



HAL
open science

Synthesis of an artificial tendon

Lise Picaut

► **To cite this version:**

Lise Picaut. Synthesis of an artificial tendon. Theoretical and/or physical chemistry. Université Pierre et Marie Curie - Paris VI, 2017. English. NNT: 2017PA066265 . tel-01763346v2

HAL Id: tel-01763346

<https://theses.hal.science/tel-01763346v2>

Submitted on 27 Apr 2018

HAL is a multi-disciplinary open access archive for the deposit and dissemination of scientific research documents, whether they are published or not. The documents may come from teaching and research institutions in France or abroad, or from public or private research centers.

L'archive ouverte pluridisciplinaire **HAL**, est destinée au dépôt et à la diffusion de documents scientifiques de niveau recherche, publiés ou non, émanant des établissements d'enseignement et de recherche français ou étrangers, des laboratoires publics ou privés.



Université Pierre et Marie Curie

École doctorale n° 397 : Physique et Chimie des Matériaux

Institut des Nanosciences de Paris

Laboratoire de Chimie et de La Matière Condensée de Paris

Synthèse d'un tendon artificiel

présentée et soutenue publiquement par

Lise PICAUT

le 09 Octobre 2017

Directeur de thèse : **Tristan BAUMBERGER**

Co-directrice de thèse : **Gervaise MOSSER**

Devant le jury composé de :

Cécile Ayako Dreiss,	Directrice de Recherche au King's College London, Royaume-Uni - IPS	Rapportrice
Charlotte Vendrely,	Maitre de Conférence HDR à l'Université de Cergy Pontoise, France ERRMECe	Rapportrice
Dominique Hourdet,	Professeur à l'Université Pierre et Marie Curie, France – SIMM	Examinateur
Sophie Asnacios,	Maitre de Conférence à l'Université Pierre et Marie Curie, France - MSC	Examinatrice
Fabien Le Grand,	Chargé de Recherche HDR CNRS, France - In- stitut de Myologie	Examinateur



Contents

Contents	iii
INTRODUCTION	1
0.1 References	3
1 Literature review specific to tendon and its repair strategies	5
1.1 Tendon	6
1.1.1 Anatomy and structure	6
1.1.1.1 Human anatomy	6
1.1.1.2 Structure	6
1.1.2 Clinical situation	13
1.1.2.1 Pathologies and injuries description	13
1.1.2.2 Incidence	13
1.1.2.3 Current strategies	15
1.2 Tissue engineering for tendon repair	23
1.2.1 Scaffold design specifications	23
1.2.2 Presentation of the main TE techniques used for tendon repair	24
1.2.3 Synthetic polymer scaffolds	26
1.2.4 Scaffolds based on natural/organic components	27
1.3 Conclusion	31
1.4 References	33
2 Methods and materials	45
2.1 Methods	47
2.1.1 Extrusion set-up	47
2.1.1.1 Key constituent part: the needle	48
2.1.1.2 Set-up performances and limits	52
2.1.1.3 Conclusion	59
2.1.2 Rheological testing of polymer solutions	60
2.1.2.1 Physical basis	60
2.1.2.2 Rheometer geometries	67
2.1.3 Mechanical testing of extruded threads	69
2.2 Materials	71
2.2.1 Collagen solutions	71
2.2.1.1 Collagen type I and its fibrillogenesis	71
2.2.1.2 Chemical properties	73
2.2.1.3 Collagen solutions preparation	75
2.2.1.4 Collagen extraction and purification	75
2.2.1.5 Collagen solutions dosage	76
2.2.1.6 Collagen solutions purity	77

2.2.1.7	Collagen solutions concentration	78
2.2.2	Model system: sodium alginate	79
2.2.2.1	Structure	79
2.2.2.2	Chemical properties	79
2.2.2.3	Solution preparation	82
2.2.3	Collagen-alginate mixtures	83
2.2.3.1	Chemical properties	83
2.2.3.2	Solution preparation	84
2.3	References	85
3	Rheological properties of collagen/alginate solutions	87
3.1	Collagen solution rheological characterization	88
3.1.1	Oscillatory shear flow	88
3.1.1.1	Complex modulus measurement	88
3.1.1.2	Comparison with Gobeaux et al. work [1]	89
3.1.2	Steady shear flow	90
3.1.2.1	Viscosity	90
3.1.2.2	First normal stress difference	92
3.1.2.3	Typical physical quantities for other concentrations	93
3.2	Alginate solutions rheological characterization	94
3.2.1	Viscosity analysis	94
3.2.1.1	Alginate concentration choice	94
3.2.1.2	Shear-thinning nature	95
3.2.2	Complex modulus analysis	96
3.2.3	First normal stress difference and Weissenberg number	97
3.3	Conclusion	99
3.4	References	100
4	Extrusion instabilities of polymer solutions	101
4.1	Quick literature overview: polymer melt extrusion instabilities	103
4.1.1	Surface instability: the sharkskin	104
4.1.2	Spurt-flow defect	104
4.1.3	Bulk distortion	104
4.1.3.1	Helical	104
4.1.3.2	Gross melt fracture	105
4.1.4	Conclusion	105
4.2	Extrusion in a bath of non-binding ions	105
4.2.1	Context and motivations	105
4.2.1.1	Conclusion	108
4.2.2	Results: Experimental evidence of helical, supercritical instability in pipe flow of shear thinning fluids	108
4.2.3	Implementation on other systems: In the "crimp" quest	122
4.2.3.1	Quick literature overview	122
4.2.3.2	Helical instability: from alginate to collagen	123
4.3	Extrusion in a bath of cross-linking ions	125
4.3.1	Overall observations	125
4.3.2	Smooth region	126
4.3.3	Die swelling	128
4.3.4	Wavy, striated patterns and smooth alternation	130
4.3.4.1	Volumetric waves and surface striations	130

4.3.4.2	Oscillating flow	134
4.3.5	Gel clogging	135
4.4	Conclusion	137
4.5	References	138
5	Preparation and characterization of collagen scaffolds	141
5.1	Threads structure characterization techniques	143
5.1.1	Photonic microscopies	143
5.1.1.1	Optical (bright field) and polarized microscopies	143
5.1.1.2	Second Harmonic Generation (SHG) Microscopy	146
5.1.2	Electron microscopies	152
5.1.2.1	Scanning Electron microscopy (SEM)	153
5.1.2.2	Transmission Electron microscopy (TEM)	154
5.1.3	Differential Scanning Calorimetry (DSC)	155
5.2	Collagen batch quality criterion	156
5.3	Fibrillogenesis buffer (Ionic strength) effect	157
5.4	Pure collagen vs collagen/alginate mixtures threads study	180
5.4.1	Pure collagen threads of different concentrations	180
5.4.1.1	Extrusion and maturation	180
5.4.1.2	Structural characterization	183
5.4.2	Collagen/alginate threads	188
5.4.2.1	Ratio choice	188
5.4.2.2	Structural characterization	189
5.4.3	Mechanical properties comparison	193
5.5	Preliminary study to cell culture	194
5.5.1	General morphology	194
5.5.1.1	Optical observations	194
5.5.1.2	Topography analysis	194
5.5.2	Diameter stability	195
5.5.3	Structural characterization	196
5.5.3.1	Pure collagen threads	196
5.5.3.2	Collagen:alginate threads	197
5.5.3.3	Collagen stability: thermal analysis	199
5.5.4	Mechanical properties	200
5.5.5	Discussion	200
5.6	Conclusion	201
5.7	References	202
6	Collagen scaffolds and cell culture	205
6.1	Biological material and techniques	207
6.1.1	Cell culture	207
6.1.2	Cell culture on threads under tension	207
6.1.3	Confocal Fluorescence Microscopy	209
6.1.4	Histology and Hybridization in situ	210
6.1.5	Real time q-PCR	212
6.1.5.1	Principle	212
6.1.5.2	Protocol	213
6.2	Cell colonization study	217
6.2.1	Mechanical properties of threads cultured with cells	217
6.2.2	Cell migration within the threads at different collagen concentrations	218

6.2.3	Preliminary In situ Hybridization results	221
6.2.4	Conclusion	222
6.3	Behavior of stem-cells cultured on collagen based threads	223
6.3.1	Load influence of threads morphologies	223
6.3.2	Cell colonization over culture time and load condition impact analysis	224
6.3.3	Genes of interest expression analysis	226
6.3.3.1	Qualitative analysis	226
6.3.3.2	Quantitative analysis: Real time qPCR	227
6.3.4	Discussion	230
6.4	Conclusion	231
6.5	References	232
	CONCLUSION	235
	List of Figures	XXIX
	List of Tables	XXXV

INTRODUCTION

Throughout the human body, about 4000 tendons have been counted [1]. These entities bind muscles to bones and stabilize the joints of the skeletal structure. Two-thirds of their content consists in water and they are known to be poorly vascularized. We use tendons in every daily motion, from the finger snap to the most arduous task. Even for passive movements and postures, our tendons work actively. During effort, they can support 17 times the average total body weight [2]! Of course, such solicitations inevitably lead to some damages and tendinopathies, tendonitis, tendosynovitis, tendon ruptures are their sworn enemies [3]. Indeed, with injured tendons, motions become painful or even impossible causing joint immobilization. Those injuries are very frequent and so far standard therapies have a low success rate, mostly coming from post-surgery complications: surrounding tissue adherence, foreign body response, inflammation, re-rupture...

For this reason, it is essential to find innovative and sophisticated solutions to repair tendons and thus to turn towards tissue engineering. To claim such amazing mechanical properties, tendons cannot be so simple as springs between bone and muscle, made of water. In fact, tendons have very well organized structures whose major protein components are collagens. To mimic tendons, scaffolds must meet many requirements including reproducing the collagen hierarchical structures from the molecular to the tissue levels.

Several tendon-like scaffolds either made of synthetic polymers or more natural components have been tested to repair tendons. Many techniques are used to produce constructs in a great variety of shapes (threads, tubings, sponges, sheets, 3D constructs etc.) However, they are still not actually close to the "ideal" artificial tendon. Indeed, when trying to reach native tendon mechanical properties, other essential properties as biocompatibility and resorbability are neglected through the use of unsuitable materials or methods. Moreover, most of the techniques used are quite complicated to be implemented.

In this general context, the present thesis aims to produce biomimetic threads which can be colonized by cells, by developing a bottom-up approach. As **collagen type I** is the main component of native tendons, we logically decided to use it as raw material and at concentrations comparable to those of tendon. Such **dense states** have never been tested before. In order to remain close to the **physiological conditions**, no chemical, cross-linking, drying or other synthetic procedures have been used. Therefore, we choose **extrusion** technique as it is the easiest way to produce threads and to be implemented in a laboratory or industry.

The main objective was thus to determine the best conditions to form collagen threads with a tendon-like structure. For this purpose, extrusion process must be perfectly harnessed. A model system, sodium alginate, which has similar collagen rheological proper-

ties was chosen to test a large range of parameters. The results, our understanding and new expertise was the transposed to the production of collagen threads. Different parameters, specific to collagen were then varied to evaluate their influence on the threads formation, ageing, microstructure, mechanical properties and cell culture.

A first chapter will briefly describe the tendon functions and structure at the different scales. Based on the clinical context of the tendon repair, the main promising tissue engineering approaches available will be presented and, in particular, those based on collagen. This state of the art part was based on the article review co-authored by Clément Rieu [4] (Appendix).

The second chapter will be devoted to the presentation of the methods and materials used during the development of our methodology. A home-made experimental set-up of extrusion will allow us to control several parameters and to observe in real-time the flow at the die exit. First, we will describe this device and techniques used to characterize rheological and mechanical properties of, respectively, solutions used and resulting synthesized threads. In a second part, the complex fluid systems and their respective physico-chemical properties will be described.

In the third chapter, rheological characterization will first be performed on collagen solution. Our results will be analyzed and compared with the work of Gobeaux et al. [5] done over a large range of concentrations. Based on these first results, alginate concentrations will then be chosen to obtain solutions exhibiting similar rheological properties as dense collagen ones.

The fourth chapter will be focused on alginate extrusion in order to better harness this technique. First, we will briefly review the polymer melt extrusion studies. Then, we will present the results obtained for alginate extrusion either in a bath without or with cross-linking ions. Based on polymer melt expertise, we will attempt to analyze and understand the extrusion instabilities observed.

The fifth chapter will present three main studies on collagen based threads production and the respective techniques used to characterize them. Criteria as the stability over time, the microstructure and the mechanical properties will determine the best condition during those studies. First, the influence of ionic strength on collagen threads will be investigated. Then, the collagen concentration (15 to 60mg/mL) will be varied and hybrid system will be tested. A last study will be performed to assess the behavior of our threads in an **in vitro** cell culture medium in absence of cells.

In the last chapter, mesenchymal stem cells seeding of collagen based threads will be performed. Behaviors are studied as a function of several parameters. Cell morphologies, migration, and gene expression will be studied in order to characterize the cells behaviors on our threads.

Finally, in the conclusion, our main results and contribution to tissue engineering for tendon repair will be outlined and several project perspectives will be provided.

0.1 References

- [1] Harrison Wein and Vickie Contie. Protect your tendons, preventing the pain of tendinitis. *NIH News in Health*, 2014. [1](#)
- [2] Marsha Rutland, Dennis O’Connell, Jean-Michel Brismée, Phil Sizer, Gail Apte, and Janelle O’Connell. Evidence-supported rehabilitation of patellar tendinopathy. *North American journal of sports physical therapy: NAJSPT*, 5(3):166, 2010. [1](#)
- [3] *Tendon Regeneration: Understanding Tissue Physiology and Development to Engineer Functional Substitutes*. Eds. Academic Press, 2015. [1](#)
- [4] Clément Rieu, Lise Picaut, Gervaise Mosser, and Lea Trichet. From tendon injury to collagen-based tendon regeneration: overview and recent advances. *Current pharmaceutical design*, 2017. [2](#)
- [5] Frédéric Gobeaux, Emmanuel Belamie, Gervaise Mosser, Patrick Davidson, and Sophie Asnacios. Power law rheology and strain-induced yielding in acidic solutions of type I-collagen. *Soft Matter*, 6(16):3769, 2010. [2](#)

Chapter 1

Literature review specific to tendon and its repair strategies

“Sometimes the right path is not the easiest one.”

Grandmother Willow in
Pocahontas

Abstract

In this chapter, we will present the tendon functions and structure at the different length scales. After establishing the clinical situation of tendon injuries and evaluating their incidence, we will present the current strategies available to repair tendons. Then, the tissue engineering (TE) approaches will be described and the tendon scaffold specifications will be set. Finally, we will give an overview of promising TE scaffolds and in particular we will focus on the collagen-based ones obtained by extrusion process.

Contents

1.1 Tendon	6
1.1.1 Anatomy and structure	6
1.1.1.1 Human anatomy	6
1.1.1.2 Structure	6
1.1.2 Clinical situation	13
1.1.2.1 Pathologies and injuries description	13
1.1.2.2 Incidence	13
1.1.2.3 Current strategies	15
1.2 Tissue engineering for tendon repair	23
1.2.1 Scaffold design specifications	23
1.2.2 Presentation of the main TE techniques used for tendon repair . . .	24
1.2.3 Synthetic polymer scaffolds	26
1.2.4 Scaffolds based on natural/organic components	27
1.3 Conclusion	31
1.4 References	33

1.1 Tendon

1.1.1 Anatomy and structure

1.1.1.1 Human anatomy

Tendon is a dense connective tissue, poorly vascularized and located between muscle and bone (Fig. 6.1) whereas ligaments connect bone to bone. It allows transmitting muscle-contraction force to the skeleton in order to produce motion or simply keep a posture. The extremities of the tendon are called the entheses. They extend from one side to the muscle to form the myotendinous junction, and on the other side to the bone to form the osteotendinous junction. They serve to dissipate stress away from interfaces and are subject to wear and tear.

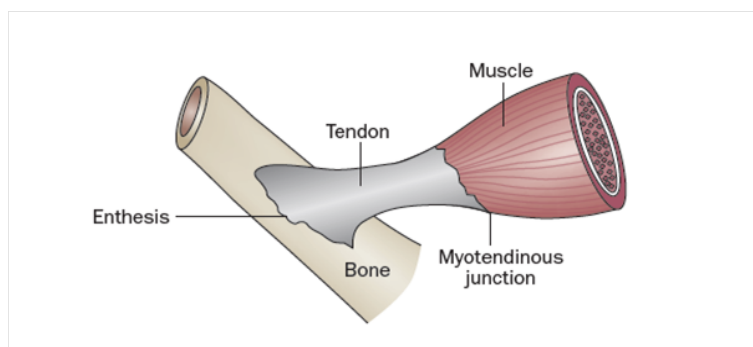


Figure 1.1: Scheme of a tendon which connects muscle to bone and allows motion [1]

There are about 4000 tendons throughout the human body and they are required for any motion in our daily life: grasp an object with the hand, rotate the shoulder, bend the knee, walk etc [1]. The tendons are well known for their incredible mechanical properties. Indeed, they can support 17 times the average total body weight while subjecting to tensile or compression forces.

Like all connective tissues in the body, the tendon is composed of some cells, called in this case tenocytes, tenoblasts and fibroblasts (about 20% of the total volume) and an abundant extracellular matrix (about 80% of this volume). This matrix contains about 65% water and 35% of solid constituents synthesized and secreted by the cells: collagen (30%) and a small amount of non-collagenous glycoproteins (5%). The collagen content represents 60 to 85% of the tendon dry weight [2].

To fulfill its goals/functions, the tendon must be highly shaped and organized as we will see below.

1.1.1.2 Structure

Tendon structure has been studied for the past decades by various techniques and under various states. Despite the information acquired, the exact organization of tendon in living tissues remains unclear. The fact that it may be adapted to each location within the body and depend on species does not help in getting a precise idea [3]. New developments in microscopy will hopefully bring some valuable keys for this understanding [4–6]. Anyhow, some general characteristics are common to all tendons and the most important are discussed in this section.

1.1.1.2.1 Hierarchical organization

Tendons have a hierarchical fibrillar organization that can be compared with russian dolls arrangement. In fact, each unit is divided into smaller units until the fundamental one (Fig. 1.2). This architecture is uniaxial as the different units are aligned along its longitudinal axis.

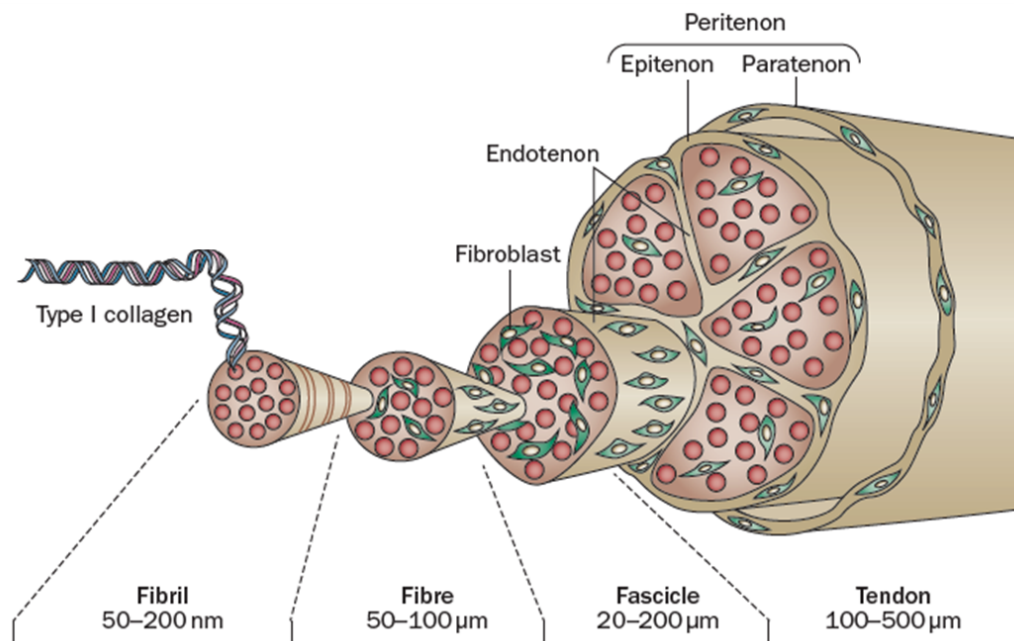


Figure 1.2: Scheme of a tendon hierarchical structure. Adapted from [1]

Surrounding sheaths

The tendon is encircled by an outer connective sheath called the epitenon (Fig. 1.2). It is further ensheathed in an another layer of loose connective tissue, the paratenon. Those sheaths give their white color/aspect to the tendon (Fig. 1.3) and contain blood vessels, nerves and cells. Their main functions are to protect the tendon fibers, to reduce friction with adjacent tissues and to facilitate tendon sliding where friction forces are very high. For tendons surrounded by other bones as in hands or feet, an other structure also helps the tendon gliding: the synovial bursae. They are enclosed cavities of various sizes which contain viscous synovial fluid. This whole system acts as a cushion to protect and lubricate the joint.

Fascicles/Bundles

The tendon largest unit is the fascicle which is composed of collagen fibers bound together. As shown in Figure 1.3, their shape is irregular and their diameter can vary from 20 to 200 μm. Each fascicle is surrounded and delineated by an interfascicular matrix called endotenon (white junctions) which contains cells.



Figure 1.3: Cross-sectional image of an equine superficial flexor tendon. The fascicles arrangement and the respective endotenon sheath (black arrows) can be seen. White scale bar: 1mm Adapted from [2]

Fibers and fibrils

A collagen fiber is composed of several collagen fibrils and has a diameter ranging from 50 to 100 μm (Fig. 1.2 and Fig. 1.4, a).

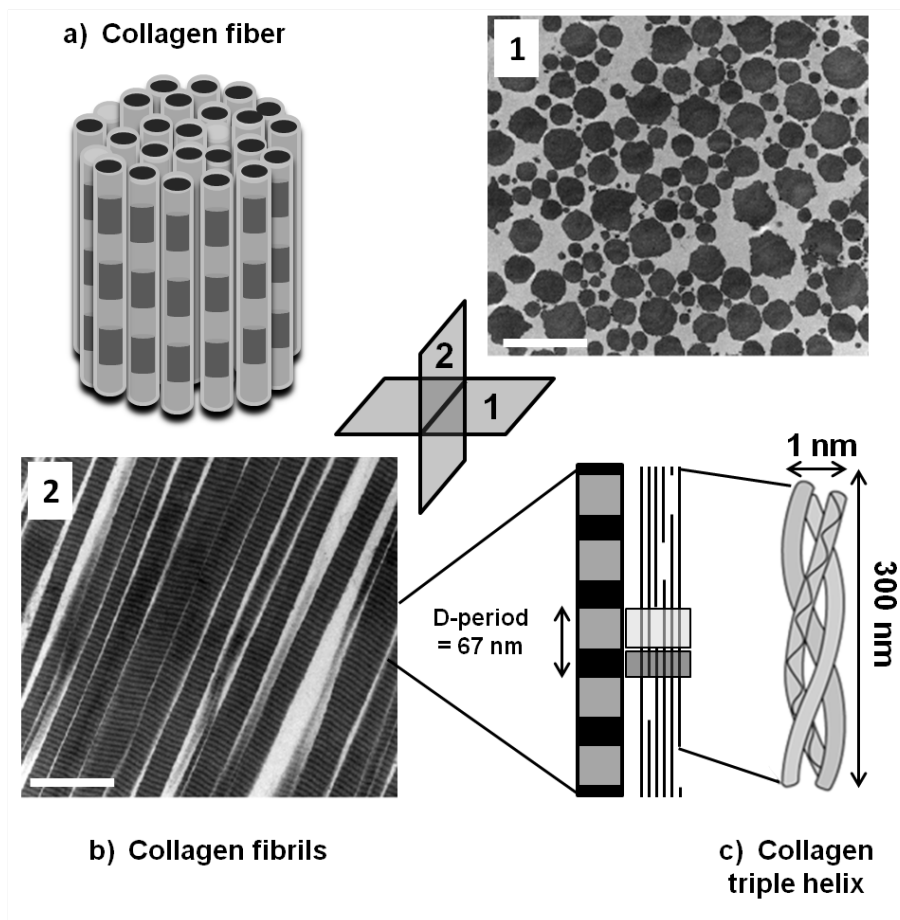


Figure 1.4: Scheme and images (TEM [7]) of a) collagen fibers and b) fibrils organization. Different views of 1. cross-sections and 2. along the fibers axis. White scale bar: 1 μm .

Collagen fibrils are parallel to each other (Fig. 1.4, 1) and are aligned along the longitudinal fiber axis (Fig. 1.4, 2). However, an axial offset called D is observed and results as a periodic striation of 67 nm recognizable as an alternation of dark and light stripes (Fig. 1.4, bottom right) visible in transmission electron microscopy (Fig. 1.4, 2). Depending on the tissues and the hydration of the fibrils, this value can vary between 64 and 68 nm. To explain this periodic striation, Hodge and Petruska developed a theoretical model in 1963 [8]. The collagen molecules are packed in a quarter staggered orientation which means that each molecule overlaps its neighbor by a quarter of its length (1.4, bottom right, c)). The resulting "empty" space is due to the triple helix length of $4.47xD$ ($=300$ nm) which is a noninteger value of the period D. The lighter space is called "gap" and measures 47 nm long while the denser stripe is called "overlap" and measures 20 nm long (1.4, bottom right). Finally, the collagen triple helix is the smallest unit of the tendon [9].

Wavy structure: the "crimp"

Collagen fibrils within tendon fascicles sheaths (endotenon, epitenon and paratenon) are not necessarily collinear to the tendon and can be found perpendicularly oriented [10]. Indeed, cross-polarized optical microscopic observations of excised rat tail tendons reveal units, from 10 to 100 μm , with alternating oblique orientations compared to the tendon axis. This feature is referred to as "crimp" (Fig.1.5).

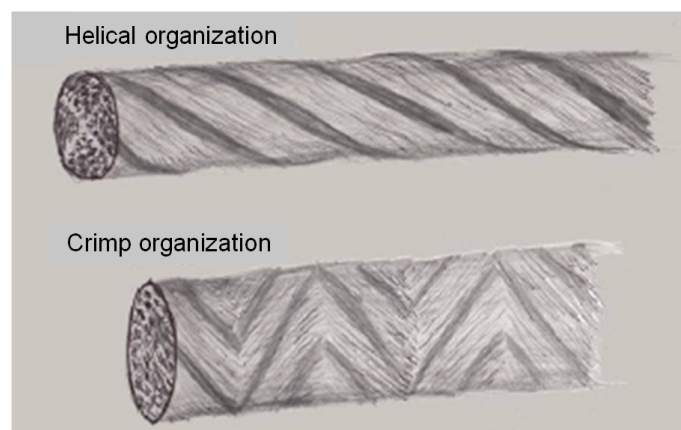


Figure 1.5: Helical (Top) and crimp organization (Bottom) of tendon fascicles. Adapted from [11]

Evidence of this crimp was further observed by atomic force and electron microscopies (scanning and transmission) [12; 13]. The crimp was suggested to be a natural shock-absorber and to play a role in elastic recoil [14].

Shah et al. (1982) reported that the crimp was only observed at day 16th during the embryonic development of chick tarsus metatarsus region. The appearance of the crimp correlated with a high increase of collagen content between day 14th and day 16th [15]. This suggests the crimp to be highly related to the presence of collagen fibrils. On the other hand, for Herchenhan et al.(2012), tenocytes may induce formation of the crimps [16]. Their conclusion relies on the fact that knocking down cells using polyoxyethylene (9–10) p-t-octyl phenol (TX-100) within a biomaterial construct presenting a crimp induces its loss. However, the authors do not take into account the fact that TX-100 also interacts with collagen and even destabilizes fibrils, possibly contributing to the loss of the crimp [17; 18].

In addition to the overall alignment and the crimp, Vidal et al. (2003) analyzed under

crossed polarizers transversal sections of tendons and showed that fascicles presented a helical organization along the tendon axis [19] (Fig. 1.5, top). This raises the question on how the crimp structure can be compatible with both a cylindrical symmetry and a helical organization. Geometrically speaking, one way to explain the crimp would be an over-winding of a helical organization. *In vivo*, under tension, it would be extended and fascicles would appear quasi collinear with the direction of the tendon. No "crimp" would be detected (Fig. 1.6, A). However, when tendons are relaxed and/or excised, the linear tension would decrease and the over-winding would collapse on itself while still being constrained transversally by the 90 ° transverse collagen sheath. The crimp would thus appear (Fig. 1.6, B).

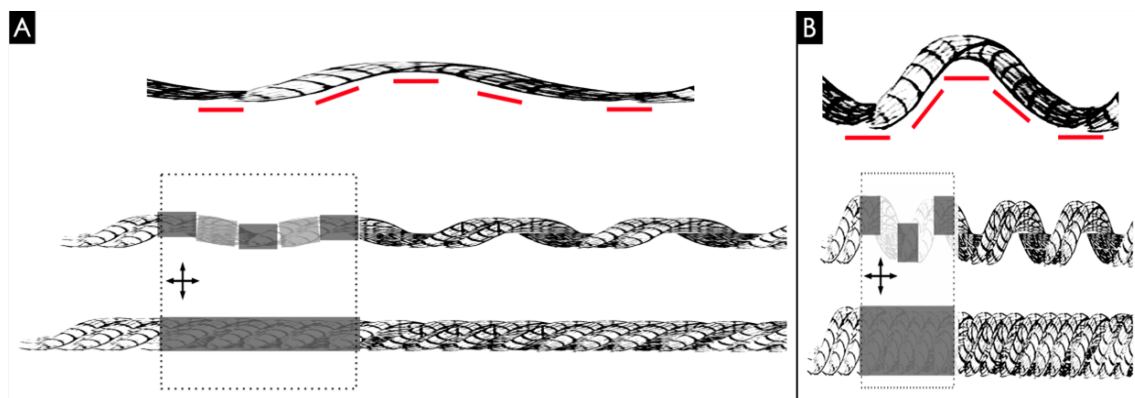


Figure 1.6: Scheme conciliating helix crimp and linear organization: A single stranded helix is schematized on top, a partial super-helix in the middle and a full super-helix on bottom. Boxed by the dotted line, their appearance when observed between crossed-polarizers. Crossed-arrows indicate directions of polarizers. (A) Top: The extended helical strand and beneath the projected collagen molecular orientations are represented by lines. All orientations are nearly aligned along the helix axis. Middle: The partial super-helix is represented and the molecular orientations being all nearly aligned along one polarizer, the crimp is hardly seen and the partial super-helix appears nearly dark. Bottom: the symmetry of the complete super-helix is cylindrical. The mean projection of the molecular directions sums up along the axis of the helix. The complete super-helix appears dark under crossed-polarizers. (B) Top: The molecular orientations vary along the axis of the helix and present a repeating unit of alternating orientations. Middle: The partial super-helix is represented and the molecular orientations varying as illustrated above, the crimp is clearly seen as banded pattern under crossed polarizers. Bottom: the symmetry of the complete super-helix remains cylindrical with the mean projection of the molecular directions summing up along the axis of the helix. The complete super-helix still appears dark under crossed-polarizers. [11]

It has been shown that super-twisted organizations could be spontaneously generated in liquid-crystals [20]. Knowing that collagen forms different liquid crystal phases [21–23] that are subject to physico-chemical parameters [24], it is not excluded, although there is no proof yet, that the over-winding helical organization of tendon may also result from simple physical-chemical laws. Most probably, cells and physicochemistry work hand in hand.

1.1.1.2.2 Mechanical properties

Tendons have to respond and adapt themselves to the loading transmitted by the muscles. Their entire structure is solicited at every hierarchical level in order to ensure their function. There are two different tendon functions: positional and energy storing. In the

first group, tendons transmit forces to bone in order to move joints and are quasi inextensible. In the second one, they act as springs and improve the locomotion efficiency. However, their intrinsic mechanical properties are lower to positional tendons. For instance, Achilles tendons are energy storing. In the following section, we will describe the characteristic mechanical properties of tendons, which are generally analyzed by traction along the tendon axis and up to the tendon rupture *in vitro*. Those experiments are typically done on traction apparatus as described in section 2.1.3. The results of this kind of tensile testing are given as stress-strain curves detailed below.

Typical stress-strain curve

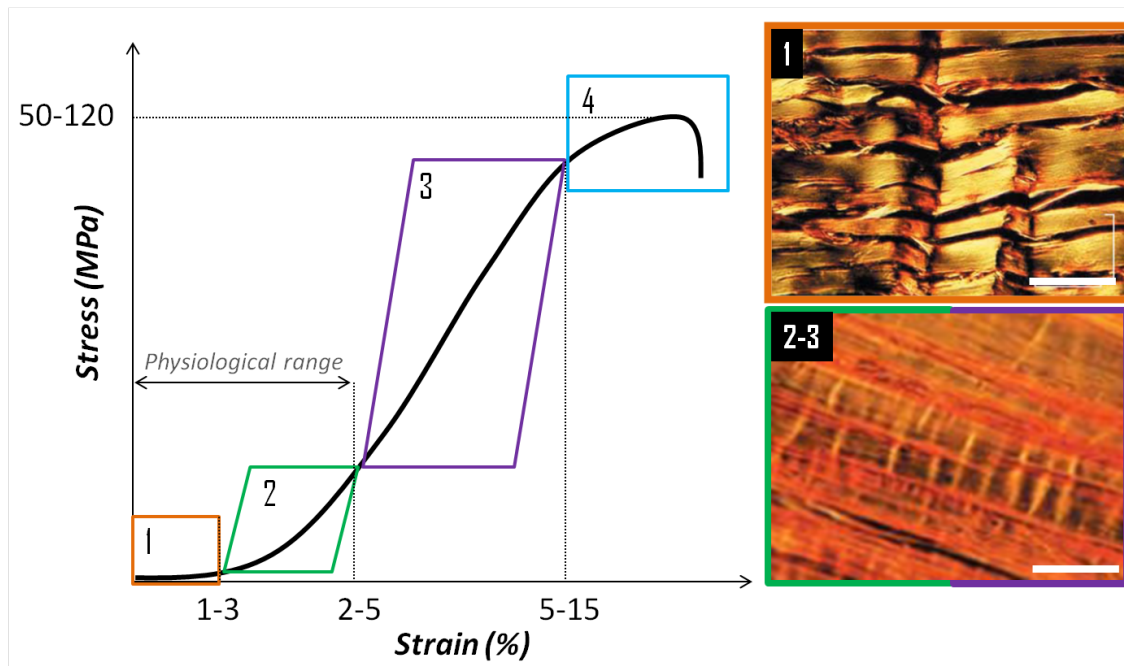


Figure 1.7: Typical stress-strain curve and corresponding images at the microscale of a rat Achilles tendon by polarized light microscopy Scale bar=100 μ m. In the toe region the macroscopic crimps disappear, in the heel region the molecular kinks in the gaps regions progressively straighten. Adapted from [14],[25]

Briefly, the force (N) is measured during the tendon extension/elongation. The stiffness (N/m) of the material is defined as the ratio of the force and the extension extracted from the gradient of the curve. In order to have characteristic variables independent of sample size, the data need to be normalized. For this purpose, stress and strain are calculated as:

$$\text{Stress (Pa)} = \frac{\text{Force (N)}}{\text{Cross-sectional area (m}^2\text{)}}$$

$$\text{Strain} = \frac{\text{Change in length (m)}}{\text{Original length (m)}}$$

The failure stress, failure strain and the modulus (stress-strain slope) will be determined from the tensile testing. Figure 1.7 shows the typical stress-strain curve obtained for such test. The tendon response to the constant elongation is clearly not linear. In fact, four different regions can be distinguished from this schematic curve:

1) Toe region: in this first region, the crimp previously described and shown in Figure 1.7 (1) Top right) by polarized light microscopy begins to stretch. As a spring initially coiled, it unfolds while elongation is applied. The tendon fibers tend to align in the loading direction which generates little effort. Mechanical tests made on tendon clearly show the difference of mechanical behavior during the elongation of the crimp and after [14]. Computational modeling best fits the mechanical experimental data when a helical arrangement is injected into the models [26]. Reese et al. (2010) further improved the fit by combining a wavy pattern with a super-helical arrangement [27]. This data comforts the idea of a super-helical structure as previously described.

2) Heel region: the tendon stiffness begins to rise. This is due to reordering at the molecular level. (Fig. 1.7 (2))

3) Linear region: a linear zone is obtained between the stress and the deformation. During this phase, micro-tears will form and start damaging the fibers of the tendon, to the macroscopic rupture zone of the tendon. (Fig. 1.7 (3))

4) Failure: the microcracks become too large and lead to the macroscopic rupture of the tendon fibers.(Fig. 1.7 (4))

Tendons display viscoelastic behaviors where the "elastic" one comes from the collagen and the "viscous" part from the interfascicular matrix. The four regions represent the tendon behaviors of most of the tendon. However, the order of magnitude of the characteristics physical values vary according to sites and persons, with Young modulus ranging from 0.5 to 1.9 GPa, ultimate tensile strength from 50 to 120 MPa and strain at break between 5 and 20% (Table 1.1) [28]. Thus, the tendinous tissue is capable of modifying its structure, and its composition is a function of the mechanical stresses which it undergoes.

Tissue	Modulus (MPa)	Ultimate Tensile Strength (MPa)	Ultimate Strain (%)
Gracilis Tendon	590-1734	111-112	7-19.4
Semitendinous Tendon	540-1081	89-124	8-23
Achilles Tendon	819 ± 208	79 ± 22	9 ± 2

Table 1.1: Mechanical properties of human tendons [28]

1.1.1.2.3 Other components

As previously mentioned, tendons present a cellular part and an extra-cellular matrix (ECM). Cells, out of which tenocytes are predominant, are found immersed into the ECM. They synthesize the bio-components and thus play a major role in the setting and renewing of the ECM. This last one is responsible for the structural and mechanical properties, and maintains the integrity of the tissue [29]. The ECM is composed of many different biochemical components such as collagens, non-collagen proteins, and proteoglycans [30; 31].

1.1.2 Clinical situation

1.1.2.1 Pathologies and injuries description

Tendons can present acute or chronic injuries caused by extrinsic or intrinsic factors, either alone or in combination (Fig. 1.8) [32]. Tendinopathies refer to the various chronic conditions that can affect tendons. They can remain silent over a large period of time, cause chronic pain and, potentially, lead to tendon tears and ruptures. These can also occur following lacerations by a sharp object or a tensile overload, in which case, it is now believed that an underlying tendinopathy is also involved [33; 34]. The term tendinitis referred to tendon micro-tears associated with acute injuries due to an overload, causing inflammation, while tendinosis accounted for chronic wound following tendon overuse. The term tendinopathies is now preferred because there is no assumption about the underlying pathology, especially since the role of inflammation is still under debate [35; 36]. They are associated with a change in remodeling activity of tendon matrix.

External causes of tendinopathies include occupational, sporting activities, and prescription drugs [37]. Intrinsic factors include age and biomechanical imbalance [32]. The etiology of tendinopathies often appears to be multifactorial [33; 34; 38].

1.1.2.2 Incidence

A UK study, performed in an acute Orthopedic Unit treating a well-defined catchment population of about 535,000 and prospectively recording the demographic details over 5 years, provided results about the incidence of musculoskeletal tissue trauma [39]. One of the findings is that about two thirds of tendon injuries relate to the hand. Among them, forearm/hand extensor tendon injuries occur with an annual incidence of 17.87/100,000, and mallet finger involving extensor tendon affecting mobility of the last phalanx, at a rate of 9.89/100,000 (Fig. 1.8). A 10-year population-based study led in the US, examining hand or wrist open wounds secondary to acute trauma and involving tendons, found an incidence rate of 33.2 tendon injuries per 100,000 person-years, with work-related injuries accounting for 24.9% of total [40].

Achilles tendon rupture occurs at an annual rate of 11.33/100,000 according to Clayton et al. (2008) [39] and has already been reported with rates ranging from 5.5 to 18/100,000 (Fig. 1.8) [41]. Most acute ruptures concern people in their thirties and forties during sports activities. Achilles tendinopathy has a 5.9% lifetime cumulative incidence among sedentary people as compared to 50% among endurance athletes [42]. Tennis elbow, also known as lateral elbow tendinopathy, is secondary to excessive use of wrist extensors and forearm supinators. It is usually reported to affect 1 to 3% of the population each year, however, a descriptive epidemiology study shows a decrease in the incidence with a rate of 3.4 per 1,000 [43]. The injury incidence in tennis players has been reported in proportions between 9 and 35% [44]. The rotator cuff, which is composed of four muscle-tendon units that originate on the scapula and cover the top of the humeral head, can also often be subject to tendinopathy. In a prospective study, the sex and age-standardized incidence of shoulder pain was evaluated to be 9.5/1,000 among the patients presenting to general practice, with a proportion of 85% related to rotator cuff tendinopathy [45]. The incidence of rotator cuff tears was reported to be 3.73/100,000 [39].

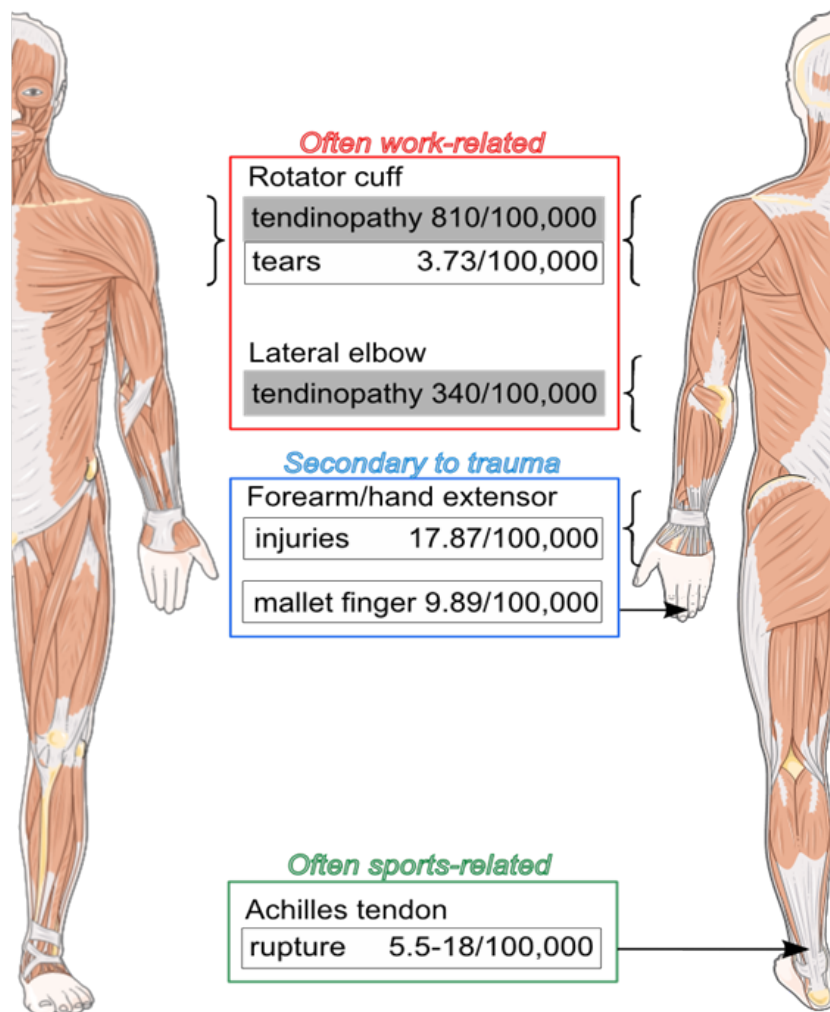


Figure 1.8: Location, annual incidence and main cause of most frequent tendon injuries. Data are referenced in the text. Sources: [39], [41],[42], [43]. Body image, courteously provided by Servier Medical Art under license <https://creativecommons.org/licenses/by/3.0/fr/>, was modified for clarity purpose.

Work-related musculo-skeletal disorders concerning tendons are evident in occupations involving prolonged periods of repetitive, static work [45]. The prevalence of work related upper limb musculoskeletal disorders in UK was estimated to be 730 per 100,000 people in year 2014/2015 [46]. There is an average of 17.7 working days lost for each case. According to the 2005 data collection of Eurostat figures on recognized occupational diseases (EODS) of 12 member states, the most common musculo-skeletal occupational disease was lateral elbow tendinopathy (14,155 cases) [45]. In the United States, shoulder injury has been found to be the second most common cause after back pain for time away from work in manual laborers [47]. 41.5% of occupational shoulder injuries required more than 31 days away from work in 2007. In Sweden in 1995 among the 9,398 reported work-related soft tissue diseases 217 cases involved rotator cuff and 538 lateral elbow [48]. Some estimates of the cost of work-related upper limb and neck musculo-skeletal disorders are between 0.5 and 2% of gross national product [48].

Due to poor vascularization and low cellularity of the tissue, there is limited spontaneous regeneration of tendon. Treatments can be conservative or surgical, or a combination of both with post-intervention rehabilitation programs [33], [36], [41], [47]. Currently

there is a high rate of re-injury. In the case of small and large rotator cuff tears surgical repairs of ruptured tendons have re-tear rates of up to 35 and 94%, respectively [49]. Clinicians assess an unsatisfactory clinical outcome after suture for 25% of patients with hand tendon lacerations, and 7.7% of these repairs re-rupture [50].

1.1.2.3 Current strategies

The gravity of the injury will determine the strategy to be used to heal the tendon. From chronic tendon injury to tendon tears, it is essential to reduce the patient's pain due to the tissue inflammation with specific drugs and with rehabilitation exercises [51], [52]. Some new treatments based on growth factors delivery through autologous whole blood or platelet rich plasma (PRP) are emerging. Even if *in vitro* studies prove that these injections improve the collagen production and degradation mechanisms [53], this kind of strategy in clinical cases is still controversial. Indeed, a standard protocol with determined parameters as the injection frequency, volume, concentration etc. is not implemented.

For acute tendon injury, the lesion severity will impose the treatment. For lesions with a gap between the two tendon extremities less than 3 mm, the tendon is able to self-heal [54]. For larger injuries, if the joint motion is altered or even completely lost then surgery is needed. The length of the gap will determine the approach to be adopted. If the gap is less than 3 cm, suture techniques are required to rejoin the tendon. In the case of Achilles tendon, the conciliation of its 2 ends requires a great force. This is why, if the rupture is in an easy access location, surgeons use some devices as bone clamp [55] or Integra™ Achillon® system [56],

1.1.2.3.1 Sutures

Three methods of suturing tendon have been developed and optimized: the non-grasping, the grasping and the locking anchors. The non-grasping method was first performed on finger flexor tendon by Bunnell in 1918 [50] (Fig. 1.9, A). This technique consists in looping the anchor around the epitendon. As a consequence, no collagen fibers bundles are injured. On the contrary, the grasping (Fig. 1.9, B) and locking anchors (Fig. 1.9, C) based respectively on an opened and a closed loop, pinch the collagen fibers. However, those two techniques bring better mechanical properties and gapping resistance to the tendon. They took the name of their authors Kessler for the grasping suture and Krakow for the locking one. The last one is assumed to be the most effective and is constantly being improved [57].

Several fibers made of polyester (Ethibond®), nylon, polypropylene or a combination of ethylene glycol and terephthalic acid (Da-cron®) are already clinically used for suture alone. They are non-resorbable as they have to maintain almost more than 1 year the end-to-end tendon extremities [50]. Other materials have been developed for suture augmentation, which is a different approach. Schliemman et al. (2015) compared the reconstruction of a tendon with a polydioxanone (PDS) or cable wire augmentation and with suture anchor repair alone. They showed that suture augmentation in both cases provides less elongation and higher loads (almost a 1.5 factor) than the simple suture [58]. A negative aspect of cable wires is that a second surgery is needed to remove them.

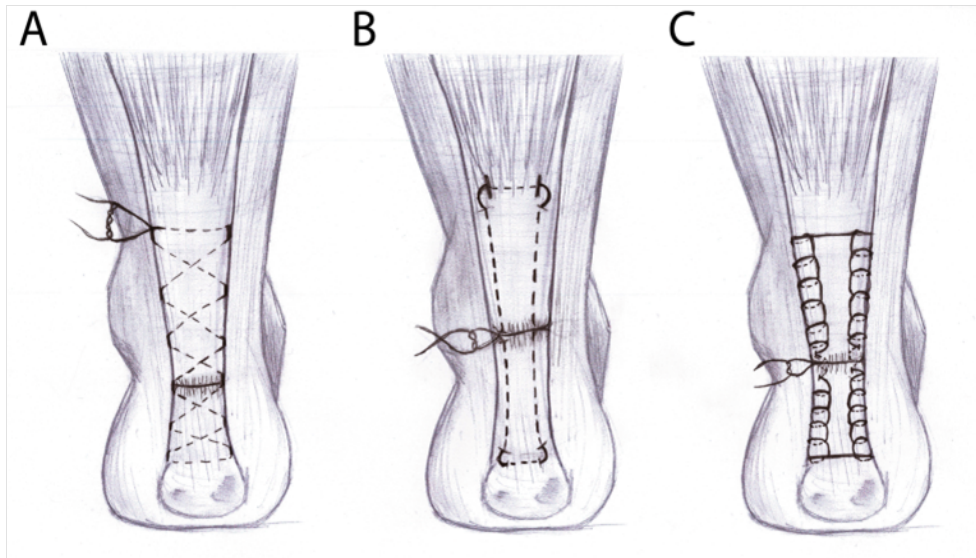


Figure 1.9: Scheme of the three sutures commonly used to repair tendon (Achilles tendon example in back view). (A): the non-grasping suture (Bunnell) consisting in looping the anchor around the epitenon. (B): the grasping suture (Kessler) based on 4 opened loops, which pinch collagen fibers. (C): The locking suture (Krackow) made of several closed loops.

Alternative methods have been proposed to avoid the use of suture. Hohendorff et al. (2008) compared post-surgery results of Achilles tendon rupture treated either with fibrin glue or suture. They note that both strategies reach almost the same results. Moreover, fewer complications are observed for the fibrin glue cohort [59]. Rose et al. (2014) also worked on the biological tissue gluing. They used solutions of silica nanoparticles (NPs) to glue mismatched tissue. They tested it *in vitro* on a piece of calf liver with a created gap of 2 cm. They glued the two ends and kept it under finger pressure during 30 s [60]. They observed that the two parts of the liver were attached together again and that the glue didn't affect the rigidity or the permeability of the tissue. This second approach is very promising as it is quite simple and fast to implement. It must be tested on tendon to know if the bonds created with the silica NPs are strong enough to support physiological loads as applied in Achilles tendon sites for months.

1.1.2.3.2 Metallic implants

With the same approach as using cable wire sutures, some other researchers have developed metallic implants. Their aim is to obtain tendon repairs with the best mechanical properties. Erol et al. (2007) developed an implant made of stainless steel wire with different spiral-shaped structure on sheep cadaveric Achilles tendon [61](Fig. 1.10, A). Briefly, the prostheses are composed of a coiled wire head, which hooks the tendon, and a wire passing through it to join the head to the other tendon end or bone. They also compared their implant with classic sutures. In some cases, they observed the breaking of the tendon-implant holding point and the fibering of tendon's ends. Indeed, they raised the problem of the material elastic properties. If the material is too stiff compared to the tendon, the rupture of the anchor will occur. To have the best mechanical properties, it is essential to use materials with the same range of elastic modulus than the tendon. In their preliminary study, they obtained good mechanical results compared to suture alone. But authors advised to use this kind of device only for bone-tendon repair.

Ağır et al. (2014) also investigated this kind of metallic implant (Fig. 1.10, B). In their

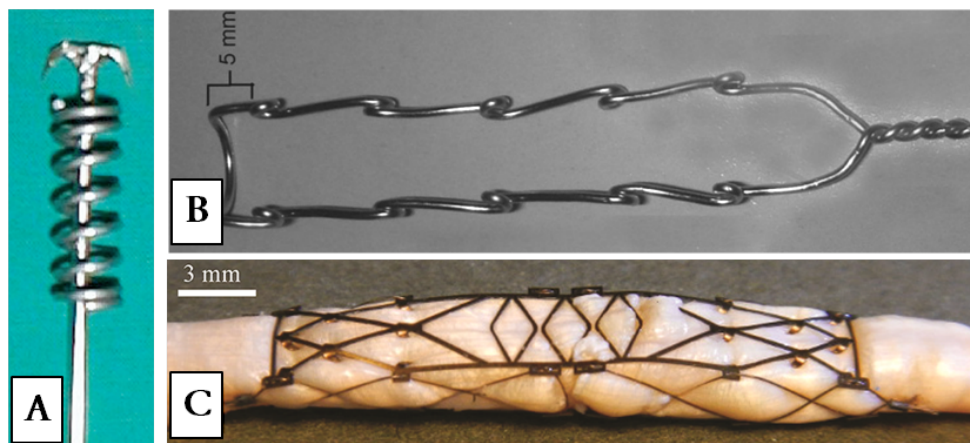


Figure 1.10: Images of different metallic implants: A: coiled spiral with a T-shaped wire stuck to the proximal end of the spiral [61]; B: stainless steel wires with several loops [62], C: nitinol device implemented on digital flexor tendon [63].

study, they also used stainless steel wires but designing it with several loops [62]. The wire is applied from outside and allows the transversal anchoring of metallic pins in it. Here again, some limitations of the device are explained: these implants cannot be used for hand injuries and are more suitable for larger body tendons as Achilles tendon. Reese et al. (2013) developed a device for digital flexor tendon repair (Fig. 1.10, C) [63]. It is made of superelastic nitinol (metal alloy of nickel and titanium) tubular parts and is designed specially for hand region (Fig. 1.10, B). They obtained promising results on cadaver model and showed that this kind of device is easy to use and may allow early mobilization of the injured finger post surgery.

Metallic devices as the Tenofix® [64] or Tenolig® [65] are already commercially available. They were tested on cadaveric tendons and on patients, respectively. Tenofix® was compared with conventional suture and no biomechanical improvements were shown passing from one to the other. Tenolig® exhibits different advantages such as the use of percutaneous surgery for the device positioning monitored with ultrasonography (noninvasive imagery technique) to target the two Achilles tendon ends, very small wound scars and complications occurring only for 1 over 75 patients and finally, the return time to sport was estimated to be 9 months. This kind of metallic implants are not largely used in clinical practice, as studies evaluating their effective improvement compared to classic sutures are still rare. Moreover, several limitations such as the site of repair tearing have been highlighted as mentioned above. Extensive improvements of these techniques are needed before becoming a common and viable strategy.

1.1.2.3.3 Grafts

If the site of the tendon injury is neglected or has a poor quality due to tendinopathy, sutures or implants are not sufficient anymore to repair it [66]. Furthermore, to avoid the re-rupture, a reinforcement of the site is needed. To meet these objectives, a source of new material called grafts must be used. The tendon augmentation with grafts consists in adding the matrix either around the defect and then suturing it (onlay surgery), or in the ruptured tendon and then closing it with suture inside (inlay surgery). The combination of the classic suture, which joins the two tendon extremities, and the graft may improve the tendon repair. The grafts can come from different origins: the patient himself (autograft), another human being (allograft), animals (xenograft) or it can be synthetic. These grafts used for tendon repair will be successively described in the following part.

Autografts

Sophisticated surgical procedures have been elaborated to overcome large tendon defects with patient's own "material". Three kinds of procedure more or less invasive allow accessing the tendon: open, mid-open and percutaneous. Beskin et al. (1987) compare four "open" techniques on 42 patients suffering from Achilles tendon rupture: Bunnell or Kessler sutures, "three bundle", and augmentation, either with the plantaris or with the peroneus brevis tendon [67]. Those last two methods consist in using local tendon transfer to reinforce the Achilles tendon. The four techniques show promising results as 85 to 92% of patients return to normal long-term activity after the surgery. However, in each case, a single long longitudinal excision is performed which is very invasive. This is why some clinicians have developed less invasive techniques. Carmont et al. (2007) also used the peroneus brevis tendon to reconstruct Achilles tendon [68]. Contrary to Beskin et al., they did two para-midline incisions. Skin wounds are clearly smaller and skin integrity is preserved. Moreover, this allows to preserve the surrounded tissues (tendon sheath) and may improve its healing. To follow through, other autologous sources for the reconstruction can be recruited. Ebied et al. (2016) repaired Achilles tendon thanks to free semi-tendinous tendon graft from upper muscles [69]. Shewy et al. (2009) used two intra-tendinous flaps from the proximal gastrocnemius-soleus complex [70] (Fig. 1.11). Briefly, they create two flaps in the musculo-tendinous junction and passed them through the Achilles tendon gap. They fix the flaps extremities to the calcaneus (bone). Few complications are observed as wound gapping or infection, and long pain after surgery. This technique showed goods results as patients recovered their pre-injury sporting activity level.

The main advantage of these two surgeries is the use of highly vascularized tissues in a close site to the injured tendon, but less invasive incisions are recommended for the future. Autografts present several key strengths such as no foreign body response, conservation of native mechanical properties and vascularization continuity. The main inconvenient is the risk of damaging the donor site tissue and thus to create new lesions. Moreover, the neo tendon reconstructed with surrounding tendons or muscles parts is thicker than the native one. This can lead to unsightly aspect repair and to a patient discomfort on the repair site. Other strategies have been developed to avoid creating more lesions in patients to repair injured tendon. Tendon augmentation with xeno-allograft may be good candidates for this purpose.

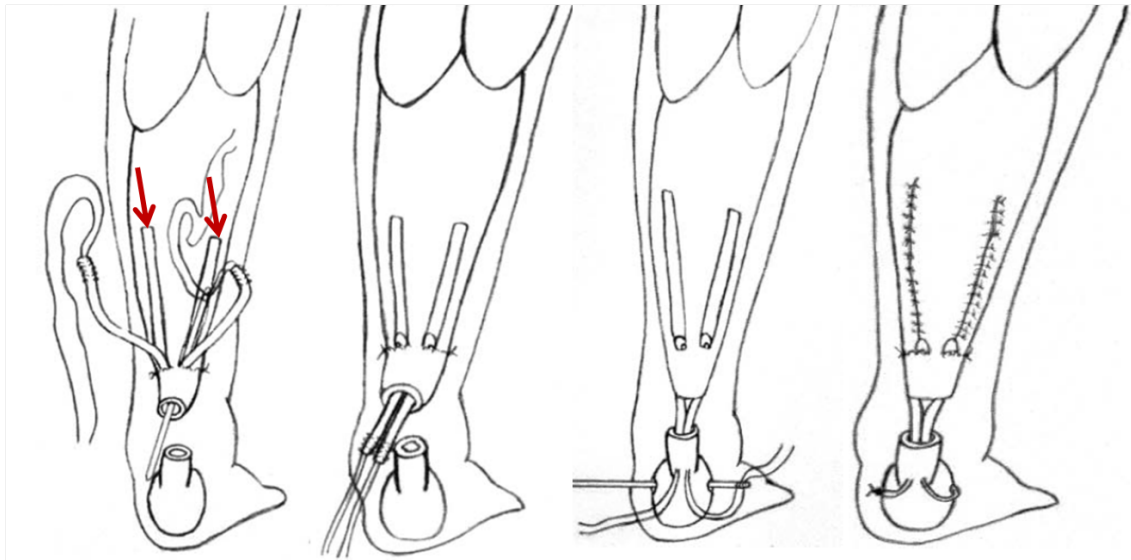


Figure 1.11: Scheme of Achilles tendon rupture repair by using autologous tendon: two flaps (red arrows) are created in the musculo-tendinous junction and passed through the Achilles tendon gap. Then, the flaps extremities are fixed to the calcaneus (bone) and finally the whole is sutured. [70]

Xeno- and allografts

Xenografts are tissues or organs coming from other species that are pre-decellularized. Porcine decellularized small intestine submucosa (SIS) is the most commonly used xenograft. Several clinical studies have been performed to assess their effectiveness for tendon repair augmentation. Phipatanakul et al. (2009) used SIS for rotator cuff repair [71]. As repairs were not convincing and as some complications (infections, skin reactions) were observed, authors did not recommend SIS for such repair augmentation. Sclamberg et al. (2004) came also to the same conclusion for this repair area as 5 over 11 patients presented worse results after the surgery [72]. Clinicians are quite unanimous on this issue. However, SIS may be adapted for tendons in other locations such as foot or ankle as only 6 % of the patients showed complications such as re-tear or patch failure.

Other sources of xenografts are also used. Berlet et al. (2014) tested the Trellis™ device (a decellularized, freeze dried and sterilized porcine dermis), in a ribbon design on human cadaveric feet [73]. They created tendon defects greater than 5 cm. The tensile testing showed that in most cases, the suture failed first. As a consequence, the xenograft collagen ribbon insured alone the load with tendon ends not joined anymore. Thus, in comparison with suture alone, the Trellis™ augmentation enhanced strength of Achilles tendon repair. Other decellularized matrices from animal origin are commercialized for other applications (Restore™, OrthADAPT™ (Fig. 1.12, A), TissueMend®, Trellis™, Zimmer®, Cuffpatch® etc.) but are already used for tendon repair.

Other strategies, based on allografts, have been developed to overcome some rejection or infection reactions. Allografts are ECMs mostly coming from human dermis or SIS. Song et al. (2010) compared two commercially available devices on a cadaveric sheep model [74]. The first one is a xenograft named TissueMend®, which is derived from fetal bovine dermis and the second one, an allograft named GraftJacket® from human skin (Fig. 1.12, B). The authors remind that grafts of dermis origin have better mechanical properties

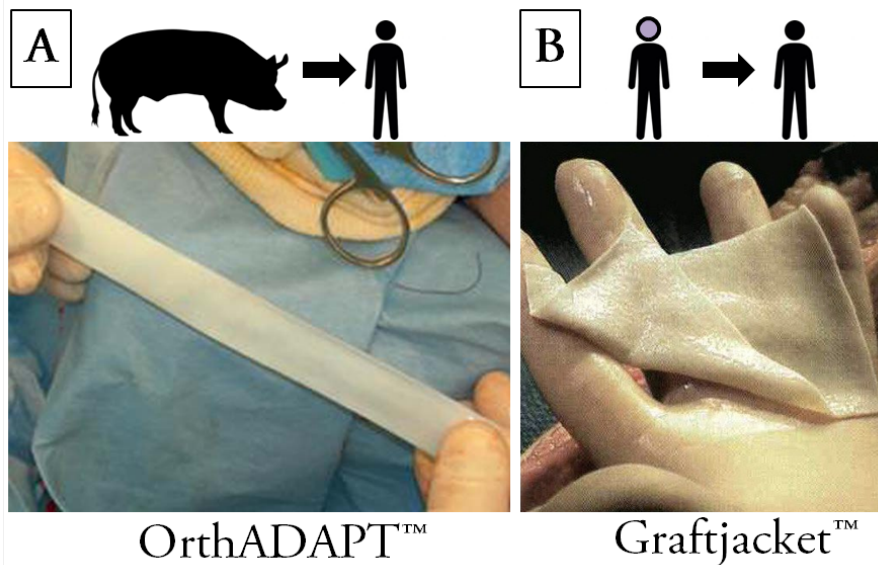


Figure 1.12: Images of commercially available A: OrthADAPT™ xenograft and B: Graftjacket® allograft.

than matrices derived from SIS, previously described. TissueMend® and GraftJacket® presented almost the same strength. They both improved tendon repair compared to suture alone. Lee et al. (2008) also used GraftJacket® matrix to augment tendon repair [75]. Clinical tests on Achilles tendon rupture were performed. At 3 months, patients recovered full range of motion and no re-rupture happened. The return-time to activity was about 12 weeks, which is quite encouraging.

Rather than choosing between xenografts and allografts, Hollawell et al. (2015) decided to combine them for Achilles tendon repair [76]. They used the allograft to span the gap between the two tendon ends and the xenograft to secure the repair site. This grafts combination improved the mechanical properties and physiological function, and patient pain was reduced. Some further investigations of this new strategy must be performed to better quantify its benefits.

Those acellular matrices either from animal or human origin show great advantages, overcoming the host reaction concerns and leading to good mechanical properties. Herbert et al. (2015) evaluated different decellularization processes needed to obtain such materials [77]. They studied the effect of using acetone or chloroform as fat agent reduction and antibiotics or peracetic acid as biodecontaminants. They showed that the tensile strength and Young modulus of acellular porcine super flexor tendons are in the same range as the native one before the decellularization. However, this process altered the matrices properties at the low strains in the toe region where the crimp should play its shock absorber role. A potential way to overcome this, is to reproduce this wavy structure. Branch et al. (2011) adopted this strategy with allograft for Achilles tendon repair [78]. They cut a human dermal acellular mesh in a z-wave shape, which finally looked like an accordion. They performed inlay surgery with a "strip and shoelace" weave. No re-rupture occurred and only one over the 3 case reports presented adhesion with the surrounding tissues.

Regarding the loss of cellular material due to the decellularization process, cell-based therapy combined with allografts emerged. Gaspar et al. (2015) reviewed the different

cell strategies [79]. Before being implanted on the tendon injury sites, grafts can be sown with cell suspension to enhance tendon regeneration. They highlighted the fact that the cell type chosen is crucial. Indeed, tenocytes or dermal fibroblasts are already differentiated, but their available quantity is limited. Progenitor stem cells overcome this issue, but can lead to bone ectopic formation. Finally, induced pluripotent stem cells may also be used on grafts. However, they raise the safety and efficiency problems. GÜngörmüs et al. (2016) used tenocytes and seeded them on decellularized rat tendons [80]. Finally, they implanted the cell-seeded scaffold in a rat model. No immune reaction occurred and their other results suggested that this scaffold improves mechanical properties of the repair.

Even if xeno- and allografts present some advantages, the matrix alteration due to the decellularization process is a problematic issue as it alters mechanical properties and leads to antigenic response [81]. It is essential to augment tendon with grafts having almost the same range of strength. To do so, synthetic grafts have been developed and are currently used in clinical practice.

Synthetic grafts

Two categories of synthetic grafts are used to augment tendon. The non-resorbable grafts persist in the body and act as a substitute to overcome the lack of tissue. On the contrary, resorbable grafts are degraded by the body and support the fibrous ingrowth [82].

Non-resorbable grafts are commonly made of synthetic polymers such as polyester (Dacron®), polytetrafluoroethylene (PTFE or Teflon®) [83], and silicone rubber [84]. Such materials are already clinically used. Morrey et al. (2016) evaluated non resorbable polypropylene mesh commercially available (Marlex®) on 8 quadriceps tendons ruptures (knee) [85]. No re-rupture occurrence and good range of motion were the main advantages of this synthetic augmentation. As they tested it on a small cohort, and as they did not perform mechanical evaluation, further studies are needed. Abdullah et al. (2015) evaluated the use of polyethylene terephthalate (PET) mesh called Orthotape® [86]. They explored this new device on two patients who needed hand surgery because of massive tendon loss. Promising physiological results were shown. Melvin et al. (2010) developed their own device Orthocoupler®, made of 32 bundles of thousand PET fibers [87]. They implanted it in a goat model. Sixty days after the surgery failure forces for the specimens with the synthetic graft were 2.5 times higher than for sutures in the control group. Sutures were too fragile compared to the Orthocoupler® which is anchored and sutured in the muscle. It allows reinforcing the musculo-tendinous junction.

Finally, another criteria is the prevention of the tendon sheath adhesion. Non-resorbable grafts made of Teflon seem to be the appropriate candidates. Indeed, Williams et al. (1964) tested them on a dog model and compared them with autologous grafts [83]. Adhesions with the surrounding tissues were clearly observed for autogenous grafts, whereas Teflon grafts surface glide and allow free joint motion. However, they reported some surgery problems as the solid anchoring of the Teflon grafts on tendon. Non-resorbable grafts present some advantages such as their biocompatibility, their strength and their non-adhesion with the tendon site. Nevertheless, they cannot be degraded, and are generally complicated to implement.

Resorbable grafts may overcome some of those issues. They can be composed of carbon ([88], [89]), polyglactin [90], polyglycolic acid (Dexon®) [91], or polylactic acid [92]. In the 70s, Jenkins et al. (1980) investigated flexible carbon implants for ligament or tendon injuries. Special affinity of the living tissue with carbon was observed [88]. Moreover, carbon based scaffolds enhance the mechanical properties of the tendon and improve the alignment of collagen neo matrix. However, fragmentation of this kind of material often occurs and may leads to some irritation of the joint. Finally, they should not to be used close to metallic implants as they can react together. To overcome these drawbacks, Alexander et al. (1983) tried to coat carbon implants with polylactic acid but could not reduce the fragmentation process [93].

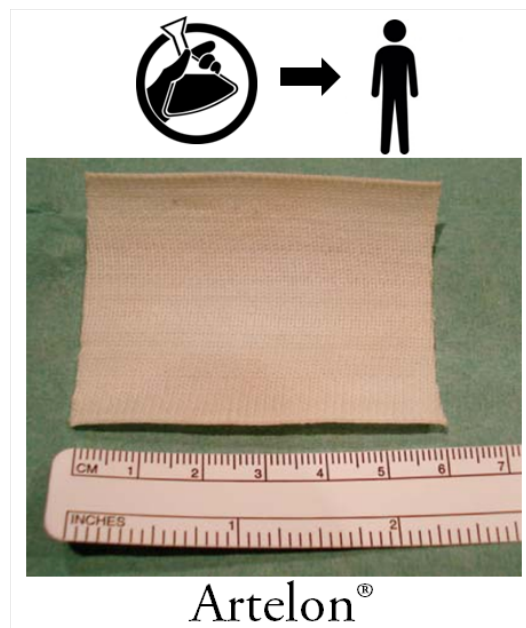


Figure 1.13: Image of commercially available synthetic graft: Artelon®. [94]

Synthetic polymer grafts are also designed as a tissue mesh. Shoaib et al. (2016) performed surgical repair in 7 patients suffering from symptomatic chronic Achilles tendon rupture with a bio-absorbable polyurethane polymer device (Artelon®) [94] (Fig. 1.13). Artelon® can be seen as the resorbable equivalent of the Orthotape® previously described. They compared this synthetic tendon augmentation to the Krakow suture alone. Better results were shown with the Artelon® graft. The authors also suggested that this device could be used for defect larger than 5 cm. Finally, they recommended to combine it with non-resorbable suture in order to secure the augmentation over the years.

We have seen that synthetic grafts show promising results for tendon repair and in particular for the mechanical properties. However, some concerns persist as they may lead to foreign body response. This is also the same for xeno-allografts, and in the case of autografts, the inherent risk of creating new lesions is too high and may lead to secondary surgery. So clinical practices or devices to repair tendon get closer to the ultimate goal but they often lack one specific criteria as strength or body tolerance. This is why, some new scaffolds based on synthetic or biocomponents are currently developed. Such engineering is not straight-forward and needs to meet several strict specifications that we will discuss below.

1.2 Tissue engineering for tendon repair

1.2.1 Scaffold design specifications

Tendon being such a specific tissue, with multiscale order and high mechanical solicitations, scaffolds for reconstruction must meet several requirements. These are dependent on the site aimed for reconstruction. Indeed, tendon size and shape can vary greatly, in function of the location in the body. Whereas rotator cuff and patellar tendons are sheet-like, length and width being in the same order and much greater than the thickness, Achilles tendons are rather unidimensional, in a rope-like manner shape [95]. Typical dimensions are given in Table 1.14.

	Requirements	Descriptions	Criteria		Refs.
Tendon mimetism	Size / Shape	Scaffold size and shape depend on the site of the tendon to be reconstructed	Rotator cuff tendon	3 x 21 x 17 mm	[Verdiyeva 2015]
			Patellar tendon	5 x 33 x 59 mm	
			Achilles tendon	5 x 14 x 120 mm	
	Mechanical Strength	Can bear usual mechanical sollicitation throughout the healing process and promote cell differentiation	Young Modulus	0.5 - 1.9 GPa	[Ladd 2011, Jung 2009]
			UTS	50 - 120 MPa	
			Strain at Break	5 - 20 %	
Alignment	Alignment in the direction of the load to promote cell alignment and differentiation	Size threshold	100 nm	[Van Delft 2008]	
Temporary biocompatible scaffold	Biotolerable	Absence of immune rejection from the scaffold and its degradation products <i>in vivo</i> (and non toxic)	Non cytotoxic, genotoxic, carcinogenic ...		
	Bioactive	The scaffold promotes cell adhesion and survival	Must be porous to allow exchange with medium Good colonization and viability of the cells on the scaffold		
	Regenerative	The scaffold fosters the formation of a new tendon by inducing cell differentiation	No observable difference between the new and old tendons		
	Biodegradable /resorbable	Degradation of the scaffold to leave room to the new tendon/and elimination of degradation products	Time range :	2 to 3 months	[Gilbert 2007, Bady-lak 1995]
Process	Tunability	The material can be shaped in a controled way to suit different location and achieve hierarchical structure	Control of the structure from molecular to macroscopic scale, and tunable size and shape of the scaffold		

Figure 1.14: Requirements for an ideal scaffold for tendon repair with description and quantitative criteria when assessable. [11]

Scaffolds must meet as much as possible the native mechanical properties to resist solicitations and promote cell differentiation [96]. Even though tendons and ligaments are sometimes indiscriminately named in papers given their similarities, they do exhibit differences when it comes to mechanical properties. Ligaments are usually not as stiff (modulus from 5 to 450 MPa) and strong (UTS between 1 and 50 MPa) as tendons and are more elastic (strain at break from 10 to 40 %) [28]. Another specificity that the scaffolds must mimic is the uniaxial structure of tendons, aligned along the direction of load. To obtain neo-tendons by promoting cell alignment and differentiation, scaffolds should mimic this anisotropy. The influence of scaffold anisotropy has been widely investigated, by using

microgrooves in the micrometer scale for instance [97][98]. Scaffold alignment may be important down to 100 nm, based on the work of Van Delft and co-workers [99].

Scaffolds for reconstruction must also comply with general specifications for regenerative scaffolds. Biocompatibility is an obvious specification but its definition is not straightforward and has evolved with time. Now, it goes further than the old definition, i.e. the absence of immune rejection or toxicity, called "bio-tolerable" by Mertz [100], adding "the ability of a device material to perform with an appropriate host response in a specific situation" [101]. Scaffolds should not be inert to the body but bioactive, promoting cell adherence and proliferation. Scaffold porosity is here paramount to ensure exchanges and cell penetration.

Besides, the scaffold must be regenerative, enabling cells to differentiate and adopt the relevant phenotype to reconstruct the ECM. Many parameters are at stake here such as mechanical properties of the scaffold, its structure and alignment as well as chemical cues [96] of the ECM or growth factors. To allow good regeneration, the scaffold should at least be biodegradable or even better, bioresorbable, based on definitions given by Vert [102]. This includes the degradation and the elimination of the polymers and by-products. Time of degradation and the subsequent change in mechanical properties are also crucial for tendon reconstruction but very seldom investigated due to the complexity of such a study. To assess the question, works on small intestinal submucosa (SIS) in canine Achilles tendon repair, carried by Badylak et al. (1995) and then Gilbert et al. (2007) are valuable. Badylak et al. (1995) reported full use of the injured leg by the dogs after 9 to 13 weeks and recovery of injured tendon strength after 12 weeks as assessed by tensile testing [103].

Degradation rate of SIS was investigated by Gilbert et al. using carbon 14 measurements, showing 60% loss after 4 weeks and total degradation after 2 months [104]. Thus, we can hypothesize that time span aimed for degradation should be around two months and that, after degradation of the scaffold, recovery and strengthening continue in the month scale. Last but not least is the processability of the material. This factor is key to meet the specifications listed above and remains one of the main challenges for biomaterials, as the processing should not degrade their properties.

We will first present the tissue engineering techniques which are mainly used to produce scaffolds for tendon repair. Then, we will review the different materials that composed suwh scaffold and we will focus on the collagen type I, which is our "raw material" for our work.

1.2.2 Presentation of the main TE techniques used for tendon repair

A variety of TE engineering techniques is currently investigated in order to produce scaffolds that fulfill all tendon criteria. Here, we report the procedures mainly used and which lead to constructs tested *in vitro* and *in vivo* for tendon repair.

As tendons exhibit hierarchical structure made of several fibers, fibrils bundles at different scales, the main idea is to produce threads and assemble them by braiding, gel embedding etc process. The synthesis of threads can be performed by different techniques as the three presented below:

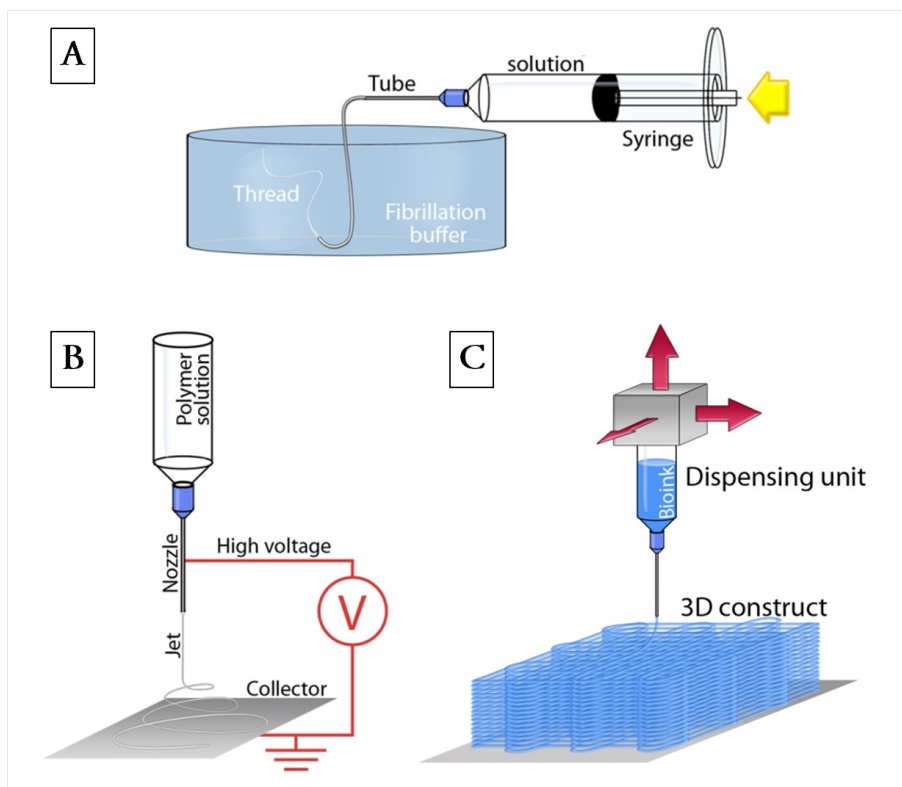


Figure 1.15: Schematic of the techniques of: A: Extrusion protocol where solution held in the syringe is forced to pass through the tubing and arrives in the buffer which induces the thread formation; B: Electrospinning protocol where a high voltage is applied between the nozzle and the collector, forming a jet of the polymer solution that dries into fiber; C: 3D printing setup where a dispensing unit is monitored in the three directions of space by a computer to deposit bio-ink layer by layer. Adapted from [11]

Extrusion

The extrusion process consists in forcing a material or a solution to pass through a die, giving its shape to the resulting extrudate. This method provides bars, tubes or fibers with a high production rate (few cm/s [105]). It is quite simple to implement as it only needs a syringe with a needle and a bath to induce the thread formation at the die exit (Fig. 1.15 A). The main advantages are its "technical simplicity" and its efficiency. Several parameters play a major role in such technique and may be well controlled in order to produce regular threads. Moreover, most of the authors used not only one extrusion bath and increase the set-up complexity by adding others baths to dehydrate the new forming thread [105]. Finally, co-extrusion procedure, directly derived from simple extrusion, is also widely used to mix directly two species or to produce hollow fibers.

Electrospinning

Electrospinning is a widespread technique for fibrous scaffold production (Fig. 1.15, B). This method, based on a simple and inexpensive set-up, uses an electrical field to cast various materials, such as polymer solutions or melts, into fiber, making it attractive for tissue engineering. Briefly, a high voltage is applied between a grounded target and a needle provided with the liquid of interest, leading to charge accumulation at its surface [106], [107]. For sufficiently high voltage, the surface tension is overcome, leading to the formation of a liquid jet that forms a fiber which dries and is collected on the target, resulting in a fibrous mat. To achieve electrospinning of a polymer solution, many requirements

must be met. In addition to the setup parameters such as voltage or solution feeding rate, and the ambient conditions such as temperature and humidity, intrinsic characteristic of the solution are paramount to electrospin it. Ideal solutions must have low surface tension and high conductivity [108], viscous enough to form a stable jet that does not break before drying [109] but not too much to ensure sufficient flowability [110] and dry fast before reaching the collector [111]. Usual solvents such as acetic acid lack the viscoelastic properties needed to form a stable jet and do not evaporate fast enough before reaching the collector [112].

3D printing

3D printing or additive manufacturing, has breached in most good manufacturing sectors in the last few years and tissue reconstruction is no exception (Fig. 1.15, C). Based on the knowledge acquired on scaffold manufacturing and facing new intrinsic problems, it gives high hopes for its capacity to design complex macroscopic shapes of scaffolds as seen in the previous paragraph, as well as enable precise cell deposition. It consists in a layer-by-layer computer aided deposition that enables the construction of 3D structure designed on the computer. This technique is currently used in research on skin, cartilage, bone, aortic valve [113]. Different methods of deposition have been developed such as inkjet, extrusion or laser-assisted bioprinting [113],[114],[115], as well as different hydrogel based inks, called bio-inks [116].

1.2.3 Synthetic polymer scaffolds

Synthetic polymer scaffolds can have a sheet-like shape for tendon augmentation repair, similar to the one of synthetic grafts or have a more tendon-like structure made of thread bundles [117]. The materials used are here based on poly(- hydroxy acids). In this category, we find the most commonly used polymer: PGA, PLA, PCL...[2]

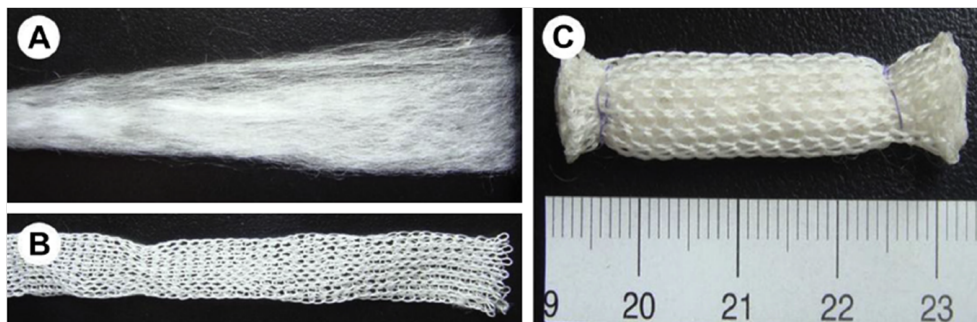


Figure 1.16: PGA/PLA scaffold example: The scaffold was composed of an inner part of PGA unweaved fibers (A) and an outer part of a net knitted with PGA/PLA fibers(B). The outcome of assembled two parts (C). [118]

In this way, Cao et al. (2001) used unweaved polyglycolic acid (PGA) fibers, which they assembled in a cord shape and wrapped with acellular intestinal submucosa membrane [119]. Tenocytes were cultured on it. Then, they created a 2.5 cm long defect in the second digital flexor profundus tendon of hen and repaired it with the cell-scaffold. They harvested the specimens at 8, 12 and 14 weeks and performed histological observations. The longer the graft stayed in the body, the better were the biomechanical properties. The authors suggested that a minimum time was required for a good tissue remodeling of the tendon. Histological results showed that the neo tendon contained a large amount of tenocytes and presented its own structure, easy to distinguish from native tendon.

Other *in vivo* studies came to the same conclusions. Indeed, Ouyang et al. (2003) tested with their biodegradable knitted poly-lactide-co-glycolide (PLGA) scaffold for Achilles tendon repair on a rabbit leg model [117]. Bone marrow cells were seeded on it before implantation. This pre-implantation step allowed a higher rate of tissue formation and remodeling than the cell-free construct. With the same approach, Deng et al. (2014) also investigated this type of polymer scaffold [118]. PGA/PLA constructs were fabricated by combining PGA unwoven fibers longitudinally arranged to form a cord with an outside net scaffold knitted with PGA and PLA fibers. The composite scaffold resulted in a cord (Fig. 1.16). They showed that the *in vitro* culture of these scaffolds before *in vivo* implantation improves the new matrix formation thanks to the *in vitro* cells already present in the scaffold. Moreover, their constructs bridged large defects of about 3 cm and displayed quite good mechanical properties ($E=50\text{MPa}$).

Synthetic polymer scaffolds present promising *in vivo* results and there is no biocompatibility concerns as for synthetic grafts. Thus, the main strength of synthetic constructs relies on their mechanical properties. However, other approaches based on natural components close to the native ones arose to avoid the question of possible inflammation or rejection reactions of the patient.

1.2.4 Scaffolds based on natural/organic components

Silk based scaffolds

Silk is increasingly investigated as a potential material for tendon repair. This protein often extracted from silkworm displays unique mechanical properties when used as a construct material. For now, scaffolds made from silk fibers are tested for the anterior cruciate ligament repair. Altman et al. (2002) designed a sophisticated silk fiber wire-rope and tested it in *in vitro* conditions [120]. Their scaffolds exhibit benefits in terms of mechanical properties (close to the native ligament ones), biocompatibility and degradation rate, which is slow. In this way, Fan et al. (2008) used knitted silk mesh filled with silk sponges, similar construct as shown in the figure 1.16. Those scaffolds were first put in contact with cells and then implanted in rabbit model [121]. Here again, after 24 weeks, remarkable results were obtained, which are promising for clinical applications.

However, some questions about the degradation rate still remain. In fact, as those matrices are slowly degraded by the body, this may lead to body foreign response, or even worse, fibrosis. Moreover, the purification of the silk must be perfectly executed: if some traces of sericin, which is a glue-like protein, are not removed, this may lead to increased adhesion of the scaffold with the surrounding tissues.

Polysaccharides

The polysaccharides represent an other source of materials for tendon TE. In this category of biopolymer, we can find: alginate, chitin, chitosan, agarose, pectin etc. In Nowotny et al. (2016) work, pure chitosan scaffolds are produced by wet electrospinning and braiding steps [122]. An example of such construct is presented in figure 1.17. The mechanical properties are improved with larger chitosan filaments and reach moduli of about 100 MPa. Cells adhered on the scaffolds in a comparable manner to the control (polystyrene 2D wells).

Other polysaccharides such as alginate may also be used. Namba et al. (2006) tested algi-

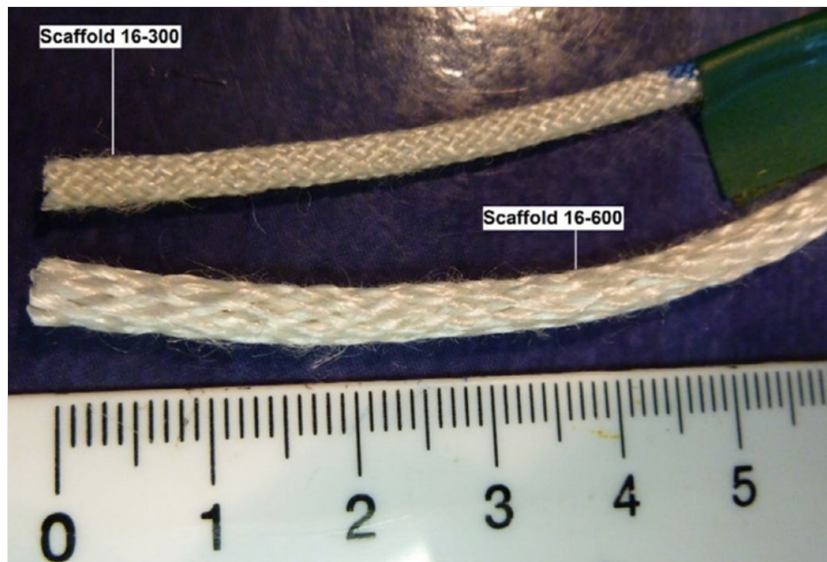


Figure 1.17: Braided chitosan scaffolds.[122]

nate solution injection post-surgery on tendon repair site in rabbits [123]. They showed that the lesions coated with alginate presented less adhesions and that the joint exion was improved. This non-adhesive property is promising for the synthesis of new scaffolds as adhesion occurs on the scared tendon areas and decreases the entire recovery of the joint motion.

Silk and polysaccharides display both amazing properties and are good candidates in the tendon gold standard quest. As some aspects need to be improved, several studies are nowadays based on hybrid scaffolds such as: silk/PLGA

Collagen based scaffolds

Collagen type I present lots of advantages as it is the main component of tendons and because it is biocompatible and degraded by enzym with low inflammatory response [81], [124]. It promotes cell adhesion [125] and differentiation [96], and is one of the most favorable biomaterials for cell survival compared to cheap and easy to use alginate for instance, or to chitosan [116]. It is thus a promising material that fuels much innovative research [105].

a) Extrusion

Collagen solution extrusion was first developed in the 1960s to create new biosutures for ophthalmic surgeries [126]. Since then, the potential of this molecule was highlighted leading to its widespread use in tissue engineering. Collagen solution extrusion is quite easy to implement requiring only a syringe, a needle or tubing, a collecting bath and a device to control the flow rate (syringe pump) (Fig. 1.15, A). Basically, to produce collagen threads the syringe is filled with a collagen solution and mounted in the syringe pump. Then, the solution will pass through the tubing and will go out in a bath containing the fibrillogenesis buffer. Finally, some other post-production processes can be performed [127–133]. Self-assembly of collagen may occur either with a pH transition when using an acidic collagen solution and a basic to neutral pH buffer, or through a temperature jump for cooled neutral collagen solution.

In most studies, the collagen is extracted from rat tail (RTT) or bovine Achilles tendons (BAT). Zeugolis et al. (2008) compared the properties of threads made of RTT or BAT acidic collagen [134]. By scanning electron microscopy, they observed no significant differences in the substructure of the collagen fibers in the two kinds of threads. Collagen concentration of solution commonly used ranges from 5 mg/mL to 30 mg/mL in acidic conditions (pH=2) [128], [130], [132; 133; 135]. For the fibrillogenesis buffer, the same basis is found in different studies: 135 mM of NaCl, 30 mM of TES (tris(hydroxymethyl)methyl-2-aminoethane sulphonic acid) and 30 mM sodium phosphate dibasic with a resulting pH of 7.5 [129; 130; 133]. Other buffers as phosphate saline buffer (PBS) [131] or polyethylene glycol in sodium phosphate dibasic and monobasic are also used. Characteristic dimensions of collagen threads, obtained by this technique, range from 100 μm to 1 mm for wet diameter and around 20 μm to 100 μm after drying [111], [129; 130; 133]. The length depends on the syringe volume capacity and the inner diameter of the tubing. In general, the order of magnitude of the collagen thread length ranges between a few centimeters to meter. Mechanical properties of collagen strands have been measured routinely in dry conditions and, less frequently, in wet conditions. Cornwell et al. (2007) measured Young modulus of wet collagen fibers around 4 MPa [132]. Regarding the elastic modulus of native tendon, those fibers are between 2 and 3 orders of magnitude "weaker". For the ultimate tensile strength (UTS), Cavallaro et al. (1994) [105], Cornwell et al. (2007) [132] and Dunn et al. (1993) [130] obtained results ranging from 1.2 to 10 MPa. Dunn et al. (1993) also observed that UTS decreases when the diameter fiber increases. So, in wet conditions, which mimic the physiological environment, mechanical properties of collagen fibers are still far from that of native tendon (Fig. 1.14). This is why different cross-linking (CXL) agents are commonly used to improve those characteristics. Cross-linking process consists in creating new bonds between collagen molecules with chemical species or external excitation sources. The most commonly used on collagen threads are glutaraldehyde, carbodiimide (EDC), cyanamide, hydroxysuccinimide (NHS) and dehydrothermal treatment (DHT), simple drying process, or ultra violet (UV) exposition.

Kato et al. (1989) have shown that they can produce collagen threads cross-linked with glutaraldehyde having an UTS of 50 to 66 MPa in wet conditions [131]. Those results are in the same range than UTS of rat tail tendons (33 to 39 MPa). The UTS is divided by a factor 2 for severe dehydration and for EDC treatment. As for Young modulus, they reach 400-500 MPa with glutaraldehyde CXL process. Zeugolis et al. (2008) evaluated mechanical properties of collagen threads dried under their own weight [136]. Young modulus of those strands ranged from 1 to 3 GPa and UTS from 0.2 to 0.3 GPa. These results have similar values as native tendon (Fig. 1.14). However, we have to keep in mind that in this case, tensile testing is performed in dry conditions, which are not close to the physiological ones. As for Kato et al. (1989) [131], they lose on average 3 orders of magnitude in wet conditions. Finally, to have as many bonds as possible, some combinations of CXL processes can be used (dehydrothermal with cyanamide [130] etc).

The alignment of collagen fibrils inside the collagen threads is also a parameter to take into account. The extrusion technique has the main advantage to induce collagen fibrils alignment in the longitudinal axis, thanks to the high strain applied when collagen solution is forced to pass through the narrow die ([105], [129]). This phenomenon can be further increased by stretching the threads [127]. Lai et al. (2011) observed that, *in vitro*, human fibroblasts cultured during 1 or 2 days have an elongated shape following the longitudinal axis of the collagen fibrils [129]. This suggests that there is some con-

tact guidance of the cells on the collagen threads structure. Cornwell et al. (2007) highlighted the problem of CXL post-process on collagen threads. Indeed, they observed that fibroblast migration rate decreased by using CXL agents [132]. A compromise between the improvement of mechanical properties with CXL techniques and the upgrading of cell proliferation must be found. To go further, Dunn et al. (1993) implanted their collagen threads in subcutaneous space of rabbit during 4 weeks. The threads were surrounded by a fibrous tissue and were colonized by inflammatory cells and fibroblasts [130]. Threads crosslinked with DHT combined with cyanamide were degraded over 4 weeks. Cavallaro et al. (1994) also had promising results in a canine ligament model and a rat abdominal repair model that can be transposed for tendon repair [105]. They noticed neovascularization and cell infiltration in the collagen threads. In both studies, no rejection of the collagen scaffolds was observed.

b) Electrospinning

Collagen electrospinning was achieved using fluoro-alcohols [137]. However, such a process was proven to denature collagen [112]. Indeed, resulting collagen is soluble in water, does not exhibit characteristic D-banding under transmission electron microscopy and has lower denaturation temperature. Further proofs were given thanks to circular dichroism, electrophoresis and infrared spectroscopy. Attempts succeeded in electrospinning collagen in benign solvent such as Phosphate Buffer Saline and ethanol mix [106] or acidic solution with poly(ethylene oxide) [138]. Bürck et al. (2013) demonstrated that electrospun collagen fiber from this solvent did not preserve much better the native structure of collagen and that part of the denatured collagen was intrinsically due to the electrospinning process and not to the solvent [111].

Recently, Elamparithi et al. (2015) reported successful electrospinning of collagen in 97:3 (acetic acid:DMSO) mix with fibers exhibiting the characteristic D-banding of native collagen [139]. However, no further investigation on native collagen content was carried out. The cross-linking of the resulting fibrous mat after electrospinning with 1-ethyl-3-(3-dimethylaminopropyl) carbodiimide hydrochloride does not allow for water solubility test and gives surprisingly low mechanical properties with modulus and tensile strength at maximum load of a few kPa. This may be suitable for non-load bearing tissue reconstruction such as cardiac tissue, aimed by the authors, but not for tendon reconstruction.

Thus, electrospinning of collagen for tendon reconstruction seems only relevant when collagen is co-electrospun with biodegradable synthetic polymers such as poly(L-lactide-co- ϵ -caprolactone) [140] or poly(L-lactic acid) [99], as it improves biocompatibility of synthetic polymers. For instance, an interesting work was published by Ladd et al. (2011) who electrospan two different polymers with collagen to reproduce the musculo-tendinous junction: the poly(L-lactic acid), being stiffer, for the tendon part and poly(ϵ -caprolactone) for the muscle part [141]. Whereas the synthetic polymers provide mechanical strength, the collagen promotes good cell viability close to 100% after 7 days of both C2C12 myoblasts and NIH3T3 fibroblasts seeded on each part.

c) 3D printing

The use of collagen as an ink for 3D printing raises an obvious interest and is investigated especially for bone [142] and cartilaginous tissue reconstruction [143]. However, current research faces difficulties to obtain self-standing 3D printed structures. Thus, collagen is often used to enhance the bioactivity of widespread bioinks such as alginate [144]

or agarose [115] that are cheap and easy to use but show lower bioactivity compared to main components of the ECM. It is also used with calcium phosphate [145] for bone reconstruction or mixed with fibrinogen [146] that is easy to crosslink.

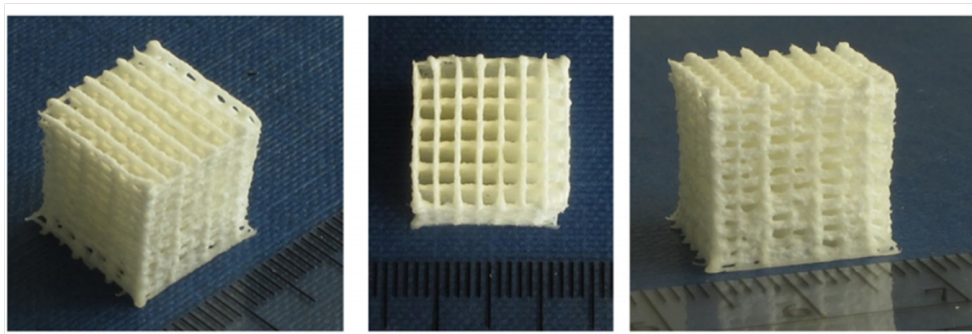


Figure 1.18: 3D plotted collagen scaffold (33 layers) in dry state [147]

Other techniques to print collagen self-standing structures are the deposition of collagen on a cold plate to freeze the solution when deposited [144], or the use of sacrificial negative molds [148],[149]. An original process that is worth mentioning is the printing of a core-sheath collagen-alginate structure [150]. Here again, collagen is sometimes used without inducing fibrillogenesis. Besides, the protocols used can be too harsh to incorporate cells in the bio-ink, preventing the use of additive manufacturing to deposit cells in an accurate and homogeneous way. A few articles deal with pure collagen self-assembled during or after printing [151], [152]. However, for collagen [152] as well as for fibrinogen [146], this leads to tedious protocols where the scaffold is incubated, after each layer printing, either at 37°C or with thrombin respectively.

One currently adopted strategy is the printing side-by-side of an artificial biodegradable polymers and a bio-ink with incorporated cells. The artificial polymer confers mechanical integrity to the scaffold whereas the bio-ink allows exact cell deposition with suitable bioactivity [146], [153]. To our knowledge, despite the control on porosity, macroscopic structure and cell incorporation that this technique offers, no article about 3D printing of collagen for tendon reconstruction has been published yet. This can be explained by the difficulty of handling collagen and the poor mechanical properties obtained with collagen in other domains such as extrusion. As collagen is often used with other bio-inks for its bioactivity, some chose gelatin instead for its lower price. For instance, Merceron et al. (2005) published the co-printing of two synthetic polymers polyurethane (PU) and poly(ϵ -caprolactone) (PCL) together with a bio-ink based on hyaluronic acid, fibrinogen and gelatin, to reproduce the musculo-tendinous junction [154]. The bio-ink contained C2C12 myoblasts on the PU side while the bio-ink on the stiffer PCL side contained NIH/3T3. The construct exhibited good cell viability, high cell alignment and characteristic musculo-tendinous gene upregulation. They highlighted the ability offered by 3D printing to deposit different cell types in precise locations, paving the way to complex multicellular scaffolds for regeneration.

1.3 Conclusion

Current tendon repair methods are mainly based on sutures and grafts that have proven to be effective but exhibit intrinsic drawbacks. Even though tendon structure is not completely understood, tendon regeneration based on bioengineered scaffold is promising.

The diversity of techniques and the increasing know-how in scaffold design allows tackling new exciting aspects such as alignment, multi-scale organization, scaffold tailoring or multi-cell deposition. Noteworthy mechanical stimulation appears also to be a key factor for tendon healing, independently of the suture, graft or scaffold used. Collagen I stands out from other biomolecules as main component of tendon and thanks to its suitable biocompatible properties. However, mechanical properties of collagen scaffolds remain an issue. Cross-linkers such as carbodiimide are mainly used to improve them but are not sufficient to bridge the gap and may introduce some drawbacks.

In this work, we thus chose collagen type I solutions to be shaped as tendon-like scaffold, at concentration range almost 20-fold higher than in other studies. We have seen that the first and easiest way used to produce threads is the extrusion technique. However, this process must be fully controlled as complex fluids extrusion may lead to severe flow instabilities, which disturb threads morphologies. Therefore, we designed a home-made extrusion set-up, where a large range of pieces and parameters are adjustable and where the exit flow is observed in real-time. A system model with similar rheological properties is chosen to study those instabilities and control them while extruding dense collagen solutions. Some hybrid threads will also be tested to combine these two systems exhibiting interesting behaviors. Finally, the collagen based threads will be cultured with cells *in vitro* under different conditions to assess their interactions with biological systems.

1.4 References

- [1] Geoffroy Nourissat, Francis Berenbaum, and Delphine Duprez. Tendon injury: from biology to tendon repair. *Nature reviews Rheumatology*, 11(4):223–233, 2015. [6](#), [7](#)
- [2] *Tendon Regeneration: Understanding Tissue Physiology and Development to Engineer Functional Substitutes*. Eds. Academic Press, 2015. [6](#), [8](#), [26](#)
- [3] Helen L. Birch. Tendon matrix composition and turnover in relation to functional requirements: *Tendon matrix composition and turnover*. *International Journal of Experimental Pathology*, 88(4):241–248, August 2007. [6](#)
- [4] Stéphane Bancelin, Charles-André Couture, Katherine Légaré, Maxime Pinsard, Maxime Rivard, Cameron Brown, and François Légaré. Fast interferometric second harmonic generation microscopy. *Biomedical Optics Express*, 7(2):399, February 2016. [6](#)
- [5] Ivan Gusachenko, Viet Tran, Yannick Goulam Houssen, Jean-Marc Allain, and Marie-Claire Schanne-Klein. Polarization-Resolved Second-Harmonic Generation in Tendon upon Mechanical Stretching. *Biophysical Journal*, 102(9):2220–2229, May 2012.
- [6] Alexandre Fouré. New Imaging Methods for Non-invasive Assessment of Mechanical, Structural, and Biochemical Properties of Human Achilles Tendon: A Mini Review. *Frontiers in Physiology*, 7, July 2016. [6](#)
- [7] Yufei Li, Gion Fessel, Marios Georgiadis, and Jess G Snedeker. Advanced glycation end-products diminish tendon collagen fiber sliding. *Matrix Biology*, 32(3):169–177, 2013. [8](#)
- [8] John A Petruska and Alan J Hodge. A subunit model for the tropocollagen macromolecule. *Proceedings of the National Academy of Sciences*, 51(5):871–876, 1964. [9](#)
- [9] Pramod B Voleti, Mark R Buckley, and Louis J Soslowky. Tendon healing: repair and regeneration. *Annual review of biomedical engineering*, 14:47–71, 2012. [9](#)
- [10] P. Kannus. Structure of the tendon connective tissue. *Scandinavian journal of medicine & science in sports*, 10(6):312–320, 2000. [9](#)
- [11] Clément Rieu, Lise Picaut, Gervaise Mosser, and Lea Trichet. From tendon injury to collagen-based tendon regeneration: overview and recent advances. *Current pharmaceutical design*, 2017. [9](#), [10](#), [23](#), [25](#)
- [12] S. P. Nicholls, L. J. Gathercole, A. Keller, and J. S. Shah. Crimping in rat tail tendon collagen: morphology and transverse mechanical anisotropy. *Int. J. Biol. Macromol.*, 5:283–288, 1983. [9](#)
- [13] J Dlugosz, L. J. Gathercole, and A. Keller. TRANSMISSION ELECTRON MICROSCOPE STUDIES AND THEIR RELATION TO POLARIZING OPTICAL MICROSCOPY IN RAT TAIL TENDON. *Micron*, 9:71–82, 1978. [9](#)
- [14] James H.-C. Wang. Mechanobiology of tendon. *Journal of Biomechanics*, 39(9):1563–1582, January 2006. [9](#), [11](#), [12](#)

- [15] J. S. Shah, E. Palacios, and L. Palacios. Development of crimp morphology and cellular changes in chick tendons. *Developmental biology*, 94(2):499–504, 1982. [9](#)
- [16] Andreas Herchenhan, Nicholas S. Kalson, David F. Holmes, Patrick Hill, Karl E. Kadler, and Lee Margetts. Tenocyte contraction induces crimp formation in tendon-like tissue. *Biomechanics and Modeling in Mechanobiology*, 11(3-4):449–459, March 2012. [9](#)
- [17] Xiao Wen Hu, David Knight, P, and John Chapman, A. The effect of non-polar liquids and non-ionic detergents on the ultrastructure and assembly of rat tail tendon collagen fibrils in vitro. *Biochimica et Biophysica Acta*, 1334:327–337, 1997. [9](#)
- [18] Jeffrey S. Cartmell and Michael G. Dunn. Effect of chemical treatments on tendon cellularity and mechanical properties. *Journal of biomedical materials research*, 49(1):134–140, 2000. [9](#)
- [19] Benedicto de Campos Vidal. Image analysis of tendon helical superstructure using interference and polarized light microscopy. *Micron*, 34(8):423–432, December 2003. [10](#)
- [20] Françoise Livolant and Amélie Leforestier. Condensed phases of DNA: structures and phase transitions. *Progress in polymer science*, 21(6):1115–1164, 1996. [10](#)
- [21] N. S. Murthy. Liquid crystallinity in collagen solutions and magnetic orientation of collagen fibrils. *Biopolymers*, 23(7):1261–1267, 1984. [10](#)
- [22] Hideatsu Maeda. An Atomic Force Microscopy Study of Ordered Molecular Assemblies and Concentric Ring Patterns from Evaporating Droplets of Collagen Solutions. *Langmuir*, 15(24):8505–8513, November 1999.
- [23] Marie-Madeleine Giraud-Guille. Liquid crystallinity in condensed type I collagen solutions: a clue to the packing of collagen in extracellular matrices. *Journal of molecular biology*, 224(3):861–873, 1992. [10](#)
- [24] Paulo De Sa Peixoto, Ariane Deniset-Besseau, Marie-Claire Schanne-Klein, and Gervaise Mosser. Quantitative assessment of collagen I liquid crystal organizations: role of ionic force and acidic solvent, and evidence of new phases. *Soft Matter*, 7(23):11203, 2011. [10](#)
- [25] Marco Franchi, Vittoria Ottani, Rita Stagni, and Alessandro Ruggeri. Tendon and ligament fibrillar crimps give rise to left-handed helices of collagen fibrils in both planar and helical crimps. *Journal of Anatomy*, 216(3):301–309, March 2010. [11](#)
- [26] Rafael Grytz and Günther Meschke. Constitutive modeling of crimped collagen fibrils in soft tissues. *Journal of the Mechanical Behavior of Biomedical Materials*, 2(5):522–533, October 2009. [12](#)
- [27] Shawn P. Reese, Steve A. Maas, and Jeffrey A. Weiss. Micromechanical models of helical superstructures in ligament and tendon fibers predict large Poisson’s ratios. *Journal of Biomechanics*, 43(7):1394–1400, May 2010. [12](#)
- [28] Ho-Joong Jung, Matthew B Fisher, and Savio L-Y Woo. Role of biomechanics in the understanding of normal, injured, and healing ligaments and tendons. *BMC Sports Science, Medicine and Rehabilitation*, 1(1), December 2009. [12](#), [23](#)

- [29] Christopher A. Squier and W. H. Bausch. Three-dimensional organization of fibroblasts and collagen fibrils in rat tail tendon. *Cell and tissue research*, 238(2):319–327, 1984. [12](#)
- [30] G. Zhang, B. B. Young, Y. Ezura, M. Favata, L. J. Soslowsky, S. Chakravarti, and D. E. Birk. Development of tendon structure and function: regulation of collagen fibrillogenesis. *J Musculoskelet Neuronal Interact*, 5(1):5–21, 2005. [12](#)
- [31] Hazel R. C. Screen, David E. Berk, Karl E. Kadler, Francesco Ramirez, and Marian F. Young. Tendon Functional Extracellular Matrix: TENDON FUNCTIONAL EXTRACELLULAR MATRIX. *Journal of Orthopaedic Research*, 33(6):793–799, June 2015. [12](#)
- [32] D. S. Morais, J. Torres, R. M. Guedes, and M. A. Lopes. Current Approaches and Future Trends to Promote Tendon Repair. *Annals of Biomedical Engineering*, 43(9):2025–2035, September 2015. [13](#)
- [33] Stavros Thomopoulos, William C. Parks, Daniel B. Rifkin, and Kathleen A. Derwin. Mechanisms of tendon injury and repair: TENDON INJURY AND REPAIR. *Journal of Orthopaedic Research*, 33(6):832–839, June 2015. [13](#), [14](#)
- [34] Jonathan S. Young and N. Maffuli. Etiology and epidemiology of Achilles tendon problems. *The Achilles Tendon*, pages 39–49, 2007. [13](#)
- [35] Graham Riley. Tendinopathy—from basic science to treatment. *Nature Clinical Practice Rheumatology*, 4(2):82–89, February 2008. [13](#)
- [36] A.J. Lomas, C.N.M. Ryan, A. Soroushanova, N. Shologu, A.I. Sideri, V. Tsioli, G.C. Fthenakis, A. Tzora, I. Skoufos, L.R. Quinlan, G. O’Laighin, A.M. Mullen, J.L. Kelly, S. Kearns, M. Biggs, A. Pandit, and D.I. Zeugolis. The past, present and future in scaffold-based tendon treatments. *Advanced Drug Delivery Reviews*, 84:257–277, April 2015. [13](#), [14](#)
- [37] Trevor Lewis and Jill Cook. Fluoroquinolones and Tendinopathy: A Guide for Athletes and Sports Clinicians and a Systematic Review of the Literature. *Journal of Athletic Training*, 49(3):422–427, June 2014. [13](#)
- [38] Francesco Oliva, Alessio Giai Via, and Nicola Maffulli. Calcific tendinopathy of the rotator cuff tendons. *Sports medicine and arthroscopy review*, 19(3):237–243, 2011. [13](#)
- [39] Robert A.E. Clayton and Charles M. Court-Brown. The epidemiology of musculoskeletal tendinous and ligamentous injuries. *Injury*, 39(12):1338–1344, December 2008. [13](#), [14](#)
- [40] Johanna P. de Jong, Jesse T. Nguyen, Anne J. M. Sonnema, Emily C. Nguyen, Peter C. Amadio, and Steven L. Moran. The Incidence of Acute Traumatic Tendon Injuries in the Hand and Wrist: A 10-Year Population-based Study. *Clinics in Orthopedic Surgery*, 6(2):196, 2014. [13](#)
- [41] Cheng Sun, Qi Zhuo, Wei Chai, Jiying Chen, Wei Yang, Peifu Tang, and Yan Wang. Conservative interventions for treating Achilles tendon ruptures. In The Cochrane Collaboration, editor, *Cochrane Database of Systematic Reviews*. John Wiley & Sons, Ltd, Chichester, UK, October 2013. [13](#), [14](#)

- [42] Alexander Scott and Maureen C. Ashe. Common Tendinopathies in the Upper and Lower Extremities:. *Current Sports Medicine Reports*, 5(5):233–241, October 2006. [13](#), [14](#)
- [43] T. L. Sanders, H. Maradit Kremers, A. J. Bryan, J. E. Ransom, J. Smith, and B. F. Morrey. The Epidemiology and Health Care Burden of Tennis Elbow: A Population-Based Study. *The American Journal of Sports Medicine*, 43(5):1066–1071, May 2015. [13](#), [14](#)
- [44] B M Pluim. Tennis injuries: occurrence, aetiology, and prevention. *British Journal of Sports Medicine*, 40(5):415–423, May 2006. [13](#)
- [45] European Agency for Safety and Health at Work. OSH in figures: Work-related musculoskeletal disorders in the EU - Facts and figures, 2010. [13](#), [14](#)
- [46] UK Health and Safety Executive. Work-related Musculoskeletal disorder (WRMSDs) Statistics, Great Britain, 2015, 2015. [14](#)
- [47] Agency for Healthcare Research and Quality. Comparative Effectiveness of the Non-operative and Operative Treatments for Rotator Cuff Tears, 2010. [14](#)
- [48] European Agency for Safety and Health at Work. Work-related neck and upper limb musculoskeletal disorders, 1999. [14](#)
- [49] Nelly Andarawis-Puri, Evan L. Flatow, and Louis J. Soslowky. Tendon basic science: Development, repair, regeneration, and healing: TENDON DEVELOPMENT, INJURY, AND REPAIR. *Journal of Orthopaedic Research*, 33(6):780–784, June 2015. [15](#)
- [50] Shelley Rawson, Sarah Cartmell, and Jason Wong. Suture techniques for tendon repair; a comparative review. *Muscles, ligaments and tendons journal*, 3(3):220, 2013. [15](#)
- [51] Marc A. Childress and Anthony Beutler. Management of chronic tendon injuries. *Am Fam Physician*, 87(7):486–490, April 2013. [15](#)
- [52] K. M. Khan and A. Scott. Mechanotherapy: how physical therapists' prescription of exercise promotes tissue repair. *Br J Sports Med*, 43(4):247–252, April 2009. [15](#)
- [53] Emily A. Sundman, Brian J. Cole, and Lisa A. Fortier. Growth factor and catabolic cytokine concentrations are influenced by the cellular composition of platelet-rich plasma. *Am J Sports Med*, 39(10):2135–2140, October 2011. [15](#)
- [54] R. H. Gelberman, M. I. Boyer, M. D. Brodt, S. C. Winters, and M. J. Silva. The effect of gap formation at the repair site on the strength and excursion of intrasynovial flexor tendons. An experimental study on the early stages of tendon-healing in dogs. *J Bone Joint Surg Am*, 81(7):975–982, July 1999. [15](#)
- [55] Patrick S. Buckley and David I. Pedowitz. Bone Reduction Clamp to Gain Length in Repairing Chronic Achilles Tendon Ruptures. *Orthopedics*, August 2016. [15](#)
- [56] M. D. Zeev Feldbrin, M. D. David Hendel, M. D. Alexander Lipkin, M. D. Dan Zin, and M. D. Louis Schorr. achilles tendon rupture and our experience with the achillon device. September 2016. [15](#)

- [57] Javier Maquirriain. Achilles Tendon Rupture: Avoiding Tendon Lengthening during Surgical Repair and Rehabilitation. *Yale J Biol Med*, 84(3):289–300, September 2011. [15](#)
- [58] Benedikt Schliemann, Niklas Grüneweller, Daiwei Yao, Clemens Kösters, Simon Lenschow, Steffen B. Roßlenbroich, Michael J. Raschke, and Andre Weimann. Biomechanical evaluation of different surgical techniques for treating patellar tendon ruptures. *International Orthopaedics (SICOT)*, 40(8):1717–1723, October 2015. [15](#)
- [59] Bernd Hohendorff, Wolf Siepen, Liesbeth Spiering, Lukas Staub, Thilo Schmuck, and Andreas Boss. Long-term Results after Operatively Treated Achilles Tendon Rupture: Fibrin Glue versus Suture. *The Journal of Foot and Ankle Surgery*, 47(5):392–399, September 2008. [16](#)
- [60] Séverine Rose, Alexandre PrevotEAU, Paul Elzière, Dominique Hourdet, Alba Marcellan, and Ludwik Leibler. Nanoparticle solutions as adhesives for gels and biological tissues. *Nature*, 505(7483):382–385, January 2014. [16](#)
- [61] Bülent Erol, Barış Kocaoğlu, and Tanil Esemeli. Spiral-shaped Metallic Implant in the Treatment of Achilles Tendon Ruptures: An Experimental Study on the Achilles Tendon of Sheep. *The Journal of Foot and Ankle Surgery*, 46(3):155–161, May 2007. [16](#), [17](#)
- [62] İsmail Ağır, Mahmut Nedim Aytekin, Onur Başçı, Barış Çaypınar, and Bülent Erol. Tendon-Holding Capacities of Two Newly Designed Implants for Tendon Repair: An Experimental Study on the Flexor Digitorum Profundus Tendon of Sheep. *Open Orthop J*, 8:135–139, June 2014. [17](#)
- [63] Shawn P Reese and Erik N Kubiak. A nitinol based flexor tendon fixation device: Gapping and tensile strength measurements in cadaver flexor tendon. *Journal of biomechanical engineering*, 136(1):014501, 2014. [17](#)
- [64] Scott W. Wolfe, Andrew A. Willis, Deidre Campbell, Jonathan Clabeaux, and Timothy M. Wright. Biomechanic Comparison of the Teno Fix Tendon Repair Device With the Cruciate and Modified Kessler Techniques. *The Journal of Hand Surgery*, 32(3):356–366, March 2007. [17](#)
- [65] S. Lacoste, J.M. Féron, and B. Cherrier. Percutaneous Tenolig® repair under intra-operative ultrasonography guidance in acute Achilles tendon rupture. *Orthopaedics & Traumatology: Surgery & Research*, 100(8):925–930, December 2014. [17](#)
- [66] Robert A Magnussen, Richard R Glisson, and Claude T Moorman III. Augmentation of achilles tendon repair with extracellular matrix xenograft: a biomechanical analysis. *The American journal of sports medicine*, 39(7):1522–1527, 2011. [18](#)
- [67] James L. Beskin, Richard A. Sanders, Stephen C. Hunter, and Jack C. Hughston. Surgical repair of Achilles tendon ruptures. *Am J Sports Med*, 15(1):1–8, January 1987. [18](#)
- [68] Michael R Carmont and Nicola Maffulli. Less invasive Achilles tendon reconstruction. *BMC Musculoskelet Disord*, 8:100, October 2007. [18](#)

- [69] Ayman M. Ebied and Adel Abdel Azim Foda. Less Invasive Reconstruction of Chronic Achilles Tendon Rupture with free Semitendinosus Tendon Autograft - A case Series. *International Journal of Orthopaedics*, 3(2):539–543, April 2016. [18](#)
- [70] Mohamed Taha El Shewy, Hassan Magdy El Barbary, and Hisham Abdel-Ghani. Repair of Chronic Rupture of the Achilles Tendon Using 2 Intratendinous Flaps From the Proximal Gastrocnemius-Soleus Complex. *Am J Sports Med*, 37(8):1570–1577, January 2009. [18](#), [19](#)
- [71] Wesley P. Phipatanakul and Steve A. Petersen. Porcine small intestine submucosa xenograft augmentation in repair of massive rotator cuff tears. *Am J. Orthop.*, 38(11):572–575, November 2009. [19](#)
- [72] Steven G. Sclamberg, James E. Tibone, John M. Itamura, and Sina Kasraeian. Six-month magnetic resonance imaging follow-up of large and massive rotator cuff repairs reinforced with porcine small intestinal submucosa. *J Shoulder Elbow Surg*, 13(5):538–541, October 2004. [19](#)
- [73] Gregory C. Berlet, Christopher F. Hyer, Thomas H. Lee, and Barbara E. Blum. Collagen Ribbon Augmentation of Achilles Tendon Tears: A Biomechanical Evaluation. *The Journal of Foot and Ankle Surgery*, 53(3):298–302, 2014. [19](#)
- [74] Lin Song, Raymond E. Olsen, Jeffrey P. Spalazzi, and Twana Davisson. Biomechanical Evaluation of Acellular Collagen Matrix Augmented Achilles Tendon Repair in Sheep. *The Journal of Foot and Ankle Surgery*, 49(5):438–441, September 2010. [19](#)
- [75] Daniel K. Lee. A Preliminary Study on the Effects of Acellular Tissue Graft Augmentation in Acute Achilles Tendon Ruptures. *The Journal of Foot and Ankle Surgery*, 47(1):8–12, January 2008. [20](#)
- [76] Shane Hollawell and William Baione. Chronic Achilles Tendon Rupture Reconstructed With Achilles Tendon Allograft and Xenograft Combination. *The Journal of Foot and Ankle Surgery*, 54(6):1146–1150, November 2015. [20](#)
- [77] Anthony Herbert, Gemma L. Jones, Eileen Ingham, and John Fisher. A biomechanical characterisation of acellular porcine super flexor tendons for use in anterior cruciate ligament replacement: Investigation into the effects of fat reduction and bioburden reduction bioprocesses. *Journal of Biomechanics*, 48(1):22–29, January 2015. [20](#)
- [78] J. Palmer Branch. A Tendon Graft Weave Using an Acellular Dermal Matrix for Repair of the Achilles Tendon and Other Foot and Ankle Tendons. *The Journal of Foot and Ankle Surgery*, 50(2):257–265, March 2011. [20](#)
- [79] Diana Gaspar, Kyriakos Spanoudes, Carolyn Holladay, Abhay Pandit, and Dimitrios Zeugolis. Progress in cell-based therapies for tendon repair. *Advanced Drug Delivery Reviews*, 84:240–256, April 2015. [21](#)
- [80] Cansın Güngörmüş, Dürdane Kolankaya, and Erkin Aydın. Histopathological and biomechanical evaluation of tenocyte seeded allografts on rat Achilles tendon regeneration. *Biomaterials*, 51:108–118, 2015. [21](#)

- [81] S. J. Kew, J. H. Gwynne, D. Enea, M. Abu-Rub, A. Pandit, D. Zeugolis, R. A. Brooks, N. Rushton, S. M. Best, and R. E. Cameron. Regeneration and repair of tendon and ligament tissue using collagen fibre biomaterials. *Acta Biomater*, 7(9):3237–3247, September 2011. [21](#), [28](#)
- [82] Mickey D. Stapp. Implantable materials and grafts in tendon surgery. *Reconstructive surgery of the foot and the leg*, pages 289–292, 1993. [21](#)
- [83] Roger D. Williams and Spencer F. August. Experimental evaluation of a Teflon tendon prosthesis. *The American Journal of Surgery*, 107(6):913–916, 1964. [21](#)
- [84] M. Holtz, M. L. Midenberg, and S. E. Kirschenbaum. Utilization of a silastic sheet in tendon repair of the foot. *J Foot Surg*, 21(4):253–259, 1982. [21](#)
- [85] Matthew C. Morrey, Jonathan D. Barlow, Matthew P. Abdel, and Arlen D. Hanssen. Synthetic Mesh Augmentation of Acute and Subacute Quadriceps Tendon Repair. *Orthopedics*, 39(1):e9–e13, January 2016. [21](#)
- [86] Shalimar Abdullah. Usage of synthetic tendons in tendon reconstruction. *BMC Proceedings*, 9(Suppl 3):A68, 2015. [21](#)
- [87] Alan Melvin, Alan Litsky, Joel Mayerson, David Witte, David Melvin, and Natalia Juncosa-Melvin. An artificial tendon with durable muscle interface. *J. Orthop. Res.*, 28(2):218–224, 2010. [21](#)
- [88] D. H. Jenkins and B. McKibbin. The role of flexible carbon-fibre implants as tendon and ligament substitutes in clinical practice. A preliminary report. *J Bone Joint Surg Br*, 62-B(4):497–499, November 1980. [22](#)
- [89] D. P. M. Corey. *Tendon grafts and implants*. 1988. [22](#)
- [90] J. M. Roberts, G. L. Goldstrohm, T. D. Brown, and D. C. Mears. Comparison of unrepaired, primarily repaired, and polyglactin mesh-reinforced Achilles tendon lacerations in rabbits. *Clin. Orthop. Relat. Res.*, (181):244–249, December 1983. [22](#)
- [91] C. B. Howard, B. McKibbin, and Z. A. Ralis. The use of Dexon as a replacement for the calcaneal tendon in sheep. *Bone & Joint Journal*, 67-B(2):313–316, March 1985. [22](#)
- [92] M. D. Liem, H. G. Zegel, F. C. Balduini, M. L. Turner, J. M. Becker, and A. Caballero-Saez. Repair of Achilles tendon ruptures with a polylactic acid implant: assessment with MR imaging. *AJR Am J Roentgenol*, 156(4):769–773, April 1991. [22](#)
- [93] H. Alexander, A. B. Weiss, and J. R. Parsons. Absorbable polymer-filamentous carbon composites—a new class of tissue scaffolding materials. *Aktuelle Probl Chir Orthop*, 26:78–91, 1983. [22](#)
- [94] Ahmed Shoaib and Viren Mishra. Surgical repair of symptomatic chronic achilles tendon rupture using synthetic graft augmentation. *Foot and Ankle Surgery*, September 2016. [22](#)
- [95] Gunay Verdiyeva, Kiron Koshy, Natalia Glibbery, Haroon Mann, and Alexander M. Seifalian. Tendon Reconstruction with Tissue Engineering Approach—A Review. *Journal of Biomedical Nanotechnology*, 11(9):1495–1523, September 2015. [23](#)

- [96] Wing Yin Tong, Wei Shen, Connie W.F. Yeung, Ying Zhao, Shuk Han Cheng, Paul K. Chu, Danny Chan, Godfrey C.F. Chan, Kenneth M.C. Cheung, Kelvin W.K. Yeung, and Yun Wah Lam. Functional replication of the tendon tissue microenvironment by a bioimprinted substrate and the support of tenocytic differentiation of mesenchymal stem cells. *Biomaterials*, 33(31):7686–7698, November 2012. [23](#), [24](#), [28](#)
- [97] Su A Park, In Ae Kim, Yong Jae Lee, Ji Won Shin, Chong-Rak Kim, Jeong Koo Kim, Young-Il Yang, and Jung-Woog Shin. Biological responses of ligament fibroblasts and gene expression profiling on micropatterned silicone substrates subjected to mechanical stimuli. *Journal of Bioscience and Bioengineering*, 102(5):402–412, November 2006. [24](#)
- [98] James HC Wang, Fengyan Jia, Thomas W Gilbert, and Savio LY Woo. Cell orientation determines the alignment of cell-produced collagenous matrix. *Journal of biomechanics*, 36(1):97–102, 2003. [24](#)
- [99] F.C.M.J.M. van Delft, F.C. van den Heuvel, W.A. Loesberg, J. te Riet, P. Schön, C.G. Figdor, S. Speller, J.J.W.A. van Loon, X.F. Walboomers, and J.A. Jansen. Manufacturing substrate nano-grooves for studying cell alignment and adhesion. *Microelectronic Engineering*, 85(5-6):1362–1366, May 2008. [24](#)
- [100] Leslie Mertz. What Is Biocompatibility?: A New Definition Based on the Latest Technology. *IEEE Pulse*, 4(4):14–15, July 2013. [24](#)
- [101] Use of International Standard ISO 10993-1, "Biological evaluation of medical devices - Part 1: Evaluation and testing within a risk management process". Technical report, U.S. Department of Health and Human Services Food and Drug Administration Center for Devices and Radiological Health, June 2016. [24](#)
- [102] Dietmar W. Huttmacher. Scaffolds in tissue engineering bone and cartilage. *Biomaterials*, 21(24):2529–2543, 2000. [24](#)
- [103] S Badylak, D Freytes, and T Gilbert. Extracellular matrix as a biological scaffold material: Structure and function. *Acta Biomaterialia*, 5(1):1–13, January 2009. [24](#)
- [104] Gilbert, Stewart-Akers, Simmons-Byrd, and Badylak. Degradation and remodeling of small intestinal submucosa in canine achilles tendon repair. *J Bone Joint Surg*, pages 621–630, 2007. [24](#)
- [105] J. F. Cavallaro, P. D. Kemp, and K. H. Kraus. Collagen fabrics as biomaterials. *Biotechnol. Bioeng.*, 43(8):781–791, April 1994. [25](#), [28](#), [29](#), [30](#)
- [106] Bin Dong, Olivier Arnoult, Meghan E. Smith, and Gary E. Wnek. Electrospinning of Collagen Nanofiber Scaffolds from Benign Solvents. *Macromolecular Rapid Communications*, 30(7):539–542, April 2009. [25](#), [30](#)
- [107] Nuanchan Choktaweasap, Kunawan Arayanarakul, Duangdao Aht-Ong, Chidchanok Meechaisue, and Pitt Supaphol. Electrospun gelatin fibers: effect of solvent system on morphology and fiber diameters. *Polymer journal*, 39(6):622–631, 2007. [25](#)
- [108] Yu-Qin Wan, Ji-Huan He, Jian-Yong Yu, and Yue Wu. Electrospinning of high-molecule PEO solution. *Journal of Applied Polymer Science*, 103(6):3840–3843, March 2007. [26](#)

- [109] Jamil A. Matthews, Gary E. Wnek, David G. Simpson, and Gary L. Bowlin. Electrospinning of Collagen Nanofibers. *Biomacromolecules*, 3(2):232–238, March 2002. [26](#)
- [110] Jamil A. Matthews, Eugene D. Boland, Gary E. Wnek, David G. Simpson, and Gary L. Bowlin. Electrospinning of collagen type II: a feasibility study. *Journal of bioactive and compatible polymers*, 18(2):125–134, 2003. [26](#)
- [111] Jochen Bürck, Stefan Heissler, Udo Geckle, Mohammad Fotouhi Ardakani, Reinhard Schneider, Anne S. Ulrich, and Murat Kazanci. Resemblance of Electrospun Collagen Nanofibers to Their Native Structure. *Langmuir*, 29(5):1562–1572, February 2013. [26](#), [29](#), [30](#)
- [112] Dimitrios I. Zeugolis, Shih T. Khew, Elijah S.Y. Yew, Andrew K. Ekaputra, Yen W. Tong, Lin-Yue L. Yung, Dietmar W. Hutmacher, Colin Sheppard, and Michael Raghunath. Electro-spinning of pure collagen nano-fibres – Just an expensive way to make gelatin? *Biomaterials*, 29(15):2293–2305, May 2008. [26](#), [30](#)
- [113] Anh-Vu Do, Behnoush Khorsand, Sean M. Geary, and Aliasger K. Salem. 3d Printing of Scaffolds for Tissue Regeneration Applications. *Advanced Healthcare Materials*, 4(12):1742–1762, August 2015. [26](#)
- [114] Jason A. Inzana, Diana Olvera, Seth M. Fuller, James P. Kelly, Olivia A. Graeve, Edward M. Schwarz, Stephen L. Kates, and Hani A. Awad. 3d printing of composite calcium phosphate and collagen scaffolds for bone regeneration. *Biomaterials*, 35(13):4026–4034, April 2014. [26](#)
- [115] Daniela Filipa Duarte Campos, Andreas Blaeser, Kate Buellesbach, Kshama Shree Sen, Weiwei Xun, Walter Tillmann, and Horst Fischer. Bioprinting Organotypic Hydrogels with Improved Mesenchymal Stem Cell Remodeling and Mineralization Properties for Bone Tissue Engineering. *Advanced Healthcare Materials*, 5(11):1336–1345, June 2016. [26](#), [31](#)
- [116] Sean V. Murphy, Aleksander Skardal, and Anthony Atala. Evaluation of hydrogels for bio-printing applications. *Journal of Biomedical Materials Research Part A*, 101A(1):272–284, January 2013. [26](#), [28](#)
- [117] Hong Wei Ouyang, James CH Goh, Ashvin Thambyah, Swee Hin Teoh, and Eng Hin Lee. Knitted poly-lactide-co-glycolide scaffold loaded with bone marrow stromal cells in repair and regeneration of rabbit achilles tendon. *Tissue engineering*, 9(3):431–439, 2003. [26](#), [27](#)
- [118] Dan Deng, Wenbo Wang, Bin Wang, Peihua Zhang, Guangdong Zhou, Wen Jie Zhang, Yilin Cao, and Wei Liu. Repair of achilles tendon defect with autologous ascsc engineered tendon in a rabbit model. *Biomaterials*, 35(31):8801–8809, 2014. [26](#), [27](#)
- [119] Yilin Cao, Yongtao Liu, Wei Liu, Qingxin Shan, Samuel D. Buonocore, and Lei Cui. Bridging tendon defects using autologous tenocyte engineered tendon in a hen model. *Plast. Reconstr. Surg.*, 110(5):1280–1289, October 2002. [26](#)
- [120] Gregory H Altman, Rebecca L Horan, Helen H Lu, Jodie Moreau, Ivan Martin, John C Richmond, and David L Kaplan. Silk matrix for tissue engineered anterior cruciate ligaments. *Biomaterials*, 23(20):4131–4141, 2002. [27](#)

- [121] Hongbin Fan, Haifeng Liu, Eugene JW Wong, Siew L Toh, and James CH Goh. In vivo study of anterior cruciate ligament regeneration using mesenchymal stem cells and silk scaffold. *Biomaterials*, 29(23):3324–3337, 2008. [27](#)
- [122] J Nowotny, D Aibibu, J Farack, U Nimtschke, M Hild, M Gelinsky, P Kasten, and Ch Cherif. Novel fiber-based pure chitosan scaffold for tendon augmentation: biomechanical and cell biological evaluation. *Journal of Biomaterials science, Polymer edition*, 27(10):917–936, 2016. [27](#), [28](#)
- [123] Jiro Namba, Kozo Shimada, Masanobu Saito, Tsuyoshi Murase, Hideaki Yamada, and Hideki Yoshikawa. Modulation of peritendinous adhesion formation by alginate solution in a rabbit flexor tendon model. *Journal of Biomedical Materials Research Part B: Applied Biomaterials*, 80(1):273–279, 2007. [28](#)
- [124] Julie Glowacki and Shuichi Mizuno. Collagen scaffolds for tissue engineering. *Biopolymers*, 89(5):338–344, May 2008. [28](#)
- [125] Malgorzata Barczyk, Sergio Carracedo, and Donald Gullberg. Integrins. *Cell Tissue Res*, 339:269–280, 2010. [28](#)
- [126] Davide Enea, Frances Henson, Simon Kew, John Wardale, Alan Getgood, Roger Brooks, and Neil Rushton. Extruded collagen fibres for tissue engineering applications: effect of crosslinking method on mechanical and biological properties. *Journal of Materials Science: Materials in Medicine*, 22(6):1569–1578, June 2011. [28](#)
- [127] George D. Pins, David L. Christiansen, Raj Patel, and Frederick H. Silver. Self-assembly of collagen fibers. Influence of fibrillar alignment and decorin on mechanical properties. *Biophysical journal*, 73(4):2164, 1997. [28](#), [29](#)
- [128] M. C. Wang, G. D. Pins, and F. H. Silver. Collagen fibres with improved strength for the repair of soft tissue injuries. *Biomaterials*, 15(7):507–512, June 1994. [29](#)
- [129] Edwina S. Lai, Claire M. Anderson, and Gerald G. Fuller. Designing a tubular matrix of oriented collagen fibrils for tissue engineering. *Acta Biomaterialia*, 7(6):2448–2456, June 2011. [29](#)
- [130] M. G. Dunn, P. N. Avasarala, and J. P. Zawadsky. Optimization of extruded collagen fibers for ACL reconstruction. *J. Biomed. Mater. Res.*, 27(12):1545–1552, December 1993. [29](#), [30](#)
- [131] Y. P. Kato, D. L. Christiansen, R. A. Hahn, S. J. Shieh, J. D. Goldstein, and F. H. Silver. Mechanical properties of collagen fibres: a comparison of reconstituted and rat tail tendon fibres. *Biomaterials*, 10(1):38–42, January 1989. [29](#)
- [132] Kevin G. Cornwell and George D. Pins. Discrete crosslinked fibrin microthread scaffolds for tissue regeneration. *Journal of Biomedical Materials Research Part A*, 82A(1):104–112, July 2007. [29](#), [30](#)
- [133] Lei Huang, Karthik Nagapudi, Robert P. Apkarian, and Elliot L. Chaikof. Engineered collagen–PEO nanofibers and fabrics. *Journal of Biomaterials Science, Polymer Edition*, 12(9):979–993, January 2001. [28](#), [29](#)

- [134] Dimitrios I. Zeugolis, Gordon R. Paul, and Geoffrey Attenburrow. Cross-linking of extruded collagen fibers-A biomimetic three-dimensional scaffold for tissue engineering applications. *Journal of Biomedical Materials Research Part A*, 89A(4):895–908, June 2009. [29](#)
- [135] W E Teo and S Ramakrishna. A review on electrospinning design and nanofibre assemblies. *Nanotechnology*, 17(14):R89–R106, July 2006. [29](#)
- [136] D.I. Zeugolis, R.G. Paul, and G. Attenburrow. The influence of a natural cross-linking agent (*Myrica rubra*) on the properties of extruded collagen fibres for tissue engineering applications. *Materials Science and Engineering: C*, 30(1):190–195, January 2010. [29](#)
- [137] Kyong Su Rho, Lim Jeong, Gene Lee, Byoung-Moo Seo, Yoon Jeong Park, Seong-Doo Hong, Sangho Roh, Jae Jin Cho, Won Ho Park, and Byung-Moo Min. Electrospinning of collagen nanofibers: Effects on the behavior of normal human keratinocytes and early-stage wound healing. *Biomaterials*, 27(8):1452–1461, March 2006. [30](#)
- [138] A. Szentivanyi, U. Assmann, R. Schuster, and B. Glasmacher. Production of bio-hybrid protein/PEO scaffolds by electrospinning. *Materialwissenschaft und Werkstofftechnik*, 40(1-2):65–72, January 2009. [30](#)
- [139] Anuradha Elamparithi, Alan M. Punnoose, and Sarah Kuruvilla. Electrospun type I collagen matrices preserving native ultrastructure using benign binary solvent for cardiac tissue engineering. *Artificial Cells, Nanomedicine, and Biotechnology*, pages 1–8, May 2015. [30](#)
- [140] T Xu, C Gregory, P Molnar, X Cui, S Jalota, S Bhaduri, and T Boland. Viability and electrophysiology of neural cell structures generated by the inkjet printing method. *Biomaterials*, March 2006. [30](#)
- [141] Mitchell R. Ladd, Sang Jin Lee, Joel D. Stitzel, Anthony Atala, and James J. Yoo. Co-electrospun dual scaffolding system with potential for muscle–tendon junction tissue engineering. *Biomaterials*, 32(6):1549–1559, February 2011. [30](#)
- [142] Kai-Feng Lin, Shu He, Yue Song, Chun-Mei Wang, Yi Gao, Jun-Qin Li, Peng Tang, Zheng Wang, Long Bi, and Guo-Xian Pei. Low-Temperature Additive Manufacturing of Biomimic Three-Dimensional Hydroxyapatite/Collagen Scaffolds for Bone Regeneration. *ACS Applied Materials & Interfaces*, 8(11):6905–6916, March 2016. [30](#)
- [143] Hyeong Jin Lee, Yong Bok Kim, Seung Hyun Ahn, Ji-Seon Lee, Chul Ho Jang, Hyeon Yoon, Wook Chun, and Geun Hyung Kim. A New Approach for Fabricating Collagen/ECM-Based Bioinks Using Preosteoblasts and Human Adipose Stem Cells. *Advanced Healthcare Materials*, 4(9):1359–1368, June 2015. [30](#)
- [144] Kai Sun, Ruixin Li, Wenxue Jiang, Yufu Sun, and Hui Li. Comparison of three-dimensional printing and vacuum freeze-dried techniques for fabricating composite scaffolds. *Biochemical and Biophysical Research Communications*, 477(4):1085–1091, September 2016. [30](#), [31](#)
- [145] B. Derby. Printing and Prototyping of Tissues and Scaffolds. *Science*, 338(6109):921–926, November 2012. [31](#)

- [146] Tao Xu, Kyle W Binder, Mohammad Z Albanna, Dennis Dice, Weixin Zhao, James J Yoo, and Anthony Atala. Hybrid printing of mechanically and biologically improved constructs for cartilage tissue engineering applications. *Biofabrication*, 5(1):015001, March 2013. 31
- [147] Anja Lode, Michael Meyer, Sophie Brüggemeier, Birgit Paul, Hagen Baltzer, Michaela Schröpfer, Claudia Winkelmann, Frank Sonntag, and Michael Gelsky. Additive manufacturing of collagen scaffolds by three-dimensional plotting of highly viscous dispersions. *Biofabrication*, 8(1):015015, February 2016. 31
- [148] C. Z. Liu, Z. D. Xia, Z. W. Han, P. A. Hulley, J. T. Triffitt, and J. T. Czernuszka. Novel 3d collagen scaffolds fabricated by indirect printing technique for tissue engineering. *Journal of Biomedical Materials Research Part B: Applied Biomaterials*, 85(2):519–528, 2008. 31
- [149] SeungHyun Ahn, SuYeon Lee, Youngseok Cho, Wook Chun, and GeunHyung Kim. Fabrication of three-dimensional collagen scaffold using an inverse mould-leaching process. *Bioprocess and Biosystems Engineering*, 34(7):903–911, September 2011. 31
- [150] MyungGu Yeo, Ji-Seon Lee, Wook Chun, and Geun Hyung Kim. An Innovative Collagen-Based Cell-Printing Method for Obtaining Human Adipose Stem Cell-Laden Structures Consisting of Core–Sheath Structures for Tissue Engineering. *Biomacromolecules*, 17(4):1365–1375, April 2016. 31
- [151] Su A Park, In Ae Kim, Yong Jae Lee, Ji Won Shin, Chong-Rak Kim, Jeong Koo Kim, Young-Il Yang, and Jung-Woog Shin. Biological responses of ligament fibroblasts and gene expression profiling on micropatterned silicone substrates subjected to mechanical stimuli. *Journal of Bioscience and Bioengineering*, 102(5):402–412, November 2006. 31
- [152] SangJun Moon, Syed K. Hasan, Young S. Song, Feng Xu, Hasan Onur Keles, Fahim Manzur, Sohan Mikkilineni, Jong Wook Hong, Jiro Nagatomi, Edward Haeggstrom, and others. Layer by layer three-dimensional tissue epitaxy by cell-laden hydrogel droplets. *Tissue Engineering Part C: Methods*, 16(1):157–166, 2009. 31
- [153] Edward Kang, Gi Seok Jeong, Yoon Young Choi, Kwang Ho Lee, Ali Khademhosseini, and Sang-Hoon Lee. Digitally tunable physicochemical coding of material composition and topography in continuous microfibres. *Nature Materials*, 10(11):877–883, September 2011. 31
- [154] Tyler K Merceron, Morgan Burt, Young-Joon Seol, Hyun-Wook Kang, Sang Jin Lee, James J Yoo, and Anthony Atala. A 3d bioprinted complex structure for engineering the muscle–tendon unit. *Biofabrication*, 7(3):035003, June 2015. 31

Chapter 2

Methods and materials

“Like so many things, it is not what’s outside, but what is inside that counts.”

The Merchant in *Aladdin*

Abstract

In this chapter, the home-made experimental set-up of extrusion is first presented and its main parts are detailed. Moreover, we quantified the new device’s performances and limits. Then, the physical bases of rheological and mechanical testing are explained and the experiments’ parameters are given. In a second part, the materials used in the following studies are described: collagen type I, sodium alginate and collagen-alginate mixtures. The solutions’ purification, preparation and their physico-chemical properties are reported here.

Contents

2.1	Methods	47
2.1.1	Extrusion set-up	47
2.1.1.1	Key constituent part: the needle	48
2.1.1.2	Set-up performances and limits	52
2.1.1.3	Conclusion	59
2.1.2	Rheological testing of polymer solutions	60
2.1.2.1	Physical basis	60
2.1.2.2	Rheometer geometries	67
2.1.3	Mechanical testing of extruded threads	69
2.2	Materials	71
2.2.1	Collagen solutions	71
2.2.1.1	Collagen type I and its fibrillogenesis	71
2.2.1.2	Chemical properties	73
2.2.1.3	Collagen solutions preparation	75
2.2.1.4	Collagen extraction and purification	75
2.2.1.5	Collagen solutions dosage	76
2.2.1.6	Collagen solutions purity	77
2.2.1.7	Collagen solutions concentration	78
2.2.2	Model system: sodium alginate	79
2.2.2.1	Structure	79
2.2.2.2	Chemical properties	79

2.2.2.3	Solution preparation	82
2.2.3	Collagen-alginate mixtures	83
2.2.3.1	Chemical properties	83
2.2.3.2	Solution preparation	84
2.3	References	85

2.1 Methods

2.1.1 Extrusion set-up

As mentioned above in section 1.2.2, extrusion consists in forcing a material to pass through a die. This method allows either to produce threads as in the textile industry and in tissue engineering (3D printing) or to study instabilities as in the microfluidics field. To fulfill the present goal, we built an in-home extrusion apparatus. This tailored set-up is designed as follows:

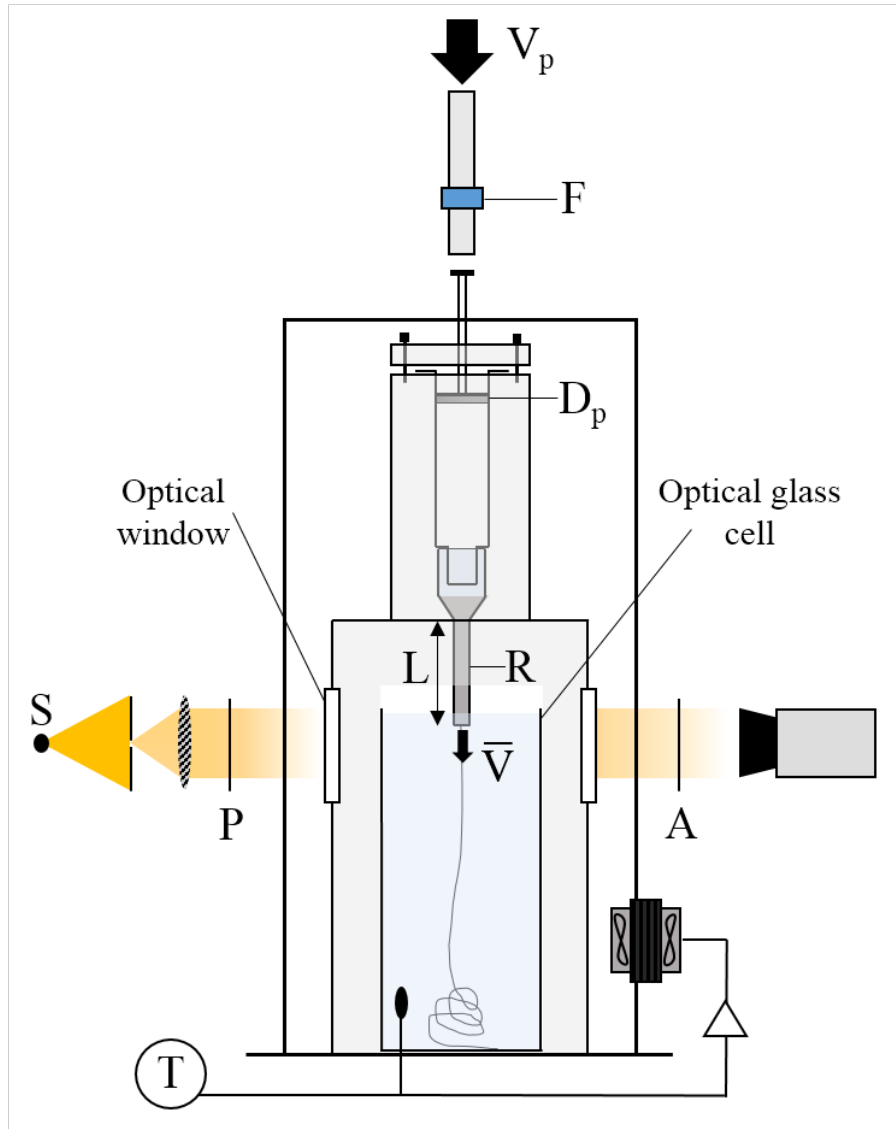


Figure 2.1: Scheme of experimental set-up of extrusion

A steel rod is clamped to a stepping motorized stage which imposes its velocity v_p ranging from 0 to 2000 $\mu\text{m/s}$. A load cell LCM201 Series from OMEGA (Fig 2.1, dark blue rectangle) was calibrated in tension for compression ranging from 100 N to 500 N. It is connected to an on-line transducer in order to assess the force F applied on the syringe piston. During the extrusion of our complex fluids, forces of 10 to 50N are reached. A syringe (Terumo) of 1 mL contains the fluid to be extruded. It has an inner diameter equal to the piston diameter D_p of 4.45 mm. Metallic needles, glass capillaries or PTFE tubings with characteristic length L and inner radius R are set at the syringe end.

A steel structure is fabricated to hold the syringe and its capillary vertically. It is composed of a cylindrical piece, which is shaped to fit tightly the syringe and a second piece to insert the optical glass cell (Hellma) containing the extrusion bath. This one can be removed so as to collect the extruded thread at any time during the process, while keeping the syringe in place. Holes are drilled on the last piece to create optical windows. The whole set-up is put inside a temperature controlled enclosure.

An optical mounting is added to observe the extrusion in real-time. A quasi-parallel beam is created with a light source (S) limited by a diaphragm placed at the focal length of a convergent lens. A polarizer (P) and an analyzer (A) are inserted so that the birefringence of the stressed fluid can be observed. The light beam illuminates the glass cell and the extrusion flow is followed thanks to a video camera equipped with a macro-objective and placed on the other side. Acquisition speeds of 600 frames/s can be reached. This optical system allows us to obtain extrusion images of a high contrast level as shown in Figure 2.2. It allows us to distinguish clearly small changes of the refractive index as well as other structural particularities.

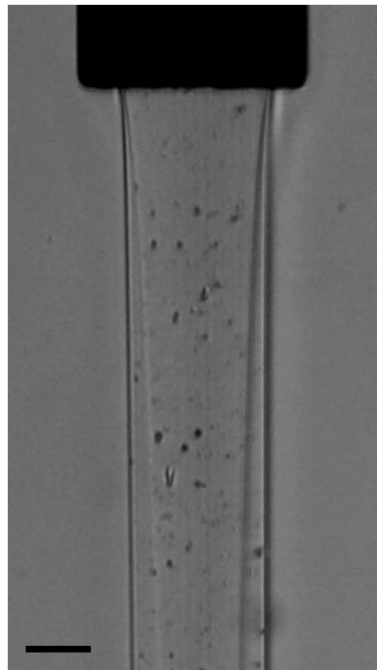


Figure 2.2: Example of an extrusion in a solution bath at the needle exit. The black rectangle is the needle exit. It is possible to see the gelation front ("black" region) growing progressively from the flow outside. Scale bar = 200 μ m

The motorized rod stage, the load cell signal and the camera are piloted by a program interface made by Olivier Ronsin to synchronize and control them easily.

2.1.1.1 Key constituent part: the needle

Our set-up allows us to control almost all the physical parameters of the extrusion such as the piston velocity, die diameter, temperature as well as chemical parameters by adjusting the collecting bath nature. Moreover, an other set-up part can be adapted to control more sensitive aspects of the extrusion as the die exit material. In fact, the die exit consists in an empty hose in which the fluid from the syringe will pass through. Along the die, this fluid will interact with the walls die. This interaction is governed by the hose material dimensions, composition and the fluid nature.

Thanks to our experimental set-up, the syringe exit can be changed and thus the material of the hose too. In the microfluidics field, typical set-up do not display such adaptability. Indeed, the polydimethylsiloxane (PDMS) is the major component used for the fabrication of devices to study flow physics. Even if some coating processings (gase-phase, plasma, sol-gel...) can be used to modify the PDMS surface nature, those strategies are not very convenient to implement [1]. In our case, hoses made of different materials (stainless steel, glass or PTFE) will be prepared and used as detailed in the following section.

2.1.1.1.1 Metallic needles

Sterile stainless steel needles with a normalized Luer nozzle were purchased from Sterican (BRAUN) and Fine-ject. Several gauges were available from 18G to 27G. A large gauge corresponds to a small diameter. Table 2.1 presents the needle characteristic dimensions supplied by the manufacturer.

Length (mm)	Outer diameter (μm)	Inner diameter (μm)	Gauge
20	400	220	27G
25	450	240	26G
25	500	250	25G
30	600	390	23G
30	700	460	22G
50	800	500	21G
120	800	500	21G
40	900	650	20G
40	1100	780	19G

Table 2.1: Chacteristic dimensions of stainless steel needles

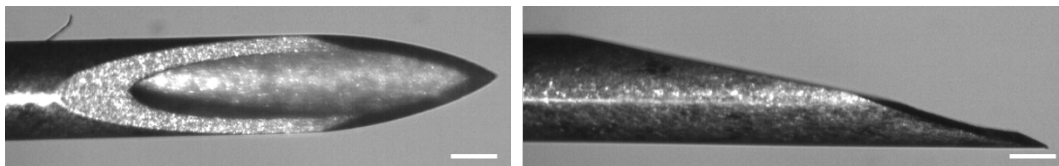


Figure 2.3: Example of a 23G needle tip, Scale bar = 250 μm

These hypodermic needles exits present almost 3 angles (2.3). The aim of this geometry is to ease penetration with less painful puncture for example during an injection or a blood sampling. In our case, this makes the extrusion study at the exit more complicated. This is why, needles were recustomized in the laboratory in order to remove the sharp lancet point and obtain a blunt tip.

For this, the needle is fixed to a support and mounted on the saw machine to cut the sharp lancet point with the diamond wire (Fig 2.4,1). The cut-needle is placed into a glass tube of the same height and sealed on its basis on a glass slide (Fig 2.4,2). The whole system is put in the heat chamber at 110 °C. A mixture of beeswax and rosin previously prepared and heated at the same temperature is filled into the glass tube(Fig 2.4,3). It is cooled at room temperature and the excess of resin is removed. The glass tube containing the needle can be handled and place in contact with a polishing lathe (Fig 2.4,4) coated with silicon carbide powder (abrasive element). The needle extremity is polished until

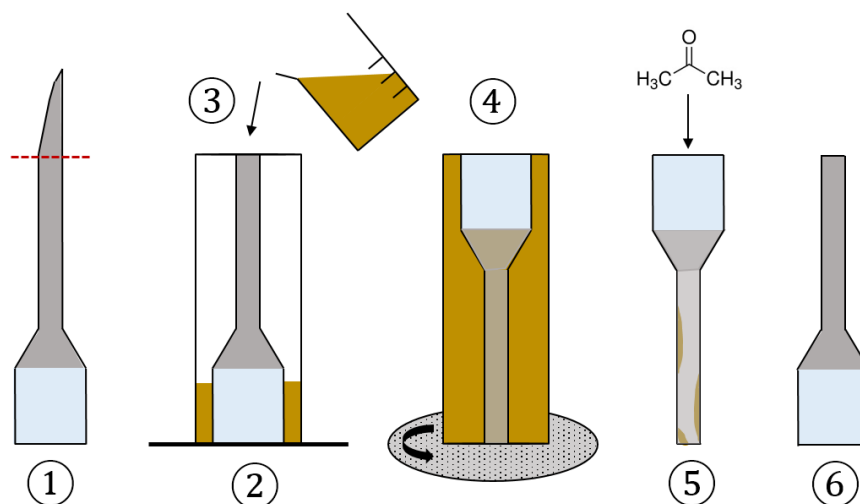


Figure 2.4: Protocol of blunt needles fabrication. 1) Cutting the sharp lancet point, 2) Needle installation for 3) Resine embedding, 4) Exit polishing, 5) Acetone cleaning to remove resin remains, 6) Needle with blunt tip

its edges are smooth, which is controlled by optical microscopy. Finally, the glass tube is removed and the blunt needle is washed with acetone to bring out resin remains (Fig. 2.4,5). The needle obtained is finally ready for use (Fig 2.4,6).

Similar procedures will be adapted to create glass capillaries of different diameters and structures as shown in the following part.

2.1.1.1.2 Glass capillaries

Borosilicate glass capillaries were purchased from CM Scientific. The outer diameter was chosen in order to be compatible with the inner diameter of stainless steel needles. In fact, the plastic extremity (Luer nozzle) of the needle is essential to be mounted on the syringe. The idea is to keep this part and to insert the glass capillary inside. Therefore glass capillaries with inner diameter of 200, 300 and 500 μm , outer diameter of respectively 330, 400 and 700 μm , were chosen.

Needles are cut at 1 cm of the input extremity with diamond wire saw (Fig 2.5 1)). Capillaries are cut to the desired length with a diamond-point and put inside the needle. The cut extremity was inside the needle and the manufactured one outside to have a clean blunt exit. The connecting point is glued and sealed horizontally with araldite (Fig 2.5 2)). The whole system is dried at room temperature overnight.

To study the input effect during the extrusion, combination of glass capillaries were fabricated. As shown in Figure 2.5 a) and b), two capillaries of different diameters were affixed to create either a branch narrowing or expansion.

Other strategies were performed to study the effects of the capillary inner surface or of the exit edges. For the first one, glass capillaries were put close to a hydrofluoric acid (HF) solution at 1% during several hours. By capillary action, the HF solution goes up to a certain height, given by the Jurin's law and react with the borosilicate glass. The idea is to control the height of the treatment and to make the inner surface more porous in order to change the fluid/capillary interaction. However, no clear effects were observed and this approach was not followed up.

For the second one, to study the effect of the sharp edges of the capillary extremity, MF-

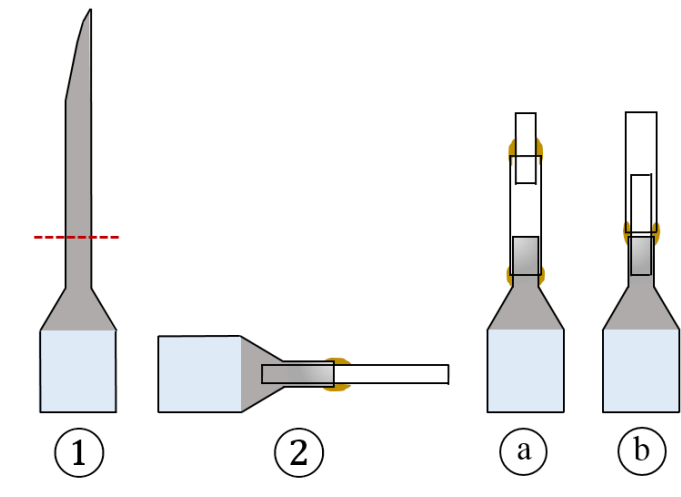


Figure 2.5: Protocol of glass needles fabrication. 1) Cutting the sharp lancet point, 2) Capillary installation and sealing with araldite, different configurations of a) narrowing and b) expansion capillaries

microforge at the laboratory *Matière et Systèmes Complexes, Paris 7* was used to fire-polish those singularities. Briefly, the glass capillary tip is heated close to the resistive electrical heating element and brought to a temperature where its surface melts. As a consequence, the glass tip becomes smooth. However, the heating seems to be too intense for those capillaries as it leads to a diameter narrowing. Some extrusions were tested with those new capillary but will not be detailed in the following chapter.

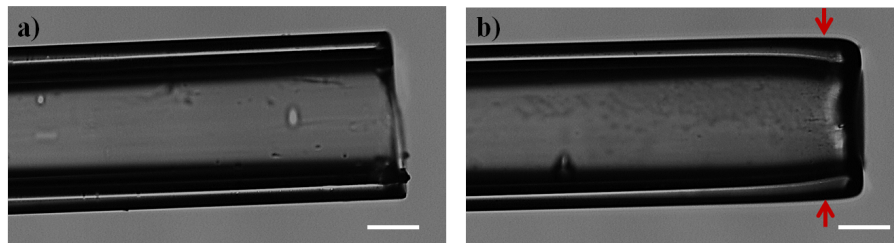


Figure 2.6: Microscope images of a) 200 μm capillary extremity without any treatment, b) Fire-polished 200 μm capillary tip. Scale bar = 100 μm

To go further in the study of the fluid/material interaction, the question of the wetting of the surface arises. Indeed, stainless steel needles and borosilicate glass are both hydrophilic materials. The idea was to study the extrusion of the fluid against a hydrophobic surface in order to lower the wall frictions and for this, we chose Teflon.

2.1.1.1.3 PTFE tubing

Polytetrafluoroethylene (PTFE, Teflon) tubing purchased from Adtech Polymer Engineering were used. The same procedure as for glass capillaries (Fig. 2.5) was performed to obtain capillary of PTFE tubing. The PTFE tubing chosen has an inner diameter of 300 μm and an outer diameter of 760 μm . As the araldite does not stick to the Teflon, the connecting point was sealed with Parafilm M.

An unexpected property of the PTFE was a great surprise during the first test with this type of capillary. In fact, the contrast obtained with the optical system is clearly enhanced

when PTFE tubing is used, making details easier to distinguish the tubing. This is due to the refractive index of the PTFE. In fact, it is close to the one of the water. For the same wavelength of 589.29 nm and temperature (20 °C), the refractive index of PTFE is 1.35 – 1.38 and 1.33 for the water. Compared to the borosilicate refractive index (1.47), PTFE tubing thus ensures a better insight of what is happening in the capillary, and helps to better understand extrusion phenomena.

2.1.1.2 Set-up performances and limits

Our experimental set-up of extrusion allows us to impose the velocity of the piston, i.e. the throughput. As for a capillary rheometer, the force applied on the piston is measured, in our case, with the load cell presented previously. The steady state is achieved when the force signal (monitored in real-time) becomes constant. In the following part, the different conditions to reach a steady flow regime will be described.

2.1.1.2.1 Friction behavior

During the extrusion experiments, force signal oscillations are observed for a restricted range of v_p values. This was first attributed to extrusion instability akin to the spurt-flow instability which manifests itself by periodic relaxation oscillations of the force. However, no flow instability was discerned at the capillary exit. To assess the origin of those signal fluctuations, we performed extrusion with an empty syringe (air), or a syringe filled with either distilled water or Rhodorsil® Oils 47V1000 (polydimethylsiloxane oils) at different piston speeds and registered the respective force signal. No capillary was mounted on the syringe. The results obtained for piston velocities of 100 and 500 $\mu\text{m/s}$ are presented in the following Figure 2.7:

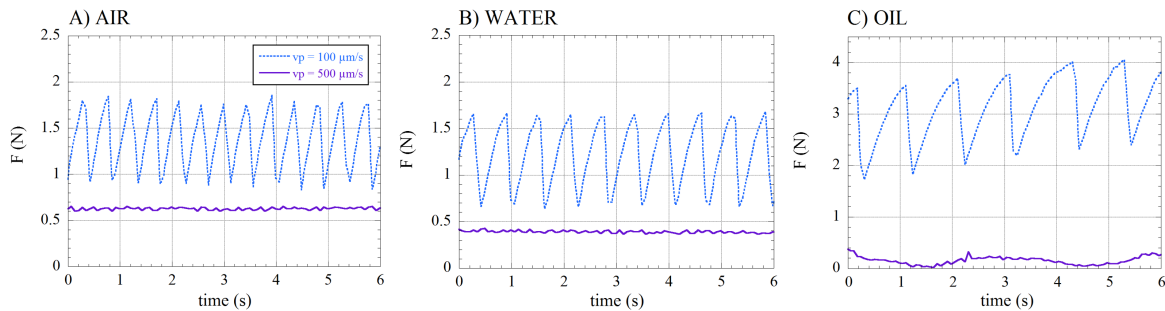


Figure 2.7: Force signals registered during the extrusion of a) Air, b) Water and c) Oil, made without capillaries at piston velocity of 100 $\mu\text{m/s}$ (dotted blue) and 500 $\mu\text{m/s}$ (purple) .

For all conditions, the force signal is constant at about 0.5 N at $v_p=500 \mu\text{m/s}$. At 100 $\mu\text{m/s}$, periodic oscillations of 1N are clearly observed even with the empty syringe. Those fluctuations are composed of two phases: a first one characterised by a slow force relaxation increase and a second one by an instantaneous decline. This can only be due to the piston frictions against the walls of the syringe. In fact, the piston rod extremity (in black, Fig. 2.8, 1)) composed of a thermoplastic latex-free elastomer is ultra-flexible to perfectly fit the inner diameter of the syringe and to create a tight seal. It plays the role of a spring. [2]

It is known that stick-slip can be suppressed either by stiffening the system or by lubricating i.e by replacing solid friction (with a threshold) by a viscous friction [3]. The inner surface of the syringe is lined by silicone oil. Despite the presence of this lubricant,

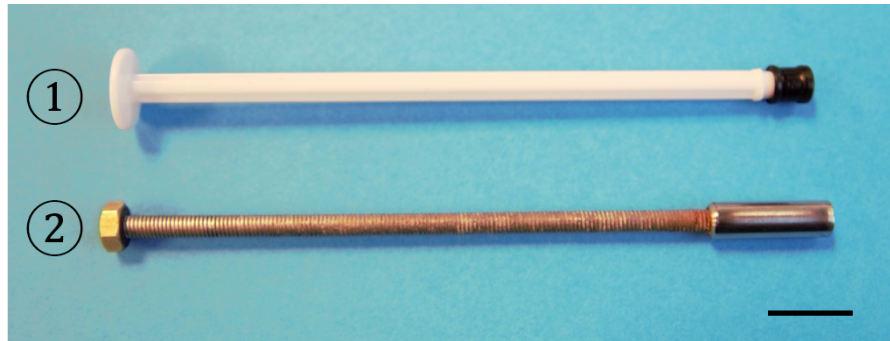


Figure 2.8: Image of 1) Terumo piston and 2) Home-made Dural piston. Scale bar = 1 cm.

stick of this piston extremity may occur. Thus, when the piston sticks to the syringe inner surface, the force signal increases and when it slips, the force signal decreases etc. This phenomenon happens for velocities ranging typically from 25 to almost 150 $\mu\text{m/s}$. As a consequence, extrusion study is not sufficiently reliable for this range of piston velocity. To assess those velocities and use the entire available velocity range, the second solution of stiffening the system is selected. To do so, a home-made Dural piston is produced (Fig. 2.8, 2)). This new piston is used for extrusion of alginate solutions of low concentration ($\leq 4\%$ (w/w)). For higher concentrations of alginate or for collagen solutions, the commercial piston is kept because no stick-slip is observed and furthermore in the second case sterility must be ensured.

2.1.1.2.2 Steady flow regime conditions

In order to study the different flow instabilities at the die exit, a steady state regime must be reached. In the following part, the different conditions to reach this regime will be described.

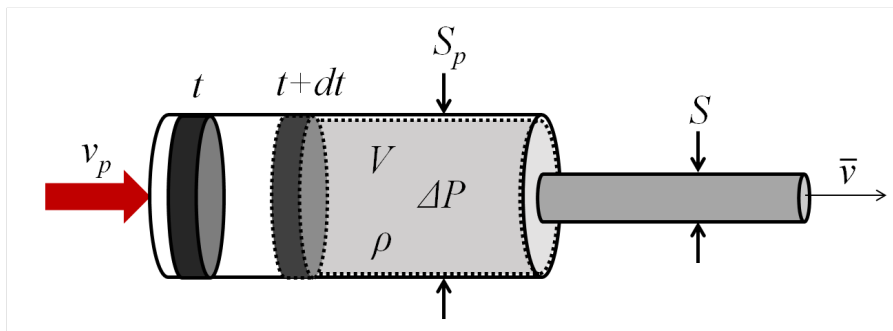


Figure 2.9: Scheme of the { syringe + capillary} system and the characteristic variables. A syringe is filled with a volume V of a solution with a density ρ . During the time t and $t + dt$ the piston (left dark gray) of section S_p advances at the velocity v_p and forces the solution at the pressure ΔP to pass through the capillary of section S and exit at the velocity \bar{v}

Figure 2.9 displays the variables of our system. A global characteristic of the exit flow rate in the capillary is the average velocity \bar{v} defined from the volumic throughput Q and related by: $\bar{v} = Q/(\pi \times R^2)$. As previously mentioned, the velocity v_p is imposed by the piston motion. However, due to the finite compressibility of the syringe and the fluid, \bar{v} will be not imposed instantaneously when imposing v_p . Indeed, a transient regime occurs during a time τ before the steady state is reached. During the time τ , a significant

portion of the fluid could be wasted. It is thus of practical importance to understand the parameters affecting τ .

Between t and $t + dt$, the mass entering in the capillary: $\rho v_p S_p dt$ is not equal to the mass emerging from the capillary: $\rho \bar{v} S dt$ as given by the continuity principle. The volume change of the fluid under pressure in the syringe must be taken into account and is written as $\frac{d(\rho V)}{dt}$. Moreover, as the capillary volume is small compared to the syringe volume, its compressibility will not be significant. All the parameters are defined as described in Figure 2.9. It can thus be written:

$$\rho \times v_p \times S_p = \rho \times \bar{v} \times S + \frac{d(\rho V)}{dt} \quad (2.1)$$

We are seeking to express the velocity \bar{v} . The steady state solution is known and given by:

$$\bar{v}(\infty) = v_p \times \frac{S_p}{S}$$

During dt , the energy due to the compression is stored either by creating volume or by compressing the fluid containing air bubbles. This is why, the syringe compliance $\chi_{syringe}$ and the fluid compressibility χ_{fluid} can be defined as:

$$\begin{aligned} \chi_{syringe} &= \frac{1}{V} \times \frac{dV}{dP} \\ \chi_{fluid} &= \frac{1}{\rho} \times \frac{d\rho}{dP} \end{aligned}$$

Thus, ρV may vary with an increase of ΔP and we can write:

$$\begin{aligned} \frac{d(\rho V)}{dt} &= \rho \frac{dV}{dt} + V \frac{d\rho}{dt} \\ &= \rho V \times (\chi_{syringe} + \chi_{fluid}) \times \frac{d(\Delta P)}{dt} \end{aligned}$$

An effective compressibility is defined as: $\chi_{eff} = \chi_{syringe} + \chi_{fluid}$ and the equation 2.1 becomes:

$$v_p \times S_p = \bar{v} \times S + V \times \chi_{eff} \times \frac{d(\Delta P)}{dt}$$

By introducing $\bar{v}(\infty)$:

$$\bar{v} + \frac{V \times \chi_{eff}}{S} \times \frac{d(\Delta P)}{dt} = \bar{v}(\infty) \quad (2.2)$$

However, the velocity \bar{v} depends on the pressure ΔP and is related to it via the relationship:

$$\Delta P = R_H \times \bar{v} \times S$$

where R_H is the hydraulic impedance for newtonian fluids and is a function of the throughput Q hence of \bar{v} .

In the case of a Newtonian fluid, R_H is constant and equation 2.2 becomes:

$$\bar{v} + V \times \chi_{eff} \times R_H \times \frac{d(\bar{v})}{dt} = \bar{v}(\infty) \quad (2.3)$$

We can thus define the system capacitance C as $V \times \chi_{eff}$ and deduce the time τ via a "RC" circuit analogy:

$$\tau = R_H \times C$$

The solution of equation 2.3 is given by:

$$\bar{v}(t) = \bar{v}(\infty) \times (1 - e^{-\frac{t}{\tau}}) \quad (2.4)$$

At **low throughput**, we measured the characteristic time τ by recording signal force during an extrusion as presented in Figure 2.10 (left).

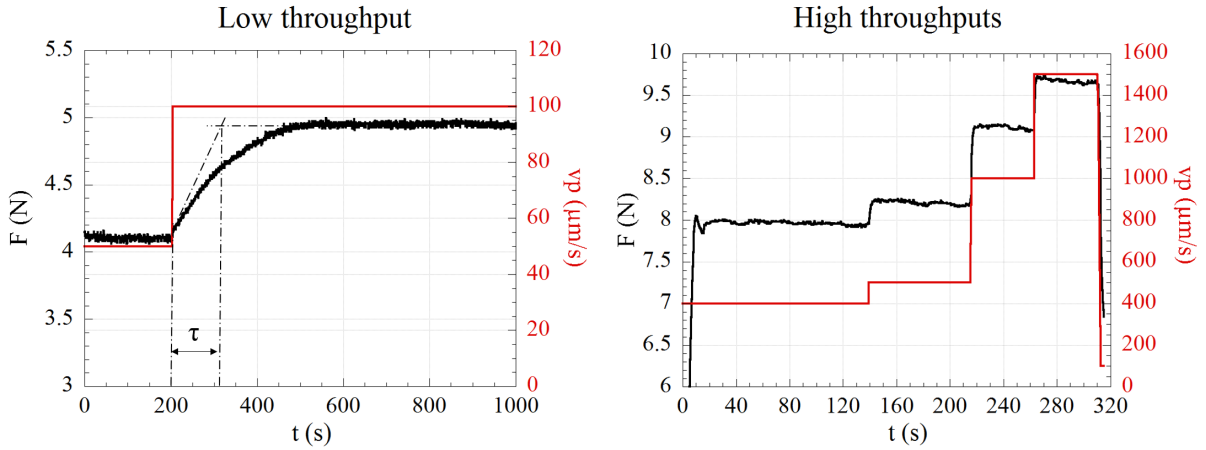


Figure 2.10: Force signals (black) and their respective piston velocities (red) over the time obtained for alginate solution extrusions at: low throughput (left) and high throughput (right). For low velocities, the force signal becomes constant after a characteristic time τ (left) whereas it is immediate (right) at high velocities.

At $v_p = 100 \mu\text{m/s}$, the transient regime is clearly observed and the steady state is reached after a time τ about 100s. At low speed, it is also possible to calculate the hydraulic resistance R_H .

– Hydraulic resistance R_H

The hydraulic resistance is determined by the Hagen-Poiseuille equation in the case of a laminar flow and a Newtonian fluid. In our case, the Reynolds number Re is defined as:

$$Re = \frac{\rho \bar{v} R}{\eta}$$

with ρ the fluid density, η the dynamic viscosity in Pa.s. Typical values for our system are: $\rho = 1000 \text{ kg/m}^3$; $\bar{v} = \text{few cm/s}$, R of $250 \mu\text{m}$ and η around 30 Pa.s . Thus, Re is about $10^{-4} \ll 1$, which means that the fluid flow is laminar. The Hagen-Poiseuille equation can be used:

$$R_H = \frac{8\eta L}{\pi R^4} \quad (2.5)$$

where L is the capillary length of 3 cm , R about $250\ \mu\text{m}$ and η around $30\ \text{Pa}\cdot\text{s}$. In this case, the hydraulic resistance is: $R_H = 5.8 \times 10^{14}\ \text{Pa}\cdot\text{s}\cdot\text{m}^{-3}$.

From the characteristic time τ and the hydraulic resistance values, we can estimate the effective compressibility of the fluid in the Newtonian regime.

– **The effective compressibility χ_{eff}**

The compressibility of liquids is of the order of $10^{-10}\ \text{Pa}$ at room temperature. We can estimate the effective compressibility χ_{eff} from the different physical parameters of our set-up by:

$$\chi_{eff} = \frac{\tau}{V_{tot} R_H}$$

where τ is about $100\ \text{s}$, V_{tot} the total volume considered of $0.2\ \text{mL} = 2 \times 10^{-7}\ \text{m}^{-3}$ and the hydraulic resistance R_H previously calculated: $5.8 \times 10^{14}\ \text{Pa}\cdot\text{s}\cdot\text{m}^{-3}$. The effective compressibility is $\chi_{eff} = 10^{-6}\ \text{Pa}^{-1} \gg \chi_{liquids}$. In microfluidics, this can be explained by the die deformability. In our case, the syringe deformability is negligible. Another possible explanation could be the presence of air in the liquid. In fact, some air bubbles may be entrapped in our solutions (Fig. 2.11). This raises the question of the effect of those air bubbles on the fluid compressibility.

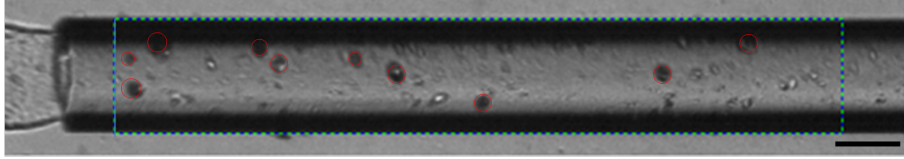


Figure 2.11: Image of extrusion with a glass capillary. Air bubbles are entrapped in the alginate solution. The volume V of interest is represented by the dotted line rectangle. Scale bar = $200\ \mu\text{m}$

We estimated the air bubbles volume V_{air} in a sodium alginate solution passing in a glass capillary of $100\ \mu\text{m}$ radius by measuring the bubbles diameter (Fig. 2.11, red circles) in a delimited solution volume V (Fig. 2.11, dotted rectangle). We obtained:

$$V_{air} = 0.03 \times V$$

The fluid compressibility is related to the air volume fraction ϕ_{air} and the pressure P by:

$$\chi_{fluid} = \frac{\phi_{air}}{P}$$

where $\phi_{air} = 3 \times 10^{-2}$ and P is considered as equal to the atmospheric pressure of $10^5\ \text{Pa}$. We thus obtain a fluid compressibility of $3 \times 10^{-7}\ \text{Pa}^{-1} \gg \chi_{water}$.

Thus, at low throughputs, characteristic physical quantities as the hydraulic resistance and the effective compressibility were calculated. χ_{eff} values seem to be overestimated and other parameters might be taken into account to explain this order of magnitude. Typical time of about $100\ \text{s}$ are observed before reaching steady state at low velocities.

At higher throughputs, the syringe would be empty before reaching a steady state. Fortunately, due to the shear thinning (viscosity decreases while increasing shear rate) behavior

of our solutions, the hydraulic resistance R_H decreases markedly as the throughput Q increases. The steady state regime is reached quasi-instantaneously as observed in Figure 2.10 (right).

To conclude, steady state regime is reached after waiting almost 100s at low throughput and few seconds for high throughput. While this signal remains constant and for laminar flows, the average velocity \bar{v} will be calculated as:

$$\bar{v} = v_p \times \left(\frac{D_p}{2 \times R} \right)^2 \quad (2.6)$$

2.1.1.2.3 Pressure drop

The pressure drop in a capillary rheometer is the difference between the pressure values measured respectively upstream (reservoir) and downstream (extrudate):

$$\Delta P = P_{up} - P_{down}$$

$$\text{with: } P_{up} = \frac{F - F_{friction}}{\pi R_{piston}^2}$$

$$\text{and: } P_{down} = p_0$$

where p_0 is the atmospheric pressure and $F_{friction}$ estimated as the force on the piston which remains when the solution is extruded without any capillary. The pressure drop is then assumed to be negligible.

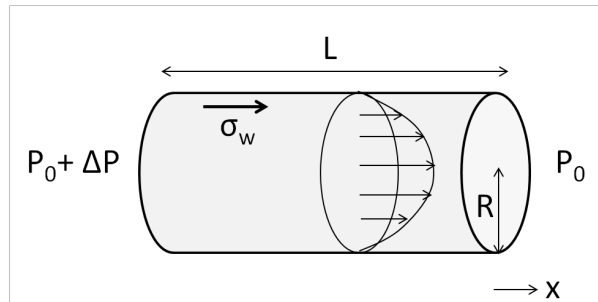


Figure 2.12: Scheme of a cylinder pipe of length L and radius R . The flow velocity is represented by the arrows and the wall shear rate σ_w acting on the lateral wall.

For example, in the case of a newtonian fluid the Hagen-Poiseuille relationship holds between ΔP and the throughput Q . In the following, we will make use of the average shear rate $\bar{\dot{\gamma}}$ (rather than Q) and the wall shear stress σ_w (rather than ΔP). These quantities are defined as:

$$\bar{\dot{\gamma}} = \frac{\bar{v}}{R} = \frac{Q}{\pi R^3}$$

and, σ_w :

$$\sigma_w = \frac{\Delta P R}{2 L}$$

The latter results from the momentum balance in steady flow (Fig. 2.12):

$$(\Delta P + P_0)\pi R^2 - P_0 \pi R^2 - \sigma_w \times 2\pi RL = 0$$

with R and L respectively the radius and length of the pipe.

The figure 2.13 displays the experimental rheological characteristics $\sigma_w(\dot{\gamma})$ obtained for ALG4 through glass capillaries of different radii.

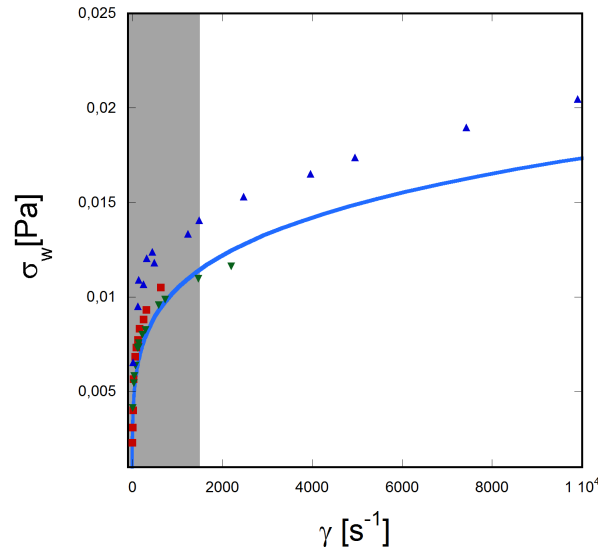


Figure 2.13: Wall shear stress as a function of shear rate for glass capillaries of different radii: $R = 100$ (blue), 150 (green) and 250 (red) μm . The blue curve has been computed from the Cross law [?] extrapolated from the range of shear rates accessible in the cone-plate rheometer (shadowed zone)

Since the range of shear rates relevant to the capillary rheometer is much larger than the one accessible for the cone plate rheometer, one may wonder whether it is legitimate to extrapolate the Cross law (well fitting the rheometer data) to the wider range. We have therefore calculated $\sigma_w(\dot{\gamma})$ for the Cross law. This means integrating:

$$\dot{\gamma} = \frac{dv}{dr}$$

with:

$$\begin{cases} \sigma(r) = \frac{\Delta P r}{2 L} \\ \sigma(r) = \eta(\dot{\gamma}) \times \dot{\gamma} \\ v(r) = 0 \text{ no slip hypothesis} \end{cases} \quad (2.7)$$

The integration must be performed numerically for the Cross law. However, it is interesting to have a look at the analytical solution corresponding to a "power law" fluid with $\eta(\dot{\gamma}) \sim \dot{\gamma}^{m-1}$ (Fig. 2.14).

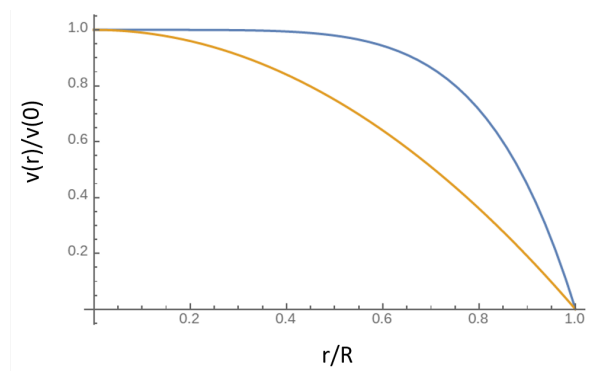


Figure 2.14: Velocity profiles for the flow of a fluid obeying a power law. Orange: $m = 1$, Blue: $m=0.8$

In this case: $v(r) = v_{max}(1 - (r/R)^\alpha)$ with $\alpha = \frac{(3-m)}{(2-m)}$. For a newtonian fluid ($m = 1$), one recovers the Poiseuille parabolic profile (for which $\sigma_w = \eta_0 \dot{\gamma}_0 (\dot{\gamma}/\dot{\gamma}_0)^n$). For lower m values, (Fig. 2.14, blue), the profile is flat over a large part of the capillary, therefore exhibiting a central plug-like flow (Fig. 2.14). When solving for $v(r)$ using the full rheological law (including the newtonian plateau) one finds that the profile evolves from the parabolic one when $\bar{\dot{\gamma}} \ll \dot{\gamma}_0$ to the power law profile when $\bar{\dot{\gamma}} \gg \dot{\gamma}_0$. Thus, from the profile $v(r)$ one can compute $\bar{\dot{\gamma}}$, $\dot{\gamma}_w$ the shear rate at the wall under no slip condition, hence $\sigma_w = \dot{\gamma}_w \times \eta(\dot{\gamma}_w)$

$$\dot{\gamma}_w \approx 5 \frac{\bar{v}}{R}$$

The pressure drop is thus quite well estimated as it gives a correct indication of pressure magnitude. Moreover, the last definition will allow us to compute the Weissenberg number for our extrusion experiments.

2.1.1.3 Conclusion

Our experimental set-up of extrusion is designed either to study extrusion instabilities origin and morphologies or to produce threads in a reproducible manner thanks to the stepping motorized rod stage. Even if the depth of focus is not sufficient to perform velocimetry measurements, the optical set-up allows us to observe with a high contrast the extrusion directly through the bath.

The particular strengths are also its adaptability as the die material and the bath can be changed, even during extrusion for the second one and its performance. Indeed, the set-up allows us to produce threads very rapidly, around several meters in few minutes.

Few set-up limitations were identified and yet analyzed in order to overcome those drawbacks before the extrusion flow studies. In fact, piston friction was observed and a new metallic one was made to remove this parasitic phenomenon. Air bubbles entrapped in the solution will be useful passive tracers in Chapter 4. The steady state regime was seen to be reached after almost 100s at low throughput. However, thanks to shear-thinning properties of our solutions, this time is close to zero at high throughput and avoids to have empty syringe before reaching the steady state. Thus, those limits are turned into

advantages and may not impact further studies. Finally, the pressure drop was estimated, giving us a correct indication of pressure magnitude.

2.1.2 Rheological testing of polymer solutions

2.1.2.1 Physical basis

Rheology is the part of the mechanics that studies elasticity and flow characteristics of a material. For the flow characteristics of a fluid, two types of experiments can be performed: the shear flow and the oscillatory shear flow that we will describe first. To characterize a solid, elongation tests are performed to assess physical quantities such as the Young Modulus.

2.1.2.1.1 Shear flow

A simple case to define the different physical quantities at play in a fluid between two parallel plates subjected to a shear stress σ is depicted in Figure 2.15:

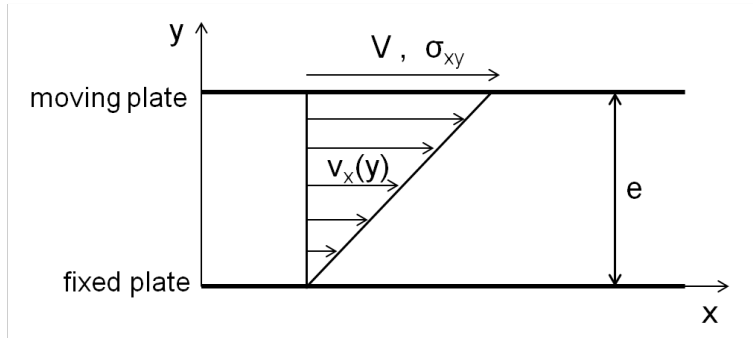


Figure 2.15: Velocity profile for a single shear flow of a newtonian liquid between two parallel plates. The upper plate is moving at a constant velocity V . The shear rate $\dot{\gamma}$ is constant along the y -axis, and is equal to: $\dot{\gamma}(y) = \frac{\partial v_x(y)}{\partial y}$. The tangential shear stress σ_{xy} is applied along the x -axis on a fluid layer surface whose normal vector \mathbf{n} is along the y -axis.

The lower plate is fixed, and the stress σ (Pa) is applied on the upper plate which then moves at a speed V . This configuration is called planar Couette flow. In laminar flow regime, the liquid can be modeled by a succession of infinitely thin layers parallel to each other and parallel to the plates. The fluid deformation is carried out by successive sliding of the layers on each other by friction without matter transport from one layer to the other but with momentum transport. The boundary conditions under the "no slip" hypothesis well verified for simple fluids are $v_x(0) = 0$ and $v_x(e) = V$. The strain rate is defined as:

$$\dot{\gamma} = \frac{d\gamma}{dt}$$

In the case of planar Couette flow with no wall slip, it reads:

$$\dot{\gamma} = \frac{V}{e}$$

For an infinitely thin liquid layer, the local shear rate is defined as:

$$\dot{\gamma}(y) = \frac{\partial v_x}{\partial y}$$

The stress σ_{xy} is the tangential force per unit area applied on the liquid layer by the surrounding fluid. One defines the shear viscosity η as $\eta = \sigma_{xy}/\dot{\gamma}$. Generally, η depends on the shear rate, so that:

$$\sigma_{xy} = \eta(\dot{\gamma}) \dot{\gamma}$$

For a newtonian fluid, the viscosity η does not depend on the shear rate $\dot{\gamma}$ and the stress σ_{xy} is proportional to the shear rate $\dot{\gamma}$. In the case of a simple shear flow, σ_{xy} is constant over the thickness e by mechanical equilibrium between the different fluid layers. When, as in the case for many fluids, σ_{xy} is a monotonous increasing function of $\dot{\gamma}$, the shear rate is also constant over the thickness e in steady state regime.

Stress tensor

For a general flow (different from simple shear) and for more complex materials (viscoelastic), it is necessary to introduce the stress tensor which reveals all the forces applied on an element of fluid by the surrounding medium.

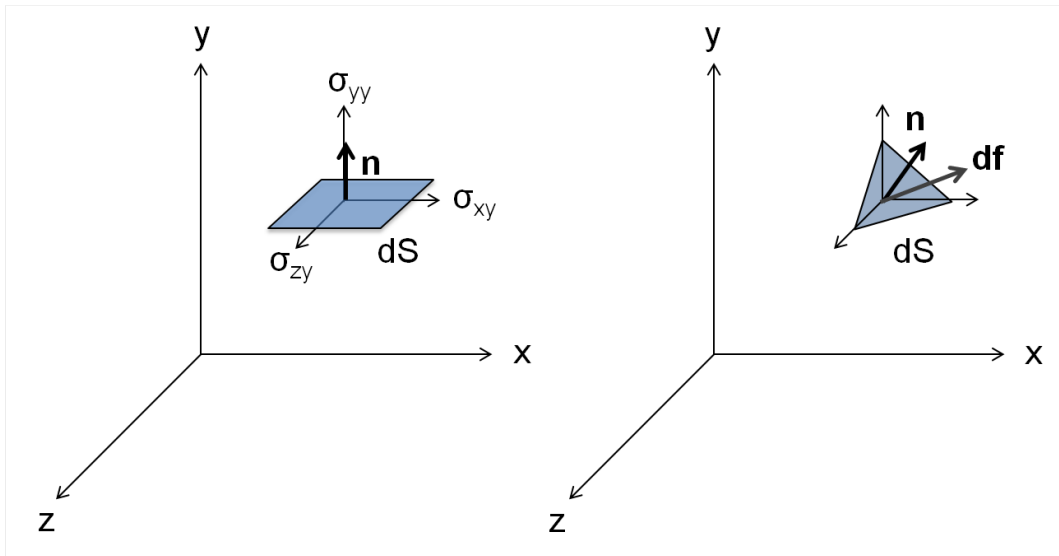


Figure 2.16: On the left: Stress components σ_{xy} , σ_{yy} and σ_{zy} applied on a surface dS with the normal \mathbf{n} oriented along the y-axis. On the right: Stress force $d\mathbf{f}$ acting on a surface dS with normal vector \mathbf{n} presents no specific orientation.

Considering a surface element dS placed horizontally: the normal \mathbf{n} to the surface dS is along the y-axis (Fig 2.16). A stress σ applied to this surface can be divided into three components along the x, y and z axes: there are respectively σ_{xy} , σ_{yy} and σ_{zy} . More generally, the notation σ_{ij} is used, where i is the stress direction and j the direction of the normal \mathbf{n} to the surface dS . The tangential stresses are σ_{xy} and σ_{zy} and the normal stress is σ_{yy} . For a force $d\mathbf{f}$ of any direction applied to the surface dS of normal vector \mathbf{n} , the stress $\sigma_{\mathbf{n}}$ applied to dS is written as:

$$\sigma_{\mathbf{n}} = \sigma \cdot \mathbf{n} = \frac{d\mathbf{f}}{dS}$$

In matrix notation:
$$\begin{pmatrix} \sigma_{xx} & \sigma_{xy} & \sigma_{xz} \\ \sigma_{yx} & \sigma_{yy} & \sigma_{yz} \\ \sigma_{zx} & \sigma_{zy} & \sigma_{zz} \end{pmatrix} \cdot \begin{pmatrix} n_x \\ n_y \\ z \end{pmatrix} = \frac{1}{dS} \times \begin{pmatrix} df_x \\ df_y \\ df_z \end{pmatrix}$$

σ is the total stress tensor and can be written as:

$$\sigma = \tau - p \delta \quad (2.8)$$

where p is the hydrostatic pressure, δ the Kronecker delta ($\delta = \delta_{ij}$, with $\delta_{ij} = 1$ if $i = j$ and 0 if $i \neq j$) and τ is the stress tensor of viscosity which appears when the fluid is moving. Under hydrostatic condition, normal stress $\sigma_n = -p$ only remains. The pressure p has a positive sign in the case of a traction. For a fluid at rest, the only non-zero terms of the tensor are the diagonal terms:

$$\sigma_{xx} = \sigma_{yy} = \sigma_{zz} = -p$$

2.1.2.1.2 Oscillatory shear flow

To simply explore the viscoelastic properties of a material in the linear response regime, it is sufficient to shear it in an oscillating manner. If the fluid sample is subjected to a sinusoidal strain of amplitude γ_0 and pulsation ω :

$$\gamma(t) = \gamma_0 e^{(i\omega t)}$$

The response stress $\sigma(t)$ is written as:

$$\sigma(t) = \sigma_0 e^{(i\omega t + \alpha)}$$

where α is the phase angle which allows the characterization of the material on a "viscoelasticity" scale. By analogy with the Hooke law, a complex modulus $\bar{G}(\omega)$ can be defined by:

$$\bar{G}(\omega) = \frac{\sigma(t)}{\gamma(t)} = \frac{\sigma_0}{\gamma_0} e^{(i\alpha)}$$

$$\bar{G}(\omega) = G'(\omega) + iG''(\omega)$$

NB: linearity implies that G does not depend of the magnitude of $\dot{\gamma}_0$. In practice, it can be achieved for small enough values of the shear rate.

This equation applies for small strains while the material structure is not modified. The total stress $\sigma(t)$ can be viewed as the combination of a viscous (imaginary) and an elastic (real) parts. Moreover, the real part of the complex modulus $\bar{G}(\omega)$, G' , refers to the in-phase component of the stress-strain relation and is associated to the elastic energy stored per unit of volume of the material during a deformation cycle. It is called the storage modulus or the elastic modulus. The imaginary part of the complex modulus, G'' , referring to the out-of-phase component is the loss modulus, or viscous modulus, associated to the viscous dissipation of energy. Those two parts are related by the phase shift α expressed as:

$$\tan(\alpha) = \frac{G''}{G'}$$

If the fluid is purely viscous the phase angle tends to 90° :

$$\begin{aligned} G'(\omega) &= 0 \\ G''(\omega) &= \eta \times \omega \end{aligned}$$

If the material is purely elastic, the phase angle will tend to zero.

$$\begin{aligned} G'(\omega) &= G \\ G''(\omega) &= 0 \end{aligned}$$

Maxwell model

The basic model for viscoelastic fluids is the Maxwell model. It consists in combining a linear elasticity and a linear viscosity models. For the linear elasticity model, it is postulated that the stress is proportional to the deformation (Hooke law), the coefficient of proportionality being the Young's modulus which is modeled by a spring of stiffness E . For Newtonian fluids, the stress is proportional to the deformation rate where the coefficient of proportionality is the viscosity η . This is modeled by a dashpot. By putting those two elements in series, we obtain the one-dimensional principle of the Maxwell model (Fig 2.17).

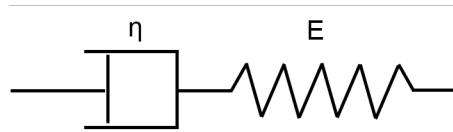


Figure 2.17: Scheme of a Maxwell liquid model: a viscoelastic fluid is modeled by a dashpot with a constant η which represents the viscous part put in series with a spring of stiffness E for the elastic part.

The spring and the dashpot obey respectively the Hooke law and the Newton law given by:

$$\begin{aligned} \sigma_s &= E \times \gamma_s \\ \sigma_d &= \eta \times \frac{d\gamma_d}{dt} \end{aligned}$$

where σ_i and γ_i are the respective stress and strain of spring (s) and dashpot (d). Equilibrium requires that the stress is the same in both elements which means: $\sigma = \sigma_s = \sigma_d$. Strains and shear rates are added:

$$\begin{aligned} \gamma &= \gamma_s + \gamma_d \\ \dot{\gamma} &= \frac{d\gamma}{dt} = \frac{d\gamma_s}{dt} + \frac{d\gamma_d}{dt} \end{aligned}$$

In the one-dimensional case, we thus obtain the following differential equation:

$$\sigma + \frac{\eta}{E} \frac{d\sigma}{dt} = \eta_M \dot{\gamma}$$

At the start of the stress-relaxation experiment, $t = 0$, and $\sigma(t=0) = \sigma_0$ is the initial stress. Solving the last differential equation, we obtain:

$$\sigma(t) = \sigma_0 e^{-\frac{E}{\eta} \times t}$$

The stress decays exponentially with a characteristic relaxation time λ defined as:

$$\lambda = \frac{\eta}{E}$$

The storage G' and loss G'' moduli are thus given by:

$$G' = E \times \frac{\omega^2 \lambda^2}{1 + \omega^2 \lambda^2}$$

$$G'' = E \times \frac{\omega \lambda}{1 + \omega^2 \lambda^2}$$

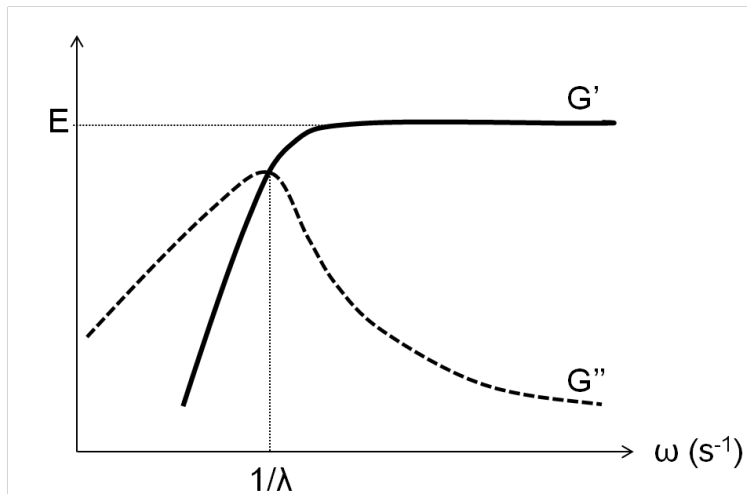


Figure 2.18: Maxwell fluid behavior for an oscillatory shear: the storage modulus G' (plain line) and the loss modulus G'' (dotted line) intersect at the pulsation $\omega = 1/\lambda$

At low frequencies, the loss modulus G'' is higher than the storage modulus G' (Fig 2.18). In this case, the viscous behavior is predominant and: $G' \propto \omega^2$ and $G'' \propto \omega$. When the frequency increases, G' tends to a plateau and G'' decreases rapidly; the elastic behavior is then predominant. At the intersection point, $G' = G''$ and $\omega\lambda = 1$.

Constitutive equations

To generalize linear models (Maxwell model) to non-linear behaviour models as for real fluids, the constitutive equation must be conformed to several principles [4]:

- **Principle of coordinates invariance:** the different constitutive variables (stress, strain, rates etc) must be expressed as tensors to ensure the invariance of the equation relationship from a coordinate frame to another (ex: Cartesian to Spherical coordinates)

- **Principle of invariance:** as a consequence from the previous principle, when passing the constitutive equation from a coordinate system to another, their orientation and scale must be invariant.
- **Principle of objectivity:** the deformation of a material is not affected by any frame rotation but only by the deformation itself.

This last principle is not applied in linear models. It is thus necessary to modify the linear Maxwell model by replacing the time derivative with an invariant one called the convected derivative:

$$\frac{D\sigma}{Dt} = \frac{\partial\sigma}{\partial t} + \overset{\nabla}{\sigma}$$

where

$$\overset{\nabla}{\sigma} = (v \cdot \nabla)\sigma - (\nabla v)\sigma - \sigma(\nabla v)^T$$

Frame invariant models are thus derived from linear one by writing the equation in a frame of reference that moves with a material element. The three most common frame invariant time derivatives are the upper- and lower-convected and the corotational time derivative. In the following, we will present the Upper Convected Maxwell, Oldroyd-B and White-Mezner models.

Upper-Convected Maxwell Model

The linear Maxwell model can be generalized for arbitrary flows by writing its frame-invariant analogue which is called the Upper-Convected Maxwell (UCM) model that takes into account the relaxation time λ . We have from the previously equation 2.8:

$$\sigma = \tau - p \delta$$

now, the stress tensor of viscosity τ obeys the UCM:

$$\tau + \lambda \overset{\nabla}{\tau} = \eta_0 \dot{\gamma}$$

where η_0 is the zero-shear polymer viscosity and $\overset{\nabla}{\tau}$ the upper-convected derivative. By combining a basic kinetic theory and a constitutive equation such as UCM equation, it is possible to link the zero-shear polymeric viscosity η_0 and the relaxation time λ to the microscopic properties of polymers. Briefly, polymer molecules are modeled by hookean dumbbells consisting of two spherical beads connected by an elastic spring. In the case of very dilute polymer solutions, the dumbbells only interact with each other through hydrodynamic interactions or intermolecular forces. After several steps of equations (motion, diffusion, forces etc), we can obtain the relationship: $\eta_0 = \lambda n k_B T$ with n the number of dumbbells, k_B the Boltzmann constant and T the temperature.

This model takes into account the memory effects of materials, but it does not consider the solvent viscosity or the shear rate dependence of the viscosity as the following models.

Oldroyd-B Model

The Oldroyd-B model is the extension of the UCM model in which the solvent viscosity η_s is taken into account. As for the UCM model, the viscoelastic fluid is modeled by a suspension of dumbbells connected by infinitely extensible springs in a newtonian solvent. If the tensor of viscosity τ obeys to the UCM, we obtain the set of equations called the Oldroyd-B model which is formulated via the total deviatoric stress $\sigma = \eta_s \dot{\gamma} + \tau$ which satisfies:

$$\sigma + \lambda \overset{\nabla}{\sigma} = \eta(\dot{\gamma} + \lambda_r \overset{\nabla}{\dot{\gamma}})$$

where λ_r is an independent time scale called the retardation time given by: $\lambda_r = \lambda(\eta_s/\eta)$; and η the total viscosity which is simply: $\eta = \eta_s + \eta_0$. This model can be simplified if:

- $\lambda_r = 0$: it reduces to the UCM model previously described
- $\lambda = \lambda_r$: it assimilates to the case of a newtonian fluid with the viscosity η_0
- $\lambda = 0$: it simplifies to a second-order fluid with a vanishing second normal stress coefficient.

When viscoelastic fluids are subjected to shear flow, normal stresses arise and are responsible for spectacular physical phenomena. The mechanism of those stresses can be explained by considering folded polymers chains at rest. While subjected to the action of a local shear, the chains will tend to align to the streamlines. However, at the same time, entropic forces are acting to make the elongated polymer chain return to its folded conformation. This leads to an extra tension in the direction of the flow. We have already defined the normal stresses differences N_1 and N_2 which can also be related to the shear rate for a linear shear flow $v(x, t) = (\dot{\gamma}y, 0, 0)$ by:

$$\begin{aligned} N_1 &= \tau_{11} - \tau_{22} = \psi_1 \dot{\gamma}^2 \\ N_2 &= \sigma_{22} - \sigma_{33} = \psi_2 \dot{\gamma}^2 \end{aligned}$$

where ψ_1 and ψ_2 are respectively the first and second normal stress difference coefficients. From the Oldroyd-B model equation, this first coefficient ψ_1 is linear in the polymer relaxation time λ and is given by: $\psi_1 = 2\lambda\eta_0$ (≥ 0). In this model, there is no second normal stress difference coefficient ($\psi_2=0$) as there are no transverse normal stresses. Moreover, the viscosity is constant and always equal to the zero-shear rate viscosity which is not representative of the real polymer solutions viscosity that often exhibits shear-thinning behavior. This is why, further models that considers those characteristic must be used.

In the case of newtonian fluids (ex: water), N_1 and N_2 are equal to zero. For non-newtonian fluids, the existence of those normal stress differences is responsible for spectacular phenomena as the Weissenberg effect or the die swell that we will observe and describe in more detail in the Chapter 4 [4.3.3](#).

White Metzner Model

Shear thinning fluids have a viscosity which is a decreasing function of the shear rate $\dot{\gamma}$. Many polymer solutions exhibit this type of behavior such as blood. This can be

easy interpreted by the presence of polymeric structures that tend to align in the flow direction while increasing the shear rate, which leads to a viscosity decrease. The White-Metzner model is suitable for this kind of fluid as it is a modified version of the UCM equation, which assumes a shear-rate dependent shear viscosity and relaxation time, here described using a Cross law:

$$\eta(\dot{\gamma}) = \frac{\eta_0}{1 + \left(\frac{\dot{\gamma}}{\dot{\gamma}_0}\right)^{1-n}}$$

2.1.2.2 Rheometer geometries

Several geometries of rheometers are available to measure those characteristic quantities. The appropriate geometry is chosen in function of solution concentrations, viscosity, pH or volume. For each geometry, geometric shape constants K relating to the viscosity can be defined by:

$$\eta = \frac{\sigma}{\dot{\gamma}}$$

where: $\sigma = M \times K_\sigma$

and: $\dot{\gamma} = \Omega \times K_\gamma$

with M the torque in N.m, Ω the angular velocity in rad/s, K_γ the strain constant and K_σ the stress constant.

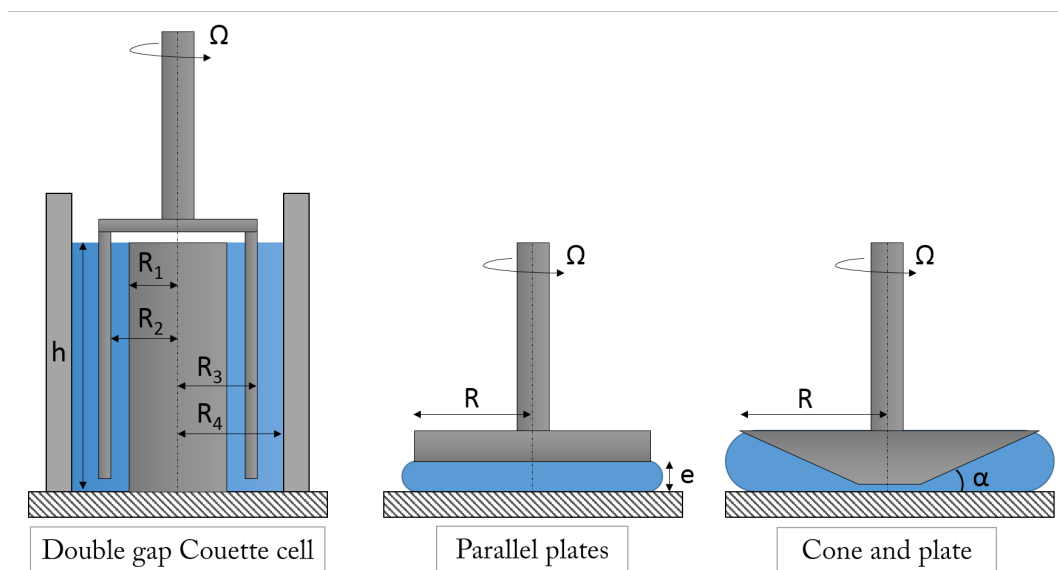


Figure 2.19: Rheometer geometries: left: Double gap Couette cell, middle: Parallel plates and right: Cone and plate

Double gap Couette cell geometry

Double gap Couette cell geometry is a concentric cylinder system suitable for solutions of low viscosity. A fixed cylinder is mounted in the center of the cup and a mobile cylinder is introduced inside the cell. This double system increases the shear area and lower torques can be determined. It was used in the case of alginate solutions of concentration lower than 1%. For this geometry, the geometric constants are:

$$K_{\gamma} = \frac{R_1^2 + R_2^2}{R_2^2 - R_1^2}$$

$$K_{\sigma} = \frac{(R_1^2 + R_2^2)}{4\pi h R_2^2 (R_1^2 + R_3^2)}$$

where R_i are the different radii and h the height of fluid in meter. For fluids with higher viscosity, other geometries must be used.

Cone-plate geometry

In a cone-plate geometry, the fluid is sheared between a plate and a cone of a radius R which makes an angle α (less than 4°) with the plate. The cone is truncated and has no contact with the lower plate. The resulting air gap corresponds to the truncation, and is generally very small (few microns). The main advantage of this geometry is the homogeneous shear rate induced in the sample. The two constants K are given by:

$$K_{\gamma} = \frac{1}{\alpha}$$

$$K_{\sigma} = \frac{3}{2\pi R^3}$$

During the experiments, the sample is kept in a humid atmosphere at 20°C thanks to a hermetically sealed cell. In our case, the rheometric tests were carried out mainly in oscillatory regime to determine the elastic modulus G' and the viscous modulus G'' . These two moduli depend on the frequency of stress. The pulsation varied between 0.01 and 100 rad/s.

This rheometer geometry was also used to measure the solution viscosity and normal stresses at different shear rates ranging from 0.01 to 100s^{-1} .

Glass parallel plate geometry

The parallel plate geometry can be considered as a simplified version of the cone and plate, having an angle of 0° . The fluid is constrained in the narrow gap between the two surfaces. For collagen solutions, the acid acetic may corrode the elements of the previous geometry (cone and plate) made of steel. We therefore used a glass parallel plate geometry that was available in the laboratory to study our collagen solution at 5 mg/mL (Chapter 5, 5.2 p 156). A small amount of solution is needed in this case which is a great advantage. However, the shear rate is not uniform and the apparent viscosity must be calculated by

using a model. In fact, the shear rate given by the rheometer is calculated at the periphery of the plate and the two constants K are then given by:

$$K_{\gamma} = \frac{R}{e}$$
$$K_{\sigma} = \frac{2}{\pi R^3}$$

2.1.3 Mechanical testing of extruded threads

Mechanical properties of extruded threads were investigated in order to assess the effect of fibrillogenesis buffer, culture medium, cells seeding or collagen concentration.

Tensile testing of extruded threads without cells were performed using a BOSE® Electro-Force® 3200 Series II Test Instrument at the Institut des Nanosciences de Paris (INSP). Specimens were attached horizontally to the stainless steel crossheads by setting each extremity on a cyanoacrylate glue drop and filter papers. Sample and crossheads were immersed in a glass Petri dish filled with either fibrillogenesis buffer or culture medium at room temperature. Initial threads diameter, d_0 , was determined by optical microscopy assuming full cylindrical symmetry. Mechanical loading of the thread was achieved by driving one crosshead at a constant velocity of 0.1 mm per second with a stepping motor (0.1-micron steps). The loading force F was measured with a 220g load cell. The cross-section S of the thread was calculated from the diameter measurements by bright field microscop and by assuming that threads are cylindrical. We defined the nominal tensile stress as:

$$\sigma(\text{Pa}) = \frac{F(\text{N})}{S(\text{m}^2)}$$

The nominal strain is defined as

$$\epsilon = \frac{L - L_0}{L_0}$$

where L is the distance between the glue points and L_0 the initial length. All measurements were performed up to the specimens rupture. The resulting stress-strain curves were thus plotted and analyzed. The Young Modulus E (Pa) of a sample is the stress-strain curve slope for small deformations and is obtained from the Hooke law:

$$\sigma(\text{Pa}) = E \times \epsilon$$

Tensile testing of threads put in cell culture were performed at the laboratory Sciences et Ingénierie de la Matière Molle-Physico-chimie des Polymères et des Milieux Dispersés (SIMM) with the help of Jingwen Zhao. In fact, with the previous instrument, threads cultured with cells splitted off from the crossheads as the cyanoacrylate was not sufficient to fix them. Instron 3343 machine is equipped with clamping jaws where sides are covered by Velcro straps. The threads with cells were put between the Velcro covered jaws vertically. The threads were immersed thanks to a tubing filled with PBS 1X solution which integrates the whole system. All tensile experiments were carried out at a velocity of 0.1mm/s with at least three measurements per condition to check the reproducibility. The set-up configuration requires a further data processing. Indeed, as the thread is immersed in the PBS solution vertically, the buoyant force exerted on the thread and equal

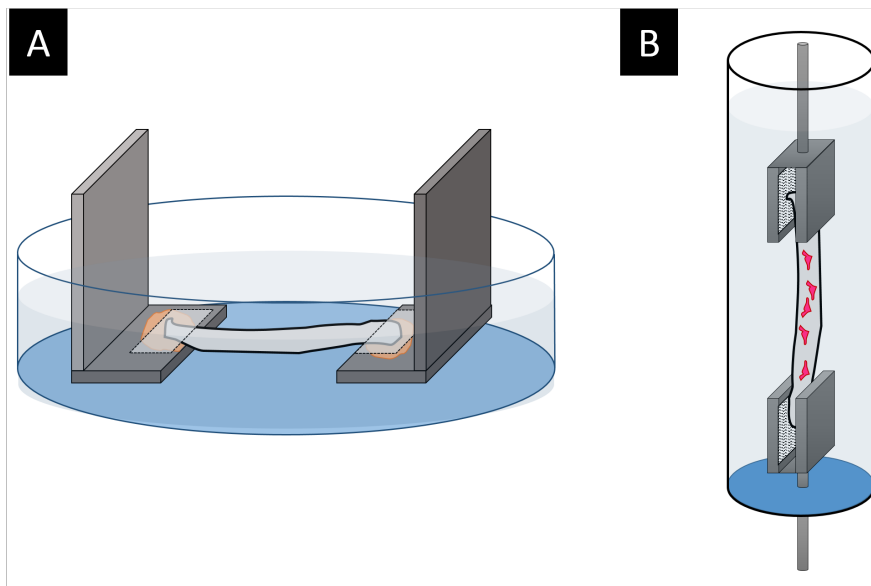


Figure 2.20: Mechanical testing configurations: A) horizontal for threads without cells and fixed with cyanoacrylate and filter paper; B) vertical for threads with cells fixed with velcro coated clamping jaws

to the weight of the fluid that the body displaces, needs to be taken into account. Briefly, after the thread rupture, data were still acquired to collect the buoyancy contribution. This was then subtracted to the force signal in order to have only the thread mechanical properties. The following data processing is then the same as the horizontal set-up.

For both configurations, Young's modulus, tensile strength, and elongation at break of the threads were derived from the stress–strain curves as described in the sections [1.1.1.2.2](#) and [2.1.3](#).

2.2 Materials

In this section, the collagen and alginate chemical properties will be described. The different protocols of purification, preparation, concentration etc. will be detailed for pure and mixed systems.

2.2.1 Collagen solutions

2.2.1.1 Collagen type I and its fibrillogenesis

Collagen is a molecule of the extracellular matrix and has large domains organized in triple helix. There are 28 types of collagen that differ in the composition of the polypeptide chains, their three-dimensional structure and their distribution in connective tissues [5]. In most collagens, the three polypeptide chains which form a α helix are identical. If the chains are different, the collagens are said to be heterotrimeric. The 28 types of collagens are divided into seven families that group together collagens with similar structural behaviors (Fig 2.21).

Family	Collagen types	Scheme
Fibril forming	I, II, III, V, XI, XXIV, XXVII	
Networking forming	IV, VIII, X	
FACIT	IX, XII, XIV, XVI, XIX, XX, XXI, XXII	
Anchoring	VII	
Transmembrane	XIII, XVII, XXIII, XXV	
Beaded filaments	VI, XVI, XXVIII	
Others with unique function	XV, XVIII, XXVIII	

Figure 2.21: Table and schemes of the seven collagen families. Blue dots are non-collagenous domains, the black line represents triple helix domain (Glycine-X-Y). Schemes adapted from [6]

Some collagens are specific to a tissue type and others are more ubiquitous. The most abundant collagen is fibrillar collagen type I and it is the one of interest in this project.

In vivo, collagen is synthesized by the cells. The synthesis begins by the production of the alpha chains in the ribosomes of the rough endoplasmic reticulum in which post-translational modifications take place (Fig 2.22 1).

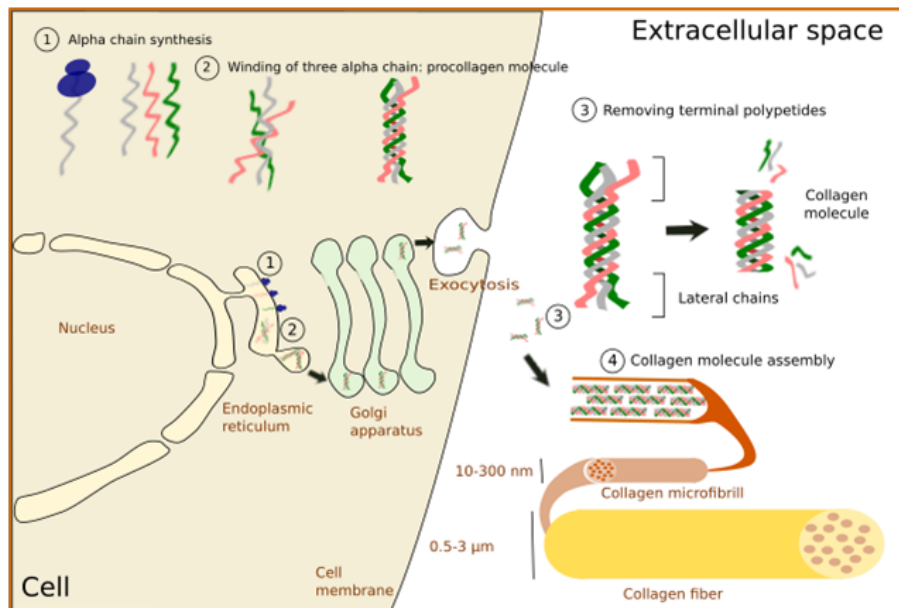


Figure 2.22: Collagen biosynthesis scheme: 1) Alpha chains synthesis, 2) Winding of the three alpha chains (procollagen molecule), 3) Removing terminal polypeptides, 4) Collagen molecule assembly. From https://mmegias.webs.uvigo.es/02-english/5-celulas/2-componentes_proteinas.php

It is followed by several steps: the hydroxylation of proline and lysine residues, the glycosylation of certain hydroxylysines and the formation of disulfide bridges between the C-terminal propeptides (which causes the three chains coiling in the N-terminal direction). The resulting molecule is called procollagen (Fig 2.22 2). Procollagen is soluble in physiological condition thanks to the presence of non-helical and charged propeptides. At this level, the procollagen molecules are found in vesicles in the Golgi apparatus before being secreted outside the cell. At the end of the process, enzymatic cleavage of the terminal N and C propeptides (Fig 2.22 3) globular domains takes place, resulting in the formation of fibrils (Fig 2.22 4). The loss of the globular domains leads to a decrease of the solubility under physiological conditions. The cleavage of the ends exposes the telopeptide sequences, which are small, non-helical domains. These telopeptides contain the binding sites for fibrillogenesis [7]. The collagen fibrils are spontaneously formed by the triple collagen helices, soluble at acidic pH but not soluble in a physiological medium during fibrillogenesis.

Collagen type I triple helix is composed of two strands $\alpha 1$ which have an identical sequence of 1056 amino acids and one strand $\alpha 2$ with a sequence of 1023 amino acids. These three strands are formed in their central part by the repetition of a sequence of three amino acids Glycine-X-Y. The glycine points towards the center of the triple helix while the larger residues of X and Y amino acids point to the outside of the triple helix, as shown in Figure 2.23 (A), and are therefore available for interactions with other molecules or with the solvent. Proline and hydroxyproline are the most encountered (30% of cases) in the X and Y positions respectively.

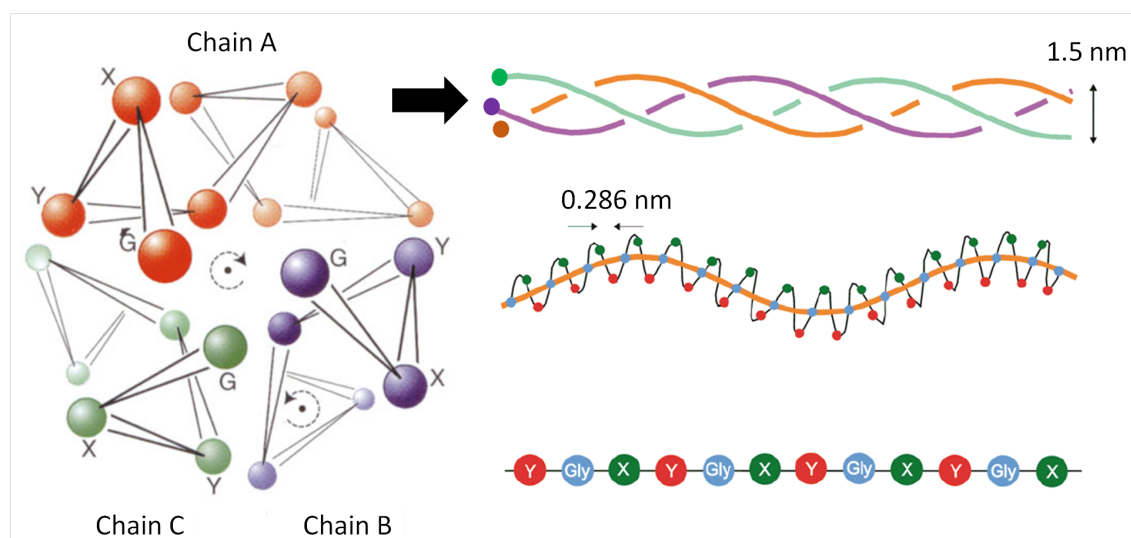


Figure 2.23: Collagen type I triple helix scheme. Left: Viewed along the molecular axis (-carbons only), showing the paths of the individual polypeptide chains and the locations of residues in the GlyX-Y triplets (G = Gly; from [8]).

The amino acid sequence corresponds to the primary structure (Fig 2.23 bottom right) and it is the folding of the left helix chain of 8.68 nm pitch, which forms the secondary structure. The folding is driven by steric repulsions between the proline residues in the X-position and the hydroxyproline residues in the Y-position. Between two residues, the axial distance is 0.286 nm (Fig 2.23 middle right). Then, the tertiary structure is formed by the folding of the secondary structures in space and the quaternary structure by the association of monomers (the chains α) between them. Indeed, the presence of numerous glycines along the chains α allows them to associate to form a right triple helix. The triple helix then has a length of 300 nm and a diameter of approximately 1.5 nm (Fig 2.23 top right). Hydrogen bonds between the glycine of one chain and the carboxyl groups of another chain ensure the stability of the triple helix. The ends of the collagen type I molecule, called telopeptides, are non-helical regions.

2.2.1.2 Chemical properties

Solubility

Collagen molecules of young tissues are soluble at acidic pH at room temperature. There are two different ways to induce the fibrillogenesis process: in physiological condition at 4 °C by increasing the temperature to 37 °C; or by increasing the pH if the collagen solution is in acidic solutions. In the case of fibrillogenesis induced by an increase of pH, the collagen solutions are subjected to other solutions at neutral pH. This induces the precipitation of the collagen molecules which assemble into fibrils. Depending on the physico-chemical conditions (pH, ionic strength), the size of the fibrils will vary, which may have consequences on the mechanical properties as we will see in Chapter 5 (5.3 p 157).

As mentioned above, the precipitation of the collagen molecules can also be induced by a thermal increasing. Gross and Kirk [9] and Jackson and Fessler [10] were the first to study this phenomenon and showed that collagen in neutral saline at 4 °C formed a fibrillar gel when the temperature rose to 37 °C for relatively low starting concentrations between 0.2 and 2 mg/mL. However, they found that the collagen could be denatured before reaching 37 °C and that the precipitation showed inhomogeneities. This second way to induce fibrillogenesis will be not used in our study.

Collagen net charge

From the physico-chemical point of view, the collagen molecule is a polyelectrolyte with an amphoteric character. Indeed, it can behave both as an acid (proton donor) or as a base (proton acceptor). Knowing the amino acid sequence of the three α -chains of the collagen molecule, it is possible to assess the distribution of the charges along the molecule which appears relatively homogeneous. Furthermore, Frederic Gobeaux estimated the net charge of the proteins as a function of the pH by using a spreadsheet provided by the University of Maine [11].

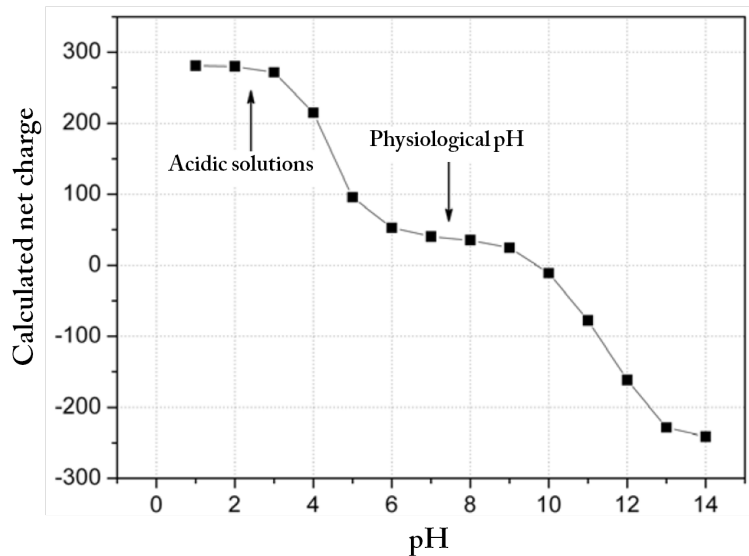


Figure 2.24: Collagen net charge plot calculated from its amino acid sequence as a function of pH. The calculation was performed with Charge Calculator III [11]

The results of those calculations are presented in Figure 2.24. In acetic acid at 500 mM, at pH 2.5, the net charge of collagen is at its maximum of 259 positive charge. The electrostatic repulsions are therefore maximal and this explains why in those conditions the collagen is soluble. On the other hand, at physiological pH (pH 7.4) and with only 38 positive charges, this condition is very close to the isoelectric point (pH \approx 9.8) and we understand why the collagen precipitates in the form of fibrils when acid solutions are neutralized. This calculation remains very approximate, because the isoelectric point depends strongly on the ions present in solution and their ionic strength, which is not taken into account here.

Flexibility and persistence length

The triple helix of collagen can be considered as a rod which is more or less flexible. This criterion may be important to interpret the collagen behavior in solution. Indeed, the flexibility impacts the conditions of the isotropic/nematic transition and the rheological properties of macromolecules in solution.

A critical parameter to characterize the flexibility of a polymer is its persistence length P , which describes the length at which two tangent vectors are correlated. The flexibility α is described as the ratio between the total contour length of the molecule L and its persistence length P :

$$\alpha = \frac{L \text{ (nm)}}{P \text{ (nm)}}$$

When $\alpha \ll 1$, the polymer is very rigid and can be modeled by a rod, while if $\alpha \gg 1$, it is very flexible. In this case, the polymer is modeled by a chain of articulated rigid segments (Kühn segments) or by the wormlike chain model. If the two quantities L and P are of the same order of magnitude, the term semi-flexible "molecule" is used. However, the persistence length of a polyelectrolyte can vary depending on its concentration, the solvent (ionic strength), or the temperature. Also, there are various values for collagen type I in the literature, depending on the experimental conditions, but also according to the method used. Some of them are reported in Table 2.2.

C (mg/mL)	Buffer	pH	P length (nm)	Ref
0.08 - 0.6	0.3 M Acetate + 6 mM NaCl	4	170	[12]
0.4 - 1.5	0.06 M potassium acetate buffer	4.8	130	[13]
0.02 - 0.03	glycerol	NA	57	[14]
0.0051	Nanopure Water	7	12.5	[15]
$6.4 \cdot 10^{-4}$	FFB	7	135	[15]
0.00051	PBS	7	165	[15]

Table 2.2: Persistence length for different buffers found in the literature. (FFB: Fibril Forming Buffer and PBS: Phosphate Buffer Saline)

The most plausible values in our case are those of the order of 165 nm, measured in PBS [15]. In this condition, the contour length is about 260nm which leads to a flexibility α of 1.6. This means that collagen triple helix molecules can be considered as "semi-flexible".

2.2.1.3 Collagen solutions preparation

Type I collagen was extracted from young wild-type non-treated Wistar or Sprague-Dawley rat tail tendons. The rats cadavers come from biological laboratories. They were initially sacrificed as controls of various experiments and not only for collagen purification. As they are a few months old, the tendon collagen is very weakly crosslinked. In the following part, the whole protocol of collagen preparation is described.

2.2.1.4 Collagen extraction and purification

The rat tail is travelled by tendons running longitudinally along its length (2.25, left scheme). To collect those tendons, the first step consists in cutting partially the skin with sterile clamps (about 1 cm from the rail extremity), twisting it and moving apart carefully the two pieces until bundles of white tendons are exposed and separated (2.25, right image). Those are the rat tail tendons.

This step is repeated every centimeter until 2-3 cm from the rat tail basis is reached. The excised tendons are then washed several times with phosphate-buffered saline (PBS) to remove cells and traces of blood coming from the veins and artery. The remaining cellular wastes are lysed by the addition of NaCl 4 M solution. Tendons are rinsed again with PBS and solubilized overnight in 500 mM acetic acid (pH=2.5). A viscous mixture containing proteoglycans, collagen, small proteins and some insoluble fibers is thus obtained. The collagen solution is purified by successive and selective precipitations. By centrifugation at high speed, the insoluble fibers are first removed. Then, the proteoglycans and polyelectrolytes of high molecular weight are precipitated by a slow step by step addition of a 4 M NaCl solution up to a final concentration of 300 mM. They can then be separated by a new centrifugation. Finally, the collagen is precipitated by a second addition of 4M NaCl solution up to a final concentration of 600 mM. After centrifuging at

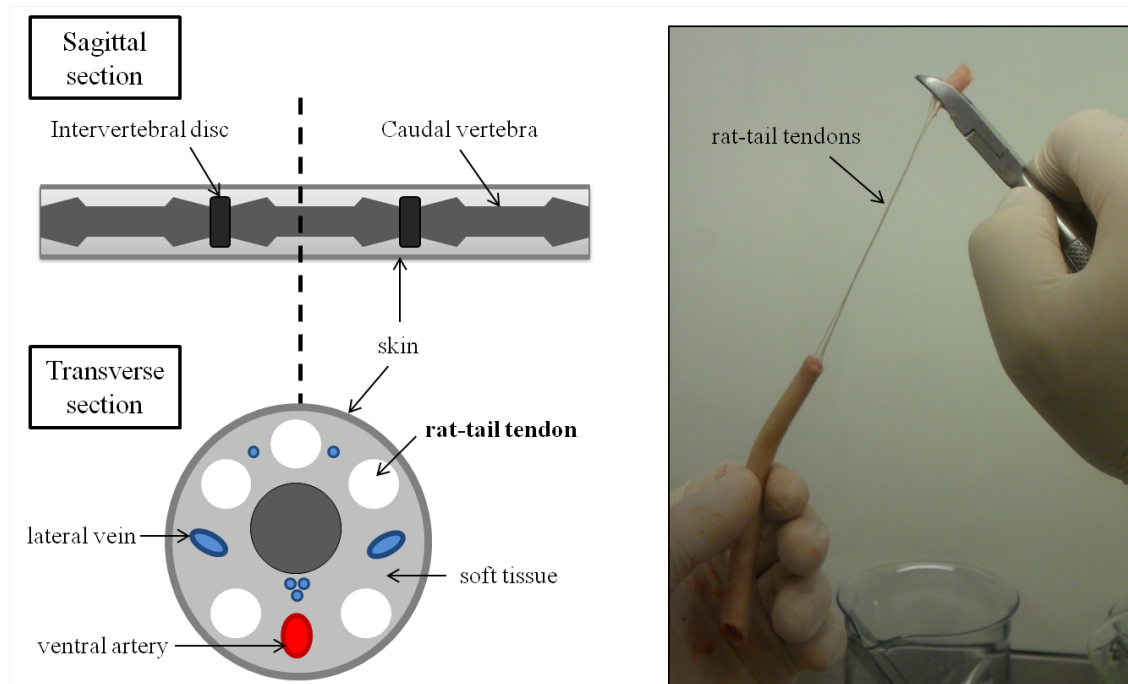


Figure 2.25: Rat tail schemes of sagittal (top left) and transverse (bottom left) sections. The rat tail is composed of several caudal vertebrae separated by intervertebral discs. All along its length it is travelled by tendons, veins and the ventral artery. The extraction of rat tail tendons is performed by cutting every centimeter the rat tail and moving apart the two pieces until tendons fascicles are exposed (right).

low speed, pellets containing the collagen I is collected. Those pellets are solubilized and dialyzed several times in 500 mM acetic acid in order to remove NaCl. The collagen solutions are kept at 4 °C and centrifuged at 41,000xg for 4 h before use. After each collagen extraction, the protein purity is checked and the collagen concentration is quantified.

2.2.1.5 Collagen solutions dosage

Collagen concentration is determined from the acidic solution by assessing the amount of hydroxyproline. In fact, the hydroxyproline (hp) is assumed to be a quasi-specific amino acid of the collagen extracted from the rat tail tendons and representing approximately 13 % of its molecular weight. To dose this amount, a volume of 50 μL of collagen solution is mixed with a the same volume of hydrochloric acid at 37% in order to release the hydroxyprolines. The mix is placed in an oven at 106 °C overnight to hydrolyse the collagen. The solvent is then evaporated and the residue obtained is re-suspended in 1 mL water. This solution is further diluted with water to obtain three samples of 400 μL of different concentration ratios(1/40, 1/20, 1/10). In each of those samples, a volume of 200 μL of Chloramine-T, perchloric acid and DMBA (4 dimethylamino-benzaldehyde) is added to provoke a colored reaction between yellow and red. The color is related to the amount of hydroxyproline present in the solution. Finally, the absorption at 557 nm is measured for each sample. A reference curve is obtained for a hydroxyproline solution which concentration is known and equal to 20 $\mu\text{g}/\text{mL}$. This curve correlates the hydroxyproline concentration with absorption. Taking into account the dilution of each sample and knowing that the type I collagen molecule contains 13% of hydroxyproline, the collagen concentration $C_{collagen}$ is calculated as follows:

$$C_{collagen} = 7.6 \times f_D \times C_{hp}$$

Where f_D is the dilution factor, and C_{hp} is the hydroxyproline concentration.

2.2.1.6 Collagen solutions purity

The purity of the solution is determined by electrophoresis under denaturing conditions on polyacrylamide gels. This allows to identify the proteins present as a function of their molecular weight.

Preparation of polyacrylamide gels

There are two types of gels: a concentration gel and a migration gel. The amount of polyacrylamide will define the size of the pores in the gel. The concentration gel at 4% of polyacrylamide and the migration gel at 6% allow to separate the different polypeptide chains from the collagen solution. The gels contain ammonium persulfate and TEMED: the first induces the polymerization and the second one accelerates this process. The two gels are cast one after the other between two glass plates held vertically, the migration gel being cast at the bottom.

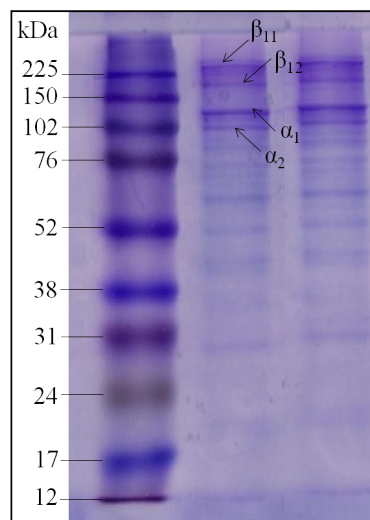


Figure 2.26: Electrophoresis gel in denaturing conditions. On the left, the rainbow molecular weight marker and the respective weights in kDa. On the right, the most marked bands are characteristic of the collagen. The two top bands correspond to the dimers β_{11} and β_{12} and the two most important bands are the α_1 and α_1 strands. Concentrations decreasing from left to the right.

Preparation of samples

The samples have a volume of 20 μL and correspond to a mixture of 10 μL of a collagen solution more or less diluted with 10 μL of sample buffer. Three different dilutions are used: 2.5, 5 and 10. The sample buffer contains SDS which will denature the collagen molecule when heated for 5 minutes at 100 $^{\circ}\text{C}$ in boiling water. The whole is then cooled for 5 minutes on ice and the samples are placed in the wells of the concentration gel. The first well is reserved for the molecular weight marker (SDS-6H, SIGMA). It enables to relate the migration distance of the molecules present in the collagen solution to a molecular weight.

Migration

The whole system (gels + samples) is immersed in a migration buffer and a potential difference is applied between the base of the migration gel and the top of the concentration gel. As long as the samples are in the concentration gel, the applied voltage is 80 V. When the migration front reaches the second gel, the voltage is fixed at 120 V.

Fixing and staining

To fix the proteins and to color them, the gel is placed for 1 hour in a solution of Coomassie blue. Then, the colored gel is placed in various bleaching baths containing water, ethanol and acetic acid in order to remove the Coomassie Blue excess. A gel obtained for one of the purifications is presented in Figure 2.26. We observe the most marked bands, which are characteristic of the collagen: the two top bands corresponding to the dimers β_{11} and β_{12} and the two most important bands being the α_1 and α_1 strands. The presence of contaminants are revealed by marked bands at other weights, which is not the case. The collagen batch is thus assumed to be pure.

2.2.1.7 Collagen solutions concentration

After purification, the stock collagen concentration c is determined by hydroxyproline dosage as previously described. To concentrate this stock solution, centrifugal concentrators (Vivaspin) are used. They are composed of two parts: an upper structure covered with a filter membrane with a 300 kD cut-off (Fig 2.27 dashed lines) and a lower part which is a traditional tube. First, the upper structure is filled with the stock collagen solution (Fig.2.27, left 1) and the introduced volume mass is recorded. Then, the two structures are combined and spinned at 4400g. By centrifuging, a solvent flux occurs (Fig.2.27 left, black arrows) through the membrane that will retain the molecules larger than the cut-off.

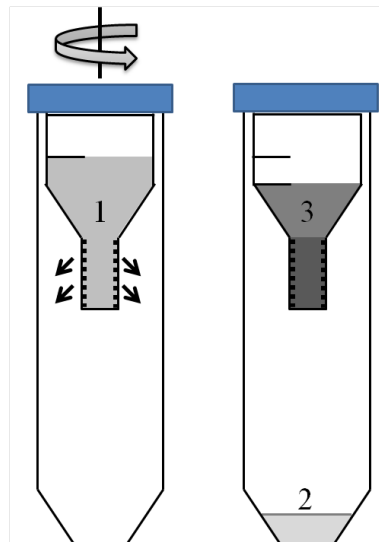


Figure 2.27: Collagen concentration scheme. The stock collagen solution (1) is put in the centrifugal concentrator tube. After centrifugation at 4400g during several hours, the solvent (2) passes through the filter membrane and the concentrated collagen solution (3) can be collected.

The pass-through solvent (Fig.2.27, right 2) is regularly removed from the lower part. Moreover, the collagen solution is frequently homogenized to avoid high concentration gradient close to the filter membrane. This whole process takes several hours or days according to the concentration c' to achieve. This concentration is reached when the desired

mass of collagen is weighed.

2.2.2 Model system: sodium alginate

2.2.2.1 Structure

Alginate is a biopolymer, more precisely a polysaccharide, extracted from cell walls of brown seaweeds [16]. It is a block copolymer composed of mannuronic acid (M) and guluronic acid (G) (Fig. 2.28, A). These two acids have the same molecular formula, but their spatial conformations are different. Indeed, the carboxyl group is either in the equatorial position (M) or in the axial position (G). An alginate chain can be composed of homo-blocks (MM and GG) (Fig. 2.28, B) and block heteropolymer (GM or MG) (Fig. 2.28, C).

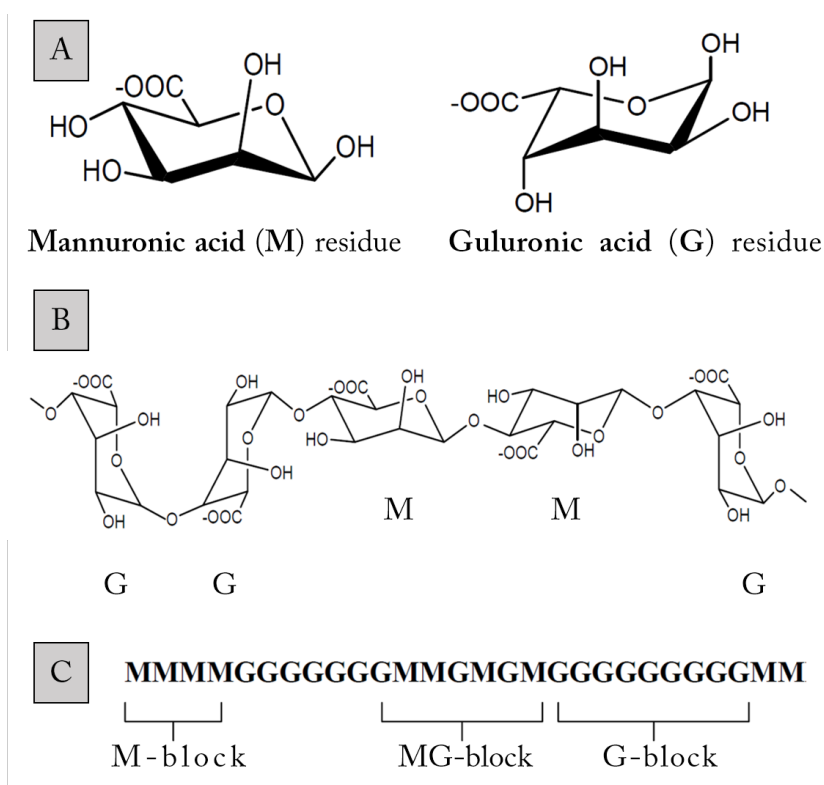


Figure 2.28: Structures of: A) the mannuronic (M) and guluronic (G) acids, B) the MM and GG homo-blocks and C) hetero-blocks. Adapted from [17]

The molar mass of the alginates depends on several parameters regarding the origin, the age and the part (top, bottom or center) of the algae from which it is extracted. The molar mass is very important as it will affect the rheological behaviors and the physico-chemical properties of the polymer. The chemical structure of the alginate chain is also modified by the origin of the algae: the blocks M and G is arranged in an order and proportion specific to each alga.

2.2.2.2 Chemical properties

Solubility, stability and charge

- The solubility of alginates depends on several parameters as the pH, ionic strength of the solvent or the "hardness" of the water (= calcium ions content). The pKa values of mannuronic acid and guluronic acid are respectively 3.38 and 3.65 [18]. For

$\text{pH} < \text{pKa}$, alginate is converted to alginic acid, which is insoluble in water. If the pH is decreased abruptly, it causes the alginic acid molecules precipitation and if it is done slowly, a gel is formed due to the controlled release of protons. The accurate pH value that causes precipitation of the alginates is dependent on the composition and the structure of the polymer [19]. In our study conditions, sodium alginate is soluble in deionized water and for the preparation of high alginate solution concentrations ($> 1\%$ (w|w)), the salts dissolution may take a few days.

- The stability of alginates depends on temperature, pH and the presence of contaminants. The glycosidic bonds may rupture when the alginate is used in acidic or basic medium. For instance, at pH below 5, the acidic hydrolysis of those bonds induces a decrease in the molar mass by cleavage of the chains. Alginate is considered stable in the pH range 5-10. The polymer degradation is thus minimal around neutral pH and increases by deviating from this pH stability area.
- Alginate is negatively charged. At low pH (around 2), it remains uncharged due to the complete protonation. While increasing the pH, the charge becomes negative and at pH 6.5, alginate is completely deprotonated. [20].

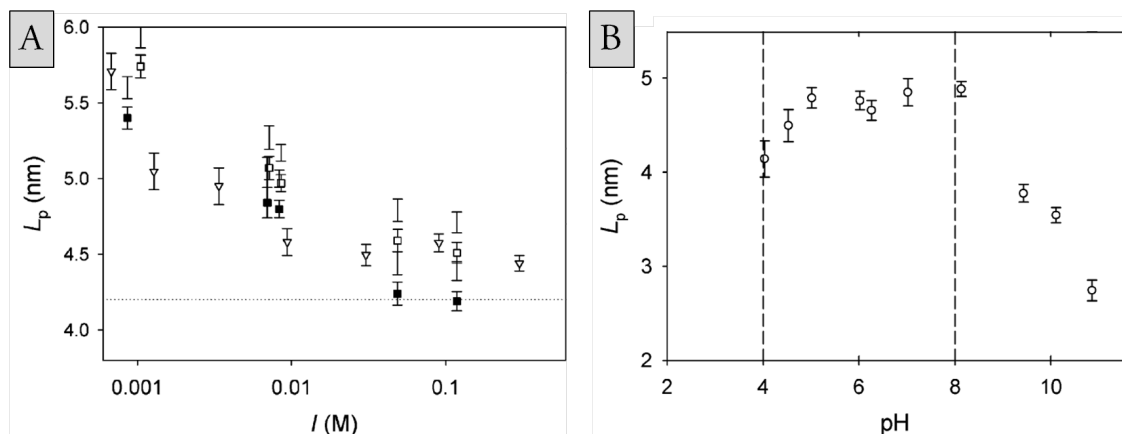


Figure 2.29: A: Total persistence lengths calculated from the Benoit-Doty equation as a function of the ionic strength I for different alginate concentration: Black square: 0.05 g/L, White square: 0.1 g/L and Triangle: 0.1 g/L with MgCl_2 . B: Influence of pH on the calculated persistence lengths for alginic acid 0.1 g/L at an ionic strength of 50 mM. Three different regimes describing the behavior of the AA molecules are thought to occur: $\text{pH} < 4$: aggregation of highly protonated alginic acid molecules; $4 < \text{pH} < 8$: increase in molecular rigidity due to an increased intramolecular electrostatic repulsion; $\text{pH} > 8$: depolymerisation. [21]

Flexibility and persistence length

In the literature, the persistence length (P) of alginate has been determined by several techniques: rheology, electron microscopy, atomic force microscopy etc. Values of P range between 5 to 17 nm ([22] [23]). Avaltroni et al. investigated the influence of both ionic strength (I) and pH on P [21]. Their experimental results are shown on the figure 2.29.

At low ionic strength ($I = 1 \text{ mM}$), P is about 5.5 nm and decreases until 4 nm for highest I values (Fig. 2.29, A). Such a length corresponds to 9-10 monomers [21].

Regarding the pH influence (Fig. 2.29, B), a slight decrease of P is observed from pH 8 to 4 while approaching the alginate pKa (around 3.2 – 3.65). As previously described, alginate is thus protonated which decreases electrostatic repulsion [21]. This increases the

molecular flexibility which is consistent with the decrease of P . From this work, we can also quantify the alginate flexibility through the parameter α which is equal to 8 for an estimated contour length of 50 nm. The alginate is assumed to be also semi-flexible even rigid for lowest P values. Moreover, M monomers chains are more flexible than G ones. As a consequence, the persistence length depends on the ratio M/G of the alginate solution.

Ionic binding of alginates/Gelation

One of the most interesting features of alginates is their ability to selectively form ionic bonds to divalent cations such as Ca^{2+} , Sr^{2+} and Ba^{2+} in order to form hydrogels. They bind more or less easily to those cations depending on their chemical nature. For example, the affinity increases following the order: $Mg^{2+} < Mn^{2+} \ll Ca^{2+} < Sr^{2+} < Ba^{2+} < Cu^{2+} < Pb^{2+}$ [18]. This affinity depends not only on electrostatic forces, but also on steric hindrance.

While sodium alginate solution is put in contact with divalent ions such as Ca^{2+} , an expanded network is formed. The structure conformation changes: alginate chains and ions form an arrangement called "egg-box" structure (Fig. 2.33), in which the ions representing the "eggs" are entrapped between two chains:

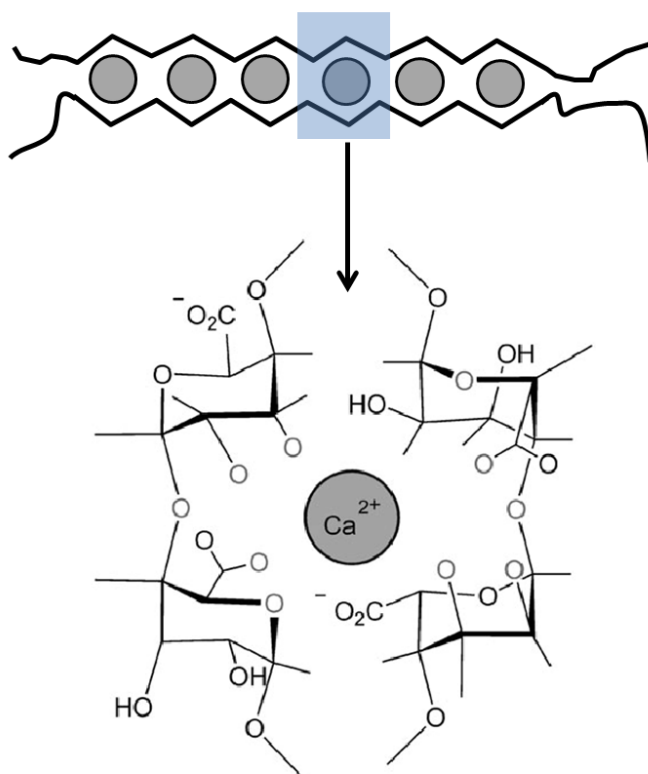


Figure 2.30: Schematic representation of the "egg-box" structure. Top: egg-box dimer, Bottom: coordination of Ca^{2+} in a cavity created by a pair of guluronate sequences along alginate chains. Adapted from [24]

For steric hindrance, calcium ions can only bind to carboxylic functions in axial positions which is the case for G-block. This mechanism is improved if the G-block exceeds 20 residues. In the case of M-blocks, their conformation assimilated to a flat ribbon, does not allow complexation with calcium ions. Thus, alginate gel formation depends on the ratio of M and G-blocks present in the polymer. From Fang et al. studies [24], this mechanism also depends on the alginate chains length. In the case of short and rigid chains, dimers

aggregate laterally through an inter-chain association, whereas in the case of longer and more flexible chains, the association occurs through intra-chain association (single chain level). Moreover, in both cases, the binding of calcium ions to alginate can be divided into three main sequential steps upon increasing calcium ions content (where R is the feeding ratio of Ca^{2+} to G residue) as shown in Figure 2.31 below:

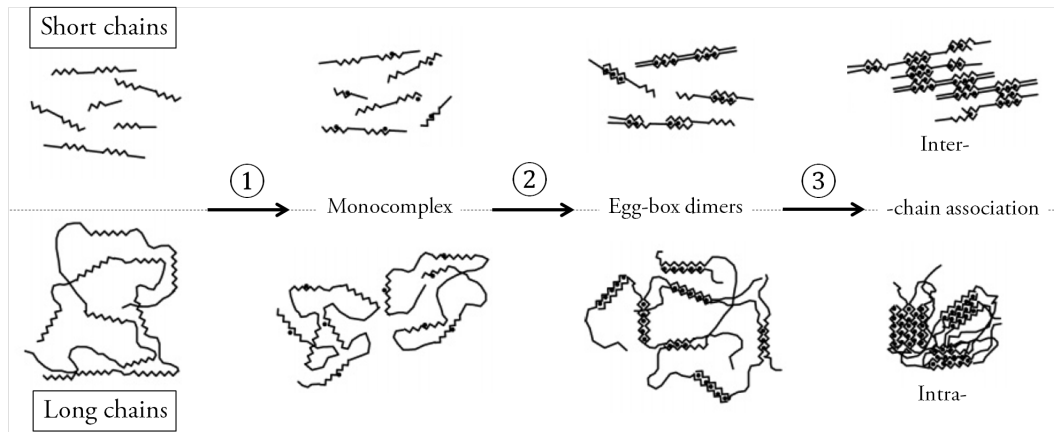


Figure 2.31: Schematic illustration of the multiple-step binding of Ca^{2+} to alginate, in the case of short (Top) and long-chain alginate (Bottom). The zigzag lines, smooth lines, and black dots stand for G blocks, M blocks, and calcium ions, respectively. Adapted from [24]

- **Step 1 ($R < 0.25$):** monocomplexation = calcium ions interaction with a single G-unit forming monocomplexes
- **Step 2 ($0.25 < R < 0.55$):** dimerization = propagation and formation of the egg-box dimers via pairing of the monocomplexes.
- **Step 3 ($R > 0.55$):** multimers formation = lateral association of the egg-box dimers.

2.2.2.3 Solution preparation

Sodium alginate was purchased from Kalys Gastronomie (average molecular mass $\overline{M}_w = 246$ kDa). Salts are dissolved in ultrapure Millipore water in order to obtain solutions at the desired concentration in % (w/w). A small amount of sodium azide solution at 3% is added to avoid bacterial growth. The water is added progressively in order to avoid the formation of clots. We have made use of solutions with alginate concentrations ranging from $c = 4, 6$ to 10 wt.% (equivalent of 40, 60 and 100 mg/mL), referred to in the following sections as ALG4, ALG6 or ALG10. At the lowest concentration $< 4\%$, the solution was magnetically stirred overnight. For higher concentrations $> 4\%$, alginate powder was left to swell and dissolved for at least 2 days under periodic gentle manual stirring. Homogeneity of the solutions is assessed from its optical aspect. For rheological measurements, a solution previously prepared at 4% is diluted to reach concentrations between 0.025 and 3%.

To induce gelation, alginate solutions were extruded in a cross-linking bath containing divalent ions (Ca^{2+}). Calcium chloride dihydrate ($M=147.02$ g/mol) was purchased from Prolabo. It is also dissolved in ultrapure Millipore water to obtain solution at 0.1, 0.5 or 1M and stirred until the complete dissolution of salts.

2.2.3 Collagen-alginate mixtures

To improve threads properties at the structural and mechanical levels compared to pure collagen based ones, we decided to mix collagen and alginate. The idea is to produce threads from the collagen-alginate mixture to benefit from key strengths of each species.

2.2.3.1 Chemical properties

While mixing proteins and polysaccharides together, different kinds of interactions may occur: steric exclusion, hydrogen bonding, hydrophobic or electrostatic interactions. In our case, the collagen and the alginate have an electrical charge under the experimental chosen conditions (pH, ionic strength...). The main interaction is thus electrostatic and may be either attractive or repulsive depending on the charge of the species involved [25] (Fig. 2.32).

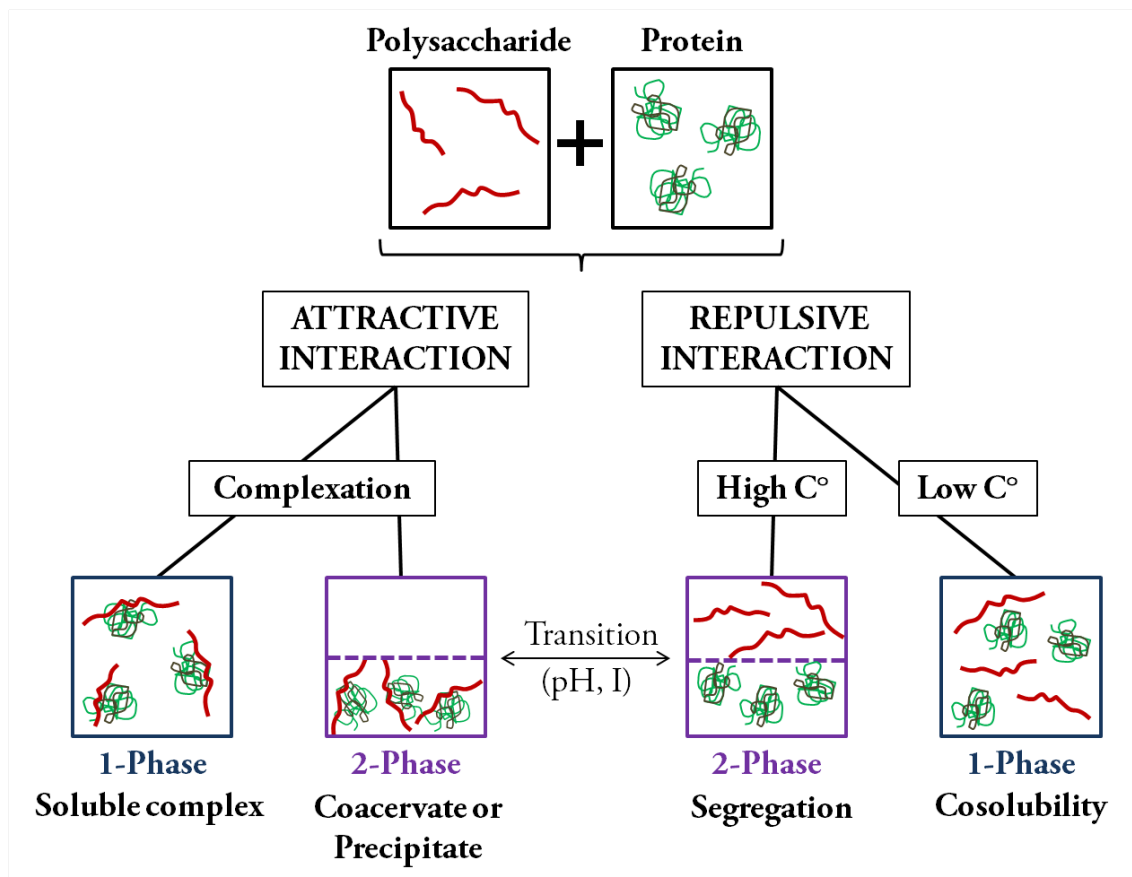


Figure 2.32: Schematic representation of the types of structural arrangements of the molecules involved that can occur when proteins and polysaccharides are mixed together. Adapted from [25], [26]

If they are oppositely charged, attractive interaction is predominant and can lead to soluble (1-phase) and/or insoluble (2-phase) complexes. This 2-phase system is composed of a phase rich in both biopolymers and a second one depleted in both species. Depending on the attraction strength and the chemical properties of the polymers, the rich phase can be a coacervate or a precipitate.

If the proteins and polysaccharides have similar electric charges or if one or both are uncharged, repulsive interaction occurs. At low biopolymer concentrations, the two species

are cosoluble and form a 1-phase solution. While increasing the concentration, segregative phase separation occurs and a 2-phase solution is then formed in which each phase is rich in one biopolymer.

To control this interaction and move from attractive to repulsive ones, it is necessary to adjust the pH, ionic strength, biopolymer ratio and other parameters [26].

2.2.3.2 Solution preparation

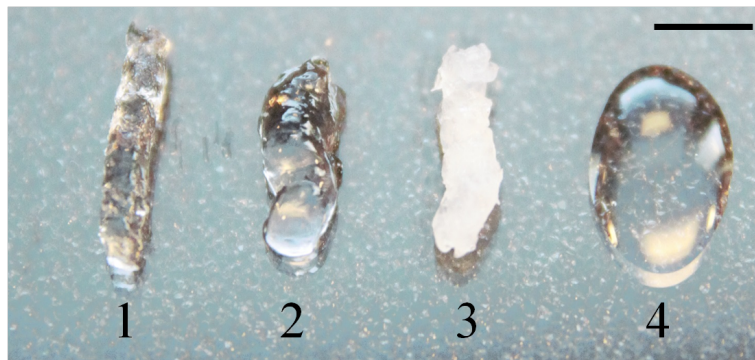


Figure 2.33: 1:Collagen 60 mg/mL, 2:Collagen 30 mg/mL, 3: Collagen/alginate (5:1) mixture; 4: Alginate 4%.

Fresh and sterile sodium alginate salt (as previously described) is dissolved in 500 mM acetic acid to obtain solution at 4 % (w/w) (Fig. 2.33, 4). A mass m_1 of collagen stock solution at 3mg/mL (500mM AA) and a mass m_2 of sodium alginate solution at 4 % (w/w) are added to a concentrator centrifugal tube. The mixture is then centrifuged at 4400 g until reaching the desired ratio Coll:Alg. Three different ratios Collagen:Alginate were tested: 1:1, 2:1, and 5:1 (Fig. 2.33, 3). The collagen-alginate mixture solution before extrusion is quite opaque that may already testify the interaction between the two species.

To induce gelation of alginate inside the mixture, solutions were extruded in a cross-linking bath containing divalent ions (Ca^{2+}) at 1M as previously detailed.

2.3 References

- [1] Jinwen Zhou, Amanda Vera Ellis, and Nicolas Hans Voelcker. Recent developments in pdms surface modification for microfluidic devices. *Electrophoresis*, 31(1):2–16, 2010. [49](#)
- [2] Tristan Baumberger and Christiane Caroli. Solid friction from stick–slip down to pinning and aging. *Advances in Physics*, 55(3-4):279–348, 2006. [52](#)
- [3] Frank Philip Bowden and David Tabor. *The friction and lubrication of solids*, volume 1. Oxford university press, 2001. [52](#)
- [4] Alexander Morozov and Saverio E Spagnolie. Introduction to complex fluids. In *Complex Fluids in Biological Systems*, pages 3–52. Springer, 2015. [64](#)
- [5] Darwin J Prockop and Kari I Kivirikko. Collagens: molecular biology, diseases, and potentials for therapy. *Annual review of biochemistry*, 64(1):403–434, 1995. [71](#)
- [6] Jyrki Heino. The collagen family members as cell adhesion proteins. *Bioessays*, 29(10):1001–1010, 2007. [71](#)
- [7] Darwin J Prockop and Andrzej Fertala. The collagen fibril: the almost crystalline structure. *Journal of structural biology*, 122(1-2):111–118, 1998. [72](#)
- [8] Konrad Beck and Barbara Brodsky. Supercoiled protein motifs: the collagen triple-helix and the α -helical coiled coil. *Journal of structural biology*, 122(1):17–29, 1998. [73](#)
- [9] Jerome Gross and David Kirk. The heat precipitation of collagen from neutral salt solutions: some rate-regulating factors. *Journal of Biological Chemistry*, 233(2):355–360, 1958. [73](#)
- [10] DS Jackson and JH Fessler. Isolation and properties of a collagen soluble in salt solution at neutral ph. *Nature*, 176(4471):69–70, 1955. [73](#)
- [11] Frédéric Gobeaux. *Phases denses de collagène de type I: transition isotrope/cholestérique, fibrillogénèse et minéralisation*. PhD thesis, Université Pierre et Marie Curie-Paris VI, 2007. [74](#)
- [12] F Henry M Nestler, Søren Hvidt, John D Ferry, and Arthur Veis. Flexibility of collagen determined from dilute solution viscoelastic measurements. *Biopolymers*, 22(7):1747–1758, 1983. [75](#)
- [13] Hiroyasu Utiyama, Kuniaki Sakato, Kenji Ikehara, Takashi Setsuiye, and Michio Kurata. Flexibility of tropocollagen from sedimentation and viscosity. *Biopolymers*, 12(1):53–64, 1973. [75](#)
- [14] Hans Hofmann, Tilman Voss, Klaus Kühn, and Jürgen Engel. Localization of flexible sites in thread-like molecules from electron micrographs: Comparison of interstitial, basement membrane and intima collagens. *Journal of molecular biology*, 172(3):325–343, 1984. [75](#)
- [15] Heather H Lovelady, Satish Shashidhara, and W Garrett Matthews. Solvent specific persistence length of molecular type i collagen. *Biopolymers*, 101(4):329–335, 2014. [75](#)

- [16] Glyn O Phillips and Peter A Williams. *Handbook of hydrocolloids*. Elsevier, 2009. 79
- [17] Leslie Rolland. *Propriétés physico-chimiques de capsules d'hydrogel à coeur liquide*. PhD thesis, Université Pierre et Marie Curie-Paris VI, 2013. 79
- [18] ARNE Haug and O Smidsrød. The effect of divalent metals on the properties of alginate solutions. *Acta Chem. Scand*, 19(2):341–351, 1965. 79, 81
- [19] KI Draget, G Skjåk Bræk, and O Smidsrød. Alginic acid gels: the effect of alginate chemical composition and molecular weight. *Carbohydrate Polymers*, 25(1):31–38, 1994. 80
- [20] Severian Dumitriu. *Polysaccharides: structural diversity and functional versatility*. CRC press, 2004. 80
- [21] Fabrice Avaltroni, Marianne Seijo, Serge Ulrich, Serge Stoll, and Kevin J Wilkinson. Conformational changes and aggregation of alginic acid as determined by fluorescence correlation spectroscopy. *Biomacromolecules*, 8(1):106–112, 2007. 80
- [22] Ivan Donati, Anna Coslovi, Amelia Gamini, Gudmund Skjåk-Bræk, Amedeo Vetere, Cristiana Campa, and Sergio Paoletti. Galactose-substituted alginate 2: conformational aspects. *Biomacromolecules*, 5(1):186–196, 2004. 80
- [23] Gjertrud Maurstad, Signe Danielsen, and Bjørn T Stokke. Analysis of compacted semiflexible polyanions visualized by atomic force microscopy: influence of chain stiffness on the morphologies of polyelectrolyte complexes. *The Journal of Physical Chemistry B*, 107(32):8172–8180, 2003. 80
- [24] Yapeng Fang, Saphwan Al-Assaf, Glyn O Phillips, Katsuyoshi Nishinari, Takahiro Funami, Peter A Williams, and Liangbin Li. Multiple steps and critical behaviors of the binding of calcium to alginate. *The Journal of Physical Chemistry B*, 111(10):2456–2462, 2007. 81, 82
- [25] Juan Miguel Rodríguez Patino and Ana MR Pilosof. Protein–polysaccharide interactions at fluid interfaces. *Food Hydrocolloids*, 25(8):1925–1937, 2011. 83
- [26] David Julian McClements. Non-covalent interactions between proteins and polysaccharides. *Biotechnology advances*, 24(6):621–625, 2006. 83, 84

Chapter 3

Rheological properties of collagen/alginate solutions

“Sweet scents of honey float through the air.”

Winnie the Pooh

Abstract

In this chapter, oscillatory and steady state shear measurements were performed on collagen at 30 mg/mL and on three alginates solutions. First, for collagen solution at 30 mg/mL, our results are presented and compared with the work of Gobeaux et al. (2010)[1]. From this study, we extracted the order of magnitude of viscosities of dense collagen solutions involved in our work. Then, selected alginate concentrations comparable with collagen ones and exhibiting quite similar behaviors were characterized. These two complex fluid systems show strong visco-elastic and shear-thinning properties.

Contents

3.1 Collagen solution rheological characterization	88
3.1.1 Oscillatory shear flow	88
3.1.1.1 Complex modulus measurement	88
3.1.1.2 Comparison with Gobeaux et al. work [1]	89
3.1.2 Steady shear flow	90
3.1.2.1 Viscosity	90
3.1.2.2 First normal stress difference	92
3.1.2.3 Typical physical quantities for other concentrations	93
3.2 Alginate solutions rheological characterization	94
3.2.1 Viscosity analysis	94
3.2.1.1 Alginate concentration choice	94
3.2.1.2 Shear-thinning nature	95
3.2.2 Complex modulus analysis	96
3.2.3 First normal stress difference and Weissenberg number	97
3.3 Conclusion	99
3.4 References	100

During the extrusion, solutions will be forced to pass through a die of a few hundred microns diameter and be subjected to high shear stresses. It is thus necessary to fully characterize the rheological properties of our complex fluids systems before extruding them in order to understand the different flow phenomena.

A complete study of collagen rheological properties at concentrations up to 112 mg/mL was already performed by Gobeaux et al. (2010) [2]. We compare our results based on the data analysis approach used in this study and Gobeaux PhD thesis [3].

Sodium alginate is our model system and will be also characterized to choose solution concentrations exhibiting similar properties as collagen.

3.1 Collagen solution rheological characterization

Rheological characterization was performed on collagen solutions at 30 mg/mL. Our results were both compared and supplemented with those of Gobeaux et al. [1] in which a study on collagen solutions at different concentrations was performed. As reported, studying complex fluids demands much attention as their rheological properties depend on their history. The solutions structure can be disturbed by strong stresses and it takes a very long time for them to recover their "rest" structure. This may explain why few investigations of collagen rheological properties at such high concentrations have been performed.

3.1.1 Oscillatory shear flow

3.1.1.1 Complex modulus measurement

Shear rheological measurements were carried out using a rheometer imposing strain. Cone-plate geometry was used in dynamic mode and allowed to probe angular frequencies ranging from 0.01 to 100 rad/s. The viscous and elastic components of the complex modulus were then measured. Results are presented in Figure 3.1.

To have systems comparable with the previous study [1], we brought the collagen solutions to the same initial state before measurements: first, the sample (30 mg/mL) was sheared during 300s at a constant shear rate of 8 s^{-1} and then left at rest for one hour.

The collagen solution exhibited a viscoelastic behavior depending on the stress frequency (Fig. 3.1). Shear storage G' and loss G'' moduli increased with frequency. According to Gobeaux analysis [3], we also modeled the two curves by power law written as:

$$G'(\omega) = G'_0 \left(\frac{\omega}{\omega_0}\right)^\alpha$$

$$G''(\omega) = G''_0 \left(\frac{\omega}{\omega_0}\right)^\beta$$

where $\omega_0 = 1 \text{ rad/s}$, $G'_0 = G'(\omega_0)$ and $G''_0 = G''(\omega_0)$. The respective exponents and prefactors are: $\alpha = 0.092 \pm 0.06$ and $\beta = 0.20 \pm 0.12$; $G'_0 \simeq 486 \pm 10 \text{ Pa}$ and $G''_0 \simeq 91 \pm 20 \text{ Pa}$.

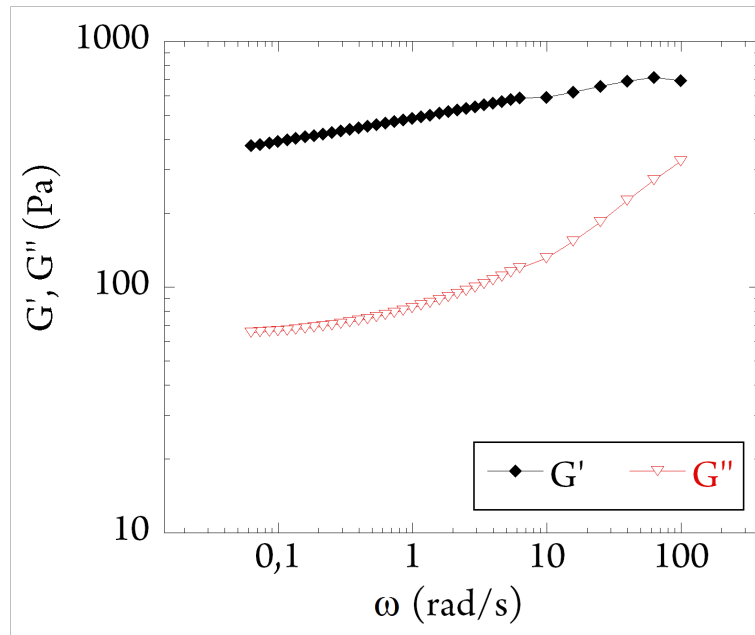


Figure 3.1: Shear storage G' (black \diamond) and loss G'' (red ∇) moduli against angular frequencies for collagen solution at 30 mg/mL

3.1.1.2 Comparison with Gobeaux et al. work [1]

According to Gobeaux et al. results (Fig. 3.2) exponents are equal to 0.3 and prefactors to $G'_0 \approx 460$ Pa and $G''_0 \approx 230$ Pa. In our case, those exponents are lower and closer to those found for very high concentrations (300 mg/mL) (Fig 3.2, red results). The previous power law fit might not be suitable for our solution. However, the shear and loss moduli are almost in the same order of magnitude.

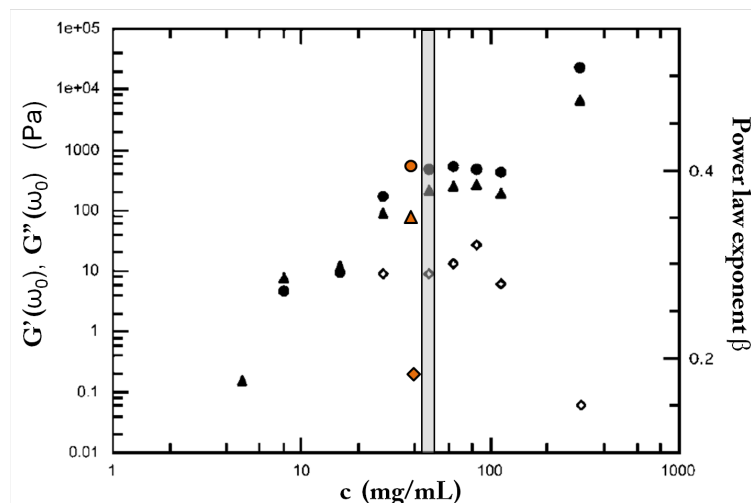


Figure 3.2: Prefactors G'_0 (\circ), G''_0 (\triangle) and power-law exponent β (\diamond) as a function of the collagen concentration. Our experimental results are added in the respective orange filled markers. The study concentration region of interest the closest to our concentration is shaded. Adapted from [1]

3.1.2 Steady shear flow

The material was sheared between the cone and the plate in which shear rate is constant within the whole sample. We measured the physical quantities of interest: viscosity, normal forces as a function of the imposed shear rate.

3.1.2.1 Viscosity

The collagen solution viscosity was measured for constant shear rates ranging from 0.1 to 100 s^{-1} . Upon increasing the shear rate, the viscosity decreases (Fig 3.3), attesting to the shear-thinning behavior of the collagen at 30 mg/mL. It could be interpreted as the entangled molecules network rupture or simply as the molecules alignment due to the imposed shear.

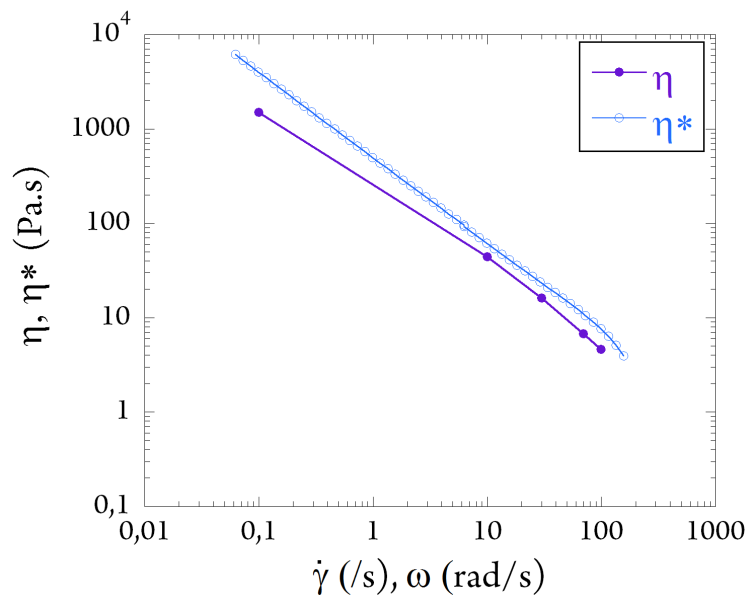


Figure 3.3: Comparison of the complex (or dynamic) viscosity η^* measured in oscillatory regime and the viscosity η measured in steady state for collagen solution at 30mg/mL. The shear-thinning behavior of collagen in dense solution is clearly observed. Moreover, Cox-Merz rule is verified.

Cox-Merz rule application

The Cox-Merz rule is an empirical correlation between dynamic and steady flow viscosity found by their respective authors [4] and was verified for almost all polymer melts, concentrated and semi-dilute polymer solutions. It is assumed that the complex viscosity η^* measured in oscillating dynamic regime and the viscosity η measured in steady state are equal while assimilating the angular frequency ω to the shear rate $\dot{\gamma}$:

$$|\eta^*(\omega)| = \eta(\dot{\gamma})|_{\omega=\dot{\gamma}}$$

$$\text{with: } |\eta^*| = \sqrt{\left(\frac{G'}{\omega}\right)^2 + \left(\frac{G''}{\omega}\right)^2}$$

In our case, the complex viscosity η^* was slightly overestimated compared to the viscosity η , but the trends were very similar. Thus, it is assumed that Cox-Merz rule is verified for our collagen solution at 30 mg/mL

Viscosity curves fitting

According to the further Gobeaux analysis, we modeled in the same way the viscosity linear domain plotted in figure 3.3 by a power law as proposed by Ostwald [5].

$$\eta \propto K \dot{\gamma}^{-n}$$

where K is a constant and n is an exponent to be determined. In the case of Newtonian fluids, $n = 0$. The exponent n_1 was measured in the steady state ($\eta = f(\dot{\gamma})$) and n_2 in the dynamic regime ($\eta^* = f(\omega)$). The results are gathered in Table 3.1 and compared with the values obtained previously at 31 mg/mL [3].

Study	C (mg/mL)	n_1 (η)	n_2 (η^*)
Picaut	30	0.83	0.91
Gobeaux	31	0.79	0.75

Table 3.1: Power law fit exponent values n_1 for η and n_2 for η^* at collagen concentration of 30 mg/mL and comparison with Gobeaux previous results [3].

Our experimental results are in good agreement with Gobeaux PhD thesis results [3]. In the range of shear rates tested, the Newtonian plateau is not reached (Fig. 3.3) and we only observe the shear-thinning part.

In fact, when the collagen solution is submitted to lower shear rates, it is possible to see the transition between the "plateau" and the linear domain and so to deduce the critical crossover shear rate $\dot{\gamma}_0$ from which the shear-thinning behavior starts [3]. From this, a characteristic time τ_c is defined as: $\tau_c = 1/\dot{\gamma}_0$, below which the collagen chains do not have time to come back to their initial entangled configuration. Gobeaux characteristic disentanglement time for high collagen concentrations are given in the figure 3.4.

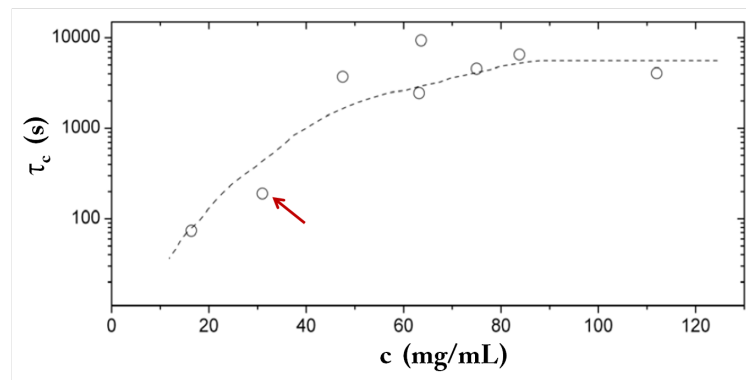


Figure 3.4: Characteristic disentanglement time τ_c as a function of the collagen concentration. The concentration corresponding to our experimental condition is pointed out by the red arrow. Results from [3]

For collagen solution at 31 mg/mL, close to our experimental condition, this time is about 200s (respectively $\dot{\gamma}_0=5 \times 10^{-3} \text{ s}^{-1}$) as shown by the red arrow in Figure 3.4. This time can reach a few hours for the highest concentrations.

3.1.2.2 First normal stress difference

Under steady shear flow, we can also measure the normal forces F_N for shear rates in the range of 0.1 to 100 s^{-1} and calculate the associated first normal stress difference N_1 defined as: $N_1 = F_N/S$ where S is the rheometer geometry surface. It is then possible to estimate the Weissenberg number Wi which is the ratio between the first normal stress difference and the shear stress:

$$Wi = \frac{N_1}{\sigma}$$

$$\text{where } \sigma = \eta(\dot{\gamma}) \dot{\gamma}$$

Wi is a dimensionless number which compares the relaxation time of the fluid to a specific process time. We calculate this number for collagen solution at 30 mg/mL from measured F_N values (Fig. 3.5, purple).

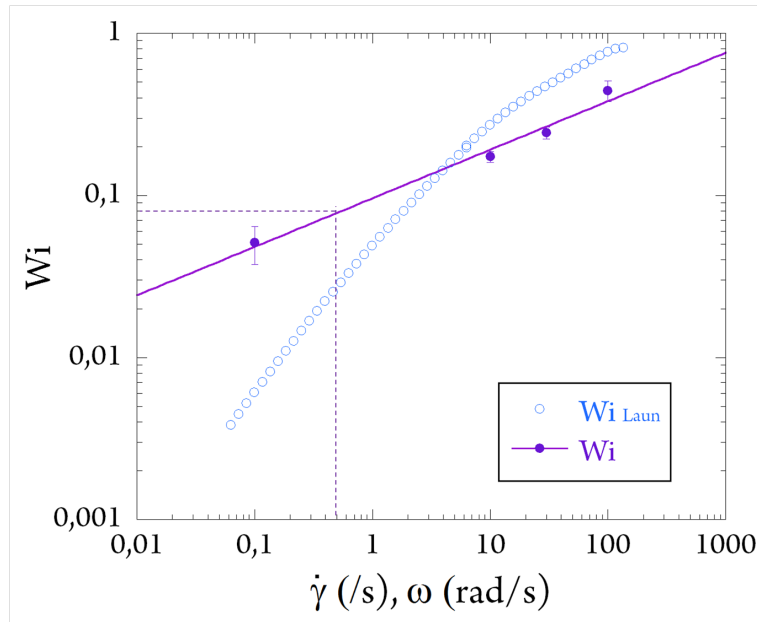


Figure 3.5: Shear rate dependent Weissenberg numbers for collagen solution at 30 mg/mL. Purple: Wi calculated from normal forces experimental measurements in steady shear flow. Blue: Wi calculated from empirical Laun relationship in oscillatory shear. The dashed line indicates the value of $\dot{\gamma}_0$ and the full line is $(\dot{\gamma}/\dot{\gamma}_0)^m$ with $m \approx 0.3$.

We also attempted to extract Wi number by using the empirical relationship proposed by Laun [6] as it is classically performed for polymer melts. It connects the first normal stress $N_1(\dot{\gamma})$ measured using steady shear flow to the storage modulus $G'(\omega)$ and loss modulus $G''(\omega)$ measured in oscillatory shear for $\dot{\gamma} = \omega$ by:

$$N_{1,Laun}|_{\omega=\dot{\gamma}} = 2G'(\omega) \left(1 + \left(\frac{G'(\omega)}{G''(\omega)} \right)^2 \right)^{0.7}$$

We thus have:

$$Wi_{Laun} = \frac{N_{1,Laun}}{\sigma}$$

$$\text{where } \sigma = \eta^*(\omega) \omega$$

Figure 3.5 shows the shear rate dependence of the Weissenberg numbers: 1) Wi calculated from the normal forces measurements and 2) Wi_{Laun} from the oscillatory shear with $G'(\omega)$ and $G''(\omega)$ (Fig. 3.5, blue).

The two Weissenberg numbers calculated from the steady and oscillatory shear experiments are not in good agreement. In fact, collagen solutions display strong anisotropic behaviors and this kind of empirical law is not suitable to model such specific fluids. However, we attempt to describe the Weissenberg number $Wi(\dot{\gamma})$ from our experimental data by a power law:

$$Wi = \left(\frac{\dot{\gamma}}{\dot{\gamma}_0} \right)^m$$

We extract from this curve fitting the physical quantities: a) the exponent: $m \simeq 0.3$, b) the crossover shear rate: $\dot{\gamma}_0 \simeq 1.2s^{-1}$ and $Wi(\dot{\gamma}_0) \simeq 0.097$. The characteristic disentanglement time τ_c is equal to 0.83 s, which is about 200 times smaller than the one found in Gobeaux et al. study (Fig. 3.4).

3.1.2.3 Typical physical quantities for other concentrations

In chapter 5, we describe the production of collagen threads at different concentrations in order to find the best condition (swelling, collagen fibrils alignment, mechanical properties etc) for the further studies. Three concentrations are tested: 15, 30 and 60 mg/mL. Based on the Gobeaux et al. work [3], we can already have an idea of the physical quantities for those conditions.

In this concentration range, different regimes may be observed. Indeed, c^* which is the overlap concentration separating the dilute and the semi-dilute regime was estimated from the specific viscosity. c^* is defined as the concentration at which polymer molecules start to contact with one another, which induces changes of the solution viscoelastic properties. For collagen solution, it is assumed to be around 3-5 mg/mL [2]. In our case, concentrations are higher than 5 mg/mL which means that even at 15 mg/mL, solutions are in the semi-dilute regime. At 30-60 mg/mL, collagen solutions are in entangled state. It would be also interesting to have an order of magnitude of the "plateau" viscosity, the crossover shear rate and the exponents of the shear-thinning linear region n_1 . To do so, we extracted those quantities from the following figure and the results presented in [3]:

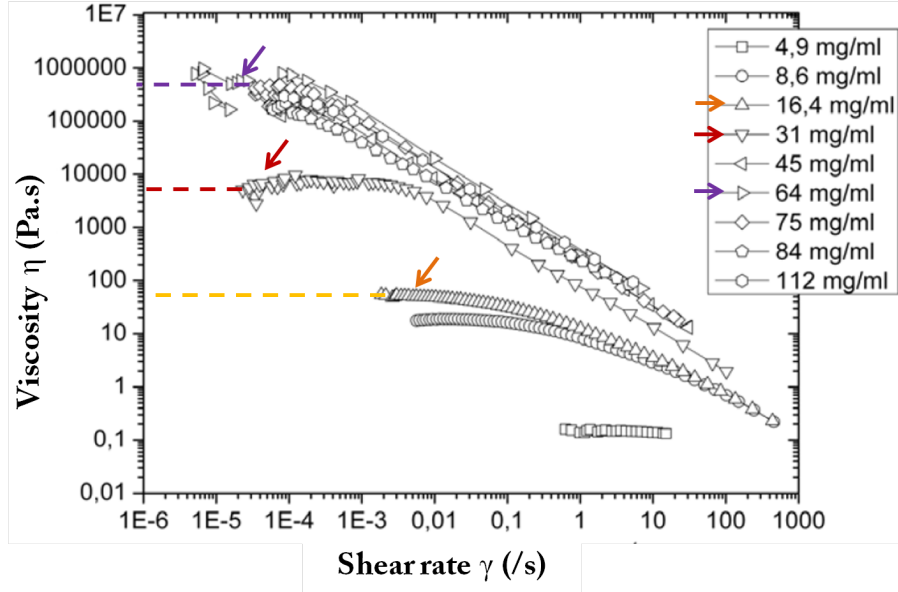


Figure 3.6: Viscosity of collagen at different concentrations as a function of the shear rate. The concentrations of interest are highlighted by colored arrows: 16.4 (orange), 31 (red) and 64 (purple) mg/mL. Eye guidelines in dashed lines are given to estimate η_0 . From [3]

The concentrations studied close to ours are highlighted by colored arrows. From this figure 3.6, we could obtain the "plateau" viscosity η_0 . We deduced the crossover shear rate from Figure 3.4 given the characteristic disentanglement time τ_c . The table 3.2 shows those quantities as a function of concentration.

C (mg/mL)	η_0 (Pa.s)	$\dot{\gamma}_0$ (/s)	n_1
16.4	50	$1.5 \cdot 10^{-2}$	0.65-0.72
31	5000	$5 \cdot 10^{-3}$	0.79
64	50 000	$4 \cdot 10^{-4}$	0.81

Table 3.2: Characteristic physical quantities of collagen solutions of interest, from [3].

3.2 Alginate solutions rheological characterization

In this section, the same rheological characterizations as collagen solutions is performed on alginate ones. The choice of the concentrations of alginate solutions was substantially motivated by the possibility to transpose the results obtained on alginate extrusion to collagen.

3.2.1 Viscosity analysis

The viscosity of sodium alginate solutions in pure water was measured at temperature $T = 20$ °C for shear rates ranging from 0.01 to 200 s^{-1} .

3.2.1.1 Alginate concentration choice

For the lowest concentrations (< 1 wt %), we used the double gap Couette cell geometry and above, the cone-plate geometry. Measurements at $c = 1$ wt % were done with the two

geometries to ensure the results continuity. Figure 3.7 displays the specific viscosity η_{sp} defined as $\eta_{sp} = (\eta_0 - \eta_s)/\eta_s$ as a function of the concentration c , where η_0 is the viscosity of the solution in the vanishing shear rate Newtonian regime and η_s is the solvent (water) viscosity. While increasing the alginate concentration, the specific viscosity increases gradually with three characteristic slopes corresponding to the usual regimes observed for polymer solutions [7]:

- $c < c^*$: dilute regime
- $c < c^* < c_E$: semi-dilute unentangled regime
- $c > c_E$: entangled regime

where c^* , as previously mentioned, is the overlap concentration ($c^*=0.35\%$) and c_E is the entanglement concentration ($c_E=1\%$). The overlap concentration for alginate was quite similar to that of collagen: $c^*_{alg} \simeq c^*_{coll} \simeq 3 - 5\text{mg/mL}$. Collagen solutions of 15 to 60 mg/mL exhibit zero-shear viscosity ranging between 50 and 50 000 Pa.s. To study alginate solutions with the same order of viscosity, we choose to use concentrations above 4 wt % (4, 6 and 10 wt %) which also correspond to the entangled state (Fig. 3.7 grey region).

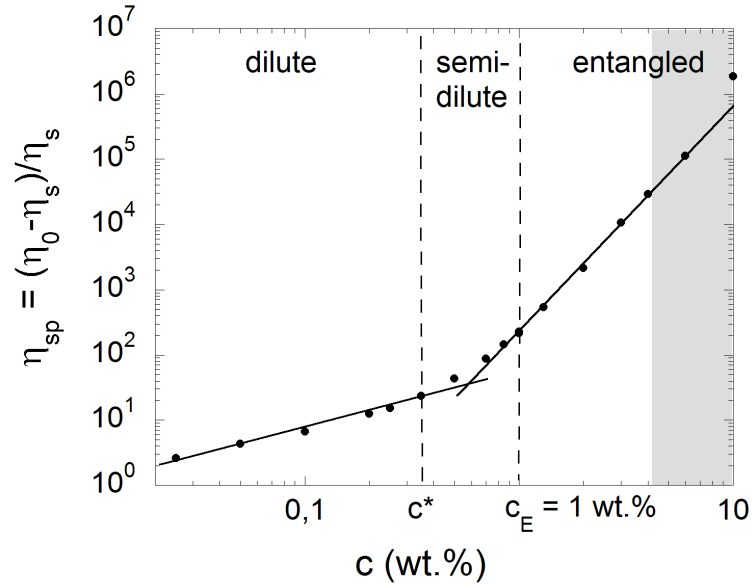


Figure 3.7: Specific viscosity of alginate solutions as a function of concentration (wt %), measured at $T = 20^\circ\text{C}$. The boundaries between the three scaling regimes define the overlap $c^* = 0,35\text{ wt \%}$ and entanglement $c_E = 1\text{ wt \%}$ concentrations. The grey zone indicates the concentration domain relevant to our work, corresponding to strongly entangled solutions.

3.2.1.2 Shear-thinning nature

Figure 3.8 shows the viscosity evolution as a function of the shear rate for the chosen solutions ALG4, ALG6 and ALG10. Each solution exhibit a marked shear-thinning behavior which can be characterized by the Cross law [8], [9]:

$$\eta(\dot{\gamma}) = \frac{\eta_0}{1 + (\dot{\gamma}/\dot{\gamma}_0)^{1-m}}$$

We found a single exponent m equal to 0.29 ± 0.02 for the three concentrations. This exponent value is compatible with that usually reported ($m \simeq 0.24$) for entangled and

random coil polysaccharide solutions [10]. Moreover, in the case of collagen solutions, we showed that: $\eta \propto \dot{\gamma}^{-n}$ with $0.65 < n < 0.81$. From the Cross law fit, it is assumed $\eta \propto \dot{\gamma}^{m-1}$ with $m=0.29$ which corresponds to an exponent $n = 1 - m = 0.71$. Thus, collagen and alginate solutions used during our study had almost the same shear-thinning behaviors.

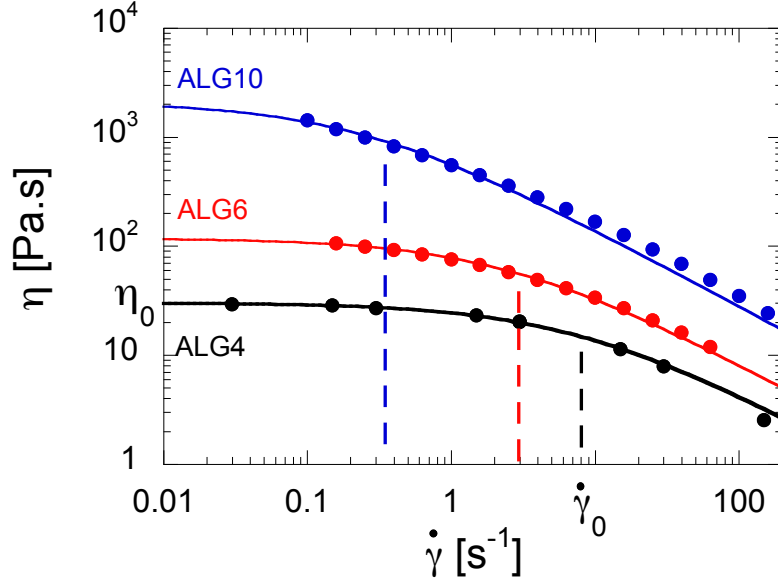


Figure 3.8: Shear-thinning behavior of the alginate solutions at 4, 6 and 10%. The solid lines are a fit by a Cross law with a common shear-thinning exponent $m = 0,29$. The dashed lines mark the crossover shear rates $\dot{\gamma}_0$.

The characteristic physical quantities (η_0 , $\dot{\gamma}_0$ and the exponent n) found from the Cross law fits for each concentration are gathered in the following table 3.3:

C^0 (wt%)	η_0 (Pa.s)	$\dot{\gamma}_0$ (/s)	τ_c (s)	n
4	30	8	0.13	0.71
6	110	3	0.33	0.71
10	1900	0.3	3.3	0.71

Table 3.3: Characteristic physical quantities of chosen alginate solutions: ALG4, ALG6 and ALG10.

NB: The characteristic times τ_c for alginate ranging from 130 ms to 3.3 s was very low compared to collagen ones ($80s < \tau_c < 30$ min for $16.4 \text{ mg/mL} < c < 60 \text{ mg/mL}$).

3.2.2 Complex modulus analysis

Storage (G') and loss (G'') moduli were measured with cone-plate geometry under oscillatory shear for angular frequencies between 0.1 and 300 rad/s. Figure 3.9 shows the results for the three alginate concentrations. Here again, it was clear that the three alginate solutions displayed viscoelastic behaviors.

Same analyses as collagen moduli were performed to assess the exponents of those two quantities in the linear region. Moreover, the crossover angular frequency allowed us to estimate the relaxation time λ of each solution. All those computed values are presented in Table 3.4.

The complex viscosity η^* was also calculated from G' and G'' measurements with the Cox-Merz rule. It was verified for those three concentrations.

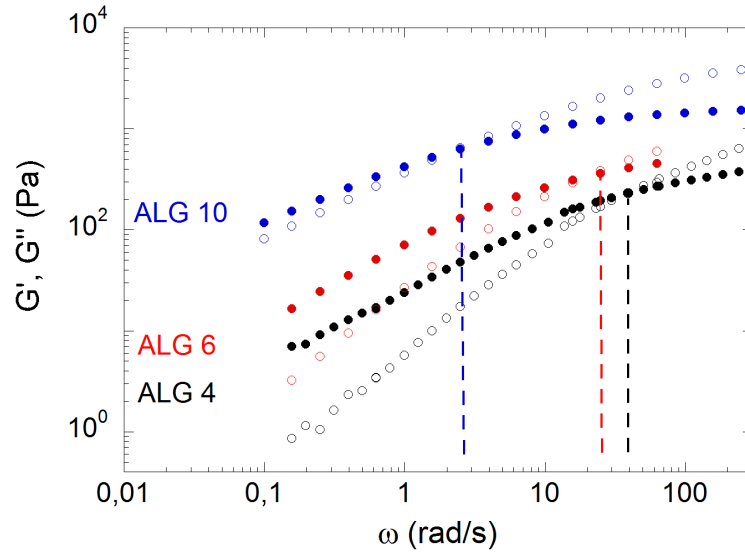


Figure 3.9: Shear storage G' (empty circle) and loss G'' (filled circle) moduli against angular frequencies for: ALG4 (black), ALG6 (red) and ALG10 (blue). The dashed lines show the crossover angular frequency for each condition.

Solution	α (G')	β (G'')	ω_c (rad/s)	λ (ms)
ALG4	1.16	0.72	30	33
ALG6	1.05	0.72	20	50
ALG10	0.65	0.53	2.5	400

Table 3.4: Fit exponents α and β for the respective storage and loss moduli; the crossover angular frequency ω_c and the relaxation time λ estimated from ω_c values for the three algininate concentrations: ALG4, ALG6 and ALG10.

3.2.3 First normal stress difference and Weissenberg number

The viscoelastic properties were also characterized by the measurement of the first normal stress difference N_1 as a function of the shear rate. The experimental results are shown in Figure 3.10 (empty circles). As previous analysis performed for collagen, we used Laun empirical relationship to also compute first normal stress difference ($N_{1,Laun}$) from the shear and loss moduli measurements (Fig 3.10 filled circles). The results from the two ways of measuring N_1 were in good agreement for ALG10 which was the most concentrated solution. For ALG4 and ALG6, the $N_{1,Laun}$ was overestimated compared to the direct measurements of N_1 . Here again, it is probably due to the N_1 measurement difficulty as the normal forces may be too low for this concentration range.

However, the $N_{1,Laun}$ allowed us to estimate the Weissenberg number Wi for algininate (Fig. 3.11)

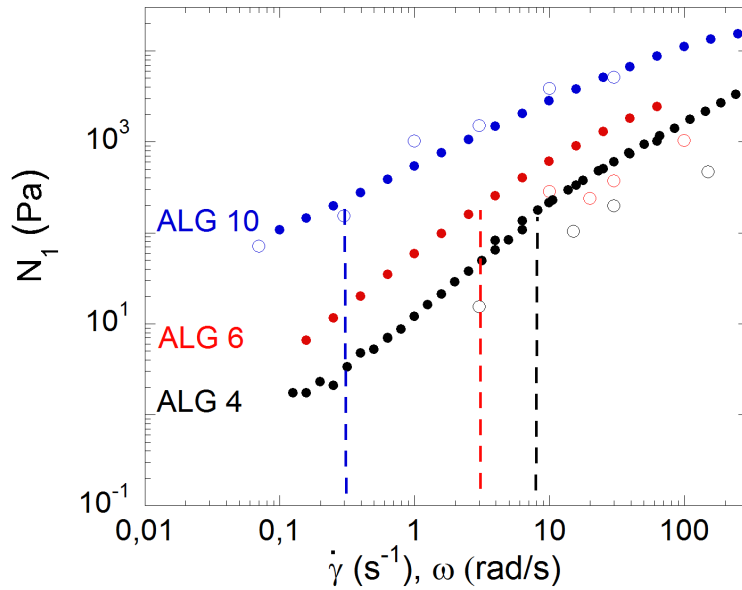


Figure 3.10: First normal stress difference measured in steady state shear (empty circles) and computed from Laun empirical relationship through G' and G'' measurements (filled circles) The dashed lines show the crossover shear rate for each condition.

For $\dot{\gamma} > \dot{\gamma}_0$, Wi number can be described by a simple power law as previously done for collagen. A common exponent equal to 0.3 was found for the three alginate concentrations. The Weissenberg number estimated for collagen at 30mg/mL had the same exponent but was lower even compared to ALG4.

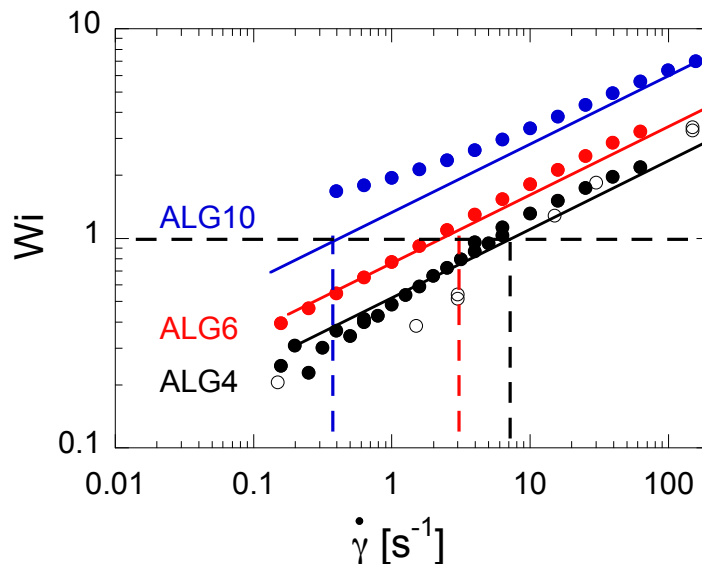


Figure 3.11: Sublinear, shear rate dependent Weissenberg number for alginate solutions. The dashed lines indicate the values of $\dot{\gamma}_0$ and the full lines are the power fit with a common exponent equal to 0.3.

3.3 Conclusion

Collagen and alginate solutions exhibit strong viscoelastic and shear-thinning behaviors which are quite similar in the concentration region of interest. Moreover, those complex fluids will be studied in the same "entanglement" state. The empirical rules and relationships are verified and in good agreement with the literature for alginate system. In the case of collagen, Cox-Merz rule can be applied but further analysis are needed to better model such specific fluid.

This rheological study makes us confident to have chosen comparable concentration condition with two different systems. It will probably help us to transpose extrusion results from one system to the other.

3.4 References

- [1] Frédéric Gobeaux, Emmanuel Belamie, Gervaise Mosser, Patrick Davidson, and Sophie Asnacios. Power law rheology and strain-induced yielding in acidic solutions of type i-collagen. *Soft Matter*, 6(16):3769–3777, 2010. [iv](#), [87](#), [88](#), [89](#)
- [2] Frédéric Gobeaux, Emmanuel Belamie, Gervaise Mosser, Patrick Davidson, and Sophie Asnacios. Power law rheology and strain-induced yielding in acidic solutions of type I-collagen. *Soft Matter*, 6(16):3769, 2010. [88](#), [93](#)
- [3] Frédéric Gobeaux. *Phases denses de collagène de type I: transition isotrope/cholestérique, fibrillogénèse et minéralisation*. PhD thesis, Université Pierre et Marie Curie-Paris VI, 2007. [88](#), [91](#), [93](#), [94](#)
- [4] W Cox and E Merz. Rheology of polymer melts—a correlation of dynamic and steady flow measurements. In *International Symposium on Plastics Testing and Standardization*. ASTM International, 1959. [90](#)
- [5] Wolfgang Ostwald. Ueber die geschwindigkeitsfunktion der viskosität disperser systeme. i. *Colloid & Polymer Science*, 36(2):99–117, 1925. [91](#)
- [6] HM Laun. Prediction of elastic strains of polymer melts in shear and elongation. *Journal of Rheology*, 30(3):459–501, 1986. [92](#)
- [7] Liang Guo, Ralph H Colby, Charles P Lusignan, and Andrew M Howe. Physical gelation of gelatin studied with rheo-optics. *Macromolecules*, 36(26):10009–10020, 2003. [95](#)
- [8] Malcolm M Cross. Rheology of non-newtonian fluids: a new flow equation for pseudoplastic systems. *Journal of colloid science*, 20(5):417–437, 1965. [95](#)
- [9] R Byron Bird, Robert C Armstrong, and Ole Hassager. Dynamics of polymeric liquids. vol. 1: Fluid mechanics. 1987. [95](#)
- [10] ER Morris, AN Cutler, SB Ross-Murphy, DA Rees, and J Price. Concentration and shear rate dependence of viscosity in random coil polysaccharide solutions. *Carbohydrate polymers*, 1(1):5–21, 1981. [96](#)

Chapter 4

Extrusion instabilities of polymer solutions

“It’s up to you how far you’ll go. If you don’t try, you’ll never know.”

Merlin in *The Sword in the Stone*

Abstract

The purpose of this chapter is to study instabilities affecting the extrusion of a viscoelastic polymer solution. Two different configurations were studied depending on the presence or not of gelling ions in the exit solution.

We have first performed an extensive study using sodium alginate solutions. The non-gelling configuration is akin to the industrial one, hence widely studied polymer melt extrusion process. Here, however, we have made use of capillaries ("dies") with unusually large length to radius ratios. We have been able to prove that in that case, the helical extrusion instability observed at high enough Weissenberg number is the mere consequence of a bulk pipe flow instability, predicted theoretically for such highly shear-thinning fluids but never observed experimentally.

In the presence of gelling Ca^{2+} ions, more complex phenomena are involved and lead to unexpected and spectacular instabilities that we will describe.

Finally, we have made use of our results on alginate to narrow the domain of control parameter in our quest of an analogous helical instability. We show that such an instability actually occurs and we give hints of a "crimp like" helical ordering of the collagen fibrils.

Contents

4.1 Quick literature overview: polymer melt extrusion instabilities	103
4.1.1 Surface instability: the sharkskin	104
4.1.2 Spurt-flow defect	104
4.1.3 Bulk distorsion	104
4.1.3.1 Helical	104
4.1.3.2 Gross melt fracture	105
4.1.4 Conclusion	105
4.2 Extrusion in a bath of non-binding ions	105
4.2.1 Context and motivations	105
4.2.1.1 Conclusion	108
4.2.2 Results: Experimental evidence of helical, supercritical instability in pipe flow of shear thinning fluids	108
4.2.3 Implementation on other systems: In the "crimp" quest	122

4.2.3.1 Quick literature overview	122
4.2.3.2 Helical instability: from alginate to collagen	123
4.3 Extrusion in a bath of cross-linking ions	125
4.3.1 Overall observations	125
4.3.2 Smooth region	126
4.3.3 Die swelling	128
4.3.4 Wavy, striated patterns and smooth alternation	130
4.3.4.1 Volumetric waves and surface striations	130
4.3.4.2 Oscillating flow	134
4.3.5 Gel clogging	135
4.4 Conclusion	137
4.5 References	138

4.1 Quick literature overview: polymer melt extrusion instabilities

It has taken a long time of sustained experimental efforts to classify the different instabilities occurring, depending on the nature (linear, branched...) of the polymers, on the geometry (die length, radius) and the throughput. Several expressions have been coined to describe these instabilities which are now recognized as misleading. For instance, melt fracture expression was used to gather and describe all polymer melt instabilities as it was first thought that they came all from local ruptures of the material. However, there is no evidence that those phenomena are all related to the rupture of polymer melt and the term "melt fracture" is not suitable but still used [1].

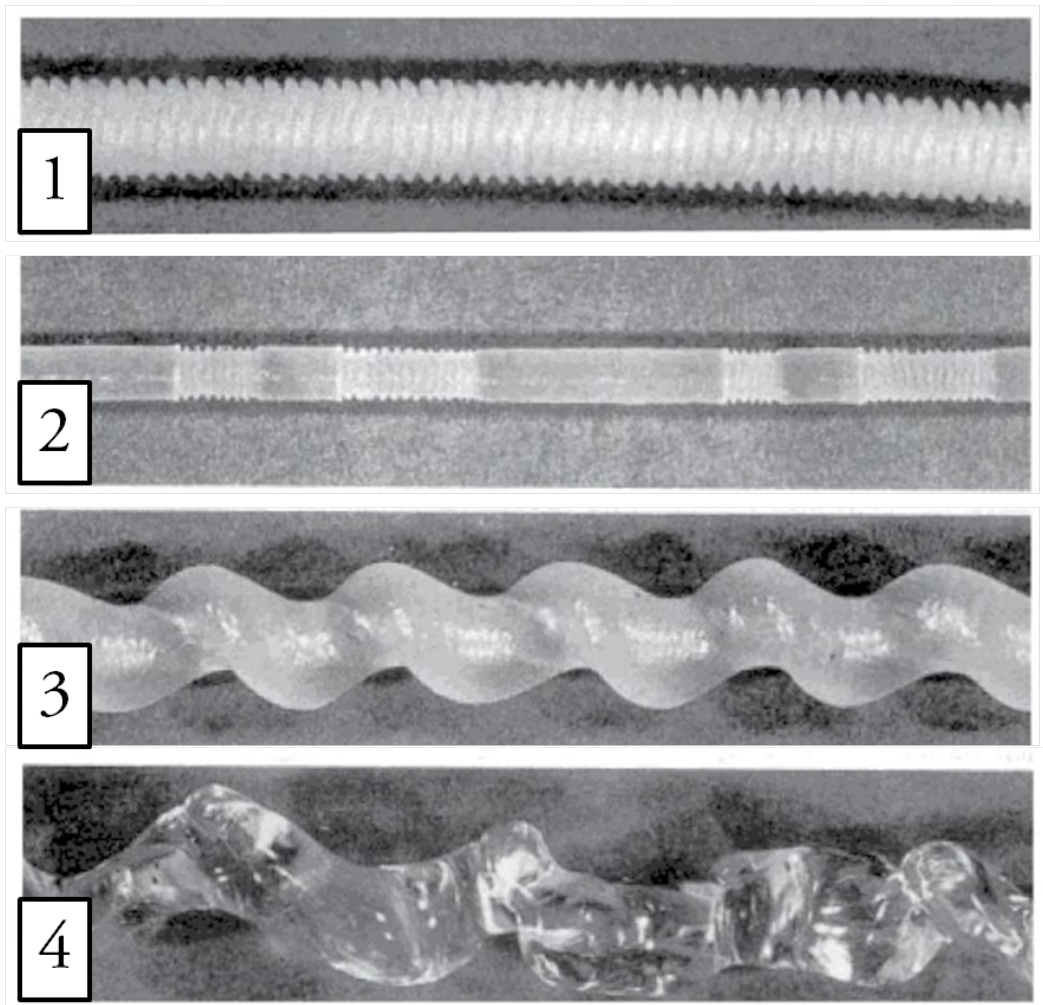


Figure 4.1: Examples of polymer melt extrudates exhibiting: 1)Sharkskin, 2)Spurt-flow, 3) Helical, and 4) Chaotic defects. Adapted from [2]

It is thus meaningful to distinguish between surface and bulk instabilities, depending on the extension of the profile perturbation with respect to the average extrudate radius: 1) the sharkskin, 2) the "spurt-flow", 3) helical and 4) chaotic defects [2]. As shown in Figure 4.1, these instabilities spoil in a more or less pronounced way the extrudate: either affecting the surface, or the volume. For each characteristic defect, we review the main observations and possible mechanisms which may initiate those instabilities.

4.1.1 Surface instability: the sharkskin

Sharkskin affects the surface of the extrudate and takes its name from its typical pattern that looks like the skin topological structure of sharks. It generally occurs at low shear rates and it is not impacted by the length of the die or the angle of the inlet. Moreover, the velocity field at distances larger than the capillary radius is not disturbed while noticing sharkskin instability. All those observations point to the idea that this defect is produced at the die exit. Moreover, surface treatment promoting wall slip in the exit vicinity has been shown to suppress sharkskin [3]. In fact, the die exit displays a singular point which is the site of high stresses and elongation.

A possible mechanism was proposed and thought to be responsible for the sharkskin pattern [2]. In fact, due to the abrupt transition from no slip to no stress boundary conditions at the capillary exit, the flow is singular at the rim, i.e. the stress field inside the pipe and the shear rate outside should diverge. This unphysical unbounded behavior must lead to localized but important changes, e.g. wall slip (e.g. via chain disentanglement) or fracture of the viscoelastic extrudate.

4.1.2 Spurt-flow defect

Several names are used to designate this instability: cycling melt fracture, stick-slip, spurt or plug flow etc. It appears as a regular succession of different morphologies areas, generally a smooth one alternating with sharkskin and this phenomenon may be very periodic [4],[5]. While imposing the flow rate, this instability is also revealed through pressure jumps [6]. It is very sensitive to the geometry of the flow and so the ratio of the pipe length L over its diameter D . If this ratio is close to 0, oscillations vanish.

From those observations, it is assumed that this defect occurs in an unstable region where it can go from a smooth regime to a surface instability one. Here again, two main explanations are given [7]:

- At first it was thought that this instability was only due to the viscoelastic nature of the material.
- A second mechanism is the succession of sliding and adhesion of the polymer chains to the wall. In the sliding phase, polymer chains keep their entangled configuration and the extrudate is smooth. In the adhesive phase, the chains are first elongated and then recover their initial entangled configuration at the outlet which leads to the "skin" fracture as previously explained.

The first hypothesis was discarded and the second one is assumed to represent the real mechanisms. Thus, the best way to kill this oscillating defect is to induce a permanent sliding on the wall by changing the roughness of the die.

4.1.3 Bulk distortion

The more spectacular instabilities are the bulk distortion which impacts the whole volume of the extrudate.

4.1.3.1 Helical

This instability affects the entire volume of the extrudate and exhibits helical shape which can be very periodic. The amplitude of the defect increases with the flow rate. It is damped while increasing the capillary length [7] and also while decreasing the angle of the die entry [8]. By observing the velocity and the stress fields in the reservoir, many authors at-

tributed the phenomena to the contraction at the die entry where destabilization of the elongational flow occurs [9], [10]. However, it should also be considered that this instability may develop itself along the pipe [11].

4.1.3.2 Gross melt fracture

The gross melt fracture or chaotic defect gives to the extrudate an extremely disturbed appearance [1]. For all materials, it is observed at very high flow rates. This instability is quite difficult to quantify but is always ascribable to too severe flow and die entry conditions.

4.1.4 Conclusion

The instabilities in the case of polymer melt extrusion can spoil either the surface or the volume of the extrudate. In some cases, both types can even be superimposed. Most of the mechanisms involved are understood but some of them are still contested and need to be further investigated. Regarding industrial concerns, it is necessary to fully improve this knowledge to be able to kill their defects and produce smooth extrudate in a wide range of velocity.

In the following sections, we study the extrusion of alginate solutions (ALG4, ALG6 and ALG10) in the presence or not of binding ions. We report for both conditions the instabilities obtained. Based on the polymer melt extrusion knowledge, we strive to give possible mechanisms involved in our case.

4.2 Extrusion in a bath of non-binding ions

4.2.1 Context and motivations

Alginate extrusion in a bath without binding ions is the simplest way to study flow stability. In fact, it avoids all parasitic phenomena which occur with divalent ions as gelation. Moreover, the presence of the solution allows to get rid of the surface tension and especially the gravity, which adds stretching due to the weight of the extrudate.

We will present here the preliminary results that initiate the thorough and quantitative investigation of such extrusion presented in 4.2.2.

At the beginning, we naively wanted to know if the instabilities observed for polymer melt were also visible with polymeric solutions. We decided to play with the different affordable parameters, one at a time: alginate concentration, velocity, die material or dimensions, and observe the flow at the die exit.

First, we decided to use the lowest concentration and extruded alginate solutions at 4% (ALG4) with glass capillary. At low throughput, the extrudate was smooth (Fig. 4.2, a). While increasing the velocity, a very fine pattern appeared (Fig. 4.2, b) black arrow) compared to the smooth one. This reminded us of the sharkskin instability but the amplitude was very low. We thus tested higher alginate concentration (ALG10) with the same material (glass). The sharkskin clearly appeared with a higher contrast which suggested a stronger amplitude. It seemed to disappear while moving away from the die exit.

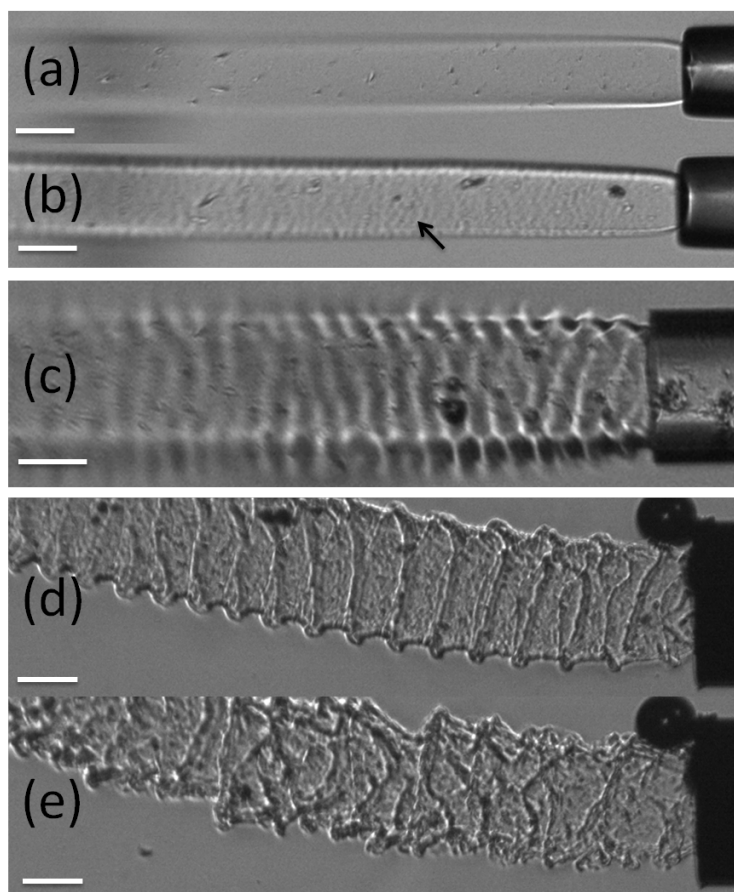


Figure 4.2: Morphologies observed during the extrusion of: ALG4 in water with a glass capillary at low a) and increased velocity; c) ALG 10 in water with a glass capillary and d) ALG 10 in $MgCl_2$ 0.5M with metallic needle. b), c) and d) extrudates exhibit sharkskin instability. White scale bar = 200 μm

NB: The extrusion bath was filled with deionized water or $MgCl_2$ 0.5M and thus no thread is formed. Mg^{2+} ions were assumed to induce very weak binding with alginate chains and we verified that results in water or $MgCl_2$ were the same. Thus, the extrudate defects could only be observed in real time as it dissolved in such bath.

However, it was only due the alginate dissolution in water. In the rest of the study, we thus extruded alginate in a solution of $MgCl_2$ as Mg^{2+} are non binding ions and alginate (strongly charged) is poorly soluble in such strongly saline solutions ($I \approx 0.5M$). We verified that the same results were obtained for extrusion in NaCl solution of same ionic strength (I).

After changing the concentration, the question of the influence of the die material arose. We then extruded then ALG10 with stainless steel needle (Fig. 4.2, c)). Here again, the sharkskin defect was clearly visible and became quite chaotic for higher throughputs (Fig. 4.2, d)).

With those qualitative observations, we already had an idea of the impact of different parameters on the **sharkskin instability**: the amplitude seemed to be higher for ALG10 compared to ALG4 and the same observation was made for glass capillary compared to the metallic needle. The metallic needle inner surface may be rougher than the glass capillary one which can explain the higher skin failure in the first case. Indeed, as previously explained, in this case, the polymer chains adhesion is stronger and leads to a higher elongational stress at the die exit.

As this first instability was obtained, we decided to further explore the **velocity parameter**. We used exactly the same conditions as presented in Figure 4.2 but we increased the velocity. For all conditions (ALG4, ALG10) and even while changing the die material, the extrudate exhibited a wavy shape (Fig. 4.3). It looked quite similar to the **helical pattern** observed for polymer melts. However, here, simple observations were not sufficient to extract a trend. In fact, it was quite difficult to observe the "birth" of such instability. When it was clearly seen, the instability was already well established and the amplitude evolution was not fully assessed even after increasing the camera acquisition frame rate.

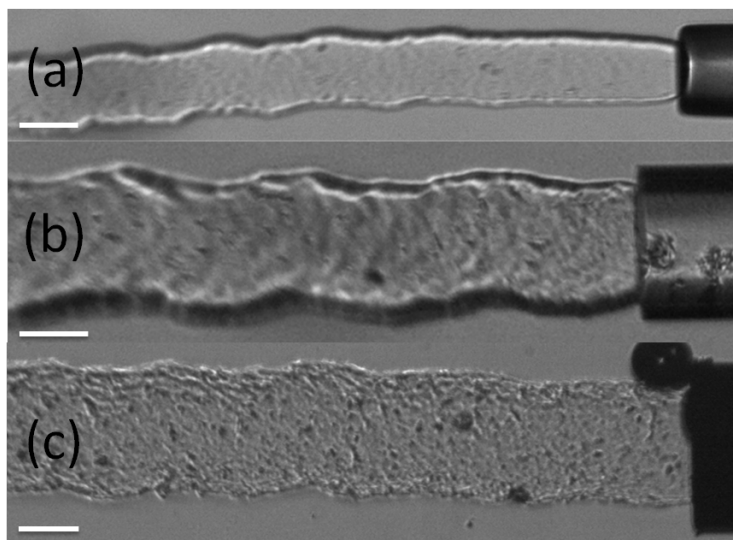


Figure 4.3: Morphologies observed during the extrusion of: a) ALG4 in water with a glass capillary; b) ALG 10 in water with a glass capillary and c) ALG 10 in $MgCl_2$ 0.5M with metallic needle, for higher velocities compared to the first set of observations 4.2. a), b) and c) extrudates have a wavy shape. White scale bar = 200 μm

We therefore faced several questions: How can we track the beginning of this instability? Has this wavy instability an helical geometry? And finally, does this instability come from the die entry or develop itself along the pipe?

Fortunately, some key "particles", which were not at first expected to be so useful, helped us to answer several questions. Those "particles" were the air bubbles entrapped in our solutions. Some may consider them as parasitic particles, but in our case, they were essential tracers of this wavy defect. As shown in the figure 4.4, some **train of bubbles** could appear during the extrusion. While the wavy instability was observed, the train path was sinuous and periodic. More interesting, we observed that a smooth extrudate contained first a straight and then a sinuous path of air bubbles while increasing the velocity. This meant that we could track the birth of this instability by looking at the form of the tracers paths.

The profile of the extrudate could then be systematically followed and analyzed from the instability "birth" in order to extract its undulation amplitude as a function of the velocity. Glass capillaries allowed us to observe those tracer inside the pipe. Thus, we could observe how this instability evolved all along the pipe.

The question of the die entry effect still remained and contrary to previous polymer melt studies, where authors directly saw this effect by using a transparent slit die, it was not possible to observe this region in our case due to the set-up configuration. However,

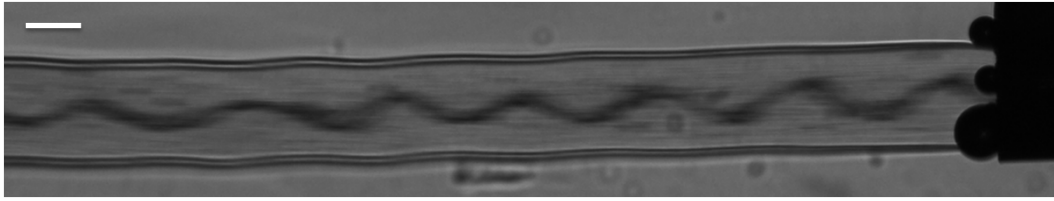


Figure 4.4: Path of train of bubbles during the extrusion of ALG10 in $MgCl_2$ 0.5M while wavy shape is observed. White scale bar = 200 μm

the different capillaries could insert into each other leading to a contraction or an expansion configuration. In other words, we produced a **second "die entry"** which is transparent and allows us to simulate the event taking place at the die entry. We can either put a stable flow or an unstable flow in the first capillary which stood as the die entry and observe what it became in the second one (Fig. 4.5)

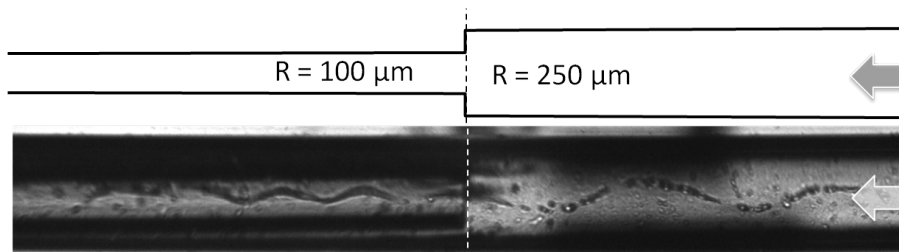


Figure 4.5: Interlocking of two capillaries of radii 250 and 150 μm which act at a die entry configuration where contraction of the flow occurs. Train of bubbles allow to see the die entry effect. Wavy to wavy state is presented. Flow direction is given by the grey arrows.

4.2.1.1 Conclusion

Without binding ions, two main instabilities observed for polymer melts are found here: the sharkskin and the helical defects. For the first, we clearly noticed the die material impact which leads to severe skin fractures in the case of metallic needles. Helical instability is more difficult to track, however, several solutions came to us and allowed us to quantify precisely its shape, amplitude and to understand the mechanisms behind this instability. The results of this thorough analysis are presented in the following article.

4.2.2 Results: Experimental evidence of helical, supercritical instability in pipe flow of shear thinning fluids

In this first study, we report the extrusion of strongly shear thinning alginate solutions through long glass capillaries (aspect ratios $L=R$ up to 200), in a bath of non-binding ions solution. The extrudate shape and the tracer paths (e.g. Fig. 4.4) are observed together in order to analyze the flow stability.

From those experiments, we provide proofs of: (i) the existence of an instability associated with the helical distortion of the extrudate, (ii) the supercritical nature of the bifurcation and (iii) concomitant emergence of undamped velocity oscillations extending along the whole length of the capillary. [12]

Experimental evidence of a helical, supercritical instability in pipe flow of shear thinning fluids.

L. Picaut, O. Ronsin, C. Caroli and T. Baumberger

*Institut des NanoSciences de Paris, CNRS, Sorbonne Université – Pierre et Marie Curie,
UMR 7588, 4 place Jussieu, 75005 Paris, France*

We study experimentally the flow stability of entangled polymer solutions extruded through glass capillaries. We show that the pipe flow becomes linearly unstable beyond a critical value ($Wi_c \simeq 5$) of the Weissenberg number, via a supercritical bifurcation which results in a helical distortion of the extrudate. We find that the amplitude of the undulation vanishes as the aspect ratio L/R of the capillary tends to zero, and saturates for large L/R , indicating that the instability affects the whole pipe flow, rather than the contraction or exit regions. These results, when compared to previous theoretical and experimental works, lead us to argue that the nature of the instability is controlled by the level of shear-thinning of the fluids. In addition, we provide strong hints that the non-linear development of the instability is mitigated, in our system, by the gradual emergence of gross wall slip.

INTRODUCTION

Extrusion, which consists in forcing viscoelastic polymer melts or solutions out of a reservoir through an axisymmetric pipe, or “die”, is an important shaping process, unfortunately prone to a variety of instabilities which spoil the surface or the bulk of the extrudate [1–3]. Among these, an ubiquitous one, usually referred to as “melt fracture”, results in a distortion of the extrudate into a more or less pronounced and regular helical shape. Visualization of the velocity and stress fields in the reservoir [3–6] has lent strong support to the idea that melt fracture was ascribable to the well documented destabilization of the elongational flow upstream of the sudden contraction at the entry of the die [4, 7]. Due to viscous damping, such velocity oscillations are expected to decay over a finite length as the fluid is advected through the pipe. Hence, it is not surprising that helical instabilities were reported by many authors as being more severe when using short dies, rather than pipes with larger length/radius (L/R) aspect ratios [3]. However, as pointed out by Larson [1], one cannot rule out that the flow in a long pipe may itself develop a bulk helical instability, in which case the amplitude of the extrudate distortion should not decrease upon increasing the die aspect ratio.

The stability of the flow in an infinitely long pipe, in the limit of vanishing Reynolds numbers, has been the subject of extensive theoretical studies, in the case of viscoelastic fluids obeying either the Oldroyd-B [8, 9] or the White-Metzner [10, 11] constitutive equations. In the first case, dealing with the peculiar class of non shear thinning fluids, it has been shown that the Poiseuille flow, although *linearly stable*, exhibits a *weakly non-linear* subcritical instability: beyond a critical value of the Weissenberg number Wi , the flow is unstable against a finite but small noise amplitude, therefore resulting in a hysteretic behavior [8, 9]. The existence of such an instabil-

ity has later been confirmed by the experimental studies of Bertola et al. [12] and Pan et al. [13] on axisymmetric pipe and 2D channel flows.

A wider class of great practical importance deals with polymeric fluids which exhibit both a large first normal stress difference and strong shear thinning in the same range of shear rates. It has been studied theoretically by Wilson and coll. [10, 11, 14] within the framework of the White-Metzner equation, under the assumption of a power law dependence of the shear-rate dependent viscosity $\eta(\dot{\gamma})$. They have shown that the base flow is *linearly unstable* provided that the shear thinning exponent $n = 1 - |d \log \eta / d \log \dot{\gamma}|$ is smaller than 0.3 [10, 11]. The non-linear behavior has not been investigated, however, so that the super- or subcritical nature of the instability remains unpredicted. Strong hints that a bulk flow instability actually occurs beyond a finite Wi value in strongly shear-thinning fluids ($n \simeq 0.2$) have been provided by Bodiguel et al. [15] who observed the emergence of sinuous tracer paths in microfluidic 2D channels. This emergence is associated with that of strong fluctuations of the velocity field, as confirmed by Poole [16] using larger scale pipe flows with $Re \simeq 100$. However, due to the difficulty of quantifying the spatio-temporal behavior of the velocity field inside the die, these studies did not permit a full characterization of the nature of the bifurcation, in terms of amplitude evolution and possible presence of hysteresis.

Here, we report on a study of the extrusion through long glass capillaries (aspect ratios L/R up to 200) of a strongly shear thinning ($n \simeq 0.3$) polymer solution exhibiting a rheology well described by a White-Metzner equation. A detailed quantitative analysis of the extrudate shape, together with the observation of tracer paths in the glass capillaries, provide experimental proof of: (i) the existence of an instability associated with the helical distortion of the extrudate, (ii) the supercritical nature of the bifurcation, which occurs beyond a critical Weissenberg $Wi_c \simeq 4-6$, with a wavelength $\lambda_c \simeq 3R$, (iii) the

concomitant emergence of undamped velocity oscillations extending along the whole length of the capillary,

On this basis, we provide what we think is the first evidence and characterization of a *helical* linear instability of the axisymmetric base flow in a long pipe, in the vanishing Reynolds number limit. We are therefore able to conclude that, at least for shear thinning viscoelastic fluids, upstream destabilization of the contraction flow is *not* the sole route to the helical extrudate instability which, though an ubiquitous phenomenon, has attracted much less attention in the theoretical literature than the “sharkskin” or “spurt flow” ones [1, 2, 17].

MATERIALS AND METHODS

Polymer solutions: preparation and rheological characterization

Polymer solutions were prepared by dissolving sodium alginate (average molecular mass $\bar{M} = 246$ kDa, Kalys S.A., France), a biopolymer extracted from seaweed, in deionized water. 500 ppm sodium azide were added to prevent bacterial development. We have made use of solutions with alginate concentration $c = 4, 6$ or 10 wt.%, referred to in the following as ALG4, ALG6 or ALG10. At the lowest concentration (ALG4), overnight magnetic stirring was sufficient to obtain a homogeneous solution. For higher concentrations, alginate powder was left to swell and dissolve for several days under periodic gentle manual stirring. Homogeneity of the solution was assessed from its optical aspect.

Rheological measurements were performed using a stress-controlled rheometer (MCR 501, Anton Paar) equipped with a 50 mm diameter, 2° cone-plate, sand-blasted cell geometry.

The concentration dependence of the zero-shear specific viscosity (see data in supplemental material) yields a concentration at the onset of the entanglement regime $c_E = 1$ wt.%, so that the three systems tested in this work are well entangled polymer solutions. Their viscoelastic properties were characterized by the measurement of both the steady flow viscosity $\eta(\dot{\gamma})$ and the first normal stress-difference $N_1(\dot{\gamma})$ for shear rates $\dot{\gamma}$ in the range 10^{-1} – 10^2 s $^{-1}$.

As seen on Fig.1, the three solutions exhibit a marked shear thinning behavior that we have characterized using a Cross law:

$$\eta = \frac{\eta_0}{1 + (\dot{\gamma}/\dot{\gamma}_0)^{1-n}} \quad (1)$$

Fitting values of the plateau viscosity η_0 and crossover shear rate $\dot{\gamma}_0$ are given in Table I. We found that a single shear-thinning exponent n was able to account for the behavior of the three solutions, namely $n = 0.29 \pm 0.02$, a value compatible with the “universal” one ($n \simeq$

0.24) reported for a broad class of entangled, random coil polysaccharide solutions [18] to which alginate belongs.

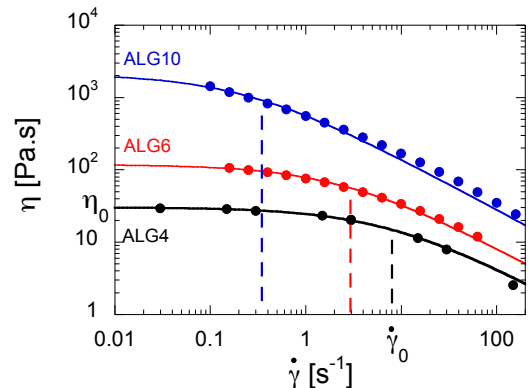


FIG. 1: Shear-thinning behavior of the alginate solutions. The solid lines are a fit by a Cross law with a common shear-thinning exponent $n = 0.29$. The dashed lines mark the crossover shear rates $\dot{\gamma}_0$. Parameters of the fit are listed in Table I.

TABLE I: Plateau viscosity η_0 and crossover shear rates $\dot{\gamma}_0$ values for the three alginate concentrations c used in this study. The last two columns give the critical values of the average shear rate and the corresponding Weissenberg number estimated at the capillary wall at the onset of the helical instability.

	c [wt.%]	η_0 [Pa.s]	$\dot{\gamma}_0$ [s $^{-1}$]	$V/R _c$ [s $^{-1}$]	Wi_c
ALG4	4	30	8	340–500	5–5.6
ALG6	6	110	3	60	4
ALG10	10	1900	0.3	8–14	4.3–5.1

Fig. 2 shows the shear rate dependence of the Weissenberg number Wi defined as:

$$Wi = \frac{N_1(\dot{\gamma})}{\eta(\dot{\gamma})\dot{\gamma}} \quad (2)$$

As commonly observed with shear-thinning viscoelastic fluids [15] $Wi(\dot{\gamma})$ exhibits a markedly sublinear growth indicative of an extended spectrum of viscoelastic relaxation times. This is reasonably well described for $\dot{\gamma} > \dot{\gamma}_0$ by a simple power law:

$$Wi \simeq (\dot{\gamma}/\dot{\gamma}_0)^m \quad (3)$$

with $m \simeq 0.3$. From $m \simeq n$, we conclude that entangled alginate solutions are well described by a White-Metzner model, yielding $\eta = G\tau$ and $N_1 = 2G(\dot{\gamma}\tau)^2$, with a constant elastic modulus G and a shear-rate dependent relaxation time $\tau \sim \dot{\gamma}^{-n}$ for $\dot{\gamma} > \dot{\gamma}_0$.

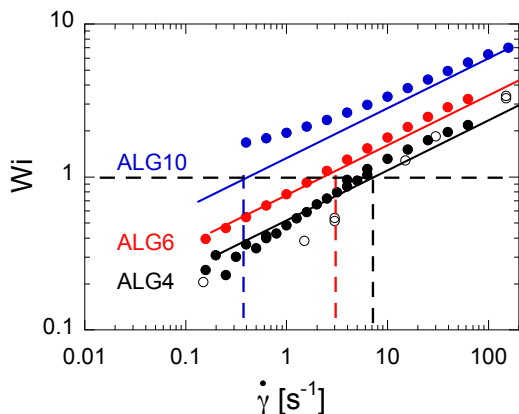


FIG. 2: Sublinear, shear rate dependent Weissenberg number for alginate solutions. The dashed lines indicates the values of $\dot{\gamma}_0$ and the full lines are $(\dot{\gamma}/\dot{\gamma}_0)^m$ with $m \simeq 0.3$.

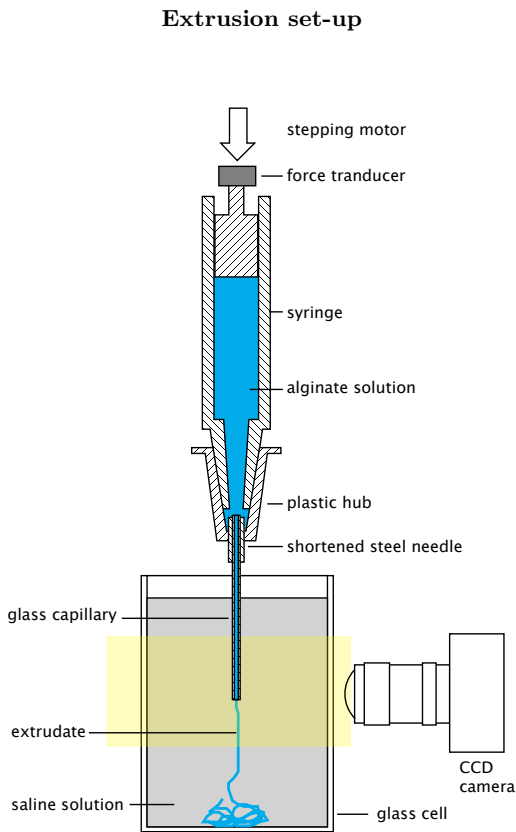


FIG. 3: Schematic representation of the extrusion setup.

Polymer solutions were extruded through cylindrical capillaries of inner radius R and length L using commercial 1 mL syringes. The body of the syringe was filled with the viscous polymer solution using a spatula. The volumetric throughput Q was prescribed by driving

the piston velocity through a home-made syringe pump operated by a stepping motor. As usual when working with microfluidic circuits, their finite compressibility associated with their large hydraulic impedance results in long transients. These were monitored by measuring the force on the piston with an on-line transducer. Fortunately, thanks to shear thinning, the impedance decreases markedly as the throughput increases so that for all Q values used in this study, the volume of fluid extruded during a transient remained negligibly small. In the following, we will characterize the steady state flow by the average velocity in the capillary $V = Q/(\pi R^2)$.

Except when specified, we have made use of cylindrical borosilicate glass capillaries with radii 100, 150 and 250 $\mu\text{m} \pm 10\%$ (VitroCom, USA). Each capillary, used as purchased, was first diamond-cut to the prescribed length, then inserted into a shortened commercial steel needle, with an inner radius chosen to tightly fit the outer radius of the capillary. The assembly was finally epoxy-glued together, with the capillary end just emerging out of the steel needle, into the tapered plastic hub (see Fig. 3).

In order to minimize surface tension and gravity-induced drawing effects on the extrudate, extrusion was carried out into a bath of aqueous liquid. We have made use of a 0.5 M MgCl_2 saline solution into which alginate is poorly soluble so that, although Mg^{2+} ions do not crosslink alginate molecules, the extrudate preserves its shape and sharp interface long enough for its distortions to be quantified.

The whole set-up (syringe, capillary and bath) was thermostated at $T = 20 \pm 0.5^\circ\text{C}$.

The extrusion bath being contained in a glass cell, significant lengths (typically $\simeq 20R$) of the capillary and the extrudate on either side of the exit plane can be monitored under direct, quasi-parallel illumination, using a video camera equipped with a macro objective and operating at speeds up to 300 frame/s. Sequences were acquired for each value of the control parameter V and stored for analysis.

Profile analysis

The undulation amplitude ΔR of the extrudate (see left panel Fig.4) is measured from the reconstruction of its profile, using the section visible at each time t within the field of view. First of all, we select one edge and determine its position $y(t)$ at a distance $x = D$ from the exit plane of the capillary (see Fig.4 for the definition of x and y). A value $D = 4R$ is chosen so as to be out of the zone of viscoelastic recovery responsible for the “die swelling” phenomenon. The edge position in the fixed framework linked to the capillary evolves with time due to the advection of the distorted extrudate along the capillary axis but also perpendicular to it due e.g. to the flagellar motion associated with the sinuous distur-

sion. The latter contribution is redundant and must be removed. We therefore determine the translation vector of the extrudate at time t in the vicinity of the abscissa D by applying a standard image correlation technique in a zone of interest between two successive frames. The y -component is used to correct the edge position while the x -one is used to map the time t onto the position x along the capillary axis. We thus obtain the shape $R(x)$ of the profile edge corresponding to an extrudate length $\simeq 300R$. It is Fourier transformed so as to get the power spectrum from which a peak is identified, centered on a spatial frequency f_0 (Fig.5). Finally, from the area of the peak, one computes the r.m.s. amplitude of the corresponding oscillations, named ΔR in the following.

EXPERIMENTAL RESULTS

The three solutions under study exhibit the same qualitative behavior when extruded at increasing values of V . Except when explicitly stated, the data presented in this section have been obtained with ALG10 solutions.

Characteristics of the instability

The following description refers to the labelled pictures on the left-side panel of Fig.4.

At very low throughput (a), the extrudate profile is cylindrical and smooth. Then (b), upon increasing V , although the extrudate remains straight, a characteristic fine pattern appears on its surface. The pattern contrast gradually increases with V , indicating the growth of the surface distortion until it shows up as a sawtooth deformation of the profile edges (c), unmistakably attributable to the “sharkskin” instability [1–3].

In the vicinity of a velocity V_c , the extrudate profile, as well as trains of micro bubbles which are sporadically coextruded, exhibit bursts of wavy distortion (c). When increasing V slightly above V_c , a wavy instability clearly develops. It manifests itself as a fairly regular, sinuous undulation of the profile edges (d). It is worth noting that the sharkskin pattern does not vanish at the onset of the larger scale undulations but remains superimposed to them, which suggests that both instabilities have independent physical and spatial origins.

The amplitude of the undulation increases rather sharply upon increasing V above V_c and reaches a plateau for $V/V_c \simeq 1.2$ (d), (e). Finally, we have observed no further qualitative changes in the extrudate aspect and/or dynamics upon further increasing V/V_c up to typically 10, i.e. the undulations remain regular and no other instability occurs.

In the following we focus on this instability — leaving the sharkskin one aside — and refer to it as “the” instability. In order to put this description on a more quan-

titative basis, we have systematically measured the rms. amplitude of the oscillations ΔR and their mean spatial frequency f_0 , when the undulating mode was present.

The instability is helical — In order to assess the full 3D symmetry of the extrudate undulation, we have measured ΔR at a single velocity $V \gtrsim V_c$, for a fixed position of the camera but different values of the azimuthal angle θ around the capillary axis. Fig. 6 shows that the undulation amplitude is θ -independent. This, together with the sinuosity of the profile, demonstrates that the extrudate is deformed into a *helical* shape.

The instability is supercritical — A possible subcritical nature of the instability would be revealed by the occurrence of hysteresis in the oscillation amplitude when ramping V up and down [12]. Fig.7 shows that, within experimental uncertainties, no hysteresis is measurable, either on the amplitude or on the spatial frequency of the undulations. We can therefore conclude that the instability occurs via a supercritical bifurcation. This is compatible with the existence of damped bursts of undulation close below the threshold. Accordingly, we determine the critical velocity V_c by extrapolating to $\Delta R = 0$ the universal behavior of the amplitude in the close vicinity of the threshold for a supercritical (Hopf) bifurcation [19], namely $(\Delta R)^2 \sim V - V_c$.

As V/V_c grows, the amplitude ΔR departs from its universal behavior and tends to plateau at a value ΔR_{max} which remains relatively small, namely $\Delta R_{max}/R \lesssim 0.1$. Accordingly, the profile edges remain quasi-sinusoidal (i.e. the non-linear terms of the underlying dynamics remain small). More precisely, the power spectra of $R(x)$ show no harmonic peak and remain relatively narrow (typ. $\Delta f/f_0 \simeq 0.2$) in the whole range ($V/V_c < 10$) investigated. The spectrum shown on Fig.5, which corresponds to $V/V_c \simeq 1.2$, i.e. to the maximum ΔR_{max} of oscillation amplitude, is therefore typical.

The instability is controlled by the Weissenberg number — Fig.8 shows the variations of ΔR and f_0 with V for ALG10 flowing through capillaries with three different radii R . Clearly, the critical velocity V_c , the maximum undulation amplitude ΔR_{max} and the spatial frequency f_0 depend on the capillary radius. Fig.9 shows that V_c , ΔR_{max} and the pitch of the helical disturbance $\lambda = 1/f_0$ depend linearly on R .

Accordingly we have replotted the data, suitably scaled by R (Fig.10). For a given alginate concentration (ALG10) the relevant control parameter is therefore the average shear-rate V/R . We have determined the critical value $V/R|_c$ for ALG4 and ALG6 as well. The values compiled in Table I are compatible with a critical value $Wi_c = 4-6$ of the Weissenberg number (evaluated at the wall, under a no-slip hypothesis, as detailed in supplemental material).

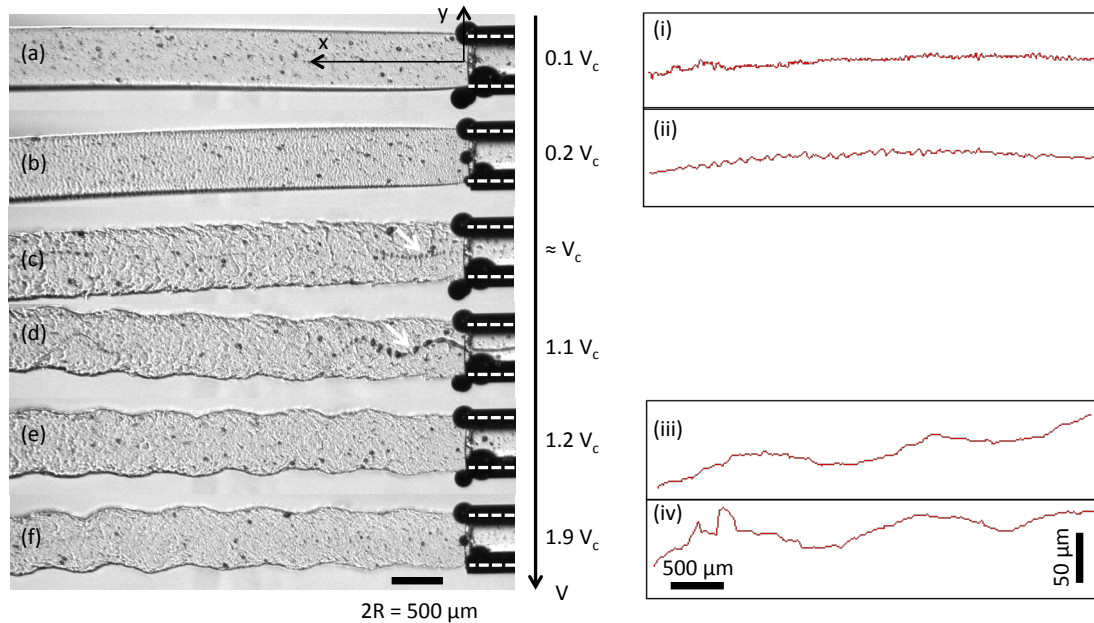


FIG. 4: Left panel: Snapshots of the extrudate exiting from a glass capillary with internal radius $R = 250 \mu\text{m}$ (see dashed white lines) for increasing average velocities V . At a critical value V_c sinuous features show up, such as trains of microbubbles arranged sinusoidally, indicated by white arrows on (c) and (d), see text. Right panel: Characteristic paths of microbubbles tracked in the end portion of the capillary extending $\simeq 20R$ upstream of the exit plane. The velocity scale is common to both panels. We have expanded the vertical scale in order to magnify the bubble displacement perpendicular to the axis.

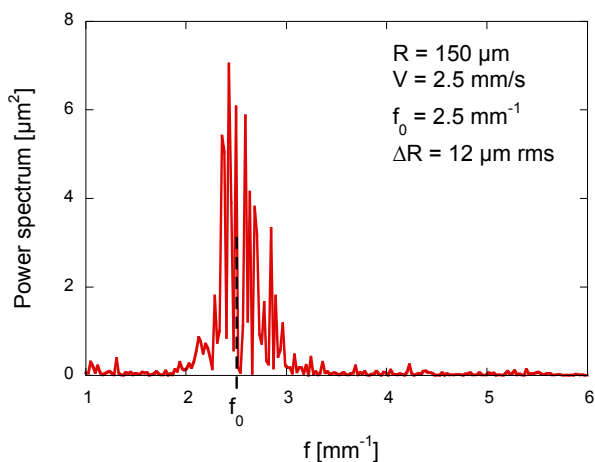


FIG. 5: Power spectrum of a sinuous extrudate profile $R(x)$ for a velocity $V \simeq 1.2 \times V_c$ with V_c the velocity at the onset of oscillations (see text).

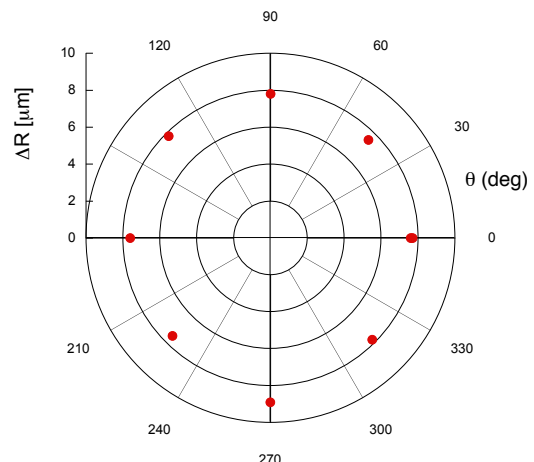


FIG. 6: Azimuthal isotropy of the rms amplitude of the extrudate undulation ($V = 2 \times V_c$) as measured by a fixed camera but for different angular positions θ of the whole extrusion setup ($R = 100 \mu\text{m}$) around its symmetry axis.

Evidence of a bulk flow instability inside the capillary

Oscillations of the extrudate necessarily result from an oscillating velocity field inside the die, at least in the close vicinity ($\simeq R$) of the exit plane. In order to check this,

we have tracked microbubbles advected along the glass capillary in the end region extending $\simeq 20R$ upstream of the exit plane. The right panel of Fig.4 shows representative paths selected at different average velocities below and above the threshold V_c . As expected, whereas for

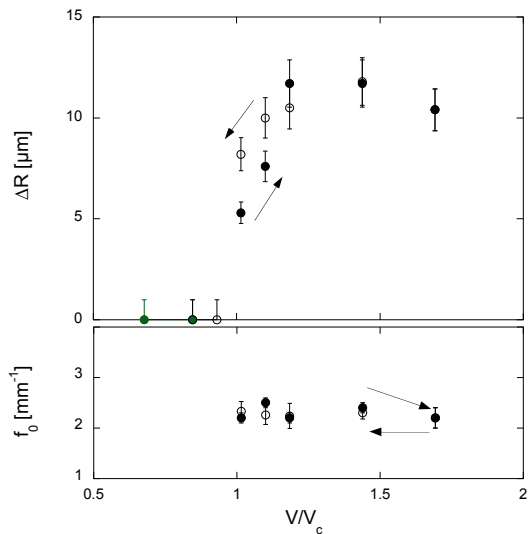


FIG. 7: Evolution of the oscillation amplitude and spatial frequency upon first increasing, then decreasing the control parameter V in the vicinity of the threshold V_c , for a capillary with $R = 150 \mu\text{m}$, showing no measurable hysteresis.

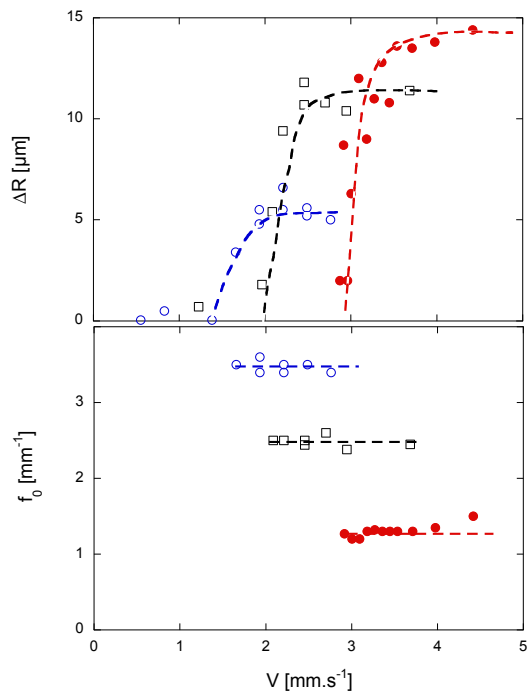


FIG. 8: Evolution of the oscillation amplitudes and spatial frequencies $R = 100 \mu\text{m}$ (red full circles), $150 \mu\text{m}$ (black squares) and $250 \mu\text{m}$ (blue open circles). The dotted lines are guides for the eyes.

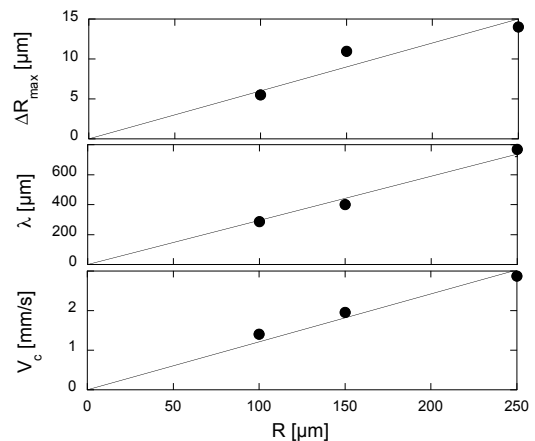


FIG. 9: Amplitude ΔR_{max} at apparent saturation, wavelength $\lambda = V_c/f_0$ of the oscillations at the onset of the oscillations, and threshold velocity V_c with respect to the capillary radius R .

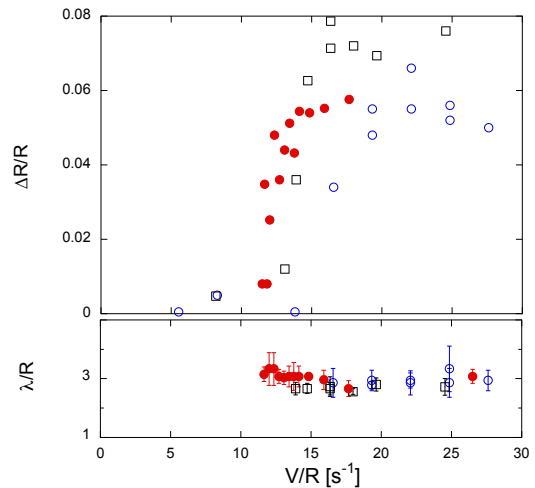


FIG. 10: Characteristics of the instability in the vicinity of its threshold, plotted in reduced form. Same symbols as on Fig.8

$V < V_c$ the paths are straight, for $V > V_c$ their projection onto the observation plane are quasi-sinusoidal.

At this stage, we must assess whether the flow instability responsible for the extrudate one is an entry, exit or bulk one. For this purpose, we have monitored for $V > V_c$ bubble paths at different locations along the capillary, up to a distance $\simeq 80R$ upstream of the exit. The observation of quasi-sinusoidal paths with comparable amplitudes and periods, whatever their location along x , illustrated on Fig. 11, indicates the presence of undamped oscillations of the velocity field, i.e. an instability which, in contradistinction to the sharkskin one [1], is *not* localized in the vicinity ($\simeq R$) of the exit plane.

Moreover, note that the wavelengths of the bubble paths are $\simeq 8R$, i.e. significantly larger than the period ($\simeq 3R$) of the extrudate distortion. This was already pointed out by Wilson and Loridan [11] in their analysis of Bodiguel et al. data [15]. Such an apparent wavelength dilatation is akin to a Doppler effect. The analysis performed in supplemental material enables us to estimate that the magnitude of the phase velocity v_φ of the oscillating perturbation is comparable with V .

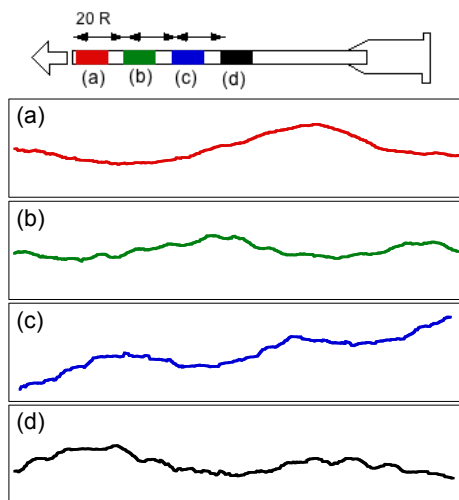


FIG. 11: Paths of lagrangian tracers recorded at different locations along a $R = 250 \mu\text{m}$ capillary. The portions of the capillary corresponding to each path are shown on the upper drawing.

Finally, the fact that the extrudate instability is observed for capillaries with aspect ratios L/R as large as 200 strongly suggests that it cannot originate from a destabilization of the flow upstream of the abrupt contraction. As pointed out by Larson [1], some unstable pipe modes must be at work in order to pump energy from the base flow and compensate for the viscous losses associated with the velocity oscillations.

In order to make a more precise statement, we have constructed capillaries with a 5:3 contraction by glueing a $R_- = 150 \mu\text{m}$ capillary inside a $R_+ = 250 \mu\text{m}$ one and cutting the narrow portion at different lengths L_{150} (see inset of Fig.12). The throughput range was chosen so that the flow in the wider capillary remained stable while enabling to cross the instability threshold — as revealed by the undulations of the extrudate — in the narrower one. Fig.12 shows the maximum amplitude ΔR_{max} of the undulations as a function of L_{150}/R_- . At large enough aspect ratios, i.e. $L_{150}/R_- \gtrsim 40$, ΔR_{max} becomes insensitive to the length. This definitely establishes that the helical deformation of the extrudate is the outer manifestation of an instability which affects the whole flow inside the capillary. The results presented so far were obtained for $L/R \simeq 200$, hence correspond to the instability of

an “infinite” pipe. For $L/R < 40$, the amplitude decreases markedly and, when extrapolated to the “orifice die” limit ($L/R \rightarrow 0$) the amplitude vanishes (Fig.12). As will be discussed in the next section, this is in strong contradistinction with the usually reported phenomenology for polymer melt extrusion where shorter dies, mostly used in practice, are also the most prone to the so-called “melt fracture” helical instability.

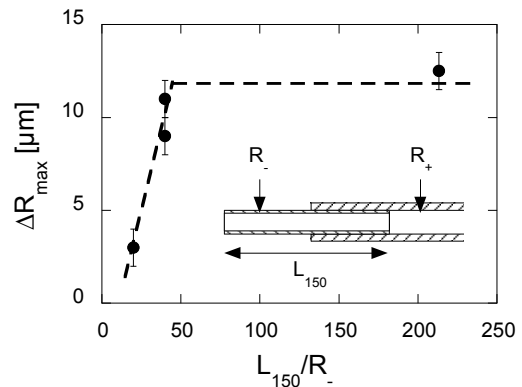


FIG. 12: Maximal amplitude of undulation of an extrudate exiting a $R_- = 150 \mu\text{m}$ capillary at a distance L_{150} downstream a 5:3 contraction with $R_+ = 250 \mu\text{m}$ (see sketch on inset). The broken lines are guides for the eyes.

DISCUSSION

Comparison with previous studies

Influence of shear-thinning on the nature of the instability — The results presented so far are in clear contradistinction with those of Bertola et al. [12] and Pan et al. [13] who evidenced a pipe instability controlled by the Weissenberg number but exhibiting a large hysteresis — an obvious *subcritical* feature, while the instability is, in our case, *supercritical*. Since the two cases differ essentially by the steady flow characteristics of the fluids under study, namely their being shear-thinning or not, we are led to conclude that it is this rheological feature which primarily controls the nature of the pipe instability. This is fully supported by the theoretical prediction that planar channel flows of “weakly” shear-thinning White-Metzner fluids ($n > 0.3$) are linearly stable [10] while “strongly” shear-thinning ones ($n \leq 0.3$) are linearly unstable. The theoretical limiting value of n for axisymmetric pipe flows is unknown but our results indicate that, in this respect, entangled alginate solutions with $n \simeq 0.3$ belong to the “strongly shear thinning” class of fluids.

Beyond proving the existence of a *linear* pipe flow instability, our results reveal that: (i) it corresponds to a

direct Hopf bifurcation — a feature which would require a *non-linear* analysis of the flow dynamics to be theoretically assessed — and (ii) the first unstable mode is *helical* — hence a relevant theoretical study of the flow stability should be *fully 3D* [17].

As far as symmetry breaking is concerned, our pipe flow helical instability is strongly reminiscent of the *sinuous* one reported by Bodiguel et al. [15] for 2D micro-channel flows. Although the high molecular weight, partially hydrolyzed polyacrylamide (PAA) solutions used in their study exhibited an exponent $n \simeq 0.2$, i.e. were highly shear thinning, the results could not be directly compared to the theoretical predictions of [10]. Indeed, on the one hand, for technical reasons [14], the theoretical flow stability was restricted to “varicose” axisymmetric modes. On the other hand, PAA does not obey the White-Metzner constitutive equation with a single exponent ruling power laws (1) and (3). In [15], $n = 0.21$ and $m = 0.43$ indicates that the elastic modulus itself is rate dependent. The consequence of this extra complication has been studied by Wilson & Lorida [11] using an extended constitutive law. Interestingly, albeit they have restrained their analysis to varicose modes, they have shown that the flow stability, i.e. the critical value of the Weissenberg number, is noticeably increased by the rate dependence of the modulus. This is an important example showing that rheological details may have quantitative consequences on a flow instability while preserving its qualitative characteristics. This would be worth being confirmed experimentally by swapping the two fluid systems — ALG and PAA — in each of the two flow configurations of [15] (2D channel flow) and the present study (axisymmetric pipe flow).

Competition between pipe and contraction flow instabilities — In the field of extrusion instabilities, a touchstone is the broad phenomenology pertaining to the so-called “melt fracture” of polymer melts [3, 5, 20]. Here we focus on the extensive study by Combeaud et al. [6, 20] of the helical extrusion instability of linear polystyrene (PS). Their polymer melts and our entangled polymer solutions exhibit a common rheological characteristic since the flow viscosity of PS is strongly shear thinning [20] with a power law exponent $n \simeq 0.2$, a plateau viscosity $\eta_0 \simeq 5 \times 10^4$ Pa.s and a cross-over shear rate $\dot{\gamma}_0 \simeq 1$ s⁻¹. It appears therefore meaningful to compare the results obtained on PS and ALG, taking advantage that in both studies, the extrudate together with the upstream (pipe or contraction) flow have been characterized.

At first sight, the two systems behave similarly since in both cases the extrudate exhibits at large enough throughput a transition from a cylindrical to a fairly regular helicoidal shape. The authors report that for PS this instability occurs at shear rates far beyond the range accessible in a cone-plate rheometer. Therefore, the critical value Wi_c of the Weissenberg could only be roughly estimated by extrapolation of their rheological

data to range between 2 and 10. Since our own estimate is $Wi_c = 5 \pm 1$, the comparison is not conclusive, even though both ranges are compatible.

Much more specific is the behavior of the pitch λ of the distorted extrudate upon increasing the shear rate. In this respect, both systems show antagonistic trends: while for ALG it is the *spatial* frequency λ^{-1} which remains constant (Fig.8), for PS it is the *temporal* one V/λ which exhibits but small variations. This strongly suggests that both systems develop instabilities of different origins. This is confirmed in [6] by the direct visualization of the velocity field in the reservoir, upstream of the inlet, which clearly indicates that emergence of the extrudate instability coincides with the destabilization of the contraction flow, a phenomenon which has been extensively studied by McKinley et al. for non shear-thinning Boger fluids [7]. Correlatively, as the die aspect ratio is reduced, the extrudate undulation becomes more pronounced for PS, whereas it vanishes for ALG (Fig.12).

Although for practical reasons extrusion of polymer melts is usually performed through short dies, Combeaud et al have extended their study to aspect ratios up to $L/R = 64$. They show that the helicoidal undulations persist up to this aspect ratio value, although strongly reduced (see Fig. 3.7 of [20]). The gradual attenuation of the helix amplitude however strongly slow down for $L/R \gtrsim 32$ (see Fig. 3.8.b. of [20]). Interestingly, this value, which could be considered a priori quite large for an “infinite die” regime to be reached, is compatible with our own finding that the “infinite pipe” limit is reached for $L/R \simeq 40$ (12). From this comparison we conclude that the main body of experiments on PS (resp. ALG) are concerned with “short” (resp. “long”) dies in which reservoir (resp. pipe) flow instabilities are favored.

In light of the present results, it should be extremely useful to focus experimentally on a contraction flow instability of ALG and a possible pipe flow instability of PS, although the high viscosity of the melts probably precludes using the long pipes required for this instability to fully develop.

Non-linear instability development *vs.* wall slip

The standard extrusion phenomenology of polymer melts involves the gradual transition from a quasi-periodic helical disturbance to a more or less chaotic one as the throughput is increased beyond a critical threshold. With this in mind we have systematically explored the evolution of the extrudate undulations beyond Wi_c . No widening of the oscillation spectrum (see Fig.5) was observed up to the experimental limit of $V \simeq 10 \times V_c$ (however only a two-fold increase in the slowly varying Wi). Surprisingly, although one could expect a slowing down of the amplitude growth due to the build-up of stabilizing non-linear terms in the flow dynamics, we sys-

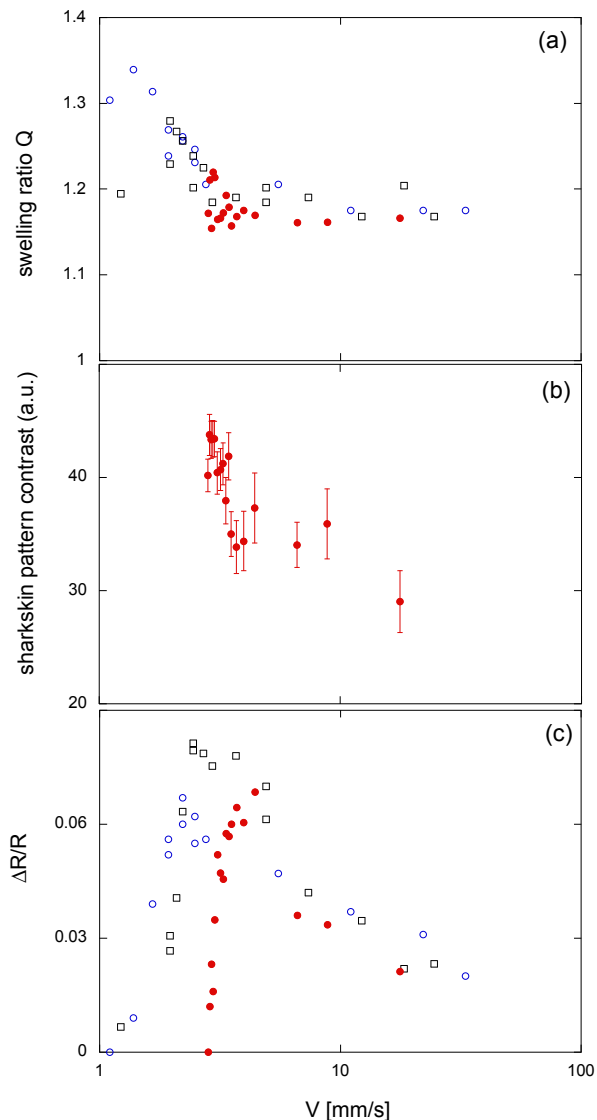


FIG. 13: Evolution with respect to V of (a) the swelling ratio Q , (b) the sharkskin contrast index (see text) and (c) the scaled oscillation amplitude. Different radii are represented by the same symbols as in Fig.8.

tematically observe a marked decrease of the amplitude, as shown on Fig.13.c. This means that the plateauing trend observed close above V_c (Fig.8) signals, in fact, the existence of a *maximum* of the amplitude. Such a behavior is, to our knowledge, quite unusual in non-linear dynamics.

Since the extrudate undulations involve some motion of the surrounding bath fluid, we have checked whether viscous damping could be involved. We have changed the saline solution (viscosity $\eta_s \simeq 10^{-3}$ Pa.s) for a 1 wt.% solution of sodium alginate (viscosity $\eta_{1\%} \simeq 10^{-1}$ Pa.s). No significant difference in the $\Delta R(V)$ curve was observed,

neither close to onset nor well beyond threshold, suggesting that the viscosity of the bath is not relevant to the undulation development.

Some further insight into the underlying physical mechanisms responsible for this behavior can be gained from the simultaneous measurement of two characteristics of the extrudate, namely the (die-)swelling ratio Q and the sharkskin amplitude. The swelling ratio in the presence of oscillations is determined by measuring the average axial velocity of the extrudate V_{out} well downstream the capillary exit. It is defined [26] as $Q = (V/V_{out})^{1/2}$. The sharkskin amplitude is estimated from the contrast of the resulting pattern, determined under constant illumination and video acquisition parameters.

Fig.13.a reveals an unusual behavior of the swelling ratio which is expected to grow as some power law of the shear rate with a small exponent [21]. Here, Q first increases with the throughput but hardly builds up to values larger than 1.3 and then decreases to a plateau value $\lesssim 1.2$ (close to the value 1.1 for a purely newtonian fluid). The same trend is exhibited by the sharkskin contrast (see Fig.13.b and Fig.4): although always superimposed to the volume oscillations, the sharkskin is less and less severe as the throughput is increased beyond threshold.

Both die swell and sharkskin are qualitative indicators of the validity of the no-slip condition at the capillary wall. Die swell is a manifestation of the sudden relaxation of the first normal stress difference which itself requires viscous shear to build up. It is therefore mitigated by wall slip. Sharkskin results from the stress singularity which develops at the exit rim where boundary conditions abruptly switch from no-slip to no-stress [22]. It is attributed to the accommodation of the singularity via tearing of the viscoelastic material [23]. Wall slip clearly smoothes out the singularity hence limits the development of sharkskin. This suggests that *the strong attenuation of ΔR is due to the concomitant build up of wall slip*.

Furthermore, the data of Fig.13.a show that, quite unexpectedly, the relevant variable when the capillary radius is changed is not the shear rate but rather the average velocity V . This can be understood as a hint for the occurrence of gross slip with a velocity $V_s \sim V$. The no slip condition is then replaced by a tribological relationship $\sigma_w = f(V_s)$ which depends on “microscopic” characteristics of the fluid-wall interface, and not on the “macroscopic” radius. So, the residual shear rate at the wall $\dot{\gamma}_w(V_s) \sim \sigma_w^{1/n}$, must be determined by V_s , hence by V rather than V/R . Accordingly, we have plotted the relative oscillation amplitudes for different radii as a function of V (Fig.13.c). It is clear that, although in the growing part of the amplitude development this variable is not the relevant one, in the decreasing part it leads to a reasonable collapse of the data.

These results, though preliminary, indicate that the non-linear development of the instability is probably mitigated by the gradual build-up of wall slip. We cannot conclude at this point whether the fact that both phenomena occur at neighbouring values of the wall shear rate is a mere coincidence or signals some correlation. Interestingly, non-trivial coupling between flow instability and wall slip can be found in the previously discussed study of Bodiguel et al. [15] (their Fig.2) although the authors have rather focussed on the drag reduction associated with the occurrence of elastic turbulence in their microfluidic channel flow.

CONCLUSION

We have studied in detail the helical instability which occurs when extruding an entangled polymer solution through glass capillaries with large aspect ratios. Coupling the quantitative analysis of the extrudate undulations with the visualization of tracer paths inside the capillaries we were able to demonstrate that this extrusion instability is the downstream manifestation of the destabilization of the base flow occurring everywhere inside the pipe. The instability exhibits the characteristics of a supercritical Hopf bifurcation occurring above a critical Weissenberg number $Wi_c = 5 \pm 1$.

As suggested by the seminal theoretical work of Wilson & Rallison [10], a key rheological characteristic of our fluid system, as regards its flow stability, is certainly its rather strong shear-thinning behavior. Recent studies have also brought out the essential role played by shear thinning in the stability of viscoelastic flows at zero [24] or moderate [25] Reynolds numbers. In serpentine micro-channels, shear thinning is found to stabilize the flow against the onset of elastic turbulence [24]. In large pipes, it yields a new type of symmetry-breaking supercritical transition [25]. In our case, as well as probably in microchannel planar flow [15], “strong” shear-thinning is responsible for the linear instability of the base flow, whereas Boger fluids designed to exhibit negligible shear-thinning are only non-linearly unstable [12, 13].

The present work therefore suggests to make use of fluid systems with increasing shear-thinning exponents n in order to study experimentally the evolution of the pipe flow instability, from weakly non-linear subcritical at small n to linear supercritical at larger ones.

An intriguing issue that the present work leaves open is the origin of the large aspect ratio ($L/R \simeq 40$) required for an “infinite” pipe regime to be reached. To our knowledge, it is the first time that this phenomenon is put forward and we hope that it will stimulate further theoretical and numerical studies.

Finally, preliminary results show that, at least for glass capillaries, the non-linear development of the helical undulations is mitigated by the gradual build-up of wall slip.

In the case studied here, the helical instability and the onset of gross slip occur in a narrow bracket of control parameter, leaving open the possibility of some causal relationship. Our set-up makes it possible to change the die material from glass to metal or even PTFE, and will therefore be suitable for future investigation of the role of wall slip in pipe flow instabilities.

-
- [1] R. G. Larson, *Rheologica Acta* **31**, 213 (1992).
 - [2] M. M. Denn, *Annual Review of Fluid Mechanics* **33**, 265 (2001).
 - [3] J.-F. Agassant, D. R. Arda, C. Combeaud, A. Merten, H. Muenstedt, M. R. Mackley, L. Robert, and B. Vergnes, *International Polymer Processing* **21**, 239 (2006).
 - [4] H. Nguyen and D. Boger, *Journal of non-Newtonian fluid mechanics* **5**, 353 (1979).
 - [5] J. Piau, N. El Kissi, and B. Tremblay, *Journal of non-newtonian fluid mechanics* **34**, 145 (1990).
 - [6] C. Combeaud, Y. Demay, and B. Vergnes, *Journal of non-newtonian fluid mechanics* **121**, 175 (2004).
 - [7] G. H. McKinley, W. P. Raiford, R. A. Brown, and R. C. Armstrong, *Journal of fluid mechanics* **223**, 411 (1991).
 - [8] B. Meulenbroek, C. Storm, A. N. Morozov, and W. van Saarloos, *Journal of non-newtonian fluid mechanics* **116**, 235 (2004).
 - [9] B. Meulenbroek, C. Storm, A. N. Morozov, and W. van Saarloos, *Journal of non-newtonian fluid mechanics* **116**, 235 (2004).
 - [10] H. J. Wilson and J. M. Rallison, *Journal of non-newtonian fluid mechanics* **87**, 75 (1999).
 - [11] H. J. Wilson and V. Loidan, *Journal of Non-Newtonian Fluid Mechanics* **223**, 200 (2015).
 - [12] V. Bertola, B. Meulenbroek, C. Wagner, C. Storm, A. Morozov, W. van Saarloos, and D. Bonn, *Physical review letters* **90**, 114502 (2003).
 - [13] L. Pan, A. Morozov, C. Wagner, and P. Arratia, *Physical review letters* **110**, 174502 (2013).
 - [14] H. J. Wilson, Ph.D. thesis, The University of Cambridge (1998).
 - [15] H. Bodiguel, J. Beaumont, A. Machado, L. Martinie, H. Kellay, and A. Colin, *Physical review letters* **114**, 028302 (2015).
 - [16] R. Poole, *Physical Review Fluids* **1**, 041301 (2016).
 - [17] H. J. Wilson, *Nonlinearity* **25**, R45 (2012).
 - [18] E. R. Morris, A. Cutler, S. Ross-Murphy, D. Rees, and J. Price, *Carbohydrate polymers* **1**, 5 (1981).
 - [19] G. Iooss and D. D. Joseph, *Elementary stability and bifurcation theory* (Springer Science & Business Media, 2012).
 - [20] C. Combeaud, Ph.D. thesis, École Nationale Supérieure des Mines de Paris (2004).
 - [21] R. Tanner, *Journal of Polymer Science Part A-2: Polymer Physics* **8**, 2067 (1970).
 - [22] G. Lipscomb, R. Keunings, and M. Denn, *Journal of non-newtonian fluid mechanics* **24**, 85 (1987).
 - [23] A. Allal, A. Lavernhe, B. Vergnes, and G. Marin, *Journal of non-newtonian fluid mechanics* **134**, 127 (2006).
 - [24] L. Casanellas, M. A. Alves, R. J. Poole, S. Lerouge, and A. Lindner, *Soft matter* **12**, 6167 (2016).

- [25] C. Wen, R. J. Poole, A. P. Willis, and D. J. Dennis, *Physical Review Fluids* **2**, 031901 (2017).
- [26] The amplitude of the extrudate undulation remains smaller than 0.1 so that the volumetric flow of the ex-

trudate can be approximated to $V \times (\pi R_{out}^2)$ with R_{out} the radius of the thread, to within a few percent.

Supplemental material

CONCENTRATION DOMAINS OF ALGINATE SOLUTIONS

The viscosity of sodium alginate solutions in pure water was measured, at temperature $T = 20^\circ\text{C}$, using a double gap Couette cell geometry. Figure 1 shows the specific viscosity $\eta_{\text{sp}}(c) = (\eta(c) - \eta_s)/\eta_s$ as a function of the concentration c , where η is the viscosity of the solution in the vanishing shear rate Newtonian regime and η_s is the solvent (water) viscosity.

The three usual regimes of polymer solutions are observed [1]:

- *dilute* regime where $\eta_{\text{sp}} \sim c$ at low concentrations $c < c^*$
- *semi-dilute unentangled* regime at intermediate concentrations $c^* < c < c_E$
- *entangled* regime where $\eta_{\text{sp}} \sim c^{3.5}$ at high concentrations $c > c_E$.

From the above results, we conclude that the $c = 4\text{--}10$ wt.% solutions used in the present work are in a rather strongly entangled state.

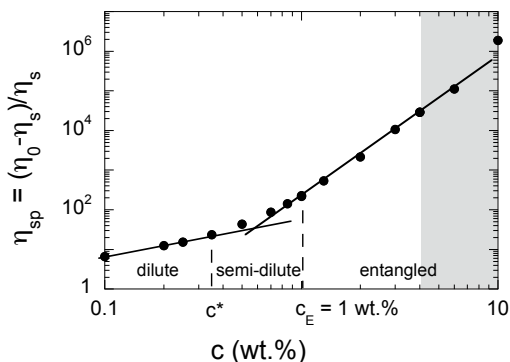


FIG. 1: Specific viscosity of alginate solutions *vs* concentration, measured at $T = 20^\circ\text{C}$. The boundaries between the three scaling regimes define the overlap $c^* = 0.35$ wt.% and entanglement $c_E = 1$ wt.% concentrations. The grey zone indicates the concentration domain relevant to this study, corresponding to strongly entangled solutions.

CALCULATED BASE FLOW VELOCITY PROFILE AND WALL SHEAR RATE

As a consequence of the strong shear-thinning rheology, well described by a Cross law:

$$\eta = \frac{\eta_0}{1 + (\dot{\gamma}/\dot{\gamma}_0)^{1-n}} \quad (1)$$

the calculated velocity profile in an infinite capillary with no-slip condition at the wall differs markedly from the Poiseuille solution for a newtonian fluid.

Whereas for $V/R \ll \dot{\gamma}_0$ the profile is indistinguishable from the Poiseuille one, when $V/R \gg \dot{\gamma}_0$, it becomes that of a power law fluid (for which $\sigma = \eta_0 \dot{\gamma}_0 (\dot{\gamma}/\dot{\gamma}_0)^n$). This profile [2] is very flat over a large part of the capillary, therefore exhibiting a central quasi-plug flow with shear localized close to the wall (Fig.2).

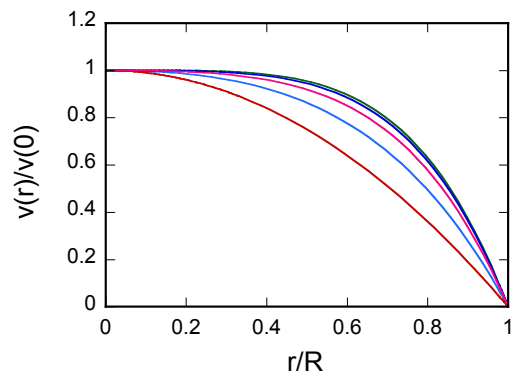


FIG. 2: Velocity profiles for the flow of a fluid obeying a Cross law with $n = 0.3$. Lower curve: the Poiseuille solution for a newtonian fluid corresponding to the limit $V/(R\dot{\gamma}_0) \ll 1$. Upper curve: solution for a power-law fluid, corresponding to $V/(R\dot{\gamma}_0) \gg 1$. Intermediate curves (bottom to top) are for: $V/(R\dot{\gamma}_0) = 2, 17, 160$, the latter being almost indistinguishable from the power law one. Note the plug-like nature of the power-law profile in a wide core zone ($0 \leq r/R \lesssim 0.5$).

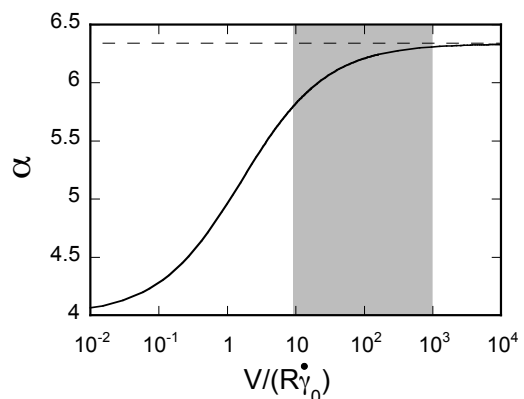


FIG. 3: Evolution of the parameter $\alpha = \dot{\gamma}_w/\dot{\gamma}_0$ with the reduced shear rate. The dashed line is the pure power law limit $\alpha = 6.3$. The grey area corresponds to the experimental range of shear rates.

It is customary to estimate the Weissenberg number $Wi(\dot{\gamma})$ at the wall, where the shear rate $\dot{\gamma} = \dot{\gamma}_w$ is maximum. We express it as:

$$\dot{\gamma}_w = \alpha V/R$$

with α a number depending on the velocity profile. In the low and high shear rate limits:

$$\alpha = \begin{cases} 4 & \text{Poiseuille } (n = 1), \\ 3 + \frac{1}{n} & \text{Power law} \end{cases}$$

We have computed the dependence of α on V/R by straightforward numerical integration of the flow equation for the Cross law (1) under a no-slip condition at the wall. This was used to estimate the wall shear rate $\dot{\gamma}_w$ and the corresponding Wi for any value of the throughput. As seen on Fig.3, in the range $10 < V/(R\dot{\gamma}_0) < 10^3$ s^{-1} relevant to this study, $\alpha \simeq 6$. We have used this value to compute the expression of the Weissenberg number for our experiments:

$$Wi \simeq 1.7 \left(\frac{V}{R\dot{\gamma}_0} \right)^{0.3}$$

ANALYSIS OF LAGRANGIAN TRACER PATHS

When a passive tracer moves along with an axisymmetric base flow $v_x(r)\vec{e}_x$ perturbed by a propagating harmonic mode of pulsation *omega* and wavelength λ_v , it experiences an oscillating velocity field which is itself moving with respect to the capillary frame at the phase velocity v_φ of the mode. Accordingly, the wavelength Λ of the tracer's path is different from λ_v . The effect is analogous to the classical Doppler effect and, accordingly, the following relationship holds [3] between the period T of the tracer oscillations and that, $2\pi/\omega$, of the velocity field:

$$T(r) = \frac{2\pi/\omega}{|1 - v_x(r)/v_\varphi|}$$

Here, it is assumed that the radial velocity perturbation is small with respect to v_x , so that the tracers remain at

a quasi-constant distance r from the capillary axis (as is actually the case for the traces of Figs. 4 and 11 of the main article).

Since $\Lambda = v_x T$ and $2\pi/\omega = \lambda_v/v_\varphi$, one gets straightforwardly:

$$\Lambda = \frac{\lambda_v}{|1 - v_\varphi/v_x(r)|}$$

We want to compare Λ with the measured wavelength λ of the extrudate undulations. Extrudate incompressibility yields: $\lambda R_{out}^2 = (2\pi/\omega)VR^2$ where we have written that the pulsation ω of the velocity perturbation at the capillary exit is also that of the undulation. In terms of the die-swelling ratio $Q = R_{out}/R$, one gets:

$$\frac{\lambda}{\lambda_v} = \frac{V}{v_\varphi} \frac{1}{Q^2}$$

And finally:

$$\frac{\Lambda}{\lambda} = \frac{v_x}{V} \frac{Q^2}{|v_x(r)/v_\varphi - 1|}$$

Knowing the imposed average flow velocity V and measuring the average axial velocity along the path v_x , we have estimated the radius r of the path using the calculated velocity profile of Fig.2. All the traces shown on Figs. 4 and 11 of the main article correspond to $r/R \simeq 0.8-0.9$, meaning that the corresponding tracers travelled in the near-wall zone where they could experience significant shear rate.

With typical values, $Q \simeq 1.3$, $v_x/V \simeq 0.7$, $\Lambda/\lambda \simeq 2.7$, one gets $|v_x/v_\varphi - 1| \simeq 0.5$, indicating that the phase velocity of the mode probed by the tracers is on the order of their average velocity, i.e. of V itself.

-
- [1] L. Guo, R. H. Colby, C. P. Lusignan, and A. M. Howe, *Macromol.* **36**, 10009 (2003).
 - [2] R. Byron Bird, R.C. Armstrong and O. Hassager, *Dynamics of Polymeric Liquids, Vol.1 Fluid Mechanics*, 2nd ed. John Wiley & Sons, New-York 1987.
 - [3] H.J. Wilson & V. Lorian, *J. Non-Newton. Fluid Mech.* **223**, 200 (2015).

4.2.3 Implementation on other systems: In the "crimp" quest

4.2.3.1 Quick literature overview

Collagen fibrils within the tendon fascicles sheaths exhibit alternating oblique orientations referring to as "crimp", as presented in Chapter 1 (1.1.1.2.1 p 9). This tendon wavy shape was suggested to act as spring or a shock-absorber, which may improve tendon mechanical properties [13]. Thus, several emerging strategies were developed in order to confer wavy shape to scaffolds and in particular to threads. We briefly report three main techniques used for this purpose.

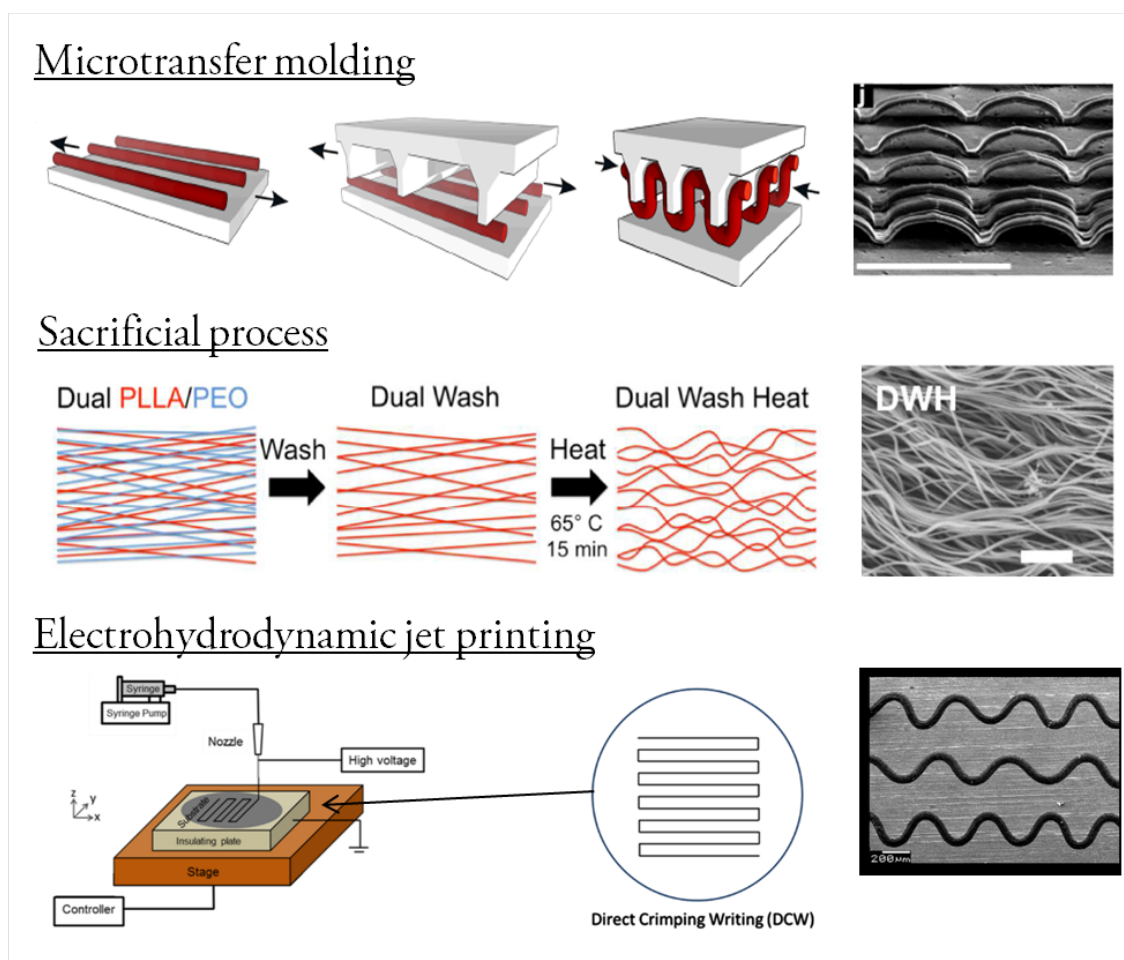


Figure 4.6: Example of protocols used to produce wavy scaffolds. Top: Microcrimping method and scanning electron microscopy of crimped collagen microfibers [14]. Scale bar = 200 μm, Middle: Sacrificial process and a representative SEM image of fabricated scaffolds containing two fiber populations. [15] Scale bar = 1 μm, Bottom: Electrohydrodynamic jet printing set-up and example of moving path and resulting fiber. [16]. Scale bar = 200 μm

A first method to produce wavy microstructures is the microtransfer molding, used by Caves et al. [14]. The system is composed of a lead-screw assembly, a base membrane on which synthetic collagen fibers are aligned parallel and a microridged membrane. After several steps of extension, compression, freezing, drying, chemical treatment, they obtained wavy sheet of collagen fibers with a wavelength of about 100 μm.

A second method consists in producing a construct made of two polymer thread (elec-

trospinning) populations from which one will be removed or "sacrificed". Szczesny et al. used this method with PLLA and PEO polymers. As shown in the figure (4.6), PEO population threads were removed by wash step [16]. The "crimped" shape is given to the remaining population by heating them.

Recently, Wu et al. used an electrohydrodynamic jet printing device to print wavy polymer (PCL) fibers (Fig. 4.6) [15]. The resulting fibers have a diameter of about $100\mu\text{m}$, a pattern wavelength of $360\mu\text{m}$ and crimp angle about 45° .

In both studies, authors showed that the mechanical properties of the scaffolds were improved by using wavy fibers compared to their respective controls. However, those techniques used synthetic polymer solutions and may be not suitable for collagen ones. Indeed, electrospinning could denature the collagen and the post-processing such as chemical cross-linking may impact the biocompatibility of the constructs. Moreover, these methods are quite sophisticated and the whole procedure may take time. Finally, the resulting scaffolds exhibit more a "2D" wavy pattern than a spring-like shape as for native tendon crimp.

Our strategy consists in transposing the helical instability observed during the extrusion of alginate solutions (without binding ions) to the collagen one and thus produced "crimped" threads.

4.2.3.2 Helical instability: from alginate to collagen

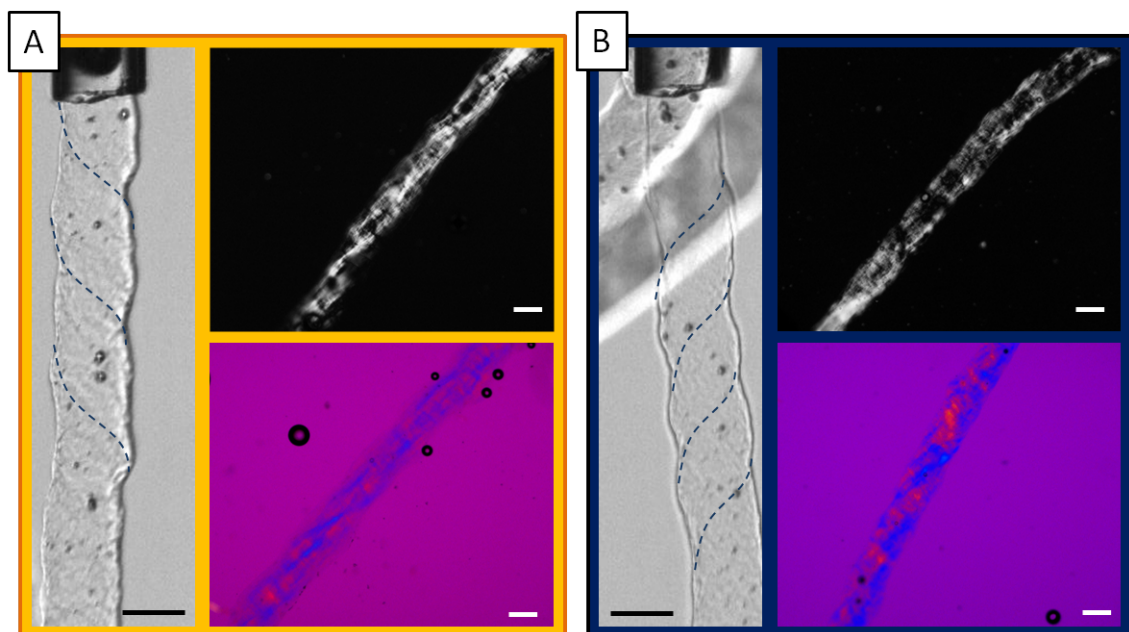


Figure 4.7: Collagen at 30 mg/mL extrusion in A) PBS 1X and B) PBS 5X observed in real time and post extrusion by polarized light microscopy with (top corner) and without quarter wave-plate (bottom corner). Eye guidelines in blue dashed lines helps the helical pattern visualization. Scale bars = $200\mu\text{m}$

The alginate solution at 10 wt % exhibited rheological properties close to the collagen solution at 30 mg/mL (Chapter 3, 3.1.2.3 p 93). From the study of alginate extrusion with

glass capillaries in the case of non-binding ions, we have found a critical velocity above which the helical instability starts appearing.

Thus, we decided to test the extrusion in almost the same conditions with collagen solution at 30 mg/mL. The idea was to produce collagen threads with inner structure presenting an helical geometry. The final goal would be to mimic the "crimp" and so to improve collagen threads properties (Chapter1, 1.1.1.2.1 p 9).

First, to induce slow fibrillogenesis of collagen molecules, phosphate buffer saline PBS (1X) was put in the extrusion bath. The helical pattern revealed quite rapidly over a large range of velocity. At higher ionic strength, with PBS 5X, this instability was also observed. Even if the helix was less pronounced than the one observed with alginate solutions, the whole inner structure followed the helix geometry as shown by polarized light microscopy.

Conclusion:

By a simple extrusion process, we induce the helical alignment of collagen inside the threads. It should be noted here that this analysis of instabilities took place in parallel to the biological tests and its application to collagen came very recently. Therefore those helical threads were not checked for their mechanical properties neither for the cell culture at the time of the writing up of my thesis. Nevertheless, those results are very promising in the "crimp" quest and may improve the quality of artificial tendon-like collagen threads.

4.3 Extrusion in a bath of cross-linking ions

Without cross-linking ions, sharkskin and helical instabilities were observed downstream. While we have shown that the latter affects the whole flow along the capillary, the former was known to be attributable to the stress and strain rate singularity generated in the exit zone due to the no-slip to no-stress boundary condition abrupt transition [12]. In the presence of binding ions in the exit zone, it is legitimate to think that sharkskin could be modified by the ions while the helical instability would remain unaffected. In addition new instabilities could appear as well. In this section, we will focus on the instabilities "zoology" obtained for alginate solution ALG4 extrusion with glass capillary in a cross-linking ions (calcium) bath while varying the velocity. The different effects due to the calcium ions or alginate concentrations and needles materials will be discussed for each instability.

4.3.1 Overall observations

The results obtained for ALG4 extruded with glass capillary in chloride calcium 0.5M bath are gathered in Figure 4.8. During the extrusion of such solutions, several instabilities are observed:

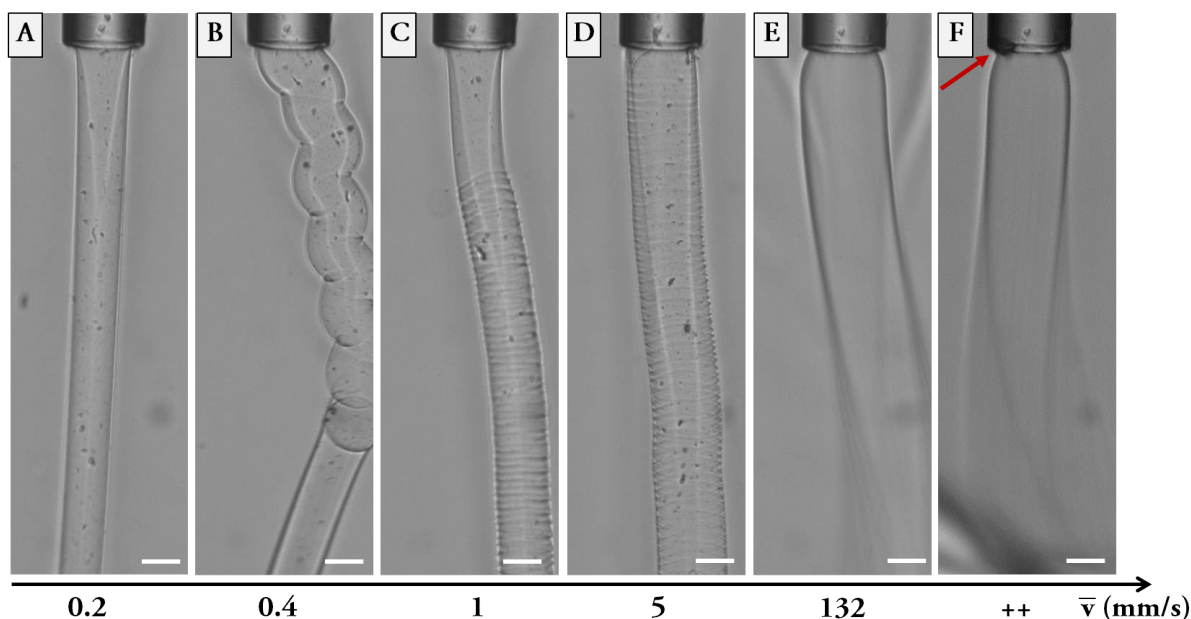


Figure 4.8: Morphologies observed during the extrusion of ALG4 in $CaCl_2$ 0.5M with a glass capillary ($R=150\mu\text{m}$) for exit velocities ranging from 0.2 to more than 132 mm/s : A) Smooth, B) Wavy, C) Alternating, D) Striated, E) Smooth, F) Narrowed. White scale bar = 200 μm

Upon increasing the velocity from rest up to 0.2 mm/s, the alginate extrudate is smooth (Fig.4.8 A) and then different patterns appear one after the other (Fig.4.8 B, C, D). First, the alginate flow has a wavy shape (B), then, tightened striations (D) appear and those two may alternate between smooth and wavy/striated pattern (C). For higher velocities (around ten times more), the alginate flow seems to be smooth again (Fig.4.8 E) but with an external diameter higher than in the first smooth region. Finally, for the highest attainable velocities, we observe a flow narrowing at the die exit and an opaque region (Fig.4.8 F) red arrow) inside the capillary is growing. Those phenomena are observed for the different capillary radii. It is quite surprising that the sharkskin defect does not appear as

previously observed in deionized water. This means that the presence of binding ions avoids the formation of sharkskin.

In the following, each instability is described in more details and discussed.

NB: For the highest velocities, camera acquisition frame rate did not allow the observation of the flow surface in real-time. In such cases, the alginate extrudate was quickly removed from the bath and observed by optical microscopy "post-extrusion".

4.3.2 Smooth region

As previously mentioned, at very low velocities, the extrudate surface was smooth (Fig. 4.8 A). Moreover, the flow diameter (D') seemed to be smaller than the die exit. To quantify this observation, D' was measured from the real-time motion pictures for different velocities. The swelling ratio D'/D was plotted as a function of the shear rate $\dot{\gamma}$ for the available stainless steel needles of inner diameters D (Fig. 4.9):

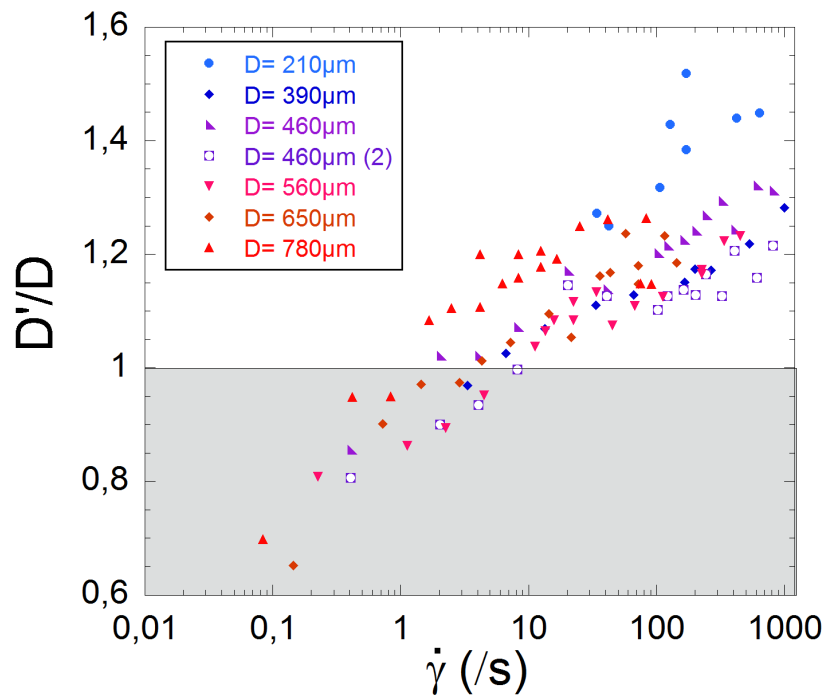


Figure 4.9: Ratio diameters D'/D plotted as a function of the shear rate for the extrusion of ALG4 in $CaCl_2 0.5M$ with stainless steel needles. D' is the measured extrudate diameter and D the inner needle diameter. In the region of interest (shaded area), the ratio is below 1 which shows that the extrudate has a smaller diameter than the needle one.

For shear rates ranging between 0.1 to 10 s^{-1} , we had: $D'/D < 1$ (the region of interest is shaded). This meant that the extrudate diameter was significantly smaller than the imposed inner diameter. This shrinkage could even reach 40% of the initial diameter for the lowest shear rates.

NB: The same measurements were performed with glass capillaries with the same order of magnitude.

How can we explain thus this remarkable shrinkage? As the shrinkage was not observed in the previous study while there was no cross-linking ions, this phenomenon can only be due to the presence of calcium ions.

Indeed, when the alginate extrudate came in contact with the calcium ions, a gel was then formed through the "egg box" mechanism previously described (2.2.2.2 p 81). The gel was formed from the outside and the gelation continued progressively to reach the extrudate core. The gelation front was visible: fine area where the contrast changes (Fig. 4.10 left). Further the die exit, the extruded thread was thus completely gelled.

However, this gelation is more complex. In fact, several mechanisms occur simultaneously: ion exchanges ($Na^{2+} \leftrightarrow Ca^{2+}$) which allow alginate/calcium binding, calcium ions diffusion through the new formed network and sodium alginate solution emergence from the die exit.

A first approach to estimate the dominant phenomena consists in analyzing dimensionless number. The two forms of species transport in a flow, that is convective and diffusive, are generally compared by the Peclet number Pe , defined as:

$$Pe = \frac{t_{diff}}{t_{conv}} = \frac{\bar{v} R}{D}$$

It relates to the fact that the typical convection time over a distance R is defined by $t_{conv} = R/\bar{v}$ whereas the diffusion time over this same distance is expressed as $t_{diff} = R^2/D$, where D is the diffusion coefficient of the species considered in the respective solvent. Alginate is a macromolecule and has a lower diffusion coefficient than calcium ions, implying that alginate should not diffuse significantly before reacting with the ions. The considered diffusive species are thus the calcium ions.

In the direction of the flow at a velocity $\bar{v} = 0.2$ mm/s, with $D \sim 10^{-9}$ m^2/s , and a capillary radius L of $150 \mu m$, we obtain $Pe_{||} \sim 30$. Since $30 \gg 1$, it means that the diffusion is negligible and convection is dominant. However, in the radial direction, since the flow is longitudinal, the Peclet number Pe_{\perp} is equal to zero as there is "no velocity". In such case, the diffusion of calcium ions is the dominant phenomenon.

Little reaction takes place in the gel, since the concentration of free alginate is very low. As the boundary between sodium alginate (liquid) and calcium alginate (gel) is continuously moving, the gel layer is growing and the liquid core decreases. We can estimate the diffusion length L_{diff} over which the gelation front is converging (Fig. 4.10). This length is related to the Peclet number by:

$$L_{diff} = \bar{v} \times t_{diff} = Pe \times R$$

As $Pe \simeq 30$, the diffusion length from this estimation is equal to: $L_{diff} \simeq 30R$. While measuring this length on the real time extrusion figure 4.10 (left), we find: $L_{diff} \simeq 8R$. This means that the effective diffusion of calcium ions is faster than the predicted one.

At the die exit (Fig. 4.10, insert), if we suppose that the diffusion and convection phenomena are comparable ($Pe \sim 1$), the physical quantity δ called the "skin depth" which corresponds to the gelled thickness at a distance h from the die exit can be estimated as:

$$Pe = 1 = \frac{\bar{v} \delta}{D}$$

$$\delta = \frac{D}{\bar{v}} \simeq 20 \mu m$$

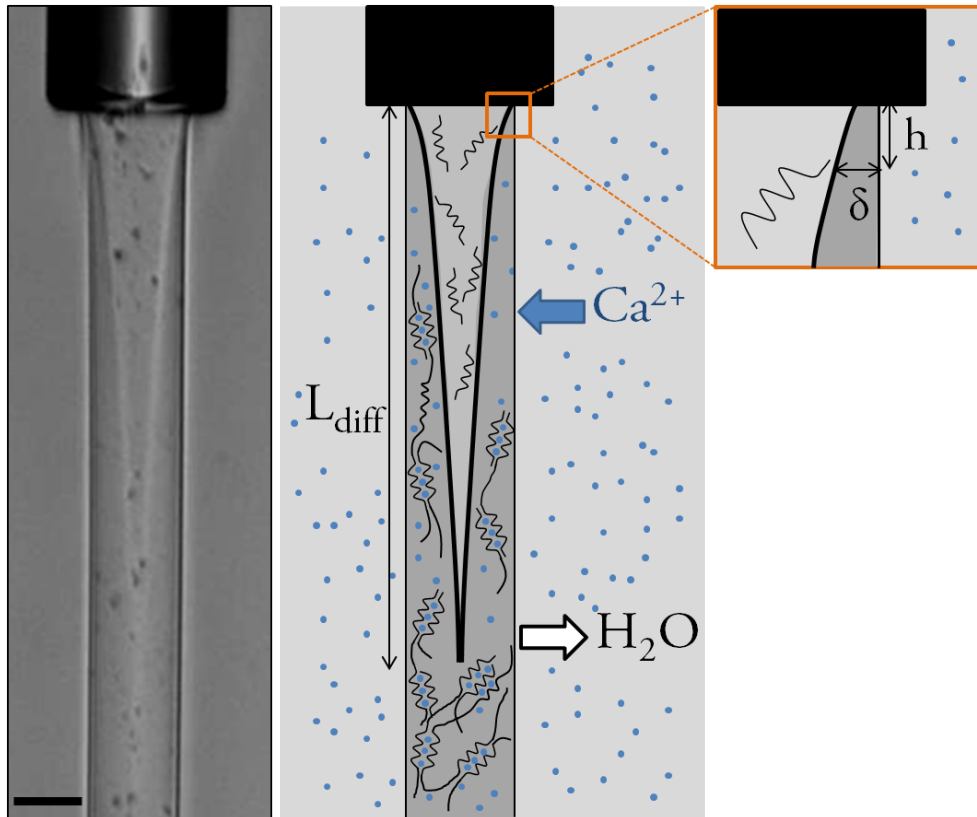


Figure 4.10: Steady and homogeneous alginate flow (left) and the scheme representation of the syneresis process occurring (right): calcium ions diffusion and water expulsion. The insert focuses on the nearly die exit zone. Black scale bar = 200 μm

While measuring this length on Figure 4.10 (left), we obtain: $\delta \approx 25 \pm 5 \mu\text{m}$ which is in good agreement with this estimate.

In parallel of calcium ions diffusion, a last phenomenon called syneresis occurs [17]. This is characterized by the contraction of alginate chains network while local divalent ions concentration is increasing. During the syneresis, the water of the gel is exuded, which has the effect of decreasing the dimensions of the extrudate and increasing locally the polymer concentration. This reorganization of the network increases the stability of the the hydrogel and reduces its porosity which may impact the calcium ions diffusion speed. Moreover, the composition of alginate plays here an important role in this mechanism as alginate solutions with long G-type sequences contract less than the alginates which possess shorter ones [17].

4.3.3 Die swelling

From the first observations, at higher velocities, the extrudate seems to be smooth (Fig.4.11, right) with a larger diameter than the die and compared to the smooth region while syneresis occurs. If we go back to the diameter ratio D'/D plot, we observe that this ratio is greater than 1 for shear rates ranging from almost 10 to 1000 s^{-1} (Fig. 4.11, shaded area). It means that the extrudate diameter is higher than the inner needle diameter which is thus called the die swelling. The swelling increases with the velocity and exceeds 1.5 times the internal diameter of the needle.

This phenomenon is due to the strong viscoelastic properties of the alginate solutions.

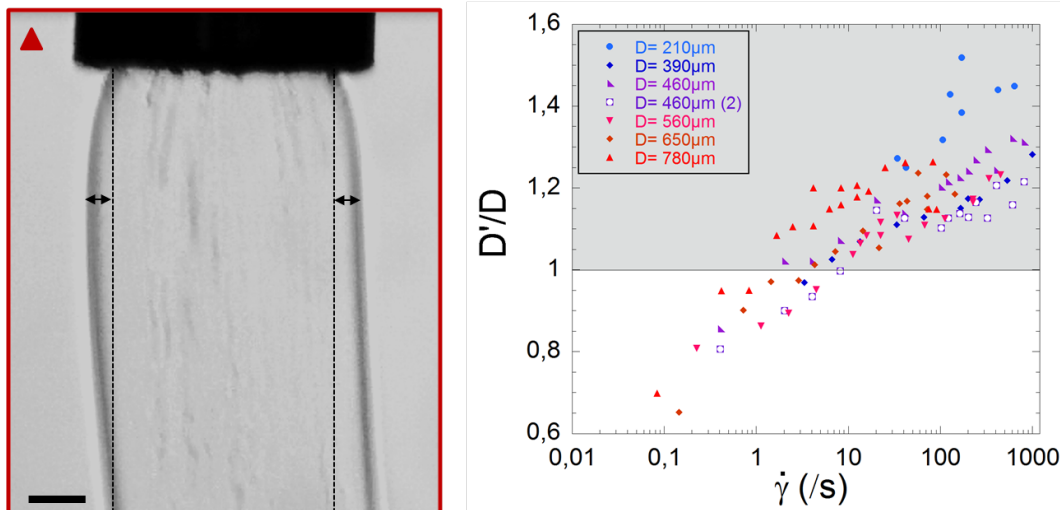


Figure 4.11: Left: Die swelling image of ALG4 extrusion in $CaCl_2 0.5M$ with metallic needle $D=780\mu m$ (Scale bar = $200\mu m$). Right: Ratio diameters D'/D plot as a function of the shear rate. In the region of interest (shaded area), the ratio is larger than 1 which shows that the extrudate has a higher diameter than the needle one.

Such fluids display also other spectacular demonstrations as the Weissenberg effect [18]:

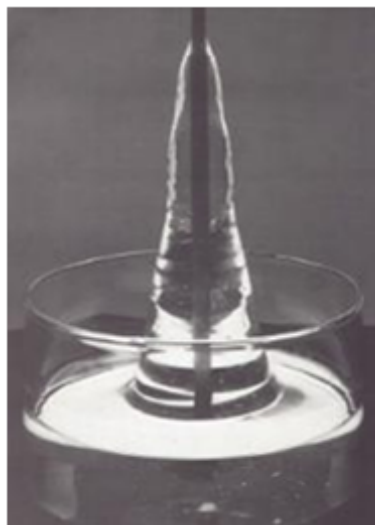


Figure 4.12: The Weissenberg or rod-climbing effect imaging [18]. The fluid is high molecular weight PIB in low molecular weight polyisobutylene. It can be compared to newtonian fluids (ex: water) behavior, where the swirling effect causes a depression vortex rather than a climbing effect as observed here.

NB: In the case of newtonian fluids, the extrudate has the same diameter as the die and the rotation of the rod creates a vortex and not a fluid climbing.

Those two effects are directly related to the normal stresses developed when such systems are submitted to a shear flow [19]. In fact, during extrusion process, the solution composed of long, entangled and coiled polymer chains, is forced to pass through a narrow die channel which elongates those chains in the flow direction and compresses them in the normal direction (Fig. 4.13). At the die exit, the release of the compressive forces and the "memory effect" of such viscoelastic fluid make the polymer chains go back to

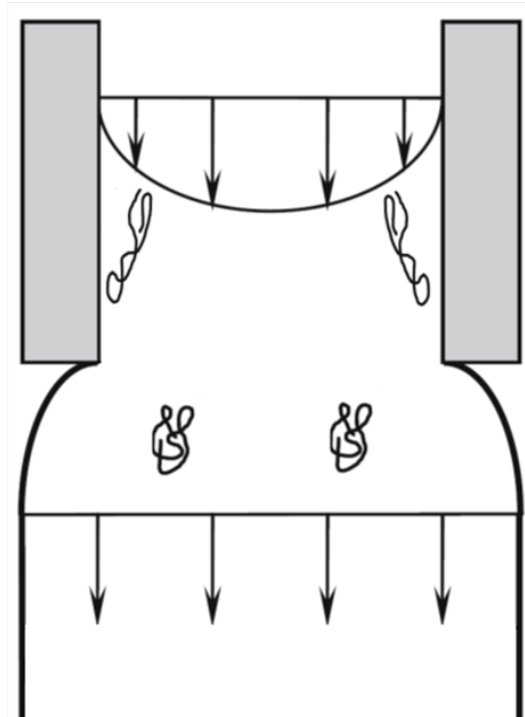


Figure 4.13: Scheme of die swelling mechanism: in the narrow channel, the polymer chains are elongated in the flow direction and compressed in the normal direction. At the die exit, the polymer chains return to the "coiled" configuration which leads to the extrudate swell. Adapted from [2].

their original configuration. Thus, there is a contraction of the chains in the flow direction and an expansion in the normal direction leading to the extrudate swell.

Moreover, from the rheological properties presented in Chapter 3, it has been shown that the alginate solutions are shear-thinning where the viscosity is constant (newtonian Plateau) for $\dot{\gamma} < \dot{\gamma}_0$ and decreases for $\dot{\gamma} > \dot{\gamma}_0$. In our study case, $\dot{\gamma} > \dot{\gamma}_0$ meaning that the viscosity function depends on the shear rate and is described by a power law. When increasing the shear rates, the viscosity decreases as the polymer chains tend to align along the shear. Thus, the swelling phenomenon is not due to the cross-linking ions but to the strong shear-thinning of alginate solutions.

4.3.4 Wavy, striated patterns and smooth alternation

4.3.4.1 Volumetric waves and surface striations

4.3.4.1.1 General observations

The wavy and striated patterns were not observed without cross-linking ions whatever extrusion speed tested. Therefore, a first assumption was that those instabilities were due to calcium ions. An easy way to verify this hypothesis was to change the calcium ions concentration. The same extrusion of ALG4 was thus performed in a calcium ions bath at 0.5M and 0.1M at the same velocity ($\bar{v} = 0.1 \text{ mm/s}$).

At $[Ca^{2+}] = 0.5M$, the extrudate showed high periodic rough striations whereas at $[Ca^{2+}] =$

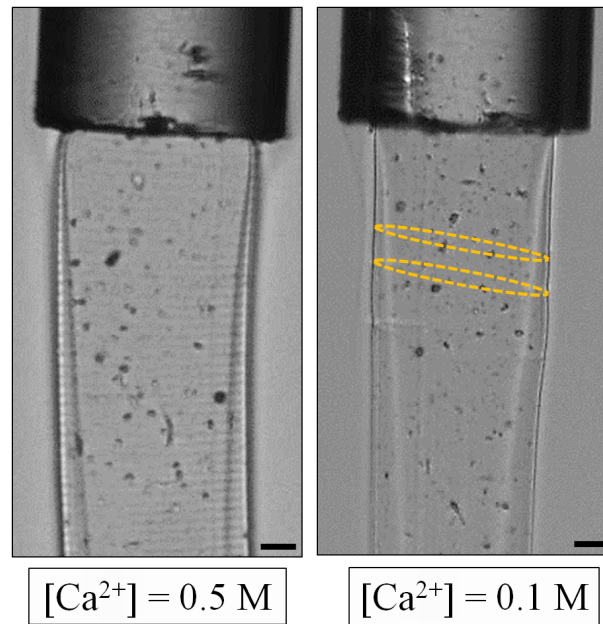


Figure 4.14: Extrusion of ALG4 in $CaCl_2 0.5M$ (left) and $CaCl_2 0.1M$ (right) with glass capillary $R=250\mu m$ at $\bar{v} = 0.1 mm/s$. Striations are periodic at 0.5M and sporadic at 0.1M.

0.1M those patterns were more sporadic and more difficult to observe as the roughness amplitude of those striations may be reduced. Therefore, striations are promoted by the gelling salt and so, the calcium ions are responsible for those instabilities.

4.3.4.1.2 Striations and waves analysis

It was very surprising to see how periodical the striated patterns were. In order to track in real-time their presence and assess their spatial wavelengths, we decided to analyze the striation using a laser beam. Unfortunately, this procedure was not suited for the real-time tracking of this instability as the laser beam illumination would suffer from numerous reflexions due to the glass tank and the solution in the bath. We therefore analyzed "post extruded" alginate threads outside of the set-up when striations were observed. The diffraction pattern is shown in Figure 4.15.

The diffraction pattern is composed of several fringes spaced at a length L . Those fringes are perpendicularly oriented to the striations found on the alginate thread surface. The striated patterns act as a diffraction grating. It is thus possible to estimate the distance between two striations:

Numerical application: From the diffraction relationship between the different physical quantities, we have:

$$a = \frac{2 \lambda D}{L}$$

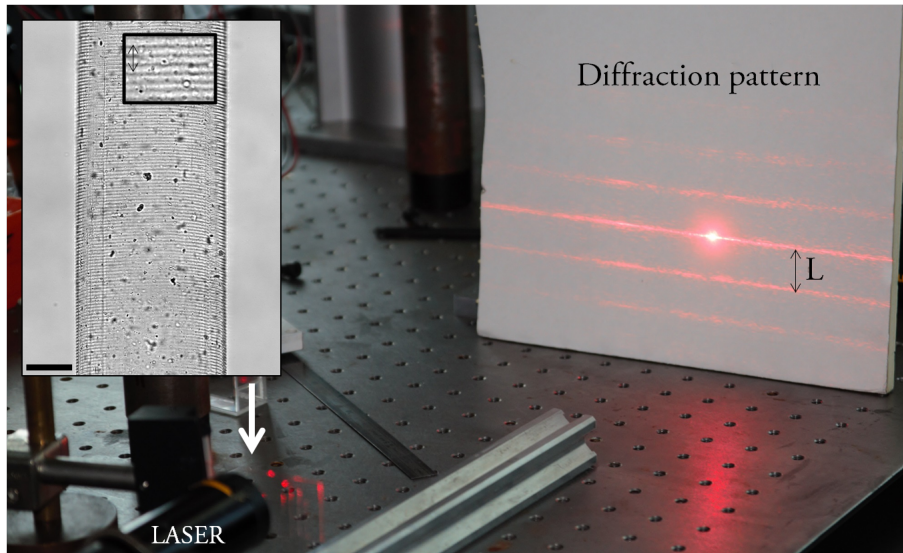


Figure 4.15: Laser diffraction experiment on an alginate thread which exhibits periodic striations and the respective diffraction pattern observed directly on a screen.

where a is the striations wavelength on alginate thread, λ is the laser beam wavelength $\lambda = 660\text{nm}$, D the length between the thread and the screen; and L the length measured on the screen between two fringe patterns ($L = 4\text{cm}$). From the relationship, we obtain: $a \approx 12\mu\text{m}$ which is consistent with the microscopical observations.

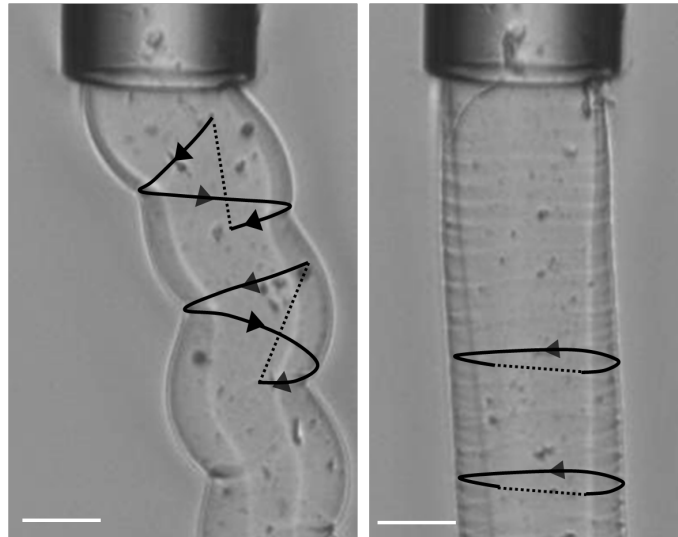


Figure 4.16: Eye guidelines of the possible mechanism which leads to wavy (left) and striated pattern (right). The gelation may occur at the die exit and propagate along the die circumference. At low throughput (left), the gelation front sticks and debonds while the solution still flows (protrusion). At higher throughput, this mechanism occurs more rapidly: the protrusions do not form and the gelation travels the entire circumference quasi instantaneously (right). Scale bar = $200\mu\text{m}$.

Possible mechanism: It is assumed that wavy and striated patterns both come from the presence of calcium ions and may be due to the same instability but at different time scales. Calcium ions might diffuse and penetrate at the die exit vicinity over a small length, but long enough to create a gelled area which sticks and moves radially away from the die

surface. In the "wavy" case, the throughput is slow enough to give to the annular gel front the time to propagate over ONE die circumference while solution continues flowing (protusion). As a consequence, the pattern is helical (Fig 4.16 left). When the throughput increases, this phenomenon occurs more rapidly and the gel "annulus" debonds from the die over the all circumference at almost the same time (Fig 4.16 right), leading to quasi entire rings which appear very periodically.

The time period T between two striated events were measured at different throughputs. The striations velocity v_s at which the striations progress, was estimated as follows:

$$v_s = \frac{2 \pi R}{T}$$

where the numerator represents the die inner periphery with R its radius and T the time period. Figure 4.17 displays the striations velocity evolution as a function of the shear rate $\dot{\gamma}$ for three different capillary radii.

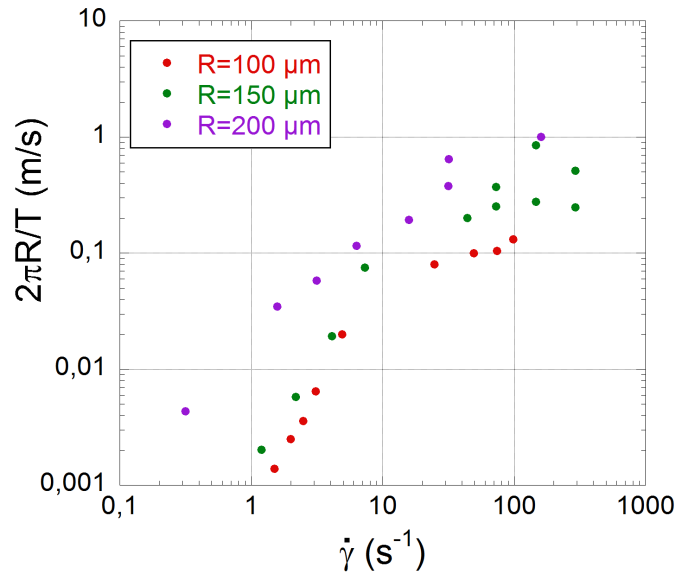


Figure 4.17: Striations velocity evolution as a function of the shear rate for three capillaries of radii: Red: 100 μm , Green: 150 μm and Purple: 200 μm

The striations velocity tend to values of about: $v_s = 0.1-1 \text{ m/s}$ for high shear rates. As a possible line of reflection, we can calculate the sound velocity of a plane transverse shear wave in a material. This velocity is related to the shear modulus G and the mass density ρ by:

$$v_{\text{sound}} = \sqrt{\frac{G}{\rho}}$$

Here, for the high shear rates, the shear modulus is about 200 Pa.s. The mass density of sodium alginate is 1600 kg/m^3 . The resulting shear wave velocity is estimated: $v_{\text{sound}} \simeq 0.35 \text{ m/s}$. The striations velocity and the shear wave velocity are of the same order of magnitude. This might suggest that the striation is an adhesive fracture process which, as such, has a limit velocity of the order of the transverse sound velocity. (Rayleigh wave speed for mode I brittle fracture, [20])

4.3.4.2 Oscillating flow

Between the wavy and striated regimes, an unstable region is observed. While the velocity is close to the lower or upper ranges, the extrudate surface alternates with smooth and respectively wavy (low) or striated (high) patterns. An example of alginate extrudate with oscillating surface is shown in figure 4.18:

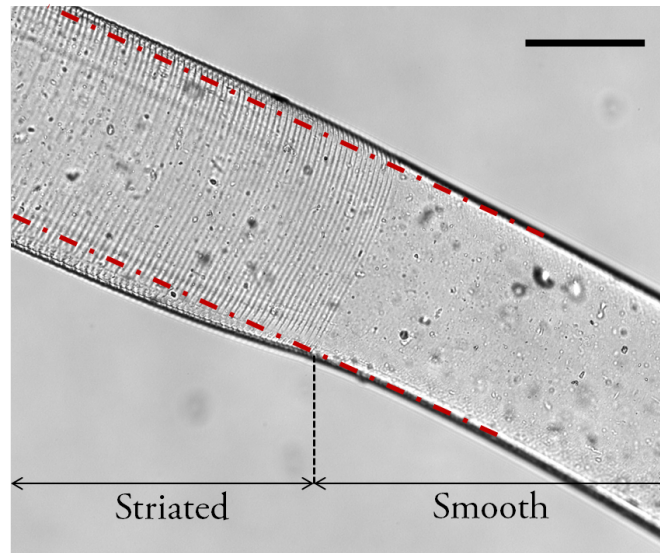


Figure 4.18: Alginate extrudate from ALG4 extrusion in CaCl_2 0.5M, with a glass capillary $R=150\ \mu\text{m}$ at $\bar{v}=1\text{mm/s}$. This extrudate displays two morphologies: right: smooth region and left: striated pattern. Red dashed lines are eyes guidelines to see the die swelling superimposed with striations defect. Scale bar = $200\ \mu\text{m}$

NB: Those instabilities were observed for glass, metallic and PTFE capillary. It was more surprising in the last case as Teflon is hydrophobic and does not promote adhesion.

We can also notice that the striations appear superimposed with a diameter increase whereas the smooth part has a diameter comparable with the inner capillary diameter (Fig. 4.18,4.19). Based on polymer melt interpretation for the stick-slip instability, it is assumed that as the swelling and striations appear together, polymer chains stick to the wall surface leading to their disentanglement and so to the die swelling at the exit where chains entangle. On the contrary, when chains are sliding on the wall, there is no die swelling and the extrudate is smooth [1].

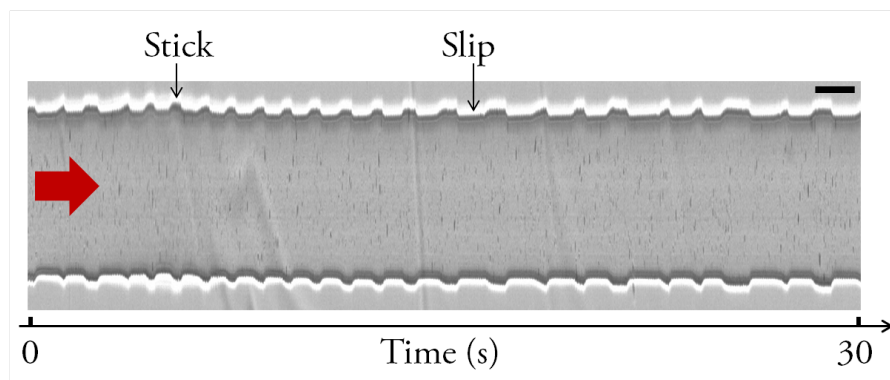


Figure 4.19: Spatio-temporal image of ALG4 extrusion with stainless steel needle of radii $760\ \mu\text{m}$ in the oscillating regime. Stick is associated to die swelling and Slip to the smooth region. Red arrow shows the flow direction. Scale bar = $200\ \mu\text{m}$.

Finally, regarding the time period of each phenomenon, we observe that, generally, the stick phase has shorter durations than the slip phase (Fig. 4.19). Moreover, both appear quite periodically. Further investigations must be performed to better quantify this oscillating regime.

4.3.5 Gel clogging

The last instability is the most surprising. While increasing extrusion velocity at its maximum, gel clogging near the die exit is observed. We first noticed this incredible instability with a metallic needle. With this material, the gel clogging can reach 50% of the die diameter! To better understand the gel clogging formation, we used glass capillaries and repeated the experiment. It was quite difficult to find it but it seems that after several experiments with the same capillary, it favored the instability. Moreover, the instability must appear on one capillary "side" in the field of view to be seen.

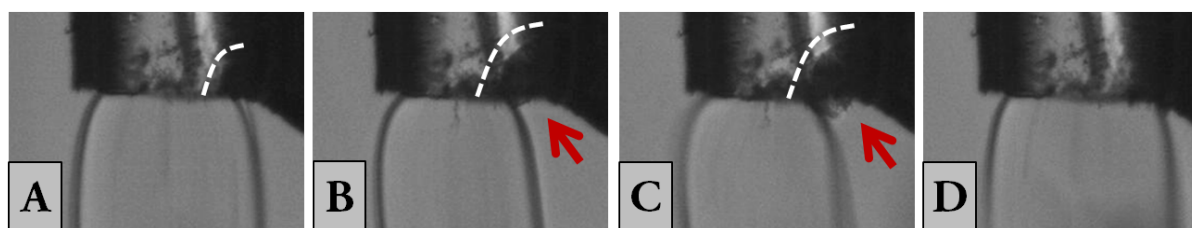


Figure 4.20: Gel clogging steps: A) The gel nucleation site appears and B) grows until C) beginning to go out and D) being expelled. The flow diameter decreases progressively. Extrusion of ALG4 in $CaCl_2$ 0.5M with glass capillary 500 μ m. Needle diameter=390 μ m.

Figure 4.20 displays the different steps of the gel clogging formation. Thanks to the glass transparent capillary, we can follow the development of the gel clogging. First, a nucleation point is observed and grows inside the capillary up to some critical size. Then, it begins to go out of the capillary and it is finally expelled. Moreover, one gel clogging event is often followed by series of other events which appear quite periodically (Figure 4.21, A) from the same "nucleation" site. In order to further investigate this gel clogging, we have used needles with different angles.

Angle effect: for an angle of 30° at the die exit (Figure 4.21, B), in the case of stainless steel needle, the gel clogging is also observed. The instability is always located on the top angle side (side where the solution is "first" in contact with the bath)

Die material effect: as previously mentioned, the gel clogging was larger for stainless steel needles than for glass capillaries. It was not yet observed in the case of PTFE tubing.

Calcium ions effect: we performed the same extrusion experiment at the highest velocity in chloride calcium solution at 0.1M (5 times lower). No gel clogging was noticed.

All those qualitative observations suggest that calcium ions are essential to induce quick gelation at the die exit and that rough material improves this instability. We can hypothesize that the roughness acts as an ion entrance favorable parameter which makes easier ion diffusion at the die exit vicinity.

Short comment: As this bulk defect spoils the extrudate and may clog half of the die (Fig. 4.22 B)), we would like to know how this large barrier impacts the force signal and then

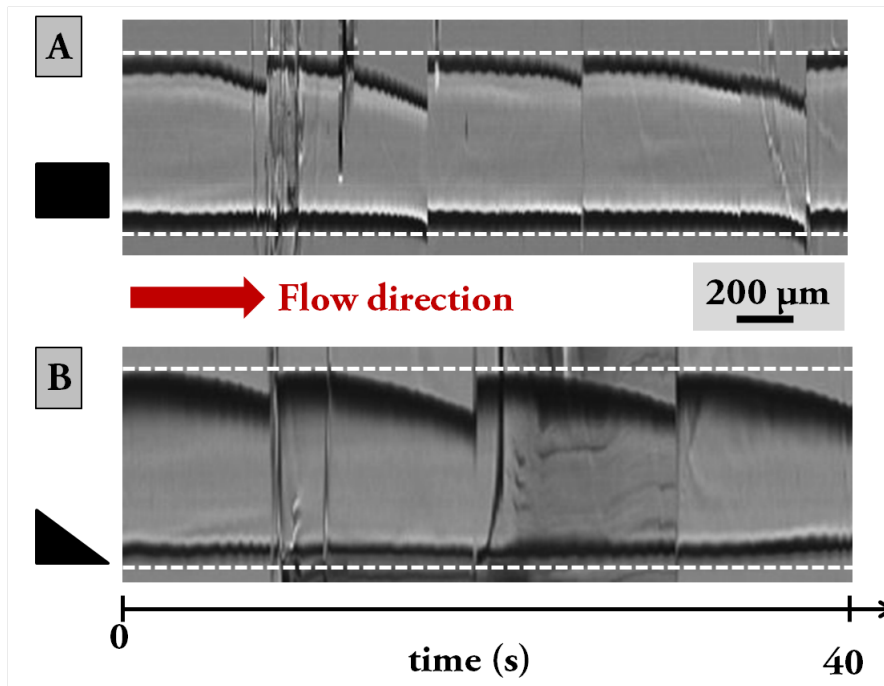


Figure 4.21: Spatio-temporal images of ALG4 extrusion with stainless steel needle of radii $460\mu\text{m}$ of A) blunt exit and B) exit angle 30° of several gel clogging events.

if it is possible to predict the gel clogging. The force signal was monitored during the extrusion of alginate solutions at exit velocity of 40 mm/s (Fig. 4.22, A)). However, even if gel cloggings were amazing and blocked almost the middle of the capillary exit, the force signal is not impacted enough to be detected. Indeed, the two events showed by the purple arrows are the gel clogging expulsions and both forces signals do not stand out from the signal noise.

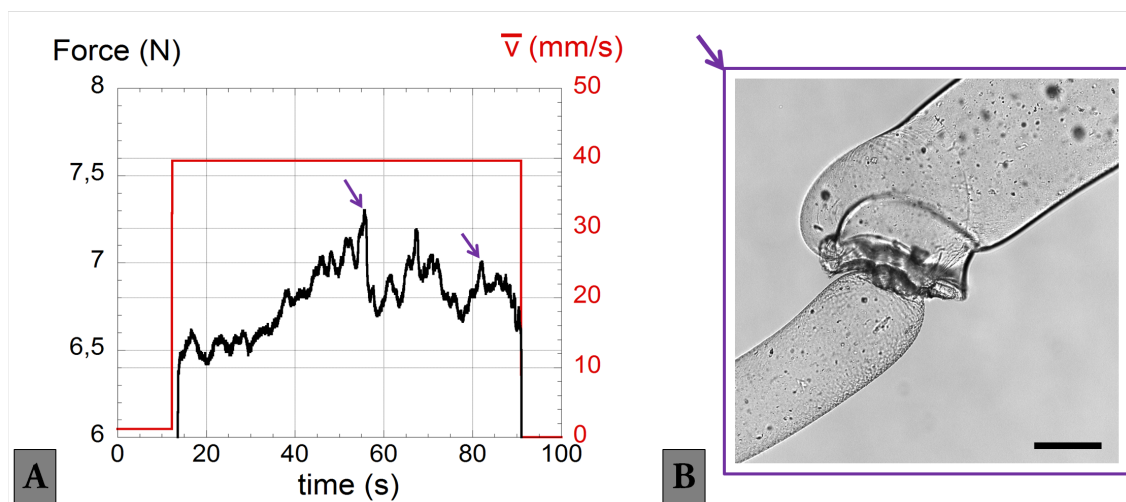


Figure 4.22: A) Force and velocity signal of the extrusion of ALG4 in $\text{CaCl}_2 0.5\text{M}$ with a glass capillary of $500\mu\text{m}$. Purple arrows point out gel clogging expulsions. B) A corresponding example of gel clogging defect on an extrudate is observed post-extrusion. Scale bar: $200\mu\text{m}$.

The gel clogging defect is quite inconsistent with the velocity range at which it appears. Indeed, it is assumed that, at high velocity, calcium ions may not diffuse inside the cap-

illary. However, they reach the internal die wall probably through singular die exit defect area which constitutes an ion entrance point and thus a gel nucleation point.

4.4 Conclusion

Sodium alginate solutions were chosen to be our model system to study the extrusion instability and harness our experimental set-up before using it with collagen solutions. First, we studied the extrusion of alginate in the absence of binding ions. Two characteristic instabilities already reported for polymer melt extrusions were observed and quantified: the sharkskin perturbing the extrudate surface and the helical instability which disturbed the extrudate volume. We proved that the die characteristic dimensions had an influence on the second one which was assumed to affect the whole pipe flow. Those observations had never been reported before in the case of polymer solutions.

In the second study, we extruded alginate solutions in a bath containing calcium ions. Quite surprisingly, instabilities were observed such as the highly periodic striations on threads surface or the gel clogging which appeared at high velocities. Indeed, in the presence of divalent ions, the gelation of alginate occurred and several phenomena could appear at the same time: calcium ions diffusion, alginate network formation, syneresis etc, making the results interpretation more complicated. Several potential mechanisms were anyway described but further experiments were needed to better understand those unique instabilities.

Finally, according to our initial idea, we attempted to transpose results obtained for alginate solutions to collagen ones. We have succeeded in reproducing helical distortion on collagen threads. This last result offers interesting prospects for providing a tendon-like structure to our collagen threads, akin the "crimp".

4.5 References

- [1] Morton M Denn. Extrusion instabilities and wall slip. *Annual Review of Fluid Mechanics*, 33(1):265–287, 2001. [103](#), [105](#), [134](#)
- [2] Bruno Vergnes. Défauts d'extrusion et instabilités d'écoulement des polymères fondus. *Rhéologie*, 25:1–25, 2014. [103](#), [104](#), [130](#)
- [3] JM Piau, N El Kissi, and B Tremblay. Influence of upstream instabilities and wall slip on melt fracture and sharkskin phenomena during silicones extrusion through orifice dies. *Journal of non-newtonian fluid mechanics*, 34(2):145–180, 1990. [104](#)
- [4] Laurent Robert. *Instabilité oscillante de polyéthylènes linéaires: observations et interprétations*. PhD thesis, Nice, 2001. [104](#)
- [5] H Münstedt, M Schmidt, and E Wassner. Stick and slip phenomena during extrusion of polyethylene melts as investigated by laser-doppler velocimetry. *Journal of Rheology*, 44(2):413–427, 2000. [104](#)
- [6] Christelle Combeaud. *Etude des instabilités volumiques en extrusion de polystyrène et polypropylène*. PhD thesis, École Nationale Supérieure des Mines de Paris, 2004. [104](#)
- [7] J-F Agassant, Dawn R Arda, Christelle Combeaud, Armin Merten, Helmut Muenstedt, Malcolm R Mackley, Laurent Robert, and Bruno Vergnes. Polymer processing extrusion instabilities and methods for their elimination or minimisation. *International Polymer Processing*, 21(3):239–255, 2006. [104](#)
- [8] Christelle Combeaud, Yves Demay, and Bruno Vergnes. Experimental study of the volume defects in polystyrene extrusion. *Journal of non-newtonian fluid mechanics*, 121(2):175–185, 2004. [104](#)
- [9] H Nguyen and DV Boger. The kinematics and stability of die entry flows. *Journal of non-Newtonian fluid mechanics*, 5:353–368, 1979. [105](#)
- [10] Gareth H McKinley, William P Raiford, Robert A Brown, and Robert C Armstrong. Nonlinear dynamics of viscoelastic flow in axisymmetric abrupt contractions. *Journal of fluid mechanics*, 223:411–456, 1991. [105](#)
- [11] Ronald G Larson. Instabilities in viscoelastic flows. *Rheologica Acta*, 31(3):213–263, 1992. [105](#)
- [12] Lise Picaut, Olivier Ronsin, Christiane Caroli, and Tristan Baumberger. Experimental evidence of a helical, supercritical instability in pipe flow of shear thinning fluids. *Physical Review Fluids*, 2017. [108](#), [125](#)
- [13] James H.-C. Wang. Mechanobiology of tendon. *Journal of Biomechanics*, 39(9):1563–1582, January 2006. [122](#)
- [14] Jeffrey M Caves, Vivek A Kumar, Wenjun Xu, Nisarga Naik, Mark G Allen, and Elliot L Chaikof. Microcrimped collagen fiber-elastin composites. *Advanced Materials*, 22(18):2041–2044, 2010. [122](#)

- [15] Yang Wu, Jerry YH Fuh, and Yoke San Wong. Crimped fiber printing via e-jetting for tissue engineering. In *ASME 2017 12th International Manufacturing Science and Engineering Conference collocated with the JSME/ASME 2017 6th International Conference on Materials and Processing*, pages V004T05A014–V004T05A014. American Society of Mechanical Engineers, 2017. [122](#), [123](#)
- [16] Spencer E Szczesny, Tristan P Driscoll, Hsiao-Yun Tseng, Pang-Ching Liu, Su-Jin Heo, Robert L Mauck, and Pen-Hsiu G Chao. Crimped nanofibrous biomaterials mimic microstructure and mechanics of native tissue and alter strain transfer to cells. *ACS Biomaterials Science & Engineering*, 2016. [122](#), [123](#)
- [17] Kurt Ingar Draget, Olav Gåserød, Ingrid Aune, Peder O Andersen, Bente Storbakken, Bjørn Torger Stokke, and Olav Smidsrød. Effects of molecular weight and elastic segment flexibility on syneresis in ca-alginate gels. *Food Hydrocolloids*, 15(4):485–490, 2001. [128](#)
- [18] David V Boger and Kenneth Walters. *Rheological phenomena in focus*, volume 4. Elsevier, 2012. [129](#)
- [19] RI Tanner. A theory of die-swell. *Journal of Polymer Science Part B: Polymer Physics*, 8(12):2067–2078, 1970. [129](#)
- [20] Jay Fineberg and M Marder. Instability in dynamic fracture. *Physics Reports*, 313(1):1–108, 1999. [133](#)

Chapter 5

Preparation and characterization of collagen scaffolds

*“In every job that must be done,
there is an element of fun.”*

Mary Poppins in *Mary Poppins*

Abstract

In this chapter, we first tested the reproducibility of collagen type I extrusion while changing the stock solution batch. We then assessed the ionic strength influence of the extrusion bath on the collagen thread stability and structure ageing. Based on several criteria, this study allowed us to select a single condition that was used to analyze the effect of collagen solution concentration. As a complementary experiment and to study the benefits of their added properties, collagen-alginate mixtures were extruded and the resulting threads were compared with the pure collagen ones. Finally, in view of cell culture experiments, the stability of the collagen based threads in culture medium was characterized

Contents

5.1 Threads structure characterization techniques	143
5.1.1 Photonic microscopies	143
5.1.1.1 Optical (bright field) and polarized microscopies	143
5.1.1.2 Second Harmonic Generation (SHG) Microscopy	146
5.1.2 Electron microscopies	152
5.1.2.1 Scanning Electron microscopy (SEM)	153
5.1.2.2 Transmission Electron microscopy (TEM)	154
5.1.3 Differential Scanning Calorimetry (DSC)	155
5.2 Collagen batch quality criterion	156
5.3 Fibrillogenesis buffer (Ionic strength) effect	157
5.4 Pure collagen vs collagen/alginate mixtures threads study	180
5.4.1 Pure collagen threads of different concentrations	180
5.4.1.1 Extrusion and maturation	180
5.4.1.2 Structural characterization	183
5.4.2 Collagen/alginate threads	188
5.4.2.1 Ratio choice	188
5.4.2.2 Structural characterization	189

5.4.3 Mechanical properties comparison	193
5.5 Preliminary study to cell culture	194
5.5.1 General morphology	194
5.5.1.1 Optical observations	194
5.5.1.2 Topography analysis	194
5.5.2 Diameter stability	195
5.5.3 Structural characterization	196
5.5.3.1 Pure collagen threads	196
5.5.3.2 Collagen:alginate threads	197
5.5.3.3 Collagen stability: thermal analysis	199
5.5.4 Mechanical properties	200
5.5.5 Discussion	200
5.6 Conclusion	201
5.7 References	202

The collagen-based threads have been studied as a function of several parameters as the time, fibrillogenesis buffers, material nature and concentration and extrusion velocity. We have characterized each thread from the nanometric to the sample scale by using different techniques. The mechanical properties of the threads that were assessed by tensile testing methods and have already been described in Chapter 2 (2.1.3 p 69). In this chapter we first present the other techniques techniques of characterization that were used, their underlying principles, as well as our main results.

5.1 Threads structure characterization techniques

Two main categories of structure characterization techniques have been used: those involving photon radiation and those involving electron radiation. The first category allowed us to characterize the collagen 3D organization and distribution inside the threads. Electron microscopy techniques have revealed the topography of the threads, the inner structure at the nanometric scale and have allowed us to measure the diameter of the fibrils and to verify their integrity. Combining those two types of techniques, we determined the most advantageous threads for the project according to the different physicochemical conditions.

5.1.1 Photonic microscopies

5.1.1.1 Optical (bright field) and polarized microscopies

Optical bright field microscopy is used to observe the threads evolution and stability as a function of several parameters (maturation time, concentration, buffer etc). It allows us to gather informations about their structural shape at the thread scale. Polarized light microscopy is performed to assess qualitatively the main orientation of collagen inside the threads.

Bright field

A light wave is an electromagnetic wave, which is composed of an electric field \vec{E} and a magnetic field \vec{B} (Fig. 5.1). These fields are perpendicular to each other and in a plane perpendicular to the direction of propagation: the wave plane. The polarization of a wave is characterized by the direction of \vec{E} . For natural lighting, the vector \vec{E} varies randomly over time, and so, this light is not polarized.

Linear polarization

When the direction of \vec{E} remains constant in the wave plane, the polarization is linear. In a (Oxy) coordinates system (Fig. 5.1), the vector \vec{E} is written as: $\vec{E} = E_x \vec{e}_x + E_y \vec{e}_y$
If α is the angle between the axis (Ox) and the vector \vec{E} , it is then expressed as:

$$\begin{cases} E_x = E_0 \cos(\alpha) \cos(\omega t) \\ E_y = E_0 \sin(\alpha) \cos(\omega t) \end{cases}$$

Elliptical polarization

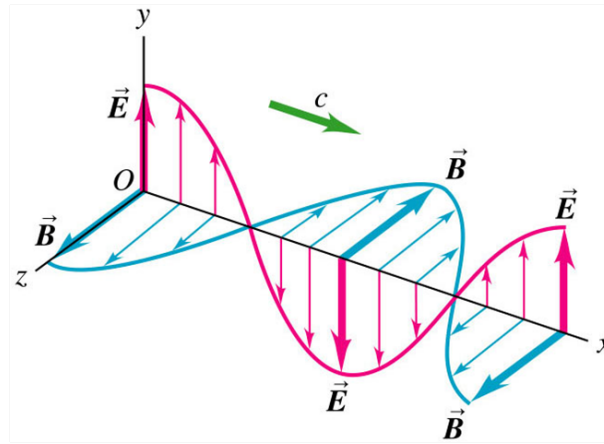


Figure 5.1: Scheme of a linearly polarized sinusoidal electromagnetic wave travelling in the positive x-direction. \vec{E} and \vec{B} are the electric and the magnetic fields respectively of the light wave, which propagates at the celerity c . (From: <https://www.miniphysics.com/>, "Electromagnetic Spectrum and Sinusoidal EM Plane Waves")

In the case of elliptical polarization, the tip of the vector \vec{E} describes an ellipse in the wave plane. If a and b are the two half-axes of the ellipse, the ellipticity is then defined by: $\tan(\psi) = b/a$.

The ellipse is said to be "right" if the tip of \vec{E} turns clockwise and "left" if it rotates in the trigonometric direction. The components of \vec{E} are given by:

$$\begin{cases} E_x = E_0 a \cos(\omega t) \\ E_y = E_0 \epsilon b \sin(\omega t) \end{cases}$$

with $\epsilon = \pm 1$.

If the major axis of the ellipse has an angle α with the axis (Ox) we have:

$$\begin{cases} E_x = E_0 (a \cos(\alpha) \cos(\omega t) - \epsilon b \sin(\alpha) \sin(\omega t)) \\ E_y = E_0 (a \sin(\alpha) \cos(\omega t) + \epsilon b \cos(\alpha) \sin(\omega t)) \end{cases}$$

Circular polarization

Circular polarization is a special case of elliptic polarization. It is obtained when $a = b$, we thus have:

$$\begin{cases} E_x = E_0 a \cos(\omega t) \\ E_y = E_0 \epsilon a \cos(\omega t) \end{cases}$$

Microscope parameters: All threads observations were performed on a Nikon Eclipse E600L microscope equipped with a digital camera DXM 1200 CCD. The samples were placed horizontally between two crossed polarizers. Between them, a collagen thread with an isotropic structure will appear black whereas if it has an anisotropic organized structure, it will be revealed colored and textured. This is due to the **birefringence** of the collagen.

Birefringence

In an isotropic material, the light propagates at the same velocity in all directions of space. The medium can therefore be characterized by a unique refractive index n , defined by the

relation $n = c/v$, where c is the light celerity in the vacuum and v the light propagation velocity in the medium.

The birefringence of a medium results from its anisotropy. Here, we focus only on an uniaxial anisotropy. Such a medium can not be characterized only by a single index of refraction. The ellipsoid of the indices is defined by its surface composed of three axes: n_o , the ordinary index (along (Ox) and (Oy) axes) and the extraordinary index n_e (Fig. 5.2). In a positive uniaxial medium, we have: $n_e > n_o$.

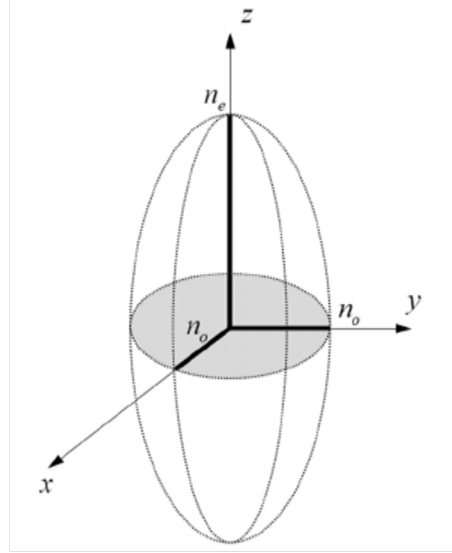


Figure 5.2: Index ellipsoid for a positive uniaxial medium: n_o and n_e are the respective ordinary and extraordinary index where $n_e > n_o$ leading to the ellipsoid.

The birefringence is determined by placing this medium between two crossed polarizers at 45° . The first polarizer selects linearly the incident light in a given direction. In the absence of a sample (or in the presence of an isotropic sample), the analyzer (second polarizer) oriented at 90° avoids the transmission of this light, causing an extinction. In the case of birefringent material, it is possible to decompose the propagating light into two components along the axes of the index ellipsoid. The transmitted light (at the analyzer output) is the combination of those two components and has an intensity I' given by:

$$I' = I \sin^2(2\alpha) \sin^2\left(\frac{\pi\delta}{\lambda}\right)$$

with: I the incident light intensity (at the polarizer input); α the angle formed between the polarizer and n_e ; δ the delay between the two parallel vibration components of the polarizer and the analyzer; and λ the light wavelength.

The path delay δ defined as $\delta = \Delta n \times e$ (with e the medium thickness) is a function of the anisotropic medium traversed. The variations of the intensity at a sample point depend on the single parameter α . The transmitted intensity is maximum for values of $\alpha = \pm \pi/4$ and is minimal or equal to zero for $\alpha = \pm \pi/2$. We can quantify the birefringence through the subtraction of the two index: $\Delta n = n_e - n_o$. The birefringence is therefore positive when $n_e > n_o$, which means that the light propagation velocity ($v = c/n$) is greater along the ordinary axis of the ellipsoid.

In practice, when an anisotropic material is observed under a polarized light microscope, the rotation of the sample plate will vary the angle α . In the case of type I collagen, its extraordinary index occurs in the axial direction of both fibrils and the molecule itself.

Sample preparation and observations parameters

All samples were put in optical observation chambers in which several drops of extrusion buffer were added to keep the samples in wet conditions at room temperature. The threads diameters were measured over two weeks for stability analysis. For polarized light microscopy observations, a wave plate (λ) was sometimes added between the crossed polarizers in order to change the linearly polarized light into circularly polarized light. This operation made easier the observations of collagen molecules orientation despite the thickness of the threads.

5.1.1.2 Second Harmonic Generation (SHG) Microscopy

With the two first optical techniques, we can easily quantify the threads stability over time and have an idea about the collagen orientation inside the thread. However, it is not precise enough to observe the possible structural changes and organization at the collagen molecule scale. To do so, more advanced and sophisticated techniques must be used such as the Second Harmonic Generation (SHG) microscopy [1]. This technique presents a much better axial resolution than the polarized light microscopy and allows to image the texture of the collagen-based threads in 3D. Two contrast modes are used on the same focal volume: SHG and 2PEF (two photon excited fluorescence).

5.1.1.2.1 Principle

Multiphoton microscopy uses non-linear interactions between light and matter as a source of contrast. SHG is a coherent process which consists in the conversion of an intense pulse laser source of frequency ω into its harmonic at 2ω , by the generation of 1 single photon at 2ω from 2 photons at ω [2]. This process is not very effective and requires focusing the energy by using femtosecond pulses. This increases the signal intensity while maintaining an average power compatible with biological samples. The signal intensity is then proportional to the square of the density of the molecules generating the harmonic response.

SHG process is due to the oscillation of polarizable electrons at the molecular scale and to the electric field of induced dipoles that will interfere at the macromolecular scale. The three-dimensional organization of the molecules in the focal volume is thus important for obtaining an SHG signal.

The interaction of an electromagnetic wave with a molecular bond or a single molecule induces the oscillation of an electron of this molecule. The potential of the excited electron evolves in the same way as the one of a harmonic oscillator according to the Lorentz model. Thus the frequency at which this electron oscillates is equal to that of the excitation wave (Rayleigh scattering, Fig. 5.3, a). In reality, the potential is not exactly parabolic, which leads to the generation of harmonics (Fig. 5.3, b). In the case of symmetric potential, only the uneven multiple harmonics of the exciter wavelength are generated. This is why, a centro-symmetric molecule can not create a SHG signal.

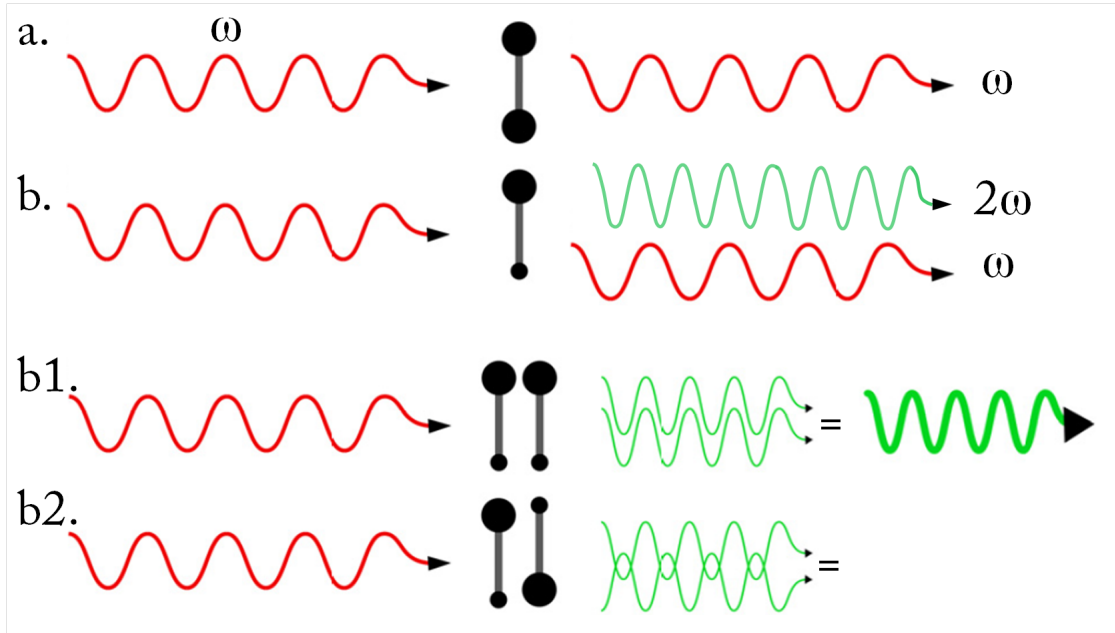


Figure 5.3: Excitation of molecules with a radiation of frequency ω . a) While exciting a symmetrical molecule, the frequency of the excitation radiations are equal to that of the scattered radiation: this is the Rayleigh scattering. b) If the molecule is non-centrosymmetric, we have both Rayleigh scattering and harmonic scattering (double frequency radiation: 2ω) at high excitation intensity. b1. If two non-centrosymmetric molecules are parallel, we have constructive interferences of the radiations at the double frequency 2ω . b2. On the contrary, for two non-centrosymmetric antiparallel molecules, the radiation is in phase opposition and there is then destructive interference with zero scattering intensity. The scattered intensity thus varies quadratically with the number of parallel non-centrosymmetric molecules. (Adapted from [3])

The polarization \vec{p} is then given by the relation:

$$\vec{p} = \alpha \vec{E} + \beta \vec{E} \cdot \vec{E} + \gamma \vec{E} \cdot \vec{E} \cdot \vec{E} + \dots$$

where α is the linear polarizability, β and γ the first and second order hyperpolarizabilities and \vec{E} , the electric field is written as:

$$\vec{E} = \vec{E}_0 e^{-i\omega t} + cc$$

with ω the wave pulsation and cc the complex conjugate.

If two non-centrosymmetric molecules, separated by a small distance ($< \lambda$: incident wavelength), are aligned parallel in the same direction, the generated harmonic radiations are the same for the two molecules. The polarization of order 2 which is identical for the two molecules is given by:

$$\vec{p}^{(2)}(2\omega) = \beta \vec{E}(\omega) \cdot \vec{E}(\omega)$$

Thus, these harmonic radiations interfere constructively and the total field is twice that of a single dipole (Fig. 5.3, b1). Since the scattered intensity is the square of the total

field, the intensity is 4 times greater than that obtained in the case of a single molecule. However, if the polarities of the molecules are opposite, destructive interference occurs resulting in zero signal (Fig. 5.3, b2).

5.1.1.2.2 Origin of the collagen SHG signal

The collagen SHG signal comes from the peptide bonds at the molecular level. As previously described, SHG is sensitive to non-centrosymmetric molecules assemblies. The collagen molecule, due to the alignment of its numerous peptide bonds (Fig. 5.4 a), b top), has a non-negligible first hyperpolarizability (Fig. 5.4 b) bottom).

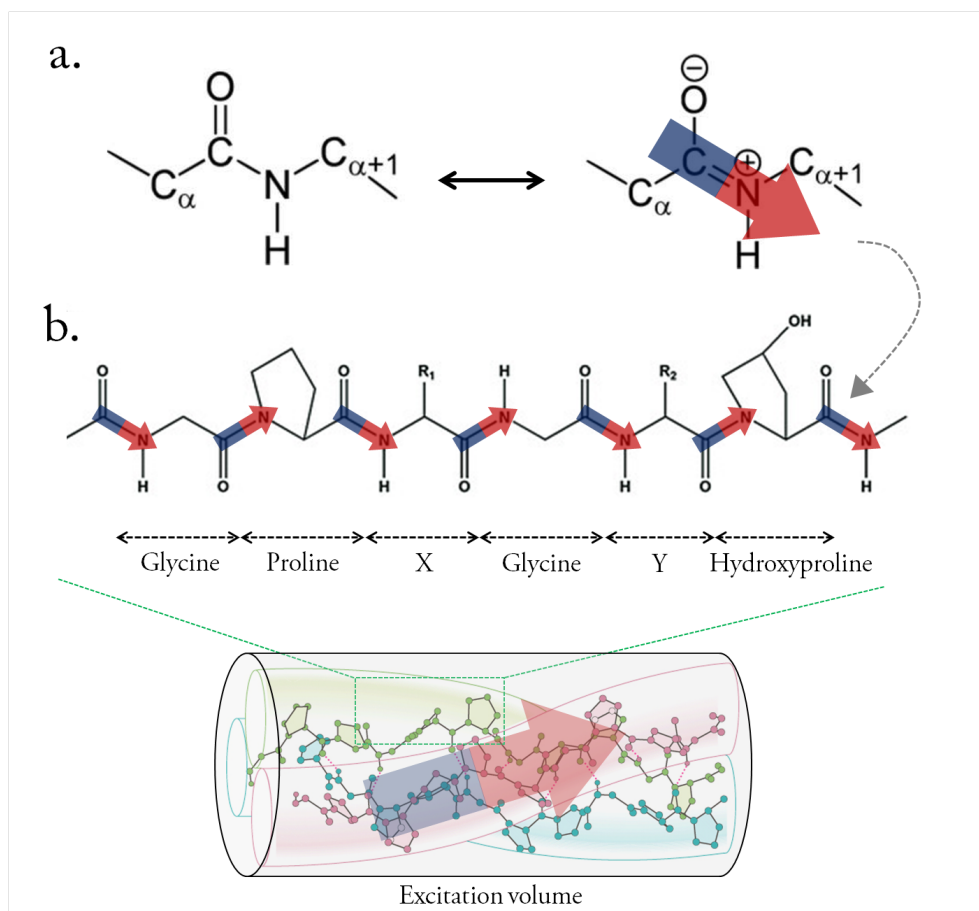


Figure 5.4: Schemes of: a) a peptide bond which is responsible for the SHG signal of the collagen molecule [4]. In fact, this bond acts as an electric dipole (arrow). b) Top: The origin of the SHG signal in collagen is related to the hyperpolarizability β of the peptide bonds present in each collagen helix. Bottom: Thus, the SHG signal will depend on the organization of these bonds in the excitation volume, therefore, of the 3D organization of the triple helices. The triple helix has C_∞ symmetry. Adapted from [5]

Because of its three α -helices, collagen has C_3 symmetry, but to simplify, it is considered as a C_∞ symmetry. The compactness and stiffness of the triple helix ensure that a large number of harmonophores (peptide bonds) are well aligned along the molecular axis, which allows the coherent built-up of SHG signal. Moreover, the coherent addition of the second harmonic signal of each triple helix within a fibril leads to an important SHG signal of the fibrillar collagen.

5.1.1.2.3 Polarization-resolved Second Harmonic Microscopy

In order to assess the three-dimensional mean orientation of collagen in the threads, we used polarization-resolved SHG. This further technique allows determining the orientation of the collagen helices in the excitation volume (Fig. 5.5 a), b)).

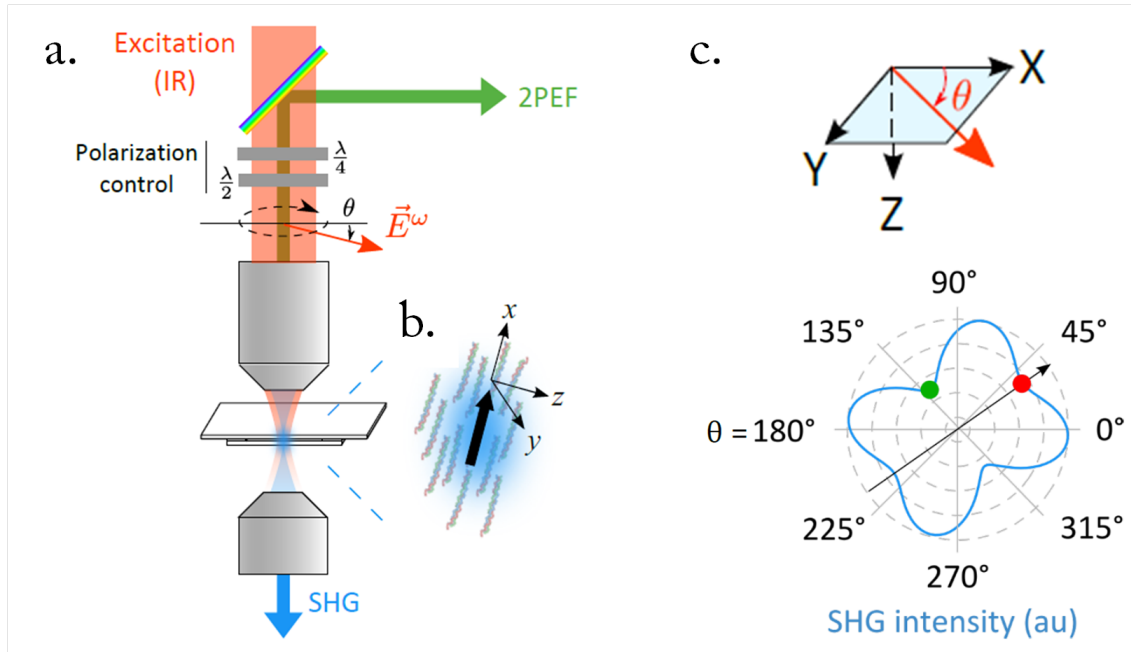


Figure 5.5: The polarization-resolved SHG consists in exciting the sample with a linearly polarized beam which angle θ is changed. a. Schematic representation of the experimental setup. The polarization angle θ of the excitation is controlled by two achromatic wave plates. The excitation field E^ω is focused through an objective. The second harmonic radiation is detected forward with a condenser (Numerical Aperture $NA \approx 1$) and the 2PEF signal backwards through the focusing lens. b. Area focus of the excitation volume. The black arrow gives the mean orientation of the triple helices present in the excitation volume. (x, y, z) is the corresponding reference with the x-axis in the mean direction of the triple helices. c. Top: (XYZ) is the laboratory coordinates reference frame. The incident polarization E^ω is represented by the red arrow and is assumed to be located in the plane of the image (XY). c. Bottom: Example of SHG intensity polarimetric diagram related to the orientation of collagen molecules within the focal volume. Adapted from [5]

It consists in exciting the sample with a linearly polarized field but whose orientation θ in the focal plane is changing. It is then possible to plot the SHG intensity as a function of θ (Fig. 5.5 c). Several structure characteristics can be deduced from this function:

- The triple helices average orientation in the image plane, which is represented by the black arrow (Fig. 5.5 b)
- The mean SHG intensity which depends on the triple helices density and organization.
- The triple helix orientation disorder which is given by a parameter ρ which corresponds to the square root of the ratio of the detected intensities for, respectively, an incident polarization parallel to the triple helices direction and a perpendicular one.

Theory

The SHG response of a medium is characterized by its second order nonlinear suscepti-

bility tensor $\chi^{(2)}$, related to the the polarizability $P^{2\omega}$ to the incident electric field E^ω by:

$$P_i^{(2\omega)} = \chi_{ijk}^{(2)} E_j^\omega E_k^\omega$$

where i, j and k correspond to the directions x, y and z. The triple helices of collagen are assumed to be aligned along x in the excitation volume with a minimal disorder. Assuming that the triple helices have cylindrical symmetry and by applying Kleinman symmetry [6], only seven tensor components are nonzero and take only two different values:

$$\chi_{xxx} \text{ and } \chi_{xzz} = \chi_{zzz} = \chi_{yxy} = \chi_{zzx} = \chi_{yyx}$$

The susceptibility tensor χ corresponds to the averaging of the hyperpolarizability tensor β in the focal volume. This implies that the polarizability at the harmonic frequency 2ω is then written:

$$\begin{cases} P_x^{(2\omega)} = \chi_{xxx}^{(2)} E_x^2 + \chi_{xyy}^{(2)} E_y^2 + \chi_{xzy}^{(2)} E_z^2 \\ P_y^{(2\omega)} = 2\chi_{xxy}^{(2)} E_x E_y \\ P_z^{(2\omega)} = 2\chi_{xxz}^{(2)} E_x E_z \end{cases}$$

If (X, Y, Z) is the laboratory reference frame, the mean orientation of the triple helices can be fully described with the polar φ and azimuth ψ angles (Fig. 5.6) . In the following figure 5.6, the two angles are represented as follows:

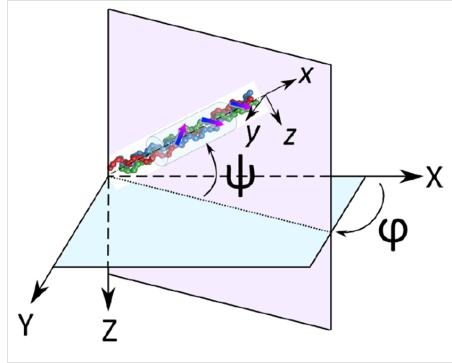


Figure 5.6: The two angles φ and ψ describe the orientation of the collagen molecules in the excitation volume: the orientation in the plane of the image φ ; and the out-of-plane orientation given by ψ , which can be measured from two parameters: the mean SHG intensity I_{mean} and the anisotropy parameter ρ .

where φ is the triple helix orientation in the image plane (XY) and is directly measured by polarization-resolved measurements; and where ψ is the off-plane angle.

For polarization-resolved SHG (P-SHG) measurements, the incident electric field is perpendicular to the propagation direction Z of the light in the laboratory reference frame (XYZ), with an angle θ with respect to the X axis. Thus its components are: $E_X^\omega = E_0 \cos(\theta)$; $E_Y^\omega = E_0 \sin(\theta)$; $E_Z^\omega = 0$

The total SHG intensity $I^{2\omega}$ is then calculated by transposing the susceptibility tensor of the triple helix (xyz) coordinates system to the laboratory reference frame (XYZ). Indeed,

the symmetries are legitimate in the reference of the triple helix but it is necessary to express the incident electric field in the laboratory reference frame. The triple helices are not necessarily in the focal plane and the total SHG intensity is written as:

$$I^{2\omega}(\theta) = \cos^2(\psi)A(\psi) \cdot \cos[4(\theta - \varphi)] + B(\psi) \cdot \cos[2(\theta - \varphi)] + C(\psi)$$

where $A(\psi)$, $B(\psi)$ and $C(\psi)$ are directly related to the components of the susceptibility tensor in the frame (XYZ) and can be expressed as a function of the susceptibility components of the triple helices in the (xyz); and ψ the off-plane angle of their mean orientation.

Finally, we can extract three quantitative parameters from this total SHG intensity (measured for different excitation angles), which will allow us to obtain a variety of informations on the 3D orientation of the triple helices.

- the orientation φ of the triple helix projections in the image plane (XY)
- the mean SHG intensity I_{mean} , which is directly connected to the angle ψ in the first order by: $I_{mean} \propto \cos^2(\psi)$. If the triple helices are in the plane of the image, the signal is more intense than if they are perpendicular to this plane.
- and, the anisotropy parameter ρ , which quantifies the "disorder" within the focal volume. It is related to the SHG intensity by: $\rho = \sqrt{I(\theta)/I(\theta + \frac{\pi}{2})}$.

5.1.1.2.4 Experimental system

The second harmonic imaging was carried out at the Ecole Polytechnique in the Laboratory of Optics and Biosciences by Guillaume Ducourthial (Post Doctoral researcher under the supervision of Marie-Claire Schanne-Klein, (CNRS) with a laser scanning microscope as already presented in the figure 5.5. The excitation is provided by a femto-second titanium-sapphire laser (Mai-Tai, Spectra-Physics) set at $860nm$ (2.60W). A circular polarization was used to image all the structures independently from their orientation in the focal plane or a linear polarization was used for P-SHG. The collagen threads imaging was performed using a 20x 0.95 NA objective with lateral resolution of $0.6 \mu m$ and an axial resolution of $3.5 \mu m$. For P-SHG experiments, SHG and two-photon excited fluorescence (2PEF) are detected in three channels equipped with photomultiplier Tubes (P25PC, Electron tubes) and spectral filters:

- Forward SHG: transmission (1 Semrock 680SP + 1 Semrock 720SP + 1 Semrock 427/10)
- Backward: 2PEF (1 GG5 + 2 Semrock 680SP)
- Backward SHG: epidetection (1 Semrock 680SP + 1 Semrock 720SP + 1 Semrock 427/10)

The polarization was changed from 0° to 360° with a 10° step.

For the imaging of collagen threads with cells, second harmonic generation was coupled with fluorescence in order to detect both SHG signal of collagen and fluorescence of cells. To do so, the different signals are detected in three channels (CH) equipped with photomultiplier tubes (P25PC, Electron tubes) and spectral filters:

- Forward: SHG (1 Semrock 680SP + 1 Semrock 720SP + 1 Interferential Filter Semrock FF01-427/10)
- Backward: Alexa (2 Semrock 680SP + Alexa 488 Filter + dichroic Filter),
- Backward: DAPI (1 Semrock 680SP + 1 Semrock 720SP + DAPI filter + dichroic Filter)

Fine plane by plane images sampling was performed every microns over the first $50\mu m$ from the thread surface and then, every $10\mu m$ until reaching the thread center. At least

two areas were observed in order to check the sample structure homogeneity. The 3D image reconstructions were done with *Imaris* software.

5.1.1.2.5 Sample preparation

Samples without cells were kept in their fibrillogenesis buffer. When cultured with cells, the threads were first fixed in paraformaldehyde 4% (PBS 1X). Then, for both conditions, they were put in an observation chamber composed of round cover glass sides separated with two Teflon torus shaped spacers (thickness of 225 μm). Few drops of PBS 1X were added in the chamber to keep the sample in wet conditions and avoid its drying.

5.1.2 Electron microscopies

Electron microscopy is based on the same principle as optical microscopy, except that the radiation used comes from electrons and not from photons (Fig. 5.7). The low wavelength of this radiation, which is of the order of the picometer (10^{-12} meter), allows us to reach an atomic-level resolution. In the following section, two types of electron microscopies used in our work are described: scanning (SEM) and transmission (TEM).

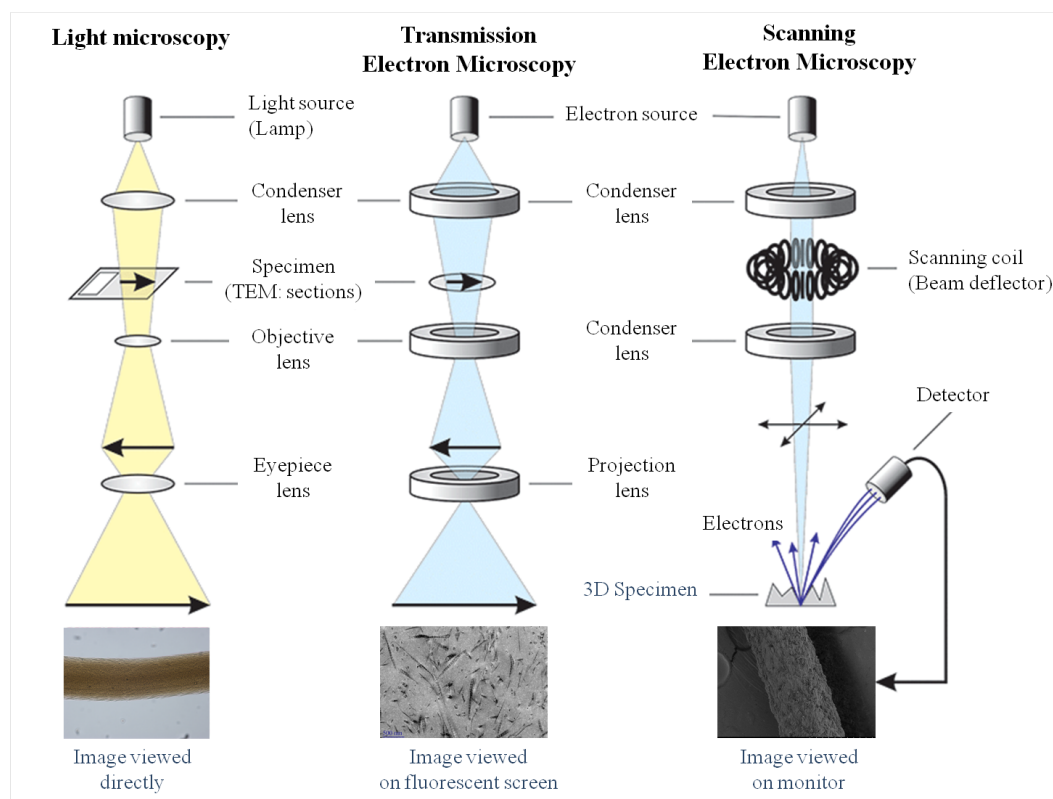


Figure 5.7: Schemes of optical and electron microscopes: The sample is illuminated by a source (photons or electrons). Several lenses (optical or magnetic) allow to focus the beam. For optical and transmission electron microscopy (TEM), the beam passes through the sample, which is observed by transmission. For scanning electron microscopy, the electrons of the focused beam interact with the sample atoms leading to the emission of secondary electrons very close to the specimen surface. Those electrons are then detected. An example of photos obtained on our samples is given for each technique. (From <https://microbiologyinfo.com>, "Differences between Light Microscope and Electron Microscope")

5.1.2.1 Scanning Electron microscopy (SEM)

Scanning Electron Microscopy is based on electron-matter interactions. It allows high-resolution images of the sample surface.

5.1.2.1.1 Principle

The main components of a Scanning Electron Microscope are: an electron source (gun) and a high voltage device, a column under a secondary vacuum, a set of electronic lenses to obtain a fine beam, a turntable for the installation of the samples, an electron detector coupled to a signal amplifier and finally an image display system (Fig. 5.7 right).

The interactions between the sample and the incident beam electrons are of different natures and induce several emissions, summarized in Figure 5.8. In this work, only the secondary electronic emissions will be of interest.

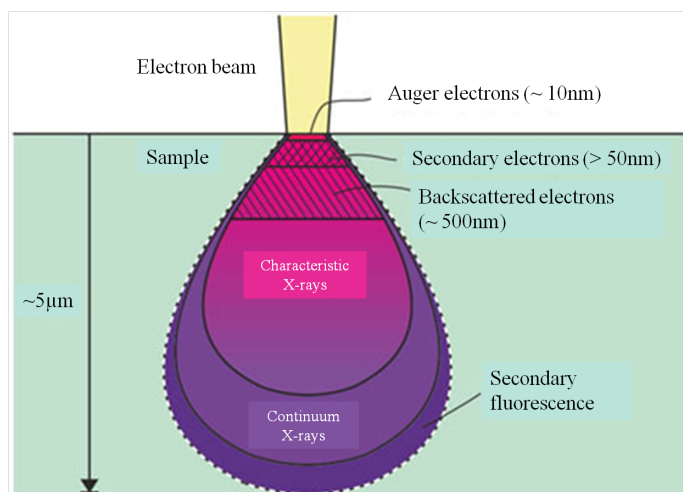


Figure 5.8: Electron-matter interaction volume scheme. (From: <http://gems-inclusions.com> "Scanning electron microscopy")

Secondary electron emissions are generally caused by inelastic scattering between primary electrons of the beam and those of the sample. These electrons have low energy (5 to 50 eV max) and the associated volume of interaction is about few nm^3 . When an incident electron interacts with the electrons of an atom of the sample, it emerges with a loss of energy. A secondary electron is then emitted and the atom is ionized by the ejection of the latter. The secondary electrons are weakly bound to the conduction band. An incident electron can cause the ejection of several secondary electrons, but their low energy causes only those near the surface (less than 10 nm) to emerge from the sample. They give a characteristic image of the surface since a topographic change will modify the number of secondary electrons emitted, useful for the visualization of the topography.

The **backscattered electrons** correspond to the primary electrons re-emitted after having undergone elastic shocks with the nuclei of the atoms as well as inelastic shocks with the orbital electrons. They have an energy close to the primary electrons (up to 50 eV) and an associated interaction volume of 0.5 to 1 μm^3 . This volume is closely related to the operating conditions. The backscattered electronic emission is sensitive to the topography

of the sample but also to its chemical composition (elements with high atomic numbers appear more clear). However, the contrast of the topography remains predominant and the differences in gray levels due to the chemical composition will only be perceived for perfectly flat samples. Thus, they provide information on the chemical composition of the sample.

X-ray photon is emitted when a primary electron, colliding with an atom, ejects an electron from an inner layer. The latter is replaced by an electron of a higher layer and thus a photon whose energy is equal to the difference of the levels of electronic energy is emitted. The associated volume of interaction is of the order of μm^3 . Quantitative chemical analysis of the sample is possible by using this type of interaction.

5.1.2.1.2 Sample preparation and observation system

All threads were fixed using 3.63 % glutaraldehyde in a cacodylate/saccharose buffer (0.05 M/0.3 M, pH 7.4) for 1 hour at 4 °C. Following fixation, samples were washed three times in a cacodylate/saccharose buffer (0.05 M/0.3 M, pH 7.4) and dehydrated through successive ethanol baths with increasing concentrations from 70% to 100% alcohol. Thereafter, samples were dried at the carbon dioxide critical point and gold sputtered (20 nm) for analysis. Samples were observed with Hitachi S-3400N SEM operating at 10 kV.

5.1.2.2 Transmission Electron microscopy (TEM)

Transmission Electron Microscopy allows to image ultrafine cross-sections of the samples. With this technique, we obtain very local information about the collagen organization inside threads at the nanometric scale.

5.1.2.2.1 Principle

A transmission electron microscope is composed of several parts: the source from which the electrons are emitted, condenser lens which focus the source beam, an objective stage where the image of the sample is formed and finally a projection area where the image of the sample is enlarged. The entire column is under a high vacuum (Fig. 5.7 middle). The different parts are detailed:

The electrons are emitted from the **canon** by heating a filament of metal which corresponds to the cathode. The extraction can be carried out by heating the metal to a temperature close to its melting temperature (2400 °C. for tungsten): this is a thermoionic emission. The electrons emitted by the gun are used by the **lenses** to create the electronic probe. The axis of the lenses is parallel to the path of the electrons and allows to focus them. The focal length of the lenses is related to the ampere-turns numbers of the coil. Thus, by varying the current which passes through the coil, the focal distance of the lens can be modified and the magnetic field is produced. The coils are often made of soft iron elements in order to increase the magnetic field. The electromagnetic lenses are directly used to focus the beam on the sample after passing the electrons through a field diaphragm.

The electron beam then passes through the **sample** where various electron-matter inter-

actions occur as previously described. There are the elastic (energy-free) and the inelastic interactions. In this case, when the electrons interact with the sample atoms, they lose energy. They will be more or less absorbed and diffracted. The resolution is limited by the optical aberrations which come essentially from the objective lens. The three main types of aberrations encountered are the following: defocusing, astigmatism and spherical aberrations. The final image is formed on a screen associated with a CCD camera which allows to image the sample section.

5.1.2.2.2 Sample preparation and observation system

Collagen threads with or without cells were fixed as described above. After fixation, samples were postfixed with 2% osmium tetroxide in cacodylate/saccharose buffer solution. They were washed in cacodylate/saccharose solution, dehydrated in successive ethanol baths (from 50° to 100°), and finally embedded in araldite. Embedded samples were sectioned on an Ultracut Reichert Jung. Thin sections (0.5 μm) were stained with toluidine blue and observed on a Nikon Eclipse E600Pol microscope equipped with a 40x (0.65 NA) objective and a DXM 1200 CCD camera. As biological samples are essentially formed by light atom, they little interact with electrons. Thus, in order to observe biological samples such as collagen, it may be useful to contrast them with heavy metals such as uranyl acetate. For this purpose, the ultrathin sections (70 nm) were contrasted with uranyl acetate and observed on a transmission electron microscope FEI Tecnai spirit G2 operating at 120 kV. Images were recorded on a CCD Camera (Orius Gatan 832 digital).

5.1.3 Differential Scanning Calorimetry (DSC)

The differential scanning calorimetry (DSC) technique allows characterizing the stability of the material by measuring the heat exchanges between the sample to be studied and a reference (here: air). Several physical quantities can then be extracted from those exchanges analysis: the glass transition (T_g), melting (T_m) and crystallization (T_c) temperatures; or the reaction enthalpies to assess the degree of crosslinking of certain polymers.

In our case, while heating the sample at a constant speed, conformation changes and thermal denaturation of the collagen molecules may occur. DSC measures the enthalpy (ΔH) resulting from the conformational changes induced by the temperature rise.

Collagen can indeed be more or less organized and structured in the threads and thus, the more stable the molecules, the higher the melting temperature.

Experimental set-up and parameters

The thermograms of the collagen-based threads were recorded using a DSC Q20 (ThermoAnalytic) device. Since the denaturation of collagen is irreversible, the threads are subjected to only one cycle of temperature rise and decrease. For this, samples of 2 cm length were cut before measurement and placed in hermetic aluminum capsules. They were then transferred to the DSC device and stabilized for 5 minutes at 20°C. Then, the temperature was increased up to 90°C at a speed of 5°C/min. For each condition, at least 3 samples were analyzed. Each sample was previously weighed to determine the mass rate of heat flow during denaturation processes.

5.2 Collagen batch quality criterion

One collagen purification of almost 30-40 rat tail tendons leads to a collagen volume of about 2 liters at 2-4 mg/mL. As we extruded dense collagen solutions of concentration range between 15 and 60 mg/mL, we "consumed" large quantities of the dilute stock solution to be concentrated. As a consequence, several collagen batches were needed to cover the totality of the different studies. It was thus necessary to verify the reproducibility of the extrusion for different batches. Figure 5.9 shows the results obtained for extrusion of 3 different collagen batches. First, batches A and B at 60 mg/mL were extruded with exactly the same parameters and buffer conditions. The two threads (Fig. 5.9 A1, B1) look very similar: they are straight and their surface and volume are homogenous. Then, the same experiment was performed between batches A and C (60mg/mL) (Fig. 5.9 A2,C2). In this case, the morphology difference is obvious: on the right, "thread C" displays non-homogeneous areas, which are more or less transparent and seem to reveal severe extrusion disturbance. On the contrary, "thread A" is still straight and homogeneous.

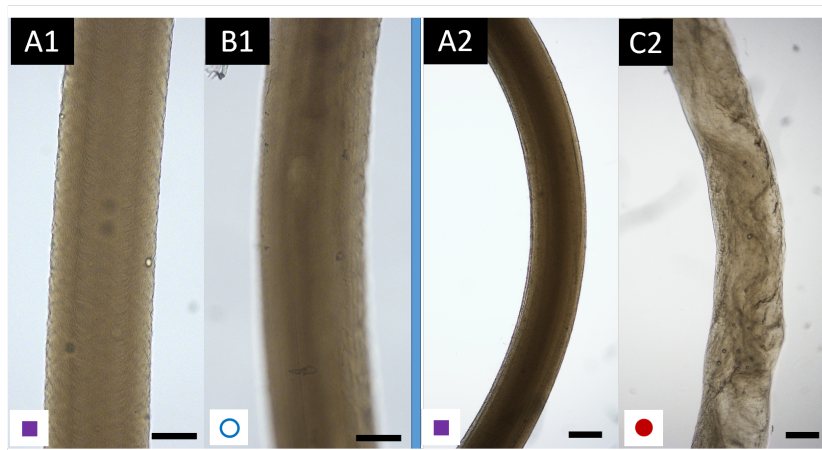


Figure 5.9: Collagen threads observed post-extrusion. Different batches (A,B,C) are tested and compared: Condition 1: PBS 10x, $D=650\mu\text{m}$; Condition 2: PBS 5X, $D=390\mu\text{m}$. A and B collagen threads show similar morphologies. A and C collagen threads are different: C displays perturbations at the surface and inside. Symbols refer to the corresponding rheological measurements. Black scale bars are $200\mu\text{m}$

Remark: one collagen batch serves for several users. For example, batch A was used for cornea or wound project. While using batch C, some users observed also different behaviors. In their case, they have to form collagen disks or sheets. However, with batch C, the collagen spreading was not a homogeneous manner and it was not possible to produce regular matrices. This kind of batch was considered as "bad" batch and the batch A as a "good" one.

As extrusion technique is very sensitive to this difference, we can rapidly conclude if a batch is good or not. However, we wanted to go further and find a physical criterion to quantify the batch quality after its purification. As the spreading of collagen was different, and the extrudate disturbed, the idea was that the rheological behaviors varied from one batch to another.

Since large quantities of collagen were needed during rheological measurements. In order to use small volumes, we performed the tests with collagen solutions at 5mg/mL rather than at high concentration with the smallest geometry available. Seven batches were analyzed and their respective concentrations were verified by hydroxyproline titration so as

to have the same for all. The results are presented in figure 5.10:

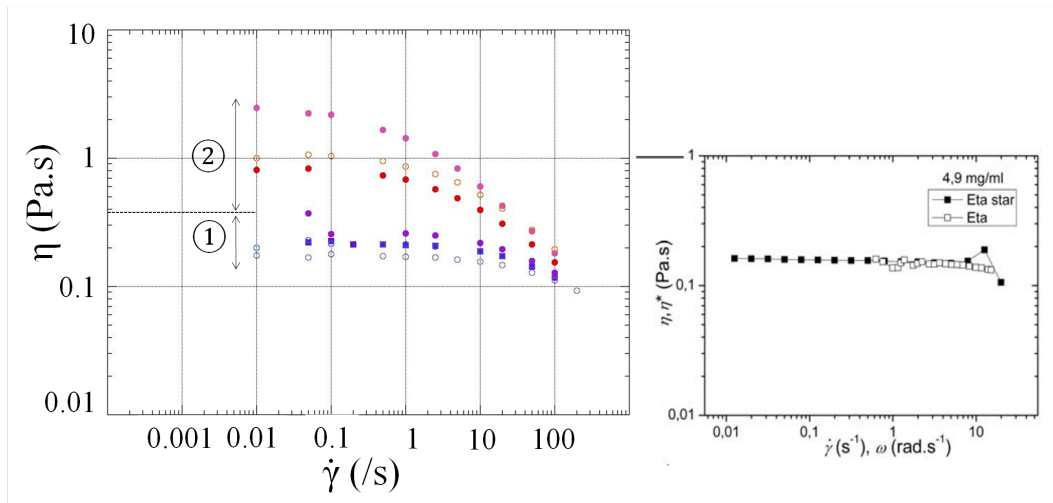


Figure 5.10: Viscosity as a function of the shear rate for: left: seven collagen batches at 5mg/mL. Two groups (1, 2) of batches can be distinguished corresponding to the "good" and "bad" respectively; right: Gobeaux PhD thesis results [7] for collagen at 4.9 mg/mL.

From Gobeaux PhD thesis rheological analysis [7], "plateau" viscosity η_0 of about 0.18 Pa.s is found for collagen solution at 4.9 mg/mL. Based on this result, we can set a viscosity threshold and distinguish two groups of batches: 1) η_0 around 0.2 Pa.s and 2) $\eta_0 > 0.8$ Pa.s. The previous batches A and B tested by extrusion are in the region 1 whereas C is in the region 2. Therefore, C has a higher viscosity than the bathes A and B. For the same velocity (thus the same shear rate), rheological behaviors are different. For example, at $\dot{\gamma}$ around 2-3 s^{-1} , batches of A and B are in the newtonian region whereas batch C exhibits shear-thinning behaviors.

By measuring viscosity at low concentration, we can already assess the quality of the collagen batch. It is assumed that several parameters as the rat age, race, or the purification process may impact the quality of a batch. But for now, no clear origin of those difference arises from this rheological characterization.

5.3 Fibrillogenesis buffer (Ionic strength) effect

The aim of this first study is to determine the best conditions to induce a stable sol-gel transition while preserving the alignment of the molecules and obtaining the best mechanical properties. For this purpose, 8 extrusion buffers of different ionic strength from 150 mM to 1.65 M are tested. They are used for the extrusion and during the ageing of the collagen threads. Therefore, all along this study, we narrow down the conditions to determine those giving threads of optimized characteristics.

The results of the present study are presented in the following article. Briefly, collagen solutions at 60 mg/mL were extruded at a constant exit speed of 3.4 cm/s in order to form threads of homogeneous diameter. The extrusion solution was varied to assess the effect of the ionic strength. It was the only parameter to be changed. One of the eight buffers led to collagen threads that fulfilled the majority of the requirements: extrusion characteristics, fibrillogenesis, storage stability and mechanical properties.

ARTICLE

Fibrillogenesis buffer influence on pure dense collagen threads ageing

Lise Picaut^{1,2}, Léa Trichet², Olivier Ronsin¹, Bernard Haye², Isabelle Genois², Tristan Baumberger¹ and Gervaise Mosser².

¹ *Institut des Nanosciences de Paris, Sorbonne Universités, UPMC Univ Paris 6 and CNRS-UMR 7588, F-75005 Paris, France*

² *Laboratoire de Chimie de la Matière Condensée de Paris, Sorbonne Universités, UPMC Univ Paris 6 and CNRS-UMR 7574, F-75005 Paris, France*

Abstract

A home-made set up built to extrude dense and highly viscous solutions was used to extrude 60 mg/mL acidic collagen solutions into meters of regular threads. Out of an analysis of eight different extruding and fibrillogenesis buffers, we have pinned down a condition (PBS 5X) in which the diameter of the extruded thread was stable throughout extrusion, fibrillogenesis and storage. In this condition, the threads observed between cross-polarizers show good anisotropy suggesting that the majority of collagen fibrils are aligned parallel to the thread axis. Transmission and scanning electron microscopy reveal the 67 nm "D" period of the fibrils, whose diameters are around 20 and 80 nm. The threads present a Young modulus of 1.66 ± 0.45 MPa and an ultimate tensile strength of 0.33 ± 0.08 MPa without the use of any cross-linkers or dehydration process, thus under conditions mimicking physiological ones.

Key words: Extrusion, Dense Collagen, Ionic Strength, Maturation.

1 Introduction

Tendons can present chronic or acute injuries due to intrinsic or external factors which can also be combined [25]. The etiology of tendinopathies is indeed often recognized as being multifactorial [36],[45],[28] with causes including work and sports activities, drugs [21], age and biomechanical imbalance[25]. Spontaneous regeneration is limited due to a poor vascularization and a low number of cells. Treatments can be conservative, surgical, or both, with or without rehabilitation programs[36],[22],[34],[1]. Surgical treatments go from sutures to insertion of metallic implants or grafts, which can be auto, xeno or allografts. Synthetic grafts made of polyester (Dacron®), polytetrafluoroethylene (PTFE or Teflon®)[33], silicone rubber[42], polypropylene (Marlex® mesh)[6], polyethylene terephthalate (PET, devices Orthotape® and Orthocoupler®)[26],[3] are also used. Depending on the system, more or less promising physiological results were obtained with, in some cases, no re-rupture occurrence observed at the level of the graft consolidation. Alongside with those synthetic grafts, grafts made out of biopolymers are also being developed with in mind the goal to mimic as well as possible the biochemistry and three-dimensional organization of tendon in order to optimize the biocompatibility (i.e. absence of immune rejection or toxicity[23], proper host-response[2], promotion of cell adherence, proliferation and differentiation). Tendons and ligaments belong to connective tissues that are characterized by the extra-cellular matrices (ECM) in which cells are embedded. The ECM is composed of many biochemical components such as collagens, non-collagen proteins, and proteoglycans[46],[32].

In tendon, collagens reach a concentration of 60-85% of the dry weight of the tissue[32], collagen I being the major structuring bio-component. Tendons and ligaments are organized in a hierarchical manner from collagen I molecules to fascicles [4]. Molecules, fibrils and fascicles are aligned in a preferred orientation in relation to the function of those tissues. For instance, excised rat-tail tendons present an overall alignment of the bundles along the tendon axis. This is clearly seen by cross-polarized optical microscopy. They also reveal units, ranging from 10 to 100 μm , of alternating oblique orientations to the tendon axis. The repetition of those units, referred to as "crimp" [27],[10], is a highly compliant element and was suggested to be a natural shock-absorber[40]. Elaborations of tendon-like scaffolds are inspired by this hierarchical construct and this anisotropy [29],[41]. Another important characteristic of tendons is their mechanical properties defined by the Young moduli, the ultimate tensile strength (UTS) and the strain at break as assessed along their longitudinal axis. Those vary from 0.5 to 1.9 GPa for the Young moduli and from 50 to 120 MPa for the UTS [19],[16]. Such values have not been yet achieved with wet simple extruded collagen-based thread scaffolds, with highest values obtained around 46 MPa for Young Modulus and 766 MPa for UTS with dehydration and stretching steps ([8],[18], [31], [11]). Higher values reaching 766 MPa and 110 MPa for Young modulus and UTS respectively are only achieved when chemical cross-linkers are being applied ([8],[18], [31], [11]). Thus future developments of scaffolds for tendon augmentation, and even more so for tendon replacements, will need to achieve higher mechanical prop-

erties. Indeed, the better the tendon structural characteristics and mechanical properties will be approached, the better the scaffold will resist solicitations and promote cell differentiation[38]. In order to address this subject, we made use of the lyotropic properties of acidic-collagen I solutions (i.e: collagen molecules self-organize into liquid crystal phases as soon as a critical concentration in collagen is reached)[12],[13]. These liquid crystals can be stabilized thanks to a pH increase to create organized fibrillar scaffolds. The pH increase triggers the fibrils formation while preserving the long-range liquid-crystalline organization[14]. We combined this approach with an extrusion process to generate high-density, anisotropic, collagen threads. Using a homemade extruding apparatus, we focused on determining the best conditions to induce a stable sol-gel transition while preserving the alignment of the molecules and achieving optimal mechanical properties.

2 Material and Methods

Collagen type I preparation

Type I collagen was purified from young Wistar or Sprague-Dawley rat tail tendons as previously described[37]. Extracted tendons were washed several times with phosphate-buffered saline (PBS) to remove blood and fat traces. They were subsequently soaked and washed in 4 M NaCl solution to remove cells. Finally, tendons were extensively rinsed again with PBS and solubilized in 0.5 M acetic acid. After successive and selective precipitations, respectively at 0.3 M and 0.6 M NaCl, the final collagen I pellets were solubilized in 500 mM acetic acid and thoroughly dialyzed against the same solvent to completely remove

salt content. The solutions were kept at 4°C and centrifuged at 41,000xg (Beckman Coulter J26-XP) for 4 h before use. Sample purity was assessed by SDS-PAGE electrophoresis. Collagen concentration was determined from the acidic solution by titrating the amount of hydroxyproline. Collagen solutions were concentrated using centrifugal filtration units (Vivaspin®[®], Sartorius, with a 100kD cutoff) spun at 3000xg, 10°C, until reaching the desired final concentrations (60 mg/mL). Solutions were then placed in 1 mL syringes and degassed by centrifugation at 3000xg for 30 min at 10°C.

Extrusion of dense collagen solutions

The home-made extrusion set-up, schematized in Figure 1, was built to allow in-sight visualization, (ii) application of great forces compatible with highly viscous solutions, (iii) precise monitoring of the extrusion speed and buffer exchange during extrusion. Briefly, a 1 mL syringe, filled with a 60 mg/mL collagen solution in 500 mM acetic acid, was mounted with a 23-gauge (inner diameter of 390 μ m) blunt stainless-steel needle, and loaded vertically. A motorized stage was used to bring down a rod in contact with the syringe piston and to impose its speed. The extruded fluid velocity was about 50 mm/s. The collecting cuvette was filled with the fibrillogenesis buffer (pH 7.4). At the blunt needle exit, extruded threads, plunging into the fibrillogenesis buffer, were observed and followed by an optical through-hole mounting. Prior to their use, the threads were kept and left for maturation in fibrillogenesis buffer at room temperature for 2 weeks under gentle agitation to prevent their sticking together.

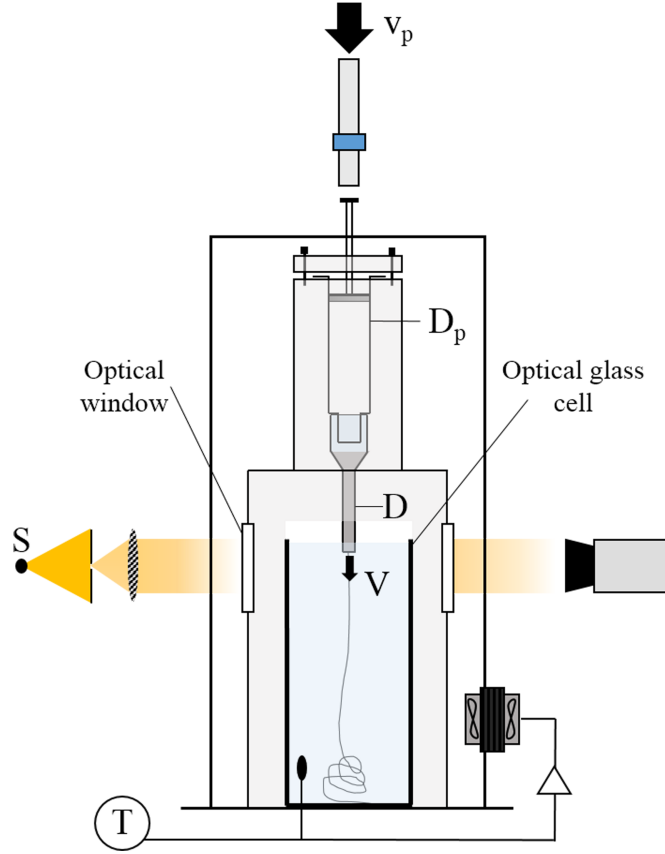


Figure 1: *Extruding homemade experimental set up. A syringe (Terumo®) of 1 mL contains the collagen solution to be extruded. It has an inner diameter D_p equal to the piston diameter of 4.45 mm. Stainless steel blunt needles (Terumo®) of 390 or 650 μm inner diameters D , respectively 23G and 20G, are set at the syringe end. A steel rod is clamped to a stepping motorized stage, which imposes a velocity v_p ranging from 0 to 2000 $\mu\text{m/s}$. The average output velocity V is calculated as follows: $V = v_p \times (\frac{D_p}{D})^2$. In order to apply the same shear condition for different inner diameters, the output velocity must be the same. The collagen solutions are extruded at $V = 50 \pm 2$ mm/s. A steel structure holds the syringe with its needle as well as an optical glass cell (Hellma®) containing the extrusion bath. Holes are drilled to create optical windows. The whole set-up is put inside a temperature-controlled enclosure. The extrusion bath can be removed at any time during the process to collect the extruded thread, while keeping the syringe in place. A quasi-parallel beam is created with a light source (S) limited by a diaphragm placed at the focal length of a convergent lens. The light beam illuminates the glass cell and the extrusion flow is followed thanks to a video camera equipped with a macro-objective and placed on the other side. Acquisition speeds of 600 frames/s can be reached. This optical system allows us to obtain extrusion images of a high contrast level as shown in Figure 2AB.*

Several fibrillogenesis buffers were tested with ionic strengths ranging from 0.15 M to 1.65 M (Table 1). For each buffer, the pH was adjusted prior to use to pH 7.4 with HCl or

NaOH solutions depending on the initial pH measured. The same buffer was used for the extrusion and the maturation. Ionic strength was calculated by taking into account all the

ions present in the solution according to the equation

$$\sum_{i=0}^n c_i z_i^2$$

, where c_i is the molar concentration of each ion and z_i the charge of that ion, assuming ideal solution.

TABLE 1				
No	Buffers	Concentrations	Ionic strength	D/D ₀
1	Na ₂ HPO ₄	50 mM	150 mM	1,4 +/- 0,1
2	PBS 1X (home made)			1,70 +/- 0,08
	NaCl	137 mM	165 mM	
	KCl	2.7 mM		
	Na ₂ HPO ₄	8 mM		
NaH ₂ PO ₄	1.5 mM			
3	PBS 1X (commercial)			1,53 +/- 0,09
	NaCl	137 mM	166 mM	
	KCl	2.7 mM		
	Na ₂ HPO ₄	8 mM		
	KH ₂ PO ₄	2 mM		
4	Na ₂ HPO ₄	100 mM	300 mM	1,7 +/- 0,1
5	Na ₂ HPO ₄	50 mM	300 mM	1,43 +/- 0,06
	NaCl	150 mM		
6	Na ₂ HPO ₄	50 mM	300 mM	1,32 +/- 0,05
	KCl	150 mM		
7	PBS 5X (home made)		825 mM	1,00 +/- 0,05
8	PBS 10X (home made)		1650 mM	0,75 +/- 0,04

Table 1: *Fibrillogenesis buffers and collagen threads diameters evolution upon ageing*

Maturation

Collagen threads (60 mg/mL in collagen), were kept over two weeks at room temperature in the different buffers listed in Table 1. Their diameters D were measured along the maturation process. We define the swelling ratio as $Q = D/D_0$ where D_0 is the inner diameter of the needle. D is measured and

plotted over time. Standard Deviation of this ratio was calculated by:

$$\Delta\left(\frac{D}{D_0}\right) = \sqrt{\left(\frac{\Delta D}{D_0}\right)^2 + \left(\frac{D \Delta D_0}{(D_0)^2}\right)^2}$$

where ΔD and ΔD_0 are the respective standard deviation of the thread diameter and the needle inner diameter measurements.

Microscopy analysis

For optical analysis, threads were put in a homemade thin glass-chamber filled with fibrillogenesis buffer to prevent dehydration during observation. Polarized light microscopy was performed using a transmission Nikon Eclipse E600 Pol, equipped with crossed polarizers and a Nikon DXM 1200CCD camera. For electron microscopy analysis, all samples were fixed using 3.63% glutaraldehyde in a cacodylate/saccharose buffer (0.05 M/0.3 M, pH 7.4) for 1 hour at 4°C. For scanning electron microscopy (SEM), the samples were then washed three times in a cacodylate/saccharose buffer (0.05 M/0.3 M, pH 7.4) and dehydrated through successive increasing concentration ethanol baths from 70% to 100% alcohol. Thereafter, samples were dried at the carbon dioxide critical point and gold sputtered (20 nm) for analysis. Samples were observed at 200M, 1kM, 5kM and 30kM with a Hitachi S-3400N SEM operating at 8 kV with a probe current around 95 μ A. For transmission electron microscopy (TEM), samples were post-fixed with 2% osmium tetroxide in cacodylate/saccharose buffer solution, washed in cacodylate/saccharose solution, dehydrated in successive ethanol baths (from 50° to 100°), and finally embedded in araldite. Embedded samples were sectioned on an Ultracut Reichert Jung as already described [37]. 500 μ m thin sections were stained with toluidine blue and observed on a Nikon Eclipse E600Pol microscope equipped with a 40x/0.65 NA objective and a DXM 1200 CCD camera. 70 nm ultrathin sections were contrasted with uranyl acetate and observed on a transmission electron microscope FEI Tecnai spirit G2 operating at 120 kV. Images were recorded on a CCD

Camera (Orius Gatan 832 digital) at 4.4kM and 15kM.

Mechanical tests

Mechanical tests were performed using a BOSE® ElectroForce® 3200 Series II Test Instrument. Specimens were attached to the stainless steel crossheads by gluing each extremity with cyanoacrylate adhesive drop. Sample and crossheads were immersed in a glass Petri dish filled with fibrillogenesis buffer at room temperature. The threads diameter, D was determined by optical microscopy assuming full cylindrical symmetry. Mechanical loading of the thread was achieved by driving one crosshead at a constant velocity of 0.1 mm per second with a stepping motor (0.1-micron steps). The loading force F was measured with a 220 g load cell. We defined the nominal tensile stress as $\sigma = \frac{4F}{\pi D^2}$. The nominal strain is defined as $e = (L-L_0)/L_0$, where L is the distance between the glue points and L_0 the initial length. All measurements were performed up to the specimens rupture. The resulting stress-strain curves were plotted and analyzed. At least 4 different threads were tested for each condition.

3 Results

Since the goal of our work was to find the best conditions to synthesize dense collagen threads that would be stable over time, present anisotropic organization of collagen fibrils and have the highest mechanical properties, we have, all along our work, narrowed down the conditions to determine those giving threads of optimized characteristics.

Extrusion and Maturation

All threads look similar at the time of the extrusion in all buffers (Figure 2; Figure SI-1). Their surfaces present a "shark-skin" roughness, characteristic of so-called viscoelastic fluids (Larson, Denn). The roughness amplitude is of the order of $20\ \mu\text{m}$ for a thread diameter of $710\ \mu\text{m}$ (2.8%) as measured on Figure 2A. Noticeably, within experimental error and after averaging the shark-skin roughness, the swelling ratio Q , measured just downstream of the die exit (the so called die swell, of mere viscoelastic origin ??) remains close to 1. Figure 2 illustrates the threads synthesized

using buffer 1, 7 and 8 as visualized during extrusion (Fig. 2A,B) thanks to the optical system, and after the two weeks of maturation under polarized light (C) and in between crossed polarizers (D). We see that, depending on the buffer, the thread diameters evolve differently. No changes are observed in condition 7, while swelling and shrinkage are respectively observed in conditions 1 and 8. In Figure 2D, threads are positioned at nearly 45° to both polarizers. They appear homogeneously bright along the thread axis. In the case of condition 1, the bright signal concerns only the central part of the thread.

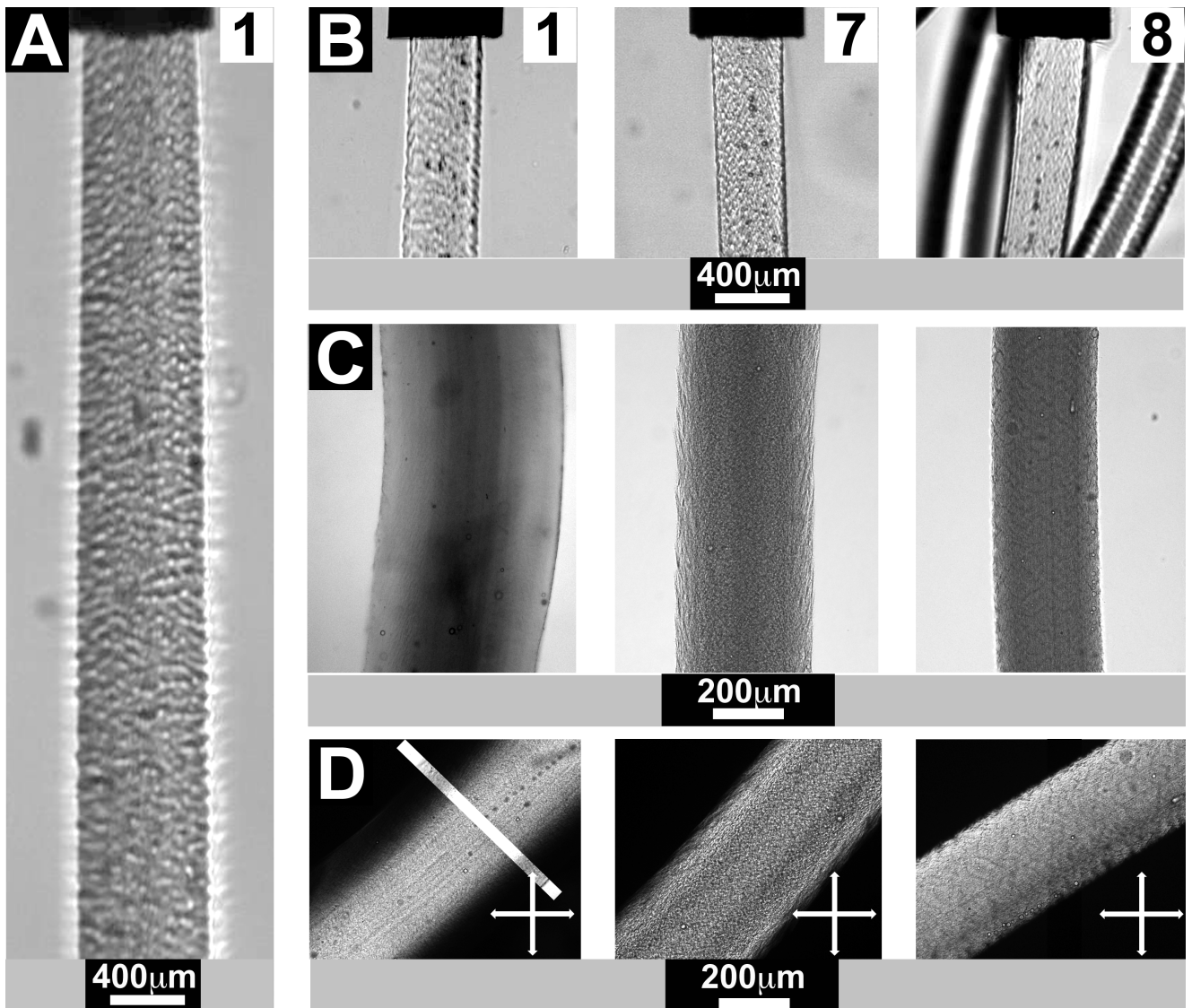


Figure 2: 60 mg/ml collagen thread extrusion and maturation. Figure 2A,B shows the threads extrusions in extrusion buffers 1, 7 and 8. Figure 2A corresponds to the extrusion through a 650 μm inner diameter needle in condition 1, while Figure 2B corresponds to extrusion in the three buffers through needle of 390 μm inner diameter. A sharkskin pattern is observed on all threads, although it less pronounced in condition 8. Figure 2C shows the threads after the two weeks of maturation in the respective extrusion buffers. We observe the increase and shrinkage in diameters of threads extruded in condition 1 and 8 respectively, while the diameter of the threads in condition 7 does not evolve. The thread extruded and matured in buffer 1 shows a core shell profile, the core being denser than the shell. Figure 2C, show the matured threads as seen in between cross-polarizers (crossed arrowed) and at around 45° from both polarizers. We see that in all the three conditions, the threads appear very bright indicating an overall alignment of the molecules. For the thread made in buffer 1, only the core shows birefringence. The shell, delineated as seen the inset appears dark and remains invisible. This suggests a loss of molecular orientation along the thread axis..

Figure 3A shows the evolution of the threads diameter over time during the maturation process for all buffers and Figure 3B shows the plot of the long term swelling ratio Q , here of osmotic nature, in function of the ionic strength. The former show that diameters evolve over 10 days and then reach a plateau. The latter reveals three groups of be-

haviors. For the first one, consisting in a cluster of conditions 1 to 6, we observe a swelling of the threads and find a $Q > 1$. For the second one, consisting in buffer 7, the diameters remain constant over time, with a ratio $Q = 1$. Finally for the third one, buffer 8, we observe a shrinkage of the collagen thread diameter ($Q < 1$). Data are summarized in Table 1.

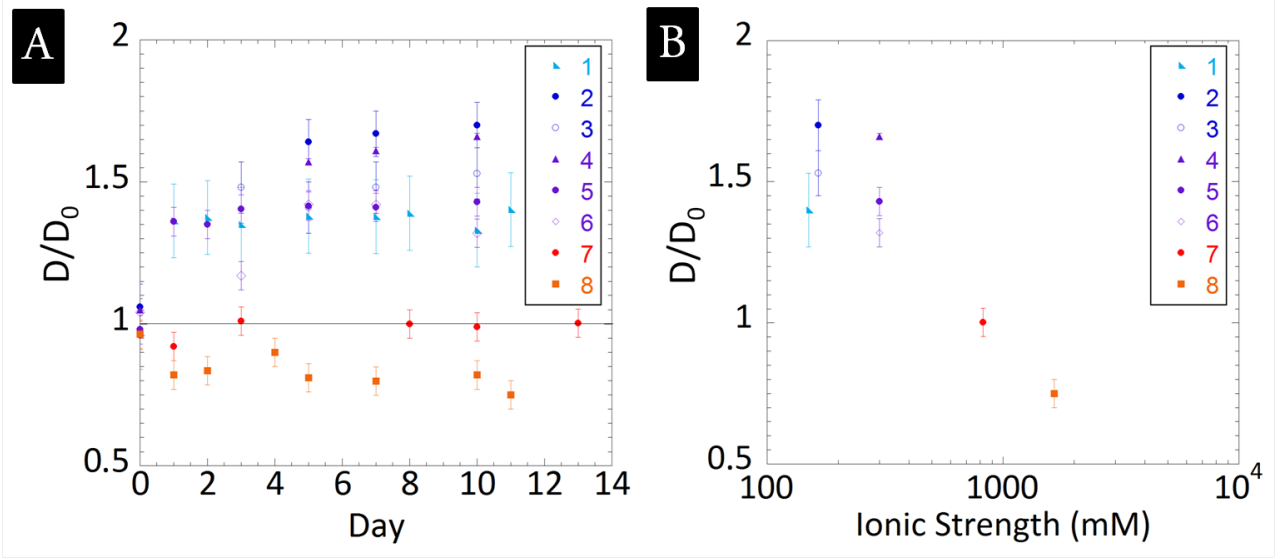


Figure 3: *Evolution of thread diameters upon maturation for the different buffers. After extrusion, the threads are left into the buffers for two weeks for a maturation process. The diameters of the thread have been measured regularly along the two weeks. We see that depending on the buffer some thread see their diameter increasing some decreasing. In condition 7 the diameter remains relatively stable throughout the two weeks period..*

At this stage, we chose to focalize only on conditions 1, as representative of the cluster of conditions 1 to 6, as well as condition 7 and 8.

Structural characterization

Figure 4 shows the external morphology and ultrastructures of threads obtained with fibrillogenesis buffers 1, 7 and 8 as seen by SEM. At low magnifications (200M, 1kM, 5 kM, top three lines), we observe the overall characteristics of the threads. In condition 1 (A),

threads present an outskirts of large "hairs" while, in condition 8 (C), threads present a smooth shell with hills and valleys with, locally some cracks revealing the internal ultrastructure. In condition 7 (B), the threads are rather smooth with a few "hairs" sticking here and there. At higher magnifications (bottom line), in condition 1, we see large ($\simeq 560$ nm) linear fibers or bunches of compact fibrils ($\simeq 150$ nm) on top of more tortuous fibrils ($\simeq 70$ nm). The fibers present a large striation of $\simeq 180$ nm and sub-striations of approximately 67 nm. In condition 8, we ob-

serve a smooth top shell under which linear fibers and fibrils (approximately 150 nm diameter) can be seen. The fibers present large striations of varied length and a sub striation of 67 nm. Clear helical fibers are also seen. In condition 7, densely packed wavy fibrils with diameters of 100 nm in average are seen with

the 67 nm cross-striation. The fibrils are fused in a more or less wavy pattern. Some larger striations can also be seen. The measurement of the diameters are indicated in Table SI-1 together with a scheme of the threads profile for each group.

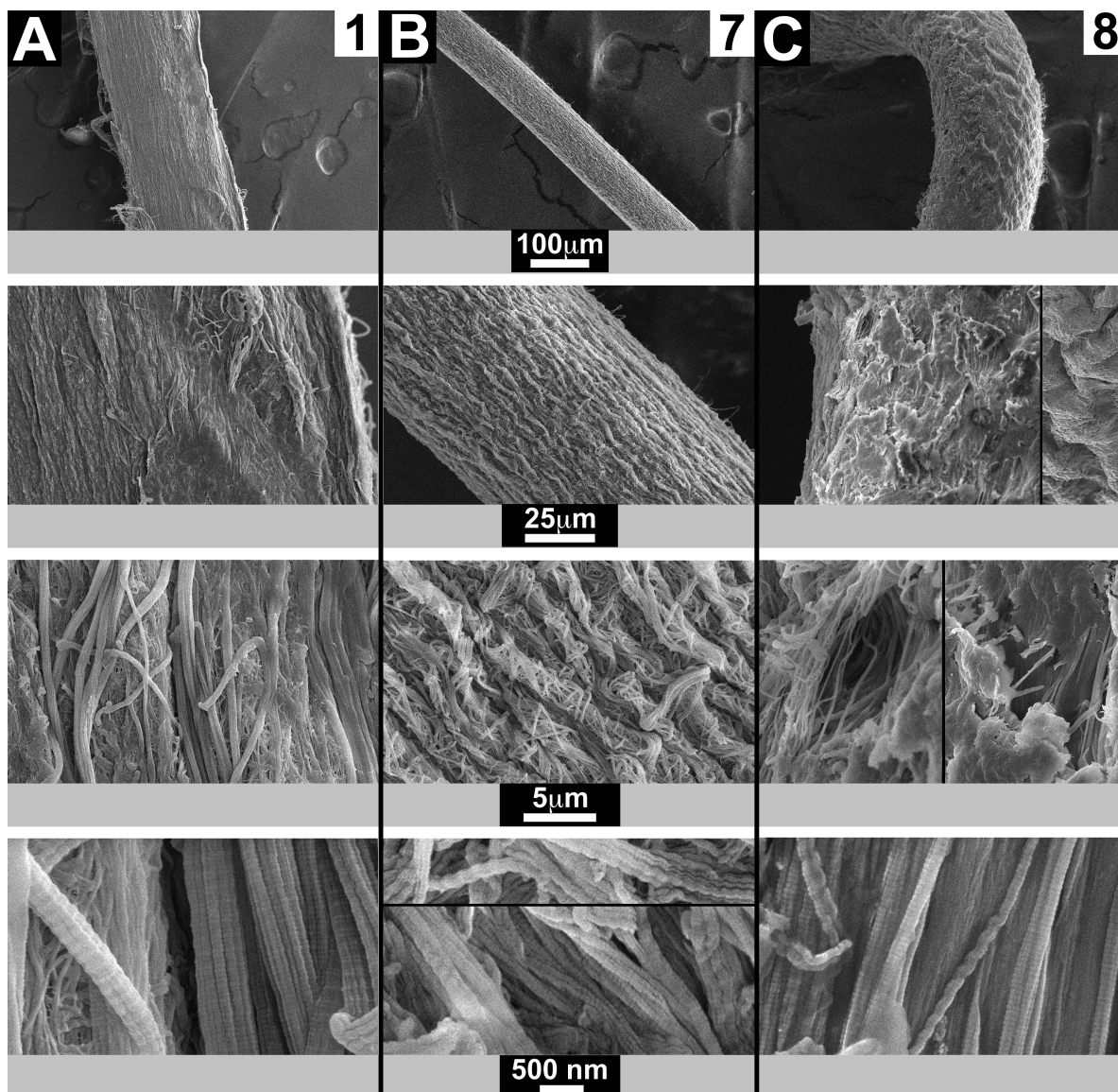


Figure 4: *Ultrastructure of threads after maturation in buffers 1, 7 and 8 as seen by SEM. Figure 4A, B, C correspond respectively to threads synthesized in condition 1,7 and 8. The magnification increases from top to bottom (200M, 1kM, 5kM, 30kM). The cross-striated appearances of fibrils and fibers are clearly seen at 30kM in all three conditions. In condition 1, a 67nm striation is further integrated in a wider one of 180 nm. In condition 7, the 67 nm striations dominate although curly or wavy undulated fibrils, fused or not, are seen locally, which wavelength or pitch give yet other repeated distances. In condition 8, the 67 nm striation is seen both on straight and on helical fibrils.*

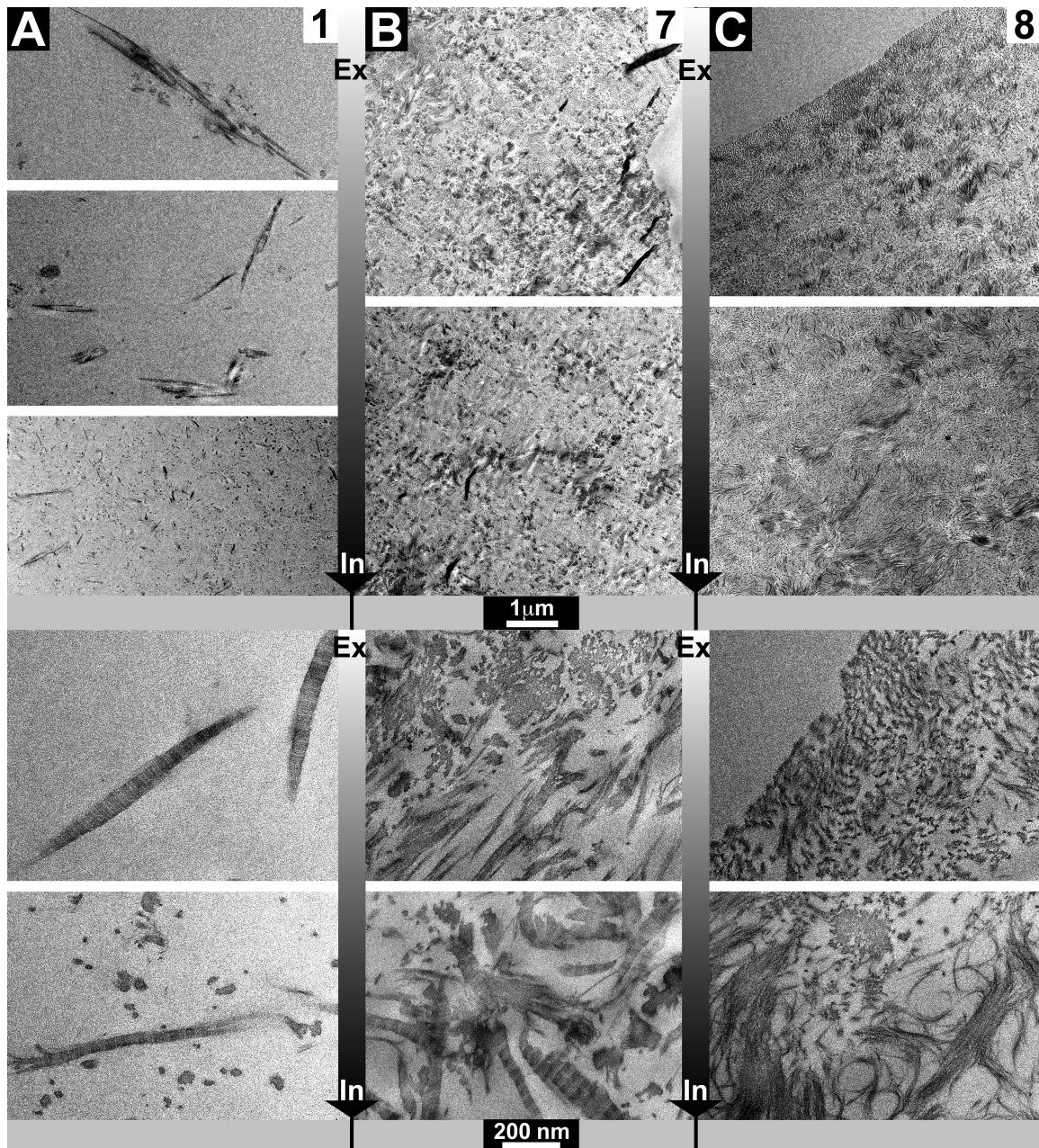


Figure 5: *Ultrastructure of threads after maturation in buffers 1, 7 and 8 as seen by TEM (transverse sections). Figure 5A, B, C correspond respectively to threads synthesized in condition 1, 7 and 8. Top: view at low magnification from the outskirts (when present) to the inner part of the thread. Bottom: view at higher magnification from the outskirts to the inner part of the thread. Collagen fibrils appear cut in all directions from longitudinal to transverse, in which case they appear as dots. In A, the thread presents three different structural characteristics when going from the outskirts of the thread to the inner part. In B and C the threads present more homogeneous appearances. In B two types of fibrils are observed, some with greater diameters than others while in C the fibrils appear homogenous in diameters but with a reduced diameter.*

Figure 5 shows the distribution of the fibrils as well as their morphology as seen by transmission electron microscopy (Table 2).

Figure 5A, 5B and 5C, are cross-sections of threads respectively made in buffer 1, 7 and 8, at low magnification on the top part and

high magnification on the lower part. The pictures show view from the external (Ex) part to the internal part (In) of the threads as indicated by the side arrows. In 5A, we see that the thread present very large fibrillar entities ($\simeq 500$ nm) on the outmost edge of the thread. The shell is constituted of large ($\simeq 250$ nm) individualized fibers that do not present any specific alignment. In the core part, thin fibrils ($\simeq 40$ nm) are more tightly packed, most of them being cut perpendicular to their axis, giving the dotted features on the photo. Fewer appear cut along their longitudinal axis. Figure 5B shows ultra structure of a thread made in buffer condition 7. We see a cohabitation of well defined thick ($\simeq 80$ nm) fibrils presenting the 67 nm cross-striation, together with packages or aggregates of thin fibrils ($\simeq 20$ nm). In the external part, the fibrils are seen in majority aligned to the longitudinal axis of the thread and thus appear as dots. In Figure 5C, we observe a section of a thread made in buffer condition 8. Here, we observe dense packages ($\simeq 200$ nm) of small fibrils ($\simeq 25$ nm) in majority aligned with the axis of the thread in the external part and more ran-

domly orientated especially in the core. The measurement of the diameters are indicated in Table SI-1 together with a scheme of the threads profile for each group

Mechanical properties

Figure 6 shows the results of the mechanical tests and the threads after breakage. Figure 6A shows typical stress curves in function of the strain obtained for the 3 selected conditions 1, 7 and 8. Figure 6B shows typical profile of thread extremities after breakage. Figure 6C shows Young modulus and Ultimate Tensile Strength obtained for the three conditions as measured over more than 4 threads for each of them. We see that the highest mechanical properties are obtained for threads extruded and matured in PBS5X that exhibit a Young's modulus of 1.66 ± 0.45 MPa and an ultimate tensile strength of 0.33 ± 0.08 MPa, while threads synthesized in two other conditions yield values of 0.30 ± 0.15 MPa and 0.13 ± 0.01 MPa respectively for the Young modulus and UTS in condition 1 and of 0.88 ± 0.14 MPa and 0.16 ± 0.02 MPa respectively for condition 8.

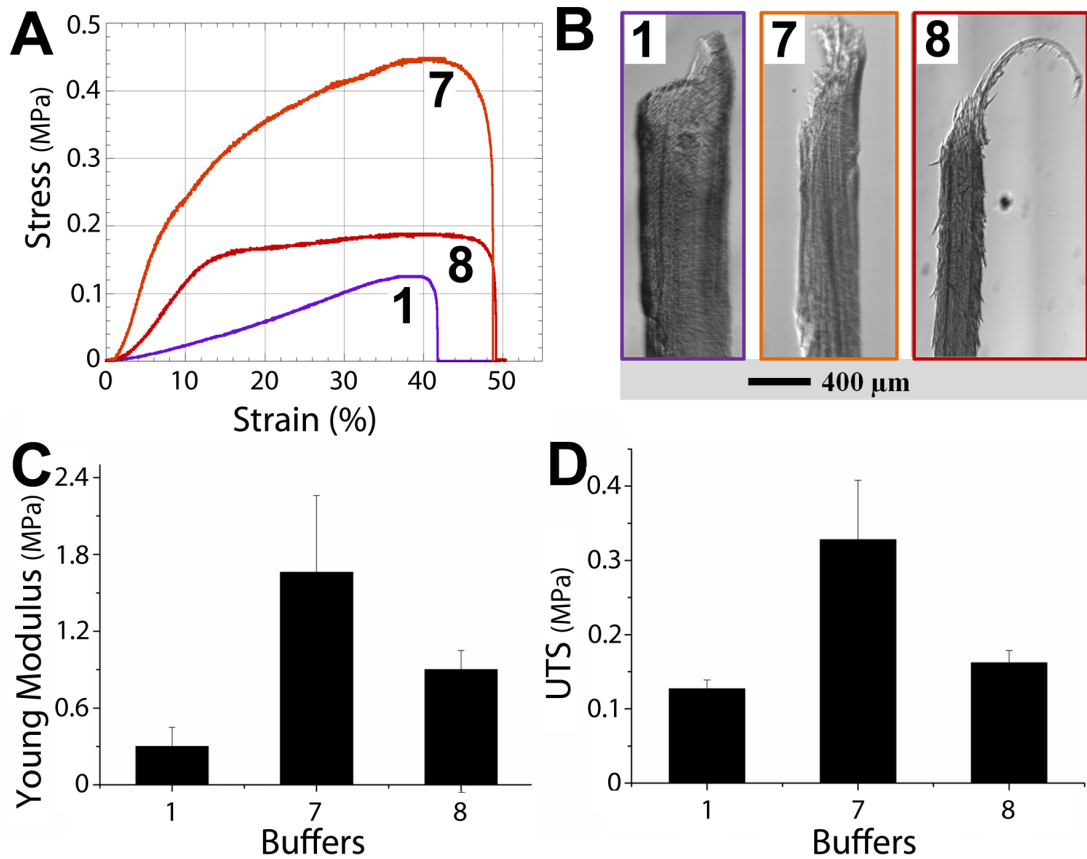


Figure 6: *Mechanical characterization.* Figure 6A shows the typical profiles obtained for the stress-strain curves in the three conditions 1, 7, 8. Figure 6B shows the three threads at the point of breakage. Note that the breakage end is rather sharp in condition 1, intermediate in condition 7 and elongated in condition 8. Figure 6C gives Young Modulus and Ultimate Tensile Strength for the three conditions 1, 7 and 8 as measured over 4 threads.

4 Discussion

The main objective of this work was to optimize the synthesis protocol in order to reproducibly obtain, homogeneous, high-density, anisotropic collagen threads with the best mechanical properties, that is high Young modulus and high UTS. As criteria we have selected: 1) the stability of the thread upon storage in the fibrillogenesis buffer to avoid swelling or contraction, 2) the ultrastructure of the threads, 3) their mechanical properties.

Another figure of merit is the linearity of the thread. This one can be affected by several gross instabilities [9] [9]. It is controlled both by the extrusion velocity and the nee-

dle diameter. In the present work, we chose the extrusion speed according to the analysis previously made on alginate samples [30] so as to limit instabilities. Since threads extruded with $D_0 = 650 \mu\text{m}$ or $390 \mu\text{m}$ diameter with adapted extrusion speeds had similar structural and mechanical properties, we did most of the present study with a needle of $390 \mu\text{m}$ diameter to limit the quantity of collagen used. Noteworthy, diameters around $390 \mu\text{m}$ make threads easier for post-production processes (such as weaving), as compared to collagen threads with similar properties produced in the other studies, which diameters range from 50 to $200 \mu\text{m}$ sys-

tem [11],[5],[17],[7].

Remarkably, upon extrusion, the threads presented the same diameter as the inner diameter of the needle with no die swelling effect, often observed in the case of highly viscous solutions and that can reach up to 2 times the internal diameter of the needle [24]. This observation is puzzling since, even for a newtonian fluid, die swelling $Q = 1.1$ [35] is observed. Gross slip would suppress wall shear and normal stresses responsible for die swelling. It is however unlikely since the presence of shark-skin is indicative of a strong adhesion of the solution at the wall. At this stage, one can tentatively suggest that the strong anisotropy of the collagen solution could be one factor precluding die swelling.

Regarding the stability of the thread diameter upon fibrillogenesis and storage, Pins et al. (1997)[31] have shown the importance of fibril alignment on the mechanical properties obtained, starting from a 10 mg/ml collagen thread, and using a multistep procedure with two air-drying-rehydration stages, interspersed by a stretching step of different spans to align and condense the collagen fibrils, and followed or not by chemical cross-linking. The authors showed that on the final products, synthesized in the absence of cross-linking, the linear Young modulus increased from 1.8 MPa at 0% stretch to 46 MPa at 50% stretch, and UTS from 0.9 MPa to 7 MPa respectively. They made no ultrastructural study but showed the overall increased orientation by the increase of birefringence values. They concluded that collagen fibrils alignment, within the thread, increased its mechanical properties. Therefore the stability of the thread diameter after extrusion, that is limited swelling or contraction, stood as a

criteria on to select the best conditions. This stability indeed provided evidence of maintenance over time of collagen density as well as limited reorganization of collagen fibrils, as a consequence of the conservation of the shear induced alignment made by the extrusion.

Now, depending on the buffer we used, we observed swelling, contraction or stability of the thread. This variation in diameter and different structures obtained with different fibrillogenesis buffers most likely reflect the involvement of hydrogen and electrostatic bonding in collagen supramolecular organizations in our systems. Several studies on the effect of ionic force and pH in diluted collagen solutions have already been reported. The intermolecular space between triple helices has indeed been negatively correlated to the osmotic pressure applied [20]. Wood et al. also reported that increasing ionic strength between 130 and 310 mM increased fibril width [44]. This increase of fibril diameter was also observed in the case of collagen solutions at high concentration (100 mg/mL)[14]. Amongst all our conditions, the threads made in conditions 7 were the least affected upon storage. The overall alignment of the threads was confirmed by polarized light microscopy for the three conditions 1, 7 and 8, but was limited to the core of the thread in condition 1. This showed that, in our case, the swelling had disturbed the alignment of the fibrils at the surface of the thread. The ultra-structural characterization of the different threads confirmed the core shell nature of the thread synthesized in buffer 1. It revealed larger fibrils and wider interspaces in the external part than the internal. The wide interspace could potentially be more favorable to cell invasion. However, the inhomogeneity

of the thread with the very large aggregated fibers at its outmost edge, together with the pronounced difference from external to internal part, was opposite to the criteria that we had set. Threads made in condition 7 and 8, both presented ultra-structure more homogeneous than in condition 1. However, in condition 8, the thread showed a diameter contraction together with the presence of a crusty and smooth surface. We believe that this crust would be unfavorable for cell attachment and colonization. It may result from an artifact of SEM preparation although TEM images also reveal a rather continuous limit of very small fibrils. In fact, the small diameter of those fibrils, smaller than those found in living tissues, exception made of cornea, may potentially be problematic. Thus, although we observed two types of fibrils by TEM and SEM in the case of condition 7, the otherwise overall homogeneity of ultra-structure seemed to be the most favorable for future development.

The effectiveness of phosphate anion in changing the rate of fibrillogenesis has been reported for long [43],[15]. Using pepsin-treated collagen (4 mg/mL) Hayashi has shown that, at pH 6.8 with equal concentrations of monovalent and divalent ions, the time length to reach opacity was at a peak for a concentration around 150 mM phosphate. In our experiments, the samples in phosphate buffer 1 were the slowest to opacify taking up to 1 hour to generate stable and easy to handle threads. Roughly, the highest was the ionic strength the fastest the opacification occurred. Compared to buffer conditions 2 to 6, the relatively reduced swelling in buffer 1, in spite of a lower ionic strength, is in agreement with the model proposed by Mertz et al. In this model, the divalent phosphate ions

form salt bridges between positively charged residues on collagen molecules, especially at low ionic strength below the physiological values[26]. The opacification occurred more rapidly in buffer 8 with higher ionic strength creating a dense and continuous shell of a network of thin fibrils on the periphery of the thread. The intermediate situation is observed in the case of buffer 7, which presents intermediate ionic strength. The fact that the shark-skin structure observed after extrusion in all different buffers seems to be preserved only in buffer 8 may indicate that the fibrillation occurs more rapidly in this condition. In the case of buffers 1 and 7, the larger fibrils observed inside the core reflect molecular reorganization and thus a slower fibrillogenesis process than in buffer 8 which only gives rise to thin fibrils. Still, at pH 6, the precipitation was first retarded from 130 to 230 mM then accelerated again at 310 mM. Our study highlights phenomena at play in dense collagen solutions moreover constrained in cylindrical geometries, and the possible role of kinetics formation in the final structures obtained. Furthermore, the probable specific binding effect of phosphate anions, already observed at low collagen concentrations, seems to be confirmed at higher concentrations in our system.

Uquillas et al. (2011) showed that the variation of PBS concentration, in the buffers used to trigger fibrillogenesis, induced an increase of UTS and Young's modulus for PBS 1X, 5X and 10X compared to PBS 0.5X [39]. This compares pretty well with our results except for PBS10X for which we find a decrease of mechanical properties. They also reported an effect of the time left in the fibrillogenesis buffer on the mechanical properties of their scaffolds: after 12 hours incubation in

PBS 1X, the UTS and Young's modulus were around 0.4-0.5 MPa for both, and reached 1.2 MPa for UTS and 6 MPa for Young's modulus after 96h. Beside, they showed using SAXS that the D-bands characteristic of fibrillary collagen was present after 12 hours incubation in PBS 1X but not in PBS 10X, and that this pattern disappeared after 96h incubation in PBS 1X. In our case, although the thread diameters evolved over four days before reaching stabilization, after two weeks of maturation, the fibrils constituting the threads still showed cross-striations indicating good and stable fibrillogenesis in our three selected conditions (1, 7 and 8).

Concerning the mechanical properties in our systems, the highest Young's modulus (1.66 ± 0.45 MPa) was obtained with condition 7 compared to conditions 1 and 8 (0.30 ± 0.15 MPa and 0.90 ± 0.17 MPa respectively). This value may seem rather low compared to other reported scaffolds. For instance, Cornwell et al. (2007) measured Young's modulus around 4 MPa and UTS around 1.5 MPa [7]. However, these values were obtained on 10 mg/mL collagen threads that were air-dried and then soaked again in PBS[34]. Kato et al. (1989)[18] and Dunn et al. (1993)[11] had already obtained threads made with the same initial collagen concentration and in a similar fibrillogenesis buffer as Cornwell and coworkers. A modulus of 13.2 MPa on threads that had been rinsed in alcohol, air-dried then rewet in PBS was reported[18]. The measured UTS ranged between 16 MPa and 2.4 approximately, with a decrease for larger thread diameters [11] [18], in accordance with Cornwell et al. results [7]. The good mechanical values they report are likely resulting from enhanced fibril alignment and density due to

thread diameter contraction induced by the dehydration processes. However, the authors did not report any ultrastructural study to assess the alignment of the fibers. Using a similar process as Pins et al. (1997)[31] but starting with a 5 mg/mL collagen solution extruded in an initial polyethylene glycol solution (20% PEG MW 8000, in 94 mM sodium phosphate dibasic and 24 mM sodium phosphate monobasic), followed by dehydration in 70% isopropanol and drying, Cavallaro et al. (1994)[5] measured UTS around 1.2 MPa, with well aligned collagen fibers. By comparison, in our present work, the use of concentrated collagen solutions enables reaching moduli in the same MPa range in the absence of any crosslinking, air-drying and dehydration. Thus, our process still leaves possibilities to further reinforce the mechanical properties by applying further treatments as air-drying or chemical cross-linking or further bottom-up post-processing like braiding. Finally, the stress-strain curve shapes and the different profiles adopted by the three types of threads after rupture, also indicate a better behavior of thread synthesized in condition 7. Indeed, in case of buffer 1, the thread breaks with a sharp fracture area, whereas in case of buffer 8, the crack propagates through a sliding mode, with fiber-like tips being visible at both ends after breakage. This mode of ductile rupture corresponds to the plateau observed in the stress-strain curve with constant stress over a large range of strain. In the case of condition 7, although no clear behavior arises from the stress-strain curve, the tip profile with several sharp breaks observed at different positions along the longitudinal axis, would be in favor with a multistep rupture. Thread in condition 7 thus present more

favorable behaviors, in between threads synthesized in condition 1 and 8.

5 Conclusion

The home-made set up build to extrude dense and highly viscous collagen solutions enabled us to extrude regular threads over meters for collagen at 60 mg/mL. Through the analysis of different buffers, we have selected a condition (PBS 5X) in which the diameter of the extruded solution was preserved during fibrillogenesis and storage. "67 nm" cross-striated collagen fibrils with two diameters (80 and 20

nm) were generated, the majority of which were aligned parallel to the thread axis. However, some fibrils appear misaligned to this axis and up to a 90° deviation. This somehow disorganization may contribute to the mechanical strength of the threads by blocking the preferential sliding direction along the thread axis. The threads synthesized in this condition present a Young modulus of 1.66 ± 0.45 MPa and an ultimate tensile strength of 0.33 ± 0.08 MPa without the use of any cross-linkers or any drying step. We suggest those threads to be good candidate for tendon repair trials.

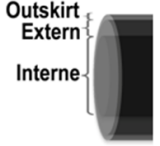
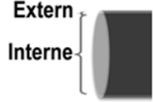
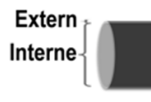
TABLE 2							
CONDITION	1			7		8	
Scheme of thread							
	Outskirt	Extern	Intern	Extern	Intern	Extern	Intern
Diameters SEM (nm)	560/150	70		100		150	
Diameters TEM (nm)	500	250	40	80/20	80/20	25	25
Striations SEM (nm)	180 at 3kV 67 at 8kV			67 at 8kV		190 at 3kV	
Striations TEM (nm)	67			67			

Table 2: *S-I*: Diameters and striations of fibrillar entities in threads synthesized in condition 1, 7 and 8.

Supplementary information

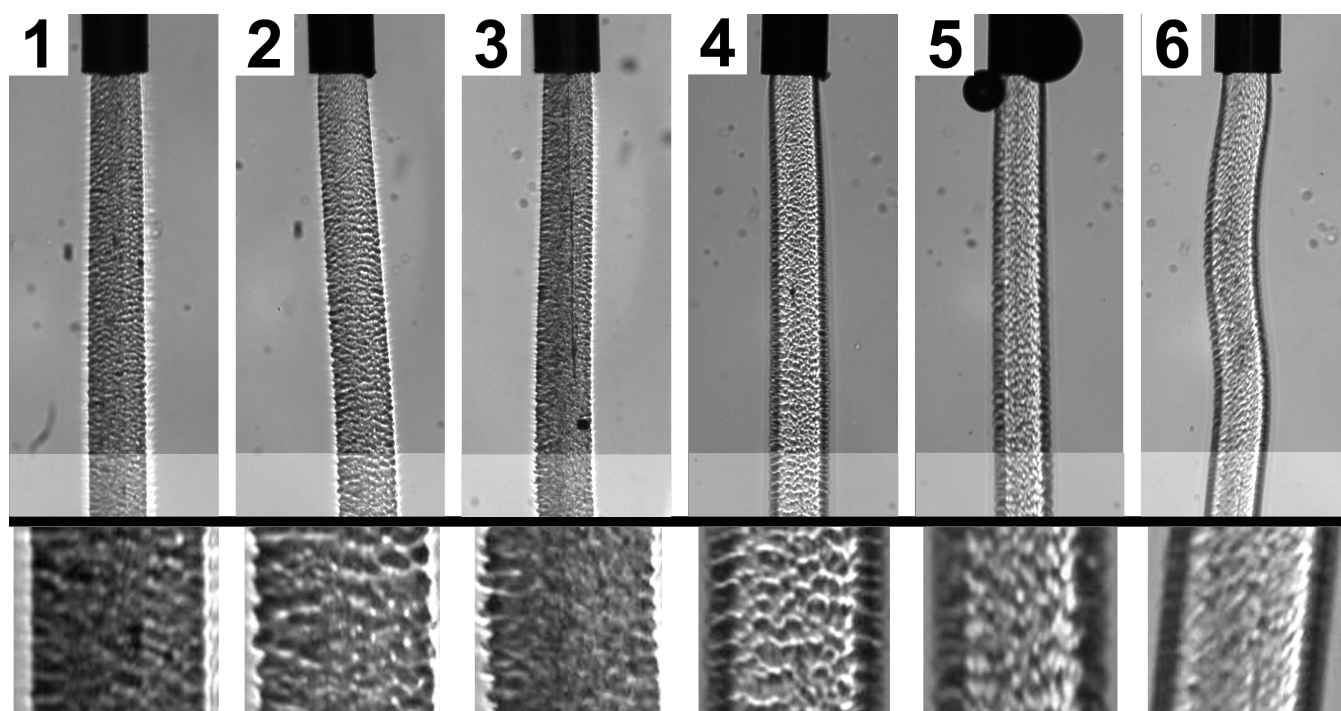


Figure 7: *Extrusion of collagen solutions through a 650 μm inner diameter needle in the first 6 buffer conditions as listed in Table 1. Bottom: higher magnification. The threads present a shark-skin like appearance and their diameter is equivalent to that of the inner diameter of the extruding needle.*

Bibliography

- [1] *Agency for Healthcare Research and Quality*. 2010.
- [2] *Use of International Standard ISO 10993-1, "Biological evaluation of medical devices - Part 1: Evaluation and testing within a risk management process"*. U.S. Department of Health and Human Services Food and Drug Administration Center for Devices and Radiological Health, 2016.
- [3] Shalimar Abdullah. Usage of synthetic tendons in tendon reconstruction. *BMC Proceedings*, 9(Suppl 3):A68, 2015.
- [4] M. Benjamin, E. Kaiser, and S. Milz. Structure-function relationships in tendons: a review. *Journal of Anatomy*, 212(3):211–228, March 2008.
- [5] J. F. Cavallaro, P. D. Kemp, and K. H. Kraus. Collagen fabrics as biomaterials. *Biotechnology and Bioengineering*, 43(8):781–791, April 1994.
- [6] A Choksey, D Soonawalla, and J Murray. Repair of neglected achilles tendon ruptures with marlex mesh. *Injury*, 27(3):215–217, 1996.
- [7] Kevin G. Cornwell, Pedro Lei, Stelios T. Andreadis, and George D. Pins. Crosslinking of discrete self-assembled collagen threads: Effects on mechanical strength and cell-matrix interactions. *Journal of Biomedical Materials Research. Part A*, 80(2):362–371, February 2007.
- [8] Kevin G. Cornwell, Pedro Lei, Stelios T. Andreadis, and George D. Pins. Crosslinking of discrete self-assembled collagen threads: Effects on mechanical strength and cell-matrix interactions. *Journal of Biomedical Materials Research Part A*, 80A(2):362–371, February 2007.
- [9] Morton M Denn. Extrusion instabilities and wall slip. *Annual Review of Fluid Mechanics*, 33(1):265–287, 2001.
- [10] J Dlugosz, LJ Gathercole, and A Keller. Transmission electron microscope studies and their relation to polarizing optical microscopy in rat tail tendon. *Micron (1969)*, 9(2):71–82, 1978.
- [11] M. G. Dunn, P. N. Avasarala, and J. P. Zawadsky. Optimization of extruded collagen fibers for ACL reconstruction. *Journal of Biomedical Materials Research*, 27(12):1545–1552, December 1993.
- [12] Marie-Madeleine Giraud-Guille. Liquid crystallinity in condensed type I collagen solutions: a clue to the packing of collagen in extracellular matrices. *Journal of molecular biology*, 224(3):861–873, 1992.
- [13] F. Gobeaux, E. Belamie, G. Mosser, P. Davidson, P. Panine, and M.-M. Giraud-Guille. Cooperative Ordering of Collagen Triple Helices in the Dense State. *Langmuir*, 23(11):6411–6417, May 2007.

- [14] Frédéric Gobeaux, Gervaise Mosser, Anny Anglo, Pierre Panine, Patrick Davidson, M-M Giraud-Guille, and Emmanuel Belamie. Fibrillogenesis in dense collagen solutions: a physicochemical study. *Journal of molecular biology*, 376(5):1509–1522, 2008.
- [15] Toshihiko Hayashi and Yutaka NAGAI. Factors affecting the interactions of collagen molecules as observed by in vitro fibril formation. *The Journal of Biochemistry*, 74(2):253–262, 1973.
- [16] Ho-Joong Jung, Matthew B Fisher, and Savio L-Y Woo. Role of biomechanics in the understanding of normal, injured, and healing ligaments and tendons. *BMC Sports Science, Medicine and Rehabilitation*, 1(1), December 2009.
- [17] Y. P. Kato, D. L. Christiansen, R. A. Hahn, S. J. Shieh, J. D. Goldstein, and F. H. Silver. Mechanical properties of collagen fibres: a comparison of reconstituted and rat tail tendon fibres. *Biomaterials*, 10(1):38–42, January 1989.
- [18] Y. P. Kato and F. H. Silver. Formation of continuous collagen fibres: evaluation of biocompatibility and mechanical properties. *Biomaterials*, 11(3):169–175, April 1990.
- [19] Mitchell R. Ladd, Sang Jin Lee, Joel D. Stitzel, Anthony Atala, and James J. Yoo. Co-electrospun dual scaffolding system with potential for muscle-tendon junction tissue engineering. *Biomaterials*, 32(6):1549–1559, February 2011.
- [20] S. Leikin, D. C. Rau, and V. A. Parsegian. Direct measurement of forces between self-assembled proteins: temperature-dependent exponential forces between collagen triple helices. *Proceedings of the National Academy of Sciences*, 91(1):276–280, 1994.
- [21] Trevor Lewis and Jill Cook. Fluoroquinolones and tendinopathy: a guide for athletes and sports clinicians and a systematic review of the literature. *Journal of athletic training*, 49(3):422–427, 2014.
- [22] A.J. Lomas, C.N.M. Ryan, A. Sorushanova, N. Shologu, A.I. Sideri, V. Tsioli, G.C. Fthenakis, A. Tzora, I. Skoufos, L.R. Quinlan, G. O’Laighin, A.M. Mullen, J.L. Kelly, S. Kearns, M. Biggs, A. Pandit, and D.I. Zeugolis. The past, present and future in scaffold-based tendon treatments. *Advanced Drug Delivery Reviews*, 84:257–277, April 2015.
- [23] Leslie Mertz. What Is Biocompatibility?: A New Definition Based on the Latest Technology. *IEEE Pulse*, 4(4):14–15, July 2013.
- [24] John C Miller. Swelling behavior in extrusion. *Polymer Engineering & Science*, 3(2):134–137, 1963.
- [25] DS Morais, J Torres, RM Guedes, and MA Lopes. Current approaches and future trends to promote tendon repair. *Annals of biomedical engineering*, 43(9):2025–2035, 2015.
- [26] Matthew C. Morrey, Jonathan D. Barlow, Matthew P. Abdel, and Arlen D. Hanssen. Synthetic Mesh Augmentation of Acute and Subacute Quadriceps Tendon Repair. *Orthopedics*, 39(1):e9–e13, January 2016.

- [27] SP Nicholls, LJ Gathercole, A Keller, and JS Shah. Crimping in rat tail tendon collagen: morphology and transverse mechanical anisotropy. *International Journal of Biological Macromolecules*, 5(5):283–288, 1983.
- [28] Francesco Oliva, Alessio Gai Via, and Nicola Maffulli. Calcific tendinopathy of the rotator cuff tendons. *Sports medicine and arthroscopy review*, 19(3):237–243, 2011.
- [29] Su A Park, In Ae Kim, Yong Jae Lee, Ji Won Shin, Chong-Rak Kim, Jeong Koo Kim, Young-Il Yang, and Jung-Woog Shin. Biological responses of ligament fibroblasts and gene expression profiling on micropatterned silicone substrates subjected to mechanical stimuli. *Journal of bioscience and bioengineering*, 102(5):402–412, 2006.
- [30] Lise Picaut, Olivier Ronsin, Christiane Caroli, and Tristan Baumberger. Experimental evidence of a helical, supercritical instability in pipe flow of shear thinning fluids. *Physical Review Fluids*, 2017.
- [31] G D Pins, D L Christiansen, R Patel, and F H Silver. Self-assembly of collagen fibers. Influence of fibrillar alignment and decorin on mechanical properties. *Biophysical Journal*, 73(4):2164–2172, October 1997.
- [32] Hazel R. C. Screen, David E. Berk, Karl E. Kadler, Francesco Ramirez, and Marian F. Young. Tendon Functional Extracellular Matrix: TENDON FUNCTIONAL EXTRACELLULAR MATRIX. *Journal of Orthopaedic Research*, 33(6):793–799, June 2015.
- [33] Mickey D. Stapp. Implantable materials and grafts in tendon surgery. *Reconstructive surgery of the foot and the leg*, pages 289–292, 1993.
- [34] Cheng Sun, Qi Zhuo, Wei Chai, Jiyang Chen, Wei Yang, Peifu Tang, and Yan Wang. Conservative interventions for treating Achilles tendon ruptures. In The Cochrane Collaboration, editor, *Cochrane Database of Systematic Reviews*. John Wiley & Sons, Ltd, Chichester, UK, October 2013.
- [35] RI Tanner. A theory of die-swell. *Journal of Polymer Science Part B: Polymer Physics*, 8(12):2067–2078, 1970.
- [36] Stavros Thomopoulos, William C Parks, Daniel B Rifkin, and Kathleen A Derwin. Mechanisms of tendon injury and repair. *Journal of Orthopaedic Research*, 33(6):832–839, 2015.
- [37] Aurélien Tidu, Djida Ghoubay-Benallaoua, Barbara Lynch, Bernard Haye, Corinne Illoul, Jean-Marc Allain, Vincent M Borderie, and Gervaise Mosser. Development of human corneal epithelium on organized fibrillated transparent collagen matrices synthesized at high concentration. *Acta biomaterialia*, 22:50–58, 2015.
- [38] Wing Yin Tong, Wei Shen, Connie W.F. Yeung, Ying Zhao, Shuk Han Cheng, Paul K. Chu, Danny Chan, Godfrey C.F. Chan, Kenneth M.C. Cheung, Kelvin W.K. Yeung, and Yun Wah Lam. Functional replication of the tendon tissue microenvironment by a bioimprinted substrate and the support of tenocytic differentiation of mesenchymal

- stem cells. *Biomaterials*, 33(31):7686–7698, November 2012.
- [39] Jorge Alfredo Uquillas, Vipuil Kishore, and Ozan Akkus. Effects of phosphate-buffered saline concentration and incubation time on the mechanical and structural properties of electrochemically aligned collagen threads. *Biomedical Materials*, 6(3):035008, 2011.
- [40] James H-C Wang. Mechanobiology of tendon. *Journal of biomechanics*, 39(9):1563–1582, 2006.
- [41] James HC Wang, Fengyan Jia, Thomas W Gilbert, and Savio LY Woo. Cell orientation determines the alignment of cell-produced collagenous matrix. *Journal of biomechanics*, 36(1):97–102, 2003.
- [42] Roger D. Williams and Spencer F. August. Experimental evaluation of a Teflon tendon prosthesis. *The American Journal of Surgery*, 107(6):913–916, 1964.
- [43] GoC Wood and M. K. Keech. The formation of fibrils from collagen solutions 1. The effect of experimental conditions: kinetic and electron-microscope studies. *Biochemical Journal*, 75(3):588, 1960.
- [44] GoC Wood and Madelaine K Keech. The formation of fibrils from collagen solutions 1. the effect of experimental conditions: kinetic and electron-microscope studies. *Biochemical Journal*, 75(3):588, 1960.
- [45] Jonathan S Young and N Maffuli. Etiology and epidemiology of achilles tendon problems. *The Achilles Tendon*, pages 39–49, 2007.
- [46] G. Zhang, B. B. Young, Y. Ezura, M. Favata, L. J. Soslowsky, S. Chakravarti, and D. E. Birk. Development of tendon structure and function: regulation of collagen fibrillogenesis. *J Musculoskelet Neuronal Interact*, 5(1):5–21, 2005.

5.4 Pure collagen vs collagen/alginate mixtures threads study

From the previous study, the threads with the best results are extruded in PBS5X. This condition is then our gold standard and we can explore other parameters as the collagen concentration and the ageing time. In this study, collagen concentration varies from 15 to 60 mg/mL. The threads are analyzed from characteristics at extrusion to their mechanical properties. Then, we produce hybrid threads composed of alginate and collagen and do the analysis to compare the two systems.

Extrusion parameters choice: in the study on the effect of buffers on fibrillogenesis, the output velocity was: $\bar{v}=50$ mm/s. This speed was chosen from alginate extrusion experiments. Indeed, as several unintended instabilities were observed in the presence of cross-linking ions at low throughput, we decided to transpose those results to the collagen and work at high throughput to avoid threads bulk distortions. We thus produced regular collagen threads and studied the influence of the ionic strength. In the current study, it was quite difficult to extrude the lowest concentration at this velocity range. Indeed, extrusion of such solution resulted in pieces of irregular "threads" of few millimeters. Therefore, the output velocity was reduced to $\bar{v}= 3.4$ mm/s for which all concentrations lead to useable threads. Of course, we checked that this decrease did not induce huge morphology or structural changes on collagen threads at 60 mg/mL before beginning the concentration impact study. As collagen solutions at 60 mg/mL extruded in PBS 5X at 50mm/s and 3.4mm/s presented the same stability and structural morphologies (SEM, TEM, SHG), we use the new velocity $\bar{v}= 3.4$ mm/s and kept the same previous needle diameter ($D=390\mu\text{m}$) for the whole following works.

5.4.1 Pure collagen threads of different concentrations

Three different concentrations were tested. In this part, A, B and C designate collagen threads at 15, 30 and 60 mg/mL respectively .

5.4.1.1 Extrusion and maturation

The collagen threads were observed from the beginning of their formation and during their ageing in the fibrillogenesis buffer. The results obtained with different techniques are presented in Figure 5.11.

During the extrusion, the collagen solution flow is steady and homogeneous (Fig. 5.11 Top). However, at 30 (B) and 60 (C) mg/mL, a surface irregularity is observed. By optical view (Fig. 5.11 middle), it is clear that the threads have different diameters: $A > B > C$. This will be quantified in the following part. They exhibit regular shapes even if some roughness appears for B and C. The thread at 15 mg/mL (A) is quite transparent and smooth. At 30 mg/mL, the thread is transparent and presents a periodic roughness of almost 25 μm depth. At 60 mg/mL, the thread is more opaque and its surface is textured by a pattern of 10 μm height. This surface pattern is due to the sharkskin instability already observed at 60mg/mL in the previous study (5.3 p 157). It is not observed at 15 mg/mL as to reach the shear-shinning region of this condition, the extrusion velocity must be considerably increased. In fact, the imposed shear rate is about 4.5 s^{-1} in our experiments. If we take a look on the viscosity plot as a function of the shear rates given in Gobeaux et al. work,

([8] 3.6 p 94) at $\dot{\gamma} = 4.5 \text{ s}^{-1}$, collagen solutions at 30 and 60 mg/mL are in the strong shear-thinning region whereas the solution at 15 mg/mL is almost at the end of the newtonian region.

During observation by polarized light microscopy (Fig. 5.11 bottom), threads are positioned at nearly 45° to both polarizers. They appear homogeneously bright along the thread axis. The birefringence signal is higher while increasing collagen concentration. For the lowest one, the thread is almost not visible (A). For threads B and C, a central part is observed, although this might be due to the cylindrical geometry. Their inner structure seems to be aligned along the thread axis.

The threads A, B and C exhibit both regular shapes even if some roughness appears for B and C. Their inner structure seem to be aligned along the thread axis for B and C.

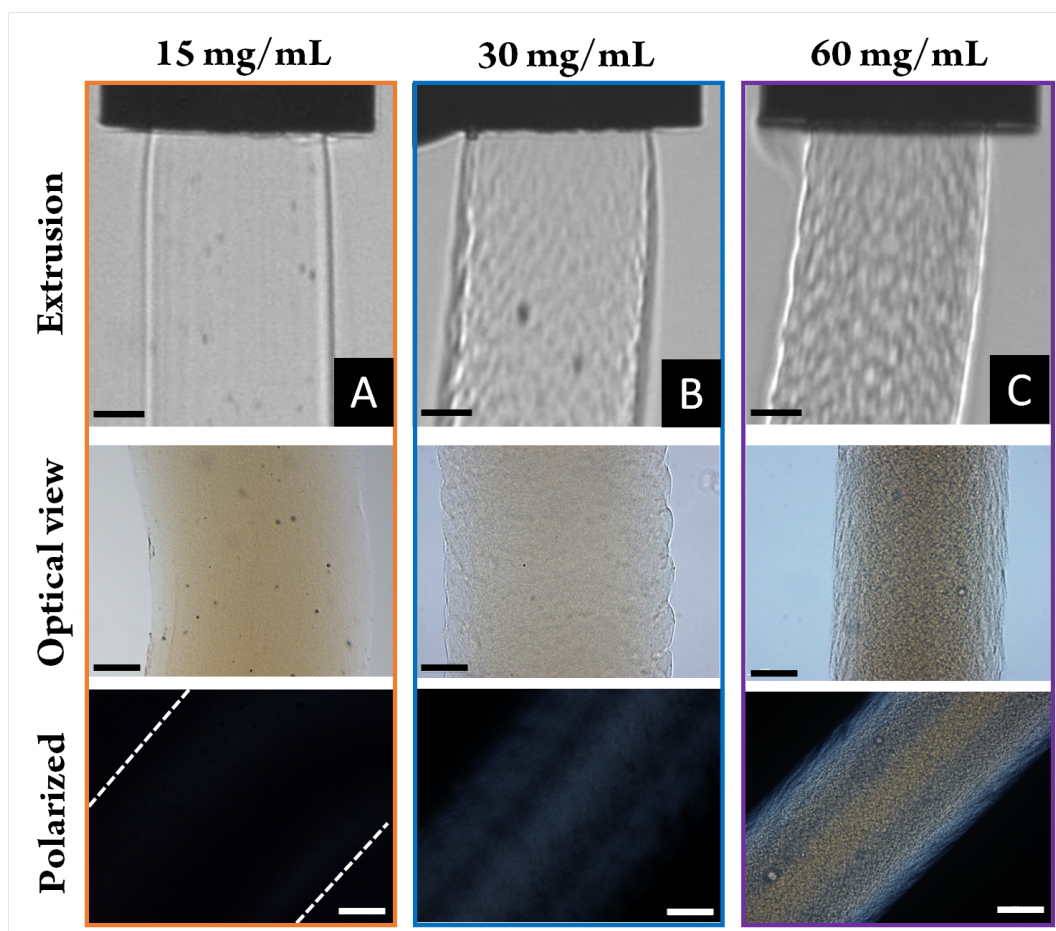


Figure 5.11: Collagen threads observed by different techniques at different concentrations. On the left, collagen thread at 15mg/mL (A). During the extrusion, the collagen flow is homogeneous and the thread seems to be smooth. It is confirmed by optical microscopy. At 30 and 60mg/mL (B and C), a pattern at the thread surface is observed during the extrusion. It is also visible by optical view where a regular roughness appears. Bottom: Polarized light microscopy technique: birefringence signal is visible for 30 and 60 mg/mL. The inner collagen organization seem to be aligned along the thread axis. Scale bars are $100\mu\text{m}$

5.4.1.1.1 Diameter stability

The collagen threads diameter was measured over 2 weeks by optical microscopy to assess their ageing evolution in the fibrillogenesis buffer (PBS 5X) chosen from the previous study. The results are presented in Figure 5.12 showing the plot of the ratio D/D_0 .

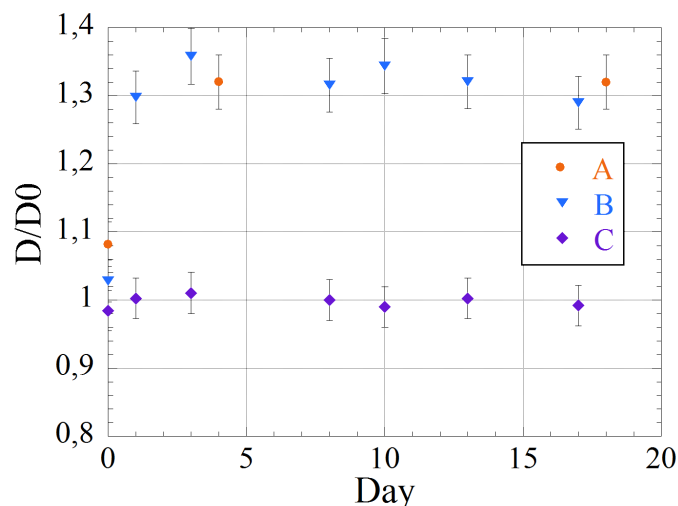


Figure 5.12: Evolution of collagen threads diameter over time. The ratio of the measured thread diameter D and the inner diameter of the needle was plotted as a function of the time (day). Dash-lines represent the diameter evolution trend. Optical microscopy images of collagen threads after 14 days of ageing in PBS 5X, at A) 15mg/mL; B) 30mg/mL and C) 60mg/mL

For collagen threads A and B, the ratio D/D_0 increases almost from 1 to 1.3 during the first two days. From the third day, D/D_0 remains constant in both cases. For collagen thread C, the diameter ratio is equal to 1 and remains constant even after 2 weeks.

5.4.1.1.2 Surface analysis

The threads topography was observed by scanning electron microscopy (SEM) over time. The results are shown in Figure 5.13.

At day 1, SEM shows that the thread A surface is quite smooth while B exhibits more pleated patterns aligned in the thread axis. For C, we observe the same pattern, which now appears constituted by "ball of wool" made of collagen fibrils (Fig. 5.13 C). After two weeks in PBS 5X, B and C surface morphology do not differ much from day 1. For the lowest concentration, fibrillar structures are revealed. Those are smaller than those constituting the "ball of wool" of thread C.

These observations are in good agreement with the results obtained with optical techniques (Fig. 5.11 p 181). Thread A is quite smooth compared to B and C. The sharkskin surface instability seems to lead to those "ball of wool" of collagen fibrils for thread C. This perturbation is lower for threads B and A resulting only in more or less pronounced pleated. The fibrillar structures are larger for C than A that suggests a different fibrillogenesis kinetic.

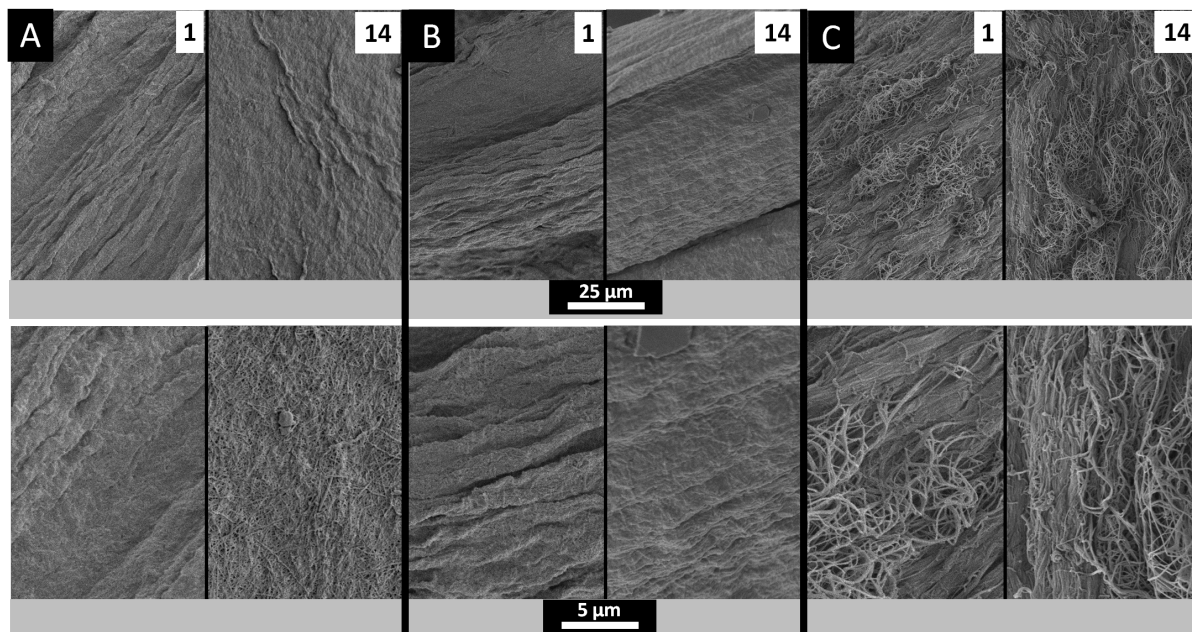


Figure 5.13: SEM images of threads surface at A) 15mg/mL, B) 30mg/mL, C) 60mg/mL at day 1 and 14. A appears quite smooth compared to B and C where a more pronounced roughness is observed.

5.4.1.2 Structural characterization

5.4.1.2.1 Fibrils characterization

Figure 5.14 shows the distribution of the fibrils as well as their morphology as seen by transmission electron microscopy (TEM) after 2 weeks in PBS 5X. Figure 5.14 A, B and C, are cross-sections of threads respectively made of collagen at 15, 30, 60 mg/mL at low magnification on the top part and at high magnification on the lower part. The pictures show view of threads center areas.

In all threads, fibrils presenting the 67 nm cross-striation are observed and their diameter is about 40-60 nm. Their length is greater for A and C and can reach almost 1 μm and seem smaller in the thread B. For thread A (low magnification), the fibrils population is smaller per unit area than threads B and C. Indeed, as A has less collagen material (low concentration) and swells during ageing, collagen fibrils are more disconnected from each other. On top images, for threads A and B, most of the fibrils are cut perpendicular to their axis, giving the dotted features and fewer appear cut along their longitudinal axis. For thread C, both populations are observed.

The concentration effect is observed by TEM on threads centers, where the fibrils population appears smaller while decreasing the concentration. Fibrils are well aligned in the thread axis, which suggests that extrusion process tends to align them along the longitudinal thread axis. For the highest concentration, a transverse fibrils population is also observed.

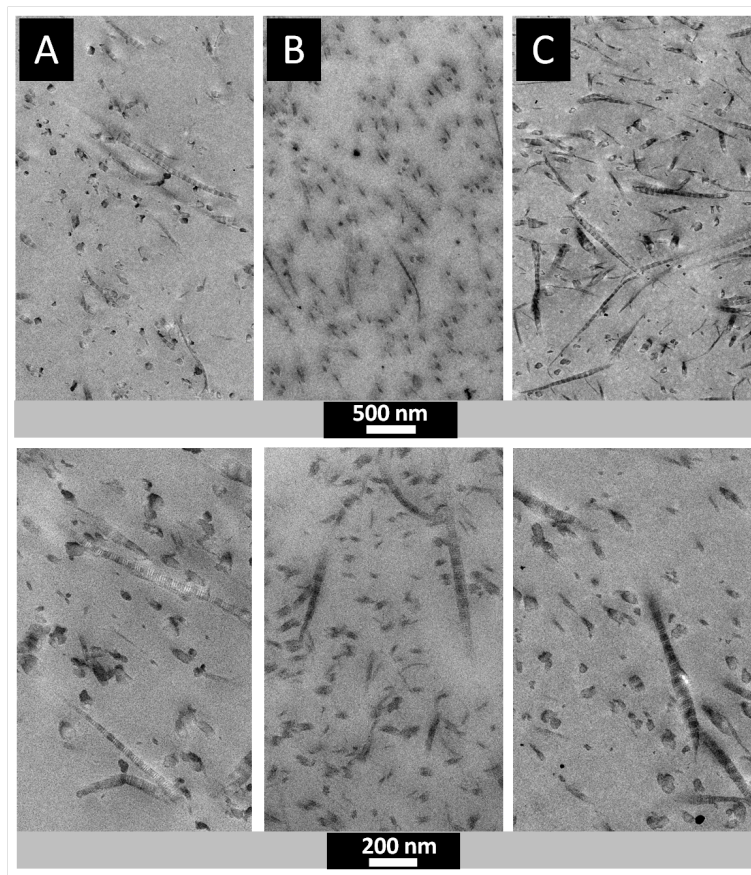


Figure 5.14: Ultrastructure of threads after 2 weeks of maturation in PBS 5X as seen by TEM (transverse sections). Figure A, B, C correspond respectively to collagen threads at concentrations 15, 30 and 60mg/mL. Top: view at low magnification of a center threads region. Bottom: view at higher magnification of near region. Collagen fibrils appear cut in all directions from longitudinal to transverse, in which case they appear as dots.

5.4.1.2.2 Collagen fibrils organization and orientation

Second Harmonic Generation microscopy (SHG) and Polarization-resolved SHG (P-SHG) were performed on the collagen threads at different concentrations as a function of time. We first present the results obtained after 2 weeks of ageing in PBS 5X (Fig. 5.15) and detail those obtained at previous times if differences are revealed.

At lower magnification, SHG intensity is homogeneous in every direction for thread A. In the case of thread B, a texture (black striations) is observed within a distance of approximately 50 μ m from the surface. This shell is radially organized as it is observed on both "sides". The thread center is homogeneous. The same structure is observed for thread C, with more pronounced striking features, and a size of about 100 μ m. All those observations suggest that more concentrated collagen threads have a shell-core structure and that the one with the lowest concentration is homogeneous. This is in good agreement with polarized light microscopy previous observations, for which some doubts about the origin of this core structure arose.

P-SHG enables to calculate the anisotropy parameter ρ and the orientation ϕ of collagen in the image plane as previously explained, and thus to assess the micrometer scale disorder in the collagen fibril distribution. In the anisotropy "map" (Fig. 5.15), ρ is constant over the thread because the thread appears as a uniform medium for all conditions. The values of the anisotropy parameter is almost the same for the three concentrations and is

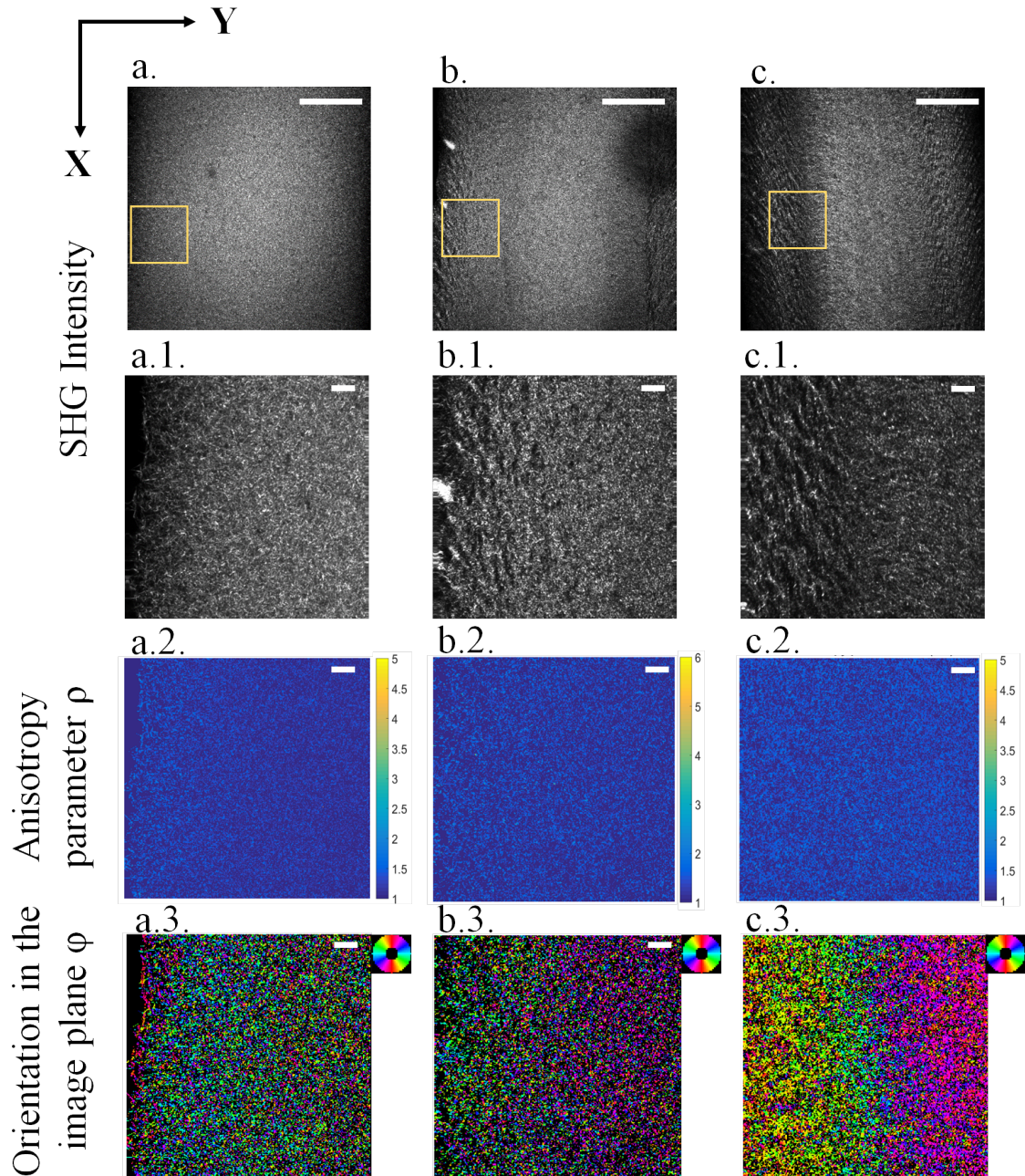


Figure 5.15: TOP: SHG imaging of collagen threads at a.15 mg/mL, b. 30 mg/mL and c. 60mg/mL in the center transverse thread planes. The threads are placed vertically and their borders are visible on each side (left and right) of the images. Scale bar: 100 μ m. P-SHG imaging a.1., b.1., c.1 : zoomed-in images taken in the yellow squared areas respectively in a., b., c. BOTTOM: images of P-SHG analysis of the anisotropy parameter (a.2, b.2, c.2) and the orientation φ of collagen in the image plane (a.3, b.3, c.3) Scale bar: 10 μ m.

equal in the superficial area to 1.34, 1.56 and 1.45 for respectively A, B and C. The same experiments were performed on native rat-tail tendons by Gusachenko et al. [9]. They found anisotropy parameters of about 1.40 ± 0.03 on the surface. Our results are almost in the same range, which may indicate that the collagen fibrils organization in the threads is close to those of tendons. Moreover, in our case, we observe that this parameter decreases, while going from the thread surface to its center (1.27, 1.52 and 1.40 are the ρ values at the center for A, B and C). This decrease is presumably an artefact due to diat-

tenuation.

The collagen fibrils orientation was also obtained by P-SHG measurements on regions of interest. Figure 5.15 (bottom) displays the resulting color maps obtained in the threads center transverse planes in the region close to the surface ("left side" in this example), as shown by the yellow squares on the top images. For the thread A, the fibrils orientation is the same in all directions, which means that it is isotropic. For threads B and C, φ varies abruptly from the textured shell to the core: from -60° to $+50^\circ$ for B and -70° to $+70^\circ$ for C. The same measurements were done at the thread "center-center" and at the other surface side for B. The results are shown in Figure 5.16.

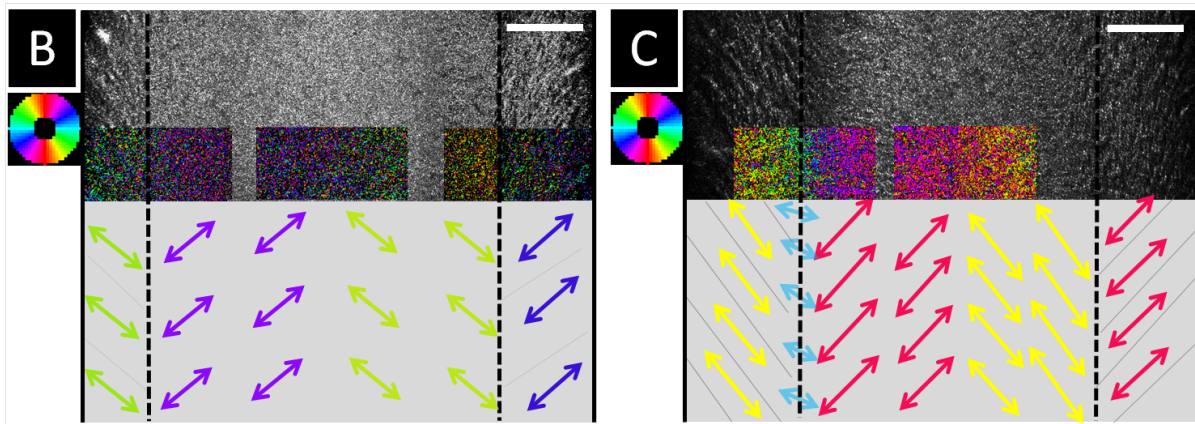


Figure 5.16: SHG imaging and P-SHG areas (colored) of surfaces and middle regions at the threads center transverse sections for B: 30mg/mL and C: 60mg/mL. Schemes of collagen fibril orientation φ are given to help to visualize the radial organization. Scale bar: 50 μ m.

Sharp angles variations are observed from the shell-core interfaces to the thread center. The angles changes are lower for thread B than C. The collagen fibrils orientation has radial symmetry. The resulting angles maps look like "ear of corn" patterns at interfaces. The mean orientation follows the thread longitudinal axis. Those complex organization may come from the sharkskin instability. Indeed, only threads B and C exhibit this pattern during extrusion. It means that strong strains are applied at the singular die exit and may lead to this collagen fibrils orientation difference between the shell (high strains) and the core. Moreover, as collagen fibrillogenesis at the thread surface occurs more rapidly for higher concentration, the matrix is "frozen" in the high strains state and can not relax. It might explain the φ angle amplitude, which is higher for C. Other parameters as the swelling of B can also be considered to understand those observations.

Remark 1: Ageing time influence

At day 1, collagen threads A and C have the same structure as presented at day 14. Only some collagen fibrillar structures at the surface were larger at day 14, these results being similar with those as observed by SEM (5.13 p 183). However, at day 1, the shell-core structure was not observed for thread B as shown on figure 5.17.

The sharp striated patterns of the shell are not visible by SHG. Surprisingly, while looking at the P-SHG measurements of φ angle at day 1, the interface between shell and core, and visible at day 14, matches an angle orientation difference (blue and red, the interface being represented by a yellow dashed line). It indicates that collagen is already oriented and during fibrillogenesis/ageing phase, this orientation becomes visible at a higher scale.

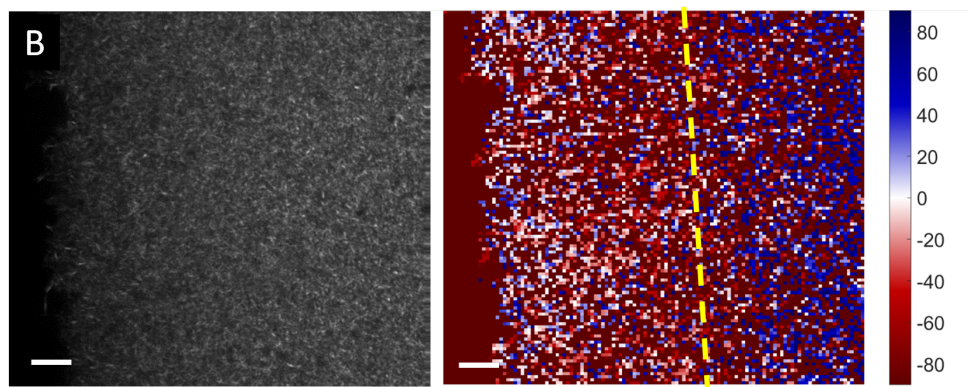


Figure 5.17: SHG and P-SHG imaging of collagen thread at 30mg/mL (B) at day 1. It is already possible to see the different orientations in the core/shell regions even if it is not visible on SHG image as in the case of 60mg/mL (C). Yellow dashed line is an eye guideline to show the core/shell interface. Scale bar: 10 μ m.

Remark 2: "Ball of wool" and 3D imaging

By SHG technique, it is also possible to do 3D imaging of the threads. This kind of plane-by-plane acquisition (each 5 μ m) takes typically 1 to 2 hours. We give here an example of 3D imaging of a collagen thread at 60 mg/mL after 2 weeks in PBS 5X. At the outer surface, the famous "ball of wool" of collagen fibrils is clearly seen (Fig. 5.18, top left 1) as already observed by SEM (5.13 p 183).

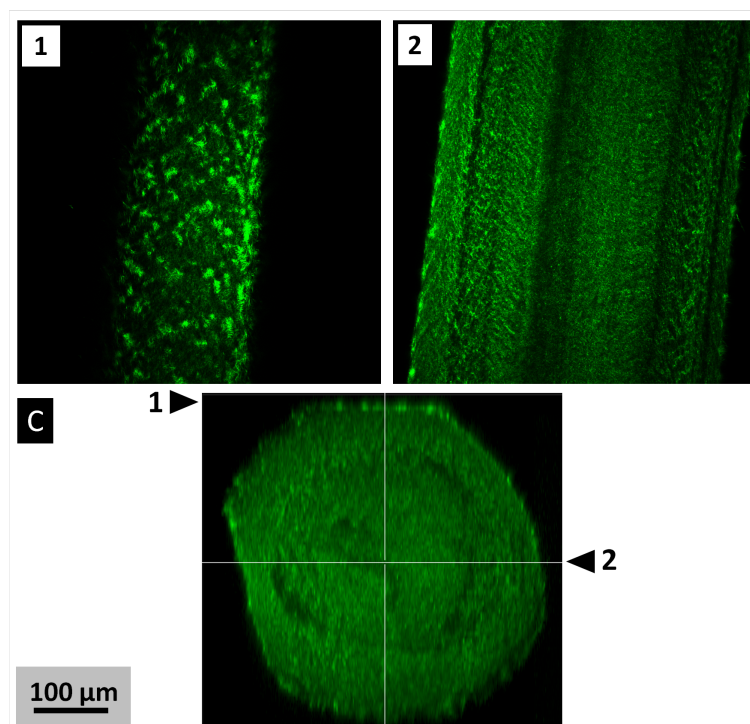


Figure 5.18: SHG images of collagen threads at 60 mg/mL after 2 weeks in PBS 5X. Images 1 and 2 correspond to the depths indicated by the arrowheads. The cross section was obtained by 3D reconstruction.

In this example, it is noticed that several concentric "layers" are revealed at the thread center depth (Fig. 5.18, top right 2). With the 3D reconstruction, we can observe the cross-section thread organization (Fig. 5.18). The main shell-core interface is visible and there, the SHG signal seems to be lower. If we come back to the scheme of thread C (Fig.

5.16 p 186, right), blue arrows were put on this area of about 10 μm , corresponding to the fact that φ is equal to 40-50 ° between the shell and the core. From these two facts, we assumed that this small area may be a depletion area or a region where collagen molecules are mainly "antiparallel" leading to decreased SHG signal. Further TEM investigations must be done to assess the fibrils size and repartition between the surface, the shell and the core of the threads.

Remark 3: discarded condition

Unfortunately, as collagen thread at 15 mg/mL was difficult to handle, we decided to remove it for the mechanical characterization as it is obviously too weak for tendon repair applications.

5.4.2 Collagen/alginate threads

Hybrid collagen-alginate threads were made in order to combine the two systems and take benefit from both of them. In fact, in chapter 1 we reported the advantages of alginate (1.2.4 p 27), which can be degraded and thus created some porosity, and which also has non adhesive properties, both interesting characteristics in the view of tendon repair. On the other hand, as we already have presented it, collagen is the main component of connective tissues. The extrusions were performed in chloride calcium 1M to induce the gelation of alginate. The pH of this bath solution is about 6-7.

5.4.2.1 Ratio choice

This kind of mixtures is not easy to achieve due to proteins and polysaccharides interactions, phase separation and precipitation that may occur leading to heterogeneous systems. In order to ease the task, we produce collagen-alginate threads with effective total material quantity similar to pure collagen of 30 milligrams per milliliter and with exactly same extrusion parameters. Several ratios (2.2.3.2 p 84) are tested and the resulting flow extrusion and threads are presented in Figure 5.19.

During extrusion, at ratios 1:1 (coll:alg) and 2:1, tortuous opaque domains are visible while the rest of the mixture solution is transparent. At ratio 5:1, the whole extrudate seems to be more homogeneous. Regarding the thread diameter uniformity, ratio 2:1 is clearly not straight and material is not well distributed inside the thread. By polarized light microscopy, the birefringence differences are more obvious. At ratio 1:1, very bright and dark regions alternates sharply, which means that some regions are rich and other poor in collagen. The material distribution is not homogeneous. For the thread at ratio 2:1, bright domain is homogeneous over a larger period. At ratio 5:1, birefringence signal is less intense but more homogeneous over the whole thread. Finally, while changing the extrusion buffer (CaCl_2 1M) for few minutes by PBS 1X, threads at ratios 1:1 and 2:1 begin to disintegrate and ratio 5:1 remain quite stable.

According to these results, we assume that the best condition for the further study is the collagen:alginate **ratio 5:1**.

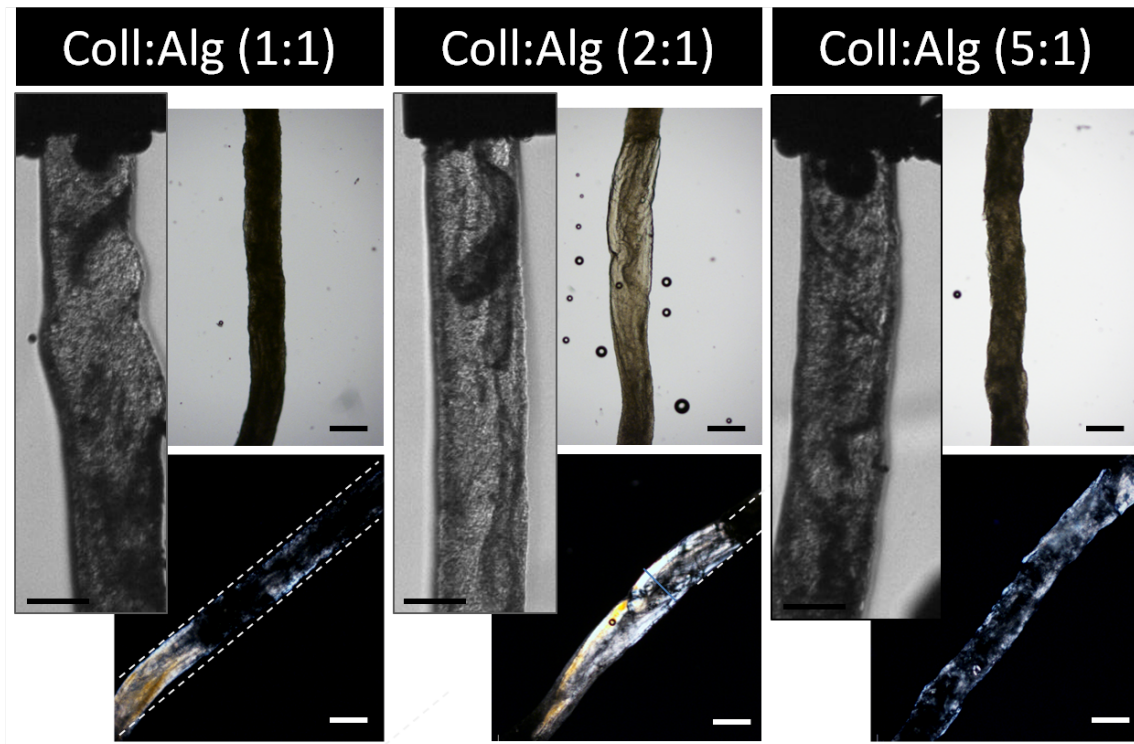


Figure 5.19: Collagen:alginate threads at ratios: 1:1, 2:1, 5:1, observed by different techniques. On the left, real-time observations during the extrusion. Right: bright field views. Bottom: Polarized light microscopy images between two crossed polarizers at 45° . Scale bar are $250\mu\text{m}$.

5.4.2.2 Structural characterization

Some plugs appear once in a while and disturb the solution flow extrusion. Therefore, we use needle diameter of $D=460\mu\text{m}$ and increase the piston velocity in order to have output velocity of $\bar{v}=3.4\text{ mm/s}$ and thus the same shear rate as for collagen threads at 30 mg/mL .

Surface analysis

The topography of collagen-alginate (5:1) thread and pure ALG4 thread as control were observed by SEM. In Figure 5.20, ALG4 thread surface appears smooth. For the mixed thread, the surface also appears smooth, but some small aggregated structures are observed on it. A higher magnification, we can see the difference between the smooth (right) surface and those aggregates. As those structures are not observed for pure alginate, it is assumed that they might be made of collagen.

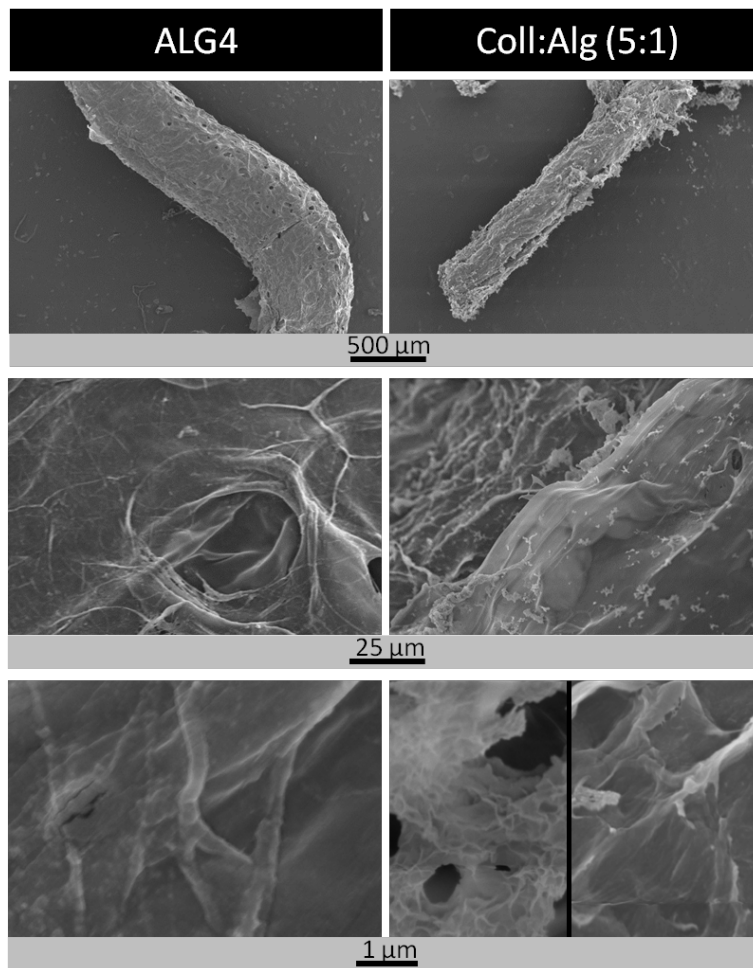


Figure 5.20: SEM imaging of pure ALG4 (control) and collagen:alginate (5:1) threads. Both thread surface are smooth, but some aggregates are observed on the hybrid thread.

Microstructural organization

As for pure collagen at 30 mg/mL, microstructural organization was assessed by TEM and SHG techniques. In Figure 5.21, TEM images of two hybrid thread areas are shown. On the **left**, straight and abrupt transitions between two populations are observed. A population (1) composed of a network of small strands (length about 60-70nm) is enclosed between two similar areas (2), which are very concentrated and compact. At high magnification, this second population seems to be composed of thin "hair"-like structures (width of 5-6 nm) that are quite aligned with the interface axis. This phase (2) seems also to be composed of several parallel layers (bottom right corner).

TEM micrographs of a second representative area of the sample are shown on the figure 5.21 **right**. The two populations (1) and (2) described in the first area are found again. Here, the interface is not abrupt as in the other region. Moreover, a third population (3) seems to be located at the interface between the void-strands and the compact "hairs" region. Several concentrated tortuous bundles are observed between these populations. They have diameters about 70nm and length ranging from 500nm to 1μm. At high magnification, few of those larger shapes seem to present striations (red arrow) akin D-spacing of collagen fibrils.

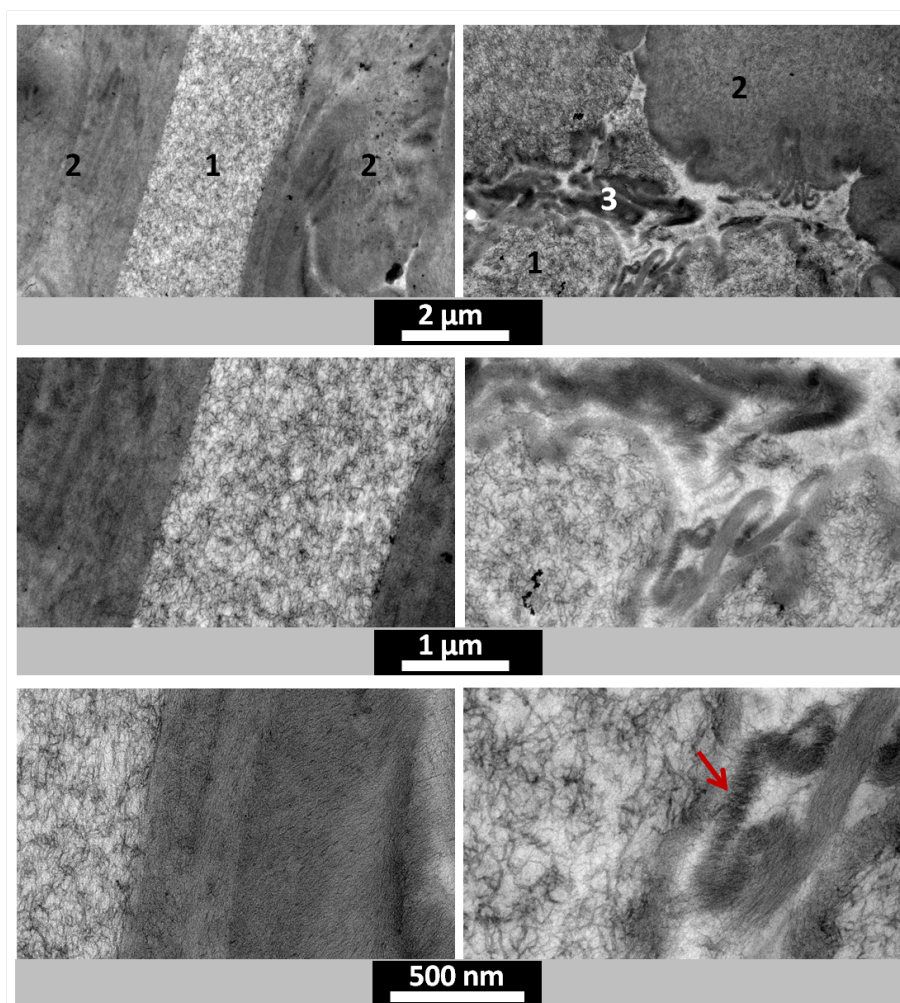


Figure 5.21: TEM longitudinal sections images of two characteristic areas of collagen:alginate (5:1) thread in CaCl_2 1M.

Based on structural studies by other authors, we attempt to identify those different populations. The figure 5.22 shows TEM images of a cross-linked alginate gel at 2 % (w|w) [11] and a fibrillated collagen gel at 100-150 mg/mL (pH 13) [12].

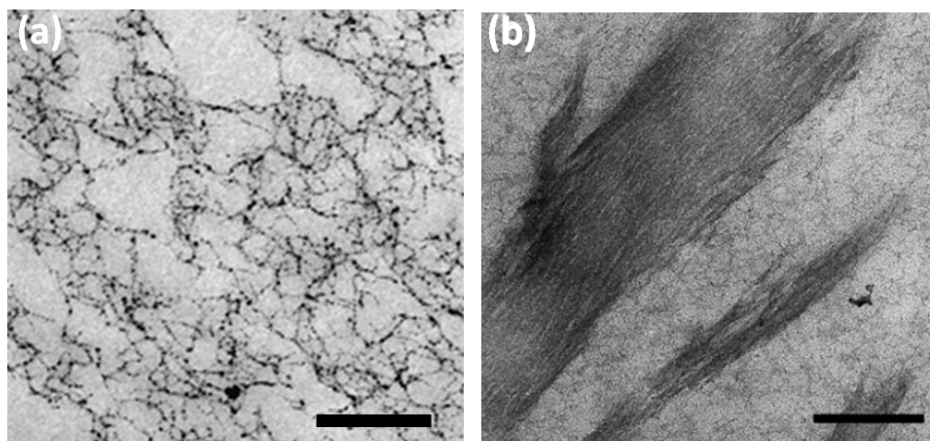


Figure 5.22: TEM micrographs obtained from studies of a cross-linked alginate gel at 2 % (w|w) [11] and a fibrillated collagen gel at 100-150 mg/mL (pH 13) [12]. Scale bar: 200 nm.

a) Schuster et al. [11] observed alginate gel networks. This network consists in polymer strands (dark) and voids (grey space), which are similar to the population (1) observed in our collagen:alginate thread.

b) Gobeaux et al. [12] obtained disordered fibrillar aggregates at 100-150 mg/mL at pH 13, that do not exhibit the typical cross-striation for collagen. They explained that these aggregates are similar to those obtained for lower pH of 6.2-12.2. Moreover, they measured the width of the nanofibrils located in the aggregates and found a width of 6 nm. These observations are in good agreement with our results for the population (2). In our case, the initial concentration is not comparable to gel at 100 mg/mL. However, as we observe phase separation, a local collagen material concentration may occur that would lead to structures similar to those of highest concentration as seen in Figure 5.22.

SHG observations

To further investigate the microstructural collagen of hybrid thread, SHG observations were performed by Adèle Mauroux (PhD student under the supervision of Laurent Muller). In Figure 5.23, section view and their projections are given. There is a diffuse SHG signal in almost the whole thread. However, some areas are more intense. It means that fibrillar collagen is located in certain regions. In fact, we observe the same structures as previously observed by TEM: tortuous collagen phase (3) pointed by the red arrow. These "steamy" bright areas are assumed to be collagen fibrillated with a lower SHG intensity than in pure collagen threads. Those structures are located almost at the thread surface. The less intense SHG areas may be those of nanofibrils corresponding to the population (2). Finally, the darker regions may consist in alginate population (1). They seem to be preferentially located deeper inside the threads than population 3.

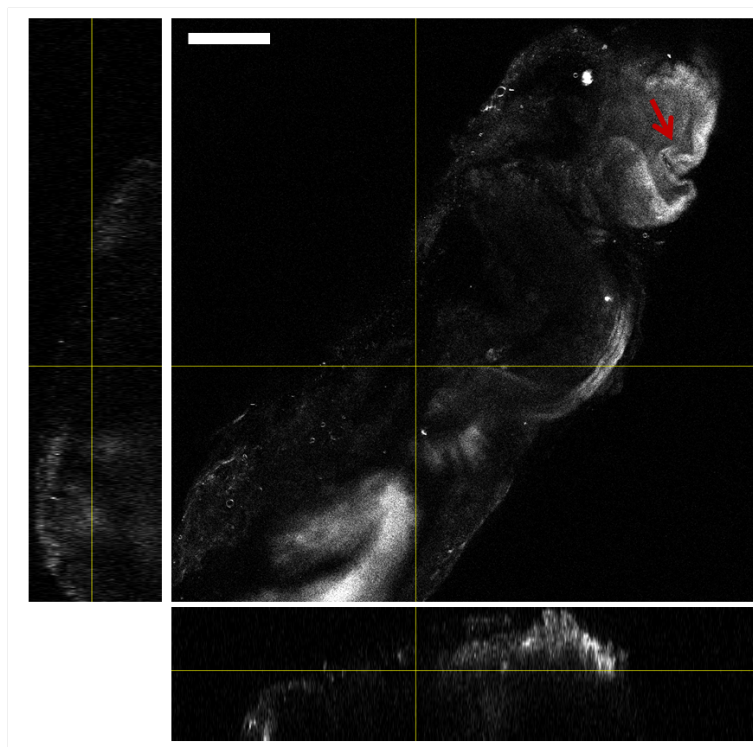


Figure 5.23: SHG images of collagen:alginate (5:1) thread in CaCl_2 section and the respective projections as given by the yellow lines. Scale bar: 100 μm . SHG signal is observed in almost the whole thread but is more or less intense in certain areas. Red arrow points to a tortuous structure.

5.4.3 Mechanical properties comparison

Stress-strain plots representative of each condition are presented in Figure 5.24. For collagen thread at 30mg/mL, a linear evolution before the rupture is observed. For the coll:alg thread, the material failure seems to be prolonged in term of strain compared to the pure collagen one. However, a better loading extent is observed for collagen 30mg/mL. Finally, at 60mg/mL, the stress roughly increases until reaching a plateau corresponding to a plastic behavior, whereas collagen 30 and its hybrid equivalent rather exhibit elastic behavior.

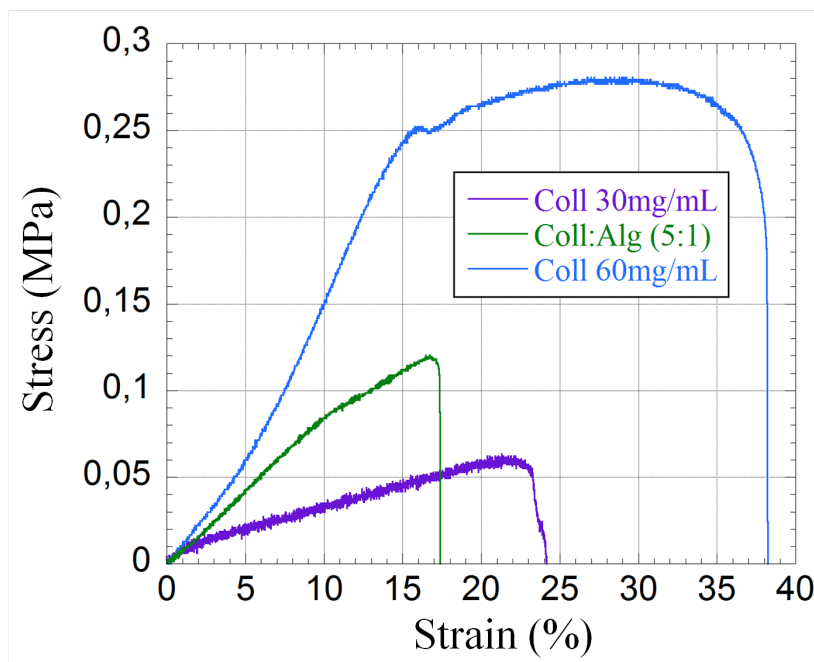


Figure 5.24: Tensile testing until rupture for collagen threads at 30 and 60mg/mL and coll:alg (5:1) thread in wet conditions and at room temperature. The characteristic stress-strain curves are given for the three conditions.

Condition	E (MPa)	UTS (MPa)	N
Coll 30 mg/mL	0.20 ± 0.06	0.081 ± 0.016	10
Coll:Alg (5:1)	0.84 ± 0.17	0.11 ± 0.06	5
Coll 60 mg/mL	1.66 ± 0.45	0.31 ± 0.08	33

Table 5.1: Tensile testing results: Young modulus E, Ultimate Tensile Strength UTS for collagen at 30 and 60 mg/mL and collagen:alginate at 5:1 ratio threads. N is the number of experiments performed.

The summary results of tensile testing are shown in table 5.1. At 30 mg/mL, E of about 0.20 MPa is reached. This value is almost 8 times larger at 60mg/mL. Collagen threads at 30 mg/mL have UTS 4times smaller than at 60 mg/mL. Here, we clearly notice the collagen concentration effect: the more material in the thread, the best mechanical properties. While comparing pure collagen and hybrid collagen:alginate, we observe that the addition of alginate improve the mechanical properties of the threads, for which E (4-fold) and UTS (1.4-fold) are higher. But, the mixture thread can support smaller strains.

5.5 Preliminary study to cell culture

Before seeding the cells on threads, it is necessary to know if the collagen-based threads are stable in the cell culture medium. In fact, this medium is composed of 90% Dulbecco's Modified Eagle's Medium (DMEM: mixture of salts, vitamins etc), 10% Foetal Bovine Serum (FBS) and a small amount of antibiotics. The ionic strength of this medium is about 0.13M [13] and is set to be at physiological pH (7.4).

PBS 5X and CaCl_2 1M have respective ionic strengths of 0.825 and 1M. The ionic strength is thus decreased while putting threads in culture with cells and this may lead to a structural change. Collagen based threads were put in DMEM in an incubated chamber maintained at 37°C and 5% CO_2 for 3 weeks. In this part, we observe the influence of complete cell culture medium, abbreviated DMEM, on these threads.

5.5.1 General morphology

5.5.1.1 Optical observations

By optical microscopy, we observe the threads morphology evolution over time. The measurements are presented in the next section (Fig. 5.27 p 195). The pure collagen thread overall aspect is the same at day 0 as at day 14 (Fig. 5.25). No difference is observed by optical microscopy and we come to the same conclusion for collagen 60mg/mL.

On the contrary, hybrid thread morphology evolves over time. First, it clearly exhibits a larger diameter after 2 weeks in DMEM. As a consequence, the thread becomes more transparent as it is less concentrated per unit area. It is assumed that the ionic strength decreases from 1M to 0.13M leading to the swelling of the thread.

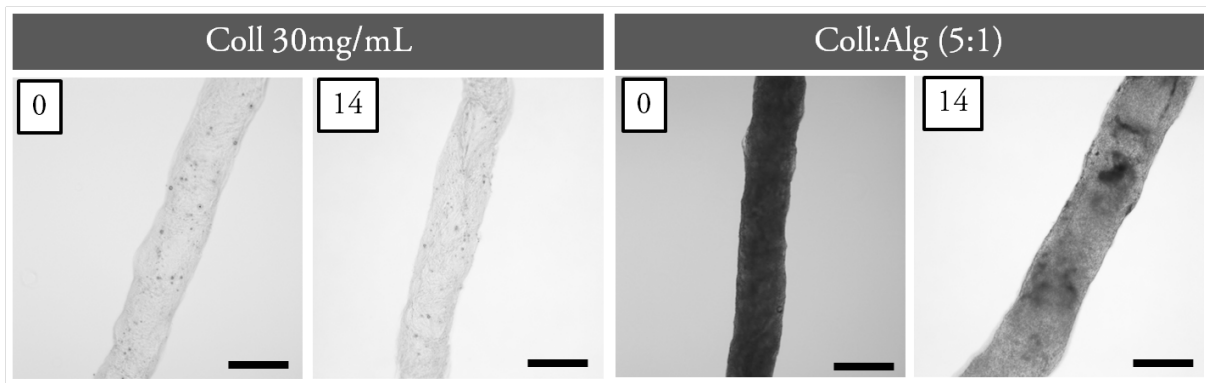


Figure 5.25: Bright field microscopy images of collagen 30 mg/mL and coll:alg (5:1) threads incubated during 0 and 14 days in DMEM at 37°C . Scale bar: $500\mu\text{m}$

5.5.1.2 Topography analysis

The topography of pure collagen threads was not changed while incubating them in DMEM, on the contrary to the collagen:alginate mixture threads (Fig. 5.26). By comparison with the threads kept in CaCl_2 1M (Fig. 5.20 p 190), the topography is rough and fibers cover the entire thread surface. At higher magnifications, those fibers appear quite thin

(< 1 μm width) and do not have clear orientation. Finally, no typical fibrillar striations are seen.

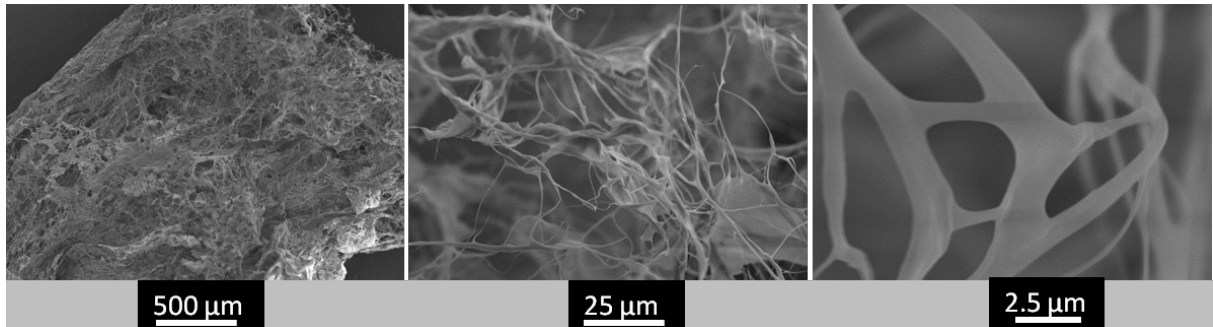


Figure 5.26: SEM images of collagen:alginate (5:1) thread surface after 3 weeks in DMEM at 37°C. Thin fibers cover the entire thread surface and have no clear orientation.

5.5.2 Diameter stability

The threads diameter D were measured on optical microscopy images before and during the incubation in DMEM at 37°C. The figure 5.27 displays the results of these measurements.

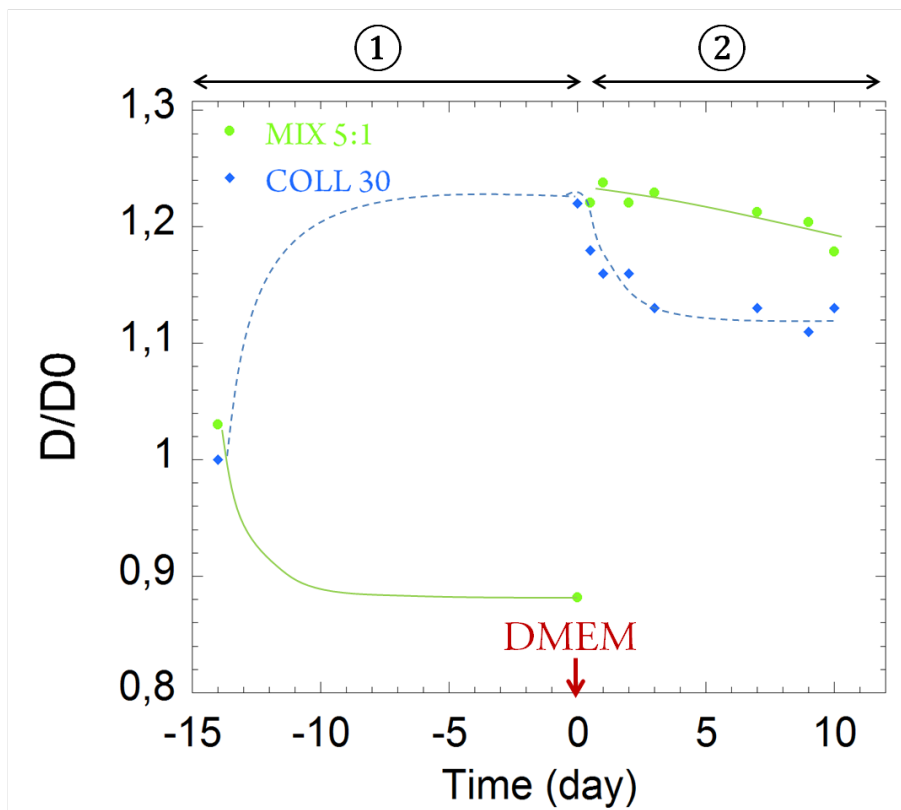


Figure 5.27: Evolution of collagen based thread diameters upon maturation for the different buffers: 1) PBS 5X for collagen 30 mg/mL, CaCl_2 1M for coll:alg (5:1) and 2) cell culture medium DMEM at 37°C. The diameters of the threads have been measured regularly along the two phases.

In the phase 1, threads remain in their extrusion solution. As previously presented, collagen thread at 30 mg/mL swells in PBS 5X and its diameter is stable after 3 days. On the

contrary, hybrid thread diameter decrease by 10%, which indicates a shrinkage caused by the high ionic strength of the extrusion solution.

At "day 0", both types of threads are put in DMEM at 37°C. In the phase 2, the ratio D/D_0 decreases from 1.22 to 1.12 for pure collagen thread 30mg/mL over 3 days and then is stable. In the case of collagen:alginate mixture, in only few hours, the diameter ratio increases from 0.88 to 1.24, which is equivalent to a swelling of 36%. Then, the ratio slightly decreases and reaches 1.18 value closer to that of pure collagen. The ionic strength difference between CaCl_2 1M and DMEM is assumed to be responsible for the strong and fast swelling of the collagen:alginate (5:1) thread. In the case of pure collagen thread, the small diameter decrease is not intuitive as one would have thought that it would also swell. The temperature is higher in the phase 2 which might also impact the thread stability.

5.5.3 Structural characterization

5.5.3.1 Pure collagen threads

Collagen threads at 30 and 60 mg/mL were observed by TEM while remaining in DMEM during 2 weeks. The following figure 5.28 displays the images comparison between the microstructure in PBS 5X and in DMEM.

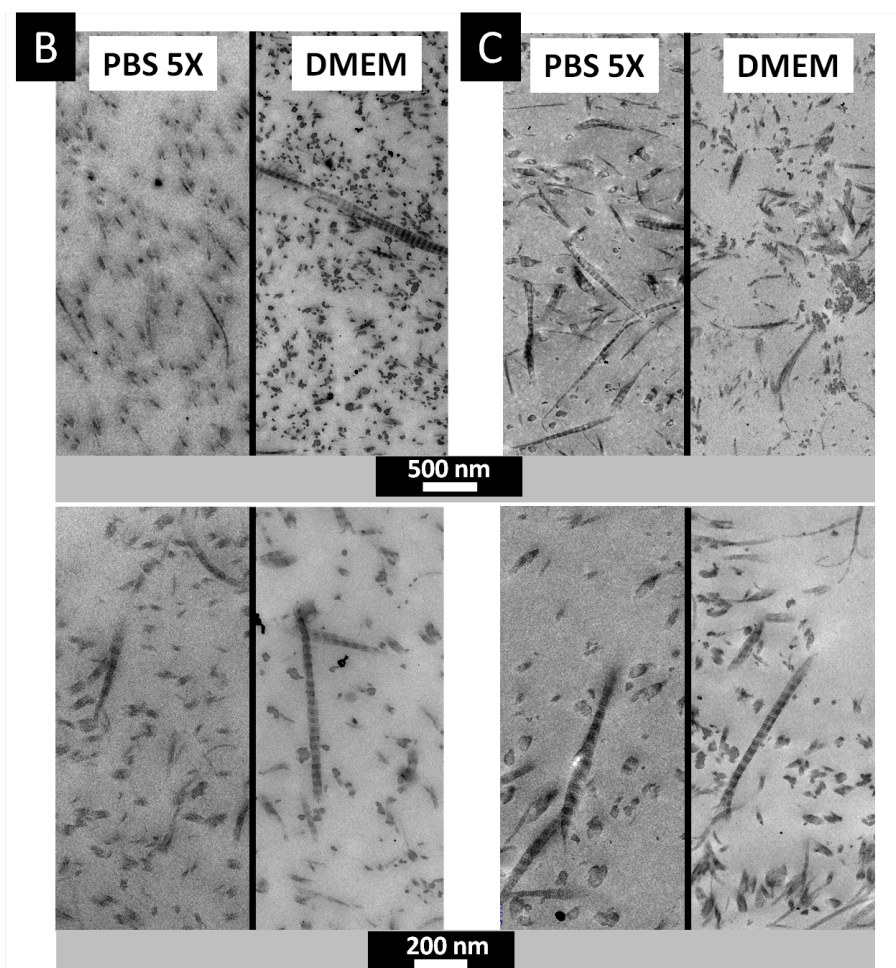


Figure 5.28: TEM cross-sections images of collagen threads at 30 mg/mL (B) and 60 mg/mL (C) either matured in PBS5X or incubated in DMEM at 37°C during 2 weeks.

For both collagen concentrations, cross-sections are very similar between the two buffers. For thread B, most of the collagen fibrils are aligned along the thread axis (dots) and very few fibrils are shifted in both buffers. The fibrils seem to be larger in DMEM than in PBS 5X. Moreover, at low magnification, we observe that there are more fibrils per unit area in DMEM. This is probably due to the small diameter decrease leading to the local collagen concentration. At 60mg/mL, the two conditions give very similar ultrastructure and no effect of the buffer change is revealed. For pure collagen threads, the passage from fibrillogenesis buffer to the cell culture medium does not change the thread structure, which remains quite stable.

5.5.3.2 Collagen:alginate threads

TEM observations were also performed on collagen:alginate threads incubated in DMEM during 3 weeks as shown in Figure 5.29:

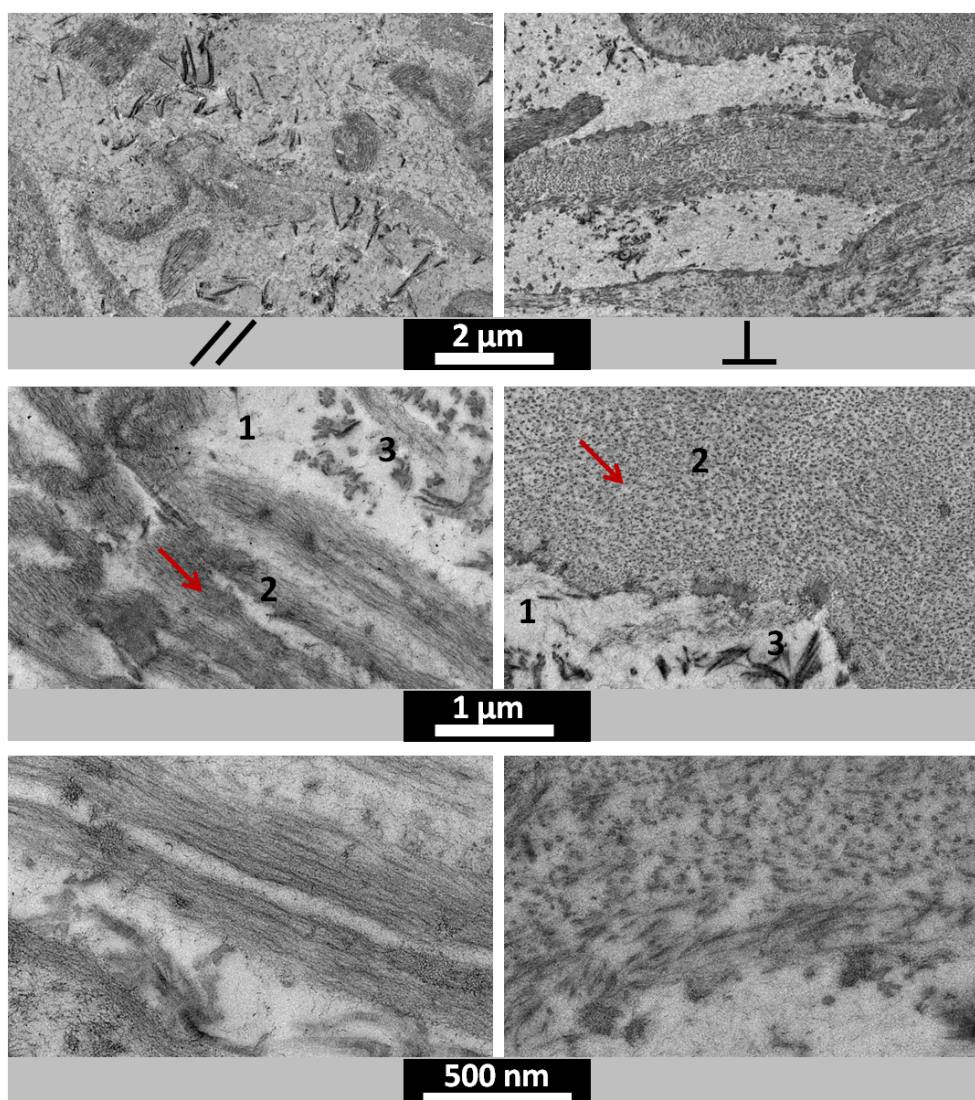


Figure 5.29: TEM sections along the thread axis (left //) and perpendicular (right ⊥) of collagen:alginate (5:1) threads incubated in DMEM at 37°C during 3 weeks.

Longitudinal (left) and perpendicular (right) threads sections images are presented in order to assess the main orientation of structures in the thread. At low magnification, fibrils

with 67 nm period striations are clearly observed and highly contrasted. The three different populations are still present: 1) alginate rich phase, 2) nanofibrils collagen phase and 3) alginate and collagen fibrils coexistence region at the interface between 1 and 2. After 3 weeks in DMEM, there are more collagen fibrils and they are larger than those found for CaCl_2 1M (Fig. 5.21 p 191), resulting in an overlap with phase 1. Regarding the phase 2, the main orientation of the nanofibrils bundles might be along the thread axis. Indeed, for perpendicular sections, those bundles appear as huge areas of dots (red arrow), which may correspond to transverse cut of collagen nanofibrils. For parallel sections, nanofibrils bundles are observed along their whole length. Finally, these bundles are separated by voids areas, which may be here again alginate phase with typical polymer chains (higher magnification).

In cell culture medium, fibrillogenesis of collagen molecules clearly continue to occur compare to CaCl_2 1M condition and leads to large striated fibrils formation in the "cosoluble" phase.

Remark: SHG observations were done on the hybrid threads (5:1) after 3 weeks of incubation in DMEM at 37°C (Fig. 5.30).

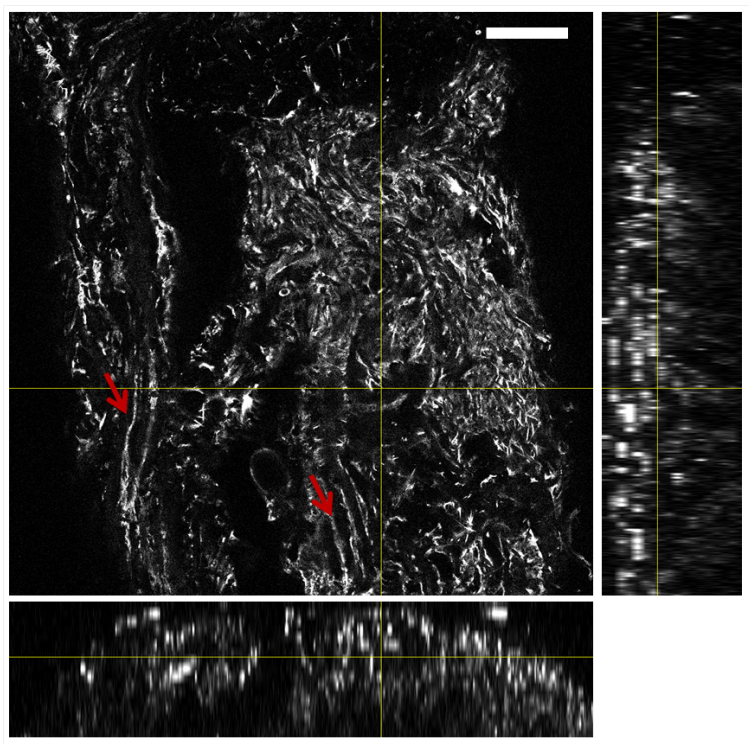


Figure 5.30: SHG image of collagen:alginate (5:1) thread section incubated 3 weeks in DMEM at 37°C and the respective projections as shown by the yellow lines. Scale bar: 100 μm .

Looking overall, SHG signal intensity is high and well-defined structures are visible, in contrast with hybrid thread left in CaCl_2 1M (Fig. 5.23 p 192). Dark areas are still observed and must correspond to alginate rich phase. On the transverse view (bottom), SHG signal appears more intense on the thread surface. This was already noticed for this thread condition in CaCl_2 1M. On the longitudinal view (right projection), we observe also the signal enhancement over 50 μm from the surface. Moreover, some light and darker layers are alternating in this outlying region. It reminds the parallel organization seen by TEM, where supposed alginate phase and collagen one are stacked on top of each other (Fig.

5.29 p 197, bottom left). Finally, straight structures parallel to the thread axis are pointed out by red arrows, suggesting an alignment in such area of collagen molecules in a overall more disordered and "tortuous" matrix.

5.5.3.3 Collagen stability: thermal analysis

The impact of cell culture medium on the collagen stability was investigated by DSC measurements on wet threads (pH 7.4) at a heating rate of 5°C/min. As shown in figure 5.31, pure collagen sample (red) has a denaturation temperature of 54°C, corresponding to the breaking of protein triple helices. This is in good agreement with values found in previous studies [14]. For pure alginate thread at 4 % (black), a non significant peak at 65°C due to thread dehydration is observed. While mixing collagen and alginate (green), a peak at 41 °C appears.

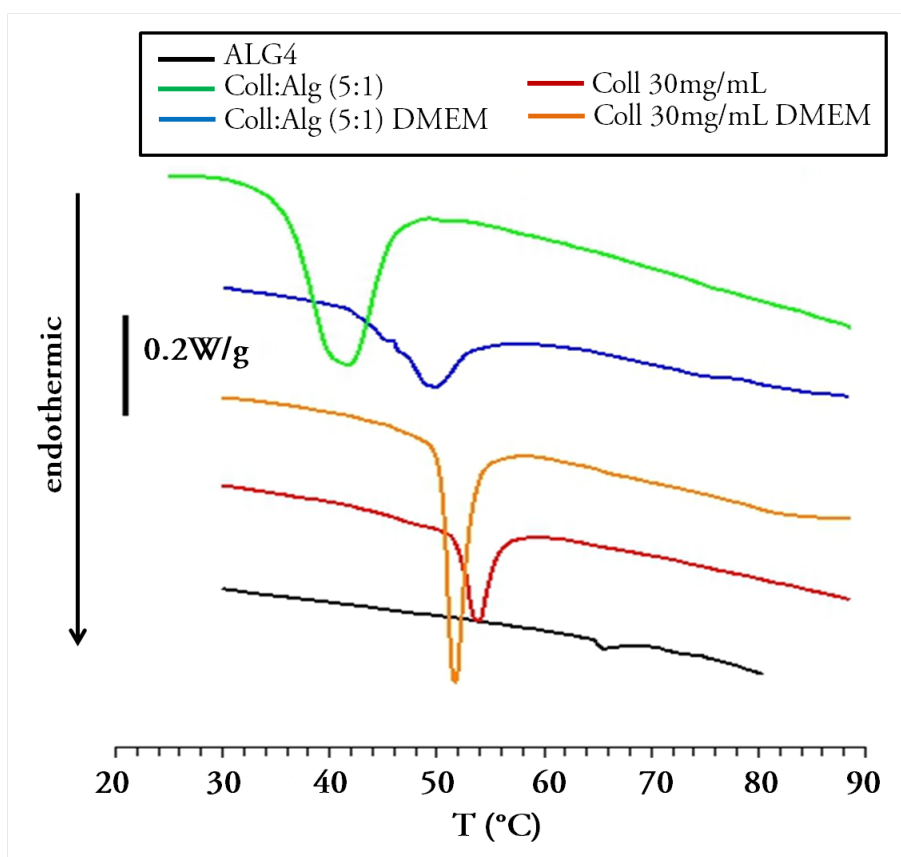


Figure 5.31: DSC measurements: denaturation of collagen 30mg/mL, coll:alg (5:1) and ALG4 threads kept either in their extrusion solutions (PBS 5X or CaCl₂ 1M respectively), or in DMEM during 2 weeks. Heating rate 5°C/min. Endotherms are down.

After 3 weeks in DMEM at 37°C, a slight temperature shift from 54 to 52°C is observed for pure collagen at 30mg/mL. In the case of hybrid thread, denaturation temperature rises from 41 to 50 °C suggesting the presence of a more stable protein conformation. In fact, we previously observed by TEM (Fig. 5.29 p 197) that fibrillar collagen population was evolving in DMEM and presented typical 67 m striations whereas in CaCl₂ 1M rare striated fibrils were seen (Fig. 5.21 p 191). As the quarter-staggered configuration is more stable, a higher temperature is needed to denature those structures.

5.5.4 Mechanical properties

Tensile testing results performed in DMEM for the three thread conditions to be seeded with cells are presented in table 5.2. According to the results obtained in extrusion buffer (table 5.1 p 193), pure collagen threads exhibit the same mechanical properties. This is consistent with results from microscopic and thermal analysis. For coll:alg (5:1), E and UTS respectively decrease from 0.84 to 0.31 and 0.11 to 0.032. Young Modulus stays higher than pure collagen thread at 30 mg/mL.

Condition	E (MPa)	UTS (MPa)	N
Coll 30 mg/mL	0.18 ± 0.03	0.066 ± 0.005	14
Coll:Alg (5:1)	0.31 ± 0.10	0.032 ± 0.08	5
Coll 60 mg/mL	1.23 ± 0.12	0.31 ± 0.01	5

Table 5.2: Tensile testing results: Young modulus E, Ultimate Tensile Strength UTS for threads made of collagen at 30 and 60 mg/mL and collagen:alginate at 5:1 ratio threads incubated in DMEM at 37°C during 3 weeks. N is the number of experiments performed.

In DMEM, hybrid threads swell resulting in a lower material concentration per unit area. From tensile testing, threads exhibit a more alginate-like behavior in CaCl_2 1M and a more collagen-like one in DMEM. In fact, calcium ions content is much lower in DMEM leading to a looser alginate network. This may be amplified and correlated with the thread swelling. Regarding collagen evolution, typical striations appear on collagen fibrils as seen by TEM (5.28) similar to the ones in pure collagen threads. We suggest that Young modulus is still higher in DMEM (than for pure collagen threads at 30mg/mL) because of collagen areas not aligned to the thread axis.

5.5.5 Discussion

While changing the thread bath condition from its fibrillogenesis buffer to cell culture medium, several structural changes were observed. In the case of pure collagen condition, threads at 30 and 60 mg/mL remain stable and only a slight diameter swelling was observed for the lowest concentration.

However, for mixed threads, several structural modifications occur leading to new properties. In fact, as presented in Chapter 2 (2.2.3.1 p 83), proteins (collagen) and polysaccharides (alginate) could interact in different way according to pH, ionic strength, temperature etc. We attempt here to explain those interactions when varying the bath condition parameters.

1) **Before extrusion**, we observed that collagen:alginate (5:1) mixed solution was opaque and white (Chapter 2, 2.33 p 84), suggesting a first interaction between the two systems. In fact, the mixed solution then in acetic acid (500mM) has a pH of about 3-4. At $\text{pH} < \text{pI}$ (isoelectric point), collagen is positively charged [15]. Moreover, at $\text{pH} > \text{pKa}$ (≈ 3.5) of alginate [16], the polysaccharide is deprotonated. In acidic solvent, collagen and alginate interaction is thus attractive and may lead to an associative phase separation ("2-phase" of precipitation) as a white solution is observed.

2) **While extruding** this mixture in CaCl_2 1M, three main changes occur: (i) pH increase to physiological value of 7.4 and (ii) alginate binding ions addition, (iii) high ionic strength.

With the pH increase, collagen fibrillogenesis begins. Moreover, collagen is still positively charged and alginate completely deprotonated. Indeed, as the ionic strength is high (1M), collagen pI value is shifted to 9 and so, $\text{pH} = 7.4 < \text{pI} = 9$, as shown by Freudenberg et al. [17]. Alginate is completely deprotonated and free G-blocks interact then with divalent ions through the gelation process and form a network of "egg-box" structures. At sight of our results (5.29), we obtained a first phase from the alginate and collagen precipitation still interacting; a second one rich in collagen for which fibrillogenesis begins, and a last one rich in gelled alginate.

3) **In cell culture medium**, the pH is the same but the ionic strength is lower than CaCl_2 1M. Here again, three main changes occur compared to previous situation "2": (i) ionic strength decrease, (ii) calcium ions content decrease, (iii) temperature increase. As the ionic strength decreases, $\text{pH} \approx \text{pI}$ for collagen [17], which becomes then almost neutral. As the calcium ions content is lower, the disassembly of alginate network begins. At the same time, ionic strength decreases, leading to thread swelling, which reveals the weakening of the network. Regarding the temperature, the conformation of the "free" chains of alginate or collagen molecules may change and turn to the unfolded state [18], increasing the number of reactive sites available for each species. From our results, we observed the growth of fibrils exhibiting the typical D-spacing of 67nm in the mixed phase of collagen and alginate. It is assumed that in culture medium, the alginate network, in which collagen was entrapped, swells and comes undone (5.29, 5.30). This gives enough space for the entrapped collagen molecules to assemble. The collagen rich phase, secondary to the repulsive interaction with alginate rich phase, can not benefit from this network expansion and the nanofibrils areas stay confined.

Thus, alginate may disturb the collagen fibrillogenesis, but when put in cell culture medium, the mixed thread are composed of collagen phases as stable as pure collagen ones and displaying better mechanical properties.

5.6 Conclusion

In this work, several physico-chemical parameters were varied in order to select the condition for which thread topography, structural organization and mechanical properties were improved.

First, we showed that the extrusion process aligns collagen inside the pure collagen threads. This effect was lower for collagen:alginate mixed threads.

Then, collagen threads extruded in PBS 5X were revealed to be more stable and present the best Young modulus and Ultimate Tensile Strength compared to those obtained for lower or higher ionic strengths. Then, we have shown that the higher the collagen concentration, the better the threads properties. Finally, the collagen:alginate mixture (5:1) equivalent to collagen at 30 mg/mL exhibited several promising properties and must be improved to reach those obtained for pure collagen at 60 mg/mL.

5.7 References

- [1] Francesco S Pavone and Paul J Campagnola. *Second harmonic generation imaging*. CRC Press, 2013. 146
- [2] A Ustione and DW Piston. A simple introduction to multiphoton microscopy. *Journal of microscopy*, 243(3):221–226, 2011. 146
- [3] Mathias Strupler. *Imagerie du collagène par microscopie multiphotonique*. PhD thesis, Ecole Polytechnique X, 2008. 147
- [4] Stéphane Bancelin. *Imagerie quantitative du collagène par génération de seconde harmonique*. PhD thesis, Ecole Polytechnique X, 2013. 148
- [5] Claire Teulon. *Imagerie quantitative de biopolymères par génération de second harmonique résolue en polarisation*. PhD thesis, Université Paris-Saclay, 2016. 148, 149
- [6] DA Kleinman. Nonlinear dielectric polarization in optical media. *Physical Review*, 126(6):1977, 1962. 150
- [7] Frédéric Gobeaux. *PHASES DENSES DE COLLAGÈNE DE TYPE I: TRANSITION ISOTROPE/CHOLESTÉRIQUE, FIBRILLOGENÈSE ET MINÉRALISATION*. PhD thesis, Université Pierre et Marie Curie-Paris VI, 2007. 157
- [8] Frédéric Gobeaux, Emmanuel Belamie, Gervaise Mosser, Patrick Davidson, and Sophie Asnacios. Power law rheology and strain-induced yielding in acidic solutions of type i-collagen. *Soft Matter*, 6(16):3769–3777, 2010. 181
- [9] Ivan Gusachenko, Gaël Latour, and Marie-Claire Schanne-Klein. Polarization-resolved second harmonic microscopy in anisotropic thick tissues. *Optics express*, 18(18):19339–19352, 2010. 185
- [10] Ivan Gusachenko, Viet Tran, Yannick Goulam Houssen, Jean-Marc Allain, and Marie-Claire Schanne-Klein. Polarization-resolved second-harmonic generation in tendon upon mechanical stretching. *Biophysical journal*, 102(9):2220–2229, 2012.
- [11] Erich Schuster, Johanna Eckardt, Anne-Marie Hermansson, Anette Larsson, Niklas Lorén, Annika Altskär, and Anna Ström. Microstructural, mechanical and mass transport properties of isotropic and capillary alginate gels. *Soft Matter*, 10(2):357–366, 2014. 191, 192
- [12] Frédéric Gobeaux, Gervaise Mosser, Anny Anglo, Pierre Panine, Patrick Davidson, M-M Giraud-Guille, and Emmanuel Belamie. Fibrillogenesis in dense collagen solutions: a physicochemical study. *Journal of molecular biology*, 376(5):1509–1522, 2008. 191, 192
- [13] Benoît GC Maisonneuve, Denis CD Roux, Peter Thorn, and Justin J Cooper-White. Effects of synthetic biomacromolecule addition on the flow behavior of concentrated mesenchymal cell suspensions. *Biomacromolecules*, 16(1):275–283, 2014. 194
- [14] Maria Victoria Tuttolomondo, Juan Manuel Galdopórpora, Lea Trichet, Hugo Voisin, Thibaud Coradin, and Martin Federico Desimone. Dye–collagen interactions. mechanism, kinetic and thermodynamic analysis. *RSC Advances*, 5(71):57395–57405, 2015. 199

- [15] John H Highberger. The isoelectric point of collagen. *Journal of the American Chemical Society*, 61(9):2302–2303, 1939. [200](#)
- [16] ARNE Haug and O Smidsrød. The effect of divalent metals on the properties of alginate solutions. *Acta Chem. Scand*, 19(2):341–351, 1965. [200](#)
- [17] Uwe Freudenberg, Sven H Behrens, Petra B Welzel, Martin Müller, Milauscha Grimmer, Katrin Salchert, Tilman Taeger, Kati Schmidt, Wolfgang Pompe, and Carsten Werner. Electrostatic interactions modulate the conformation of collagen i. *Biophysical journal*, 92(6):2108–2119, 2007. [201](#)
- [18] Amit K Ghosh and Prasun Bandyopadhyay. Polysaccharide-protein interactions and their relevance in food colloids. In *The complex world of polysaccharides*. InTech, 2012. [201](#)

Chapter 6

Collagen scaffolds and cell culture

“Even miracles take a little time.”

Fairy Godmother in *Cinderella*

Abstract

In this chapter, the mesenchymal stem cells (C3H10 T1/2) behavior was studied as a function of several parameters. First, we investigated the collagen concentration influence on cell morphologies and ability to colonize the threads. Preliminary in situ hybridization results of the target genes were given in order to assess qualitatively their expressions. Those first observations were promising. As cellular penetration was enhanced on collagen threads at 30 mg/mL, further quantitative analysis was performed enabling the comparison with corresponding collagen-alginate based threads. With this second study we tested the influence of : thread material, cell culture time, and mechanical loading during culture. We used Real time qPCR to quantify the expression of genes of interest (Col1a1, Tnmd and Scx) in order to characterize cell behavior. Characteristic tendon gene markers were expressed, which reflect the differentiation of C3H10 T1/2 into tendon-like cells.

Contents

6.1 Biological material and techniques	207
6.1.1 Cell culture	207
6.1.2 Cell culture on threads under tension	207
6.1.3 Confocal Fluorescence Microscopy	209
6.1.4 Histology and Hybridization in situ	210
6.1.5 Real time q-PCR	212
6.1.5.1 Principle	212
6.1.5.2 Protocol	213
6.2 Cell colonization study	217
6.2.1 Mechanical properties of threads cultured with cells	217
6.2.2 Cell migration within the threads at different collagen concentrations	218
6.2.3 Preliminary In situ Hybridization results	221
6.2.4 Conclusion	222
6.3 Behavior of stem-cells cultured on collagen based threads	223
6.3.1 Load influence of threads morphologies	223
6.3.2 Cell colonization over culture time and load condition impact analysis	224
6.3.3 Genes of interest expression analysis	226

6.3.3.1 Qualitative analysis	226
6.3.3.2 Quantitative analysis: Real time qPCR	227
6.3.4 Discussion	230
6.4 Conclusion	231
6.5 References	232

6.1 Biological material and techniques

Checking behavior of cells *in vitro* in contact with putative implantable scaffolds is a prerequisite before studying *in vivo* models. In the present work, we chose the cell line C3H/10T1/2 to check cells behavior, such as migration, adopted morphology and eventual differentiation when cultured on dense collagen threads.

6.1.1 Cell culture

Cell type: C3H/10T1/2

The C3H/10T1/2 cell line was established by CA. Reznikoff, D.Branchow and C.Heidelberg in 1973 from C3H mouse embryos. According to their studies, these cells have similar properties and stability as murine fibroblasts after prolonged culture. The cells are very sensitive to post confluence inhibition of cell division. C3H/10T1/2 are functionally similar to mesenchymal stem cells or multipotent stromal cells that means that they can differentiate into different cell types (bone, cartilage, adipose cells etc). This cell line was chosen to be cultured on dense collagen threads in order to observe their morphologies, migration and behaviors on them.

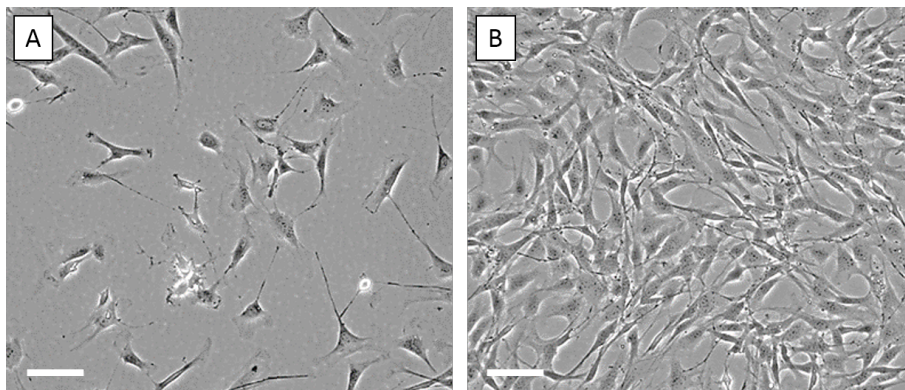


Figure 6.1: C3H/10T1/2 cells morphology at: A) low and B) high densities. Images from ATCC, scale bars: 100 μm .

Cell culture

C3H10T1/2 cells were cultured on culture flask of 75 or 150 cm^2 with Dulbecco's Modified Eagle's Medium (DMEM low glucose, pyruvate) supplemented with 10% fetal bovine serum (FBS), and penicillin/streptomycin (100 U/100 μg per mL). Cells are put in an incubated chamber maintained at 37°C and 5% CO₂. Passages 18 to 23 were used during experiments.

6.1.2 Cell culture on threads under tension

The protocol from Kapacee et al. [1] is adapted in order to put threads under static tension during the cell culture. Figure 6.2 presents the protocol used in our study. Threads are cut into segments of about 2 – 3 cm length and put under tension on already prepared SYLGARD silicon gel-covered wells (Dow Chemical, Midland, MI, USA), in which two 8 mm sutures (Ethican, Sommerville, NJ, USA) are pinned 20 mm apart as shown in Figure 6.2. Each collagen thread is seeded with 2 mL of cells in culture medium with 350000 cells and placed to incubation conditions. Control collagen threads without cells are also followed. Culture medium is renewed every two days. After 1, 7, 14 and 21 days,

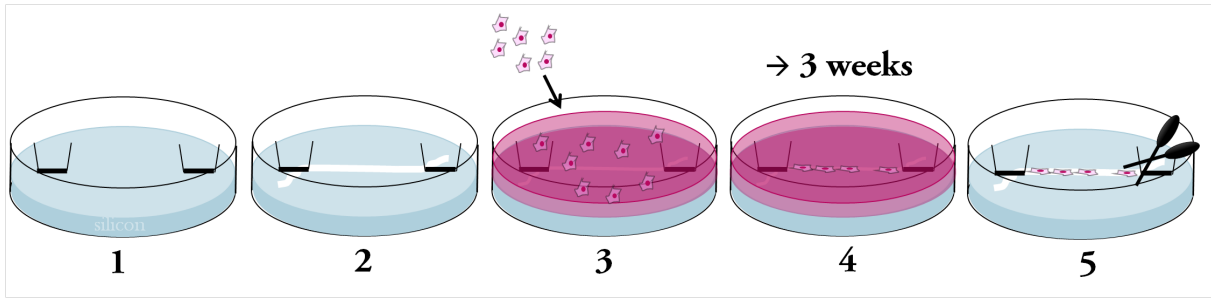


Figure 6.2: Protocol of cell culture under tension. 1) 6-well plate bases were covered with silicon gel (SYLGARD) and silk sutures are pinned with needles. 2) Threads are put under tension between the two sutures and 3) C3H10 T1/2 are added. 4) After 3 weeks of culture, 5) threads extremities are cut and observed by different techniques.

the threads in presence of cells and the controls were retrieved by cutting the two extremities. For microscopic analysis, they are fixed in a 4% of paraformaldehyde (PFA) in PBS solution. Cell cultures were performed both at the LCMCP and in collaboration with Delphine Duprez and Marie-Ange Bonnin from the Laboratoire de Biologie du Développement.

Static load range estimation

The explanation given below provides a reliable underestimate of the force applied. This estimation relies on the fact that the only force applied on the threads under tension is gravitational. Still, the threads extremities were also pinned apart in order to apply an additional tangent force, but the reproducibility was not easy and there was no possibility to measure these potential additional forces accurately.

A collagen thread pinned 20 mm (= 2L) apart can be considered as a flexible chain suspended between two points at the same height (Fig. 6.3). The thread is assumed to be almost cylindrical about its lowest point which is located at a height a from the anchored point altitude. The horizontal tension T_h is estimated from the catenary curve equation which relates this constant tension with the respective lengths L , a , the apparent linear density μ_{app} of the thread, and the gravitational force g [2]:

$$T_h = \frac{L^2 - a^2}{2a} \mu_{app} g$$

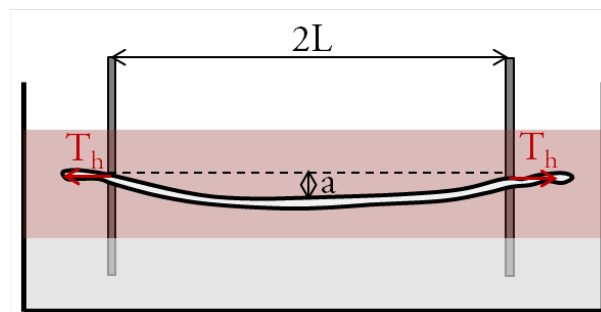


Figure 6.3: Scheme of collagen thread cell culture configuration under tension. The horizontal tension T_h is estimated by assuming that this situation is alike flexible chain suspended between two anchoring points.

Numerical application: The different values of the physical quantities are: $2L = 20\text{mm}$, $a \approx 1\text{mm}$, $g = 10\text{m/s}^2$. The apparent linear density μ_{app} is the linear density of the thread adjusted by the buoyancy: $\mu_{app} = \mu_{thread} - \mu_{water} = 0.12\text{ g/m}$ with $\mu_{thread} = 0.25\text{ g/m}$ and $\mu_{water} = \pi R^2 \rho_{water}$. We found an estimated horizontal tension of about: $T_h = 62.10^{-3}\text{mN}$. This corresponds to a strain of: $\frac{l-l_0}{l} = \sigma/E = \frac{T}{E\pi R^2}$ where E is the Young modulus of the thread and is about 0.3 MPa . We found a static strain $\Delta l/l_0 = 0.16\%$. This is small compared to strain order of magnitude (about 1%) in the study of Kuo et al.[3] while using cycling loading.

6.1.3 Confocal Fluorescence Microscopy

Principle

Confocal fluorescence microscopy allows 3D high resolution imaging (lateral: 140 nm ; axial: $1\text{ }\mu\text{m}$) of labeled biological samples with little background noise. In a confocal fluorescence microscope (Fig 6.4), the labeled sample is excited by a laser beam emitting generally in the field of visible or ultraviolet. The fluorescence is excited over almost the entire path of the beam. Thus, the fluorescence arising from out-of-focus positions represents an undesirable signal. In order to eliminate the majority of this spurious fluorescence, a pinhole is placed before the detector in the image focal plane of the microscope objective. This hole allows to obtain a very good axial resolution but also to improve the lateral resolutions. It is thus possible to scan the sample plane by plane at various depths and finally reconstruct 3D images.

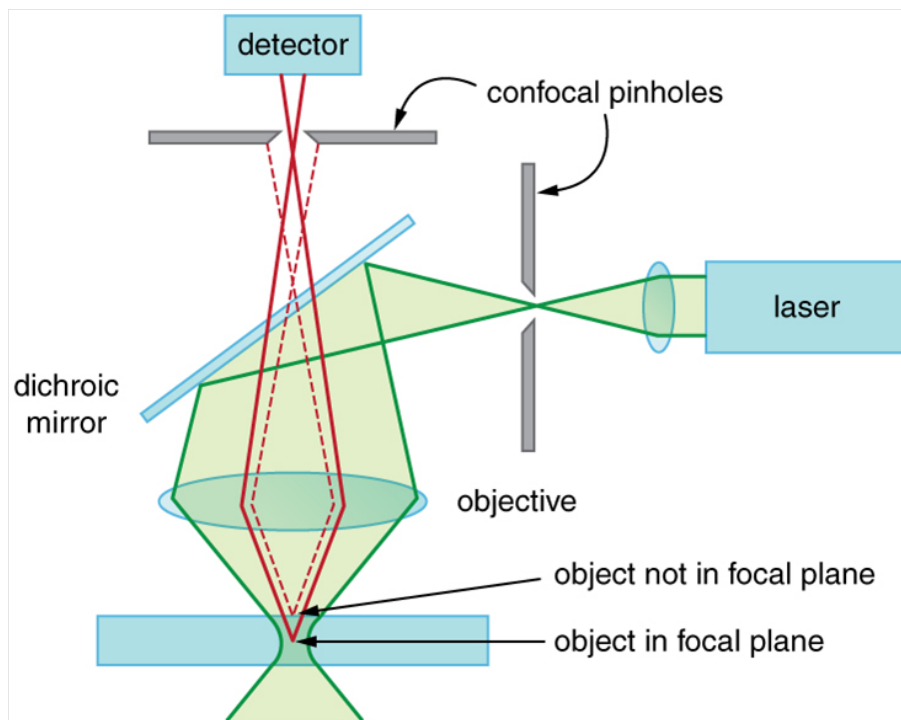


Figure 6.4: Scheme of confocal microscope: the laser beam illuminates a tiny region (through a first pinhole) of the sample in the focal plane. This light passes through the dichroic mirror and the second pinhole to a detector and a computer. The out-of-focus light is thus blocked. The pinhole is scanned sideways to form an image of the entire focal plane. The pinhole can then be scanned up and down to gather images from different focal planes and finally reconstruct 3D images. From "2-photons microscopy vs confocal microscopy" <https://cogsci.stackexchange.com>

The observations were performed with an inverted Leica SP5 or Leica SP2 multipho-

ton laser scanning confocal microscope by Adèle Mauroux (PhD student under the direction of Laurent Müller) at the Collège de France. Images analysis and projections were done with ImageJ software.

Fluorescent sample staining

Two fluorochromes are used to image the cells cultured on the collagen threads: DAPI (4',6-diamidino-2-phenylindole) which binds to DNA (nucleus) and Alexa Fluor 488 Phalloidin which binds to cells actin filaments (cytoskeleton). DAPI and Alexa Fluor excitation wavelengths are respectively 358 and 495 nm and their emission wavelengths 461 nm and 518 nm (Fig 6.5). There is an overlap region, which can lead to receive some DAPI signal in the Alexa channel.

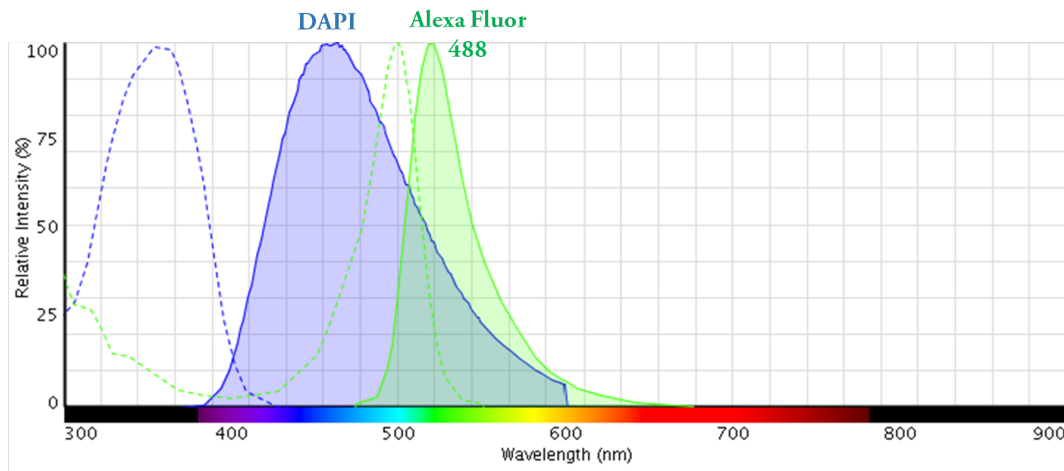


Figure 6.5: Fluorescence spectra of DAPI (blue) and Alexa Fluor 488 Phalloidin (Green). Dashed lines are the excitation plots. Emission plots are represented by colored area. From "Fluorescent SpectraViewer" <https://www.thermofisher.com>.

Sample preparation: Threads cultured with cells are fixed in solution of 4% PFA (diluted in PBS). Cells are then permeabilized by using 0.2% Triton X-100 for 15 min. This step allows the different fluorochromes to access their respective targets inside the cells. After rinsing with PBS solution, threads with cells are immersed in Alexa Fluor 488 Phalloidin (dilution: 1:200 in PBS) left in the dark at 4°C during 1 hour. Several PBS rinsing are needed to remove Alexa excess. Finally, the DAPI solution (dilution: 1:50000 in PBS) is added during 15 min and rinsed before the microscope observations. The same procedure is performed for SHG observations coupled with fluorescent microscopy.

6.1.4 Histology and Hybridization in situ

To examine the morphology, architecture and composition of the cells potentially present in threads, several techniques are available such as histology and in situ hybridization (ISH). ISH was also performed in collaboration with Delphine Duprez and Marie-Ange Bonnin from the Laboratoire de Biologie du Développement. Threads with cells are first removed and fixed at day 1, 7, 14 and 21 in a 4% of paraformaldehyde diluted in PBS solution. Then, they are dehydrated by successive graded ethanol baths, xylene solutions, and finally liquid paraffin. The successive baths gradually expose the sample to changes in hydrophobicity, and avoid damaging cells. Threads in liquid paraffin are placed into a mold with more paraffin. The wax finally cools down and forms a block that can be held

in a microtome and sliced . The transverse threads sections of $8\mu\text{m}$ are mounted on a slide in preparation for component identification via staining or in situ hybridization.

Commonly used staining of **Hematoxylin and Eosin** is performed on those threads slices. Hematoxylin colors the cell nucleus in dark blue and Eosin colors the remaining cell components in pink. This staining allows us to know if there are cells or not in the threads.

In situ hybridization allows localizing the expression of a gene of interest in its cellular environment. First, successive pre-treatments (deparaffinization, enzymatic digestion, permeabilization...) are performed on threads sections mounted on slides in order to avoid non specific hybridization and to access the cell genetic material.

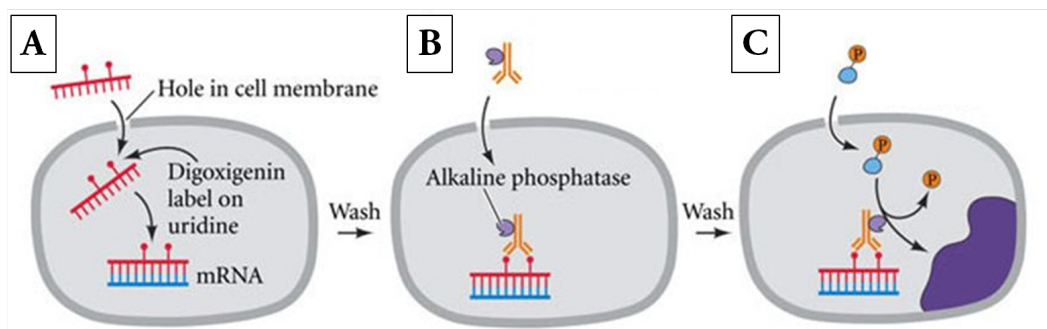


Figure 6.6: In situ hybridization main steps: A) Membrane permeabilization, denaturation and addition of the probe. Hybridization occurs when the probe combine to the targeted RNA single strand. B) Addition of the antibody which binds to the probe. C) Colorless compound addition which becomes purple if the gene of interest was present. Adapted from [4].

Then, the mRNA contained in cells and probes are denaturated (double to simple stranded RNA) by increasing the temperature. The probe is RNA strand labeled with a dioxygenin molecule (DIG). This probe will specifically hybridize (combine, base-pair to the corresponding mRNA single strand) to the mRNA of interest (Fig 6.6, A). An alkaline phosphatase conjugated with anti-DIG antibody is designed to detect the dioxygenin on the probe (Fig 6.6, B). Finally, a colorless compound that becomes purple when the phosphatase is removed, is added (Fig 6.6, C). Washing steps are necessary between the different probe and antibody additions to remove non-reagents excess.

Choice of genes of interest: Based on the literature [5] , four mouse genes were chosen for the in situ hybridization:

- **Myogenic Differentiation1 (MyoD1):** this gene encodes a nuclear protein which plays a major role in the regulation of muscle differentiation. It was chosen as a control: if mesenchymal stem cells (MSC) differentiate into muscle-like cells, ISH will reveal this character. On the contrary, if MSC differentiate into another cell type, the expression will be lower and so its signal by ISH too. [5]
- **Collagen, type I, alpha 1 (Col1a1):** this gene encodes the alpha-1 subunit of the fibril-forming type I collagen which is the most abundant protein in most of connective tissues such as tendon. [5]
- **Scleraxis (Scx):** this gene encodes a protein (transcription factor) involved in mesoderm and expressed during the embryonic development of tendons and ligaments. [6]
- **Tenomodulin (Tnmd):** this gene encodes a type II transmembrane glycoprotein which is expressed at high levels in tenocytes and ligamentocytes. [7]

6.1.5 Real time q-PCR

6.1.5.1 Principle

The Real-time quantitative Polymerase Chain Reaction allows to quantify the amplification of a targeted DNA molecule in real-time. It is divided in three main steps as shown in Figure 6.9.

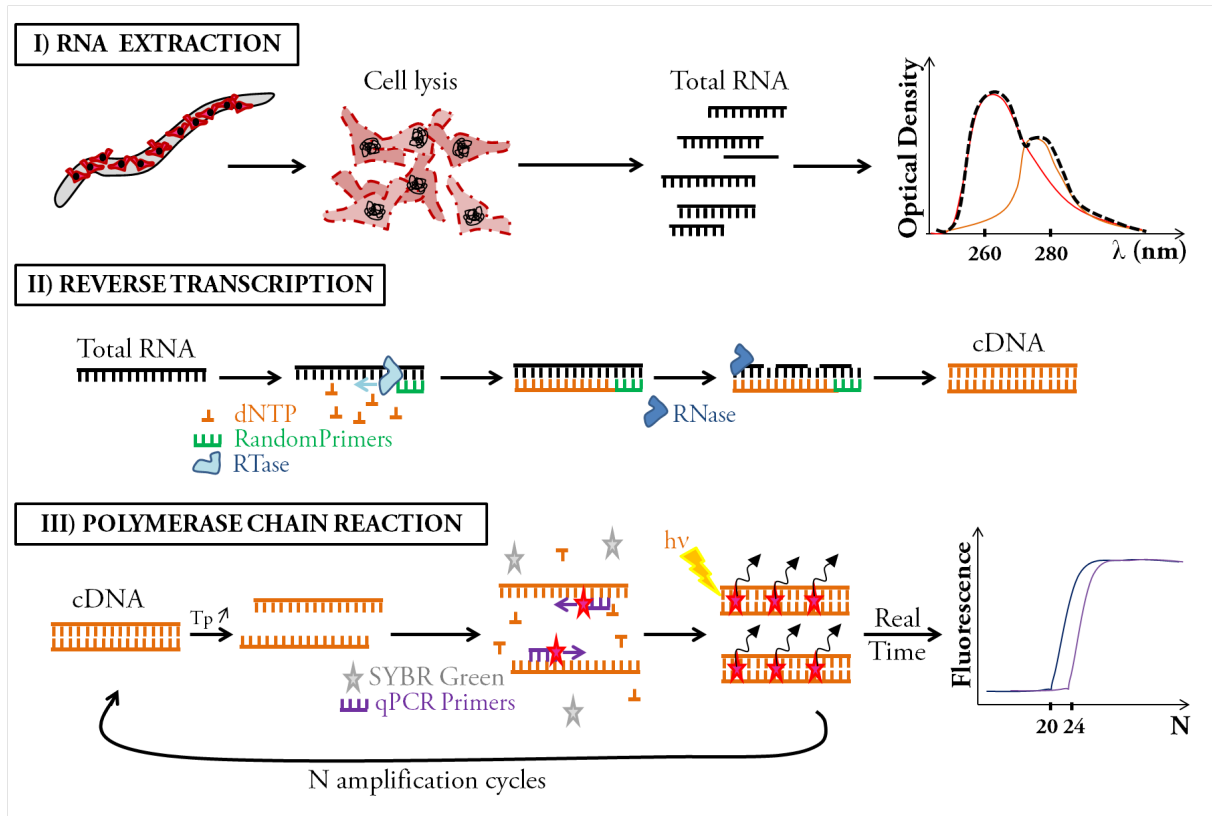


Figure 6.7: Scheme of real time qPCR main steps: I) RNA extraction of cells cultured on collagen threads, II) Reverse transcription to synthesize cDNA from RNA strands, III) Polymerase Chain Reaction, which allows the amplification of cDNA material and thus quantification of gene expression.

- I) **RNA extraction**: the collagen threads cultured with cells are removed from the 6-well plates and cell lysis is performed with Trizol in order to collect all the genetical material. Then, the RNAs are extracted through several phase separation, purification and centrifugation steps. All this procedure must be performed in very clean environment as RNase components and contaminants are present everywhere. Finally, the total RNAs concentrations are measured by spectrophotometry.
- II) **Reverse transcription (RT)**: this step consists in synthesizing a complementary double-stranded DNA from total RNA. First, a short single-stranded random primer anneals to the RNAs, which provides an initiation point for the reverse transcriptase (RTase) enzyme. In the presence of deoxynucleotide triphosphates dNTPs (dA, dT, dG, dC), the reverse transcriptase extends the primer to make a complementary DNA strand. Then, the RNA template is digested by ribonuclease (RNase) and the complementary strand of first cDNA is synthesized.
- III) **Polymerase Chain Reaction (PCR)**: this last step amplifies the DNA fragments of interest in order to be detected. First the temperature is increased in order to denature double-stranded into single -stranded cDNA. Then, specific chosen primers

anneal to their cDNA of interest. In the presence of dNTPs elongation of the complementary strand occurs. Then, SYBR green which can bind to all types of double-stranded nucleic acids, is intercalated while the strand is elongated. Once fixed, it becomes a very good fluorophore and can be detected under excitation. All this corresponds to one cycle. After one cycle, we obtained 2^n copies of labeled cDNA where n is the initial number of double-stranded cDNA. At the end of each cycle, the fluorescent signal is measured allowing the quantification of the gene expression.

6.1.5.2 Protocol

RT-qPCR was performed to assess the mechanical load and time influence on the gene expression. For this purpose, collagen-based threads seeded with cells under static tension or not were removed at day 1, 7, 14, 21 to extract cells genetical material. For each condition, biological samples (threads with cells) sixplicat were analyzed by RT-qPCR.

Extraction and purification of total RNAs

The collagen-based threads cultured with cells are first immersed in a guanidium thiocyanate-phenol-chloroform solution, called TRIzol, which contains phenol (pH = 6). This solution allows lysing the cells and extracting the RNAs. The guanidium thiocyanate forms a complex with RNAs and protect them. In order to be sure to extract all the RNAs and to lyse the maximum number of cells that may have penetrated the matrix, the threads are scraped with cell scrapers. The supernatant is then collected in tubes and placed for storage at $-80\text{ }^{\circ}\text{C}$.

After thawing and centrifugal steps, it is possible to eliminate all aggregates of collagens which would have been dragged in TRIzol. The supernatants are then collected and chloroform solution is added. After stirring, an emulsion is formed with RNAs will moving into the chloroform phase. Centrifugation allows separating the two phases: the phenol containing the cell debris and the genomic DNA at the bottom, and, the chloroform containing the RNAs at the top (and between them a phase composed of proteins). The RNAs are then purified with an RNeasy kit (Qiagen, France). Briefly, the supernatants (chloroform + total RNA) are removed and 70% ethanol is added. The samples are then poured onto extraction columns. Total RNAs greater than 200 nucleotides in size bind to the column membrane and the other elements are removed by centrifugation. The column is then washed with a solution containing guanidine. A solution containing a high concentration of NaCl is added and allows the elution of the proteins still present. This is repeated a second time and the tubes are then eluted with RNase-free distilled water. This operation is repeated and the final aliquot is constituted by the total RNAs considered to be purified. The purified samples are stored at $-80\text{ }^{\circ}\text{C}$.

Determination of total RNAs concentration

Before carrying out the reverse transcription, the total RNAs concentrations are first measured by spectrophotometry. The absorption spectrum of the nucleotides shows a maximum peak at 260 nm, that of the aromatic amino acids at 280 nm. Thus, a double reading at 260 and 280 nm and the ratio of optical densities (OD) $\text{OD}_{260}/\text{OD}_{280}$ determines the degree of contamination by proteins. A ratio lower than 2 is a sign of high protein contamination while ratios between 1.8 and 2.2 are considered acceptable.

Reverse transcription (RT)

The aim of the reverse transcription is to transform the extracted RNA into complementary DNA (cDNA) in order to carry out the polymerase chain reaction (PCR). To do so, non-specific primers capable of binding randomly to the RNAs are added to the RNAs aliquots. A first step at 65°C allows the denaturation of the secondary structures of the RNAs and fixing the primers. The tubes are then placed in ice and several reactants are added: 5X reaction buffer, DTT (Dithiothreitol), a reducing agent which destabilizes the Rnases, dNTPs and the necessary enzyme (reverse transcriptase of the Moloney virus of murine leukemia). A step at 37°C allows the action of the enzyme and it is followed by a passage at 70°C which stops the reaction. The products of the RT are stable cDNAs which can be stored at -20°C.

Choice of PCR primers

In order to prepare the necessary primers for qPCR, the sequences of the mRNAs of the genes were searched in the NCBI database (www.ncbi.nlm.nih.gov).

Name	Direction (F or R)	Sequence
36B4	F	ACCTCCTTCTTCCAGGCTTT
36B4	R	CTCCCACCTTGTCTCCAGTC
Colla1	F	TGGAGAGAGCATGACCGATG
Colla1	R	GAGCCCTCGCTTCCGTACT
Scx	F	CCTTCTGCCTCAGCAACCAG
Scx	R	GGTCCAAAGTGGGGCTCTCCGTGACT
Tnmd	F	AACACTTCTGGCCCGAGGTAT
Tnmd	R	AAGTGTGCTCCATGTCATAGGTTTT

Table 6.1: Table of the primers

The primers are in freeze-dried form and must be reconstituted in 1 mL of sterile water and then diluted in order to reduce their concentration to 7 µM. The primers pairs (Reverse R and Forward F) are then tested in conventional PCR under the conditions that will be used for the PCRs. For each pair, two mixtures are made: one contains a standard cDNA load, which is a mixture of 1 µL of all the samples, and makes it possible to verify that the primers amplify the target in a specific manner; an other mix contains no cDNA, but sterile water and ensures that the primers do not form dimers after 40 cycles. Once these two steps have been validated, the primers can be used in qPCR.

Quantitative Polymerase Chain Reaction (qPCR)

Genes of interest have been studied in qPCR in order to compare their expression under different conditions and as a function of time. This technique consists in measuring the quantity of amplicons produced in each cycle thanks to a fluorescent intercalator, here SYBER Green. The intensity of the fluorescence increases with each cycle until it exceeds the detection threshold defining the Ct (cycle threshold), ie the number of cycles after which the number of amplicons formed exceeds the background noise. The smaller the Ct, the higher the initial target cDNA amount. It is thus possible to compare the number of initial copies between the different samples because at Ct, each tube has the same number of amplicons.

Initially, the pairs of primers are tested under the conditions of qPCR using standard samples. On a 96-well plate, for each tested pair of primers, a 5-point standard range, which

are dilutions of the standard (the same as for testing the primers in conventional PCR), are carried out at dilutions: 1/5, 1/25, 1/125, 1/625, 1/3125 with two negative controls (sterile distilled water) per range. Each range point is made in duplicate. The mixtures are prepared using the LightCycler 480 SYBR green I master kit containing the SYBR Green intercalant which attaches to the double-stranded DNA. The implemented temperature program is identical to that used in conventional PCR (but where the cycle times are reduced to a few seconds, here 10s-15s-15s) and the intensity is measured at the end of each cycle by a Light Cycler 480 system (Roche). The results are then analyzed using the LightCycler 480 software and allows us to determine the efficiency of the PCR.

First, the specificity of the amplification is determined through the calculation of the melting curve (Fig. 6.9). The melting curve corresponds to the fluorescence variation as a function of the temperature. When the temperature reaches the T_m (melting temperature) of the amplicon, it degrades and the fluorescence falls. Thus, when only one amplicon is present, a single fluorescence drop is recorded, which proves the specificity of the pair of primers (R and F). This step allows us to verify that the T_m of the amplicon corresponds to the one expected during the preparation of the primers.

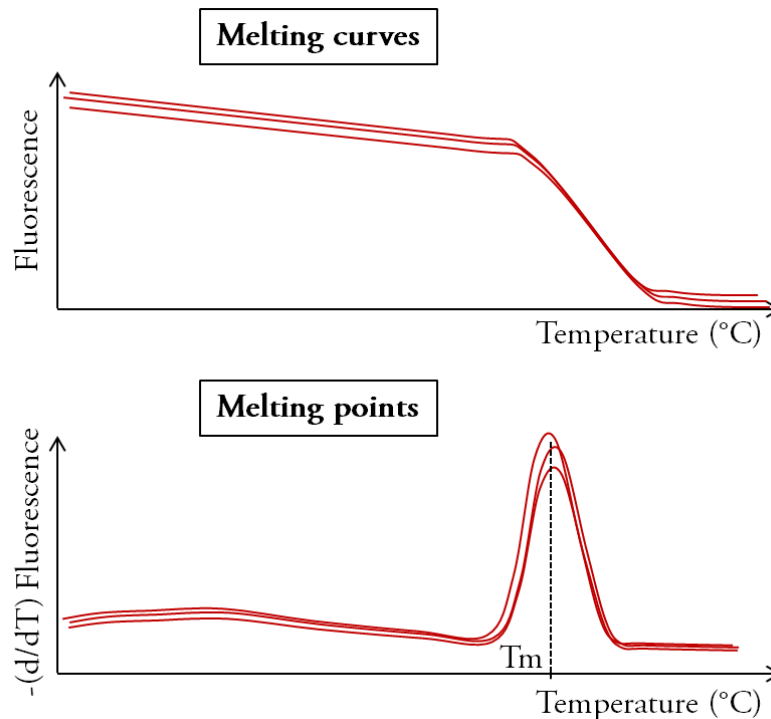


Figure 6.8: Schemes of melting curves for the calibration points (top) and its respective derivative curve (bottom) with the melting temperature T_m .

Then, the efficiency (curve slope) of each pair is calculated by introducing the cycle threshold C_t (Fig. 6.9) and by assigning arbitrary values to the (1/5, 1/25, 1/125, 1/625, 1/3125) dilutions. If the efficiency is greater than 1.85 then the pair of primers may be used for qPCR under these conditions.

For each gene tested, a 384-well plate was used. Each sample (thus each biological triplicate for each condition for each time) is made in triplicate, for the gene of interest and for the 36B4 reference gene [8]. Moreover, on each plate, two reference ranges (for the gene of

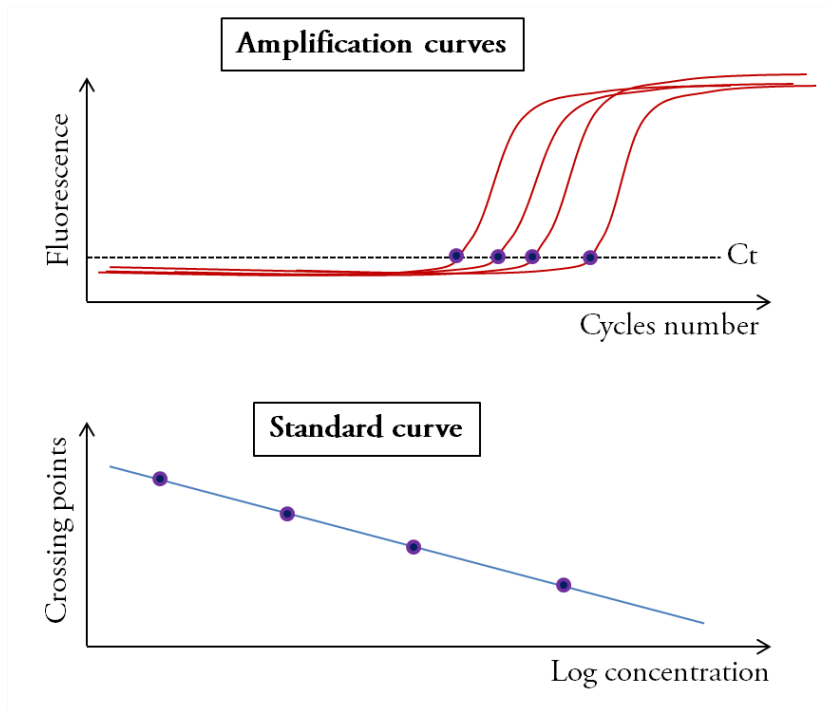


Figure 6.9: Scheme of the amplification curves with the cycle threshold C_t definition and the standard curve for the efficiency calculation

interest and for the reference gene) are produced identical to those made for primers testing. The relative quantification technique used consists in transferring the C_t obtained on the standard points realized at the same time as the samples, which gives arbitrary values for each C_t measured. The arbitrary values of the samples of the target gene are then compared with the arbitrary values of the samples of the reference gene, which gives a ratio Target Gene/Reference Gene for each sample of the plate. It is this ratio, given by the software and that takes into account the efficiency, which we then use to compare the different conditions. For this purpose, a sample is chosen as the calibrator point and a second ratio of Studied condition ratio/Reference condition ratio is calculated.

Here the reference condition used is one of the biological triplicatas: **Coll 30mg/mL D7 under static load** which therefore has a ratio of 1. The ratios of the other conditions are then compared to each other and presented in the form of histograms.

Statistical analysis

The gene expression results of real time qPCR are presented as the mean value \pm SD (standard deviation). The statistical significance was assessed using one way analysis of variance (ANOVA) followed by Tukey posthoc test (comparing all pairs of groups) while comparing 3 data sets. We used this test for evaluating the influence of cell culture time as 3 different times. The significance level in all statistical analyses was set at a probability of $P < 0.05$. Example: collagen 30 mg/mL under static load at 1w, 2w and 3w were compared together and if there was a significant difference, it also referred to the time = 1 week. If significance was revealed between 2 and 3 weeks, it was signaled. For the comparison of two relevant data sets (ex: coll 30 mg/mL and col:alg both under static load at 1w), unpaired t test was used. Here again, the significance level was set at a probability of $P < 0.05$. We performed all data analysis with the software Prism (Graphpad).

6.2 Cell colonization study

In this first study, the cell colonization is studied as a function of collagen threads concentration (30 and 60 mg/mL) produced as previously described (Chapter 5 5.4.1 p 180). The collagen threads with cells are put under static load during 3 weeks. First, we will present the tensile testing results of the threads seeded with cells. Then, we will observe the cell adhesion and migration by SHG microscopy coupled with fluorescence. Finally, four genes will be tested to assess qualitatively the mesenchymal stem cells character after being cultured 3 weeks on collagen threads.

6.2.1 Mechanical properties of threads cultured with cells

Tensile testing were performed after 3 weeks of cell culture on collagen threads under static load. Figure 6.10 shows the results obtained for such threads and the respective control either in fibrillogenesis buffer or DMEM as previously analyzed.

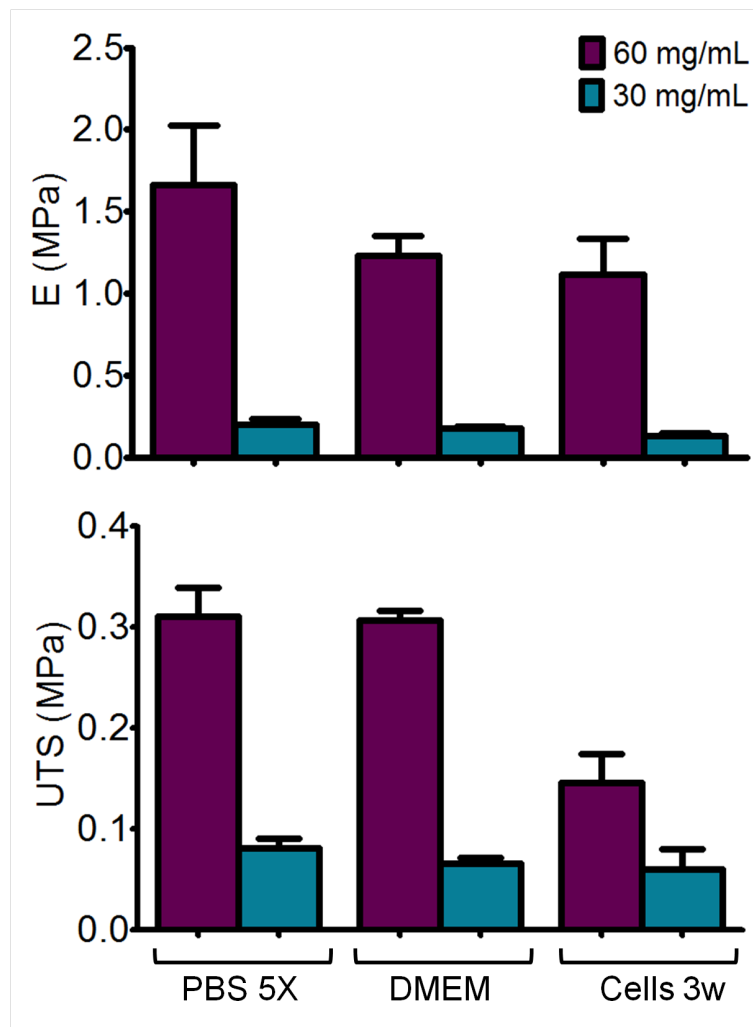


Figure 6.10: Tensile testing results of collagen threads at 30 mg/mL (blue) and 60 mg/mL (purple) seeded with cells and cultured over 3 weeks under static load and their respective controls. Top: Young's modulus and Bottom: Ultimate Tensile Stress

Collagen threads at 60 mg/mL seeded with cells exhibit the best mechanical properties with $E = 1.11 \pm 0.30 \text{ MPa}$ and $UTS = 0.14 \pm 0.04 \text{ MPa}$ compared to collagen threads with

cells at 30 mg/mL. Young modulus is almost 10-fold and UTS 3-fold higher when the collagen thread concentration is 60 mg/mL. We can also notice that there is a slight decrease of both E and UTS for threads with cells compared to their controls in PBS 5X and in DMEM without cells for the two concentrations. UTS for collagen threads at 60 mg/mL with cells has a higher decrease compared to the controls. These decreases might be explained by the cell sheath around the threads which sometimes breaks away at the clamping jaw level leading to a few sliding of the thread during the tensile testing. Some set-up improvements will be performed to avoid this kind of artifacts.

Limited literature was found about the mechanical properties of collagen scaffolds seeded with cells *in vitro*. In most of the studies, cells were directly put inside the collagen based construct.

Gentleman et al. performed tensile testing until failure of collagen threads at 10 mg/mL [9]. Post extrusion process of dehydration and cross-linking improved their mechanical properties as explained in the previous Chapter 5. However, relative analysis can be done from their collagen constructs study with and without cells. These collagen fibers (N=50) were embedded in a cell laden collagen gel (2.77 mg/mL) and cultured under static load during 25 days. The tangent moduli were compared with the corresponding scaffold without cells. They found a significant difference between the two constructs: the moduli of cell laden construct is almost 1.7-fold higher than the one without cells. In this case, cells improve mechanical properties of the constructs.

Kim et al. used 3D bioprinting to fabricate collagen based construct laden with cells and prior cross-linked with tannic acid [10]. In the case of pure cell laden collagen scaffold (40 mg/mL), they obtained Young's modulus E of 0.04 MPa. In our case, with collagen threads at 30 mg/mL, E is 3-fold higher which is quite promising.

Chen et al. produced cell laden collagen rings at various collagen concentrations (0.5 to 2 mg/mL) [11]. No post processing was performed. They showed that the modulus and UTS decreases while increasing the collagen concentration of their cell constructs. Its maximum (about 80 kPa and 35 kPa for modulus and UTS respectively) is reached for the collagen concentration of 0.5mg/mL. In our case, the opposite trend is observed and our results are significantly higher. But it should be kept in mind that cells may act differently if they are put from the outside or directly inside the collagen scaffold.

6.2.2 Cell migration within the threads at different collagen concentrations

Cell migration within the threads was followed by SHG microscopy coupled with fluorescence at 3 and 4 weeks of cell culture for both collagen concentrations. Figure 6.11 displays the results obtained for collagen signal (Green) and cells fluorescence (Red and Blue).

Collagen concentration effect: at 30 mg/mL and 60 mg/mL, C3H10 T1/2 cells covered the entire threads surface resulting in a cell multilayer of about $50\mu m$ representing around 5 cellular layers. In the case of collagen thread at 30 mg/mL at 4 weeks, we suspect the cell sheath to be ripped of the thread during handling. In all cases, cells adhere on the threads and proliferate a lot. The most notable concentration effect is the cell penetration. At

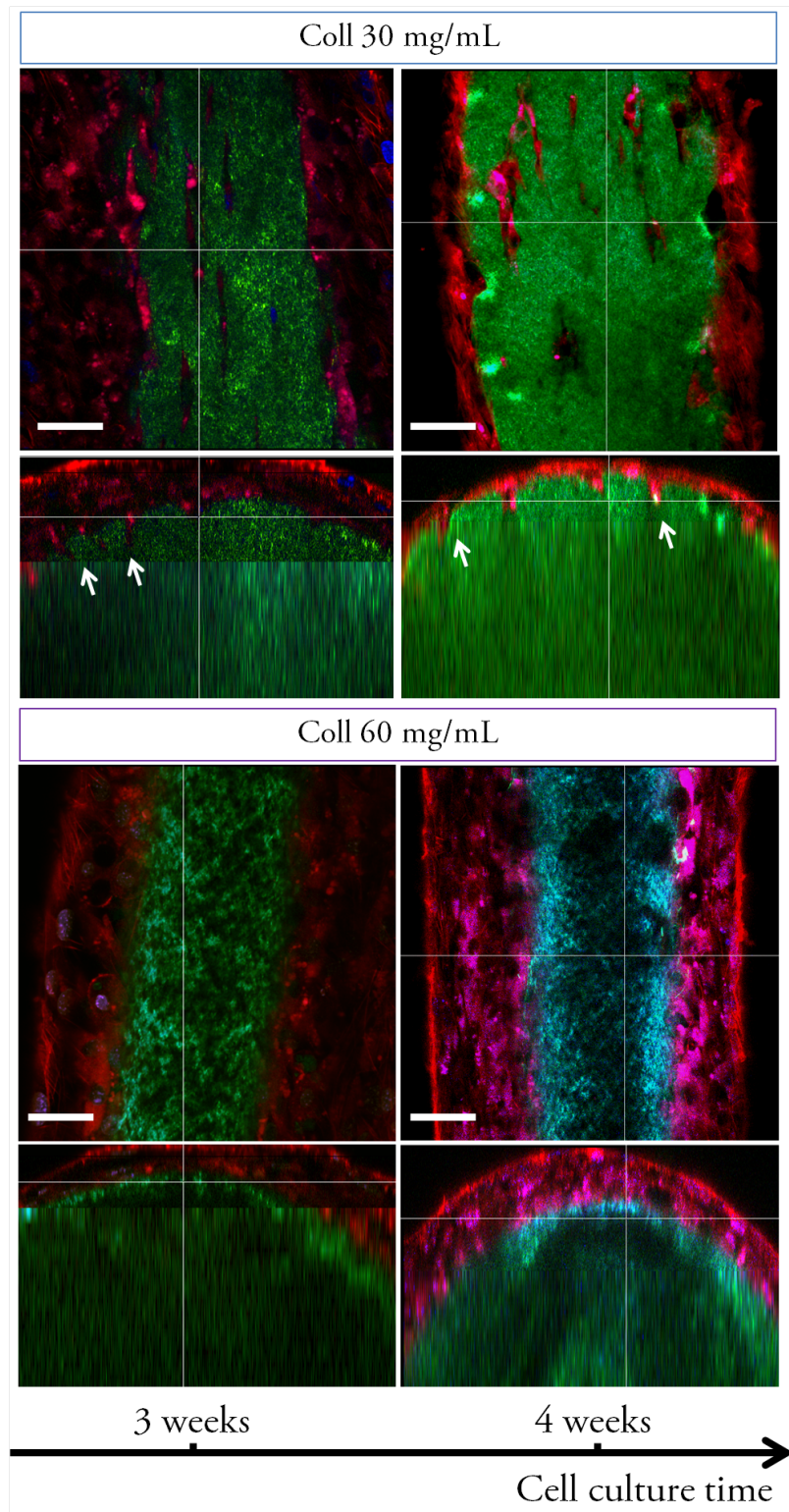


Figure 6.11: SHG images coupled with fluorescence of collagen threads seeded with C3H10 T1/2 cells during 3 weeks at 30mg/mL and 60mg/mL, under static load. Their respective cross sections projection are also given (bottom). Green: SHG signal; Red: Alexa Fluor 488 Phalloidin; Blue: DAPI. Scale bar = 50 μ m.

30 mg/mL, several holes are observed in the collagen threads where SHG signal is zero. Cells clearly invade those holes which are assumed to be created by cells through collagen matrix digestion as shown by Helary et al. [12]. In fact, without cells, such straight holes

were not observed (Chapter 5 5.4.1 p 180) on collagen threads. Thus, cells penetrate over $30\mu\text{m}$ at 30 mg/mL whereas at 60 mg/mL, they stay at the threads surface. This might be explained by the collagen density which is higher for 60 mg/mL and so the collagen "network" does not allow the cells to enter easily. Moreover, the stiffness is not the same which can also explain this observation.

Cell culture time effect: for cell cultures time of 3 or 4 weeks, the cell sheath thickness is almost the same for both conditions. No clear effect on the cell penetration is observed at 30 mg/mL. We can notice that cells do not seem to suffer from the high confluence and stay alive event after 4 weeks of culture.

Axis effect: at 30 mg/mL, straight holes in the collagen thread are observed. Each hole is equivalent to the size of one or two elongated cells. Their shape is aligned along the static load axis. Moreover, it has been shown that collagen thread surface is aligned along its longitudinal axis which can also induce cell orientation. Figure 6.12 shows the cell sheath surfaces. The cell actin filaments give the main orientation of the cells which is underlined by orange arrows. They follow the axis of the thread which is the same as the load axis. Thus it cannot be yet distinguished which mechanism is responsible for this cell direction. Observations of collagen threads seeded with cells without tension would be performed to answer it.

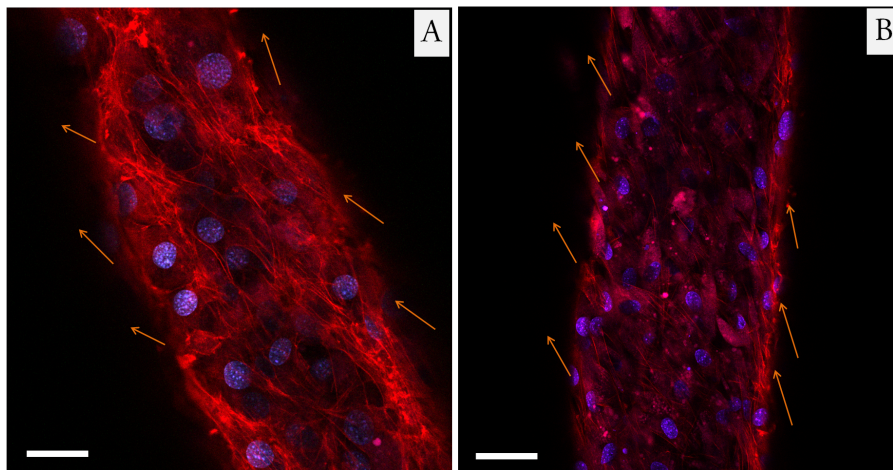


Figure 6.12: SHG images coupled with fluorescence of cell sheath surfaces on collagen threads at A)30mg/mL and B)60mg/mL, under static load. Red: Alexa Fluor 488 Phalloidin; Blue: DAPI. Orange arrows are eye guidelines to see the cell actin filaments main orientation. Scale bar = 50 μm .

6.2.3 Preliminary In situ Hybridization results

In situ hybridization was performed on collagen threads at 30 and 60 mg/mL after 3 weeks of cell culture with C3H10 T1/2. As previously introduced ISH allows us to assess qualitatively the gene expression of cells. These mesenchymal stem cells may differentiate under appropriate conditions (transcription factors, growth factors or mechanical stimulation) [13]. Figure 6.13 presents the results obtained with the four genes of interest. First, we can notice that cells penetrate more in the collagen thread at 30 mg/mL than collagen 60 mg/mL as previously observed by SHG with fluorescence. It is clearly visible on Tnmd images (Fig. 6.13 bottom left).

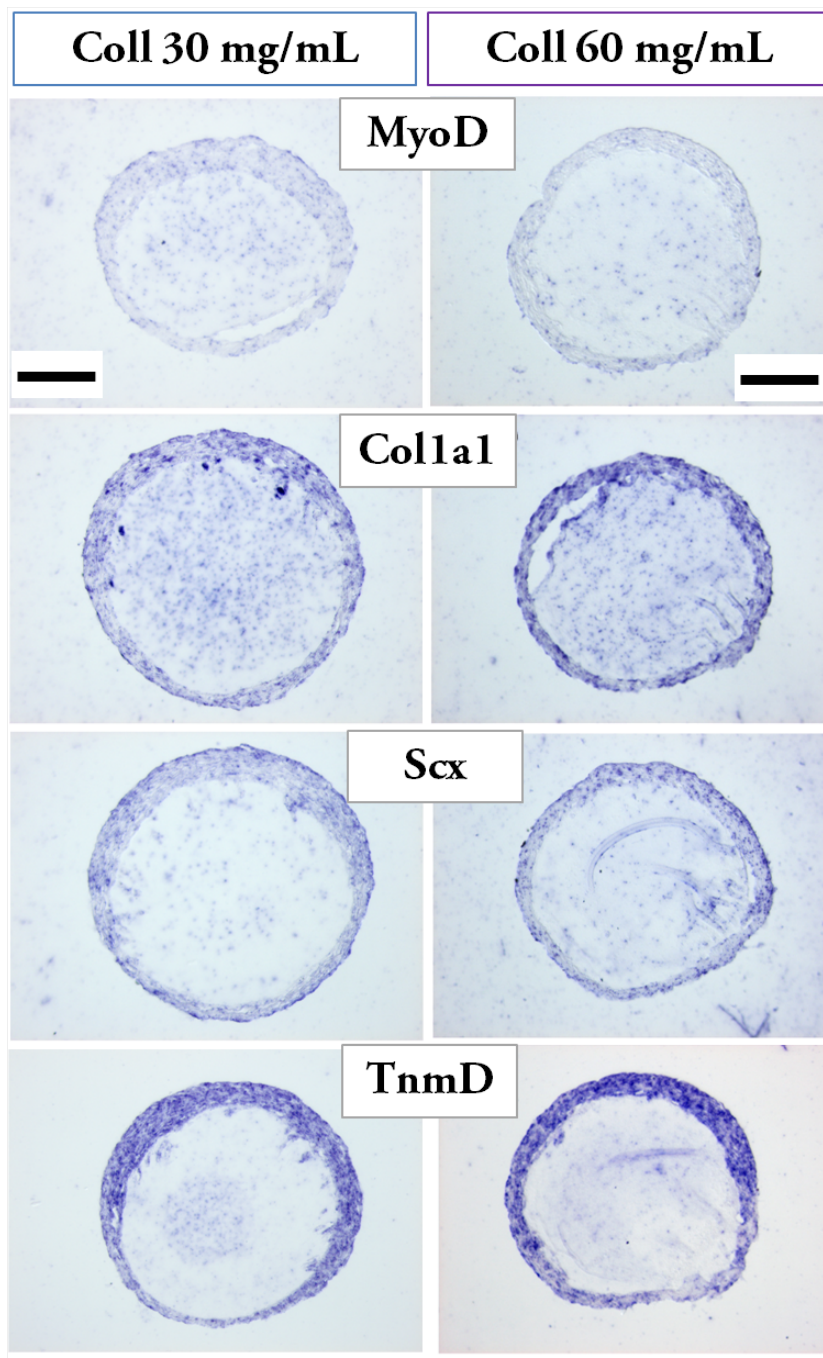


Figure 6.13: In situ hybridization on collagen threads cross sections at 30 and 60 mg/mL seeded with C3H10 T1/2 cells during 3 weeks. Four genes were labeled: MyoD, Coll1a1, Scx and Tnmd. Tnmd and Coll1a1 exhibit stronger color level labeling in both conditions. Scale bar = 100 μ m.

As explained in the previous section, ISH reveals the expression of a gene if the dye reacts. In other words, if a cell is colored for the tested gene, it means that the gene is expressed. If it is not, the gene is low or not expressed.

ISH experiments on threads cross-sections reveals that for both collagen concentrations, myoD is not expressed as the cell sheath is not "colored". Considering a purple level, Tnmd is more expressed than Colla1 and Scx. However, compared to myoD, it is assumed that Colla1, Scx and Tnmd are expressed which suggests that mesenchymal stem cells C3H10 T1/2 do not exhibit muscle character and may differentiate into tendon-like cells on our collagen threads whether at 30 or 60 mg/mL. Further quantitative analysis are performed in the second study in order to assess more precisely the gene expression.

6.2.4 Conclusion

In this first study, we showed that mesenchymal stem cells adhered on pure collagen threads and could even penetrate over a depth of 30 μ m, leading to straight holes at the collagen thread surface as shown by SHG (6.11 p 219). The cellular sheath of thickness about 50 μ m was quite aligned along the thread axis. We assumed that this cell orientation may come from the static tension or the thread topography at which striated patterns were observed without cells by SEM (Chapter 5 5.4.1 p 180). Mechanical properties were not affected by the presence of the cells. However, measurements improvements must be done in order to avoid cellular sheath gliding during the tensile testing. Finally, the first qualitative analysis of the gene expression of the mesenchymal stem cells cultured on threads were very promising and indicated that these cells may differentiate into tendon-like ones. A further study of cell behavior on threads was thus needed to quantify their gene expression level.

6.3 Behavior of stem-cells cultured on collagen based threads

In this second study, collagen thread at 30 mg/mL is chosen for quantitative analysis of stem cells behaviors as cells adhere and penetrate significantly into it. We also decided to compare this condition with the best corresponding collagen-alginate ratio thread (Chapter 5 5.4.2 p 188). The idea is to evaluate the effect of alginate addition on cell behavior.

6.3.1 Load influence of threads morphologies

Collagen based threads morphologies were observed by phase contrast microscopy over the cell culture time and as a function of the load condition. Figure 6.14 shows the morphologies of such threads at 3 weeks. Under static load (A), threads are straight. Coll:Alg (5:1) thread is opaque as previously noticed (Chapter 5 5.4.2 p 188). Without static load (B), Coll:Alg (5:3) is also quite straight whereas collagen thread at 30 mg/mL collapses and looks like a ball of wool. The thread contour is discernable through the cell sheath. This phenomenon due to the contraction of the thread by the cells begins between the first and the second week of culture.

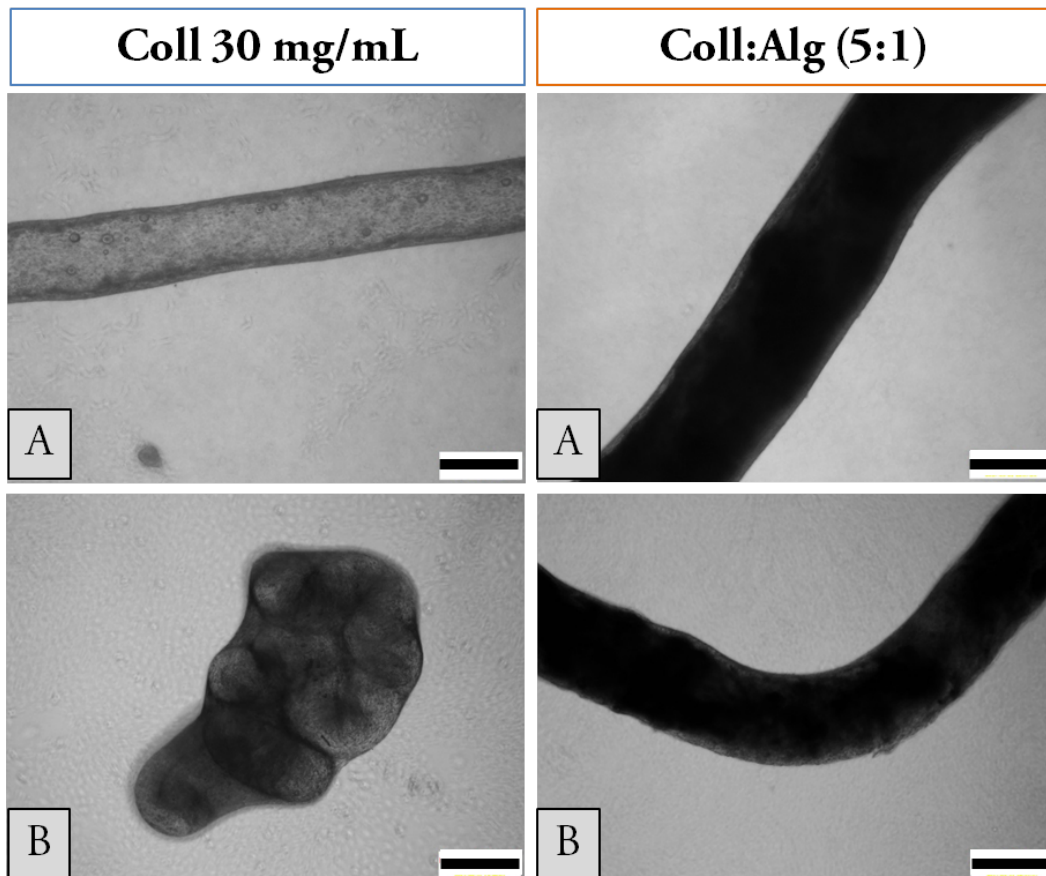


Figure 6.14: Morphologies observed by phase contrast microscopy of collagen thread at 30 mg/mL (left) and collagen:alginate (5:1) thread (right) after being seeded with cells and cultured during 3 weeks A) under static load and B) without load. Scale bar = 500 μm .

Chen (M-Y) et al. investigated the contraction of cell-laden collagen gels either as a function of the cell or collagen initial concentrations [14]. The collagen matrix contraction can be divided into three phases: a lag phase, a linear rapid contraction phase, and a slow contraction phase [15]. While increasing collagen concentration, the lag phase

is longer. Moreover, while increasing the initial number of cells inside the gel, this first phase is shortened. They found a lag phase of 14 days for collagen cell-laden gel at 2 mg/mL. Following this affirmation, lag phase for our collagen threads must be longer as concentration is 10-fold higher. However, in our case, cells number increases over time as cells have enough space to multiply and are not confined in a gel. This is why contraction occurs more rapidly. We also removed during 1 day the static load on a collagen thread at 30 mg/mL after 3 weeks of cell culture. The cells contract the threads as if no tension had been applied during 3 weeks. This is in good agreement with Chen et al. results [14] who found a lag phase of 0 to 2 days for initial cell concentration of 1 to $0.25 \times 10^6 \text{ cells/mL}$.

For coll:alg condition, threads keep straight with and without tension. A small inflection is visible for some threads (Fig 6.14, right B)). Regarding the mechanical properties of such thread, it may be too stiff to be contracted by the cells (6.2.1 p 217). Moreover, coll:alg threads diameter is larger than collagen one and the contraction cell force per area unit is thus lower. The lag phase might be too long to be observed within our culture time scale.

Remark: in Figure 6.14, we can distinguish cells on the well plate which suggests that cells migrate and proliferate rapidly as threads were put in a new 6-well plate every 2 days.

6.3.2 Cell colonization over culture time and load condition impact analysis

Cell colonization was assessed over time by confocal microscopy. After 3 days of cell culture under static load, several cell-deserted areas are observed.

At day 7, these holes disappear for collagen 30 mg/mL threads and remain for coll:alg thread. In fact, the thread surface is smaller than for the mixed one. Thus, cells cover more rapidly this surface.

At day 21, the two types of threads are entirely covered by the cells and several cell layers can be distinguished. Here again we see the thread contraction due to the cells at 30 mg/mL (Fig. 6.15, bottom left). In all cases, the outer layer of cells seems to be aligned along the longitudinal thread axis. However, for condition coll:alg no effect of the tension is visible. For pure collagen, some cell layers follow this thread axis orientation and other are perpendicular to it (Fig. 6.15 arrows). Without tension, on the thread part located on the left, which is still straight, cells are aligned along the thread axis (Fig. 6.15 arrows). Cell morphologies may be induced to the thread topography "orientation".

From those observations, it is assumed that the static load does not induce the cell orientation but this phenomena is due to the thread surface topology. Kishore et al. studied the effect of electrochemically collagen threads topography on cell morphology [16]. They fabricated either random or aligned collagen threads and put cells on it. Cells cultured on random threads exhibit a polygonal phenotype, whereas they are well aligned and have spindle shape on aligned collagen threads.

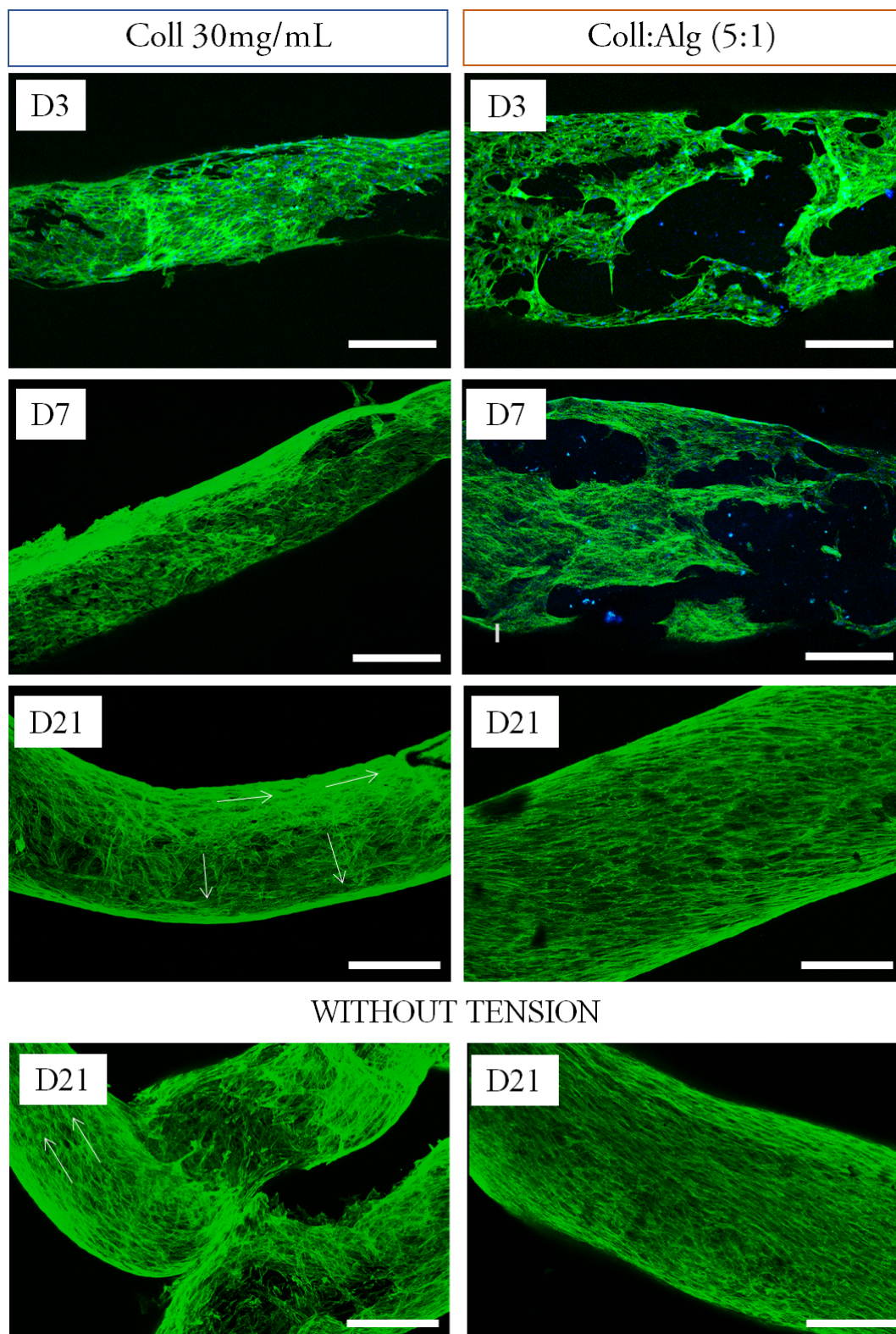


Figure 6.15: Confocal microscopy images of collagen thread at 30 mg/mL (left) and mixture coll:alg (5:1) (right) for different times: days 3, 7, 21 and without tension at 21 days. Alexa Phalloidin 488 and DAPI labeling. White arrows are eye guides for the cell sheet orientation on the thread surface. Scale bar = 250 μ m.

Remark: as collagen threads at 30 and 60 mg/mL, SHG coupled with fluorescence was performed on coll:alg (5:1) thread in order to observe how cells interact with the matrix.

The figure 6.16 displays the image of collagen (green) and cellular actin filaments (red) signals for a mix thread with cells cultured without tension.

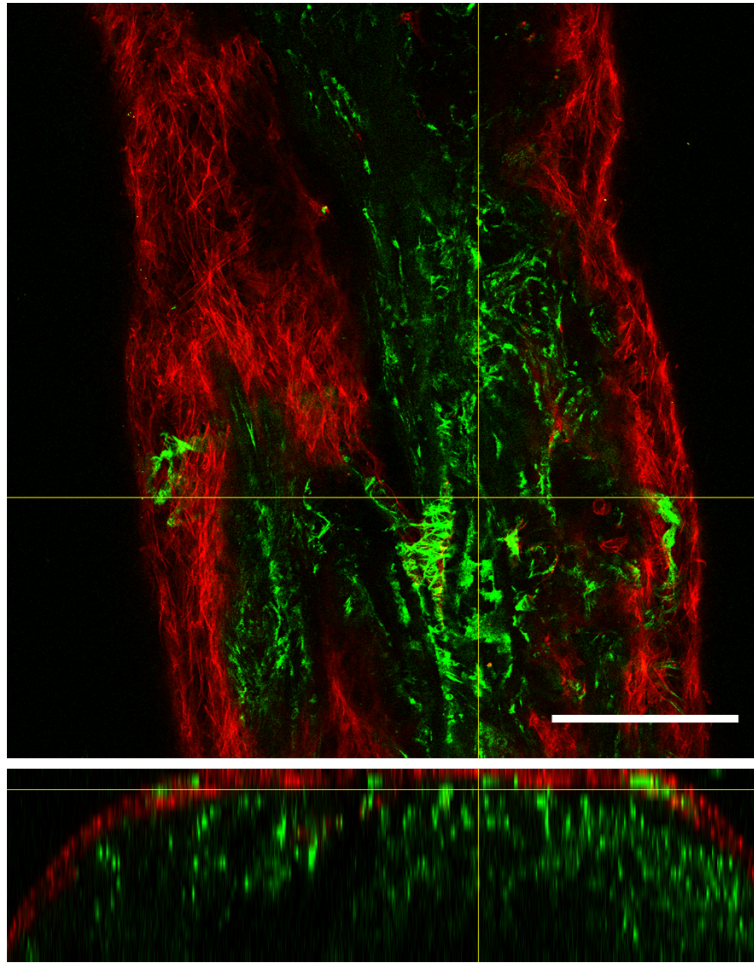


Figure 6.16: SHG image coupled with fluorescence of coll:alg (5:1) thread at 2 weeks of culture with cells without static load. Cross sectional projection is given on the bottom. Green: collagen SHG signal, Red: Alexa Fluor 488 Phalloidin. Scale bar = 200 μ m.

Cells interpenetrate the surface of the collagen-based thread. Several "SHG signal" holes are present in the thread structure meaning that those areas are mainly composed of alginate. Cells do not colonize those areas. The alginate phase may degrade over time leading to new porosity inside the thread giving enough space for cells to invade.

6.3.3 Genes of interest expression analysis

The expression of the genes of interest were analyzed first qualitatively by ISH and then by Real-time qPCR.

6.3.3.1 Qualitative analysis

ISH allows us to estimate gene expression prior Real-time qPCR. ISH reveals the expression of Scx in both conditions: collagen 30 mg/mL and coll:alg (5:1) thread. Coll1a1 seems to be more expressed on coll:alg with brighter color level. Tnmd is lower expressed than Scx and Coll1a1 for both threads.

The myoD gene is not expressed attesting that mesenchymal stem cells C3H10 T1/2 do not exhibit muscle character. As tendon markers are more or less expressed for each type

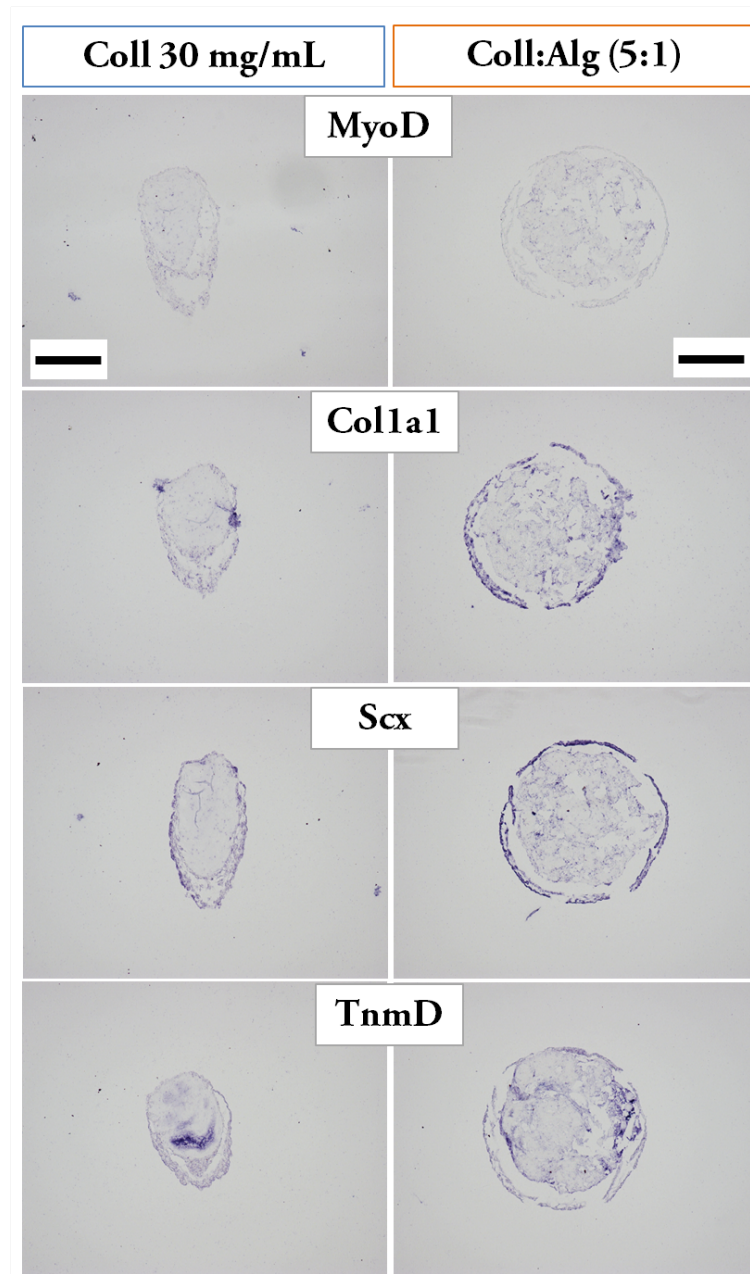


Figure 6.17: In situ hybridization on collagen threads at 30 mg/mL (left) and coll:alg (5:1) thread (right) with C3H10 T1/2 cells at 3 weeks, under static load. Four genes were labeled: MyoD, Coll1a1, Scx and TnmD. Scale bar = 200 μ m.

of threads, it is assumed that C3H10 T1/2 may differentiate into tendon like cells. This effect seems to be more pronounced for threads with alginate than pure collagen one.

Remark: no significant difference was noticed in the case of no load condition.

6.3.3.2 Quantitative analysis: Real time qPCR

The gene expression of Coll1a1, TnmD and Scx was analyzed quantitatively with real time qPCR and by using statistical tests to reveal the significant differences. For each gene, we will describe the results by varying one parameter at a time.

6.3.3.2.1 Coll1a1 gene expression analysis

Cell culture time effect: For collagen 30 mg/mL threads, coll1a1 gene expression increases over time with and without tension. Significant difference is noticed between 1 week and 3 weeks of culture. For coll:alg, coll1a1 gene expression tends to decrease over time but no significant differences are observed.

Material condition effect: Significant differences are observed between pure collagen and mixed alginate threads for the first two weeks of cell culture. The gene expression is higher for cells cultured on coll:alg threads. At 3 weeks, coll1a1 expression is almost the same for all conditions.

Static load influence: No clear effect of the tension is observed. Only one significant difference is noticed for mix threads at 3 weeks.

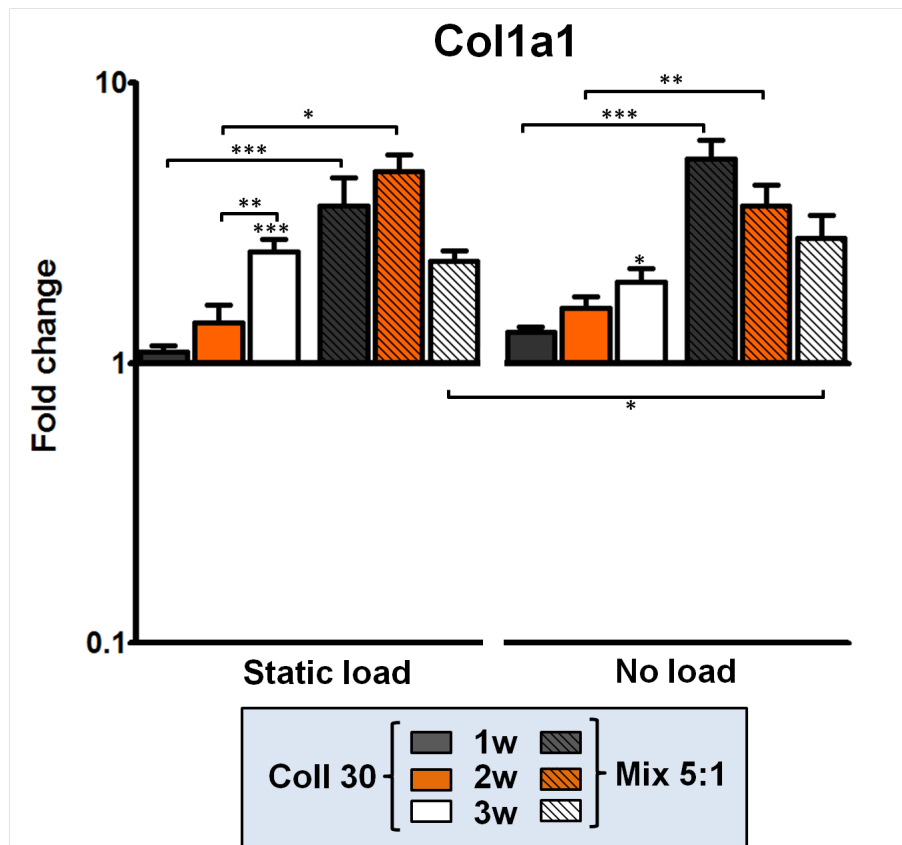


Figure 6.18: Collagen 1a1 gene: effect of cell culture time, load and material (pure collagen or mixed with alginate threads) conditions on tenogenic differentiation of mouse mesenchymal stem cells C3H10T1/2. (*P < 0.05, **P < 0.01, ***P < 0.001).

Conclusion

Coll1a1 expression increases over time on pure collagen threads and decreases on mixed ones, on which the initial expression is higher than with pure collagen. However, after 3 weeks, expression tends to the same level in case; the expression of the cells is different at the beginning depending on the conditions but tends to the same value after three weeks. The static tension does not seem to present any stimulating effect and rather decreases the stimulating effect of the presence of alginate. Indeed, at 3 weeks, the expression in the non-loaded mix is higher than the loaded mix.

6.3.3.2.2 Tnmd gene expression analysis

Cell culture time effect: At 1 week, Tnmd is overexpressed for all conditions. The gene expression decreases significantly over the time in all cases.

Material condition effect: Tnmd expression is low for collagen 30 mg/mL (static load) at all times. It is significantly lower compared to coll:alg threads.

Static load influence: Tension has a significant increasing effect at 2 weeks of cell culture for both material conditions but at other time points, there is no difference.

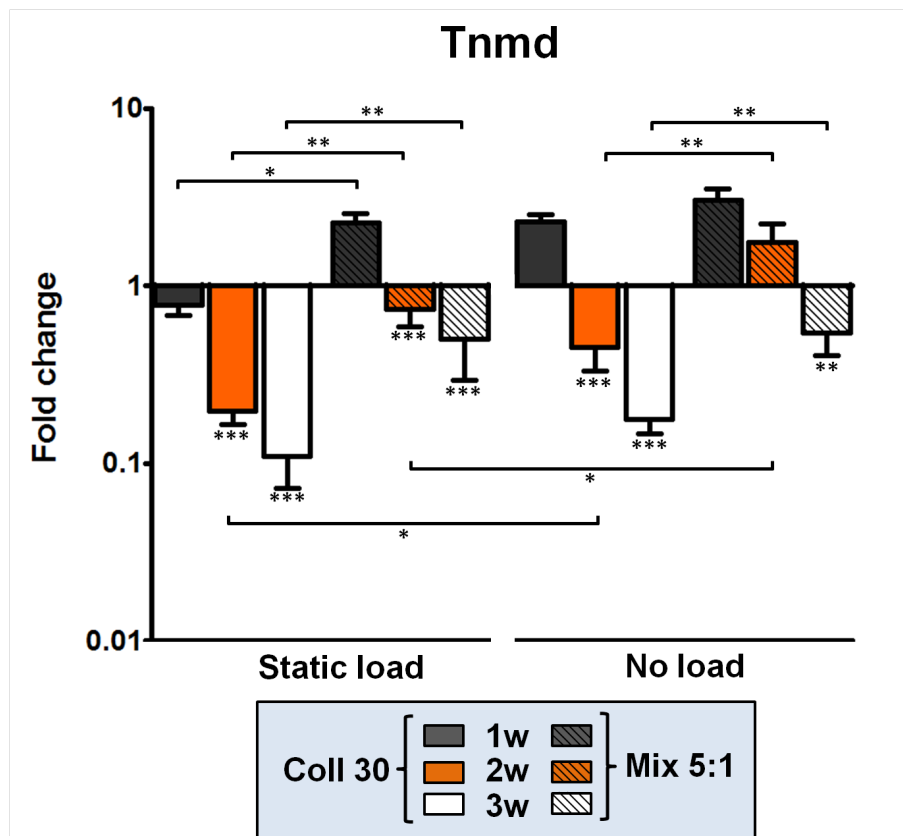


Figure 6.19: Tenomodulin gene: effect of cell culture time, load and material (pure collagen or mixed with alginate threads) conditions on tenogenic differentiation of mouse mesenchymal stem cells C3H10T1/2. (*P < 0.05, **P < 0.01, ***P < 0.001)

Conclusion

Tnmd gene is expressed at the beginning for all conditions but decreases over time. The material has an effect on its expression as it is significantly less expressed for pure collagen threads. Here again, it seems that the static load has no impact or a slight negative one.

6.3.3.2.3 Scx gene expression analysis

Cell culture time effect: Scx expression decreases significantly over time for pure collagen. It is quite constant over time for mixed threads.

Material condition effect: Scx is less expressed for pure collagen compared to coll:alg threads which exhibit very significant increase compared to pure collagen.

Static load influence: Static load has a positive effect at 1 week for pure collagen and a negative impact at 3 weeks for alginate mixtures.

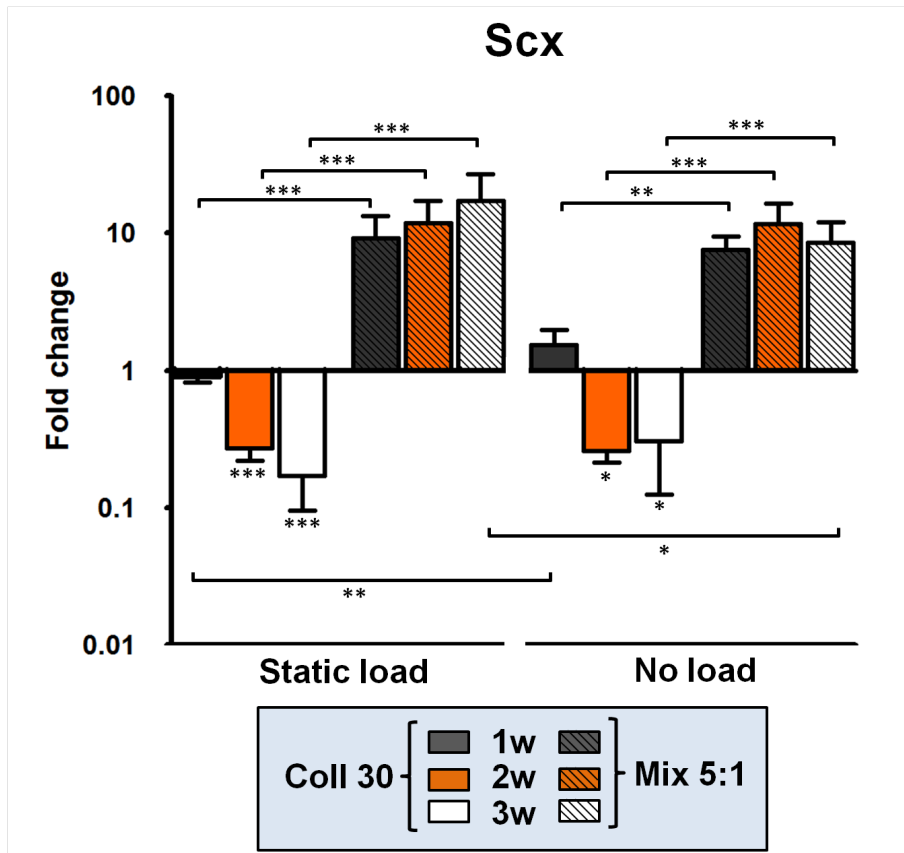


Figure 6.20: Scleraxis gene: effect of cell culture time, load and material (pure collagen or mixed with alginate threads) conditions on tenogenic differentiation of mouse mesenchymal stem cells C3H10T1/2. (* $P < 0.05$, ** $P < 0.01$, *** $P < 0.001$)

Conclusion

The thread material has clearly an influence on Scx expression as it is around 10-fold higher on coll:alg threads. Moreover, Scx expression is constant and remains at high level over the three weeks with or without load, whereas the expression decreases for pure collagen condition and the load has a negative effect at one week.

6.3.4 Discussion

From this gene expression analysis, the fact that the mesenchymal stem cells on the coll:alg mix threads express all tendon markers stands out. It is assumed that the cells behave as tenocytes while cultured on mix. The differentiation seems to be lower for pure collagen threads. This is in good agreement with the qualitative observations made from ISH images.

Kishore et al. studied the gene expression of Scx and Tnmd on random and aligned collagen threads. Scx expression is higher at day 3 on aligned collagen threads [16]. For Tnmd, they showed that its expression is 3-fold higher at day 7, and 10-fold higher when compared to random surfaces. The same trend is observed in our study. Based on their results, we can hypothesise that our coll:alg threads exhibit more aligned surface than the

pure collagen. This would favor tenogenic differentiation. Further investigations of surface characterization must be performed to verify this assumption.

Regarding the loading effect, Kuo et al. studied bone marrow mesenchymal stem cells gene expression [17]. Cells are put inside collagen gels at 3 mg/mL. They performed either static or cycling loading on those gels and cell culture was done over 7 days. They did not notice any difference while increasing the collagen gel concentration. Scx expression decreases over time for static loading, whereas Kuo et al. showed that static loading maintains Scx expression.

In our study, several hypotheses can be considered: the static load of about 125 mN is may not be sufficient enough to induce a difference with no tension condition. From this, we can conclude that thanks to its higher stiffness, coll:alg threads provide a better environment for cell differentiation. Based on Kuo et al. work [17], it will be interesting to perform the same study with cycling loading.

6.4 Conclusion

Mesenchymal stem cells were cultured on collagen-based threads over 3 weeks. From the studies of the cell colonization and behaviors on the threads, we showed that the cells could proliferate on the threads (pure or mixed condition) leading to a cellular sheath of about a width of 50 μ m. For pure collagen at 30 mg/mL, cells even digested collagen material and penetrated over a depth of 30 μ m from the thread surface. The cell sheath covered the whole thread surface available and seemed to be aligned along its axis. In Chapter 5, pure collagen threads exhibited striated patterns along the thread axis as shown by SEM. This oriented topography may guide and induce cell morphologies [18]. Moreover, the larger collagen structures (ball of wool) observed for collagen thread at 60 mg/mL could improve the cell adhesion. After 3 weeks, cells did not seem to suffer from the high confluence and preliminary ISH results proved that they could express specific genes of tenocytes.

The expression of these tendon specific genes were quantified by RT q-PCR for cells either cultured on pure collagen threads at 30mg/mL or its coll:alginate mixed equivalent ones. This was done as a function of time and mechanical loading. The ISH results were confirmed by this technique. Quite surprisingly, gene expression was higher in the case of collagen:alginate mixed thread than for pure collagen for *Tnmd* and *scx*. For *Coll1a1* gene, gene expression was almost the same after 3 weeks. Finally, the static mechanical loading was assumed to not have any effect on gene expression. This last parameter may be further investigated.

6.5 References

- [1] Zoher Kapacee, Susan H Richardson, Yinhui Lu, Tobias Starborg, David F Holmes, Keith Baar, and Karl E Kadler. Tension is required for fibripositor formation. *Matrix Biology*, 27(4):371–375, 2008. [207](#)
- [2] *Differential equations*. D. C. Heath and Company, 1952. [208](#)
- [3] Catherine K. Kuo, Joseph E. Marturano, and Rocky S. Tuan. Novel strategies in tendon and ligament tissue engineering: advanced biomaterials and regeneration motifs. *BMC Sports Science, Medicine and Rehabilitation*, 2(1):20, 2010. [209](#)
- [4] *Developmental Biology*. Sinauer Associates, 2010. [211](#)
- [5] Ava E Brent and Clifford J Tabin. Developmental regulation of somite derivatives: muscle, cartilage and tendon. *Current opinion in genetics & development*, 12(5):548–557, 2002. [211](#)
- [6] Chisa Shukunami, Aki Takimoto, Miwa Oro, and Yuji Hiraki. Scleraxis positively regulates the expression of tenomodulin, a differentiation marker of tenocytes. *Developmental biology*, 298(1):234–247, 2006. [211](#)
- [7] Chisa Shukunami, Yuki Yoshimoto, Aki Takimoto, Hiroshi Yamashita, and Yuji Hiraki. Molecular characterization and function of tenomodulin, a marker of tendons and ligaments that integrate musculoskeletal components. *Japanese Dental Science Review*, 52(4):84–92, 2016. [211](#)
- [8] Jorge Laborda. 36b4 cDNA used as an estradiol-independent mRNA control is the cDNA for human acidic ribosomal phosphoprotein p0. *Nucleic acids research*, 19(14):3998, 1991. [215](#)
- [9] Eileen Gentleman, Andrea N Lay, Darryl A Dickerson, Eric A Nauman, Glen A Livesay, and Kay C Dee. Mechanical characterization of collagen fibers and scaffolds for tissue engineering. *Biomaterials*, 24(21):3805–3813, 2003. [218](#)
- [10] Won Jin Kim, Hui-Suk Yun, and Geun Hyung Kim. An innovative cell-laden α -tcp/collagen scaffold fabricated using a two-step printing process for potential application in regenerating hard tissues. *Scientific Reports*, 7(1):3181, 2017. [218](#)
- [11] Xiao Chen, Zi Yin, Jia-lin Chen, Wei-liang Shen, Huan-huan Liu, Qiao-mei Tang, Zhi Fang, Lin-rong Lu, Junfeng Ji, and Hong-wei Ouyang. Force and scleraxis synergistically promote the commitment of human ES cells derived MSCs to tenocytes. *Scientific reports*, 2:977, 2012. [218](#)
- [12] Christophe Helary, Ludmila Ovtracht, Bernard Coulomb, Gaston Godeau, and Marie Madeleine Giraud-Guille. Dense fibrillar collagen matrices: a model to study myofibroblast behaviour during wound healing. *Biomaterials*, 27(25):4443–4452, 2006. [219](#)
- [13] Giselle Chamberlain, James Fox, Brian Ashton, and Jim Middleton. Concise review: mesenchymal stem cells: their phenotype, differentiation capacity, immunological features, and potential for homing. *Stem cells*, 25(11):2739–2749, 2007. [221](#)

- [14] Meng-Yi Chen, Yulong Sun, Chunfeng Zhao, Mark E Zobitz, Kai-Nan An, Steven L Moran, and Peter C Amadio. Factors related to contraction and mechanical strength of collagen gels seeded with canine endotenon cells. *Journal of Biomedical Materials Research Part B: Applied Biomaterials*, 82(2):519–525, 2007. [223](#), [224](#)
- [15] Toshio Nishiyama, Naoki Tominaga, Keisuke Nakajima, and Toshihiko Hayashi. Quantitative evaluation of the factors affecting the process of fibroblast-mediated collagen gel contraction by separating the process into three phases. *Collagen and related research*, 8(3):259–273, 1988. [223](#)
- [16] Vipuil Kishore, Whitney Bullock, Xuanhao Sun, William Scott Van Dyke, and Ozan Akkus. Tenogenic differentiation of human mscs induced by the topography of electrochemically aligned collagen threads. *Biomaterials*, 33(7):2137–2144, 2012. [224](#), [230](#)
- [17] Catherine K Kuo and Rocky S Tuan. Mechanoactive tenogenic differentiation of human mesenchymal stem cells. *Tissue Engineering Part A*, 14(10):1615–1627, 2008. [231](#)
- [18] Giulio Abagnale, Antonio Sechi, Michael Steger, Qihui Zhou, Chao-Chung Kuo, Gülcän Aydin, Carmen Schalla, Gerhard Müller-Newen, Martin Zenke, Ivan G Costa, et al. Surface topography guides morphology and spatial patterning of induced pluripotent stem cell colonies. *Stem Cell Reports*, 2017. [231](#)

CONCLUSION

The main objective of this thesis was to produce dense collagen threads mimicking the native tendon structure to repair it in the future. For this multidisciplinary project, it was thus necessary to combine both physico-chemical skills, due to the complexity of its structure and biological ones, due to the final TE goal. As a consequence, a large range of parameters from those different fields needed to be explored in order to fully understand their influence and continuously improve the collagen threads properties until reaching the best condition.

For this purpose, extrusion technique was chosen as it is quite convenient to implement in a laboratory and is the first/intuitive method used to fabricate threads. We developed a home-made set-up in order to control a large range of parameters and also to be able to observe in real-time the thread production. Then, we decided to use a system model similar to collagen that we could extrude in a vast amount to harness our experimental device and first explore the influence of each parameter. Finally, we produced dense collagen threads in a reproducible manner and in vitro studies were performed to assess the behaviors of the cells cultured on our scaffolds.

First, we studied the extrusion of sodium alginate in the presence or not of binding ions (Chapter 4). In the first case, two characteristic instabilities of polymer melt extrusion were observed and quantified thanks to our experimental set-up configuration, which allows the visualization of the flow at the die exit and even inside the capillary. By varying die dimensions, we showed that the bulk undulation of the extrudate vanished for ratio of length over radius close to zero, indicating that the instability affected the whole pipe flow. Moreover, the shear-thinning level of such fluid solution may control the nature of the instability. It was the first time that such instabilities were reported in the case of polymer solutions. In the presence of binding ions, we reported several surprising instabilities such as the striated patterns on the thread surface or the gel clogging at the die exit. Such phenomena have never been previously described and further investigations were necessary to fully understand the mechanisms of alginate and calcium ions interaction during the extrusion.

Then, the new expertise on the complex fluid extrusion was used for the production of collagen threads. We extruded for the first time collagen solutions at concentrations up to 60 mg/mL (10-fold higher than in other studies) and succeeded to produce regular threads in a reproducible manner, while controlling their quality in real time. The preparation and extrusion process allowed to obtain in only a few hours several meters of collagen threads about 500 μ m in diameter. We proved also that this method tends to align collagen molecules along the thread axis. Moreover, the studied alginate instability was successfully transposed on collagen systems, leading to the production of collagen threads exhibiting helical morphology, similar to the tendon "crimp" structure. This was obtained

at the end of the thesis and is promising compared to the previous studies on crimp replication (Chapter 4).

Hybrid threads were made of both collagen and alginate in order to take benefit from their respective properties (Chapter 5). After selecting the best collagen:alginate ratio, we showed that the addition of even a small amount of alginate improved the mechanical properties of the threads compared to the pure collagen ones.

Finally, mesenchymal stem cells were cultured on the collagen-based threads (Chapter 6). The cells colonized the threads surface and penetrated over a distance of 50 μm from the surface. They expressed the different genes characteristic of tendon-like cells suggesting that they differentiate into tenocytes when seeded on our threads. No difference was observed between cells cultured on threads with or without static load. However, the gene expression was improved on hybrid threads.

Although our threads exhibited promising properties, there is still a long way to repair the tendon and have a scaffold ready for clinical applications. This is why several further studies must be done on this subject and we will here detail many perspectives raised by our results.

Perspectives

Extrusion parameters investigation

Regarding the knowledge of the extrusion technique, several parameters still need to be further investigated. As we changed one parameter at a time, it was difficult to test each of them over a wide range. In fact, we began studying the effect of the die material and some corresponding results for alginate were presented. As the condition at the die wall seems to be critical to obtain some instability, it would be interesting to use PTFE tubing to remove stick effect on the wall and study the impact on instabilities. Then, we showed that the die exit angle can be shaped at a desired angle. From preliminary results, instabilities might be amplified by using sharp exit angles and this may be helpful to produce more pronounced crimped threads. Finally, the extrusion velocity range needs to be further explored and in particular for collagen solutions. Our experimental set-up also offers the possibility to impose the temperature during the extrusion. This parameter was not varied during this project. Such complex fluids may exhibit different behaviors while increasing or decreasing the temperature. In the case of collagen:alginate mixed solutions, it would be interesting to extrude them at lower temperatures which might enable to delay the two systems interactions so as to obtain more homogeneous threads.

Threads properties improvement

Composition

In this thesis, no cross-linking agent or post-processing was used. In fact, those may decrease the biocompatibility of the scaffolds or lead to the denaturation of the collagen respectively. However, some natural cross-linking agents, present in the tendon, may be used to reinforce our threads. To do so, it would be interesting to introduce proteoglycans which bridge collagen molecules to each other. As shown in the Chapter 5, the threads produced from the higher collagen concentration exhibit the best properties. It may be possible to extrude collagen solution at concentration higher than 60mg/mL. This would lead to highly dense threads as shrinkage phenomenon might increase the local concen-

tration. Moreover, the strategy of mixing alginate and collagen seems to be very promising. By exploring the interactions between these proteins and polysaccharides, we would assess the best conditions to obtain quite cosoluble systems at high concentrations.

Structure

Regarding its shape, the "crimp" like morphology was obtained at the end of this thesis project. It deserves to be further studied as it is easy to implement and does not need plenty of chemical treatments as in molding strategy. The die material may have an influence on this bulk "defect", which needs to be explored. Moreover, we did not have enough time to test the production of a "multiple"-based thread: the idea is to insert a metallic grid either upstream or downstream (to be chosen) in order to separate the flow into several parts that can be put back together downwards. This way we expect the alignment of collagen to be improved also in the core thread. A last approach would be to incorporate the cells directly inside the solution and extrude threads with cells inside. The cells may reorganize the collagen matrix at their length scale and improve the collagen structure.

Scaffold assembly

Plenty of strategies may be applied to construct elaborated scaffolds from our threads. The first idea would be to braid several threads together as presented in Chapter 1 and form a cord-like construct. It would also be possible to assemble those cords and form a scaffold at a higher level. In our work, we observed the forces developed by the cells cultured on threads without static load. Some collagen threads were completely folded. It could be possible to assemble several threads pinned at their extremities and close enough to each other to allow the cell adhesion between threads. They would bind the threads together and produce their own extracellular matrix between them. In a similar approach, several threads "layers" could be aligned in a mold, which could also be filled with a collagen solution at a lower concentration and already containing cells.

Cells behaviors

Mesenchymal stem cells expressed tendon-like cells gene while cultured on our collagen-based threads. Cell cultures on higher collagen concentration threads could be performed to assess the influence of this parameter on cell behaviors. The static load did not impact the cell behaviors. However, it would be interesting to test cell cultures on threads under cyclic load. This would be closer to the physiological situation. Some devices as Flexcell™ are available to perform such testing under cell culture.

List of abbreviations

- 36B4 : reference gene
- AA : acetic acid
- ALG: sodium alginate
- C3H10T1/2 : mesenchymal stem cell from mouse embryos
- C : concentration
- $CaCl_2$: calcium chloride
- cDNA : complementary strand DNA
- χ : compressibility
- Coll1a1: collagen type 1 alpha 1 gene
- coll : collagen
- C_t : cycle threshold
- DAPI 4',6-diamidino-2-phenylindole dihydrochloride
- D_p : piston diameter
- DSC : Differential Scanning Calorimetry
- DMEM Dulbecco's Modified Eagle's Medium
- DNA : Deoxyribonucleic acid
- E: Young Modulus
- ECM Extracellular matrix
- EDC : carbodiimide
- η : viscosity
- η_0 : plateau viscosity
- η^* : complex viscosity
- $\dot{\gamma}$: shear rate
- $\dot{\gamma}_0$: zero shear rate
- γ : strain
- f : frequency
- F : force
- FACITs : Fibril Associated Collagen with Interrupted Triplehelix
- \bar{G} : complex modulus
- G' : storage modulus
- G'' : loss modulus
- Gly : Glycine
- I : ionic strength
- ISH : In situ Hybridization
- KCl : potassium chloride
- L : capillary length
- λ : relaxation time
- λ_r : retardation time
- M : torque
- MPa : Mega Pascal (Pressure unit)

- mRNA: Messenger RNA
- myoD : myogenic differentiation gene
- N: Newton (Force unit)
- N_1, N_2 : normal stress differences
- ∇ : upper-convected derivative
- NaCl : sodium chloride
- Na_2HPO_4 : sodium phosphate
- nDNA Compacted DNA
- ω : angular frequency
- Ω : angular velocity
- P: pressure
- P (length): persistence length
- PBS : Phosphate Buffer Saline
- PCR Polymerase chain reaction
- Pe : Peclet number
- PFA : paraformaldehyde
- ϕ : orientation in the image plane (SHG)
- pI : isoelectric point
- ψ_1, ψ_2 : normal stress difference coefficients
- P-SHG: Polarization-resolved SHG
- PTFE: Polytetrafluoroethylene, Teflon
- Q: throughput
- q-PCR : quantitative PCR
- R: capillary radius
- Re : Reynolds number
- R_H : hydraulic resistance
- ρ : bulk density
- ρ (SHG) : anisotropy parameter
- RNA : Ribonucleic acid
- RNase : Ribonuclease
- RT : Reverse Transcription
- σ : shear stress
- Scx: scleraxis gene
- SEM : Scanning Electron Microscopy
- SHG : Second Harmonic Generation
- S_p : piston surface
- t: time
- τ : stress tensor
- TE: Tissue Engineering
- TEM : Transmission Electron Microscopy
- Tnmd: tenomodulin gene
- T_m : melting temperature
- UTS: Ultimate Tensile Strength
- V: volume
- v_p : piston velocity
- \bar{v} : output velocity
- Wi : Weissenberg number

Appendix

REVIEW ARTICLE

From Tendon Injury to Collagen-Based Tendon Regeneration: Overview and Recent Advances

Clément Rieu^{a,†}, Lise Picaut^{a,b,†}, Gervaise Mosser^a and Léa Trichet^{a,*}

^aSorbonne Universités, UPMC Université Paris 06, CNRS, Collège de France, Laboratoire de Chimie de la Matière Condensée de Paris, F-75005, France; ^bSorbonne Universités, UPMC Université Paris 06, CNRS UMR 7588, Institut des NanoSciences de Paris, F-75005, Paris, France

ARTICLE HISTORY

Received: March 24, 2017
Accepted: May 5, 2017

DOI:

10.2174/1381612823666170516130515

Keywords: Tendon, injury, repair, biomaterial, graft, collagen, scaffold.

Abstract: Tendon injury is a clinical, societal and economical issue. Moreover, tendon repair represents an important clinical challenge, partly due to the mechanical constraints that occur at the junctions with muscle and bone. Several strategies have been developed for tendon repair. In this review, we first assess the importance of tendon injuries from different sites and their causes. After a short overview of tendon three-dimensional organization, the complexity of the perfect repair quest is presented ranging from current clinical procedures to new engineering scaffolds. We then sum up tendon engineering requirements and focus on new collagen-based scaffolds, which raise promising prospects to mimic and repair tendon. In particular, we survey quantitatively a large panel of techniques to produce these scaffolds, detailing their principle and recent improvements.

1. INTRODUCTION: CLINICAL CHALLENGES

Tendons can present acute or chronic injuries caused by extrinsic or intrinsic factors, either alone or in combination (Fig. 1) [1]. Tendinopathies refer to the various chronic conditions that can affect tendons. They can remain silent over a large period of time, cause chronic pain and, potentially, lead to tendon tears and ruptures. These can also occur following lacerations by a sharp object or a tensile overload, in which case, it is now believed that an underlying tendinopathy is also involved [2], [3]. The term tendinitis, previously used, referred to tendon micro-tears associated with acute injuries due to an overload, causing inflammation, while tendinosis accounted for chronic wound following tendon overuse. The term tendinopathies is now preferred because there is no assumption about the underlying pathology, especially since the role of inflammation is still under debate [4], [5]. They are associated with a change in remodeling activity of tendon matrix.

External causes of tendinopathies include occupational, sporting activities, and prescription drugs [6]. Intrinsic factors include age and biomechanical imbalance [1]. The etiology of tendinopathies often appears to be multifactorial [2], [3], [7].

A UK study, performed in an acute Orthopedic Unit treating a well-defined catchment population of about 535, 000 and prospectively recording the demographic details over 5 years, provided results about the incidence of musculoskeletal tissue trauma [8]. One of the findings is that about two thirds of tendon injuries relate to the hand. Among them, forearm/hand extensor tendon injuries occur with an annual incidence of 17.87/100, 000, and mallet finger involving extensor tendon affecting mobility of the last phalanx, at a rate of 9.89/100, 000 (Fig. 1). A 10-year population-based study conducted in the US, examining hand or wrist open wounds secondary to acute trauma and involving tendons, found an incidence rate

of 33.2 tendon injuries per 100, 000 person-years, with work-related injuries accounting for 24.9% of total [9].

Achilles tendon rupture occurs at an annual rate of 11.33/100, 000 according to Clayton *et al.* (2008) [8] and has already been reported with rates ranging from 5.5 to 18/100, 000 (Fig. 1) [10]. Most acute ruptures concern people in their thirties and forties during sports activities. Achilles tendinopathy has a 5.9% lifetime cumulative incidence among sedentary people as compared to 50% among endurance athletes [11]. Tennis elbow, also known as lateral elbow tendinopathy, is secondary to excessive use of wrist extensors and forearm supinators. It is usually reported to affect 1 to 3% of the population each year, however, a descriptive epidemiology study shows a decrease in the incidence with a rate of 3.4 per 1, 000 [12]. The injury incidence in tennis players has been reported in proportions between 9 and 35% [13]. The rotator cuff, which is composed of four muscle-tendon units that originate on the scapula and cover the top of the humeral head, can also often be subject to tendinopathy. In a prospective study, the sex and age-standardized incidence of shoulder pain was evaluated to be 9.5/1, 000 among the patients presenting to general practice, with a proportion of 85% related to rotator cuff tendinopathy [14]. The incidence of rotator cuff tears was reported to be 3.73/100, 000 [8].

Work-related musculo-skeletal disorders concerning tendons are evident in occupations involving prolonged periods of repetitive, static work [14]. The prevalence of work related upper limb musculoskeletal disorders in UK was estimated to be 730 per 100, 000 people in year 2014/2015 [15]. There is an average of 17.7 working days lost for each case. According to the 2005 data collection of Eurostat figures on recognized occupational diseases (EODS) of 12 member states, the most common musculo-skeletal occupational disease was lateral elbow tendinopathy (14, 155 cases) [14]. In the United States, shoulder injury has been found to be the second most common cause after back pain for time away from work in manual laborers [16]. 41.5% of occupational shoulder injuries required more than 31 days away from work in 2007. In Sweden in 1995, among the 9, 398 reported work-related soft tissue diseases, 217 cases involved rotator cuff and 538 lateral elbow [17].

*Address correspondence to this author at the Laboratoire de Chimie de la Matière Condensée de Paris, UPMC, Tour 43-44, Et. 4, 4 place Jussieu, 75252 Paris Cedex 05, France; Tel/Fax: +33-1-44276553, +33-1-44278102; E-mail: lea.trichet@upmc.fr

[†]These authors contributed equally to this work.

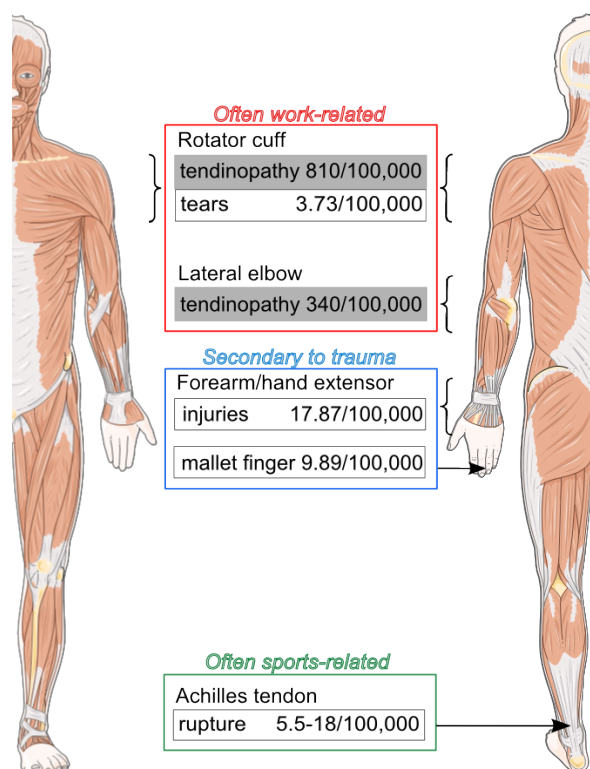


Fig. (1). Location, annual incidence and main cause of most frequent tendon injuries. Data are referenced in the text. Sources: [8], [10]-[12]. Body image, courteously provided by Servier Medical Art under license <https://creativecommons.org/licenses/by/3.0/fr/>, was modified for clarity purpose.

Some estimates of the cost of work-related upper limb and neck musculo-skeletal disorders are between 0.5 and 2% of gross national product [17].

Due to poor vascularization and low cellularity of the tissue, there is limited spontaneous regeneration of tendon. Treatments can be conservative or surgical, or a combination of both with post-intervention rehabilitation programs [2], [5], [10], [16]. Currently there is a high rate of re-injury. In the case of small and large rotator cuff tears, surgical repairs of ruptured tendons have re-tear rates of up to 35 and 94%, respectively [18]. Clinicians assess an unsatisfactory clinical outcome after suture for 25% of patients with hand tendon lacerations, and 7.7% of these repairing re-rupture [19].

2. TENDON STRUCTURE AND REMAINING QUESTIONS

Tendons and ligaments belong to connective tissues that present a cellular part and an extra-cellular matrix (ECM). Cells, out of which tenocytes are predominant, are found immersed into the ECM. They synthesize the bio-components and thus play a major role in the setting and renewing of the ECM. This last one is responsible for the structural and mechanical properties, and maintains the integrity of the tissue [20]. ECM is composed of many different biochemical components such as collagens, non-collagen proteins, and proteoglycans [21][22].

Collagens are widespread and play major roles in organisms. They constitute a family of 28 members [23], all being formed by three polypeptides chains. Each chain has repeating amino-acid triplet units $-(\text{Glycine-XY})_n-$, that extend variably depending on the family member, and with X and Y positions frequently occupied by proline and hydroxyproline. The presence of those $-(\text{Glycine-XY})_n-$, repeats leads to polyproline-II segments that supercoil into a right-handed helix. Each member of the family has different functions

and members can be, or not, co-localized, depending on the connective tissue considered. In tendon, collagens reach a concentration of 30-31.6% of the wet weight [24], and 60-85% of the dry weight of the tissue [22]. In the collagen family, collagen I is the major structuring bio-component of the tendon, where it is found in its fibril form and arranged into a hierarchical manner as we will see later.

Among the other components found in the ECM, some regulate collagen fibril diameters and/or fibrils interdistance and mechanical properties. For instance, polysaccharides form bridges between fibrils maintaining the equidistance between them and contribute in holding the three-dimensional network. Those bridges are formed by small carbohydrate chains of about 15 kDa [25]. *In vitro*, it was also reported that, in the synthesis of collagen scaffolds, the addition of decorin increased their mechanical properties.

Tendon structure has been studied for the past decades and by various techniques and under various states. Despite the information acquired, the exact organization of tendon in living tissues remains unclear. The fact that it may be adapted to each location within the body and depend on each species, does not help in getting a precise idea [26]. New developments in microscopy will hopefully bring some valuable keys for this understanding [27]-[29]. Anyhow, some general characteristics are common to all tendons and ligaments and the most important are discussed below.

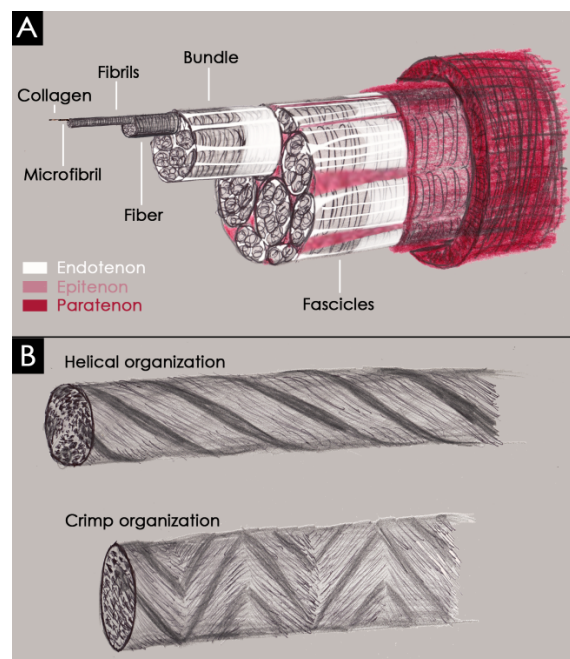


Fig. (2). Schemes illustrating the major structural characteristics of extracellular matrix of tendon: (A) Hierarchical organization of tendon unit. (B) Helical and crimp organization of fascicles (resp. top and bottom).

Tendons and ligaments are organized in a hierarchical manner that starts with collagen I molecules, which, associated by five into "microfibrils", pack into fibrils [30]. The fibrils are further associated into fibers that are joined into bundles delineated by the endotenon, a fine ECM of another composition and organization. The endotenon is continuous with the surrounding connective tissues and facilitates sliding between adjacent structures. In particular, it is in continuity with the epitendon that further tightens together bundles of fibers into fascicles. Depending on the tendon, fascicles may present another covering layer named "paratenon" (Figure 2A). Finally, several fascicles may be bound together to give larger units [31].

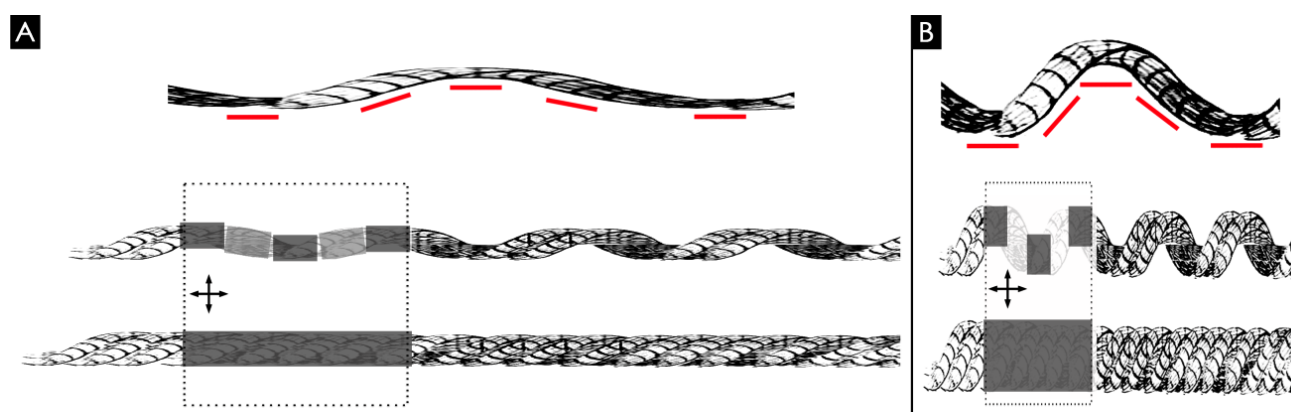


Fig. (3). Scheme conciliating helix crimp and linear organization: A single stranded helix is schematized on top, a partial super-helix in the middle and a full super-helix on bottom. Boxed by the dotted line, their appearance when observed between crossed-polarizers. Crossed-arrows indicate directions of polarizers. (A) **Top:** The extended helical strand and beneath the projected collagen molecular orientations are represented by lines. All orientations are nearly aligned along the helix axis. **Middle:** The partial super-helix is represented and the molecular orientations being all nearly aligned along one polarizer, the crimp is hardly seen and the partial super-helix appears nearly dark. **Bottom:** the symmetry of the complete super-helix is cylindrical. The mean projection of the molecular directions sums up along the axis of the helix. The complete super-helix appears dark under crossed-polarizers. (B) **Top:** The molecular orientations vary along the axis of the helix and present a repeating unit of alternating orientations. **Middle:** The partial super-helix is represented and the molecular orientations varying as illustrated above, the crimp is clearly seen as banded pattern under crossed polarizers. **Bottom:** the symmetry of the complete super-helix remains cylindrical with the mean projection of the molecular directions summing up along the axis of the helix. The complete super-helix still appears dark under crossed-polarizers.

Collagen fibrils within endotenon, epitenon and paratenon are not necessarily collinear to the tendon and can be found perpendicularly oriented [32]. Those layers possibly maintain the integrity at each level from bundles to tendon. They also possibly take part in its mechanical properties. Blood and lymphatic vessels, as well as nerves, are found in the endotenon, epitenon and paratenon.

Cross-polarized optical microscopic observations of excised rat tail tendons reveal an overall alignment of the bundles along the tendon axis. They also reveal units, from 10 to 100 μm , with alternating oblique orientations compared to the tendon axis. This feature is referred to as “crimp” (Fig. 2B bottom). Evidence of this crimp was further observed by atomic force and electron microscopies (scanning and transmission) [33][34]. The crimp was suggested to be a natural shock-absorber and to play a role in elastic recoil [35].

Shah *et al.* (1982) reported that the crimp was only observed at day 16th during the embryonic development of chick tarsus metatarsus region. The appearance of the crimp correlated with a high increase of collagen content between day 14th and day 16th [36]. This suggests the crimp to be highly related to the presence of collagen fibrils. On the other hand, for Herchenhan *et al.*, (2012) tenocytes, cells found inside tendon, induce formation of crimps [37]. Their conclusion relies on the fact that, knocking down cells using polyoxyethylene (9-10) *p-t*-octyl phénol (TX-100) within a biomaterial construct presenting a crimp, induces its loss. However, the authors do not take into account the fact that TX-100 also interacts with collagen and even destabilizes fibrils, possibly contributing to the loss of the crimp [38][39].

In addition to the overall alignment and the crimp, Vidal *et al.* (2003) analyzed under crossed polarizers transversal sections of tendons and showed that fascicles presented a helical organization along the tendon axis [40] (Fig. 2B top). This raises the question on how the crimp structure can be compatible with both a cylindrical symmetry and a helical organization. Geometrically speaking, one way to explain the crimp would be as over-winding of a helical organization. *In vivo*, under tension, it would be extended and fascicles would appear quasi collinear with the direction of the tendon. No “crimp” would be detected (Fig. 3A). However, when tendons

are relaxed and/or excised, the linear tension would decrease and the over-winding would collapse on itself while still being constrained transversally by the 90° transverse collagen sheath. The crimp would thus appear (Fig. 3B).

Mechanical tests made on tendon clearly show the difference of mechanical behaviors during the elongation of the crimp and after [35]. Computational modeling best fits the mechanical experimental data when a helical arrangement is injected into the models [41]. Reese *et al.* (2010) further improved the fit by combining a wavy pattern with a super-helical arrangement [42]. This data comforts the idea of a super-helical structure.

It has been shown that super-twisted organizations could be spontaneously generated in liquid-crystals [43]. Knowing that collagen forms different liquid crystal phases [44][45][46] that are subject to physico-chemical parameters [47], it is not excluded, although there is no proof yet, that the over-winding helical organization of tendon may also result from simple physical-chemical laws. Most probably, cells and physico-chemistry work hand in hand.

Modifications upon aging, injury and recovery have been studied at different levels: biochemical, fibrils (diameter, orientation) and crimp (presence or not, period) [21][48]. Here, again, it seems that there is not a unique scheme of evolution with different observations being made depending on tissues and/or species. To further highlight the complexity of the living tissues, their studies and the different routes to achieve their healing, reconstruction or replacement, it should be noted that control tendons, which are generally contralateral tendons, also see their characteristics being modified, possibly due to stress and postural changes during healing process.

Tendon wound healing process is characterized by three different stages: inflammation, repair, and remodeling [5], [49]. After injury there is a high release in growth factors, cytokines, and an increase in the expression of tendon-associated molecules, which cellular origins are still difficult to trace back [50]. During the repair phase, collagen type III is mainly synthesized, leading to the formation of a scar tissue with increased cross section area. During matrix remodeling, which can last months to years, collagen type I synthesis is increased and the newly formed fibers are aligned along

the longitudinal axis of the tendon. The tissue obtained often displays reduced mechanical properties due to the presence of disorganized collagen, as well as improper non-collagenous molecules and exogenous cells recruited at the wound site. These cells can lead to the formation of fibrous peritendinous adhesions with the surrounding tissue, impairing the normal stress transmission and hence the restoration of normally aligned collagen fibers [1].

The ultimate tendon repair is based on several requirements. The prior physiological criteria include, among others, the initial strength recovery, the joint gliding, the re-rupture avoidance and the shorter return-time to activity. Early active mobilization of the repaired tendon is advocated to improve those properties [19]. It was also proved that this early post-surgery stimulation increases the collagen type I cell production and that the quick tension restoration induces the parallel alignment of this renewed collagen [51]. In the following part, the different strategies clinically used from sutures to decellularized matrices will be described.

3. CURRENT CLINICAL STRATEGIES

The route chosen to induce healing of the tendon must take into account the gravity of the injury. From chronic tendon injury to tendon tears, the first objective is to reduce the patient's pain due to the tissue inflammation with specific drugs and with rehabilitation exercise [52], [53]. Then, emerging treatments consist in delivering growth factors through autologous whole blood or platelet rich plasma (PRP). Although *in vitro* studies show that these injections impact favorably the collagen production and degradation mechanisms [54], their use in clinical cases are controversial. Indeed, several questions regarding the injection frequency, volume, concentration etc. still remain open.

For acute tendon injury, the treatment depends on the lesion severity. If the gap between the two tendon extremities is less than 3 mm, the self-healing mechanism is engaged [55]. For larger injuries, if the joint motion is altered or even completely lost then surgery is needed. The length of the gap will determine the approach to be adopted. If the gap is less than 3 cm, suture techniques are required to rejoin the tendon. In the case of Achilles tendon, the conciliation of its 2 ends requires a great force. This is why, if the rupture is in an easy access location, surgeons use some devices as bone clamp [56] or Integra™ Achillon® system [57], [58], to join the tendon and then suture it. It should be kept in mind that the more handled is the injured tendon the more severe are the tissue trauma and adhesion. Wang *et al.* (2006) have even shown in a murine model that the suture directly affects the cellular healing process. The acellular zone does not heal and present inflammatory signs [59].

For gaps larger than 3 cm, augmentation of the ruptured tendon with additional implants or grafts is recommended [56]. Several types of devices from metallic implants to synthetic grafts are commercially available and already used by clinicians (Table 1, [60]).

3.1. Sutures

Three methods of tendon suturing have been developed and optimized: the non-grasping, the grasping and the locking anchors. The non-grasping method was first performed on finger flexor tendon by Bunnell in 1918 [19] (Fig. 4A). This technique consists in looping the anchor around the epitenon. As a consequence, no collagen fibers bundles are injured. On the contrary, the methods based on grasping, (opened loop, Fig. 4B) and locking anchors (closed loop, Fig. 4C) pinch the collagen fibers.

However, those two techniques bring better mechanical properties and gapping resistance to the tendon. They took the name of their authors Kessler for the grasping suture and Krakow for the locking one. The last one is assumed to be the more effective and is continuously being improved [61].

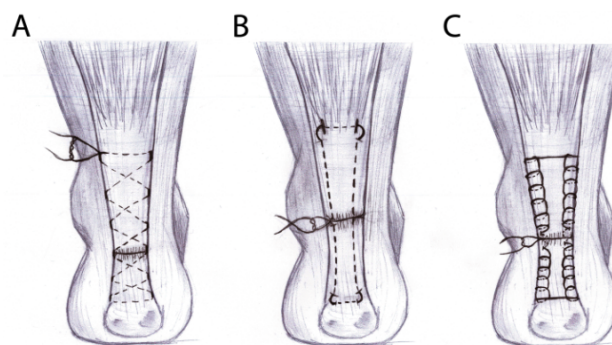


Fig. (4). Scheme of the three sutures commonly used to repair tendon (Achilles tendon example in back view). (A): the non-grasping suture (Bunnell) consisting in looping the anchor around the epitenon. (B): the grasping suture (Kessler) based on 4 opened loops, which pinch collagen fibers. (C): The locking suture (Krackow) made of several closed loops.

Several fibers made of polyester (Ethibond®), nylon, polypropylene or a combination of ethylene glycol and terephthalic acid (Dacron®) are already clinically used for suture alone. They are non-resorbable as they have to maintain more than one year the end-to-end tendon extremities [19]. Other materials have been developed for suture augmentation, which is a different approach. Schliemman *et al.* (2015) compared the reconstruction of a tendon with a polydioxanone (PDS) or cable wire augmentation and with suture anchor repair alone. They showed that suture augmentation in both cases provides less elongation and higher loads (almost a 1.5 factor) than the simple suture [62]. A negative aspect of cable wires is that a second surgery is needed to remove them.

Alternative methods have been proposed to avoid the use of sutures. Hohendorff *et al.* (2008) compared post-surgery results of Achilles tendon rupture treated either with fibrin glue or sutures. They noted that both strategies reached almost the same results. Moreover, fewer complications were observed for the fibrin glue cohort [63]. Rose *et al.* (2014) also worked on the biological tissue gluing. They used solutions of silica nanoparticles (NPs) to glue mismatched tissue. They tested it *in vitro* on a piece of calf liver with a created gap of 2 cm. They glued the two ends and kept it under finger pressure during 30 s [64]. They observed that the two parts of the liver remained attached and that the glue did not affect the rigidity or the permeability of the tissue. This second approach is very promising as it is quite simple and fast to implement. It must be tested on tendon to know if the bonds created with the silica NPs are strong enough to support physiological loads as applied in Achilles tendon sites for months *in vivo*.

3.2. Metallic implants

Some other researchers have developed metallic implants to achieve tendon repair with the best mechanical properties.

Erol *et al.* (2007) developed an implant made of stainless steel wires with different spiral-shaped structures on sheep cadaveric Achilles tendons [65]. Briefly, the prostheses are composed of a coiled wire head, which hooks the tendon, and a wire passing through it to join the head to the other tendon end or bone. They also compared their implant with classical sutures. In some cases, they observed the breaking of the tendon-implant holding point and the fibering of tendon's ends, raising the problem of the material elastic properties. If the material is too stiff compared to the tendon, the rupture of the anchor will occur. To have the best mechanical properties, it is essential to use materials with the same range of elastic modulus as tendon. In their preliminary study, they obtained good mechanical results compared to sutures alone. But authors advised to use this kind of device only for bone-tendon repair. Ađır *et al.* (2014) also investigated this kind of metallic implant. In their

Table 1. Commercially available grafts or implants for tendon repair. The devices written in bold italic are detailed in sections 3.2 and 3.3.

Type	Name	Source	Company	Refs.
Metallic implants	<i>Teno Fix</i> ®	Stainless steel	Ortheon Medical, Winter Park (USA)	[Wolfe 2007]
	<i>Tenolig</i> ®	Stainless steel (with Dacron fibers)	FH Orthopedics, (FR)	[Lacoste 2014]
Xenografts	Bio-Blanket®	Bovine dermis	Kensey Nash Corp. (USA)	[Gomes 2015]
	Conexa®	Porcine dermis	Tornier/Wright Medicals (TN)	
	CuffPatch®	Porcine SIS	Organogenesis (MA, USA) Licensed to Arthrotek (IN, USA)	
	<i>Inforce</i> ® Reinforcement matrix	Porcine dermis	Integralife Sciences (NJ USA)	[Hollawell 2015]
	OrthADAPT®	Equine pericardium	Pegasus Biologic Inc. (USA)	[Gomes 2015]
	<i>Restore</i> ™	Porcine SIS	DePuy Orthopedics (IN,USA)	[Phipatanakul 2009]
	Shelhigh No-React® Encuff Patch	Bovine or porcine pericardium	Shelhigh Inc. (NJ, USA)	[Gomes 2015]
	<i>TissueMend</i> ®	Bovine fetal dermis	TEI Biosciences (MA, USA) licensed to Stryker Orthopedics (NJ, USA)	[Song 2010]
	<i>Trellis</i> ™ Collagen Ribbon/ Bio-tape XM	Porcine dermis	Wright Medical Technology, Inc. (USA)	[Berlet 2014]/[Gomes 2015]
	Zimmer® or Permacol™	Porcine dermis	Tissue Science Laboratories (MA, USA) licensed to Zimmer (IN, USA)	[Gomes 2015]
	Allografts	Arthroflex®	Human dermis	Arthrex, LifeNet Health Inc. (USA)
<i>GraftJacket</i> ®		Human dermis	Wright Medical Technology (USA)	[Song 2010, Lee 2008]
Matrix™ HD		Human dermis	RTI Surgical (USA)	[Gomes 2015]
TenSIX™		Human dermis	Solana, Wright Medical (USA)	
Synthetic grafts	<i>Artelon</i> ® and <i>Sportmesh</i> ™	(Polyurethane urea) polymer	Artimplant AB (SWE) Biomet Sports Medicine (IN, USA)	[Schoaib 2016]
	<i>Biomerix</i> ™ RCR Patch	Polycarbonate (polyurethane urea) with polyester fibers	Biomerix (USA)	[Gomes 2015]
	<i>Dacron</i> ® mesh	Polyethylene terephthalate (PET)		
	<i>Gore-Tex</i> ®	Polytetrafluoroethylene	WL Gore and Associates (USA)	
	<i>LARS ligament</i>	PET	LARS (FR)	
	<i>Leeds-Keio</i> ® or <i>Poly-tape</i> ®	Polyester ethylene terephthalate	Xiros plc, Neoligaments (UK) Yufu Itonaga Co. Ltd (JPN)	
	<i>Marlex</i> ® mesh	Polyethylene polymer	C R Bard (USA)	[Morrey 2016]
	<i>Orthocoupler</i> ™	PET	bioLOGIC Corp., Surgical Energetics LLC (USA)	[Melvin 2010]
	<i>Ortho-Tape</i> ®	PET	Neoligaments (UK)	[Abdullah 2015]
	Sericuff™	Silkworm silk	Serica, Allergan (USA)	[Gomes 2015]
	STR GRAFT™	Poly-L-Lactide	Soft Tissue Regeneration Inc. (USA)	
	X-repair™ X-repair-SL	Poly-L-Lactide	Synthasome (USA)	

study, they used stainless steel wires but designed it with several loops [66]. The wire is applied from outside and allows the transversal anchoring of metallic pins in it. Here again, some limitations of the device are explained: these implants cannot be used for hand injuries and are more suitable for larger body tendons as Achilles tendons.

Metallic devices such as the Teno Fix® [67] or Tenolig® [68] are already commercially available. They were tested on cadaveric tendons and on patients respectively. Teno Fix® was compared with conventional sutures and no biomechanical improvement was shown switching from one to the other. Tenolig® exhibits different advantages such as the use of percutaneous surgery for the device positioning with ultrasonography monitoring to target the two Achilles tendon ends, very small wound scars and complications occurring only for 1 over 75 patients. The return time to sport was estimated to be 9 months. This kind of metallic implant is not largely used in clinical practice, as studies evaluating their effective improvement compared to classic sutures are still rare. Moreover, several limitations such as tearing of the site repair have been highlighted as mentioned above. Extensive improvements of these techniques are needed before becoming a common and viable strategy.

If the tendon injury has been neglected or if the site of injury has a poor quality due to tendinopathy, sutures or implants are not sufficient anymore to repair it [69]. Furthermore, to avoid the re-rupture, a reinforcement of the site is needed. To meet these objectives, grafts can be used. The tendon augmentation with grafts consists in adding a matrix either around the defect and then suturing it (onlay surgery), or in the ruptured tendon and then closing it with suture inside (inlay surgery). The combination of the classic sutures, which join the two tendon extremities, with the graft, may improve tendon repair. The grafts can come from different origins: the patient himself (autograft), another human being (allograft), animals (xenograft) or from synthetic materials. These different grafts are successively described in the following part.

3.3. Grafts

Autografts.

Sophisticated surgical procedures have been elaborated to overcome large tendon defects with patient's own "material". Three kinds of procedures more or less invasive allow accessing the tendon: open, mid-open and percutaneous. Beskin *et al.* (1987) compared four "open" techniques on 42 patients suffering from Achilles tendon rupture: Bunnell or Kessler sutures, "three bundle", and augmentation, either with the plantaris or with the peroneus brevis tendon [70]. These last two methods consist in using local tendon transfer to reinforce the Achilles tendon. The four techniques show promising results as 85 to 92% of patients return to normal long-term activity after the surgery. However, in each case, a single long longitudinal excision is performed which is very invasive, urging some clinicians to develop less invasive techniques. Carmont *et al.* (2007) also used the peroneus brevis tendon to reconstruct Achilles tendon [71]. Contrary to Beskin *et al.*, they did two para-midline incisions. Skin wounds are clearly smaller and skin integrity is preserved. Moreover, this allows preserving the surrounded tissues (tendon sheath) and may improve tendon's healing. To follow through, other autologous sources for reconstruction can be recruited. Ebied *et al.* (2016) repaired Achilles tendons thanks to free semi-tendinous tendon grafts from upper muscles [72]. Shewy *et al.* (2009) used two intratendinous flaps from the proximal gastrocnemius-soleus complex [73]. Briefly, they created two flaps in the musculo-tendinous junction and passed them through the Achilles tendon gap. They fixed the flaps extremities to the calcaneus (bone). Few complications were observed as wound gapping or infection, and long pain after surgery. However, this technique showed good results as patients recovered their pre-injury sporting activity level.

The main advantage of these two surgeries is the use of highly vascularized tissues in a site close to the injured tendon, but less invasive incisions are recommended for the future. Autografts present several key strengths such as absence of foreign body response, conservation of native mechanical properties and vascularization continuity. The main inconvenience is the risk of damaging the donor site tissue and thus creating new lesions. Moreover, the neo-tendon reconstructed with surrounding tendons or muscles parts is thicker than the native one. This can lead to unsightly aspect repair and to patient discomfort on the repair site.

Other strategies to repair injured tendons have been developed to avoid creating more lesions in patients. Tendon augmentation with xeno- or allograft may be good candidates for this purpose.

Xeno- and allografts

Xenografts are tissues or organs coming from other species that are pre-decellularized. Porcine decellularized small intestine submucosa (SIS) is the most commonly used xenograft. Several clinical studies have been performed to assess their effectiveness for tendon repair augmentation. Phipatanakul *et al.* (2009) used SIS (Restore™) for rotator cuff repair [74]. As repairs were not convincing and as some complications (infections, skin reactions) were observed, authors did not recommend SIS for such repair augmentation. Scramberg *et al.* (2004) came also to the same conclusion for this repair area as 5 over 11 patients presented worse results after the surgery [75]. Clinicians are quite unanimous on this issue. However, SIS may be adapted for tendons in other locations such as the foot or ankle as only 6 % of the patients showed complications such as re-tear or patch failure.

Other sources of xenografts are also used. Berlet *et al.* (2014) tested the Trellis™ device (a decellularized, freeze dried and sterilized porcine dermis), in a ribbon form on human cadaveric feet [76]. They created tendon defects greater than 5 cm. The tensile testing showed that in most cases, the suture failed first. As the tendon ends are not joined anymore, the load is only borne by the graft. Thus, in comparison with suture alone, the Trellis™ augmentation enhanced strength of Achilles tendon repair.

Other strategies, based on allografts, have been developed to overcome some rejection or infection reactions. Allografts are ECMs mostly coming from human dermis or SIS. Song *et al.* (2010) compared two commercially available devices on a cadaveric sheep model [77]. The first one is a xenograft named TissueMend®, which is derived from fetal bovine dermis and the second one, an allograft named GraftJacket® from human skin. The authors remind that grafts of dermis origin have better mechanical properties than matrices derived from SIS that were previously described. TissueMend® and GraftJacket® presented almost the same strength. They both improved tendon repair compared to suture alone. Lee *et al.* (2008) also used GraftJacket® matrix to augment tendon repair [78]. Clinical tests on Achilles tendon rupture were performed. At 3 months, patients recovered full range of motion and no re-rupture happened. The return-time to activity was about 12 weeks, which is quite encouraging.

Rather than choosing between xenografts and allografts, Hollawell *et al.* (2015) decided to combine them for Achilles tendon repair [79]. They used the allograft to span the gap between the two tendon ends and the xenograft (Inforce® Reinforcement Matrix) to secure the repair site. This graft combination improved the mechanical properties and physiological function, and patient pain was reduced. Some further investigations of this new strategy must be performed to better quantify its benefits.

Those acellular matrices either from animal or human origin show great advantages, overcoming the host reaction concerns and leading to good mechanical properties. Herbert *et al.* (2015) evaluated different decellularization processes needed to obtain such materials [80]. They studied the effect of using acetone or chloroform as fat agent reduction and antibiotics or peracetic acid as

biodecontaminants. They showed that the tensile strength and Young modulus of acellular porcine super flexor tendons are in the same range as the native one before the decellularization. However, this process altered the matrices properties at the low strains in the toe region where the crimp should play its shock absorber role. A potential way to overcome this problem is to reproduce this wavy structure. Branch *et al.* (2011) adopted this strategy with allograft for Achilles tendon repair [81]. They cut a human dermal acellular mesh in a z-wave shape, which finally looked like an accordion. They performed inlay surgery with a “strip and shoelace” weave. No re-rupture occurred and only one over the 3 case reports presented adhesion with the surrounding tissues.

Regarding the loss of cellular material due to the decellularization process, cell-based therapy combined with allografts emerged. Gaspar *et al.* (2015) reviewed the different cell strategies [82]. Before being implanted on the tendon injury sites, grafts can be sewn with cell suspension to enhance tendon regeneration. They highlighted the fact that the cell type chosen is crucial. Indeed, tenocytes or dermal fibroblasts are already differentiated, but their available quantity is limited. Progenitor stem cells overcome this issue, but can lead to bone ectopic formation. Finally, induced pluripotent stem cells may also be used on grafts. However, they raised the safety and efficiency problems. Güngörmüş *et al.* (2016) used tenocytes and seeded them on decellularized rat tendons [83]. Finally, they implanted the cell-seeded scaffold in a rat model. No immune reaction occurred and their other results suggested that this scaffold improve mechanical properties of the repair.

Even if xeno- and allografts present some advantages, the matrix alteration due to the decellularization process is a problematic issue as it alters mechanical properties and leads to antigenic response [84]. Since it is essential to augment tendon with grafts having similar range of strength, synthetic grafts have been developed and are currently used in clinical practice.

Synthetic grafts

Two categories of synthetic grafts are used to augment tendon. The non-resorbable grafts persist in the body and act as a substitute to overcome the lack of tissue. On the contrary, resorbable grafts are degraded by the body and support the fibrous ingrowth [85].

Non-resorbable grafts are commonly made of synthetic polymers such as polyester (Dacron®), polytetrafluoroethylene (PTFE or Teflon®) [86], and silicone rubber [87]. Such materials are already clinically used. Morrey *et al.* (2016) evaluated non resorbable polypropylene mesh commercially available (Marlex®) on 8 quadriceps tendons ruptures (knee) [88]. No re-rupture occurrence and good range of motion were the main advantages of this synthetic augmentation. As they tested it on a small cohort, with no mechanical evaluation, further studies are needed. Abdullah *et al.* (2015) evaluated the use of polyethylene terephthalate (PET) mesh called Ortho-Tape® [89]. They explored this new device on two patients who needed hand surgery because of massive tendon loss. Promising physiological results were shown. Melvin *et al.* (2010) developed their own device Orthocoupler®, made of 32 bundles of thousand PET fibers [90]. They implanted it in a goat model. Sixty days after the surgery failure forces for the specimens with the synthetic graft were 2.5 times higher than for sutures in the control group. Sutures were too fragile compared to the Orthocoupler® which is anchored and sutured in the muscle reinforcing the musculo-tendinous junction. It allows reinforcing the musculo-tendinous junction.

Finally, another criteria is the prevention of the tendon sheath adhesion. Non-resorbable grafts made of Teflon seem to be the appropriate candidates. Indeed, Williams *et al.* (1964) tested them on a dog model and compared them with autologous grafts [86]. Adhesions with the surrounding tissues were clearly observed for autogenous grafts, whereas Teflon graft surfaces glided and allowed

free joint motion. However, they reported some surgery problems as the solid anchoring of the Teflon grafts on tendon.

Non-resorbable grafts present some advantages such as their biocompatibility, their strength and the absence of adhesion with the tendon site. Nevertheless, they cannot be degraded, and are generally complicated to implement.

Resorbable grafts may overcome some of those issues. They can be composed of carbon ([91], [92]), polyglactin [93], polyglycolic acid (Dexon®) [94], or polylactic acid [95]. In the 1970s, Jenkins *et al.* (1980) investigated flexible carbon implants for ligation or tendon injuries. Special affinity of the living tissue with carbon was observed [91]. Moreover, carbon based scaffolds enhance the mechanical properties of the tendon and improve the alignment of collagen neo matrix. However, fragmentation of this kind of material often occurs and may lead to some irritation of the joint. Finally, they should not to be used close to metallic implants as they can react together. To overcome these drawbacks, Alexander *et al.* (1983) tried to coat carbon implants with polylactic acid but could not reduce the fragmentation process [96].

In this way, Cao *et al.* (2001) used unwoven polyglycolic acid fibers, which they assembled in a cord shape and wrapped with acellular intestinal submucosa membrane [97]. Tenocytes were cultured on it. Then, they created a 2.5 cm long defect in the second digital flexor profundus tendon of hen and repaired it with the cell-scaffold. They harvested the specimens at 8, 12 and 14 weeks and performed histological observations. The longer the graft stayed in the body, the better were the biomechanical properties. The authors suggested that a minimum time was required for a good tissue remodeling of the tendon. Histological results showed that the neo-tendon contained a large amount of tenocytes and presented its own structure, easy to distinguish from native tendon.

Synthetic polymer scaffolds can also be designed as a tissue mesh. Shoaib *et al.* (2016) performed surgical repair in 7 patients suffering from symptomatic chronic Achilles tendon rupture with a bio-absorbable polyurethane polymer device (Artelon®) [98]. Artelon® can be seen as the resorbable equivalent of the Ortho-Tape® previously described. They compared this synthetic tendon augmentation to the Krakow suture alone. Better results were shown with the Artelon® graft. The authors also suggested that this device could be used for defect larger than 5 cm. Finally, they recommended combining it with non-resorbable suture in order to secure the augmentation over the years.

We have seen that synthetic grafts show promising results for tendon repair and in particular for the mechanical properties. However, some concerns persist as they may lead to foreign body response. This is also the same for xeno-allografts, and in the case of autografts, new lesions are created that may lead to secondary surgery in case of local degradation. Clinical practices or devices to repair tendon get closer to the ultimate goal, but they often lack specific criteria as strength or body tolerance. This is why some new scaffolds based on biocomponents are currently being developed. Such engineering is not straight-forward and needs to meet several strict specifications that we will discuss below.

4. SCAFFOLD DESIGN SPECIFICATIONS FOR TENDON REGENERATION

Scaffolds for reconstruction must meet several requirements as tendons are such specific tissues, with multiscale order and high mechanical solicitations. These are dependent on the site aimed for reconstruction. Indeed, tendon size and shape can vary greatly, in function of the location in the body. Whereas rotator cuff and patellar tendons are sheet-like, length and width being in the same order and much greater than the thickness, Achilles tendons are rather unidimensional, in a rope-like manner shape [99]. Typical dimensions are given in Table 2. Mechanical properties can also vary according to sites and persons, with Young modulus ranging from

0.5 to 1.9 GPa, ultimate tensile strength from 50 to 120 MPa and strain at break between 5 and 20% [100] [101]. Scaffolds must meet as much as possible these properties to resist solicitations and promote cell differentiation [102]. Even though tendons and ligaments are sometimes indiscriminately named in papers given their similarities, they do exhibit differences when it comes to mechanical properties. Ligaments are usually not as stiff (modulus from 5 to 450 MPa) and strong (UTS between 1 and 50 MPa) as tendons and are more elastic (strain at break from 10 to 40 %) [101]. Another specificity that the scaffolds must mimic is the uniaxial structure of tendons, aligned along the direction of load. To obtain neo-tendons by promoting cell alignment and differentiation, scaffolds should mimic this anisotropy. The influence of scaffold anisotropy has been widely investigated, by using microgrooves in the micrometer scale for instance [103][104]. Scaffold alignment may be important down to 100 nm, based on the work of Van Delft and co-workers [105].

Scaffolds for reconstruction must also comply with general specifications for regenerative scaffolds. Biocompatibility is an obvious specification but its definition is not straightforward and has evolved with time. Now, it goes further than the old definition, i.e. the absence of immune rejection or toxicity, called “bio-tolerable” by Mertz [106], adding “the ability of a device material to perform with an appropriate host response in a specific situation” [107]. Scaffolds should not be inert to the body but bioactive, promoting cell adherence and proliferation. Scaffold porosity is here paramount to ensure exchanges and cell penetration. Besides, the scaffold must be regenerative, enabling cell to differentiate and adopt the relevant phenotype to reconstruct the ECM. Many parameters are at stake here such as mechanical properties of the scaffold, its structure and alignment as well as chemical cues [102] of the ECM or growth factors. To allow good regeneration, the scaffold should at least be biodegradable or even better, bioresorbable, based on definitions given by Vert [108]. This includes the degradation and the elimination of the polymers and by-products. Time of degradation and the subsequent change in mechanical properties are also crucial for tendon reconstruction but very seldom investigated due to the complexity of such a study. To assess the question, works on small intestinal submucosa (SIS) in canine Achilles tendon repair, carried by Badylak *et al.* (1995) and then Gilbert *et al.* (2007) are valuable. Badylak *et al.* (1995) reported full use of the injured leg by the dogs after 9 to 13 weeks and recovery of injured tendon strength after 12 weeks as assessed by tensile testing [109]. Degradation rate of SIS was investigated by Gilbert *et al.* using carbon 14 measurements, showing 60% loss after 4 weeks and total degradation after 2 months [110]. Thus, we can hypothesize that time span aimed for degradation should be around two months and that, after degradation of the scaffold, recovery and strengthening continue in the month scale.

Last but not least is the processability of the material. This factor is key to meet the specifications listed above and remains one of the main challenges for biomaterials, as the processing should not degrade their properties.

In this review, we will focus on the use of collagen I for tendon reconstruction as it is the main component of tendons and because it is biocompatible and degraded by enzyme with low inflammatory response [111][112]. It also promotes cell adhesion [113][114] and differentiation [102], and is one of the most favorable biomaterials for cell survival compared to cheap and easy to use alginate for instance, or to chitosan [115]. It is thus a promising material that fuels much innovative research [116].

5. COLLAGEN BASED TECHNIQUES

As collagen I fulfills the requirements for regenerative scaffolds listed in Table 2, the main challenge is to process it to obtain significant mechanical properties and structure for tendon repair. This section will describe collagen-based techniques, which favor the

production of anisotropic complex architectures, with a particular emphasis on collagen alignment at multiple length scales to better mimic tendon structure. Although promising results for tendon repair have been obtained with isotropic materials such as collagen sponges [117], the focus will be laid on the development of scaffolds which 3D organization aims at providing mechanical support and cell guidance for regeneration.

5.1. Extrusion

The extrusion process consists in forcing a material or a solution to pass through a die, giving its shape to the resulting extrudate. This method provides bars, tubes or fibers with a high production rate (few cm/s [118]). Collagen solution extrusion was first developed in the 1960s to create new biosutures for ophthalmic surgeries [119]. Since then, the potential of this molecule was highlighted leading to its widespread use in tissue engineering. Collagen solution extrusion is quite easy to implement requiring only a syringe, a needle or tubing, a collecting bath and a device to control the flow rate (syringe pump) (Fig. 5A). Basically, to produce collagen threads the syringe is filled with a collagen solution and mounted in the syringe pump. Then, the solution will pass through the tubing and will go out in a bath containing the fibrillogenesis buffer. Finally, some other post-production processes can be performed [118], [120]-[126]. Self-assembly of collagen may occur either with a pH transition when using an acidic collagen solution and a basic to neutral pH buffer, or through a temperature jump for cooled neutral collagen solution. In most studies, the collagen is extracted from rat tail (RTT) or bovine Achilles tendons (BAT). Zeugolis *et al.* (2008) compared the properties of threads made of RTT or BAT acidic collagen [121]. By scanning electron microscopy, they observed no significant differences in the substructure of the collagen fibers in the two kinds of threads. Collagen concentration of solution commonly used ranges from 5 mg/mL to 30 mg/mL in acidic conditions (pH=2) [118], [121], [123], [125]-[127]. For the fibrillogenesis buffer, the same basis is found in different studies: 135 mM of NaCl, 30 mM of TES (tris(hydroxymethyl)methyl-2-aminoethane sulphonic acid) and 30 mM sodium phosphate dibasic with a resulting pH of 7.5 [122], [123], [125], [126]. Other buffers as phosphate saline buffer (PBS) [124] or polyethylene glycol in sodium phosphate dibasic and monobasic [118] are also used. Characteristic dimensions of collagen threads, obtained by this technique, range from 100 μ m to 1 mm for wet diameter and around 20 μ m to 100 μ m after drying [118], [122], [123], [125]. The length depends on the syringe volume capacity and the inner diameter of the tubing. In general, the mean thread length obtained by this technique ranges from few centimeters to about one meter. Mechanical properties of collagen strands have been measured in a routine manner for dry conditions and, less frequently, in wet conditions. Cornwell *et al.* (2007) measured Young modulus of wet collagen fibers around 4 MPa [127]. Regarding the elastic modulus of native tendon, those fibers are between 2 and 3 orders of magnitude “weaker”. For the ultimate tensile strength (UTS), Cavallaro *et al.* (1994) [118], Cornwell *et al.* (2007) [127] and Dunn *et al.* (1993) [125] obtained results ranging from 1.2 to 10 MPa. Dunn *et al.* (1993) also observed that UTS decreases when the fiber diameter increases. So, in wet conditions, which mimics physiological environment, mechanical properties of collagen fibers are still far from that of native tendon (Table 2). This is why different cross-linking (CXL) agents are commonly used to improve those characteristics. Cross-linking process consists in creating new bonds between collagen molecules with chemical species or external excitation sources. The most commonly used on collagen threads are glutaraldehyde, carbodiimide (EDC), cyanamide, hydroxysuccinimide (NHS) and dehydrothermal treatment (DHT), simple drying process, or ultra violet (UV) exposition.

Kato *et al.* (1989) have shown that they can produce collagen threads cross-linked with glutaraldehyde having an UTS of 50 to 66 MPa in wet conditions. Those results are in the same range than

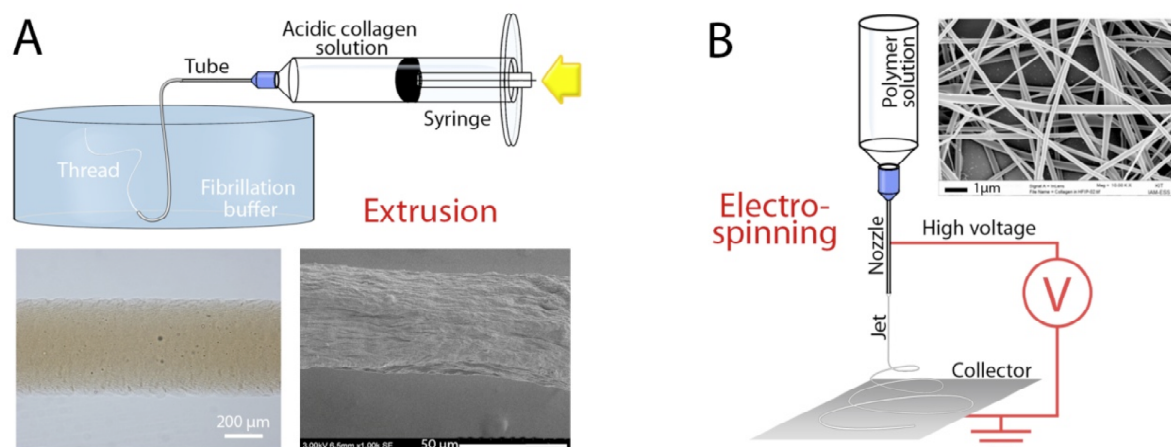


Fig. (5). Schematics and resulting scaffolds of extrusion (A) and electrospinning (B) techniques. (A) Top: Schematic of the extrusion protocol where acidic collagen solution held in the syringe is forced to pass through the tubing and arrives in the fibrillogenesis buffer which induces the thread formation. Bottom: collagen thread extruded from an acidic solution at 30 mg/mL observed under optical microscope (left) and under scanning electron microscope (right) (Authors, non-published work). (B) Schematic of the electrospinning protocol where a high voltage is applied between the nozzle and the collector, forming a jet of the polymer solution that dries into fiber. Inset: Resulting fibrous mat from a solution in 1,1,1,3,3,3-hexafluoro-2-propanol (Adapted with permission from Bürck *et al.* (2013) [133]. Copyright 2016 American Chemical Society).

UTS of rat tail tendons (33 to 39 MPa). The UTS is divided by a factor 2 for severe dehydration and for EDC treatment. As for Young modulus, they reach 400-500 MPa with glutaraldehyde CXL process. Zeugolis *et al.* (2008) evaluated mechanical properties of collagen threads hung and dried at room temperature [121]. Young modulus of those strands ranged from 1 to 3 GPa and UTS from 0.2 to 0.3 GPa. These results have similar values as native tendon (Table 2). However, we have to keep in mind that in this case, tensile testing is performed in dry conditions, which are not close to the physiological ones. As for Kato *et al.* (1989), they lose on average 3 orders of magnitude in wet conditions. Finally, to have as many bonds as possible, some combinations of CXL processes can be used (dehydrothermal with cyanamide [125] etc).

The alignment of collagen fibrils inside the collagen threads is also a parameter to take into account. The extrusion technique has the main advantage to induce collagen fibrils alignment in the longitudinal axis, thanks to the high constraints applied when collagen solution is forced to pass through the narrow die ([118], [124]). This phenomenon can be further increased by stretching the threads [122].

Lai *et al.* (2011) observed that, *in vitro*, human fibroblasts cultured during 1 or 2 days have an elongated shape following the longitudinal axis of the collagen fibrils [124]. This suggests that there is some contact guidance of the cells on the collagen threads structure. Cornwell *et al.* (2007) highlighted the problem of CXL post-processes on collagen threads. Indeed, they observed that fibroblast migration rate decreased by using CXL agents [127]. A compromise between the improvement of mechanical properties with CXL techniques and the upgrading of cell proliferation must be found. To go further, Dunn *et al.* (1993) implanted their collagen threads in subcutaneous space of the rabbit during 4 weeks. The threads were surrounded by a fibrous tissue and were colonized by inflammatory cells and fibroblasts [125]. Threads crosslinked with DHT combined with cyanamide were degraded over 4 weeks. Cavallaro *et al.* (1994) also had promising results in a canine ligament model and a rat abdominal repair model that can be transposed for tendon repair [118]. They noticed the neovascularization and the cell infiltration in the collagen threads. In both studies, no rejection of the collagen scaffolds was observed.

5.2. Electrospinning

Electrospinning is a widespread technique for fibrous scaffold production. This method, based on a simple and inexpensive set-up, uses an electrical field to cast various materials, such as polymer solutions or melts, into fibers, making it attractive for tissue engineering. Briefly, a high voltage is applied between a grounded target and a needle supplied with the liquid of interest, leading to charge accumulation at the liquid surface [128], [129]. For sufficiently high voltage, the surface tension is overcome, leading to the formation of a liquid jet that forms a fiber which dries and is collected on the target, resulting in a fibrous mat (Figure 5B).

To achieve electrospinning of a polymer solution, many requirements must be met. In addition to the setup parameters such as voltage or solution feeding rate, and the ambient conditions such as temperature and humidity, intrinsic characteristic of the solution are paramount to electrospin it. Ideal solutions must have low surface tension and high conductivity [130] and must be viscous enough to form a stable jet that does not break before drying [131] but not too much to ensure sufficient flowability [132] and dry fast before reaching the collector [133]. Usual solvents such as acetic acid lack the viscoelastic properties needed to form a stable jet and do not evaporate fast enough before reaching the collector [133]. Collagen electrospinning was achieved using fluoro-alcohols such as 1, 1, 1, 3, 3, 3-hexafluoro-2-propanol [134]-[136] and 2, 2, 2-trifluoroethanol [137]. However, such a process was proven to denature collagen [133], [138]. Indeed, resulting collagen is soluble in water, does not exhibit characteristic D-banding under transmission electron microscopy and has lower denaturation temperature. Further proofs were given thanks to circular dichroism, electrophoresis and infrared spectroscopy. Attempts succeeded in electrospinning collagen in benign solvent such as Phosphate Buffer Saline and ethanol mix [130] or acidic solution with poly(ethylene oxide) [139], [140]. Bürck *et al.* (2013) demonstrated that collagen fiber electrospun from this solvent did not preserve much better the native structure of collagen and that part of the denatured collagen was intrinsically due to the electrospinning process and not to the solvent [133].

Recently, Elamparithi *et al.* (2015) reported successful electrospinning of collagen in 97: 3 acetic acid: DMSO mix with fibers exhibiting the characteristic D-banding of native collagen [141].

Table 2. Requirements for an ideal scaffold for tendon repair with description and quantitative criteria when assessable.

	Requirements	Descriptions	Criteria		Refs.
Tendon mimetism	Size / Shape	Scaffold size and shape depend on the site of the tendon to be reconstructed	Rotator cuff tendon	<i>3 x 21 x 17 mm</i>	[Verdiyeva 2015]
			Patellar tendon	<i>5 x 33 x 59 mm</i>	
			Achilles tendon	<i>5 x 14 x 120 mm</i>	
	Mechanical Strength	Can bear usual mechanical sollicitation throughout the healing process and promote cell differentiation	Young Modulus	<i>0.5 - 1.9 GPa</i>	[Ladd 2011, Jung 2009]
			UTS	<i>50 - 120 MPa</i>	
			Strain at Break	<i>5 - 20 %</i>	
Alignment	Alignment in the direction of the load to promote cell alignment and differentiation	Size threshold	<i>100 nm</i>	[Van Delft 2008]	
Temporary biocompatible scaffold	Biotolerable	Absence of immune rejection from the scaffold and its degradation products <i>in vivo</i> (and non toxic)	Non cytotoxic, genotoxic, carcinogenic ...		
	Bioactive	The scaffold promotes cell adhesion and survival	Must be porous to allow exchange with medium Good colonization and viability of the cells on the scaffold		
	Regenerative	The scaffold fosters the formation of a new tendon by inducing cell differentiation	No observable difference between the new and old tendons		
	Biodegradable /resorbable	Degradation of the scaffold to leave room to the new tendon/and elimination of degradation products	Time range :	<i>2 to 3 months</i>	[Gilbert 2007, Bady-lak 1995]
Process	Tunability	The material can be shaped in a controled way to suit different location and achieve hierarchical structure	Control of the structure from molecular to macroscopic scale, and tunable size and shape of the scaffold		

However, no further investigation on native collagen content was carried out. The cross-linking of the resulting fibrous mat after electrospinning with 1-ethyl-3(3-dimethylaminopropyl) carbodiimide hydrochloride does not allow for water solubility test and give surprisingly low mechanical properties with modulus and tensile strength at maximum load of a few kPa. This may be suitable for non-load bearing tissue reconstruction such as cardiac tissue, aimed by the authors, but not for tendon reconstruction.

Thus, electrospinning of collagen for tendon reconstruction seems only relevant when collagen is co-electrospun with biodegradable synthetic polymers such as poly(l-lactide-co-ε-caprolactone) [142] or poly(L-lactic acid) [100], as it improves biocompatibility of synthetic polymers. For instance, an interesting work was published by Ladd *et al.* (2011) who electrospan two different polymers with collagen to reproduce the musculo-tendinous junction: the poly(L-lactic acid), being stiffer, for the tendon part and poly(ε-caprolactone) for the muscle part [100]. Whereas the synthetic polymers provide mechanical strength, the collagen promotes good cell viability close to 100% after 7 days of both C2C12 myoblasts and NIH3T3 fibroblasts seeded on each part.

5.3. Freeze-casting

Freeze-casting, also called ice-templating, is a common technique to produce highly porous scaffolds from solutions or suspensions in solvents such as water or camphene. Considering a water based polymer solution, by simply freezing it, phase segregation occurs between ice crystals and a phase concentrated in polymer (Fig. 6A & B). After freezing, the sample is freeze-dried under vacuum, sublimating ice crystals (Fig. 6B) and results in a dried polymer sponge (Fig. 6C). Depending on the protocol used and the parameters chosen, such as cooling rate, final temperature or size and shape of the vessel, it is possible to favor different crystalline structures and grow ice crystals of different sizes, thus tuning size and shape of the pores [143].

Enabling production of highly porous and anisotropic scaffolds, ice templating of collagen seems promising to promote cell proliferation, alignment and differentiation required for tendon reconstruction. The pores usually obtained in freeze-cast collagen sponges, ranging from 50 to 300 μm, are optimal for cell culture. Switching from small to large pores can be easily done, by decreasing final temperature or cooling rate, or by crystal annealing [144].

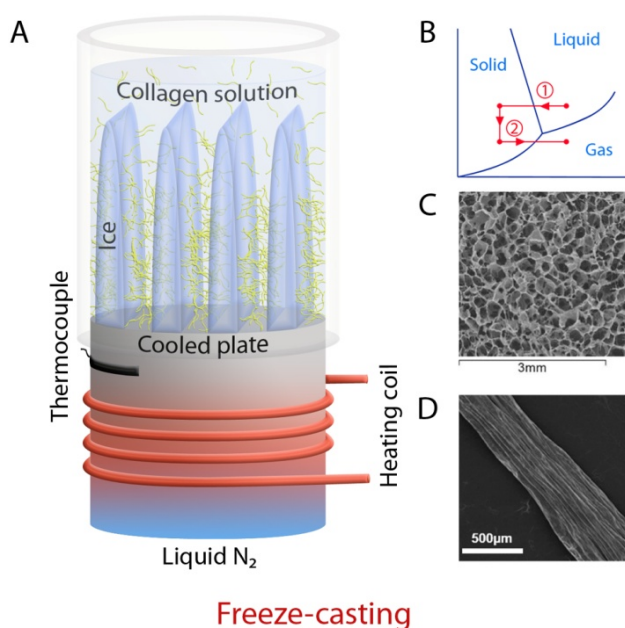


Fig. (6). Freeze-casting setup schematics (A) with the paths followed on the water phase diagram (B) and a resulting collagen sponge observed under SEM (C) and a pre-fibrillated collagen scaffold after freeze-casting (D). (A) Freeze-casting schematic where a collagen solution is directionally frozen on a metallic cooled plate, which other side is dipped in liquid nitrogen and which temperature is controlled thanks to a thermocouple and a heating coil; causing segregation between ice crystals and a concentrated phase in collagen. (B) Water phase diagram schematic where the path followed during freeze-casting (1) and then freeze-drying (2) is drawn. (C) An isotropic collagen sponge observed under SEM (Adapted from Davidenko *et al.* 2015 [150], Creative Common License). (D) SEM picture of Lowe *et al.*'s longitudinal scaffold, pre-fibrillated before freeze-casting in a high aspect ratio vessel (Adapted with permission from Lowe *et al.* 2016 [151]. Copyright 2016 American Chemical Society)

Even though the principle of freeze-drying seems simple, the physics behind is not straightforward. Pawelec and co-workers have realized interesting observations on collagen solution freeze-casting and the dependence of pore size [145] and anisotropy [146] upon parameters. They also investigated the effect of the addition of NaCl and sucrose [147], and of heat transfer between the mold and the heat sink [148] on collagen freeze-casting. They took their work one step further by culturing ovine primary patellar tendon cells on freeze-casted collagen uniaxial and anisotropic sponges in a fibrin gel [149], exhibiting higher cell proliferation, metabolism and matrix production thanks to fibrin gels and a cell phenotype control by the collagen scaffold structure.

Whereas Pawelec and coworkers mainly focused on the freeze-casting of the collagen itself, Caliri and coworkers rather investigated cell culture on freeze-casted scaffolds for tendon reconstruction. Using collagen mixed with glycosaminoglycan (10: 1) (Coll-GAG), Caliri and Harley demonstrated that pores above 150 µm were more favorable for cell proliferation and metabolism [152] while a mix of Insulin Growth Factor 1 (IGF-1) with Growth/ Differentiation Factor 5 (GDF-5) was more effective to promote cell proliferation, collagen production and tendon associated structural protein gene expression [153]. Given the relatively low mechanical properties of collagen sponges (modulus around 800 kPa in dry state), Caliri *et al.* (2011) made an attempt to compensate this by wrapping the freeze-casted scaffold in a collagen air dried membrane crosslinked with 1-ethyl-3-[3-dimethylaminopropyl] carbodiimide hydrochloride and N-hydroxysulfosuccinimide, resulting in a

core shell scaffold with a 8 MPa modulus, UTS between 0.3 and 0.9 MPa and strain at break from 10 to 25 % [154]. Ice templating being also promising for bone reconstruction research, they also produced a bi-component material Coll-GAG/ Calcium phosphate mineralized Coll-GAG (CaP Coll-GAG) scaffold to mimic bone-tendon junction, together with specific growth factors on each side to study the impact on mesenchymal stem cells (MSCs) [155]. Each side exhibited up-regulation of pro-osteogenic and pro-tenogenic genes in the CaP Coll-GAG and Coll GAG parts respectively.

In most articles, two points are not tackled. The first and more important one is the self-assembly of collagen, which could improve mechanical properties, cell adhesion and differentiation [113], [114]. The second one is the shape of the scaffolds that differs from tendons. Since the geometry of the vessel and its filling height highly impact the scaffold structure, any modification of the former will impact the latter. This increases the difficulty to mimic living tissues with this method. However, Lowe *et al.* addressed those two problems [151]. By ice-templating self-assembled collagen, they produced high aspect ratio and highly aligned porous collagen scaffolds (Figure 6D) that could be suitable for Achilles tendon for instance. Uniaxial micro features at the surface enabled rat dermal fibroblasts and chick dorsal root ganglia explants alignment. Precise pore analysis was not reported, neither cell culture inside the scaffold. It should be noted that the scaffolds were obtained without any cross-linkers, and that even though the mechanical properties of the scaffold are low (Young modulus ~600 kPa, UTS 150 kPa, strain at break 110%), they are in the same range as those obtained with cross-linked but not fibrillated scaffolds [154]. The addition of carbodiimide cross-linker could further stiffen the material.

On the way to improve mechanical strength and modulus of scaffolds, an innovative design was developed by Mozdzen *et al.* [156]. They freeze-casted a collagen-GAG solution into a 3D printed acrylonitrile butadiene styrene (ABS) array. Even though ABS may not be the most suitable polymer for tendon reconstruction because of its lack of biocompatibility [157], the composite design of this scaffold is of interest. It combines the mechanical strength of ABS with the high biocompatibility of collagen sponges. Comparing sinusoidal ABS fiber arrays of different amplitude to straight ABS fiber arrays, they were able to tune elastic properties of the scaffold in a crimp-like fashion. This gives a glimpse of the promises held by 3D printing for tissue reconstruction.

5.4. 3D Printing

3D printing, or additive manufacturing, has breached in most good manufacturing sectors in the last few years and tissue reconstruction is no exception. Based on the knowledge acquired on scaffold manufacturing and facing new intrinsic problems, it gives high hopes for its capacity to design complex macroscopic shapes of scaffolds as seen in the previous paragraph, as well as enable precise cell deposition. It consists in a layer-by-layer computer aided deposition that enables the construction of 3D structure designed on the computer.

This technique is currently used in research on skin, cartilage, bone, aortic valve [158]. Different methods of deposition have been developed such as inkjet, extrusion (Figure 7A left) or laser-assisted bioprinting [158]-[160], as well as different hydrogel based inks, called bio-inks [115]. The use of collagen as an ink for 3D printing raises an obvious interest and is investigated especially for bone [161]-[163] and cartilaginous tissue reconstruction [164], [165]. However, current research face difficulties to obtain self-standing 3D printed structures. Thus, collagen is often used to enhance the bioactivity of widespread bioinks such as alginate [166], [167] or agarose [162] that are cheap and easy to use but show lower bioactivity compared to main components of the ECM. It is also used with calcium phosphate [161] for bone reconstruction or mixed with fibrinogen [168] that is easy to crosslink.

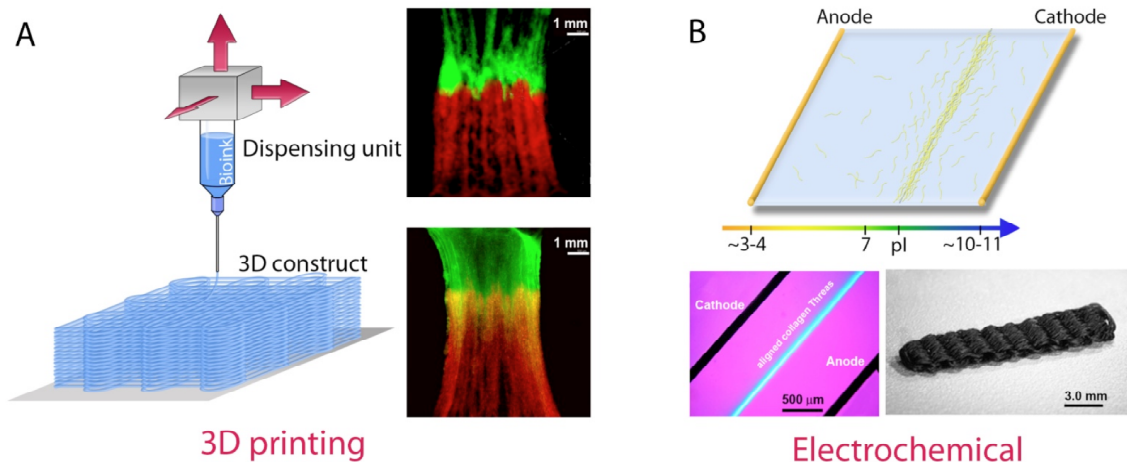


Fig. (7). Schematics and resulting scaffolds of extrusion 3D printing and electrochemical techniques (B). (A) Left: schematic of 3D printing setup where a dispensing unit is monitored in the three directions of space by a computer to deposit bio-ink layer by layer. Top right: 3D printed scaffold to reproduce myo-tendinous junction, accurately seeded with DiO-labeled C2C12 myoblasts (green - top) and DiI-labeled NIH/3T3 fibroblasts (red - bottom) after 1 day in culture. Bottom right: Same scaffold after 7 days in culture exhibiting the interface region in yellow. (B) Top: schematic of the electrochemical technique where a voltage is applied to a collagen solution between the anode and the cathode, creating a pH gradient and inducing collagen migration to the isoelectric point (pI) region and alignment of the molecules. Bottom left: picture of a thread of electrochemically aligned collagen (ELAC) between the two electrodes observed with polarized microscopy. Bottom right: picture of a scaffold woven from triple ELAC threads twisted together. (A, top and bottom right) adapted with permission from Merceron *et al.* (2015) [176]. (B, bottom) adapted with permission from Younesi *et al.* (2015) [179].

Other techniques to print collagen self-standing structures are the deposition of collagen on a cold plate to freeze the solution when deposited [169], [170], or the use of sacrificial negative molds [171], [172]. An original process that is worth mentioning is the printing of a core-sheath collagen-alginate structure [173].

Here again, collagen is sometimes used without inducing fibrillogenesis. Besides, the protocols used can be too harsh to incorporate cells in the bio-ink, preventing the use of additive manufacturing to deposit cells in an accurate and homogeneous way. A few articles deal with pure collagen self-assembled during or after printing [164], [174]. However, for collagen [174] as well as for fibrinogen [168], this leads to tedious protocols where the scaffold is incubated, after each layer printing, either at 37°C or with thrombin respectively.

One currently adopted strategy is the printing side-by-side of an artificial biodegradable polymers and a bio-ink with incorporated cells. The artificial polymer confers mechanical integrity to the scaffold whereas the bio-ink allows exact cell deposition with suitable bioactivity [168], [175]. To our knowledge, despite the control on porosity, macroscopic structure and cell incorporation that this technique offers, no article about 3D printing of collagen for tendon reconstruction has been published yet. This can be explained by the difficulty of handling collagen and the poor mechanical properties obtained with collagen in other domains such as extrusion. As collagen is often used with other bio-inks for its bioactivity, some chose gelatin instead for its lower price. For instance, Merceron *et al.* (2005) published the co-printing of two synthetic polymers polyurethane (PU) and poly(ϵ -caprolactone) (PCL) together with a bio-ink based on hyaluronic acid, fibrinogen and gelatin, to reproduce the musculo-tendinous junction [176]. The bio-ink contained C2C12 myoblasts on the PU side while the bio-ink on the stiffer PCL side contained NIH/3T3 (Figure 7A top right). The construct exhibited good cell viability (Figure 7A bottom right), high cell alignment and characteristic musculo-tendinous gene upregulation. They highlighted the ability offered by 3D printing to deposit different cell types in precise locations, paving the way to complex multicellular scaffolds for regeneration.

5.5. Electrochemical Techniques

Applying an electric field to a collagen I monomer solution enables to control the spatial aggregation of molecules, resulting in collagen membranes [177] or bundles measuring 50 to 400 μm in diameter and several centimeters in length [178]. Electrochemical reactions primarily due to the electrolysis of water create a pH gradient. In the pH region corresponding to the isoelectric point, the collagen becomes less sensitive to the electric field and stops migrating due to global neutral charge (Figure 7B top and bottom left, [179]). In these biomimetic constructs small fibers are highly oriented along the bundle axis, increasing the mechanical properties as compared to randomly oriented controls, and inducing an alignment of tendon derived fibroblasts that migrate into braided bundles [178]. Isoelectric focusing technology was further adapted to enhance directional neuronal growth [180]. This study also unraveled the underlying hierarchical structure, with nanofibrils aggregating into ~ 500 nm diameter D-banded fibrils that align to form larger entities. The influence of phosphate buffer and incubation time on strength and D-banding pattern of the electrochemically aligned collagen (ELAC) threads was also studied and advocated PBS 1X during 12h as the optimal fibrillation buffer [181]. After 96h incubation, Young modulus could attain 6 MPa in wet conditions. The ability to induce tenogenic differentiation of human MSCs was evidenced on the threads with the increase of tendon specific markers such as scleraxis and tenomodulin [182]. An *in vivo* study was led to assess the response of rabbit patellar tendon (PT) to braided ELAC threads [183]. Four months post-implantation, cross-sectional area, mechanical properties and tendon-fascicles content of the PTs treated with ELAC were optimized as compared to controls, but these differences were not evident anymore after 8 months. A low-grade granulomatous inflammation was observed at 4 months but it spontaneously diminished between 4 and 8 months. Different crosslinking strategies were investigated to improve the mechanical properties of ELAC threads, and the increase of genipin concentration in conjunction with highly concentrated ethanol was advocated [184]. Further processing was made with the fabrication of collagen textiles (Fig. 7B bottom right) by weaving ELAC triple threads after twisting continuous ELAC threads obtained with a

kinematically rotating linear electrode pair [185]. MSCs seeded in the porous scaffolds underwent tenogenic differentiation, and the mechanical properties reproduced some aspects of the functional mechanics of native tendon, in particular comparable load-displacement curves in the linear regions. Computer aided design that helped produce patterned electrodes enabled to obtain highly porous collagen scaffolds with controlled geometries that can be further combined to form layered structures [186]. The elastic modulus of these different types of constructs ranged from 5-40 MPa.

5.6. Cell-mediated Collagen Gel Compaction

Cells embedded in loose collagen hydrogels have the ability to compact them into denser tridimensional constructs. This cell-mediated collagen gel contraction was first reported in 1979 by Bell and coworkers [187]. Among the first investigators studying this phenomenon, Stopak and Harris showed that it stems from cell contractility [188]. They also embedded fibroblastic cell explants in collagen gels and observed both fiber alignment and cell orientation along the axis between the explants. They carried out other experiments in which fibroblasts, initially dispersed within a gel, could contract the matrix between fixed posts (Fig. 8A). This resulted in complex patterns of crisscrossing strands. In order to explain the reorientation of the different components of cellularized gels Barocas and Tranquillo proposed in 1997 a mathematical model in which fibril alignment results from traction forces exerted by the cells under anisotropic conditions, such as a mechanical constraint or inhomogeneous cell distribution. According to this model, cells then align along the fibrils by contact guidance [189]. Huang *et al.* (1993) showed an increase in stiffness over time of fibroblast-populated collagen constructs between fixed posts, and demonstrated that lysyl-oxidase crosslinking activity was necessary for this mechanical enhancement [190]. Autologous bone derived MSCs were further used for Achilles tendon repair in rabbits [191]. In these experiments Young *et al.* (1998) used a cell-gel composite contracted onto a pre-tensioned suture (Fig. 8B). They showed that the mechanical properties were greatly enhanced 12 weeks after implantation in 1-cm-long gastrocnemius tendon gaps compared to controls implanted with suture material only. MSC-collagen composites, implanted into central patellar tendon defects of rabbits, showed a significant improvement of the biomechanical properties as compared to natural repairs, with cells remaining within the repair site [192], [193]. No additional benefit of increasing cell density, from 1 to 8 million per ml, was observed. Formation of ectopic bone in 28% of the composite grafted repairs was noticed. Lowering the cell to collagen ratio in a different system, where the MSCs were placed into silicon dishes between fixed posts 2 weeks prior to implantation (Fig. 8A), showed no significant difference in material and histological properties between implants with 40,000 cells/mg collagen or 80,000 cells/mg collagen twelve weeks after surgery [194]. There was also no significant difference in mechanical properties between these implants and acellular ones, with an average modulus reaching 20% of normal patellar tendons.

Scaffold-free constructs were also obtained by self-assembly of collagen and non-collagenous molecules produced by rat Achilles tendon cells grown to confluence between two pinned sutures, serving as anchor points, for 2 weeks [195] (Fig. 8C). The obtained cylinders presented a tangent modulus of 17 MPa, as compared to 27 MPa for embryonic chicken extensor tendons. Tendon-skeletal muscle constructs were also engineered *in vitro* in scaffold-free environment, with the reconstitution of myo-tendinous junctions either by co-culturing fibroblasts and myoblasts between fixed posts [196] or by pinning tendon constructs on muscle cell monolayer [197]. Fibrin has also been used as a material for tendon engineered constructs. Kapacee *et al.* showed that in fixed length fibrin gels made with tendon embryonic cells, fibrin was replaced by

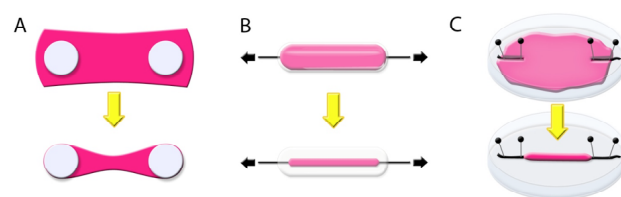


Fig. (8). Schemes of various types of tendon constructs based on cell-mediated gel compaction. On these top-views cell-gel mixtures are depicted pink, and the contraction process is represented over time, from top to bottom. (A): Principle of collagen matrix contraction between fixed posts, depicted white, as introduced in [187] and further developed in [188], where cells and collagen gels are first pipetted into wells. The cells contract the gels around two posts located at the base of each well. (B): Collagen gel-cell composite contracted onto a pre-tensioned suture, as introduced in [191]. Each construct was created in a glass trough, which contained a tensioned suture (horizontal arrows). (C): Tendon construct formation between pinned sutures, in the presence of cells only [195], fibrin-cell mixture [198], or collagen-cell mixture [201].

aligned collagen fibrils within 6 days [198]. Similar tendon constructs were also used to investigate the role of transcription factor EGR1 towards tendon differentiation by means of forced *Egr1* expression programmed MSCs in a fibrin gel [199]. Neal *et al.* (2014) developed a method using a PDMS mold and a second sacrificial mold, made of gelatin, and placed inside, to produce thin fascicle-like constructs, ~100 μm in diameter, of fibrin hydrogel with cells embedded in it [200]. This strategy enabled to combine molding and cell-mediated gel compaction of the freely suspended hydrogel anchored to the PDMS walls. C2C12 mouse myoblasts alignment and maturation were promoted. According to preliminary work, the method could also be extended to 3T3 fibroblasts and horse tenocytes. More recent studies, led by two different groups, showed that fibrin gels enhance the properties of tendon-engineered constructs over collagen-based materials. Yeung *et al.* (2015) led a comprehensive study of chick tendon fibroblast transcriptomes inside gels between pinned sutures and showed that fibrin-based constructs recapitulated more closely gene expression that occurs during tendon development as compared with collagen-based ones [201]. Cell-synthesized collagen matrix also exhibited better fibrils alignment in the fibrin-based gels. Breidenbach *et al.* (2014) showed that for approximately 14 days in cell-gel mixtures between posts embryo tendon/ligament progenitor cells exhibited enhanced tenogenic expression, collagen alignment and linear modulus with fibrin [202]. Still, a reduction in mechanical, biological and mechanical properties was observed in fibrin constructs submitted to cyclic stretching (2.4% strain, 1Hz, 3000 cycles/day) whereas this was beneficial to collagen constructs. The main conclusion is that the various parameters of mechanical stimulation must be fine-tuned for each type of construct.

5.7. Other Promising Methods

In this section we will describe some other methods, which have been applied to the generation of a high anisotropy inside collagen solutions. They often rely on the combination of multiple physical phenomena, and adapted for a better processability they may be promising candidates to generate biomaterials for tendon repair.

Magnetic Alignment

Torbet and Ronzière were the first to propose the magnetic alignment of collagen during self-assembly in solutions at low concentration [203]. They used magnetic field strengths between 1.9 and 5.6 T. Aligned fibrils being in the same plane as the field, they

inferred the additional ordering effects of surface interactions. Guido and Tranquillo further showed that fibril orientation could be controlled by independently varying the magnetic field strength or temperature during fibrillogenesis, pointing out the possible orienting effect of the magnetic field acting over an extended fibrillogenesis period due to a lower temperature [204]. When human foreskin fibroblasts are cultured in the gel, their orientation correlates with that of the fibrils. Chen *et al.* (2011) showed that, in tilapia fish-scale collagen solutions, fibril alignment can also be induced after fibrillogenesis with magnetic fields of 6 or 12 T [205]. The rheological properties obtained were similar in both cases, with either non-prefibrillated or fibrillated and crosslinked collagen prior to magnetic treatment, with higher values than those of un-oriented gels. Those properties were dependent on strength and application time of the magnetic treatment. In both cases, collagen fibrils maintained a typical D-periodic structure of 60-70 nm. Guo and Kaufman (2007) showed that it was also possible to obtain fibril alignment with a small magnet by combining flow and magnetic field effect [206]. Surface modified paramagnetic iron oxide beads placed inside collagen solutions induce collagen alignment within areas of hundreds of square microns, the domains being larger when timescales of gelation and bead motion to the magnet poles are similar. Multiple layers of collagen are obtained. C6 glioma cells embedded in the matrix were able to remodel it by bundling the fibers.

Microfluidic alignment

Lee *et al.* (2006) proposed the microfluidic alignment of collagen fibrils in dilute solutions under flow, and the orientation obtained appeared to be particularly efficient within PDMS microchannels 10 to 100 μm wide [207]. They inferred that the rapid attachment of fiber precursors along the channel walls and the subsequent influence on new fiber growth were involved, but mentioned that no firm conclusion could be drawn from their experiments to provide an explanation. Aortic bovine endothelial cells grown on the UV-crosslinked collagen matrix aligned along the direction of the fibers. Saeidi *et al.* (2009) studied the formation of fibrils on glass surface under the influence of flow between two plates [208]. The height of the microchamber could be changed which enabled to vary the shear rate at the walls. In this context self-assembly process is influenced by shear rate, as well as self-assembly energetics and surface energy. Moderately aligned collagen fibrils were obtained. They result from the aggregation of 3-5 nm microfibrils and present no D-banding, possibly due to the distortion of the fibrillar structure by the surface energy of the glass. The best alignment was observed at shear rates between 20 and 80 s^{-1} , and above these values the fibrils would often turn down-stream due to instabilities. Surface bound aligned collagen I matrices were produced on copolymer-coated or glass substrates thanks to a microfluidic system [209]. Collagen deposited under flow was either pre-fibrillated or not. The morphology of the matrices obtained could be controlled. Fibril coverage was directly dependent on collagen concentration, with extended matrices at 0.8 mg/ml as compared to 0.2 and 0.4 mg/ml. The flow rate also had a direct impact on the alignment of pre-fibrillated collagen, with highest alignment degree at 11 $\mu\text{l}/\text{min}$ as compared to 4 and 0.45 $\mu\text{l}/\text{min}$. A slight decrease of alignment was seen on more hydrophilic surfaces. Pre-conditioning of non-fibrillated collagen (0.8 mg/ml) in heated tubing before entering the channel had a direct impact on the fibers obtained, which are longer and more individual after 30 minutes as compared to 5 and 10 minutes.

Recently Haynl *et al.* (2016) used a microfluidic chip connected to three syringes to produce collagen microfibers upon an increase in the pH and the presence of PEG [210]. The diameters of the fibers can be varied depending on the extrusion buffer and the flow rates. With a collagen flow rate of 50 $\mu\text{l h}^{-1}$ and buffer flow rates in between 235 and 550 $\mu\text{l h}^{-1}$ the fibers could be collected using a rotating spool. The diameters obtained under these conditions are

around 10 μm and after air-drying from 3 to 6 μm . Alignment of the fibrils within the microfibers was evidenced by scanning electron microscopy and polarized FTIR spectroscopy. Young moduli obtained were 4138 \pm 512 MPa after drying. Neuronal cells cultured on the microfibers aligned along the longitudinal axes.

Rotary shearing

Yunoki *et al.* (2015) produced thick collagen gel bundles with aligned fibrils by means of rotary shearing to a dense collagen solution (1.8%), with gelation triggered upon rotation [211]. Well-aligned fibrils, as evidenced by scanning electron microscopy and birefringence measurements, were observed in the marginal regions of 1-3 mm thick disc-shaped gels. The optimal shear-rates for fibrils alignment were between 2-5 s^{-1} . Rectangles and dumb-bell-shaped specimens cut from the discs (7*12mm and 4*16mm respectively) in the direction of the rotation had Young modulus of 180 kPa after crosslinking with genipin, as compared to 30 kPa for the rectangles perpendicular to the rotation. After EDC/NHS crosslinking the values reached were 280 and 130 kPa, respectively. 3T3 cultured on aligned matrices were spindle-shaped in the fibril alignment direction.

Imprinting

An innovative technique was invented by Tong *et al.* to study the role played by the biophysical and biochemical environment, as well as mechanical properties, on MSCs differentiation into tenocytes [102]. They replicated tendon structure by imprinting longitudinal sections of bovine Achilles tendons with PDMS, making a negative then a positive replica reaching sub-micron precision (Fig. 9).

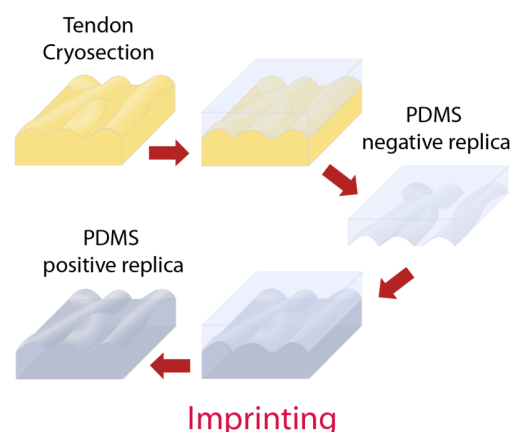


Fig. (9). Schematics of the imprinting technique. A PDMS negative replica of a longitudinal tendon cryo-section is made to produce a subsequent PDMS positive replica.

By changing monomer concentration, they were able to tune the elastic modulus of the imprint from 0.35 to 3.5MPa. They demonstrated that surface topography, collagen coating, and stiffness were paramount to promote MSCs differentiation. In addition to such valuable information, this technique could be used to mold scaffold for tendon reconstruction, resulting in optimal surface topography.

Fiber drawing

Another interesting, yet simple technique, has been reported by Paten *et al.* (2016) [212]. They were able to draw centimeter-long collagen fibers with a diameter around 50 μm , just by poking a collagen solution drop left a few minutes under dry nitrogen atmosphere with a glass micro-needle (Fig. 10). The flow-induced crystallized fibers presented outstanding aligned structure on the outer

shell. Fibers were stable when kept under strain or in polyethylene glycol solution. This could help understanding tendon morphogenesis and, above all, by weaving such fibers, it could provide a promising and simple scaffold production, with inherent high porosity and alignment to promote cell proliferation and differentiation.

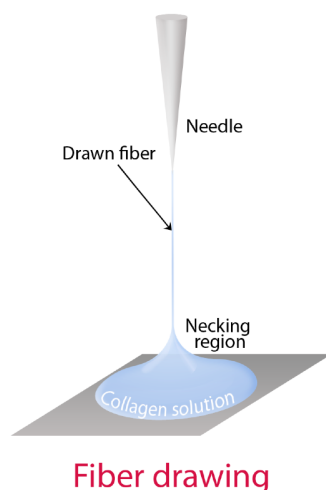


Fig. (10). Schematics of the fiber drawing technique. A glass micro-needle is used to poke the surface of a collagen solution left 150s to concentrate under nitrogen atmosphere, and draw a fiber.

Plastic compression and gel aspiration-ejection

Plastic compression is a cell-free, controlled process first introduced by Brown *et al.* [213], to produce dense, cellular, mechanically strong native collagen structures. This technique relies on external mechanical loading and capillary fluid flow to expel interstitial liquid. The cell viability is high during and after compression of cellular collagen gels, even surpassing highly hydrated collagen gel counterparts, with an increase in proliferation over time [214]. Plastic-compressed collagen gels seeded or not with rabbit flexor tendon cells, 20-40 μm thick, were rolled in order to produce spiral rolls 22 mm in length x 2.25 mm in diameter [215]. These rolls were placed in a test site across intercostal spaces in rabbits to provide tensile cyclic loading *in vivo* for 5 weeks. Collagen remodeling and tensile mechanical strength were enhanced in the cell-seeded gels. Gel aspiration-ejection (GAE) technique was further developed to produce anisotropic, cell-seeded, injectable collagen, without the use of crosslinking [216]. After incubation of low concentrated collagen solutions the resulting gels are aspirated into capillaries by means of a negative pressure applied with a syringe. Fibril alignment was evidenced by scanning electron microscopy and polarized ATR-FTIR spectra. 3T3-seeded collagen gels submitted to GAE showed a rapid orientation of the cells along the direction of the fibrils within one day. Constructs obtained through this process and exposed to the appropriate supplements also accelerated the differentiation of seeded murine MSCs towards osteoblastic and neuronal lineage, as compared to plastic-compressed cell-seeded constructs.

6. DETERMINANT IMPACT OF MECHANICAL STIMULATION

Tendon development, homeostasis and healing are influenced by their loading environment [2]. During rehabilitation, a fine balance between complete immobilization and loading is necessary to improve ECM production and tendon repair [217]. Before implantation, engineered constructs can be exposed to static and dynamic loads in order to better mimic the *in vivo* conditions and potentially improve their properties. The results obtained may also give in-

sights into the influence of mechanical stimulation on cell differentiation, activity and on biomechanical enhancement (Table 3).

The influence of uniaxial loads on ECM components was studied using collagen constructs without cells. Static stretching of self-assembled collagen fibers extruded in phosphate buffer, then air dried and rehydrated, induced a modulus increase from 1.82 MPa with 0% stretch to 45 MPa after 50% stretch, measured after air drying [218]. Increased collagen fibril orientation was supposedly involved based on birefringence values. Static stretching of PDMS substrates coated with a multilayer film composed of collagen and alginate enabled to produce surfaces with aligned collagen fibrils, that were further stabilized with genipin crosslinking, with an optimal strain of 100% for alignment [219]. Cyclic loading of strips of collagen gels obtained by plastic compression promoted fibril fusion as evidenced by transmission electron microscopy [220]. Tensile tests showed a modulus increase from 244 kPa after 1 cycle to 535 kPa after 144 cycles, with 20% maximum strain for each cycle. There was also an increase in break strain and a 4.5 fold rise in break stress. Regarding the mechanical stimulation of cells alone, a cyclic axial strain applied on human tendon fibroblasts showed a strong influence on cell proliferation, highlighting the need to fine-tune the stretch [221].

Continuous cyclic strain inhibited proliferation of four types of cells including rabbit flexor tendon derived cells, whereas an intermittent cyclic strain could enhance cell proliferation in adipose-derived stem cells and sheath fibroblasts [222]. Rat bone marrow MSCs submitted to an uniaxial cyclic stretching of 10% at 1Hz for durations ranging from 3 to 36 h showed an increased expression of collagen types I and III and of tenascin-C [223]. The percentage of cells oriented along or close to the stretch axis was decreased, as previously noticed with ligament fibroblasts [103] as well as with epitenon tenocytes [222]. The reorientation of the different components of cellularized gels under mechanical stimulation thus appears complex.

Garvin *et al.* imposed a uniaxial strain on bioartificial tendons made of avian flexor tendon cells in a collagen gel, with an elongation pattern of 1% at 1 Hz for one hour each day [224]. Results obtained in the first week of culture showed an alignment of the cells along the direction of strain and a nearly 3-fold increase in ultimate tensile strength as compared to the non-loaded constructs. Human bone-marrow derived MSCs in a collagen gel were also submitted to a similar stimulation protocol for 30 minutes each day [225]. Expression of scleraxis, the main tendon marker during vertebrate development, was up-regulated in the 3D constructs as compared to 2D culture, but this was maintained over time only in the constructs submitted to cyclic loading. The observed tendinous neo-tissue development could be associated with matrix remodeling activity, in agreement with the noticed modulation of matrix metalloproteinases expression. Another study led by Scott *et al.* (2011) with multipotent mesenchymal cell line C3H10T1/2 in the same 3D model optimized the protocol of stimulation based on the expression of scleraxis and type I collagen [226]. The insertion of a 10 s resting period between each repetition of stretching cycle (10% strain, 0.1 Hz) appeared to be a critical parameter.

Mechanical stimulation of another type of scaffold based on collagen type I sponge, with rabbit bone marrow MSCs applied on it, was also investigated prior and after surgical implantation into patellar tendon central third defects [227], [228]. When the peak strain was 2.4%, applied every 5 minutes for 8 hours each day for two weeks, the stimulated constructs had 4 times the linear modulus and 2.5 times the linear stiffness of their non-stimulated counterparts *in vitro* [228].

This was associated with increased expressions of collagen type I and type III. Repair tissues formed with constructs stimulated 2 weeks with 4% strain prior to implantation showed improved

Table 3. Mechanical stimulation protocols and main results reported for cells alone, collagen constructs, and mixtures of cells and collagen.

Scaffold	Cells	Stimulation	Main results	Refs.
Collagen thread		Static axial strain for 24h	Elastic modulus: 45 MPa after 50% stretch / 1.82 for the controls (air-dried). Increased axial fibril orientation (birefringence)	[Pins 1997]
Strips of collagen gels obtained by plastic compression		Cyclic loading 20% strain maintained 5 min for each cycle (20 min total)	Elastic modulus: 535 kPa after 144 cycles / 244 kPa after 1 cycle. UTS : 4.5-fold increase	[Cheema 2007]
PDMS substrate coated with multiple layers of collagen/alginate		Static stretching	Fiber alignment in the stretching direction with optimal strain of 100%. Cell alignment with the fibrils	[Chaubaroux 2015]
	Rabbit flexor tendon derived cells /Adipoderived stem cells /Bone marrow derived stem cells	Continuous cyclic strain 8% - 1 Hz	Proliferation inhibited	[Riboh 2008]
		Intermittent cyclic strain 4% - 0.1 Hz On/off : 1h /2h or 1h/5h	Enhanced proliferation and collagen expression. Cells perpendicular to the strain axis	
	Rat bone marrow MSCs	Uniaxial cyclic stretching 10% - 1 Hz Duration : 3 to 36h	Increased expression of collagens type I and III and tenascin-C. Cell reorientation with less cells along the stretch axis	[Zhang 2008]
Collagen gel	Avian flexor tendon cells	1% – 1 Hz 1h/day	Alignment of the cells along the direction of strain. UTS: 3-fold increase compared to controls	[Garvin 2003]
Collagen gel	Human bone marrow MSCs	1% – 1 Hz 30 min/day	Scleraxis up-regulation maintained with cyclic loading Regulation of matrix metalloproteinases expression	[Kuo 2008]
Collagen gel	Mesenchymal cell line C3H10T1/2 (mouse)	Variable strain -0.1 Hz	Increased expression of scleraxis and collagen type I with 10% strain. Further increase when a 10s resting period is inserted between each cycle repetition	[Scott 2011]
Collagen sponge	Rabbit bone marrow MSCs	4% – 1Hz cycle every 5 min 8h/day	2.5-fold rise in linear stiffness <i>in vitro</i> 12 weeks after <i>in vivo</i> implantation into patellar tendon central third defects: maximal forces sustained are 70% of normal tendons / 55% for non-stimulated constructs	[Juncosa-Melvin 2006]
Collagen sponge	Rabbit bone marrow MSCs	2.4% – 1Hz cycle every 5 min - 8h/day	4-fold rise in linear modulus and 2.5-fold rise in linear stiffness <i>in vitro</i> Increased expressions of collagen type I and type III	[Juncosa-Melvin 2007]
Collagen sponge	Rabbit bone marrow MSCs	Variable strain – 0.1Hz Variable cycle number and cycle repetition	Constructs stimulated with 2.4% strain, 3000 cycles/day, and one cycle repetition produced the stiffest constructs, peak strain appearing as the most critical parameter	[Nirmalanandhan 2008]
Collagen gel combined with collagen sponge	Rabbit bone marrow MSCs	2.4% – 1Hz cycle every 5 min - 8h/day	12 weeks after <i>in vivo</i> implantation into patellar tendon central third defects: enhanced mechanical properties in the repair tissue obtained with stimulated constructs	[Shearn 2007]

Table 4. Summary of experiments and main results obtained using newly developed collagen-based scaffolds in animal models.

Technique	Scaffold/parameters	Animal models / Sample size	Implantation site / Controls	Main results		Refs.
Extrusion	Parallel crosslinked collagen fibers (200) in an uncrosslinked collagen matrix -Fiber diameter: 20 or 50 μm -Cross-linking: GLUT or DHTC	Rabbit n=5 for each group	Subcutaneous	After 4 weeks: <ul style="list-style-type: none"> DHTC-crosslinked fibers mostly degraded and replaced by fibrous tissue GLUT-crosslinked fibers mostly intact, surrounded by inflammatory cells No influence of initial fiber diameter 		[Dunn 1993]
	Knitted collagen fabrics -Dry diameter: 25 μm -Cross-linking : EDC	Dog	Anterior Cruciate Ligament	After 12 weeks: <ul style="list-style-type: none"> Applied force by the operated limb at 70% of control Threads remain intact with disorganized cellular ingrowth Neovascularization, normal size collagen fibrils in the neoligament 		[Cavallaro 1994]
		Rat n=5	Abdominal wall defect	After 3 weeks: <ul style="list-style-type: none"> Neovascularization and fibroblastic cellular infiltrate 	After 12 weeks: <ul style="list-style-type: none"> No herniation 	
Electrochemical techniques	Braided ELAC threads (9) -Threads diameter : 200-300 μm thick, 400-500 μm wide -Cross-linking: Genipin	Rabbit Sacrificed at 4 and 8 months (n=3 each)	Patellar tendon (incised along the length) Controls: incised contralateral knees	After 4 months: <ul style="list-style-type: none"> Low degradation of the ELAC scaffold Cross-sectional area, mechanical properties and tendon-fascicles content of the PTs treated with ELAC optimized / controls Low-grade granulomatous inflammation 	After 8 months : <ul style="list-style-type: none"> Differences / controls less evident Diminished inflammation 	[Kishore 2012]
Cell-mediated gel compaction	Bone derived MSCs-collagen gel composite - Contraction: pre-tensioned suture	Rabbit Sacrificed at 4, 8, or 12 weeks (n=16 each) 5 animals used for establishing normal biomechanical properties	Achilles tendon (1 cm long gap defect) Controls: contralateral tendons implanted with suture material only	After 4 weeks: <ul style="list-style-type: none"> Stiffness is 1/2 and maximum force 2/3 of normal tendons, 2X / controls 	At 12 weeks: <ul style="list-style-type: none"> Modulus 1/2 of normal tendons, 2X / controls Histology: collagen bands which volume, density and crimp pattern are enhanced over time, more mature / controls 	[Young 1998]

(Table 4) Contd....

Technique	Scaffold/parameters	Animal models / Sample size	Implantation site / Controls	Main results		Refs.
	Bone marrow MSCs-collagen composites <i>-Contraction: sutures</i>	Rabbit 2 groups (n=43 each): -with 1. 10 ⁶ /ml cells and 4. 10 ⁶ /mL cells composites in each tendon, -with 8.10 ⁶ /mL cells in first tendon and defect left untreated in the second one 8 animals to assess tendon normal properties	Patellar tendon central defects	At 12 and 26 weeks: <ul style="list-style-type: none">Significant improvement of the biomechanical properties / natural repairs	At 26 weeks: <ul style="list-style-type: none">Maximum stress is 1/4 of normal tendon portionNo additional benefit of increasing cell densityFormation of ectopic bone in 28% of all composite grafted repairs	[Awad 2003]
	MSCs-collagen composites <i>-Contraction: in silicon dishes between two posts</i>	Rabbit 2 groups : -with cells : 40.000 or 80.000 cells/mg collagen)(n=16) - without cells (n=6)	Patellar tendon central third defects	After 12 weeks: <ul style="list-style-type: none">No significant difference in material and histological properties between the two cell concentrations and similar to acellular implantsAverage linear modulus ~ 20% of normal values		[Juncosa-Melvin 2005]
Plastic compression	Plastic-compressed collagen gels <i>-Seeded or not with rabbit flexor tendon cells</i> <i>-20-40 μm thick</i> <i>-rolled to produce spiral rolls 22 mm in length x 2.25 mm in diameter</i>	Rabbit Sacrificed at 3 time points: 1 week (n=5), 3 weeks (n=4), 5 weeks (n=4)	Intercostal spaces 3 cellular constructs on one side of the chest and 3 acellular constructs on the other one	After 5 weeks: <ul style="list-style-type: none">Vascularization with a stronger response in the cellular constructsCollagen remodeling and tensile mechanical strength enhanced in the cell-seeded gels		[Mudera 2007]
Mechanical stimulation	Collagen type I sponge with rabbit bone marrow MSCs <i>Either stimulated or non-stimulated constructs (2 weeks with 4% strain, 1 Hz cycle every 5 min, 8 h/day)</i>	Rabbit n=10	Patellar tendon central third defects	After 12 weeks: <ul style="list-style-type: none">Maximal force 70% of normal tendons, vs 55% for non-stimulated constructs		[Juncosa-Melvin 2006] [Juncosa-Melvin 2007]
	Mixture of rabbit bone marrow MSCs and collagen gels combined with collagen sponges <i>Either non stimulated or stimulated constructs (2 w. with 4% strain, 1 Hz cycle every 5 min, 8 h/day)</i>	Rabbit n=6	Patellar tendon central third defects	After 12 weeks: <ul style="list-style-type: none">Averaged linear stiffness 80% of normal values, vs 50% for non-stimulated constructsMaximal force 65% vs 60% for non-stimulated constructs		[Shearn 2007]

biomechanical properties twelve weeks after surgery, the maximal force being 70% of the one sustained by normal tendons, versus 55% with non-stimulated constructs [227]. The stimulated constructs also presented a 2.5 rise in linear stiffness *in vitro* prior to implantation. The stimulation protocol was further optimized, and peak strain appeared to be a more important parameter than cycle

number and cycle repetition to enhance *in vitro* stiffness, with an optimized value of 2.4% (Table 3) [229]. Constructs made of a mixture of cells and collagen gels combined with collagen sponges showed a different behavior, with no significant change of the biomechanical properties measured prior to implantation in the

stimulated constructs, the improvement related to preconditioning being only present in the repair tissues [230].

CONCLUDING REMARKS AND PERSPECTIVES

In the present review, we have seen how current tendon repair methods are mainly based on sutures and grafts that have proven to be effective while still exhibiting intrinsic drawbacks. We have seen that, even though tendon structure is not completely understood, tendon regeneration based on bioengineered scaffolds is promising. Among the different routes available, we focused on collagen-based scaffolds, as collagen I stands out from other biomolecules as being the main structural component of tendon, as well as for its suitable biocompatibility. The diversity of techniques and the increasing know-how in scaffold design allows tackling new exciting aspects such as alignment, multi-scale organization, scaffold tailoring or multi-cell deposition.

However, mechanical properties of collagen scaffolds still remain an issue while some other artificial materials compete or even overtake tendons. Still, several authors report that, while cross-linking improves mechanical properties and resistance to degradation, it may also damage collagen or decrease its biocompatibility. A fine balance must then be found. Cross-linking methods can be classified into two categories: chemical and physical cross-linking. Among chemical cross-linkers, widespread glutaraldehyde was proven to be cytotoxic [116]. EDC, that exhibits significant increase in mechanical properties may also decrease biocompatibility and collagen I production by cells [120]. More biological cross-linking methods such as lysyl-oxidation or glycation may be used [116]. Physical cross-linking can be achieved thanks to UV irradiation or dehydrothermal process. In some preclinical studies, the moderate mechanical properties of uncrosslinked collagen scaffolds have been shown to increase *in vivo*. Table 4 compares results obtained in animal models with various types of collagen scaffolds, among them cross-linked, compacted through cell-mediated contraction process, plastic-compressed and mechanically stimulated prior to implantation. After several weeks or months *in vivo*, most scaffolds exhibited partial replacement by neo-fibers and neo-vascularization in certain cases. The importance of mechanical pre-stimulation of cellularized scaffolds prior to implantation is highlighted in the works from Juncosa-Melvin *et al.* (2006, 2007) [227], [228], and Shearn *et al.* (2007) [230]. Twelve weeks after implantation in rabbit patellar tendon defects the maximal force obtained could reach 70% of normal tendons, which is comparable to the study led by Cavallaro *et al.* (1993) [118] using knitted EDC-crosslinked fibers with results obtained twelve weeks after implantation in dog anterior cruciate ligament.

Finally, this review shows that as bioengineering techniques improve, more complex tissues are achievable. Thus, some examples of myo-tendinous or bone-tendon junction reconstructions have been presented, illustrating the further increase of complexity. The development of artificial junctions could be paramount to improve overall scaffold efficiency and reliability, as well as to increase our understanding on the interactions between different biomaterials and cells.

CONSENT FOR PUBLICATION

Not applicable.

CONFLICT OF INTEREST

The authors declare no conflict of interest, financial or otherwise.

ACKNOWLEDGEMENTS

The authors would like to thank David Pinto, Francisco M. Fernandes and Léa-Laetitia Pontani for critical reading of the manuscript. C. R. and L. P. were supported by a French Ministère de la Recherche fellowship.

REFERENCES

- [1] Morais DS, Torres J, Guedes RM, *et al.* Current approaches and future trends to promote tendon repair. *Ann Biomed Eng* 2015; 43: 2025-35.
- [2] Thomopoulos S, Parks WC, Rifkin DB, *et al.* Mechanisms of tendon injury and repair: TENDON INJURY AND REPAIR. *J Orthop Res* 2015; 33: 832-9.
- [3] Young JS, Maffulli N. Etiology and epidemiology of Achilles tendon problems. In: Maffulli N, Almekinders L, Eds. *The Achilles Tendon*. Springer 2007: pp. 39-49.
- [4] Riley G. Tendinopathy—from basic science to treatment. *Nat Clin Pract Rheumatol* 2008; 4: 82-9.
- [5] Lomas AJ, Ryan CNM, Sorushanova A, *et al.* The past, present and future in scaffold-based tendon treatments. *Adv Drug Deliv Rev* 2015; 84: 257-77.
- [6] Lewis T, Cook J. Fluoroquinolones and Tendinopathy: A Guide for Athletes and Sports Clinicians and a Systematic Review of the Literature. *J Athl Train* 2014; 49: 422-27.
- [7] Oliva F, Via AG, Maffulli N. Calcific tendinopathy of the rotator cuff tendons. *Sports Med Arthrosc Rev* 2011; 19: 237-43.
- [8] Clayton RAE, Court-Brown CM. The epidemiology of musculoskeletal tendinous and ligamentous injuries. *Injury* 2008; 39: 1338-44.
- [9] De Jong JP, Nguyen JT, Sonnema AJM, *et al.* The incidence of acute traumatic tendon injuries in the hand and wrist: A 10-Year Population-based Study. *Clin Orthop Surg* 2014; 6: 196.
- [10] Sun C, Zhuo Q, Chai W, *et al.* Conservative interventions for treating Achilles tendon ruptures (Protocol). *Cochrane Database of Systematic Reviews* 2013. The Cochrane Collaboration. Published by John Wiley & Sons, Ltd. DOI: 10.1002/14651858.CD010765
- [11] Scott A, Ashe MC. Common Tendinopathies in the Upper and Lower Extremities. *Curr Sports Med Rep* 2006; 5: 233-41.
- [12] Sanders TL, Maradit KH, Bryan AJ, *et al.* The Epidemiology and Health Care Burden of Tennis Elbow: A Population-Based Study. *Am J Sports Med* 2015; 43: 1066-71.
- [13] Pluim BM. Tennis injuries: occurrence, aetiology, and prevention. *Br J Sports Med* 2006; 40: 415-23.
- [14] European Agency for Safety and Health at Work. OSH in figures: Work-related musculoskeletal disorders in the EU - Facts and figures; 2010. Available from: osha.europa.eu/fr/tools-and-publications/publications/reports/TERO09009ENC
- [15] Health and Safety Executive, UK. Work-related Musculoskeletal disorder (WRMSDs) Statistics, Great Britain, 2015. Available from: hse.gov.uk/statistics/
- [16] Agency for Healthcare Research and Quality. Comparative Effectiveness of the Nonoperative and Operative Treatments for Rotator Cuff Tears; 2010. Available from: ahrq.gov
- [17] European Agency for Safety and Health at Work. Work-related neck and upper limb musculoskeletal disorders; 1999. Available from: osha.europa.eu/en/tools-and-publications/publications/reports/201
- [18] Andarawis-Puri N, Flatow EL, Soslowky LJ. Tendon basic science: Development, repair, regeneration, and healing. *J Orthop Res* 2015; 33: 780-4.
- [19] Rawson S, Cartmell S, Wong J. Suture techniques for tendon repair; a comparative review. *Muscles Ligaments Tendons J* 2013; 3: 220.
- [20] Squier CA, Bausch WH. Three-dimensional organization of fibroblasts and collagen fibrils in rat tail tendon. *Cell Tissue Res* 1984; 238: 319-27.
- [21] Zhang G, Young BB, Ezura Y, *et al.* Development of tendon structure and function: regulation of collagen fibrillogenesis. *J Musculoskelet Neuronal Interact* 2005; 5: 5-21.
- [22] Screen HRC, Berk DE, Kadler KE, *et al.* Tendon Functional Extracellular Matrix. *J Orthop Res* 2015; 33: 793-9.
- [23] Kadler KE, Baldock C, Bella J, *et al.* Collagens at a glance. *J Cell Sci* 2007; 120: 1955-8.
- [24] Pohlhammer J, O'Brien Jr WD. Dependence of the ultrasonic scatter coefficient on collagen concentration in mammalian tissues. *J Acoust Soc Am* 1981; 69: 283.
- [25] Scott JE. Chemical morphology: The chemistry of our shape, *in vivo* and *in vitro*. *Struct Chem* 2007; 18: 257-65.
- [26] Birch HL. Tendon matrix composition and turnover in relation to functional requirements. *Int J Exp Pathol* 2007; 88: 241-8.

- [27] Bancelin S, Couture CA, Légaré K *et al.* Fast interferometric second harmonic generation microscopy. *Biomed. Opt. Express* 2016; 7: 399-408.
- [28] Gusachenko I, Tran V, Houssen YG, *et al.* Polarization-Resolved Second-Harmonic Generation in Tendon upon Mechanical Stretching. *Biophys J* 2012; 102: 2220-9.
- [29] Fouré A. New imaging methods for non-invasive assessment of mechanical, structural, and biochemical properties of human achilles tendon: A Mini Review. *Front Physiol* 2016; 7: 324.
- [30] Hulmes DJS. Building Collagen Molecules, Fibrils, and Suprafibrillar Structures. *J Struct Biol* 2002; 137: 2-10.
- [31] Benjamin M, Kaiser E, Milz S. Structure-function relationships in tendons: a review. *J Anat* 2008; 212: 211-28.
- [32] Kannus P. Structure of the tendon connective tissue. *Scand J Med Sci Sports* 2000; 10: 312-20.
- [33] Nicholls SP, Gathercole LJ, Keller A, *et al.* Crimping in rat tail tendon collagen: morphology and transverse mechanical anisotropy. *Int J Biol Macromol* 1983; 5: 283-8.
- [34] Dlugosz J, Gathercole LJ, Keller A. Transmission electron microscope studies and their relation to polarizing optical microscopy in rat tail tendon. *Micron* 1978; 9: 71-82.
- [35] Wang J H-C. Mechanobiology of tendon. *J. Biomech* 2006; 39: 1563-82.
- [36] Shah JS, Palacios E, Palacios L. Development of crimp morphology and cellular changes in chick tendons. *Dev Biol* 1982; 94: 499-504.
- [37] Herchenhan A, Kalson NS, Holmes DF, *et al.* Tenocyte contraction induces crimp formation in tendon-like tissue. *Biomech Model Mechanobiol* 2012; 11: 449-59.
- [38] Hu XW, Knight DP, Chapman JA. The effect of non-polar liquids and non-ionic detergents on the ultrastructure and assembly of rat tail tendon collagen fibrils in vitro. *Biochim Biophys Acta* 1997; 1334: 327-37.
- [39] Cartmell JS, Dunn MG. Effect of chemical treatments on tendon cellularity and mechanical properties. *J. Biomed Mater Res* 2000; 49: 134-40.
- [40] Vidal B de C. Image analysis of tendon helical superstructure using interference and polarized light microscopy. *Micron* 2003; 34: 423-32.
- [41] Grytz R, Meschke G. Constitutive modeling of crimped collagen fibrils in soft tissues. *J Mech Behav Biomed Mater* 2009; 2: 522-33.
- [42] Reese SP, Maas SA, Weiss JA. Micromechanical models of helical superstructures in ligament and tendon fibers predict large Poisson's ratios. *J Biomech* 2010; 43: 1394-400.
- [43] Livolant F, Leforestier A. Condensed phases of DNA: structures and phase transitions. *Prog Polym Sci* 1996; 21: 1115-64.
- [44] Murthy NS. Liquid crystallinity in collagen solutions and magnetic orientation of collagen fibrils. *Biopolymers* 1984; 23: 1261-7.
- [45] Maeda H. An atomic force microscopy study of ordered molecular assemblies and concentric ring patterns from evaporating droplets of collagen solutions. *Langmuir* 1999; 15: 8505-13.
- [46] Giraud-Guille MM. Liquid crystallinity in condensed type I collagen solutions: a clue to the packing of collagen in extracellular matrices. *J Mol Biol* 1992; 224: 861-73.
- [47] De Sa Peixoto P, Deniset-Besseau A, Schanne-Klein MC, *et al.* Quantitative assessment of collagen I liquid crystal organizations: role of ionic force and acidic solvent, and evidence of new phases. *Soft Matter* 2011; 7: 11203.
- [48] Williams IF, Craig AS, Parry DAD, *et al.* Development of collagen fibril organization and collagen crimp patterns during tendon healing. *Int J Biol Macromol* 1985; 7: 275-82.
- [49] Müller SA, Todorov A, Heisterbach PE *et al.* Tendon healing: an overview of physiology, biology, and pathology of tendon healing and systematic review of state of the art in tendon bioengineering. *Knee Surg Sports Traumatol Arthrosc* 2015; 23: 2097-105.
- [50] Nourissat G, Berenbaum F, Duprez D. Tendon injury: from biology to tendon repair. *Nat Rev Rheumatol* 2015; 11: 223-33.
- [51] Wada A, Kubota H, Miyayoshi K, *et al.* Comparison of postoperative early active mobilization and immobilization in vivo utilising a four-strand flexor tendon repair. *J Hand Surg Edinb Scotl* 2001; 26: 301-6.
- [52] Childress MA, Beutler A. Management of chronic tendon injuries. *Am Fam Physician* 2013; 87: 486-90.
- [53] Khan KM, Scott A. Mechanotherapy: how physical therapists' prescription of exercise promotes tissue repair. *Br J Sports Med* 2009; 43: 247-52.
- [54] Sundman EA, Cole BJ, Fortier LA. Growth factor and catabolic cytokine concentrations are influenced by the cellular composition of platelet-rich plasma. *Am J Sports Med* 2011; 39: 2135-40.
- [55] Gelberman RH, Boyer MI, Brodt MD, *et al.* The effect of gap formation at the repair site on the strength and excursion of intra-synovial flexor tendons. An experimental study on the early stages of tendon-healing in dogs. *J Bone Joint Surg Am* 1999; 81: 975-82.
- [56] Buckley PS, Pedowitz DI. Bone reduction clamp to gain length in repairing chronic achilles tendon ruptures. *Orthopedics* 2016; 39: e1223-5.
- [57] Feldbrin Z, Hendel D, Lipkin A, *et al.* Achilles tendon rupture and our experience with the achillon device. *Isr Med Assoc J* 2010; 12: 609-12.
- [58] Huffard B, O'Loughlin PF, Wright T *et al.* Achilles tendon repair: Achillon system vs. Krackow suture: An anatomic in vitro biomechanical study. *Clin Biomech* 2008; 23: 1158-64.
- [59] Wang JHC. Mechanobiology of tendon. *J Biomech* 2006; 39: 1563-82.
- [60] Gomes ME, Reis RL, Rodrigues MT, Eds. *Tendon Regeneration: Understanding Tissue Physiology and Development to Engineer Functional Substitutes*. Academic Press 2015.
- [61] Maquirriain J. Achilles tendon rupture: Avoiding tendon lengthening during surgical repair and rehabilitation. *Yale J Biol Med* 2011; 84: 289-300.
- [62] Schliemann B, Grüneweller N, Yao D, *et al.* Biomechanical evaluation of different surgical techniques for treating patellar tendon ruptures. *Int Orthop* 2016; 40: 1717-23.
- [63] Hohendorff B, Siepen W, Spiering L, *et al.* Long-term results after operatively treated achilles tendon rupture: Fibrin glue versus suture. *J Foot Ankle Surg* 2008; 47: 392-9.
- [64] Rose S, PrevotEAU A, Elzière P, *et al.* Nanoparticle solutions as adhesives for gels and biological tissues. *Nature* 2014; 505: 382-5.
- [65] Erol B, Kocaoglu B, Esemeli T. Spiral-shaped metallic implant in the treatment of achilles tendon ruptures: An experimental study on the achilles tendon of sheep. *J Foot Ankle Surg* 2007; 46: 155-16.
- [66] Ağır İ, Aytekin MN, Başçı O, *et al.* Tendon-holding capacities of two newly designed implants for tendon repair: An experimental study on the flexor digitorum profundus tendon of sheep. *Open Orthop J* 2014; 8: 135-9.
- [67] Wolfe SW, Willis AA, Campbell D, *et al.* Biomechanical Comparison of the Teno Fix Tendon Repair Device With the Cruciate and Modified Kessler Techniques. *J Hand Surg* 2007; 32: 356-66.
- [68] Lacoste S, Féron JM, Cherrier B. Percutaneous Tenolig® repair under intra-operative ultrasonography guidance in acute Achilles tendon rupture. *Orthop Traumatol Surg Res* 2014; 100: 925-30.
- [69] Magnussen RA, Glisson RR, Moorman CT. Augmentation of achilles tendon repair with extracellular matrix xenograft a biomechanical analysis. *Am J Sports Med* 2011; 39: 1522-27.
- [70] Beskin JL, Sanders RA, Hunter SC, *et al.* Surgical repair of Achilles tendon ruptures. *Am J Sports Med* 1987; 15: 1-8.
- [71] Carmont MR, Maffulli N. Less invasive Achilles tendon reconstruction. *BMC Musculoskelet Disord* 2007; 8: 100.
- [72] Ebied AM, Foda AAA. Less invasive reconstruction of chronic achilles tendon rupture with free semitendinosus tendon autograft - A case series. *Int J Orthop* 2016; 3: 539-43.
- [73] Shewy MTE, Barbary HME, Abdel-Ghani H. Repair of chronic rupture of the achilles tendon using 2 intratendinous flaps from the proximal gastrocnemius-soleus complex. *Am J Sports Med* 2009; 37: 1570-7.
- [74] Phipatanakul WP, Petersen SA. Porcine small intestine submucosa xenograft augmentation in repair of massive rotator cuff tears. *Am J Orthop Belle Mead NJ* 2009; 38: 572-5.
- [75] Sciamberg SG, Tibone JE, Itamura JM, *et al.* Six-month magnetic resonance imaging follow-up of large and massive rotator cuff repairs reinforced with porcine small intestinal submucosa. *J Shoulder Elb Surg* 2004; 13: 538-41.
- [76] Berlet GC, Hyer CF, Lee TH, *et al.* Collagen ribbon augmentation of achilles tendon tears: A biomechanical evaluation. *J Foot Ankle Surg* 2014; 53: 298-302.
- [77] Song L, Olsen RE, Spalazzi JP, *et al.* Biomechanical evaluation of acellular collagen matrix augmented achilles tendon repair in sheep. *J Foot Ankle Surg* 2010; 49: 438-41.

- [78] Lee DK. A preliminary study on the effects of acellular tissue graft augmentation in acute achilles tendon ruptures. *J Foot Ankle Surg* 2008; 47: 8-12.
- [79] Hollowell S, Baione W. Chronic achilles tendon rupture reconstructed with achilles tendon allograft and xenograft combination. *J Foot Ankle Surg* 2015; 54: 1146-50.
- [80] Herbert A, Jones GL, Ingham E. A biomechanical characterisation of acellular porcine super flexor tendons for use in anterior cruciate ligament replacement: Investigation into the effects of fat reduction and bioburden reduction bioprocesses. *J Biomech* 2015; 48: 22-9.
- [81] Branch JP. A tendon graft weave using an acellular dermal matrix for repair of the achilles tendon and other foot and ankle tendons. *J Foot Ankle Surg* 2011; 50: 257-65.
- [82] Gaspar D, Spanoudes K, Holladay C, *et al.* Progress in cell-based therapies for tendon repair. *Adv Drug Deliv Rev* 2015; 84: 240-56.
- [83] Güngörmüş C, Kolankaya D, and Aydin E. Histopathological and biomechanical evaluation of tenocyte seeded allografts on rat Achilles tendon regeneration. *Biomaterials* vol. 2015; 51: 108-18.
- [84] Kew SJ, Gwynne JH, Enea D, *et al.* Regeneration and repair of tendon and ligament tissue using collagen fibre biomaterials. *Acta Biomater* 2011; 7: 3237-47.
- [85] Stapp MD. Implantable materials and grafts in tendon surgery. In: *Reconstructive surgery of the foot and leg: update '93*. Tucker, GA: Podiatry Institute Publishing Co. 1993; pp. 289-92.
- [86] Williams RD, August SF. Experimental evaluation of a Teflon tendon prosthesis. *Am J Surg* 1964; 107: 913-6.
- [87] Holtz M, Midenberg ML, Kirschenbaum SE. Utilization of a silastic sheet in tendon repair of the foot. *J Foot Surg* 1982; 21: 253-9.
- [88] Morrey MC, Barlow JD, Abdel MP, *et al.* Synthetic Mesh Augmentation of Acute and Subacute Quadriceps Tendon Repair. *Orthopedics* 2016; 39: e9-e13.
- [89] Abdullah S. Usage of synthetic tendons in tendon reconstruction. *BMC Proc* 2015; 9: p. A68.
- [90] Melvin A, Litsky A, Mayerson J, *et al.* An artificial tendon with durable muscle interface. *J Orthop Res Off Publ Orthop Res Soc* 2010; 28: 218-24.
- [91] Jenkins DH, McKibbin B. The role of flexible carbon-fibre implants as tendon and ligament substitutes in clinical practice. A preliminary report. *J Bone Joint Surg Br* 1980; 62-B: 497-9.
- [92] Corey SV. Tendon grafts and implants. In: *Reconstructive surgery of the foot and leg: update '88*. Tucker, GA: Podiatry Institute Publishing Co. 1988; pp. 58-61.
- [93] Roberts JM, Goldstrohm GL, Brown TD, *et al.* Comparison of unrepaired, primarily repaired, and polyglactin mesh-reinforced Achilles tendon lacerations in rabbits. *Clin Orthop* 1983; 181: 244-9.
- [94] Howard CB, McKibbin B, Ralis ZA. The use of Dexon as a replacement for the calcaneal tendon in sheep. *Bone Jt J* 1985; 67-B: 313-6.
- [95] Liem MD, Zegel HG, Balduini FC, *et al.* Repair of Achilles tendon ruptures with a polylactic acid implant: assessment with MR imaging. *AJR Am J Roentgenol* 1991; 156: 769-73.
- [96] Alexander H, Weiss AB, Parsons JR. Absorbable polymer-filamentous carbon composites--a new class of tissue scaffolding materials. *Aktuelle Probl Chir Orthop* 1983; 26: 78-91.
- [97] Cao Y, Liu Y, Liu W, *et al.* Bridging tendon defects using autologous tenocyte engineered tendon in a hen model. *Plast Reconstr Surg* 2002; 110: 1280-9.
- [98] Shoaib A, Mishra V. Surgical repair of symptomatic chronic achilles tendon rupture using synthetic graft augmentation. *Foot Ankle Surg* 2016. doi.org/10.1016/j.fas.2016.04.006
- [99] Verdiyeva G, Koshy K, Glibbery N. Tendon reconstruction with tissue engineering approach—A review. *J Biomed Nanotechnol* 2015; 11: 1495-523.
- [100] Ladd MR, Lee SJ, Stitzel JD, *et al.* Co-electrospun dual scaffolding system with potential for muscle-tendon junction tissue engineering. *Biomaterials* 2011; 32: 1549-59.
- [101] Jung H-J, Fisher MB, Woo S L-Y. Role of biomechanics in the understanding of normal, injured, and healing ligaments and tendons. *BMC Sports Sci Med Rehabil* 2009; 1: 1-9.
- [102] Tong WY, Shen W, Yeung CWF, *et al.* Functional replication of the tendon tissue microenvironment by a bioimprinted substrate and the support of tenocytic differentiation of mesenchymal stem cells. *Biomaterials* 2012; 33: 7686-98.
- [103] Park SA, Kim IA, Lee YJ, *et al.* Biological responses of ligament fibroblasts and gene expression profiling on micropatterned silicone substrates subjected to mechanical stimuli. *J Biosci Bioeng* 2006; 102: 402-12.
- [104] Wang JH, Jia F, Gilbert TW, *et al.* Cell orientation determines the alignment of cell-produced collagenous matrix. *J Biomech* 2003; 36: 97-102.
- [105] van Delft FCMJM, van den Heuvel FC, Loesberg WA, *et al.* Manufacturing substrate nano-grooves for studying cell alignment and adhesion. *Microelectron Eng* 2008; 85: 1362-6.
- [106] Mertz L. What Is Biocompatibility?: A New Definition Based on the Latest Technology. *IEEE Pulse* 2013; 4: 14-5.
- [107] Use of International Standard ISO 10993-1, 'Biological evaluation of medical devices - Part 1: Evaluation and testing within a risk management process'. U.S. Department of Health and Human Services Food and Drug Administration Center for Devices and Radiological Health, Jun 2016.
- [108] Hutmacher DW. Scaffolds in tissue engineering bone and cartilage. *Biomaterials* 2000; 21: 2529-43.
- [109] Badylak SF, Tullius R, Kokini K, *et al.* The use of xenogeneic small intestinal submucosa as a biomaterial for Achille's tendon repair in a dog model. *J Biomed Mater Res* 1995; 29: 977-85.
- [110] Gilbert TW, Stewart-Akers AM, Simmons-Byrd A, *et al.* Degradation and remodeling of small intestinal submucosa in canine achilles tendon repair. *J Bone Jt Surg Am* 2007; 89: 621-30.
- [111] Kew SJ, Gwynne JH, Enea D, *et al.* Regeneration and repair of tendon and ligament tissue using collagen fibre biomaterials. *Acta Biomater* 2011; 7: 3237-47.
- [112] Glowacki J, Mizuno S. Collagen scaffolds for tissue engineering. *Biopolymers* 2008; 89: 338-44.
- [113] Barczyk M, Carracedo S, Gullberg D. Integrins, *Cell Tissue Res* 2010; 339: 269-80.
- [114] Jokinen J. Integrin-mediated cell adhesion to type I collagen fibrils. *J Biol Chem* 2004; 279: 31956-63.
- [115] Murphy SV, Skardal A, Atala A. Evaluation of hydrogels for bioprinting applications. *J Biomed Mater Res A* 2013; 101A: 272-84.
- [116] Walters BD, Stegemann JP. Strategies for directing the structure and function of three-dimensional collagen biomaterials across length scales. *Acta Biomater* 2014; 10: 1488-501.
- [117] Muller SA, Durselen L, Heisterbach P, *et al.* Effect of a simple collagen type I sponge for achilles tendon repair in a rat model. *Am J Sports Med* 2016; 44: 1998-2004.
- [118] Cavallaro JF, Kemp PD, Kraus KH. Collagen fabrics as biomaterials. *Biotechnol Bioeng* vol. 1994; 43: 781-91.
- [119] Truhlsen SM, Fitzpatrick J. The extruded collagen suture: tissue reaction and absorption. *Arch Ophthalmol* 1965; 74: 371-4.
- [120] Enea D, Henson F, Kew S, *et al.* Extruded collagen fibres for tissue engineering applications: effect of crosslinking method on mechanical and biological properties. *J Mater Sci Mater Med* 2011; 22: 1569-78.
- [121] Zeugolis DI, Paul RG, Attenburrow G. Factors influencing the properties of reconstituted collagen fibers prior to self-assembly: Animal species and collagen extraction method. *J Biomed Mater Res A* 2008; 86A: 892-904.
- [122] Pins GD, Christiansen DL, Patel R, *et al.* Self-assembly of collagen fibers. Influence of fibrillar alignment and decorin on mechanical properties. *Biophys J* 1997; 73: 2164-72.
- [123] Wang MC, Pins GD, Silver FH. Collagen fibres with improved strength for the repair of soft tissue injuries. *Biomaterials* 1994; 15: 507-12.
- [124] Lai ES, Anderson CM, Fuller GG. Designing a tubular matrix of oriented collagen fibrils for tissue engineering. *Acta Biomater* 2011; 7: 2448-56.
- [125] Dunn MG, Avasarala PN, Zawadzky JP. Optimization of extruded collagen fibres for ACL reconstruction. *J Biomed Mater Res* 1993; 27: 1545-52.
- [126] Kato YP, Christiansen DL, Hahn RA, *et al.* Mechanical properties of collagen fibres: a comparison of reconstituted and rat tail tendon fibres. *Biomaterials* 1989; 10: 38-42.
- [127] Cornwell K. Collagen and Fibrin Biopolymer Microthreads for Bioengineered Ligament Generation: a Dissertation. GSBS Diss. Theses, May 2007.
- [128] Huang Z-M, Zhang YZ, Kotaki, M, *et al.* A review on polymer nanofibers by electrospinning and their applications in nanocomposites. *Compos Sci Technol* 2003; 63: 2223-53.
- [129] Teo WE, Ramakrishna S. A review on electrospinning design and nanofibre assemblies. *Nanotechnology* 2006; 17: R89-R106.

- [130] Dong B, Arnoult O, Smith ME, *et al.* Electrospinning of Collagen Nanofiber Scaffolds from Benign Solvents. *Macromol Rapid Commun* 2009; 30: 539-42.
- [131] Choktaweasap N, Arayanarakul K, Aht-Ong D, *et al.* Electrospun gelatin fibers: effect of solvent system on morphology and fiber diameters. *Polym J* 2007; 39: 622-31.
- [132] Wan YQ, He JH, Yu JY, *et al.* Electrospinning of high-molecule PEO solution. *J Appl Polym Sci* 2007; 103: 3840-3.
- [133] Bürck J, Heissler, Geckler U, *et al.* Resemblance of electrospun collagen nanofibers to their native structure. *Langmuir* 2013; 29: 1562-72.
- [134] Matthews JA, Wnek GE, Simpson DG, *et al.* Electrospinning of collagen nanofibers. *Biomacromolecules* 2002; 3: 232-8.
- [135] Matthews JA, Boland ED, Wnek GE, *et al.* Electrospinning of collagen type II: a feasibility study. *J Bioact Compat Polym* 2003; 18: 125-34.
- [136] Rho KS, Jeong L, Lee G, *et al.* Electrospinning of collagen nanofibers: Effects on the behavior of normal human keratinocytes and early-stage wound healing. *Biomaterials*, 2006; 27: 1452-61.
- [137] Zhong SP, Teo WE, Zhu X, *et al.* Development of a novel collagen-GAG nanofibrous scaffold via electrospinning. *Mater Sci Eng C* 2007; 27: 262-6.
- [138] Zeugolis DI, Khew ST, Yew ESY, *et al.* Electro-spinning of pure collagen nano-fibres - Just an expensive way to make gelatin? *Biomaterials* 2008; 29: 2293-305.
- [139] Szentivanyi A, Assmann U, Schuster R, *et al.* Production of biohybrid protein/PEO scaffolds by electrospinning. *Mater Werkst* 2009; 40: 65-72.
- [140] Buttafoco L, Kolkman NG, Engbers-Buijtenhuijs P, *et al.* Electrospinning of collagen and elastin for tissue engineering applications. *Biomaterials* 2006; 27: 724-34.
- [141] Elamparithi A, Punnoose AM, Kuruvilla S. Electrospun type I collagen matrices preserving native ultrastructure using benign binary solvent for cardiac tissue engineering. *Artif Cells Nanomedicine Biotechnol* 2016; 44: 1318-25.
- [142] Xu Y, Wu J, Wang H, *et al.* Fabrication of electrospun poly(L-Lactide-co-ε-Caprolactone)/collagen nanoyarn network as a novel, three-dimensional, macroporous, aligned scaffold for tendon tissue engineering. *Tissue Eng Part C Methods* 2013; 19: pp. 925-36.
- [143] Deville S. Ice-templating, freeze casting: Beyond materials processing. *J Mater Res* 2013; 28: 2202-19.
- [144] Haugh MG, Murphy CM, O'Brien FJ. Novel freeze-drying methods to produce a range of collagen-glycosaminoglycan scaffolds with tailored mean pore sizes. *Tissue Eng Part C Methods* 2009; 16: 887-94.
- [145] Pawelec KM, Husmann A, Best SM, *et al.* A design protocol for tailoring ice-templated scaffold structure. *J R Soc Interface* 2014; 11: 1.
- [146] Pawelec KM, Husmann A, Best SM, *et al.* Understanding anisotropy and architecture in ice-templated biopolymer scaffolds. *Mater Sci Eng C* 2014; 37: 141-7.
- [147] Pawelec KM, Husmann A, Wardale RJ, *et al.* Ionic solutes impact collagen scaffold bioactivity. *J Mater Sci Mater Med* 2015; 26: 91.
- [148] Pawelec KM, Husmann A, Best SM, *et al.* Altering crystal growth and annealing in ice-templated scaffolds. *J Mater Sci* 2015; 50: 7537-43.
- [149] Pawelec KM, Wardale RJ, Best SM, *et al.* The effects of scaffold architecture and fibrin gel addition on tendon cell phenotype. *J Mater Sci Mater Med* 2015; 5349.
- [150] Davidenko N, Bax DV, Schuster CF *et al.* Optimisation of UV irradiation as a binding site conserving method for crosslinking collagen-based scaffolds. *J Mater Sci Mater Med* 2016; 27: 14.
- [151] Lowe CJ, Reucroft IM, Grota MC, *et al.* Production of highly aligned collagen scaffolds by freeze-drying of self-assembled, fibrillar collagen gels. *ACS Biomater Sci Eng* 2016; 2: 643-51.
- [152] Caliarì SR, Harley BAC. The effect of anisotropic collagen-GAG scaffolds and growth factor supplementation on tendon cell recruitment, alignment, and metabolic activity. *Biomaterials* 2011; 32: 5330-40.
- [153] Caliarì SR, Harley BAC. Composite Growth Factor Supplementation Strategies to Enhance Tenocyte Bioactivity in Aligned Collagen-GAG Scaffolds. *Tissue Eng Part A* 2013; 19: 1100-12.
- [154] Caliarì SR, Ramirez MA, Harley BAC. The development of collagen-GAG scaffold-membrane composites for tendon tissue engineering. *Biomaterials* 2011; 32: 8990-8.
- [155] Caliarì SR, Weisgerber DW, Grier WK, *et al.* Collagen scaffolds incorporating coincident gradations of instructive structural and biochemical cues for osteotendinous junction engineering. *Adv Healthc Mater* 2015; 4: 831-7.
- [156] Mozdzen LC, Rodgers R, Banks JM, *et al.* Increasing the strength and bioactivity of collagen scaffolds using customizable arrays of 3D-printed polymer fibers. *Acta Biomater* 2016; 33: 25-33.
- [157] McCullough EJ, Yadavalli VK. Surface modification of fused deposition modeling ABS to enable rapid prototyping of biomedical microdevices. *J Mater Process Technol* 2013; 213: 947-54.
- [158] Murphy SV, Atala A. 3D bioprinting of tissues and organs. *Nat Biotechnol* 2014; 32: 773-85.
- [159] Derby B. Printing and Prototyping of Tissues and Scaffolds. *Science* 2012; 338: 921-6.
- [160] Do AV, Khorsand B, Geary SM, *et al.* 3D printing of scaffolds for tissue regeneration applications. *Adv Healthc Mater* 2015; 4: 1742-62.
- [161] Inzana JA, Olvera D, Fuller SM, *et al.* 3D printing of composite calcium phosphate and collagen scaffolds for bone regeneration. *Biomaterials* 2014; 35: 4026-34.
- [162] Duarte Campos DF, Blaeser A, Buellesbach K, *et al.* Bioprinting organotypic hydrogels with improved mesenchymal stem cell remodeling and mineralization properties for bone tissue engineering. *Adv Healthc Mater* 2016; 5: 1336-45.
- [163] Lin K-F, He S, Song Y, *et al.* Low-temperature additive manufacturing of biomimic three-dimensional hydroxyapatite/collagen scaffolds for bone regeneration. *ACS Appl Mater Interfaces*, 2016; 8: 6905-16.
- [164] Park JY, Choi JC, Shim J-H, *et al.* A comparative study on collagen type I and hyaluronic acid dependent cell behavior for osteochondral tissue bioprinting. *Biofabrication* 2014; 6: 035004.
- [165] Legemate K, Tarafder S, Jun Y, *et al.* Engineering Human TMJ Discs with Protein-Releasing 3D-Printed Scaffolds. *J Dent Res* 2016; 95: 800-7.
- [166] Lee HJ, Kim YB, Ahn SH, *et al.* A New Approach for Fabricating Collagen/ECM-Based Bioinks Using Preosteoblasts and Human Adipose Stem Cells. *Adv Healthc Mater* 2015; 4: 1359-68.
- [167] Wu Z, Su X, Xu Y, *et al.* Bioprinting three-dimensional cell-laden tissue constructs with controllable degradation. *Sci Rep* 2016; 6: 24474.
- [168] Xu T, Binder KW, Albanna M, *et al.* Hybrid printing of mechanically and biologically improved constructs for cartilage tissue engineering applications. *Biofabrication* 2013; 5: 015001.
- [169] Sun K, Li R, Jiang W, *et al.* Comparison of three-dimensional printing and vacuum freeze-dried techniques for fabricating composite scaffolds. *Biochem Biophys Res Commun* 2016; 477: 1085-91.
- [170] Lode A, Meyer M, Brüggemeier S, *et al.* Additive manufacturing of collagen scaffolds by three-dimensional plotting of highly viscous dispersions. *Biofabrication* 2016; 8: 015015.
- [171] Liu CZ, Xia ZD, Han ZW, *et al.* Novel 3D collagen scaffolds fabricated by indirect printing technique for tissue engineering. *J Biomed Mater Res B Appl Biomater* 2008; 85: 519-28.
- [172] Ahn S, Lee S, Cho Y, *et al.* Fabrication of three-dimensional collagen scaffold using an inverse mould-leaching process. *Bioprocess Biosyst Eng* 2011; 34: 903-11.
- [173] Yeo M, Lee J-S, Chun W, *et al.* An innovative collagen-based cell-printing method for obtaining human adipose stem cell-laden structures consisting of core-sheath structures for tissue engineering. *Biomacromolecules* 2016; 17: 1365-75.
- [174] Moon S, Hasan SK, Song YS, *et al.* Layer by layer three-dimensional tissue epitaxy by cell-laden hydrogel droplets. *Tissue Eng Part C Methods* 2009; 16: 157-66.
- [175] Kang H-W, Lee SJ, Ko IK, *et al.* A 3D bioprinting system to produce human-scale tissue constructs with structural integrity. *Nat Biotechnol* 2016; 34: 312-9.
- [176] Merceron TK, Burt M, Seol Y-J, *et al.* A 3D bioprinted complex structure for engineering the muscle-tendon unit. *Biofabrication* 2015; 7: 035003.
- [177] Baker HR, Merschrod S EF, Poduska KM. Electrochemically Controlled Growth and Positioning of Suspended Collagen Membranes. *Langmuir* 2008; 24: 2970-2.
- [178] Cheng X, Gurkan UA, Dehen CJ, *et al.* An electrochemical fabrication process for the assembly of anisotropically oriented collagen bundles. *Biomaterials* 2008; 29: 3278-88.

- [179] Younesi M, Islam A, Kishore V, et al. Fabrication of compositionally and topographically complex robust tissue forms by 3D-electrochemical compaction of collagen. *Biofabrication* 2015; 7: 035001.
- [180] Abu-Rub MT, Billiar KL, van Es MH, et al. Nano-textured self-assembled aligned collagen hydrogels promote directional neurite guidance and overcome inhibition by myelin associated glycoprotein. *Soft Matter* 2011; 7: 2770-81.
- [181] Uquillas JA, Kishore V, Akkus O. Effects of phosphate-buffered saline concentration and incubation time on the mechanical and structural properties of electrochemically aligned collagen threads. *Biomed Mater* 2011; 6: 035008.
- [182] Kishore V, Bullock W, Sun X, et al. Tenogenic differentiation of human MSCs induced by the topography of electrochemically aligned collagen threads. *Biomaterials* 2012; 33: 2137-44.
- [183] Kishore V, Uquillas JA, Dubikovsky A, et al. In vivo response to electrochemically aligned collagen bioscaffolds. *J Biomed Mater Res B* 2012; 100B: 400-8.
- [184] Uquillas JA, Kishore V, Akkus O. Genipin crosslinking elevates the strength of electrochemically aligned collagen to the level of tendons. *J Mech Behav Biomed Mater* 2012; 15: 176-89.
- [185] Younesi M, Islam A, Kishore V, et al. Tenogenic Induction of Human MSCs by Anisotropically Aligned Collagen Biotextiles. *Adv Funct Mater* 2014; 24: 5762-70.
- [186] Islam A, Chapin K, Younesi M, et al. Computer aided biomufacturing of mechanically robust pure collagen meshes with controlled macroporosity. *Biofabrication* 2015; 7: 035005.
- [187] Bell E, Ivarsson B, Merrill C. Production of a tissue-like structure by contraction of collagen lattices by human fibroblasts of different proliferative potential in vitro. *Proc Natl Acad Sci* 1979; 76: 1274-8.
- [188] Stopak D, Harris AK. Connective tissue morphogenesis by fibroblast traction: I. Tissue culture observations. *Dev Biol* 1982; 90: 383-98.
- [189] Barocas VH, Tranquillo RT. An anisotropic biphasic theory of tissue-equivalent mechanics: the interplay among cell traction, fibrillar network deformation, fibril alignment, and cell contact guidance. *J Biomech Eng* 1997; 119: 137-45.
- [190] Huang D, Chang TR, Aggarwal A, et al. Mechanisms and dynamics of mechanical strengthening in ligament-equivalent fibroblast-populated collagen matrices. *Ann Biomed Eng* 1993; 21: 289-305.
- [191] Young RG, Butler DL, Weber W, et al. Use of mesenchymal stem cells in a collagen matrix for Achilles tendon repair. *J Orthop Res* 1998; 16: 406-13.
- [192] Awad HA, Boivin GP, Dressler MR, et al. Repair of patellar tendon injuries using a cell-collagen composite. *J Orthop Res* 2003; 21: 420-31.
- [193] Butler DL, Juncosa-Melvin N, Boivin GP, et al. Functional tissue engineering for tendon repair: A multidisciplinary strategy using mesenchymal stem cells, bioscaffolds, and mechanical stimulation. *J Orthop Res* 2008; 26: 1-9.
- [194] Juncosa-Melvin N, Boivin GP, Galloway MT, et al. Effects of cell-to-collagen ratio in mesenchymal stem cell-seeded implants on tendon repair biomechanics and histology. *Tissue Eng* 2005; 1: 448-57.
- [195] Calve S, Dennis RG, Kosnik PE, et al. Engineering of functional tendon. *Tissue Eng* 2004; 10: 755-61.
- [196] Swadison S, Mayne R. Formation of highly organized skeletal muscle fibers in vitro. Comparison with muscle development in vivo. *J Cell Sci* 1992; 102: 643-52.
- [197] Larkin LM, Calve S, Kostrominova TY, et al. Structure and Functional Evaluation of Tendon-Skeletal Muscle Constructs Engineered *in Vitro*. *Tissue Eng* 2006; 12: 3149-58.
- [198] Kapacee Z, Richardson SH, Lu Y, et al. Tension is required for fibroblast formation. *Matrix Biol* 2008; 27: 371-5.
- [199] Guerin M-J, Charvet B, et al., Nourissat G, et al. Transcription factor EGR1 directs tendon differentiation and promotes tendon repair. *J Clin Invest* 2013; 123: 3564-76.
- [200] Neal D, Sakar MS, Ong L-LS, et al. Formation of elongated fascicle-inspired 3D tissues consisting of high-density, aligned cells using sacrificial outer molding. *Lab Chip* 2014; 14: 1907.
- [201] Yeung C-YC, Zeef LAH, Lallyett C, et al. Chick tendon fibroblast transcriptome and shape depend on whether the cell has made its own collagen matrix. *Sci Rep* 2015; 5: 13555.
- [202] Breidenbach AP, Dymant NA, Lu Y, et al. Fibrin gels exhibit improved biological, structural, and mechanical properties compared with collagen gels in cell-based tendon tissue-engineered constructs. *Tissue Eng Part A* 2015; 21: 438-50.
- [203] Torbet J, Ronziere M-C. Magnetic alignment of collagen during self-assembly. *Biochem J* 1984; 219: 1057-9.
- [204] Guido S, Tranquillo RT. A methodology for the systematic and quantitative study of cell contact guidance in oriented collagen gels. Correlation of fibroblast orientation and gel birefringence. *J Cell Sci* 1993; 105: 317-31.
- [205] Chen S, Hirota N, Okuda M, et al. Microstructures and rheological properties of tilapia fish-scale collagen hydrogels with aligned fibrils fabricated under magnetic fields. *Acta Biomater* 2011. 7: 644-52.
- [206] Guo C, Kaufman LJ. Flow and magnetic field induced collagen alignment. *Biomaterials* 2007; 28: 1105-14.
- [207] Lee P, Lin R, Moon J, et al. Microfluidic alignment of collagen fibers for in vitro cell culture. *Biomed Microdevices* 2006; 8: 35-41.
- [208] Saeidi N, Sander EA, Ruberti JW. Dynamic shear-influenced collagen self-assembly. *Biomaterials* 2009; 30: 6581-92.
- [209] Lanfer B, Freudenberg U, Zimmermann R, et al. Aligned fibrillar collagen matrices obtained by shear flow deposition. *Biomaterials* 2008; 29: 3888-95.
- [210] Haynl C, Hofmann E, Pawar K, et al. Microfluidics-produced collagen fibers show extraordinary mechanical properties. *Nano Lett* 2016; 16: 5917-22.
- [211] Yunoki S, Hatayama H, Ebisawa M, et al. A novel fabrication method to create a thick collagen bundle composed of uniaxially aligned fibrils: An essential technology for the development of artificial tendon/ligament matrices. *J Biomed Mater Res A* 2015; 103: 3054-65.
- [212] Paten JA, Siadat SM, Susilo ME, et al. Flow-Induced Crystallization of Collagen: A Potentially Critical Mechanism in Early Tissue Formation. *ACS Nano* 2016; 10: 5027-40.
- [213] Brown RA, Wiseman M, Chuo C-B, et al. Ultrarapid engineering of biomimetic materials and tissues: fabrication of nano- and microstructures by plastic compression. *Adv Funct Mater* 2005; 15: 1762-70.
- [214] Ghezzi CE, Muja N, Marelli B, et al. Real time responses of fibroblasts to plastically compressed fibrillar collagen hydrogels. *Biomaterials* 2011; 32: 4761-72.
- [215] Mudera V, Morgan M, Cheema U, et al. Ultra-rapid engineered collagen constructs tested in an in vivo nursery site. *J Tissue Eng Regen Med* 2007; 1: 192-8.
- [216] Marelli B, Ghezzi CE, James-Bhasin M, et al. Fabrication of injectable, cellular, anisotropic collagen tissue equivalents with modular fibrillar densities. *Biomaterials* 2015; 37: 183-93.
- [217] Killian ML, Cavinatto L, Galatz LM, et al. The role of mechanobiology in tendon healing. *J Shoulder Elbow Surg* 2012; 21: 228-37.
- [218] Pins GD, Huang EK, Christiansen DL, et al. Effect of static axial strain on the tensile properties and failure mechanisms of self-assembled collagen fibers. *J Appl Polym Sci* 1997; 63: 1429-40.
- [219] Chaubroux C, Perrin-Schmitt F, Senger B, et al. Cell alignment driven by mechanically induced collagen fiber alignment in collagen/alginate coatings. *Tissue Eng Part C Methods* 2015; 21: 881-8.
- [220] Cheema U, Chuo C-B, Sarathchandra P, et al. Engineering functional collagen scaffolds: Cyclical loading increases material strength and fibril aggregation. *Adv Funct Mater* 2007; 17: 2426-31.
- [221] Zeichen J, van Griensven M, Bosch U. The proliferative response of isolated human tendon fibroblasts to cyclic biaxial mechanical strain. *Am J Sports Med* 2000; 28: 888-92.
- [222] Riboh J, Chong AKS, Pham H, et al. Optimization of flexor tendon tissue engineering with a cyclic strain bioreactor. *J Hand Surg* 2008; 33: 1388-96.
- [223] Zhang L, Kahn CJF, Chen H-Q, et al. Effect of uniaxial stretching on rat bone mesenchymal stem cell: Orientation and expressions of collagen types I and III and tenascin-C. *Cell Biol Int* 2008; 32: 344-52.
- [224] Garvin J, Qi J, Maloney M, et al. Novel system for engineering bioartificial tendons and application of mechanical load. *Tissue Eng* 2003; 9: 967-79.
- [225] Kuo CK, Tuan RS. Mechanoactive Tenogenic Differentiation of Human Mesenchymal Stem Cells. *Tissue Eng Part A* 2008; 14: 1615-27.

- [226] Scott A, Danielson P, Abraham T, *et al.* Mechanical force modulates scleraxis expression in bioartificial tendons. *J Musculoskelet Neuronal Interact* 2011; 11: 124-32.
- [227] Juncosa-Melvin N, Shearn JT, Boivin GP *et al.* Effects of mechanical stimulation on the biomechanics and histology of stem cell-collagen sponge constructs for rabbit patellar tendon repair. *Tissue Eng* 2006; 12: 2291-300.
- [228] Juncosa-Melvin N, Matlin KS, Holdcraft RW, *et al.* Mechanical Stimulation Increases Collagen Type I and Collagen Type III Gene Expression of Stem Cell-Collagen Sponge Constructs for Patellar Tendon Repair. *Tissue Eng* 2007; 13: 1219-26.
- [229] Nirmalanandhan VS, Shearn JT, Juncosa-Melvin N *et al.* Improving linear stiffness of the cell-seeded collagen sponge constructs by varying the components of the mechanical stimulus. *Tissue Eng. Part A* 2008; 14: 1883-91.
- [230] Shearn JT, Juncosa-Melvin N, Boivin GP *et al.* Mechanical stimulation of tendon tissue engineered constructs: effects on construct stiffness, repair biomechanics, and their correlation. *J Biomech Eng* 2007; 129: 848-54.

List of Figures

1.1	Scheme of the tendon location	6
1.2	Scheme of the hierarchical organization of the tendon	7
1.3	Scheme of a equine superficial flexor tendon	8
1.4	Scheme of collagen fibers and fibrils organization	8
1.5	Schemes illustrating the major structural characteristics of extracellular matrix of tendon	9
1.6	Scheme conciliating helix crimp and linear organization	10
1.7	Scheme of collagen fibers and fibrils organization	11
1.8	Location, annual incidence and main cause of most frequent tendon injuries.	14
1.9	Scheme of the three sutures techniques currently used	16
1.10	Images of different metallic implants for tendon repair	17
1.11	Scheme of Achilles tendon rupture repair by using autologous tendon	19
1.12	Images of commercially available A: OrthADAPT™ xenograft and B: Graf-jacket® allograft.	20
1.13	Image of commercially available synthetic graft: Artelon®.	22
1.14	Pictures of different metallic implants for tendon repair	23
1.15	Schematic of the techniques used to produce scaffolds for tendon repair	25
1.16	PGA/PLA scaffold example	26
1.17	Braided chitosan scaffolds	28
1.18	3D plotted collagen scaffold (33 layers) in dry state	31
2.1	Experimental set-up of extrusion scheme	47
2.2	Example of a complex fluid extrusion	48
2.3	Example of a 23G needle tip	49
2.4	Protocol of stainless steel blunt needles preparation	50
2.5	Protocol of glass needles fabrication	51
2.6	Images of fire-polished glass capillary	51
2.7	Piston stick-slip behaviors	52
2.8	Pistons	53
2.9	Scheme of the { syringe + capillary } system and the characteristic variables	53
2.10	Force signals and their respective piston velocities obtained for alginate solution extrusion	55
2.11	Image of extrusion with a glass capillary where air bubbles are entrapped in the solution	56
2.12	Scheme of a cylinder pipe of length L and radius R.	57
2.13	Wall shear stress as a function of shear rate for glass capillaries of different radii	58
2.14	Velocity profiles for the flow of a fluid obeying a power law.	59

2.15 Velocity profile for a single shear flow of a newtonian liquid between two parallel plates.	60
2.16 Scheme of shear flow tensor definition in 3 dimensions	61
2.17 Maxwell liquid model scheme	63
2.18 Maxwell fluid behavior for an oscillatory shear	64
2.19 Rheometer geometries: left: Double gap Couette cell, middle: Parallel plates and right: Cone and plate	67
2.20 Two configurations of mechanical testing	70
2.21 Table of collagen families	71
2.22 Collagen biosynthesis scheme	72
2.23 Collagen type I triple helix scheme.	73
2.24 Collagen nat charge plot as a function of the pH	74
2.25 Rat tail tendons anatomy and extraction	76
2.26 Electrophoresis gel	77
2.27 Centrifugal concentrator scheme	78
2.28 Sodium alginate chemical structures	79
2.29 Alginate persistence length as a function of Ionic Strength and pH	80
2.30 Schematic representation of the "egg-box" structure	81
2.31 Schematic illustration of the multiple-step binding of Ca^{2+} to alginate	82
2.32 Proteins and polysaccharides mixtures schematic representation	83
2.33 Solutions aspects before being extruded	84
3.1 Collagen Shear storage and loss moduli as a function of the angular frequency	89
3.2 Prefactors G'_0 , G''_0 and power-law exponent β as a function of the collagen concentration	89
3.3 Comparison of the complex (or dynamic) viscosity η^* for a collagen solution at 30 mg/mL	90
3.4 Characteristic disentanglement time τ_c as a function of the collagen concentration	91
3.5 Shear rate dependent Weissenberg numbers for collagen solution at 30 mg/mL.	92
3.6 Viscosity of collagen at different concentrations as a function of the shear rate.	94
3.7 Specific viscosity of alginate solutions as a function of concentration (wt %)	95
3.8 Shear-thinning behavior of the alginate solutions.	96
3.9 Alginate shear storage G' (empty circle) and loss G'' (filled circle) moduli against angular frequencies	97
3.10 Alginate first normal stress difference measured in steady state shear (empty circles) and computed from Laun empirical relationship	98
3.11 Alginate shear storage G' (empty circle) and loss G'' (filled circle) moduli against angular frequencies	98
4.1 Examples of polymer melt extrudates	103
4.2 Morphologies observed during the extrusion of alginate while changing the polymer concentration, and die material without binding ions	106
4.3 Morphologies observed during the extrusion of alginate while changing the polymer concentration, and die material without binding ions for higher velocities	107
4.4 Path of train of bubbles during the extrusion	108
4.5 Interlocking of two capillaries of radii 250 and 150 μm	108
4.6 Example of protocols used to produce wavy scaffolds.	122

4.7	Collagen at 30 mg/mL extrusion in A) PBS 1X and B) PBS 5X observed in real time and post extrusion	123
4.8	Morphologies observed during the extrusion of sodium alginate solution at 4 % in $CaCl_2$ 0.5M	125
4.9	Ratio diameters D'/D plot as a function of the shear rate for the extrusion of ALG4 in $CaCl_2$ 0.5M with stainless steel needles	126
4.10	Steady and homogeneous alginate flow and the scheme representation of the syneresis process occurring	128
4.11	Die swelling image and the respective plot of swelling ratio for stainless steel needles	129
4.12	The Weissenberg or rod-climbing effect imaging	129
4.13	Scheme of die swelling mechanism	130
4.14	Extrusion of ALG4 in $CaCl_2$ 0.5M (left) and $CaCl_2$ 0.1M (right) with glass capillary $R=250\mu m$ at the same velocity.	131
4.15	Laser diffraction experiment on an alginate thread which exhibits periodic striations	132
4.16	Eye guidelines of the possible mechanism which leads to helical (left) and striated pattern (right)	132
4.17	Striations velocity evolution as a function of the shear rate for three capillaries of radii	133
4.18	Striations velocity evolution as a function of the shear rate for three capillaries of radii	134
4.19	Spatio-temporal image of ALG4 extrusion with stainless steel needle of radii $760\mu m$ in the oscillating regime.	134
4.20	Gel clogging steps	135
4.21	Spatio-temporal images of ALG4 extrusion	136
4.22	A) Force and velocity signal of the extrusion of ALG4 in $CaCl_2$ 0.5M with a glass capillary of $500\mu m$	136
5.1	Scheme of a linearly polarized sinusoidal electromagnetic wave travelling in the positive x-direction.	144
5.2	Index ellipsoid for a positive uniaxial medium	145
5.3	Excitation of molecules with a radiation of frequency ω	147
5.4	Schemes of the origin of the collagen signal	148
5.5	Scheme of SHG microscope set-up and the main orientation parameters definition	149
5.6	The two angles φ and ψ describe the orientation of the collagen molecules in the excitation volume	150
5.7	Schemes of optical and electron microscopes	152
5.8	Electron-matter interaction volume scheme.	153
5.9	Batches analysis: Collagen threads observed post-extrusion	156
5.10	Viscosity as a function of shear rate for seven collagen batches at 5mg/mL.	157
5.11	Collagen threads observed by different techniques at different concentrations.	181
5.12	Evolution of collagen threads diameter over the time	182
5.13	SEM images of threads surface at different concentrations	183
5.14	Ultrastructure of threads after 2 weeks of maturation in PBS 5X as seen by TEM (transverse sections) at different concentrations	184
5.15	P-SHG imaging of collagen threads at a.15 mg/mL, b. 30 mg/mL and c. 60mg/ mL	185

5.16 SHG imaging and P-SHG areas (colored) of surfaces and middle at the center thread transverse section	186
5.17 SHG and P-SHG imaging of collagen thread at 30mg/mL (B) at day 1.	187
5.18 SHG images of collagen threads at 60 mg/mL after 2 weeks in PBS 5X.	187
5.19 Collagen:alginate threads at ratios: 1:1, 2:1, 5:1, observed by different techniques.	189
5.20 SEM imaging of pure ALG4 (control) and collagen:alginate (5:1) threads.	190
5.21 TEM longitudinal sections images of two characteristic areas of collagen:alginate (5:1) thread	191
5.22 TEM micrographs obtained from other studies to be compared with hybrid thread microstructure.	191
5.23 SHG image of collagen:alginate (5:1) thread section and the respective projections	192
5.24 Tensile testing until rupture for collagen threads at 30 and 60mg/mL and coll:alg (5:1) thread in wet conditions and at room temperature	193
5.26 SEM images of collagen:alginate (5:1) thread surface after 3 weeks in DMEM at 37°C.	195
5.27 Evolution of collagen based thread diameters upon maturation for the different buffers	195
5.28 TEM cross-sections images of collagen threads at 30 mg/mL (B) and 60 mg/mL (C) either matured in PBS5X or incubated in DMEM at 37°C during 2 weeks.	196
5.29 TEM sections along the thread axis (left //) and perpendicular (right ⊥) of collagen:alginate (5:1) threads incubated in DMEM at 37°C during 3 weeks.	197
5.30 SHG image of collagen:alginate (5:1) thread section incubated 3 weeks in DMEM at 37°C	198
5.31 DSC measurements: denaturation of collagen 30mg/mL, coll:alg (5:1) and ALG4 threads kept either in their extrusion solutions (PBS 5X or CaCl ₂ 1M respectively), or in DMEM during 2 weeks.	199
6.1 Cell C3H/10T1/2 morphology	207
6.2 Protocol of cell culture under tension	208
6.3 Scheme of collagen thread cell culture configuration under tension.	208
6.4 Confocal Fluorescence Microscope scheme	209
6.5 Fluorescence spectra of DAPI and Alexa Fluor 488	210
6.6 In situ hybridization main steps	211
6.7 Scheme of real time qPCR main steps	212
6.8 Schemes of melting curves for the calibration points (top) and its derivative curve (bottom) with the melting temperature T _m	215
6.9 In situ hybridization main steps	216
6.10 Tensile testing results of collagen threads at 30 mg/mL (blue) and 60 mg/mL (purple) seeded with cells and cultured over 3 weeks under static load and their respective controls.	217
6.11 SHG images coupled with fluorescence of collagen threads seeded with C3H10 T1/2 cells during 3 weeks at 30mg/mL and 60mg/mL, under static load.	219
6.12 SHG images coupled with fluorescence of cell sheath surfaces on collagen threads	220
6.13 In situ hybridization on collagen threads at 30 and 60 mg/mL seeded with C3H10 T1/2 cells during 3 weeks	221

6.14 Morphologies observed by phase contrast microscopy of collagen thread at 30 mg/mL (left) and collagen:alginate (5:1) thread (right) after being seeded with cells and cultured during 3 weeks	223
6.15 Confocal microscopy images of collagen thread at 30 mg/mL (left) and mixture coll:alg (5:1) (right) for different times: days 3, 7, 21 and without tension at 21 days.	225
6.16 SHG image coupled with fluorescence of coll:alg (5:1) thread at 2 weeks of culture with cells without static load.	226
6.17 In situ hybridization on collagen threads at 30 mg/mL (left) and coll:alg (5:1) thread (right) with C3H10 T1/2 cells at 3 weeks, under static load.	227

List of Tables

1.1	Mechanical properties of human tendons	12
2.1	Characteristic dimensions of stainless steel needles	49
2.2	Persistence length for different buffers found in the litterature.	75
3.1	Power law fit exponent values of viscosities for collagen at 30 mg/mL	91
3.2	Characteristic physical quantities of collagen solutions of interest	94
3.3	Characteristic physical quantities of chosen alginates solutions	96
3.4	Fit exponents α and β for the respective storage and loss moduli; the crossover angular frequency ω_c and the relaxation time λ	97
5.1	Characteristic physical quantities of collagen solutions of interest	193
5.2	Characteristic physical quantities of collagen solutions of interest after incubation in DMEM	200
6.1	Table of the primers	214